ATMOSPHERIC ULTRAVIOLET ABSORPTION SPECTROSCOPY

by

J.L. Lean, B.Sc.(Hons)
Australian National University

A thesis submitted for the degree of
Doctor of Philosophy
at the
University of Adelaide
Department of Physics

December 1980

C O N T E N T S

CONTENTS Continued..... Page

CONTENTS Continued..... Page

CONTENTS Continued..... Page

CONTENTS Continued..... Page

CONTENTS Continued..... Page

SUMMARY

Because the earth's atmosphere consists of atoms and molecules which absorb radiation of wavelength shorter than 300 nm, very little of the sun's ultraviolet radiation reaches the earth's surface. Monitoring the atmospheric transmission of incident ultraviolet flux with rocket borne optical instruments enables *in situ* measurements of the concentrations of these absorbing species. Experimental applications of this technique, called atmospheric ultraviolet absorption spectroscopy, are described in this thesis. Specifically, the densities of the four primary neutral constituents N_2, O_2, O and O_3 of the upper atmosphere are determined from their absorption at various wavelength intervals within the extreme, far and middle ultraviolet spectral regions.

Such composition analyses require knowledge of the solar ultraviolet spectrum, absorption cross-sections for the atmospheric gases and *a priori* estimates of their altitude distributions. These aspects are considered in the first chapter; so too is the deposition of solar ultraviolet energy in the atmosphere and some characteristic phenomena which it initiates. In the second chapter, principles of atmospheric absorption spectroscopy are discussed. Some examples of experimental investigations of the densities of the primary neutral atmospheric constituents are provided. The three remaining chapters pertain to the instrumental details, data analyses and results of three particular absorption spectroscopy experiments which are summarized below.

Solar extreme ultraviolet radiation was monitored by a scanning grazing incidence monochromator whose design and operation are described. This instrument was flown on an Aerobee rocket, launched from Woomera, S.A., just after sunrise. Extraterrestrial extreme ultraviolet radiation is

absorbed primarily in the thermosphere by N_2, O_2 and O since each of these species exhibits significant absorption at these wavelengths. Analysis of absorption at 9.6 nm, utilizing O_2 densities and the density ratios O/N_2 measured by other instrumentation on the Aerobee vehicle, facilitated deduction of N_2 and O densities.

On the same rocket, an Ebert-Fastie spectrometer was used to scan the far ultraviolet solar spectrum in the wavelength interval corresponding to the strong Schumann-Runge continuum of molecular oxygen's absorption spectrum. Oxygen's absorption in its Schumann-Runge continuum exhibits a temperature effect and new laboratory data were used to generate a semi-empirical model for the temperature dependence of the absorption cross-sections. This model was incorporated into the analysis of the monochromatic absorption profiles to provide estimates of O_2 densities in the lower thermosphere.

Thus the concentrations of N_2, O_2 and O in the early morning thermosphere were measured using dispersive spectroscopic instruments carried on a pointed rocket vehicle. Jacchia's (1977) thermospheric composition model, evaluated at the time of the Aerobee launch, is compared with the results of these experiments.

Ozone densities in the stratosphere and mesosphere were derived from ozone's Hartley band absorption of middle ultraviolet radiation, as measured by broad band photometers. Six rockets, each carrying one detector comprising two middle ultraviolet photometers, were launched at different times of the day. A seventh rocket with three identical detectors each having three middle ultraviolet photometers was launched at the time of a full moon and provided estimates of the nighttime ozone densities. Design, laboratory calibration and payload integration of these detectors are detailed, as are the retrieval and analysis of the raw data.

Results from these flights form a suitable basis for characterizing diurnal ozone variations and the number of flights provided greater statistical reliability for the experimental ozone profiles than is generally afforded from *in situ* measurements with a single rocket.

P R E F A C E

This thesis contains no material which has been accepted for the award of any other degree or diploma in any University. To the best of the author's knowledge and belief it contains no material previously published or written by another person, except where due reference is made in the text.

Judith Lean
December 1980

ACKNOWLEDGEMENTS

This thesis evolved under the excellent supervision of Alistair Blake, who provided invaluable guidance and whose interminable sanity and persistent sense of humour made many things easier.

The rocket experiments which are described reflect the research activities of the Space Group, directed with infectious enthusiasm by John Carver and, on his departure, by Brian Horton. In particular, the excellent efforts of Bob Hurn in designing the experiment electronics, his competence in all aspects associated with the successful launching of rocket vehicles and his unfailing co-operation are gratefully acknowledged.

Construction of the instruments in Chapters 3 and 5 was ably performed by Graham Eames and Keith Merry of the Physics Workshop while Peter Schebella and others were valuable sources of information on a variety of topics. Many members of the Physics Department were also helpful, especially John Wright and Pat Coe.

NASA's Goddard Space Flight Centre was responsible for launching the Aerobee rocket while the construction, testing and launching of the seven rockets which provided the data for Chapter 5 occurred at Wallops Flight Centre, Virginia. The successful execution of these latter experiments was largely due to the efficiency and enthusiasm of the Wallops personnel who also provided generous hospitality during the payload integration period. Additionally, the experience of working with the other experimenters who participated in this program was unique and rewarding.

ACKNOWLEDGEMENTS Continued....

Handling of the data generated by the rocket experiments proceeded more smoothly and skilfully through the efforts of the Computing Centre of the University of Adelaide. Peter Wadey, Bob Jones, George Joss and Tom Nemeth were approached many times for advice which they gave willingly and patiently.

Financial support during the production of this thesis was provided by a Commonwealth Postgraduate Research Scholarship and also, in 1980, by the World Meteorological Organization via the authorization of Dr Sundararaman of the FAA.

My parents, and Jennifer, Elizabeth and Cynthia were always available to share the difficult times and to offer much appreciated additional financial support; Jennifer, especially, provided great sustenance.

All of the people mentioned above, and many others, contributed to this thesis and for that I sincerely thank them.

INTRODUCTION

Absorption spectroscopy utilizing atmospheric attenuation of extraterrestrial ultraviolet radiation is intrinsically capable of providing a complete compositional analysis of the earth's neutral upper atmosphere.

Experimentally, the technique is most usually facilitated by monitoring the extinction of radiation from the sun, using rocket borne photodetectors sensitive to small wavelength increments of the ultraviolet spectrum. The absorption path is defined by the contents of a column from the detector to the sun, and the absolute concentration of the absorbing species in this column can be determined if the absorbing properties of the gases are known.

Application of absorption spectroscopy techniques to the atmosphere is therefore contiguous with an understanding of how the earth's atmosphere absorbs solar radiation. This is the basis of aeronomy, and crucial for an understanding of a wide range of physical processes in the atmosphere, the most important of which are the primary photochemical reactions, formation of the ionosphere, heating and dynamical processes and airglow emissions. An analysis of any absorption related phenomenon requires information about the solar spectrum, the physical structure of the atmosphere and the absorption cross-sections of the gases.

Solar photons of wavelengths between 300 nm and 10,000 nm represent 99% of the total solar emission and exhibit the spectral distribution of a black body radiating at 6000 K, this being the approximate temperature of the photosphere and lower chromosphere. The remaining 1% emission is at ultraviolet wavelengths. Down to 130 nm

the average spectrum follows the spectral distribution of a black body at less than 5000 K, with Fraunhofer absorption superimposed on the emission continuum. Below 122 nm the spectrum is dominated by strong monochromatic emissions, with the shortest wavelengths originating in the corona at temperatures as high as 10^6 K. While the integrated solar flux, being strongly weighted by 'quiet' photospheric emission, does not vary significantly with time, the UV fluxes, especially at the shortest wavelengths, vary markedly, reflecting large changes in density and temperature in the upper chromosphere and corona.

The atmosphere is opaque to ultraviolet photons of wavelengths shorter than 300 nm. Penetration is uniquely controlled for each wavelength by the particular absorbing properties of the atmosphere at that wavelength.

Extreme ultraviolet fluxes, between 5 and 110 nm, are absorbed by thermospheric O_2, N_2 and O which, above 120 km, are roughly distributed according to the requirements of diffusive equilibrium. Virtually all photons less than 102.7 nm are absorbed by photoionization, resulting in the formation of the E and F regions of the ionosphere. Energetic photoelectrons and ions produced by this mechanism are instrumental in heating the thermosphere, via complicated collision and excitation processes.

Hydrogen Lyman-alpha, at 121.6 nm , is singularly the most unique line of all the solar emissions, due to its extreme intensity at a wavelength for which the molecular oxygen absorption spectrum has a deep window. Thus it penetrates to about 70 km, into the mesosphere, where it is absorbed by O_2, H_2O and CO_2, and ionizes NO, producing the ionospheric D region.

Molecular oxygen in the lower thermosphere completely absorbs far ultraviolet radiation between 125 and 175 nm. Photodissociation

in the Schumann-Runge continuum is the dominant heat source below 170 km, and has wider implications for atmospheric photochemistry because of the production of oxygen atoms.

From 175 to 203 nm, the absorption of solar radiation is determined by mesospheric molecular oxygen. However, the highly structured and temperature dependent nature of the Schumann-Runge bands has so far precluded an exact quantitative analysis. Atmospheric absorption studies at these wavelengths require an understanding of complicated predissociation mechanisms in molecules, and are essential because this process controls the photochemistry by which ozone is formed.

The weak O_2 Herzberg continuum and the strong O_3 Hartley band both absorb solar radiation between 200 and 240 nm, but longer middle ultraviolet wavelengths are extinguished primarily by ozone. It is this strong absorption in the stratosphere and mesosphere that prevents any ultraviolet radiation reaching the ground, simultaneously augmenting a major energy input to the stratosphere and initiating an intrigue of photochemical reactions. The delicate balance of this network has implied the vulnerability of ozone to atmospheric pollutants which may easily be assimilated into chemical pathways that destroy it.

Those altitude regions of the atmosphere in which only one species is responsible for absorption at a particular wavelength interval are most appropriate for absorption spectroscopy experiments, especially if the wavelength variation of the absorption spectrum for that species is not too sharp.

Two examples of this condition are absorption by molecular oxygen, above 100 km, in the Schumann-Runge continuum of its absorption

spectrum; and Hartley band absorption by ozone, below 80 km. Extensive use has been made of atmospheric absorption, in both these wavelength regions, for composition studies, using detectors with bandwidths varying from a few tenths of nm to over ten nm.

Ultraviolet absorption spectroscopy at other altitudes and in different ultraviolet wavelength regions is more or less suitable, depending on the characteristics of the detector's spectral response relative to the absorption cross-sections of the constituent gases, and on the sophistication of the analysis. For example, high resolution detectors and complicated band analysis techniques have been employed to deduce mesospheric O_2 densities, via O_2 absorption in the Schumann-Runge bands.

A complete understanding of the atmosphere demands that absorption at each ultraviolet wavelength be accurately defined. As this is effected so will the practical applications of atmospheric ultraviolet absorption spectroscopy be extended. The quintessent parameters are the absorption cross-sections. Fundamental limitations are imposed on laboratory measurements with regard to spectral resolution and inability to simulate appropriate atmospheric conditions. Ignorance of the absorption cross-sections of atomic oxygen is a pertinent example.

Despite present practical limitations in some spectral regions, atmospheric ultraviolet absorption spectroscopy has proven itself a powerful tool for determining neutral densities. Since the first rocket experiments, over twenty years ago, the importance of regular and reliable measurements of the neutral composition has been reinforced by the increasing number of physicists who rely on this data as input for theories descriptive of a broad range of atmospheric behaviour.

Currently, the most popular quest is for definitive ozone density measurements, with a precision and frequency capable of

establishing and identifying quantitatively any long term trends, such as permanent pollution-related depletion. While measurements of the neutral thermospheric densities exhibit a more subtle significance, they are equally important as tracers of atmospheric variability with time, height and geographic location, as well as solar and geomagnetic activity.

Many theoretical models are employed in an attempt to define observed atmospheric phenomena. For example, there are semi-empirical composition models, energy transfer models, photochemical models and general 3-D transport models. Such models must be based on physical concepts, and their general inadequacy is largely reflective of the lack of experimental measurements to provide these concepts.

Atmospheric ultraviolet absorption spectroscopy is essential for atmospheric studies because of its usefulness in providing *in situ* composition measurements, and because of the nature of its theory, integral in explaining atmospheric absorption processes.

CHAPTER ONE

SOLAR ULTRAVIOLET RADIATION AND THE ATMOSPHERE

1.1 THE SOLAR ULTRAVIOLET SPECTRUM

The solar ultraviolet spectrum, with designated sub-regions, is illustrated in Figure 1.1.

For the purpose of aeronomy, it is necessary to make moderate spectral resolution measurements of the absolute ultraviolet flux from the whole solar disc and to determine the temporal variations of these fluxes for time scales ranging from hours and days to the 27-day period of solar rotation.

Experimental studies of the sun emphasize either high spatial and spectral resolution, reflecting the requirements of solar physicists, or wide spectral coverage of the full solar disc, as required by the aeronomist. The techniques are complementary since a final understanding of the variability of solar irradiances throughout a solar cycle will be achieved only through a detailed analysis of the behaviour of the solar plasma. And solar emission models require confirmation by regular monitoring of the complete solar disc.

A review of theoretical and semi-empirical models that are used to determine the structure of the photosphere, chromosphere and transition region between the chromosphere and corona has recently been given by Avrett (1977). Comprehensive experimental solar flux data for the entire ultraviolet spectrum have been compiled by Donnelly and Pope (1973) and Working Group IV of Cospar (Delaboudinière *et al*, 1977), while a broad perspective of current knowledge of the solar output and its variation has been provided by White (1977).

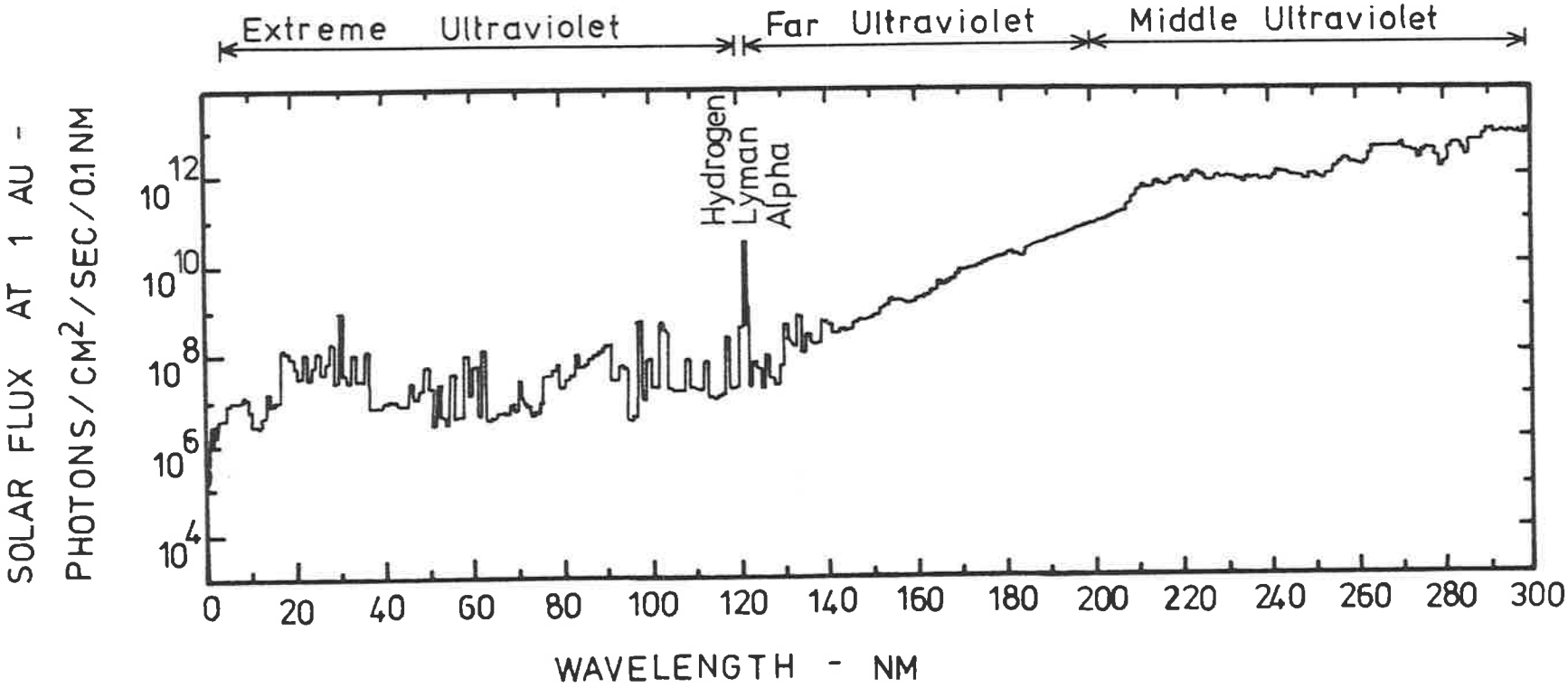

Figure 1.1 The solar ultraviolet flux in 1 nm wavelength intervals.

(Donnelly & Pope, 1973)

a. Extreme Ultraviolet Radiation : 5 - 120 nm

Since the photoionization limits for O_2, O and N_2 occur at wavelengths 102.8, 91.0 and 79.6 nm respectively, the solar extreme ultraviolet (EUV) radiation is the dominant energy source of the upper atmosphere, controlling heating, ionization, most of the airglow emissions and many other properties.

This spectral region is comprised of a multitude of emission lines produced by neutral atoms and ionized species in the solar chromosphere, transition region and corona layers of the outer solar atmosphere. Here, the temperature varies over a wide range, from 8×10^3 to 6×10^6 K, causing the shape of the spectrum to differ dramatically for radiation emitted from active regions, average quiet regions or coronal holes.

Between 30 and 120 nm the major constituents of the solar atmosphere, H and He, are responsible for a number of strong lines and recombination continua, with additional lines from intermediate constituents C, O and N. These emissions arise in the solar chromosphere and transition regions where the temperature is typically less than 10^6 K, and vary only moderately with solar activity. During a solar rotation there may be changes of the order of ± 15%, while over the 11-year solar cycle there is evidence for long term variability, although the magnitude of this is disputed (White, 1977).

Below 30 nm the spectrum is far more variable and characterized by coronal lines emitted primarily by ions of Ni, Fe, Si and Mg, at temperatures in excess of 10^6 K.

b. *Hydrogen Lyman-Alpha : 121.57 nm*

The solar hydrogen Lyman-alpha line is a broad self- reversed line of about 0.1 nm width, having peaks separated by about 0.05 nm. It is emitted from the chromosphere with a flux equivalent to all other solar flux at wavelengths less than 150 nm.

Studies of Lyman-alpha absolute intensity, its variability, line shape and distribution over the solar disc have been reviewed by Vidal-Madjar (1977). The average flux of Lyman-alpha photons, estimated with 30% accuracy, is $3 \times 10^{11} cm^{-2} s^{-1}$. Flux variation with solar rotation, observed between 1969 and 1970, appears well correlated with the $F_{10.7}$ cm radio flux and is no greater than 30% (Vidal-Madjar *et al*, 1973). Over the eleven year cycle this may vary, from maximum to minimum, by a factor of two. Absolute intensity measurements are complicated by hydrogen absorption of this solar line in the earth's geocorona.

c. *Far Ultraviolet Radiation : 130 - 200 nm*

It can be seen in Figure 1.1 that beyond 140 nm the far ultraviolet (FUV) solar spectrum involves a nearly linear exponential increase in flux intensity with wavelength.

Radiation of wavelength greater than 176 nm is emitted from the solar photosphere, the opaqueness of which causes the character of the solar spectrum to be essentially that of absorption. Below 168 nm the spectrum comes from the chromosphere and is composed primarily of emission lines. In the transition region the emergent solar continuum originates in progressively higher layers of the solar atmosphere, going to shorter wavelengths, and the changing equivalent brightness temperature of the solar continuum reflects the temperature across the photosphere-chromosphere transition. This can be determined by absolute intensity measurements of the continuum near 160 nm.

Variations associated with the 27-day solar rotational period decline exponentially with increasing wavelength, from about 25% at 120 nm to about 6% at 175 nm, which is comparable to the variation associated with the changing sun-earth distance. It is not yet understood whether or not the solar FUV fluxes change over the 11-year cycle, although a factor of two variability has been suggested near 170 nm (White, 1977).

d. Middle Ultraviolet Radiation : 200 - 300 nm

Solar continuum middle ultraviolet (MUV) radiation emanates from the photosphere. Between 207.5 and 210 nm the intensity rises rapidly, following which the spectrum exhibits superimposed absorption line structure which becomes less pronounced at longer wavelengths. The character of the solar MUV radiation arises from the ionization edges and associated continua of H, Mg, Si, Fe and C, and these elements are responsible for solar opacity at these wavelengths.

There appears to be little variation of the MUV flux with solar activity and only 1% change at 300 nm associated with the 27-day solar rotation period (White, 1977).

1.2 STRUCTURE OF THE NEUTRAL ATMOSPHERE

Very little of the sun's ultraviolet energy reaches the earth's surface. Instead, it contributes to a variety of complicated interactions involving energetics, photochemistry and dynamics, which act together to define the structure of the neutral upper atmosphere, and hence its own absorption.

a. Temperature Profile

Temperature is important as a variable for describing, together with pressure and density, the physical and chemical states of the

atmosphere and because identification of the primary atmospheric regions is based on its variation with altitude. An average temperature profile, recommended by the United States Standard Atmosphere, 1976 , is shown in Figure 1.2, together with the appropriate nomenclature for the atmospheric layers.

At the earth's surface the temperature is determined by a balance between the incoming solar radiation, which is characteristic of a black body at 6000 K, and the outgoing terrestrial radiation, which is represented by a grey body at 290 K. In the atmosphere, the structure of the temperature profile is controlled by absorption of radiation.

The troposphere exhibits a negative temperature gradient because re-emitted infrared radiation is absorbed by water vapour and carbon dioxide, both having densities which decrease with altitude.

In the stratosphere the temperature gradient becomes positive, with ozone absorption in the Hartley band providing the principal input of thermal energy.

Above 50 km, in the mesosphere, the decrease in O_3 production, coupled with cooling through the emission to space by CO_2 at 15 μm, re-establishes a negative temperature gradient which persists until about 85 km. By these altitudes, increasing atomic oxygen densities mean that solar heating through EUV absorption becomes important. Between 95 and 120 km the vertical temperature profile is complicated and variable, resulting as it does from the combined effect of solar heating and of turbulent and molecular heat transfer.

At altitudes 120 to 200 km heating is primarily from EUV absorption, reinforced by the lack of any effective means of emission. Consequently, there is a large positive temperature gradient in this

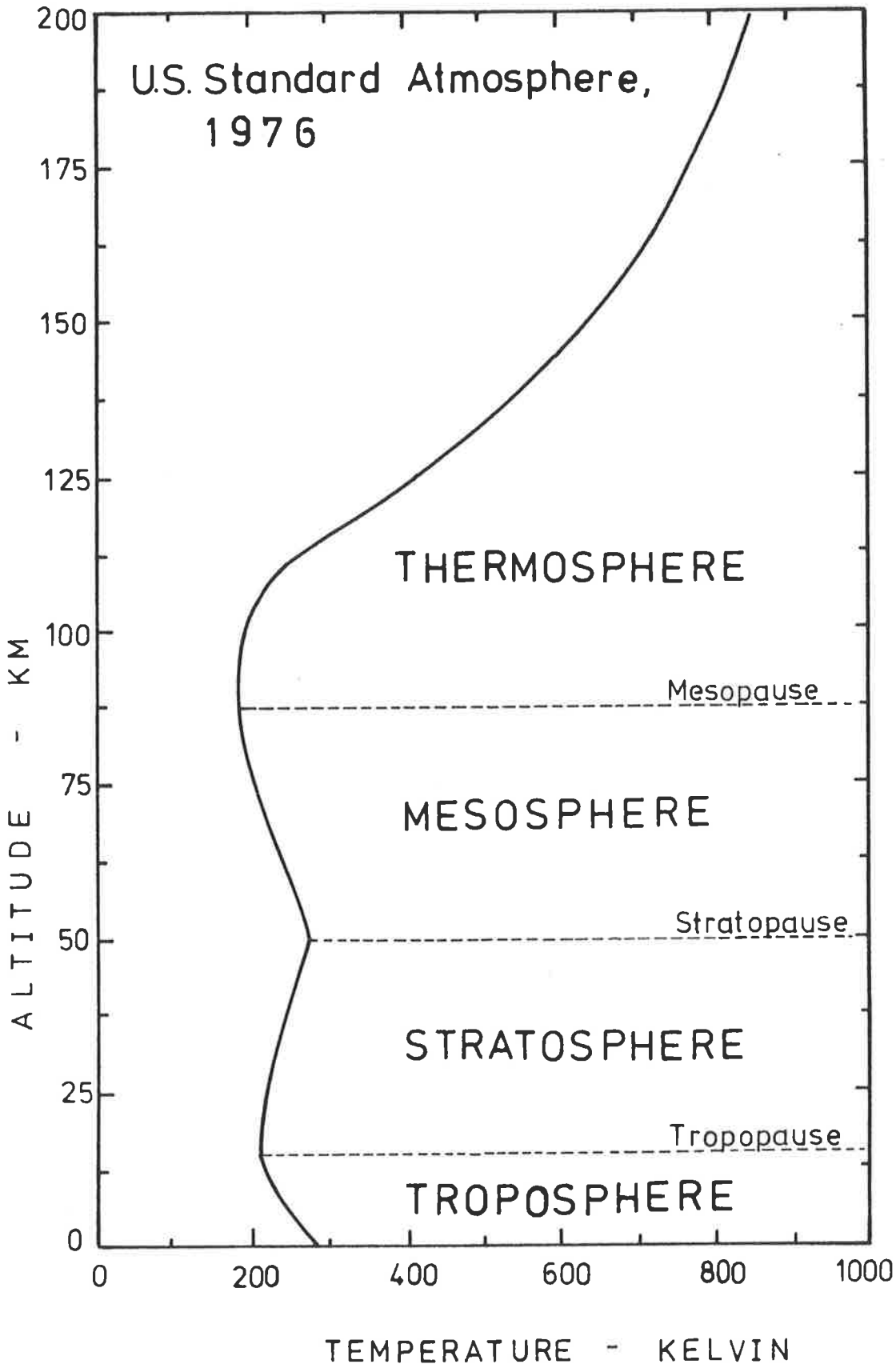

Figure 1.2 Atmospheric temperature and nomenclature.

region of the thermosphere. Above 200 km quasi-equilibrium thermal conditions are established, modified by the dependence of the thermospheric heat budget on variations of solar energy and on diurnal, seasonal, geographic and annual parameters.

Since the sun is the origin of all atmospheric heat, changes in solar flux, caused primarily by solar activity and the diurnal cycle, will cause the temperature profile of Figure 1.2 to vary, the effect becoming increasingly important at higher altitudes in the thermosphere.

Below about 90 km the average temperature is not significantly perturbed by solar activity variations. For example, the summer stratospheric temperature at 35 and 50 km, throughout solar cycle 20, was observed to change from near solar maximum to near solar minimum by only -3° to -6° (Quiroz, 1979).

At altitudes between 95 and 135 km the temperature is weakly altered by solar flux, but by 150 km the correlation is large and positive. Corresponding to a decay of the solar radio flux from 150 to $70 \times 10^{-22} Wm^{-2} Hz^{-1}$, between 1967 and 1975, Alcayde *et al* (1979) reported a temperature decrease of 40 K.

Temperature variations related to seasonal and semi-annual induced solar flux changes are also weak in the lowest regions of the thermosphere but the amplitude increases at higher altitudes. It has been noted that in winter the mesopause is higher (100 km) and broader than in summer (95 km) and that the vertical temperature gradient near 120 km in winter is twice the summer value (Alcayde *et al*, 1979).

It is above 300 km, where its increase with height has almost ceased, that the temperature varies most dramatically in response to changes in the EUV radiation, and is attuned to the daily rhythm, the

27-day sunspot cycle, the 11-year solar cycle, as well as to erratic solar activity. During the day this exospheric temperature T_{EXO} varies by 30%, from a minimum at 0400 hours local time to a maximum near 1600 hours. For solar minimum conditions the diurnal temperature ranges from 600 to 800 K, but for times of solar maximum its variation shifts to the range 900 to 1200 K (King-Hele, 1978).

The thermospheric temperature is observed to increase over the entire globe by as much as 500 K (King-Hele, 1978) in response to geomagnetic activity, which originates in fluctuations of solar wind particles interacting with the earth's magnetic field. At high latitudes the temperature variation is significantly stronger than at lower latitudes and the energy is dissipated and transferred via gravity waves and meridional circulation (Richmond, 1979).

b. *Composition*

On the basis of the hydrodynamic behaviour of its composition, the upper atmosphere can be conveniently divided into two regions. Below about 90 km, down to sea level, is the homosphere in which the composition is kept constant by winds and turbulent mixing at a mean molecular mass of 28.96. By volume, the principal constituents are N_2(78.08%), O_2(20.95%), A(0.93%) and CO_2(0.03%), with a variety of minor constituents and pollutants comprising the remaining 0.04%. Above 90 km, in the heterosphere, this homogeneity is destroyed by a combination of O_2 dissociation, followed by diffusion, which influences each of the constituents N_2, O_2, O, Ar, He and H to assume a density and pressure consistent with its mass and with the temperature. The distributions of the four neutral upper atmosphere constituents N_2, O_2, O and O_3, which together absorb the entire solar ultraviolet energy

radiated at wavelengths shorter than 300 nm, are shown in Figure 1.3.

In the stratosphere, in addition to the normal background of well-mixed, clean, 'dry' air, whole families of substances are present which participate in aeronomic reactions, effecting changes in their concentrations from the mixing distributions. Current knowledge of the sources, sinks and densities of species that are important in determining the physical and chemical state of the stratosphere is reviewed in the recent and very comprehensive compilation edited by Hudson and Reed (1979).

Some neutral particles of importance to the stratosphere are listed in Table 1.1 and can be classified into three groups; radical precursors, radicals and reservoirs. The radical precursors are relatively stable source molecules, of natural or industrial origin, which are introduced to the troposphere and gradually enter the stratosphere. These species are the halocarbons, nitrous oxide, odd-nitrogen, carbon dioxide, water vapour, methane and non-methane hydrocarbons and sulfur compounds. In the stratosphere the radical precursors are converted through photochemistry to chemically active 'radicals' such as NO, NO_2, OH, HO_2, Cl and ClO, which are more generally referred to as odd N, odd H and odd Cl because, within each family, chemical forms transfer rapidly from one to the other. Some of the radicals combine with each other to form 'reservoirs', which are typically inactive as catalysts but constitute a form of storage from which radicals can be released photochemically, or which are steadily and slowly transported back into the troposphere where they are removed by rain. Examples of reservoirs are HCl, HNO_3, $ClONO_2$, H_2O_2, HO_2NO and HOCl. Other constituents such as SO_2, COS, NH_3 and H_2SO_4 are important in the formation of atmospheric aerosols which are molecular clusters suspended near about 20 km, where their interaction with the direct and diffused solar radiation field, via scattering and

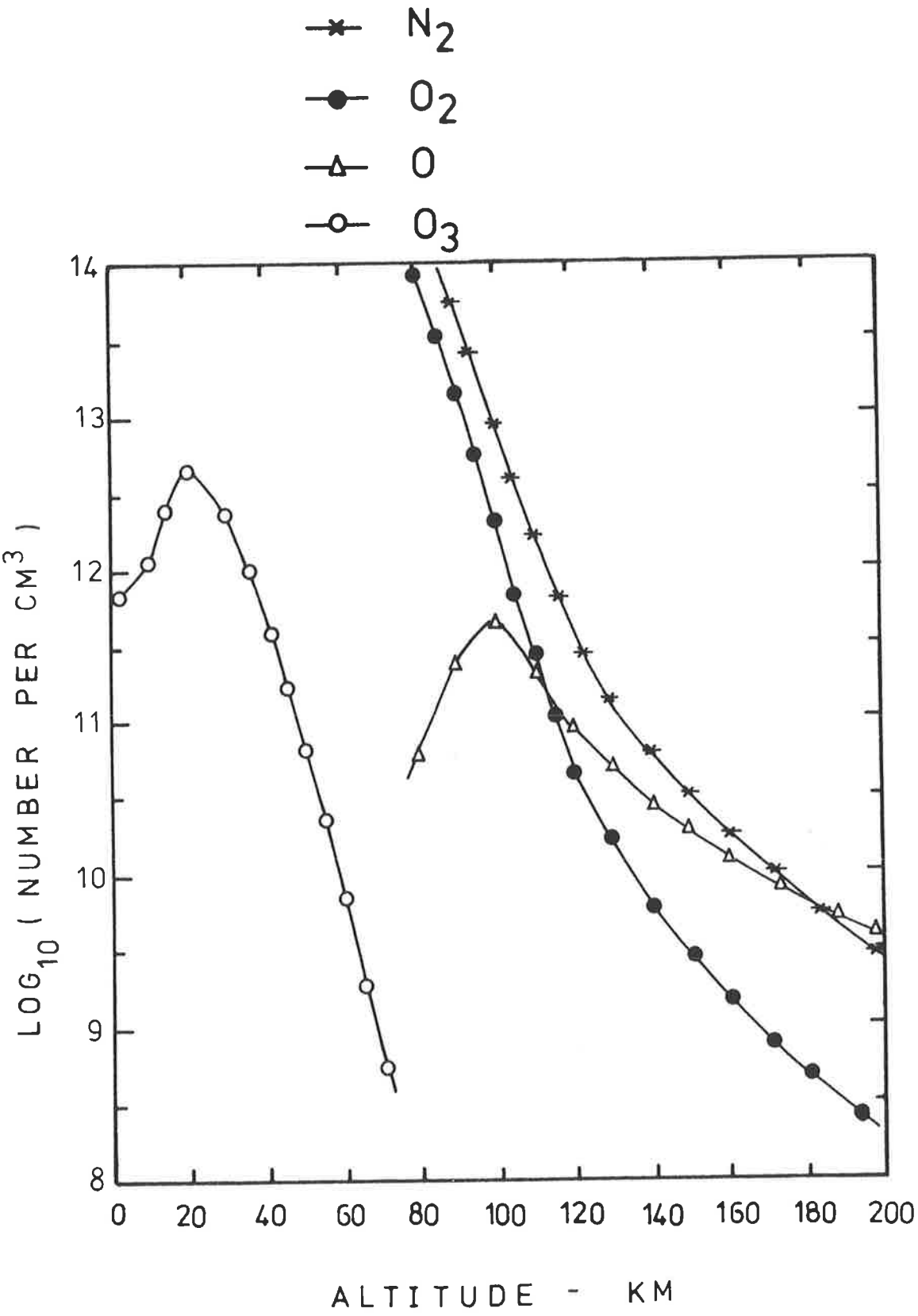

Figure 1.3 Neutral composition of the upper atmosphere.
(U.S. Standard Atmosphere, 1976)

TABLE 1.1 Neutral species of interest to the stratosphere.
(Hudson and Reed, 1979)

$O(^3P)$, $O(^1D)$, $O_2(^1\Delta)$, $O_2(^1\Sigma)$, O_3

H, OH, HO_2, H_2, H_2O, H_2O_2

N, NO, NO_2, NO_3, N_2O_5

NH_3, HNO, HONO, $HONO_2$, HO_2NO_2

Cl, ClO, OClO, ClO_2, ClO_3, HCl, HOCl, $ClONO_2$

Br, BrO, OBrO, BrO_2, HBr, HOBr, $BrONO_2$

F, FO, HF, FOH, $FONO_2$

S, SO, SO_2, SO_4, HS, H_2S, COS, CS_2

CO, CH_2O, CH_3O_2, CH_3OH, CH_3, CH_3O

CHO, CH_3OOH, CH_3ONO, CH_3ONO_2

C_2H_5, HCOOH, CH_3CHO, C_2H_5ONO, $C_2H_2O_2$, OC_2H_2O

absorption, may have important consequences for the transfer of radiative energy in the stratosphere.

Measurements of the densities of the species in Table 1.1 are difficult because the concentrations are small, so that, with the primary exception of O_3, knowledge of the distribution of the majority of species remains poor. Application of chemistry to the problem of stratospheric composition is complicated by the need to incorporate atmospheric dynamics when studying the great number of species for which chemical time scales are much greater than those of transport. This is especially true of O_3 in the lower stratosphere.

Important minor constituents in the mesosphere include: odd nitrogen, NO_2 and particularly NO and N which are transported down from the thermosphere; odd oxygen, O_3 and O and also excited molecular oxygen $O_2(^1\Delta_g)$; water vapour and other hydrogen species H_2, OH, HO_2 and H, of which the latter escapes from here up to the exosphere; and the carbon compounds CO_2 and CO. While the concentration of species such as N, OH, HO_2 and O_3 are strongly influenced by photochemistry, other species such as NO, H_2 and H_2O have longer chemical lifetimes so that mixing and transport have more influence on their distributions. O_3, H_2O and CO_2 are of special importance because they are radiatively active and control the thermal balance of the mesosphere.

In contrast to the stratosphere and mesosphere, where the activities of the minor constituents are important, the structure of the thermosphere reflects the gross features of the major constituents. A number of reviews have discussed the properties of this atmospheric region; its composition (Carignan, 1975) and solar-related variations (Jacchia, 1975), temperature and winds (King-Hele, 1978), general meteorology (Dickinson, 1975a) and dynamics (Mayr *et al*, 1978).

The concentration of the thermospheric species can be roughly assumed to decrease at a rate proportional to M/T, where M is the molecular weight and T is the temperature. Density variations therefore increase at higher altitudes which are characterized by wider excursions of the temperature, and have been confirmed to reflect the exospheric temperature dependence on, for example, solar activity. The total density is approximately in phase with the diurnal temperature, and reaches a maximum at 1400 hours local time with a minimum at 0200 hours, but each individual constituent peaks at a different local time which is a function of altitude. Semi-annual and season-latitudinal variations have also been identified for the thermospheric constituents.

Relatively systematic temperature-density changes can be distorted by atmospheric motions such as tidal waves, horizontal diffusion and gravity waves which propagate to higher altitudes from the troposphere or meridionally from high to low latitudes. More generally, the upper atmosphere is in a continuous state of motion, primarily that of rotation, with a large scale pattern of prevailing winds that are predominantly zonal (eastward or westward). Superimposed are diurnally recurring motions caused by atmospheric tides, modified by irregular motions, turbulence and gravity waves.

c. *Models*

Collation of the sparse experimental data for atmospheric constituents, acquired from observations parameterized by an extensive range of geophysical conditions, into a coherent and meaningful representation of the upper atmosphere is provided, via theoretical interpretations, by models. Because of the lack of a single credible, comprehensive and self consistent model of the radiation, chemistry and

dynamics of any of the regions of the upper atmosphere, there has developed a hierarchy of models that separately emphasize different fundamental processes. Some examples of the more recent of these models are provided below.

It is possible to reproduce the general zonally averaged circulation of the stratosphere and mesosphere by using three dimensional dynamic models. Schoeberl and Strobel (1978a) have thus described such essential features as the radiatively driven pole-to-pole circulation at solstice and the associated cold summer mesopause, warm isothermal winter mesosphere and polar night jets. They have also calculated (Schoeberl and Strobel, 1978b) that predicted ozone reductions would not substantially alter the transport and mixing of the minor atmospheric constituents. The transient behaviour of the stratosphere, as evidenced by temporal and spatial variations, has been considered by Hunt (1978) in relation to fluctuations in tropospheric-stratospheric coupling, driven dynamically from the troposphere. While three dimensional models are more effective than one or two dimensional models, deficiencies still exist, which will only be understood when sufficiently correlated measurements of the stratospheric number densities become available (Tuck, 1979).

Photochemical reactions between O , H and N species must be incorporated with atmospheric dynamics if the observed distributions of the minor stratospheric species, such as O_3, are to be adequately modelled. London and Park (1974) used time dependent photochemistry and a 3-D global circulation model to explain the variations of ozone densities with the weather patterns, seasons and latitude, and were able to reproduce the maximum found at high latitudes in spring. The diurnal variations of the minor stratospheric species have been modelled by

Shimazaki and Ogawa (1974) with steady-state photochemistry. They allowed for dynamic variability as parameterized by the vertical eddy diffusion coefficient, and noted this to be generally unsuccessful, in view of the importance of horizontal transport.

The emphasis of the recent model of Cunnold *et al* (1980) is on the reproduction of the zonal mean ozone distribution by use of a well developed 3-D dynamic model but with only an approximate chemical framework. Hence they have reported excellent simulation of observed ozone and have provided detailed qualitative explanations of the breakdown of the seasonal variations, and of the transition between photochemical and transport control of the ozone distribution.

Models of the concentrations of minor species at higher altitudes, in the mesosphere and lower thermosphere, have tended to employ extensive photochemistry but inadequate dynamics, typically accommodated by vertical eddy mixing, eddy diffusion, turbulent diffusivity, or eddy transport. Keneshea *et al* (1979) have reviewed the development of physical models for these regions of the atmosphere, with specific consideration of the inclusion of dynamic concepts. It is in this aspect that the ability of the models to reproduce observed diurnal (Shimazaki and Laird, 1970) and seasonal (Shimazaki and Laird, 1972) variations is predominantly limited, and the need to include planetary scale circulations (Strobel, 1972) such as horizontal, meridional transport is acknowledged. This is especially necessary to explain the experimentally determined spatial variations of the airglows in the Meinel bands and at 557.7 nm and 1.27 μm, due respectively to the species hydroxyl, atomic oxygen and excited molecular oxygen $O_2(^1\Delta_g)$, and also for reproducing the concentration of NO whose chemical lifetime in the mesosphere is much longer than the transport time.

The importance of co-ordinated experimental measurements to provide input parameters for models has been recently well illustrated by Keneshea *et al* (1979). Using a 1-D, time dependent model, they successfully reproduced the densities of minor constituents O, O_3, $O_2(^1\Delta_g)$, OH and Ar in the altitude range 50 to 150 km, which had been measured simultaneously by experiments which also provided dynamical parameters, mass densities and the temperature structure for inputs.

Above 120 km, where the composition of the atmosphere is generally assumed to be controlled by molecular scale diffusion processes, models have been developed on an empirical basis to provide realistic estimates of the constituent number densities. Both CIRA 1972 and the U.S. Standard Atmosphere, 1976 (Krueger and Minzner, 1976; Minzner, 1977) are idealized steady-state representations of the earth's atmosphere at mid latitudes and moderate solar activity.

With the availability of large data bases of total density from satellite drag measurements, as well as *in situ* satellite mass spectrometer measurements of individual densities, the static models have been superceded by three dimensional semi-empirical models which attempt to represent the composition variations induced by geophysical perturbations, specifically solar and geomagnetic activity and the diurnal, annual and seasonal-latitudinal cycles. Currently, there are four such models derived from a variety of data sources and, according to the comparison of Barlier *et al* (1979), none can represent correctly all geophysical aspects of the terrestrial atmosphere.

Satellites provide extensive coverage of densities predominantly between the altitudes 200 and 1200 km, while the disagreement between the models in the lower thermosphere reflects a lack of data, as well as the difficulty in modelling the temperature between 100 and 200 km.

Additional problems arise here because the models must assume a lower boundary for calculating the vertical profiles of the individual species, and this will depend, in a realistic model, on the solar UV flux, the downward kinetic and turbulent heat conduction and the transport of oxygen. Of all the lower thermospheric species, O_2 is the least well modelled because dissociation and transport invalidate the conditions of diffusive equilibrium assumed by the models.

The model of Barlier *et al* (1977, 1978) is based on satellite drag measurements of total density, covering almost two solar cycles, and the experimentally determined exospheric temperature model of Thuillier *et al* (1977). Concentrations for each of He, O and N_2 are derived from a fixed lower boundary at 120 km.

In situ mass spectrometer measurements during periods of low solar activity, at low altitudes (240 to 320 km) from ESRO-4 (von Zahn *et al*, 1977) have been combined with similar measurements above 400 km during high solar activity from OGO-6 (Hedin *et al*, 1974) in a model which incorporates variations in the height of the turbopause between 90 and 115 km (Blum *et al*, 1978). Exospheric temperatures for the model were obtained from N_2 densities, under assumptions of diffusive equilibrium conditions.

The framework of the MSIS model (Hedin *et al*, 1977a, 1977b) is the composition data from mass spectrometers on five satellites, collected over the period 1969 to 1975, and temperature data from incoherent scatter measurements at four ground stations. Allowance was made for variations in the lower boundary conditions at 120 km and for departures from diffusive equilibrium at altitudes below 200 km.

Of all the models, those of Jacchia have been most widely used and their evolution since 1961 represents a survey of how knowledge of the

upper atmosphere has increased. The most recent model (Jacchia, 1977) combines the mass spectrometer data from OGO-6 and ESRO-4 with satellite drag densities and the Doppler temperature model of Thuillier *et al* (1977). Although the lower boundary is fixed at 90 km, empirical corrections are allowed between 90 and 120 km to simulate departures from diffusive equilibrium.

Jacchia (1978) has compared the Jacchia (1977) model with the MSIS model and reports that these two completely independent representations of the same atmospheric variations are overall in good agreement. Although the MSIS model appears superior for diurnal variations below 200 km, its incorporation of the geomagnetic effect is relatively poor. Barlier *et al* (1979) have reported that none of the models agree about the amplitude and phase of the diurnal variations of individual constituents below 200 km. More generally, the largest discrepancies in all aspects of the models occur at altitudes below 200 km, especially for periods of solar activity when $F_{10.7} < 100$ or $F_{10.7} > 150$ x $10^{-22} Wm^{-2} Hz^{-1}$.

Semi-empirical thermospheric models attempt to fit analytic expressions such as spherical harmonics to observed variations of the earth's atmosphere. Explanation of the observations in terms of wave motions, circulation and turbulence is not their explicit aim. Rather, this is provided by a wide range of dynamical models (Volland and Mayr, 1977; Roble *et al*, 1977; Forbes, 1978; Forbes and Garrett, 1979; Frederick, 1979; Mayr and Harris, 1979). The importance of the semi-empirical models is confirmed by the many atmospheric investigations, including atmospheric absorption spectroscopy studies, which make use of them as input parameters.

1.3 ABSORPTION SPECTRA OF ATMOSPHERIC GASES

Deposition of solar ultraviolet energy in the upper atmosphere depends on the distributions of the constituent species and their ultraviolet absorption spectra which must be determined by laboratory experiments.

a. Absorption Processes in Gases

Processes by which gases absorb electromagnetic radiation have been described in detail for atoms (Herzberg, 1944; Kuhn, 1969), diatomic molecules (Herzberg, 1950; Banwell, 1972) and polyatomic molecules (Herzberg, 1966). This section provides a brief account of some aspects which promote an understanding of the absorption spectra of gases.

Atoms and molecules can only exist in certain discrete energy states whose properties are determined by the relative motions and interactions of the electrons and nuclei. Information about the dynamical properties of any such system are contained in the appropriate Schrödinger equation. If this can be solved, the eigenfunctions provide the probability density distribution function of the electrons and the eigenvalues are measures of the discrete energies of the stationary states, each of which is uniquely distinguished by a set of quantum numbers.

Absorption of electromagnetic radiation by atoms and molecules corresponds to a transition from one energy state to another. The energy of the absorbed photon is represented by the increment in the eigenvalues of the two states, with the quantum numbers providing a basis for selection rules which indicate whether or not the transition is 'allowed'. The intensity of a particular transition can be determined from the eigenfunctions of the states involved.

Atomic electrons move about the nucleus in orbitals of different angular momentum. In the simplest case the angular momenta of the individual electrons couple together to give a resultant orbital angular momentum $\underset{\sim}{L}$. Similarly, there is a resultant spin momentum $\underset{\sim}{S}$, which adds to $\underset{\sim}{L}$ to define the total angular momentum $\underset{\sim}{J}$ of the electrons in the atom. Energy states of the atom are conveniently designated as follows. For L=0, 1, 2, 3.... the energy levels of the atom are respectively called S, P, D, F.... terms. The multiplicity $2S + 1$ is added as a left superscript and the J value is a right subscript to the term value. Transitions between different energy levels are allowed when

$$\Delta S = 0 \qquad \Delta L = 0, \pm 1 \qquad \Delta J = 0, \pm 1.$$

Atomic absorption is represented, in its simplest form, by the alkali-like spectra. These are typically series of lines, called Rydberg series, corresponding to the changes in energy caused by the valence electron making one of the allowed transitions. Each absorption series represents all possible transitions from a common lower energy state which, at room temperature, is the ground state. At short wavelengths the lines converge to a series limit which identifies the ionizing wavelength of the atom. Adjoining the series limit, the absorption spectrum is continuous because energy in excess of the ionization energy is removed by a free electron whose energy is not quantized.

When two or more electrons participate in atomic absorption the observed spectrum is more complicated and has predominantly multiplet

rather than series structure. If two terms of different electron configuration of the same atom have approximately the same energy, the states influence each other; the eigenfunctions of the resulting states are mixtures of the two originally degenerate states and the observed spectral line is broadened by this perturbation. If an excited state of an atom has the same energy as a non-bound state consisting of the ground state ion and a free electron, it is possible for these states also to perturb each other. An electron excited to the discrete state can make a transition to the continuum in a radiationless procedure called autoionization. Spectral lines equivalent to the energy of these states are generally broadened because the probability for the radiationless transition is usually greater than the probability for a transition to an energetically lower state with radiation.

In a diatomic molecule, in addition to the energy of the electrons, there are vibrational and rotational contributions to the total energy. At ultraviolet wavelengths, the coarse structure of absorption spectra is interpreted as transitions between different electronic states, while the finer details arise from the vibrational and rotational levels.

The electronic energy depends on the instantaneous internuclear distance. Each electronic state is identified by a potential curve and is stable only if this curve has a minimum value. Molecular electronic states are classified analogously to those of atoms. However, because the orbital angular momentum $\underset{\sim}{L}$ and the spin momentum $\underset{\sim}{S}$ precess about the internuclear axis, it is appropriate to consider the components M_L and M_S of the vectors along this axis. Accordingly, as the value of M_L is $\Lambda = 0, 1, 2, 3.$, the molecular state is designated $\Sigma, \pi, \Delta, \Phi$. Any plane through the internuclear axis is a plane of

symmetry and the electronic non-degenerate (Σ) states are classified as Σ^+ or Σ^- if the eigenfunction is respectively unchanged or changed by reflection in this plane. Additionally, if the two nuclei have the same charge there is a point of symmetry on the internuclear axis. An even state (Σ_g) remains unchanged in sign when reflected at this point but an odd state (Σ_u) does not. Some allowed transitions for homonuclear diatomic molecules are listed in Table 1.2.

Absorption by a molecule at room temperature is dominated by a transition from the lowest vibrational level (v"=0) of the ground electronic state to any of the vibrational levels v' of an upper electronic state. The totality of the transitions comprises a band system (v', v"), within which the intensity distribution of the lines is determined by the overlapping of the eigenfunctions of the v" and v' levels. This is expressed by the Frank-Condon principle and is represented diagramatically in Figure 1.4. Because the electron transition in a molecule is rapid compared with the vibrational motion, the nuclei remain relatively invariant, and in Figure 1.4 the transition can thus be represented by a vertical line between two potential curves.

A transition to a continuous upper state causes the molecule to dissociate and this is evident in the absorption spectrum as a continuum joining on to the converging bands. If a discrete energy level of an upper electronic state is overlapped by a continuous range of levels from another state, as illustrated in Figure 1.4, the molecule can dissociate via a radiationless transition. The widths of the corresponding spectral lines are usually broadened by this predissociation and, if the process occurs more rapidly than the molecule rotates, any rotational structure in the absorption spectrum is destroyed. Dissociation and predissociation features are generally more frequent in diatomic

TABLE 1.2 Allowed electronic transitions for diatomic molecules. (Herzberg, 1950)

Unequal Nuclear Charge	Equal Nuclear Charge
$\Sigma^+ \leftrightarrow \Sigma^+$	$\Sigma_g^+ \leftrightarrow \Sigma_u^+$
$\Sigma^- \leftrightarrow \Sigma^-$	$\Sigma_g^- \leftrightarrow \Sigma_u^-$
$\Pi \leftrightarrow \Sigma^+$	$\Pi_g \leftrightarrow \Sigma_u^+$, $\Pi_u \leftrightarrow \Sigma_g^+$
$\Pi \leftrightarrow \Sigma^-$	$\Pi_g \leftrightarrow \Sigma_u^-$, $\Pi_u \leftrightarrow \Sigma_g^-$
$\Pi \leftrightarrow \Pi$	$\Pi_g \leftrightarrow \Pi_u$
$\Pi \leftrightarrow \Delta$	$\Pi_g \leftrightarrow \Delta_u$, $\Pi_u \leftrightarrow \Delta_g$
$\Delta \leftrightarrow \Delta$	$\Delta_g \leftrightarrow \Delta_u$

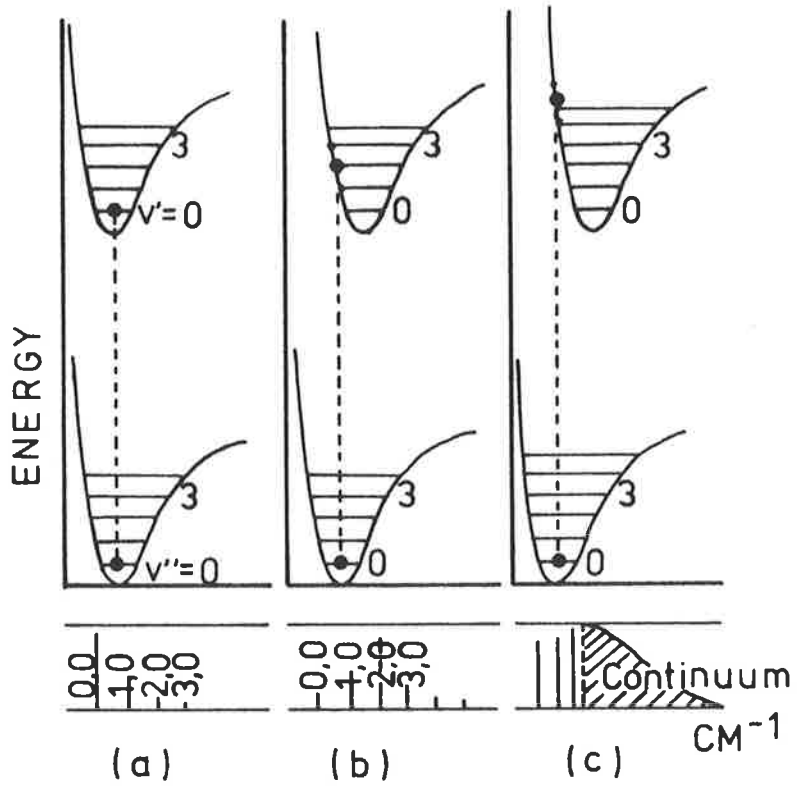

Explanation of the spectral intensity distribution in electronic bands when the internuclear distance is (a) unchanged, (b) little changed, (c) greatly changed.

(Banwell, 1972)

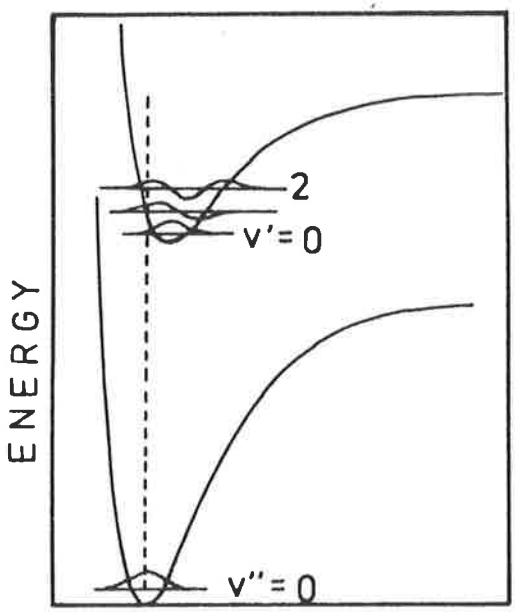

Wave mechanics: overlapping of the eigenfunctions is greatest for $v''=0$ and $v'=2$.

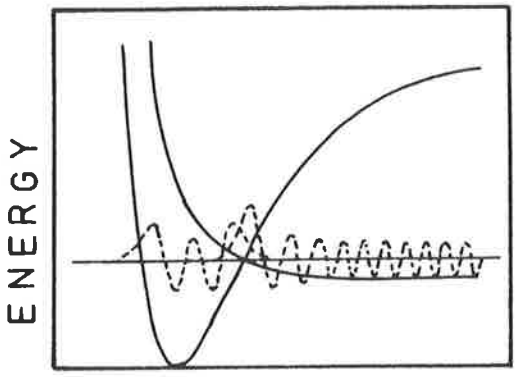

Predissociation: the broken curves are the eigenfunctions.

(Herzberg, 1950)

Figure 1.4 Interpretations of diatomic molecular spectra by the Franck-Condon principle.

molecular absorption spectra than ionization and preionization, although examples of the latter are also observed.

Triatomic molecules have many more degrees of freedom than diatomic molecules and triatomic molecular absorption hence involves many more dissociation and predissociation processes. By comparison, the continuous ranges of energy levels are numerous, due to the wider variety of products that may arise from dissociation, and the selection rules are generally less restrictive. Consequently, continuous and diffuse absorption spectra are frequently observed for triatomic molecules.

For every electronic state of a triatomic molecule the potential energy under which the nuclei move is represented, not by a potential curve, but by a potential surface. Different electronic states are often described by vastly different potential surfaces because the potential minima generally occur for quite different configurations of the nuclei. If the nuclei arrangement is highly symmetric the electronic state will be highly degenerate. As the symmetry is lost, via electronic, vibrational and rotational interactions, so this degeneracy is removed. This is represented by a splitting of the original potential surface, as described by the Jahn-Teller theorem. Figure 1.5 is a graphical representation of these concepts.

The ground state of a triatomic molecule may have a number of potential minima so that when a transition is induced by absorption of energy, it can originate in any one of these minima and terminate somewhere on the upper potential surface. Hence, from a ground state transition there is not just one band, but a number. As for diatomic molecules, the intensity distribution of the observed spectra is governed by the Frank-Condon principle, as modified by the Herzberg-Teller

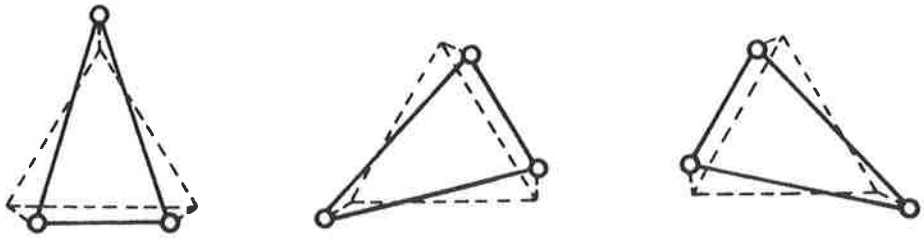

Three equilibrium conformations of a symmetrical X_3 molecule before (- - -) and after (——) introduction of vibronic interaction.

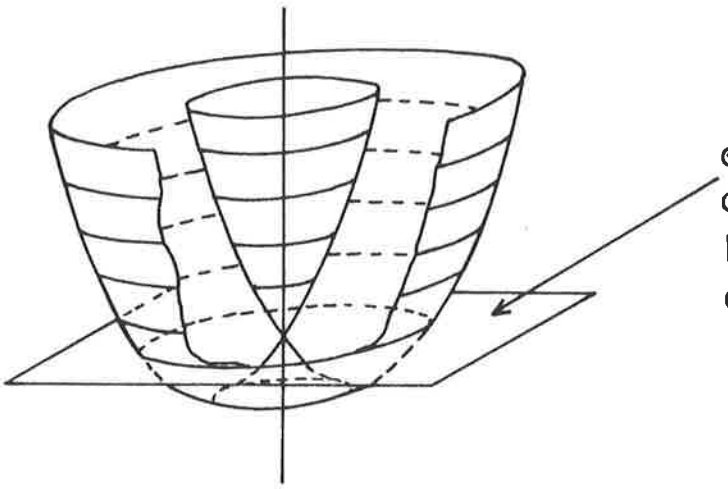

energy of the minimum of potential energy before vibronic interaction is introduced

Approximate potential surface of a non-linear molecule.

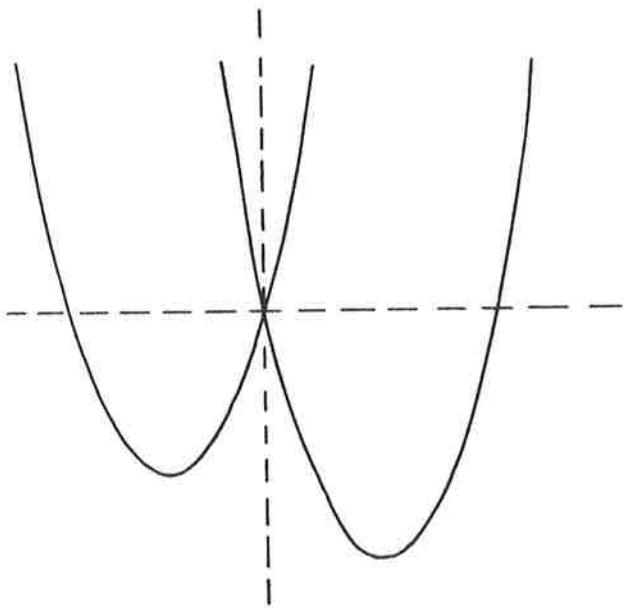

Higher approximation of the cross section of the potential function when higher order terms in the vibronic interaction are taken into account: the trough in the previous diagram now has three minima.

Figure 1.5 Graphical representation of the potential energy surface of a non linear molecule. (Herzberg, 1966)

formulation for polyatomics, but now the eigenfunctions are more complicated and the potential surfaces multidimensional.

Theoretical interpretations of the diffuseness observed in polyatomic spectra have tended to invoke predissociation mechanisms analogous to diatomic theory. The validity of this assumption has been questioned by Pack (1976) who was able to synthesize typical polyatomic spectra from simply associative upper electronic states, and therefore suggests that simple dissociation is a possible explanation for the progressions of diffuse vibrational bands typically superimposed on the continuum in the UV spectra of polyatomic molecules.

b. *Experimental Determination of Absorption Cross-Sections*

Gases can absorb radiation via multiple and complex processes but, without exception, any absorption phenomenon effects a decrease in the incident radiant intensity. The attenuation of incident intensity I_0 by a path length x cm in a gas with n molecules per cm^3, is given by the Lambert-Beer law as

$$I = I_0 \exp(- n . \sigma . x)$$

where σ cm^2 is the absorption cross-section of the molecule.

Aeronomic calculations require accurate values of the absorption cross-sections of atmospheric gases, but definitive laboratory investigations are difficult because the most important wavelengths are in the vacuum ultraviolet and because the fine structure of the wavelength dependence of the cross-sections may demand higher resolution and a more complete spectral coverage than is readily attainable.

Typically, an experiment for measuring absorption cross-sections is as follows. Light from either a continuum or line emission source is dispersed by a monochromator into a narrow wavelength interval which

emerges from the exit slit and passes through an absorption cell. This is of known length and contains the specimen gas at a suitable temperature and pressure. Then, the ratio of the monochromatic flux transmitted by the cell to the incident flux provides, directly from the Lambert-Beer law, the magnitude of the absorption cross-section. At wavelengths shorter than the ionization threshold of the gas the absorption cell may be replaced by an ionization chamber. The techniques of vacuum ultraviolet spectroscopy appropriate for absorption cross-section measurements have been reviewed in excellent detail by Samson (1967).

Ultraviolet radiation can be produced in the laboratory by a high voltage discharge through a gas confined to a narrow capillary (Hunter, 1962; Huffman *et al* 1965; Paresce *et al*, 1971; Cantu and Tondello, 1975) or via a sliding spark, as in the BRV source (Garton *et al*,1969; Fox and Wheaton, 1973). The intensity of the radiation from, for example, a pulsed discharge depends on the frequency of the discharge as well as the current density through the lamp, and sophisticated triggering mechanisms, such as thyratrons, and associated electronic circuitry must be used. High voltage switching generates high frequency electromagnetic 'noise' which interferes with sensitive detector electronics unless the lamp supply is shielded (Institute of Electronic Engineers, Conference Publications No. 65, 1970), and, preferably, the detector electronics gated. Emission lines from laboratory sources are unable to simulate the width of solar emission lines and thus are not completely ideal for measuring aeronomically important absorption cross-sections.

Synchrotrons produce continuous radiation over a wider spectral range than is available from conventional laboratory sources, but manifest

other problems, notably increased higher order and scattered radiation (Madden *et al*, 1967; Saloman, 1975). At grazing incidence angles these detrimental effects are even more significant and necessitate the use of thin metal windows as broad optical filters or gratings in tandem (Jaeglé *et al*, 1977).

It is preferable, in absorption cross-section experiments, for the specimen gas to be in a temperature and pressure environment representative of atmospheric conditions. This requires a facility to maintain the absorption cell at a constant temperature, higher or lower than ambient. Low pressure measurements are impractical when the absorption cross-section is small because the absorption cell would need to be unrealistically long. Additional complications may arise from pressure gradients generated in a gas flow-through system, which must be employed at wavelengths less than the cut-off of lithium fluoride windows (105 nm).

In principle, if the resolution is sufficiently high, the measured cross-sections will be independent of pressure but in practice this condition may not be easily achieved. Where the absorption spectrum exhibits complicated structure, unfolding the experimental data becomes extremely difficult, and curve-of-growth analyses are necessary (Hill, 1979).

Absorption cross-section data are influenced by the different experimental parameters pertaining to each individual measurement and this must be considered in any comparison of the results. Hudson (1971) has provided a critical review of photoabsorption cross-sections for molecules of aeronomic interest and has included a discussion of measurement techniques. Huffman (1969) and Ackerman (1972) have also reviewed absorption cross-section data through the entire ultraviolet region, while measurements at EUV wavelengths have been compiled

by Stolarski and Johnson (1972) and Kirby *et al* (1979), and the FUV and MUV wavelengths, important for stratospheric absorption, have been considered by Hudson (1974).

General features of the absorption spectra of O, O_2, N_2 and O_3 are illustrated in Figure 1.6 for the extreme ultraviolet, Figure 1.7 for the far ultraviolet and Figure 1.8 for the middle ultraviolet spectral regions. The four following sections describe the properties of the absorption spectrum of each gas, as discerned primarily from laboratory investigations.

c. *Atomic Oxygen*

Prominent features of atomic oxygen absorption are located either in the infrared or the vacuum (far + extreme) ultraviolet regions of the spectrum. Because atomic oxygen is a many-valence-electron system, its interaction with radiation includes more possible pathways than are available to nearly-closed-shell systems. Transitions from the ground state $(1s^2\ 2s^2\ 2p^4)\ ^3P$ which involve the $2p$ valence shell electron lead to the three lowest states of the ion, $O^+(\ ^4S^\circ)$, $O^+(\ ^2D^\circ)$ and $O^+(\ ^2P^\circ)$, for which the thresholds are, respectively, 91.04, 73.2 and 66.5 nm. Removing a $2s$ inner shell electron gives rise to $O^+(\ ^4P^e)$ and $O^+(\ ^2P^e)$ with thresholds at 43.5 and 31.5 nm. The absorption spectrum of atomic oxygen is therefore expected to have an ionization continuum below 91.04 nm , together with Rydberg series converging to each of the three OII states. This has been confirmed experimentally by Huffman *et al* (1967a), who reported nine Rydberg series. In addition, they observed some series for which the lower states were identified as excited metastable atomic oxygen terms ^2D and ^1S (Huffman *et al*, 1967b).

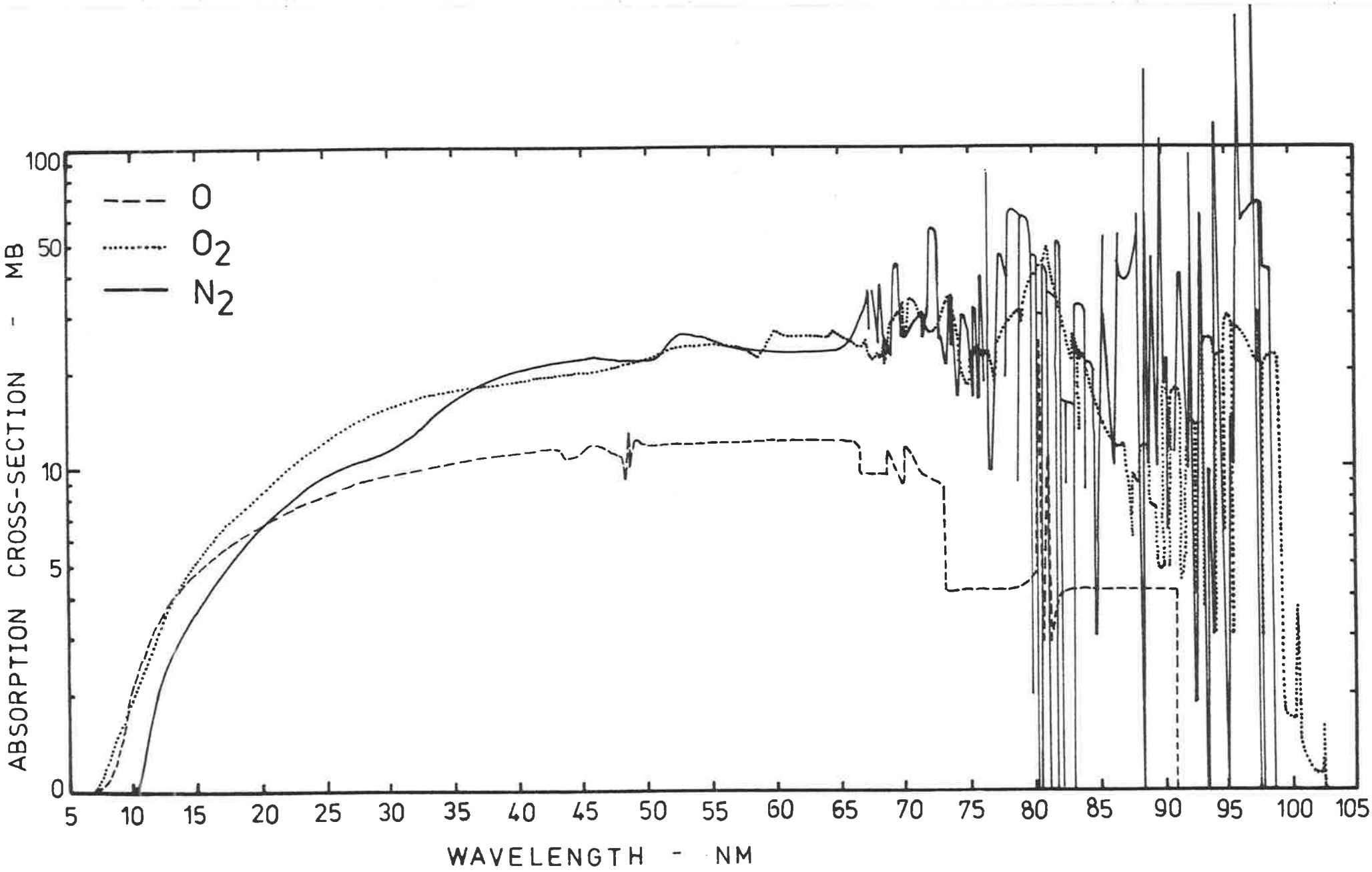

Figure 1.6 Extreme ultraviolet absorption cross-sections. (Kirby et al , 1979)

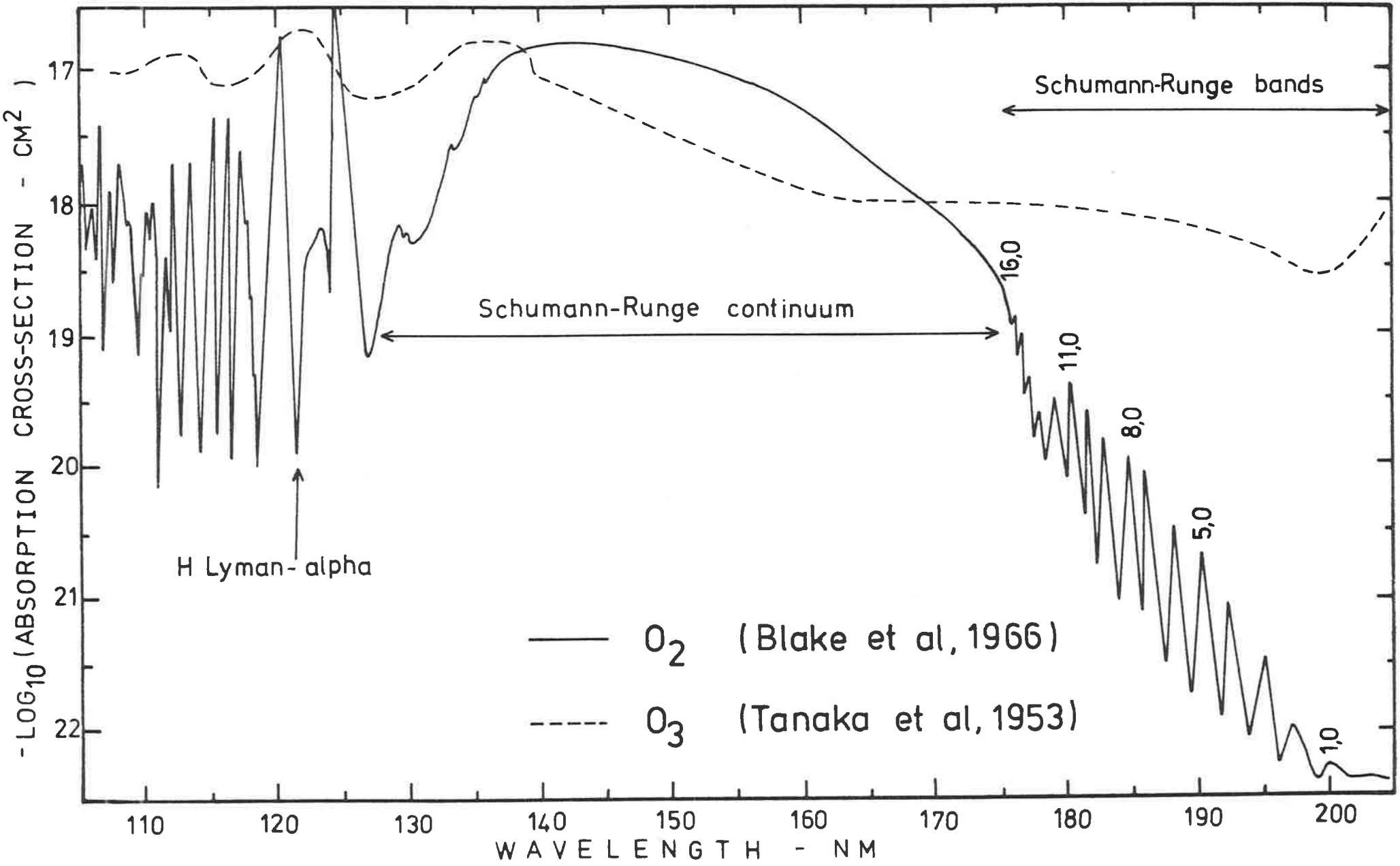

Figure 1.7 Far ultraviolet absorption cross-sections.

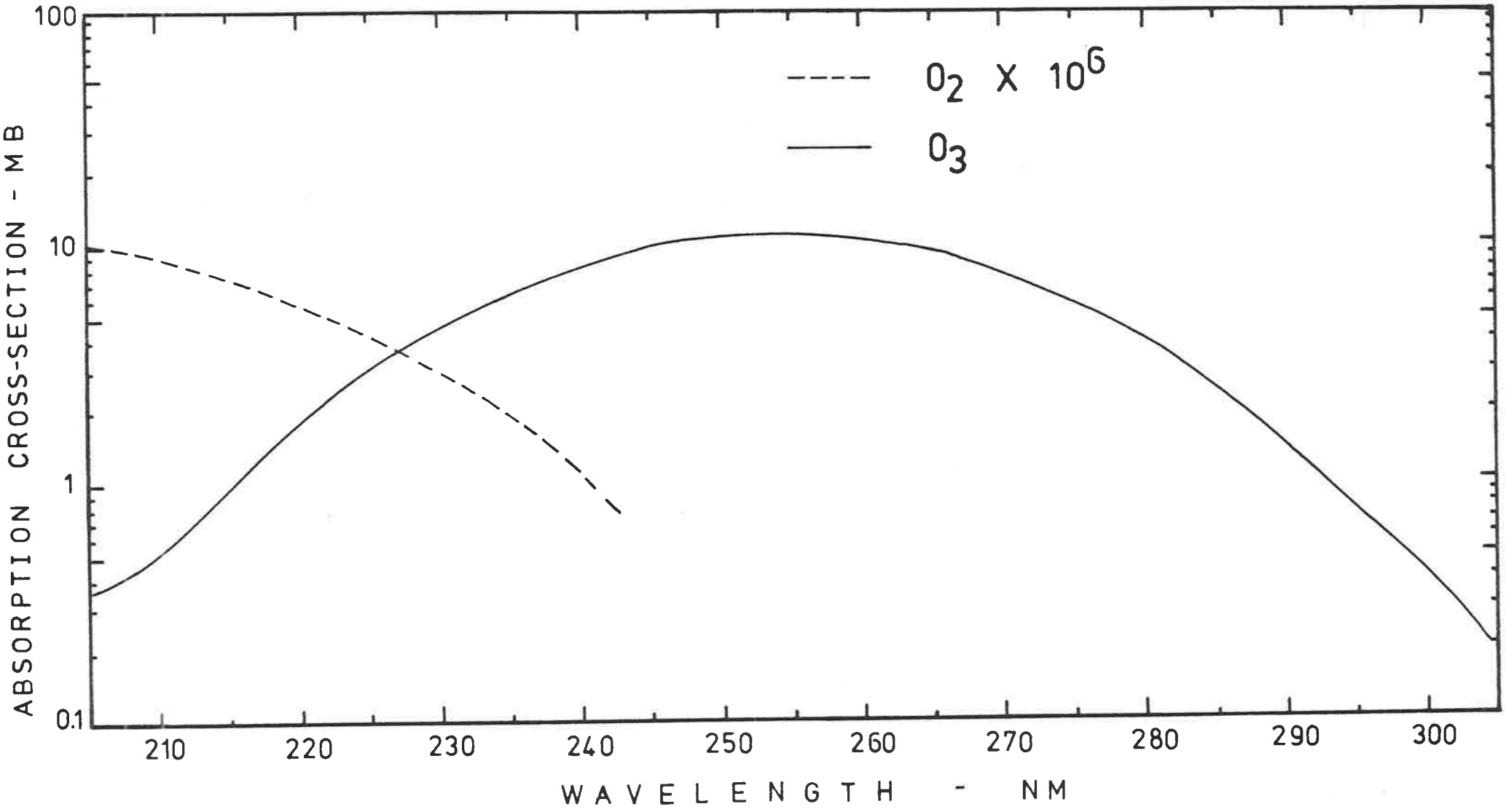

Figure 1.8 Middle ultraviolet absorption cross-sections (Nicolet, 1980).

Autoionization structure has been observed for all the transitions seen in absorption by Huffman *et al* (1967a, 1967b) (Dehmer *et al*, 1973). Relative photoionization cross-section measurements from 92 nm to 65 nm revealed that the two most intense autoionization peaks in the spectrum, at 87.8 - 87.9 nm and 79.1 - 79.3 nm, corresponded to transitions for which autoionization is actually forbidden.

Absolute magnitudes of the absorption cross-sections in the continuum and for the many strong lines have been acquired, both theoretically (Dalgarno *et al*, 1964; Henry, 1967; Taylor and Burke, 1976; Pradhan and Saraph, 1977) and experimentally (Cairns and Samson, 1965; Comes *et al*, 1968; Kohl *et al*, 1978), with difficulty. They are probably the least certain of all the ultraviolet absorption cross-sections. The strongest line in the spectrum, the resonance triplet at 130.2 - 130.6 nm, has a maximum measured absorption cross-section of 7.3×10^4 Mb (Parkes *et al*, 1967; Huffman and Larrabee, 1968) while the continuum cross-section varies from 12 Mb to less than 1 Mb at short wavelengths. However, absorption at the lines remains largely unquantified, but could possibly be greater than 100 Mb (Huffman and Larrabee, 1968).

d. Molecular Oxygen

Molecular oxygen is dissociated by photons with wavelength less than 242 nm. It is therefore a significant atmospheric absorber throughout the entire ultraviolet spectrum. Potential energy curves for different electronic states of the molecule and the ion are illustrated in Figure 1.9 and the observed absorption spectrum is discussed with reference to transitions between these levels.

Ionization commences at 102.7 nm, corresponding to a transition from the ground state $X^3\Sigma_g^-$ of the molecule to the ground state $X^2\pi_g$ of the ion. At wavelengths from 102.7 to 50 nm the absorption

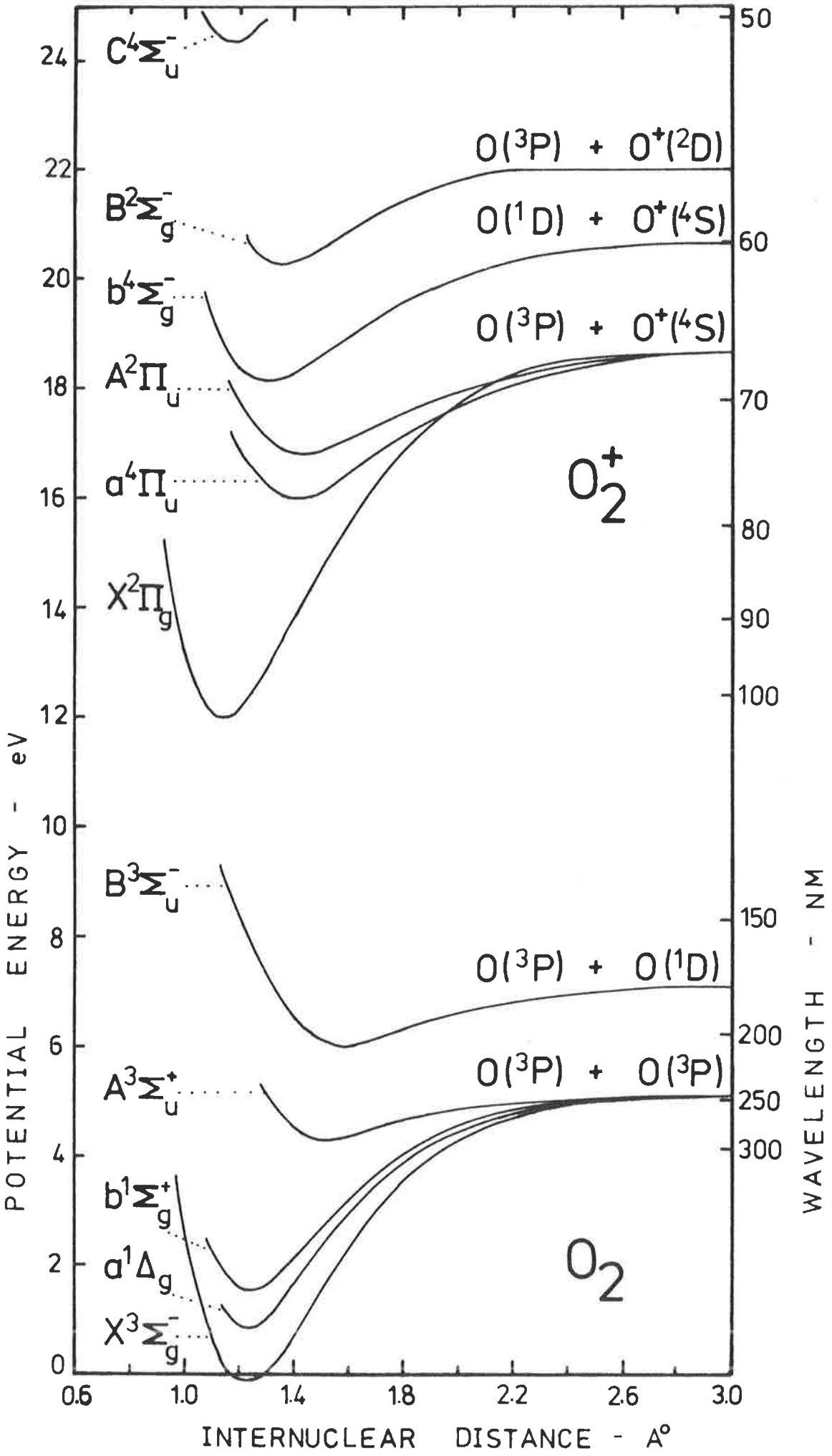

Figure 1.9 Potential curves for O_2. (Gilmore, 1965)

spectrum is complex, and comprised of diffuse and ionized bands superimposed on a continuum (Watanabe and Marmo, 1956; Samson and Cairns, 1964; Huffman *et al*, 1964 a; Cook and Metzger, 1964). This underlying continuum arises from both ionization and dissociation, and has been roughly divided into five separate maxima (Cook and Metzger, 1964).

Between 102.7 and 84 nm the continuum rises monotonically to about 13 Mb. In this region, across the diffuse and preionized bands, the variation of the absorption cross-section is the most dramatic. Successive maxima occur in the continuum near 80.9 , 76 , 72.5 and 63.5 nm. Below 74 nm, in the fourth continuum region, a large number of the bands have been identified as members of Rydberg series converging to the three lowest vibrational levels of $O_2^+(b^4\Sigma_g^-)$, at 68.2 nm. Weak structure between 68 and 59 nm is associated with the $O_2^+(B^2\Sigma_g^-)$ Rydberg series, and between 59 and 50 nm with that of $O_2^+(C^4\Sigma_u^-)$ (Lee *et al*, 1973). Here, the average magnitude of the continuum is about 20 Mb, and from 50 nm this decreases smoothly going to shorter wavelengths (De Reilhac and Damany, 1977).

Extending from 103 to 125 nm is a complex structure of diffuse and predissociated bands. In particular, there are seven 'windows' in the absorption spectrum, for which the magnitude is less than 5×10^{-2} Mb (Metzger and Cook, 1964). One of these windows coincides almost exactly with the wavelength of the hydrogen Lyman-alpha line. Here, the cross-section is 0.01 Mb, and is temperature dependent (Carver *et al*, 1977a).

In the Schumann-Runge continuum, between 125 and 175 nm, molecular oxygen dissociates into $O(^3P) + O(^1D)$. The absorption cross-section for this process is asymmetric about a broad maximum of 14.9 Mb

at 142.5 nm (Blake *et al*, 1966). On the short wavelength side the cross-section falls sharply and there are three diffuse maxima at 129.4, 132.4 and 135.4 nm while, at longer wavelengths, the cross-section decreases slowly and smoothly to the adjoining Schumann-Runge bands at 175 nm.

There are more than 20 bands between 175 and 203 nm, representing transitions from the lowest vibrational level v"=0 of the ground state $X^3\Sigma_g^-$ to successive vibrational levels of the $B^3\Sigma_u^-$ state. The bands are strongly predissociated and the cross-section, which exhibits temperature dependence, decreases from about 0.1 Mb at the (20,0) band to less than 1×10^{-4} Mb at (1,0) (Lewis *et al*, 1978, 1979; Blake, 1979).

Underlying the Schumann-Runge band system, at its long wavelength extremity, is the pressure-dependent Herzberg continuum due to the transition $X^3\Sigma_g^- \rightarrow O(^3P) + O(^3P)$. The Herzberg bands result from a forbidden transition from the ground state to the $A^3\Sigma_u^+$ state, and the whole Herzberg system extends from 185 to 260 nm (Hasson and Nicholls, 1971a, 1971b).

e. Molecular Nitrogen

In the ultraviolet, the molecular nitrogen absorption spectrum can be divided into three regions. Above 100 nm there are six absorption bands which are weak and forbidden; from 100 to 60 nm many sharp bands, which become increasingly diffuse toward shorter wavelengths, are superimposed on a continuum, which becomes increasingly stronger toward shorter wavelengths; and beyond 60 nm the absorption cross-section decreases smoothly and monotonically to the shortest wavelengths of the extreme ultraviolet.

Each of the six band systems above 100 nm derive from electronic transitions originating in the ground state $X^1\Sigma_g^+$ and

terminating in low-lying excited states of the molecule (Wilkinson and Mulliken, 1959; Tanaka *et al*, 1964; Shemansky, 1969). With reference to the potential energy curves of Figure 1.10, the corresponding upper electronic states are $A^3\Sigma_u^+$ (Vegard-Kaplan bands), $B'^3\Sigma_u^-$, $a'^1\Sigma_u^-$, $a^1\pi_g$ (Lyman-Birge-Hopfield bands), $w^1\Delta_u$ and $C^3\pi_u$. The LBH bands are the most intense and the transitions to $a'^1\Sigma_u^-$ the weakest. For the entirety of the band systems, the magnitude of the absorption cross-section is of the order of 10^4 to 10^5 times less than the strong systems which appear in the adjoining region, below 100 nm (Tanaka *et al*, 1964). This region thus has negligible significance for atmospheric absorption.

Between 105 and 80 nm there are many closely-spaced narrow bands which are strongly pressure dependent due to the presence of clear rotational structure (Watanabe and Marmo, 1956; Cook *et al*, 1964). At the maxima of these bands the cross-section may be in excess of 40 Mb. In particular, at 97.25 nm, the wavelength of Lyman-γ, the cross-section is 36 Mb and varies across the width of the line (Samson and Cairns, 1964). Additional to the bands are prominent Rydberg series converging to the ground state and first excited state of the ion, respectively $X^2\Sigma_g^+$ (Worley-Jenkins Rydberg series) and $A^2\pi_u$ (Ogawa and Tanaka, 1962). The complex and extensive band system in this region, initially correlated with many single electronic states, has more recently been ordered into six vibrational progressions of three valence states and of three Rydberg states (Dressler, 1969). As a consequence of an associated deperturbation analysis, the energy scheme for the higher excited states of N_2 has been greatly simplified. Non-Rydberg levels between 12.5 eV and the first ionization threshold have been assigned to a single electronic state $b^1\pi_u$ and, similarly, non-Rydberg bands are assigned to a single state $b'^1\Sigma_u^+$ (Carroll and Collins, 1969;

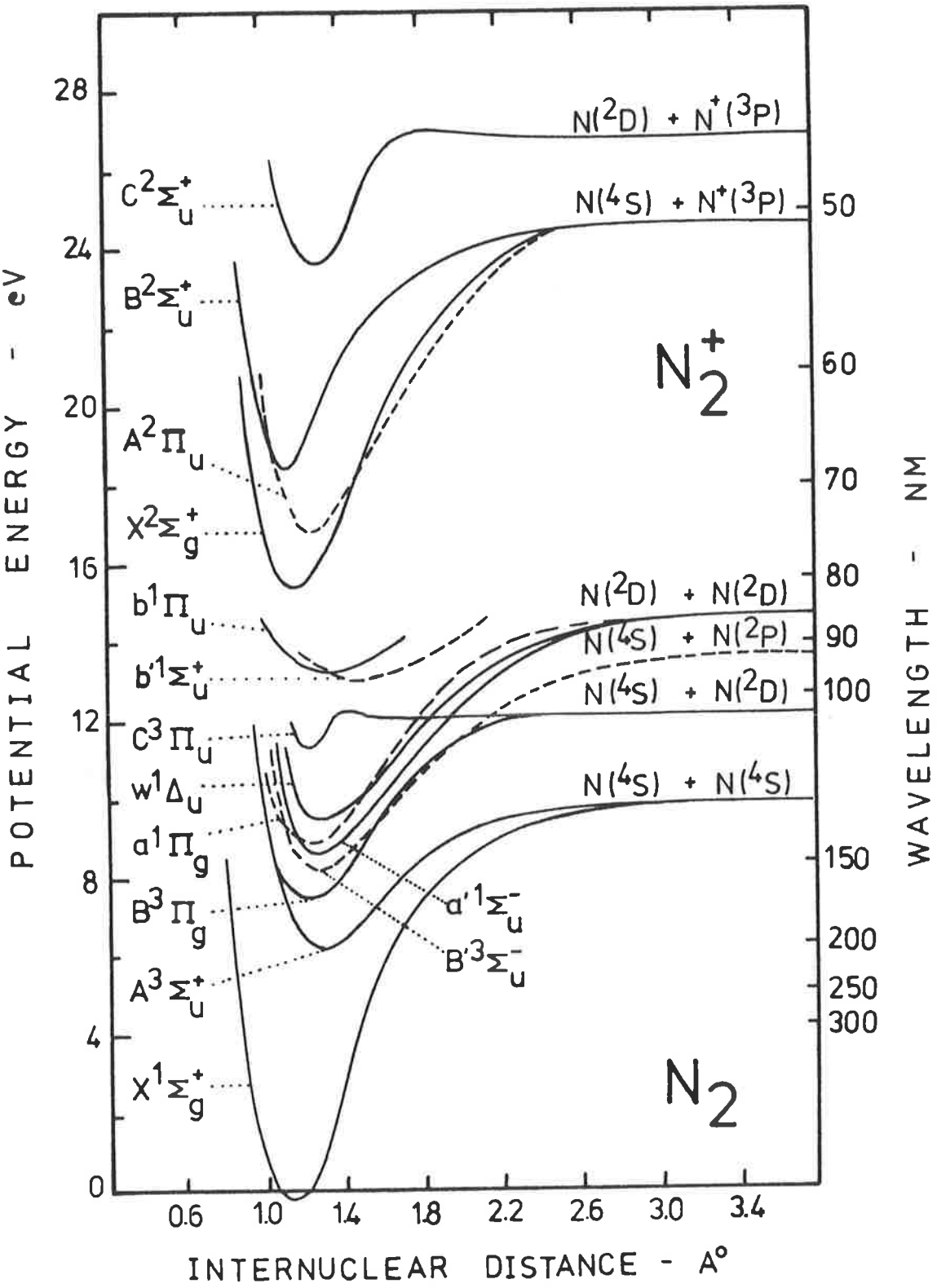

Figure 1.10 Potential curves for N_2.

(Adapted from Gilmore, 1965)

Gurtler *et al*,1977; Peatman *et al*,1978). These states are indicated in Figure 1.10.

With the onset of ionization at 79.6 nm, the many bands between 80 and 66 nm become more diffuse because they are preionized (Cook and Metzger, 1964). From 79.6 nm the continuum rises slowly to 15 Mb at 74.2 nm , which is the threshold for ionization to the $A^2\pi_u$ state of the ion. This gradual rise is different from the abrupt threshold expected for typical ionization continua where there is only a small change in internuclear distance (see Figure 1.4) (Huffman *et al*, 1963). The prominent feature of the absorption spectrum between 74.2 and 66.1 nm is the Hopfield Rydberg series which converges to $B^2\Sigma_u^+$. Beneath these lines the continuum rises, toward shorter wavelengths, from 15 Mb to 30 Mb.

At 66.1 nm, the threshold for $B^2\Sigma_u^+$ ionization, there is an abrupt rise in the continuum cross-section, following which the magnitude remains constant at about 36 Mb, until 58 nm. Beyond 66.1 nm absorption cross-section measurements are complicated by the onset of fluorescence (Cook and Metzger, 1964; Huffman *et al*, 1963) but additional Rydberg states associated with N_2^+ ($B^2\Sigma_u^+$) and N_2^+ ($C^2\Sigma_u^+$) have been identified (Codling, 1966; Lee *et al*, 1973). The structureless character of the absorption spectrum below about 47 nm has been confirmed by a number of workers (Lee *et al*, 1973; De Reilhac and Damany, 1977).

6. Ozone

In contrast to the absorption spectra of both O_2 and N_2 in which, over an extremely small wavelength interval, the cross-section may vary widely, the absorption spectrum of ozone has little dynamic structure and is described by a few well-defined continua with superimposed diffuse bands.

Ozone absorbs radiation over a wide spectral range, from the infrared to the extreme ultraviolet. In the visible region, from 750 to 400 nm, are the diffuse Chappuis bands. Here, the absorption cross-section is low, with a magnitude of 4.7×10^{-3} Mb at the strongest bands, which are located at 602 and 573 nm. The wavelength interval 345 to 300 nm is identified as the Huggins region, and comprises temperature-dependent bands which are also diffuse, but sharper than the Chappuis bands. At 343 nm the absorption cross-section is 1×10^{-3} Mb, increasing to 0.4 Mb at 300 nm. Adjoining the Huggins band system and extending to 200 nm is the strong Hartley band, a broad continuum with a high, almost symmetric peak of magnitude 11.5 Mb located at 255 nm. Overlapping the continuum are weak, diffuse bands which exhibit moderate temperature dependence near 300 nm and which may belong to the Huggins bands (Herzberg, 1966). In the vacuum ultraviolet the absorption spectrum remains continuous, with a few diffuse, overlapping bands. The continuum can be subdivided into six regions, with maxima occurring at 172.5, 145 , 133 , 121.5 , 112 and 75 nm. Toward shorter wavelengths the magnitude of the cross-section increases, from 0.3 Mb at 201.5 nm to 15.6 Mb at 133 nm, and reaches a maximum value of 36 Mb at 75 nm (Tanaka *et al*, 1953; Ogawa and Cook, 1958). Since the ionization threshold is 95 nm, it is possible that the continuum below this is caused by ionization.

Although the shape and magnitude of the ozone absorption spectrum has been well defined experimentally (Inn and Tanaka, 1953; Hearn, 1961; Vigroux, 1969; Griggs, 1968; Simons *et al*, 1973) the theoretical interpretation of the observed absorption properties remains tentative. Only in the past decade have calculations been of adequate

sophistication to generate such useful facilities as potential energy surfaces for the ground and excited states, and to reproduce the intensity distribution of the observed spectrum.

Analytical functions for the potential energy surfaces of electronic states of ozone have been constructed by combining spectroscopic data with quantum mechanics and kinetic data relating to the features of the surface (Sorbie and Murrell, 1975; Murrell *et al*, 1976; Murrell and Farantos, 1977). A potential representation of the ground state is illustrated by the contour diagram in Figure 1.11.

Extensive configuration interaction calculations on the ground state and excited states of ozone, as a function of both bond length and bond angle, have implied the existence of three low-lying excited states of the molecule that are bound with respect to dissociation into the ground states of $O_2 + O$ (Hay and Goddard, 1972; Hay *et al*, 1973; Hay *et al*, 1975). In particular, they concurred that the Hartley band was the transition $^1B_2 \leftarrow 1^1A_1$ and suggested that the Huggins band was just a non-vertical transition to another part of the same potential surface, where the energy was too low for dissociation to $O_2(^1\Delta_g) + O(^1D)$.

An alternate investigation of ozone's electronic states, using a molecular orbital approach, has been reported by Messmer and Salahub (1976). They confirmed the existence of three low-lying excited states, but observed that this technique was inadequate for describing highly excited states.

1.4 UPPER ATMOSPHERE ENERGETICS

The gross feature of the absorption by the upper atmosphere of solar ultraviolet radiant energy is the decrease in solar flux with decreasing altitude. This proceeds at a rate dependent on the local

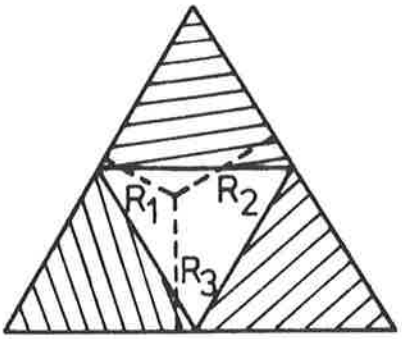

$$X = (2R_2 + R_3)/3^{1/2}$$

$$Y = R_3$$

$$R_1 + R_2 + R_3 = 4.709 A^{\circ}$$

Contour a = -6.25 eV

Contour increment = 0.5 eV

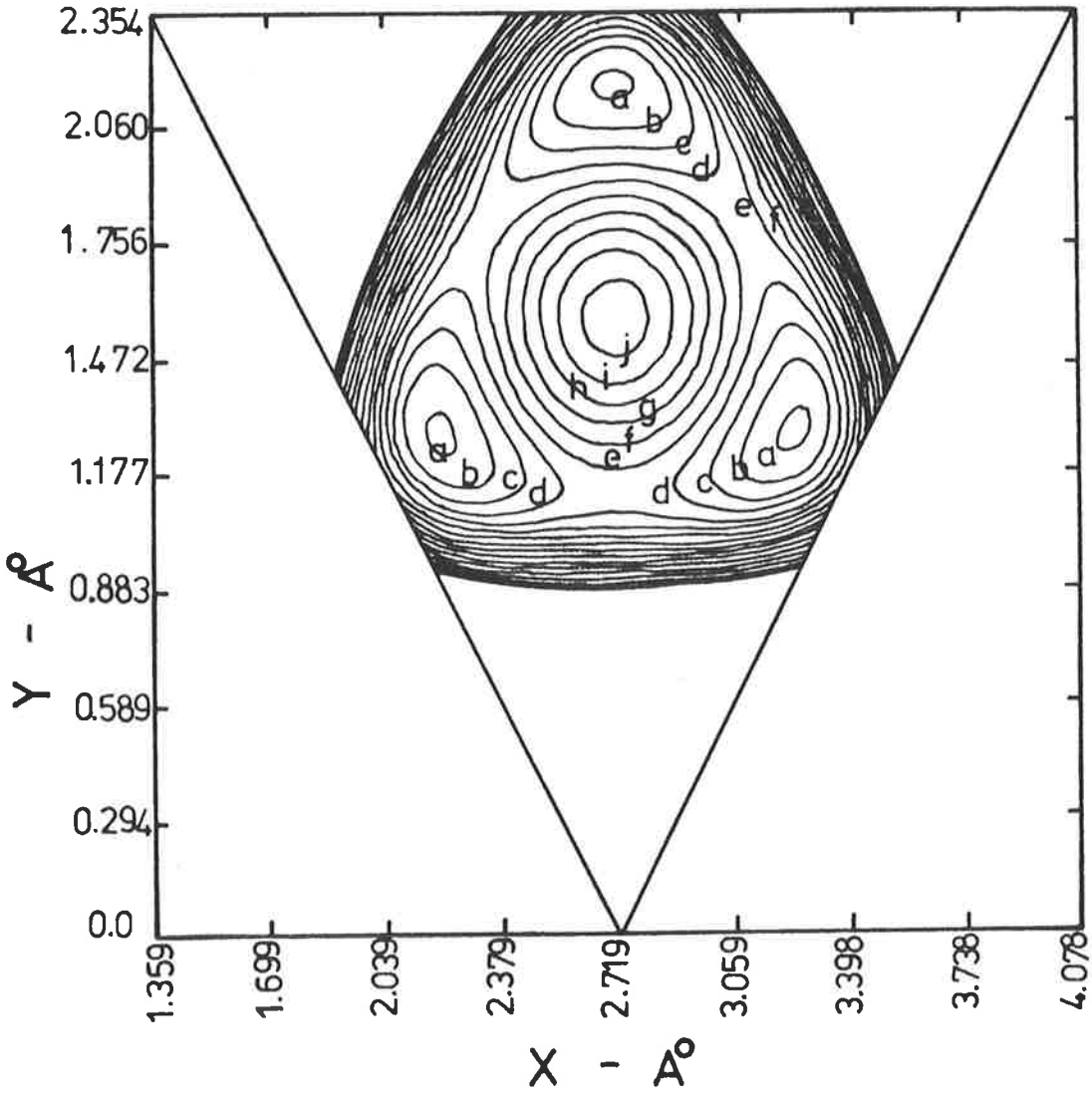

Figure 1.11 Analytical potential function for ozone, ground state. (Murrell et al, 1976)

densities of the species and the magnitude of their absorption cross-sections, and it is this effect which is utilized in absorption spectroscopy for atmospheric diagnostics. Figure 1.12 illustrates the penetration of UV radiation in the upper atmosphere.

However, the consequences of this absorption are fundamentally more complex. Solar ultraviolet energy, deposited in the atmosphere via photoionization and photodissociation of the constituent gases, is partitioned into various channels, thereby initiating a myriad of additional phenomena which define the character of the upper atmosphere. Most of the solar energy is eventually converted to thermal energy through chemical pathways controlled by a complex chain of aeronomic reactions between neutral and ionized atoms and molecules, in different excited states, and also electrons.

Some important aeronomic reactions, which have been discussed in greater detail by Banks and Kockarts (1973), are listed in Table 1.3, and in the following sections the absorption processes and resulting energetics are described for each of the atmospheric regions identified in Figure 1.2. It must be noted that delineation of the atmosphere into these regions, while useful for characterizing the absorption itself, is less satisfactory for discussion of the prominent aeronomic behaviour since in this aspect the integral nature of the entire upper atmosphere is strongly manifested.

a. Thermosphere

It was established in Section 1.3 that EUV radiation is absorbed by photoionization of each of the major thermospheric species N_2, O_2 and O . This occurs over the altitude range 150 to 300 km, with initial attenuation at higher altitudes of wavelengths corresponding to

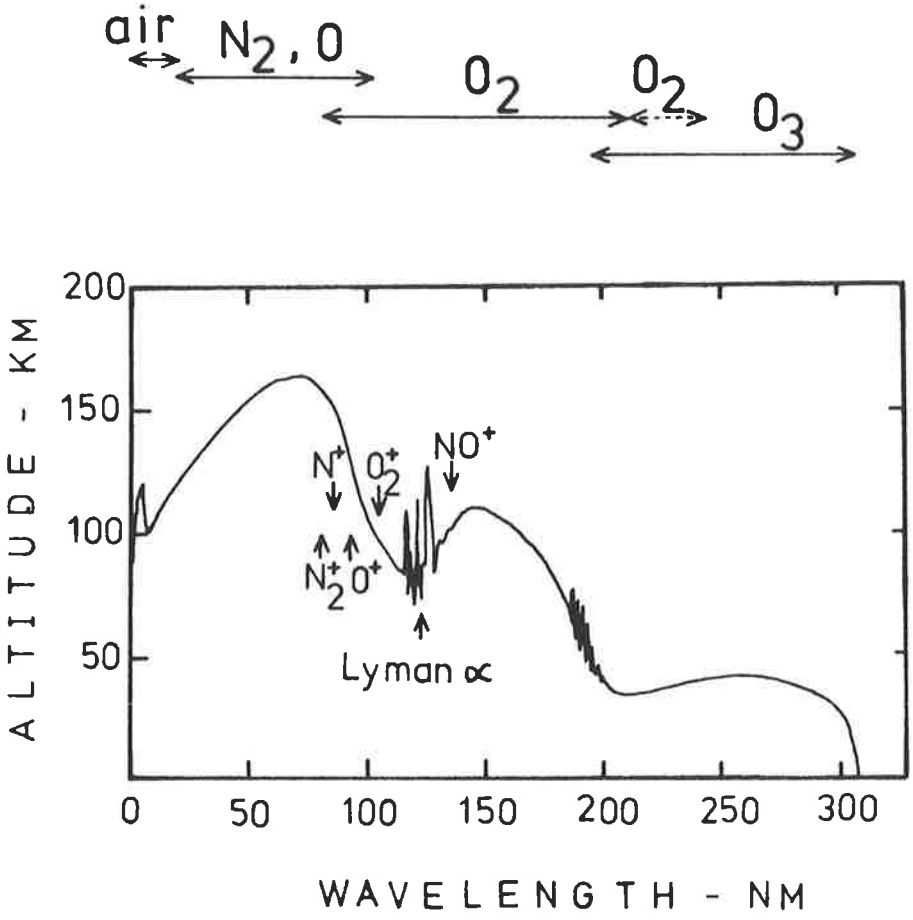

Figure 1.12 Altitude at which the intensity of solar UV radiation drops to $1/e$ of its value outside the earth's atmosphere, for vertical incidence.

(Chamberlain, 1978)

TABLE 1.3 Aeronomic reactions in the upper atmosphere. (Banks and Kockarts, 1973)

1	Photoionization $X + h\nu \rightarrow X^+ + e$
2	Photodissociation $XY + h\nu \rightarrow X + Y$
3	Electron excitation $X + e^* \rightarrow X^* + e$
4	Emission $X^* \rightarrow X + h\nu$
5	Radiative recombination of atoms $X + Y \rightarrow XY + h\nu$
6	Recombination of atoms by three-body collisions $X + Y + M \rightarrow XY + M$
7	Atom interchange $XY + Z \rightarrow XZ + Y$
8	Radiative recombination of atomic ions $e + X^+ \rightarrow X + h\nu$
9	Dissociative recombination of ions $XY^+ + e \rightarrow X + Y$
10	Ion-atom interchange $X^+ + YZ \rightarrow Y + ZX^+$
11	Charge transfer $X^+ + YZ \rightarrow X + YZ^+$
12	Cluster reactions of positive ions
13	Reactions of negative ions

the peaks of the strong N_2 absorption bands, evident in Figure 1.6 between 80 and 100 nm. Far ultraviolet radiation is absorbed predominantly by O_2. Wavelengths between 125 and 175 nm are absorbed in the Schumann-Runge dissociation continuum (Figure 1.7) between 100 and 150 km, but here the oxygen concentration is insufficient to attenuate longer FUV wavelengths for which the absorption cross-section is smaller, and this radiation is transmitted through the thermosphere to the mesosphere. Figure 1.13 depicts schematically how the solar ultraviolet radiation is apportioned by thermospheric processes.

EUV absorption, as initiator of thermospheric energetics and source of thermal energy, has been frequently discussed (Hunt, 1970; Chandra and Sinha, 1973; Stolarski *et al*, 1975; Stolarski, 1976; Kolesnik and Chernyshev, 1978; Chernyshev *et al*, 1978; Torr *et al*, 1980a). Photoionization energy is distributed to the atmosphere approximately equally via an ion, mainly with chemical energy stored in one of its excited states, and a photoelectron, which carries away excess kinetic energy. The final state of the ions O_2^+ and N_2^+ may be any one of the excited ionic states represented by the potential curves in Figures 1.9 and 1.10 respectively.

Photoelectrons lose their kinetic energy locally, to thermal electrons via Coulomb collisions and to the neutral gas via elastic collisions with O, O_2, N_2, NO, H and He, vibrational and rotational excitations of N_2 and O_2, and electron excitation of atomic oxygen to its ^1D, $^3P_1$ and $^3P_0$ states (Chandra and Sinha, 1973). Excited molecular states which may arise from electron excitation of O_2 and N_2 have also been illustrated in Figures 1.9 and 1.10. In addition, photoelectrons with energy in excess of about 12 eV can cause secondary ionization.

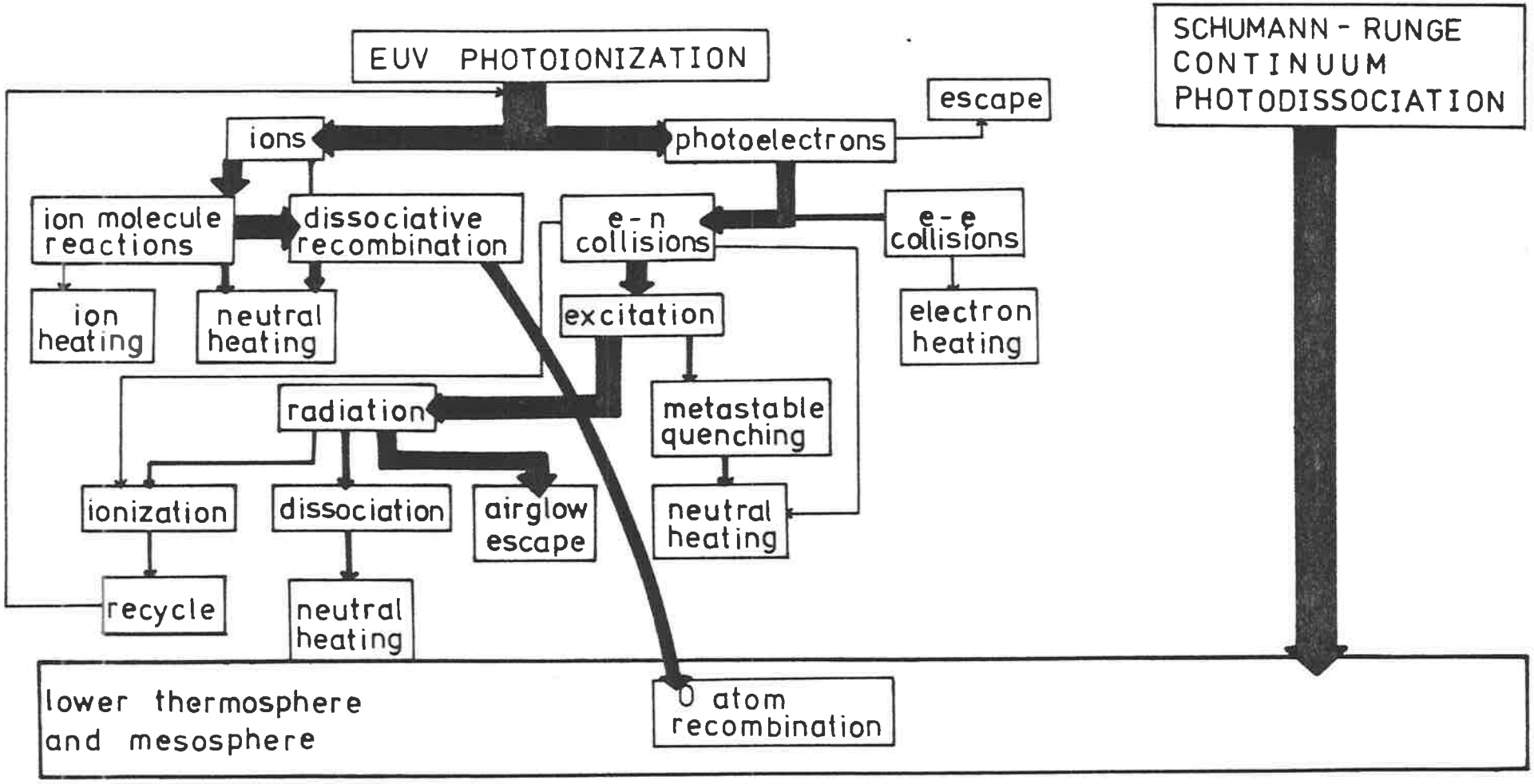

Figure 1.13 Flow of solar ultraviolet energy through the thermosphere. (Adapted from Stolarski et al (1975) and Stolarski (1976))

Ions retain their portion of the solar EUV energy for much longer than do electrons, participating in many ion-neutral reactions which are generally exothermic, the reaction energy appearing either as excitation energy or kinetic energy of the reaction products. Consequently, excited species of both ions and neutrals are abundant in the upper atmosphere, produced as they are by the majority of photochemical reactions in a low pressure environment where quenching is relatively infrequent.

Aspects of the behaviour of excited species in the upper atmosphere have been reviewed by Dalgarno (1970), and more extensively by Vlasov (1976), who has constructed a preliminary model. The net result of excitation is either quenching or airglow emission. Quenching leads directly to neutral gas heating, and has been discussed in detail by Hunten and McElroy (1966) and Zipf (1969). Airglow generally represents energy lost to the atmosphere and may be as much as 40-50% of the incident EUV energy (Stolarski, 1976), although emissions below 175 nm are absorbed. In particular, electron excitation of metastable species at high latitudes is responsible for the aurora. Experimental observations of the spectral distribution, spatial and altitude characteristics and intensities of airglow and aurora radiation provide a useful tool for understanding the physical and chemical processes in the upper atmosphere. Many such investigations have occurred and an example is the global monitoring from satellite of vacuum ultraviolet airglow and aurora reported recently by Huffman *et al* (1980). Figure 1.14 identifies the wavelengths and excited states for prominent airglow emissions.

According to the discussion of Vlasov (1976), the excited species important in the thermosphere include $N(^2D)$, $O(^1D)$, $O(^1S)$ and

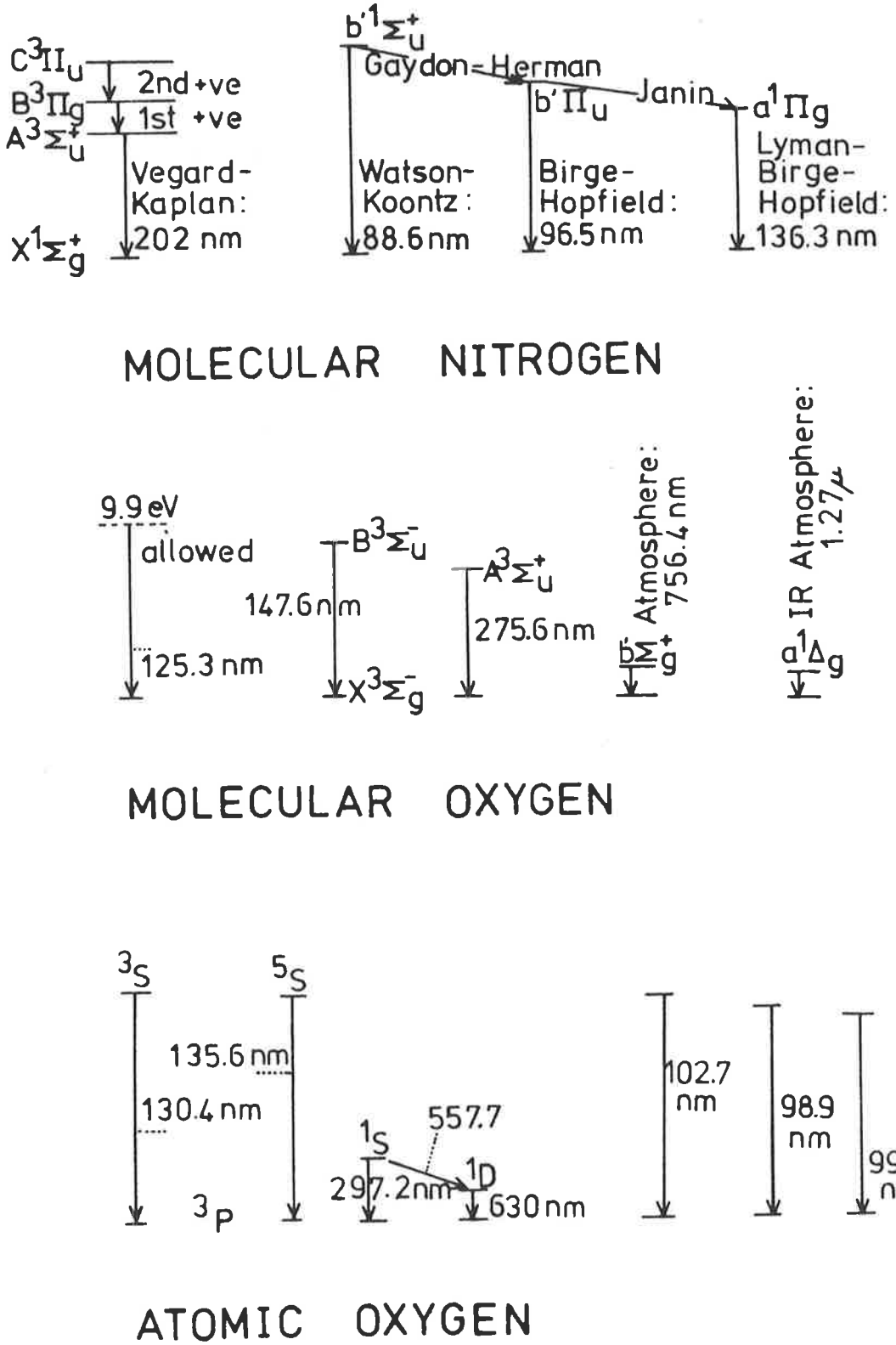

Figure 1.14 Airglow emissions resulting from transitions from excited atomic and molecular energy levels. (Stolarski et al, 1975)

vibrationally excited N_2. The rate constant of the atom interchange reaction

$$N(^2D) + O_2 \rightarrow NO + O(^1D)$$

is four orders of magnitude greater than a similar reaction involving ground state atomic nitrogen and this reaction is a primary source of thermospheric NO, and possibly also of $O(^1D)$ above 150 km (Torr *et al*, 1980b). An understanding of its importance for nitrogen photochemistry in the atmosphere has been promoted by experimental measurements of the emission from $N(^2D)$ at 520 nm (Rusch *et al*, 1975a), from $O(^1D)$ at 630 nm (Rusch *et al*, 1975b) and from the NO gamma and delta bands between 191 and 236 nm (Feldman and Takacs, 1974).

Above about 200 km, $O(^1D)$ is formed by dissociative recombination of O_2^+ and so its height distribution and variation, as well as that of $O(^1S)$, is directly related to the electron density, for which the emission at 630 nm provides a sensitive indicator (Hays *et al*, 1978).

The role of vibrationally excited N_2 in thermospheric photochemistry depends on the degree of excitation. In particular, the ion-atom interchange

$$O^+ + N_2 \rightarrow NO^+ + N$$

is accelerated when N_2 has excess vibrational energy and this has promoted interest in the very efficient quenching of N_2^* by atomic oxygen (Breig *et al*, 1973; McNeal *et al*, 1974).

As well as excited neutral species, there are metastable ions such as $O^+(^2D)$, $O^+(^2P)$ and $O_2^+(a^4\pi_u^+)$ which have very long radiative lifetimes. Above about 200 km the charge exchange reaction

$$O^+(^2D) + N_2 \rightarrow N_2^+ + O$$

provides a source of N_2 ionization additional to photoionization and must be included in the N_2^+ chemical scheme at these higher altitudes (Torr and Torr, 1979; Torr *et al*, 1980c).

Each of the ions N_2^+, O_2^+, NO^+ and O^+ (via ion-atom interchange with N_2) eventually recombines dissociatively, releasing energy and producing the atom fragments N and O in a number of different excited states. In fact, Stolarski (1976) has emphasized that every ionization ultimately results in the dissociation of O_2 into two O atoms. Examples of the sequences illustrating this are provided in Table 1.4.

While N atoms remain in the thermosphere and contribute significantly to the odd nitrogen aspect of its photochemistry (Oran *et al*, 1975; Strobel *et al*, 1976; Ogawa and Kondo, 1977), O atoms, unable to recombine through two body collisions, are transported down to 90 to 100 km where they release their energy in three-body processes.

It is at lower altitudes also that dissociation of O_2 yields additional oxygen atoms $O(^3P)$ and $O(^1D)$, with an associated thermal input to the thermosphere comparable to all other energy sources combined (Chandra and Sinha, 1973). Of the incident FUV solar energy, Torr *et al* (1980a) report that 33% is transported to below 120 km by atomic oxygen. As a consequence of dissociation and transport processes, molecular oxygen below 150 km is neither in photochemical equilibrium (Nicolet and Mange, 1954) or complete diffusive equilibrium (Oran and Strobel, 1976, 1977).

From a quantitative analysis of the reaction pathways in Figure 1.13, it is possible to estimate the efficiency with which the atmosphere converts solar VUV energy to thermal energy. However, there is little agreement between the results of different calculations.

TABLE 1.4 Examples of ionization recombination chains leading to the net dissociation of one O_2 molecule to two O atoms. (Stolarski, 1976)

	$h\nu + O \rightarrow O^+ + e$ (fast)	- 13.6 eV
	$O^+ + N_2 \rightarrow NO^+ + N$	+ 0.9 eV
	$NO^+ + e \rightarrow N + O$	+ 2.7 eV
	$N + O_2 \rightarrow NO + O$	+ 1.3 eV
	$N + NO \rightarrow N_2 + O$	+ 3.6 eV
NET:	$h\nu + O_2 \rightarrow 2O$	- 5.1 eV

	$h\nu + N_2 \rightarrow N_2^+ + e$ (fast)	- 15.6 eV
	$N_2^+ + e \rightarrow N + N$	+ 5.6 eV
	$N + O_2 \rightarrow NO + O$	+ 1.3 eV
	$N + NO \rightarrow N_2 + O$	+ 3.6 eV
NET:	$h\nu + O_2 \rightarrow 2O$	- 5.1 eV

	$h\nu + N_2 \rightarrow N_2^+ + e$ (fast)	- 15.6 eV
	$N_2 + O \rightarrow N_2 + O^+$	+ 2.0 eV
	$O^+ + N_2 \rightarrow NO^+ + N$	+ 0.9 eV
	$NO^+ + e \rightarrow N + O$	+ 2.7 eV
	$N + O_2 \rightarrow NO + O$	+ 1.3 eV
	$N + NO \rightarrow N_2 + O$	+ 3.6 eV
NET :	$h\nu + O_2 \rightarrow 2O$	- 5.1 eV

Chandra and Sinha (1973) reported that the heating efficiency was 0.5 for photoionization and 0.3 for photodissociation. Stolarski *et al* (1975) determined that for photoionization the heating efficiency was approximately constant at 0.33, between 150 and 400 km, but Torr *et al* (1980a) have noted that the heating efficiency for all UV radiation is a strong function of altitude, with a peak value of 0.5 between 160 and 200 km.

Such inconsistencies reflect an incomplete understanding of cumulative thermospheric processes. They are transmitted to other investigations of thermospheric behaviour, such as dynamic modelling (Amayenc *et al*, 1975), where this data is required as input, and provoked examination of the experimental model of the absolute solar fluxes proposed by Hinteregger (1970), which were inconsistent with observed thermospheric temperatures (Roble and Dickinson, 1973), low heating efficiencies (Breig, 1973) and electron-ion recombination rates estimated from measured electron density profiles (Swartz and Nisbet, 1973). The ensuring dilemma about the need to double the solar EUV fluxes (Prasad and Furman, 1974) has been largely resolved in favour of Hinteregger's fluxes for solar minimum conditions. Improved ionospheric models (Roble, 1976; Roble and Schmidtke, 1979) and calculations relating solar flux and ionospheric parameters (Heroux *et al*, 1974; Chakrabarty *et al*, 1977; Oppenheimer *et al*, 1978) imply that for any self consistent examination of thermospheric energetics the variability of the EUV fluxes, which may be a factor of two from solar maximum to solar minimum, must be recognized for its influence on all ionospheric and atmospheric properties. The tentative nature of the overall concepts has been further emphasized by Kockarts (1980) who has suggested that NO emission at 5.3 μm may be cooling process superior to that of atomic oxygen.

b. *Lower Thermosphere and Mesosphere*

Over the altitude range 60 to 100 km solar FUV radiation of wavelengths between 175 and 205 nm is absorbed primarily by O_2 in the Schumann-Runge bands region of its absorption spectrum. Because the Schumann-Runge bands are predissociated, this process is an important source of O atoms for the mesosphere and stratosphere. However, the absorption is temperature dependent, with finer spectral structure than is evident in Figure 1.7, so that it is difficult to obtain accurate spectroscopic values in the laboratory and to perform accurate quantitative atmospheric calculations (Kockarts, 1971, 1976; Nicolet and Peetermans, 1979; Blake, 1979; Nicolet, 1980; Frederick and Hudson, 1980a).

Throughout the mesosphere MUV radiation is absorbed by the O_3 Hartley band, principally in the spectral range 242 to 277 nm, but this process is more important at altitudes below about 60 km where the O_3 concentration is greater.

The coincidence of the wavelength of solar Lyman-alpha radiation with a window in the O_2 absorption spectrum has been previously noted (Section 1.3d). In the mesosphere Lyman-alpha is absorbed by O_2, but, more significantly, it ionizes NO and initiates the formation of the ionospheric D region. Another source of ionization derives from solar flux between 102.7 and 111.8 nm which is transmitted to the mesosphere through windows in the O_2 absorption spectrum (Section 1.3d and Figure 1.7) where, as well as being absorbed by CO_2, it ionizes $O_2(^1\Delta_g)$ (Thomas, 1971). Solar X-rays and EUV radiation less than about 7.5 nm also contribute to ionization in the mesosphere.

As noted in the previous section, there is a net downward flux of atomic oxygen from the thermosphere, and a distinctive feature of the upper atmosphere near 100 km is the emission by $O(^1S)$ at 557.7 nm, as

a consequence of atomic oxygen recombination. The mechanism for this is either the Chapman three body reaction

$$O + O + O \rightarrow O^{*} + O_2$$

or the two stage process suggested by Barth;

$$O + O + M \rightarrow O_2^{*} + M$$

$$O_2^{*} + O \rightarrow O^{*} + O_2$$

While observations by Petitdidier and Teitelbaum (1979) and Misawa *et al* (1980) suggest predominance of the Chapman mechanism, those of Witt *et al* (1979) are more consistent with the Barth mechanism.

The participation of atomic oxygen in mesospheric photochemistry, initially described by Chapman, can be summarized, after Thomas *et al* (1980), as follows:

$$O_2 + h\nu \rightarrow O + O \qquad (h\nu < 242 \text{ nm}) \qquad 1.1$$

$$O + O_2 + M \rightarrow O_3 + M \qquad 1.2$$

$$O_3 + h\nu \rightarrow O + O_2 \qquad 1.3$$

$$O + O + M \rightarrow O_2 + M \qquad 1.4$$

$$O + O_3 \rightarrow 2O_2 \qquad 1.5$$

However, there is a strong photochemical coupling between odd oxygen $(O + O_3)$ and odd hydrogen $(H + OH + HO_2)$ and the latter must also be included in the reaction scheme through the following cycles which act to reduce the ozone concentration;

$$H + O_3 \rightarrow OH + O_2 \qquad 1.6$$

$$OH + O \rightarrow H + O_2 \qquad 1.7$$

$$\text{NET: } O_3 + O \rightarrow 2O_2$$

$$O + OH \rightarrow H + O_2 \qquad 1.8$$

$$H + O_2 + M \rightarrow HO_2 + M \qquad 1.9$$

$$HO_2 + O \rightarrow OH + O_2 \qquad 1.10$$

NET: $O + O \rightarrow O_2$

Odd hydrogen is produced by the photodissociation of water vapour, in the lower thermosphere and mesosphere by Lyman-alpha and in the lower mesosphere by radiation in the Schumann-Runge band spectral region (Strobel, 1972; Frederick and Hudson, 1980b). Another source is the oxidation of water vapour by $O(^1D)$. The sinks of odd hydrogen are the reactions

$$OH + HO_2 \rightarrow H_2O + O_2$$

and

$$H + HO_2 \rightarrow H_2O + O$$

$$H + HO_2 \rightarrow H_2 + O_2$$

Photodissociation of O_3 occurs for all wavelengths less than 1.08 μm but in the mesosphere it is primarily due to radiation in the interval 198 to 312.5 nm, producing $O(^1D)$ and the extremely important, long lived metastable molecular oxygen species $O_2(^1\Delta_g)$. De-activation of $O_2(^1\Delta_g)$ is attributed to

$$O_2(^1\Delta_g) + O_2 \rightarrow O_2(^3\Sigma_g^-) + O_2$$

and also by emission at 1.27 μm. Experimental observations of this dayglow are useful for validating mesospheric photochemical theories (Evans *et al*, 1968; Evans and Llewellyn, 1970; Llewellyn and Witt, 1977).

At nighttime, that the formation of $O_2(^1\Delta_g)$ proceeds via two reactions;

$$O + O + M \rightarrow O_2(^1\Delta_g) + M$$

and

$$H + O_3 \rightarrow OH^* + O_2(^1\Delta_g)$$

is indicated by the results of simultaneous observations of 1.27 μm radiation and the emission in the OH meinel bands (Evans and Llewellyn, 1973; Llewellyn and Solheim, 1978).

Three body atomic oxygen recombination (Reaction 1.4) is also responsible for the production of other molecular oxygen excited states $b^1\Sigma_g^+$ and $A^3\Sigma_u^+$, corresponding to nightglow emissions at 762 nm (Deans *et al*, 1976) and in the Herzberg bands (Llewellyn *et al*, 1979).

The major ions in the lower thermosphere and mesosphere are O_2^+, particularly $O_2^+(^1\Delta_g)$, and NO^+, and the importance of odd nitrogen in these atmospheric regions is in its strong coupling with ionic compounds, rather than in its participation in the neutral reaction scheme of the oxygen and hydrogen species, which however assumes greater significance in the stratosphere. A complete description of the mesosphere and lower thermosphere requires that the chemical reactions and transport of each of the species oxygen, hydrogen, nitrogen, carbon and the ionic compounds be considered simultaneously. Ogawa and Shimazaki (1975) have reported a photochemical-diffusive model consisting of 24 photodissociations, 7 photoionizations, 71 reactions for neutral species and 46 reactions for ion species!

c. *Stratosphere*

Ozone concentration increases sufficiently in the stratosphere (Figure 1.3) for the strong Hartley band of the O_3 absorption spectrum to completely attenuate solar MUV flux. MUV photons at wavelengths shorter than 242 nm are also absorbed by O_2 in its Herzberg continuum (Figure 1.8) but between altitudes 35 and 55 km it is the ozone absorption that facilitates the dominant energy input.

Solar radiation longer than 300 nm is not strongly absorbed by the earth's atmosphere and can undergo scattering by molecules and particles. The spectral range 310 to 400 nm is of particular importance because it contains the dissociation limits of the absorption spectrum of H_2O_2, H_2CO, NO_2, N_2O_5, HNO_2, HNO_3, $ClONO_2$ and HOCl (Nicolet, 1980) so that calculations of the photodissociation rates of all these species must include Rayleigh scattering and albedo effects (Luther and Gelinas, 1976; Mugnai *et al*, 1979).

At wavelengths longer than 310 nm ozone is dissociated in both the Huggins bands and the Chappuis bands and here too atmospheric scattering, especially by aerosols, significantly modifies the vertically incident radiation field, necessitating the use of radiative transfer models for the determination of ozone dissociation (Fiocco *et al*, 1978) and atmospheric heating (Strobel, 1978) in the lower stratosphere and troposphere.

Ultraviolet energy from the sun is available to the stratosphere via the dissociation of ozone but the ensuring photochemistry, defined by numerous temperature dependent reactions, acts to modify and redistribute the initial energy input. Atomic oxygen is the instigator of this photochemistry. Ozone can be produced because the photodissociation of O_2 provides atomic oxygen. Then, Hartley band dissociation of ozone creates additional atomic oxygen, in particular the metastable species $O(^1D)$ which is certainly the most important excited species in the stratosphere (Cvetanović, 1974). Because the transition to the ground state, with emission at 630 nm, is strongly forbidden, the radiative lifetime of $O(^1D)$ is relatively long and de-excitation is primarily by collisions with N_2 and O_2, but also proceeds, to a lesser extent, via a few

aeronomically significant chemical reactions. Below 50 km metastable atomic oxygen is responsible for the formation of the two primary stratospheric radicals; OH from H_2O, CH_4 and H_2, and also NO from N_2O (Nicolet, 1980).

More generally, the primary reactions describing the photochemistry of an oxygen atmosphere are the Reactions 1.1 to 1.5 of the previous section. In the stratosphere, because ozone absorbs solar UV much more strongly than O_2, the interconversion of odd oxygen (Reactions 1.2 and 1.3) proceeds far more rapidly than their formation by Reaction 1.1 or removal by Reaction 1.5. And Reaction 1.4, although important in the mesosphere, is too slow to be of chemical significance in the stratosphere. Thrush (1979) has estimated that the Chapman mechanism (Reactions 1.1 to 1.5) can only account for about 20% of the actual rate of removal of odd oxygen (ozone) in the stratosphere.

Explanation of the observed ozone distribution therefore demands that other chemical schemes for reducing ozone be considered. The odd hydrogen cycle, Reactions 1.6 to 1.10, is the predominant such process in the mesosphere, but in the stratosphere an additional odd hydrogen cycle becomes important (Thomas *et al*, 1980) :

$$OH + O_3 \rightarrow HO_2 + O_2$$

$$HO_2 + O_3 \rightarrow OH + 2O_2$$

Below about 40 km there is insufficient photodissociation of H_2O to produce sufficient odd hydrogen for its effects to remain significant. Instead, odd nitrogen chemistry must be introduced to explain the observed ozone concentrations, viz;

$$NO + O_3 \rightarrow NO_2 + O_2 \qquad 1.11$$

$$NO_2 + O \rightarrow NO + O_2 \qquad 1.12$$

$$\text{NET:} \quad O + O_3 \rightarrow 2O_2$$

Sources of NO, in addition to the oxidation of N_2O by $O(^1D)$, include the photodissociation of NO_2.

Both the Reactions 1.6 and 1.7 for odd hydrogen and 1.11 and 1.12 for odd nitrogen are specific examples of the destruction of ozone by the mechanism (Thrush, 1979)

$$X + O_3 \rightarrow XO + O_2$$

$$XO + O \rightarrow X + O_2$$

$$\text{NET:} \quad O + O_3 \rightarrow 2O_2$$

with X = NO in the stratosphere and X = OH and X = H in the upper stratosphere and mesosphere. Halogens, such as Cl, can also play the role of X.

As well as the specific cycles, described above, which destroy ozone, are numerous additional reactions which describe the participation in stratospheric chemistry of all of the species listed in Table 1.1. The totality of reactions between members of the major families O_x, HO_x, NO_x and ClX is an extremely complex photochemical scheme which has been the subject of many detailed investigations (Hunt, 1966; Crutzen, 1971; Wofsy and McElroy, 1974; Stolarski and Cicerone, 1974; Whitten and Turco, 1974; Herman, 1979). Perhaps the most comprehensive review of stratospheric ozone is that of Nicolet (1975).

Recently, Johnston and Podolske (1978) have assembled the multiple elementary reactions into cycles that either produce odd oxygen, cause a loss of odd oxygen or which have no effect on odd oxygen. Examples of this concept have been provided by Thrush (1979) and the reactions in Table 1.5 illustrate such cycles for NO_x and ClX.

Photochemistry is able to explain the ozone distribution only in the upper stratosphere, above about 35 km, since here the time required

TABLE 1.5 Photochemical cycles for NO_x and ClX in the stratosphere.
(Thrush, 1979)

NO_x	ClX
ozone destruction cycle	
$NO + O_3 = NO_2 + O_2$	$Cl + O_3 = ClO + O_2$
$O + NO_2 = NO + O_2$	$O + ClO = Cl + O_2$
$O + O_3 = O_2 + O_2$	$O + O_3 = O_2 + O_2$
'no effect' cycle	
$NO + O_3 = NO_2 + O_2$	$ClO + NO = Cl + NO_2$
$NO_2 + h\nu = NO + O$	$NO_2 + h\nu = NO + O$
	$Cl + O_3 = ClO + O_2$
$O_3 = O_2 + O$	$O_3 = O_2 + O$
holding cycle	
$HO + NO_2 + M = HONO_2 + M$	$Cl + CH_4 = CH_3 + HCl$
$HNO_3 + h\nu = HO + NO_2$	$HO + HCl = H_2O + Cl$
$HO + HNO_3 = H_2O + NO_3 (\xrightarrow{h\nu} NO_2)$	and also
	$ClO + NO_2 + M = ClONO_2 + M$

to reach photochemical equilibrium is less than one day. Below 20 km this time increases to 20 years (Nicolet, 1975), signifying a complete departure from photochemical equilibrium and the need to invoke transport mechanisms to redistribute the ozone sources and sinks. At intermediate altitudes, 20 to 35 km, the times for transport and ozone photochemistry are comparable and the interaction of the two must be considered. For example, photochemistry dominates the ozone changes in the sub-solar middle stratosphere and transport processes carry the ozone poleward and downward into the troposphere where it is destroyed at the earth's surface (London and Park, 1974). But the initial parameter for any general atmospheric circulation model is the conversion of solar UV energy by heating the ozone layer.

A quantitative description of the stratosphere demands proper treatment of the interactive radiative-chemical-dynamical system and although certain aspects have been successfully modelled, a complete understanding has, as yet, eluded stratospheric investigators.

CHAPTER TWO

DETERMINATION OF THE NEUTRAL COMPOSITION OF THE ATMOSPHERE

2.1 ABSORPTION SPECTROSCOPY TECHNIQUES

When a particular wavelength interval of radiation from the sun, the moon or a star is monitored by a detector carried on a rocket or satellite, the intervening atmosphere acts as an absorption cell. The total number density in the absorption path is the sum of the number densities of each atmospheric gas which exhibits strong absorbing features at these wavelengths. As the detector moves through the atmosphere the amount of absorbing gas changes, and from the intensity profile measured by the detector it is possible to extract the individual number densities if the absorption cross-sections of the gases are known.

The form of analysis necessary to interpret experimental absorption spectroscopy data depends on the resolution of the detector relative to the structure of the solar spectrum and the absorption cross-section spectra of the gases. If the absorption cross-sections are constant across the wavelength interval defined by the detector bandwidth, the relative solar flux distribution within the detector bandwidth remains constant as the integrated solar flux is attenuated by the atmosphere. Otherwise, the more strongly absorbed parts of the spectrum are filtered out and the effective cross-section for the absorbing species exhibits altitude dependence as a consequence of this radiation hardening.

Absorption spectroscopy with broad band rocket borne detectors has been employed for studies of the neutral atmosphere, in particular molecular oxygen and ozone. Such non-dispersive techniques, which monitor

integrated intensities over various regions of the solar spectrum, have been described by Carver *et al* (1967) and Carver (1969). Analysis of the particular case of Lyman-alpha extinction, measured by ion chambers and used for O_2 density determination, has been examined by Hall (1972). Here, it is necessary to allow for changes in the molecular oxygen absorption across the line profile and to account for the possibility of absorption by minor constituents.

Monochromatic absorption of solar EUV radiation has been established as a powerful tool for quantitative thermospheric composition analysis by Hinteregger (1962) who described the determination of O_2, N_2 and O densities above 90 km. The more difficult example of absorption of the solar spectrum by a gas for which the absorption spectrum is highly structured and temperature dependent, consisting of bands superimposed on a continuum, has been investigated by Longmire *et al* (1979). For the case of molecular oxygen absorption in the Schumann-Runge bands, integrated transmittances were used to determine O_2 column densities.

Extension of classical absorption spectroscopy, traditionally applied to rocket borne detectors, to detectors carried on satellites requires occultation techniques to extract the number densities, as established by Hays and Roble (1968) and Roble and Hays (1972) for application to O_2 and O_3 density measurements.

Theoretical formulation of absorption spectroscopy techniques, for specific examples defined by experimental parameters, are given in the following sections.

a. Absorption of Radiation

Solar photon flux of wavelength λ is absorbed by the neutral atmosphere according to the Lambert-Beer law in the form

$$\phi(h, \lambda) = \phi_0(\lambda) \exp [- \tau(h, \lambda)] \qquad 2.1$$

where $\phi(h, \lambda)$ is the transmitted flux of wavelength λ at height h,

$\phi_0(\lambda)$ is the flux of wavelength λ incident on the atmosphere, and

$\tau(h, \lambda)$ is the optical depth.

In a multiconstituent atmosphere, each species contributes to the attenuation of the incident flux in proportion to its absorption cross-section and column density so that the optical depth may be written as

$$\tau(h, \lambda) = \int_h^\infty \sum_i n_i(s) \, \sigma_i(\lambda) \, ds$$

in which $n_i(h)$ is the concentration of constituent i at height h,

$\sigma_i(\lambda)$ is the monochromatic absorption cross-section of type i absorber at wavelength λ and may depend on pressure and temperature, and the integration is taken from the observation altitude h along the optical ray path s.

b. Optical Depth Factor

To evaluate the optical depth it is necessary to determine the content of a column of molecules making an angle χ with the zenith. If χ is not too large ($< 65°$) the atmosphere can be considered to be plane stratified and the column density is different from the vertical column density by a factor $\sec \chi$, since

$$ds = - \sec \chi \, dh \qquad 2.2$$

As the sun moves toward the horizon, the atmospheric column content becomes progressively larger and the $\sec \chi$ factor becomes incorrect since the curvature of the earth makes the column content a complicated function of the solar zenith angle.

Chapman (1931) computed the column content of an exponentially distributed atmospheric constituent along a slant column as

$$\int_h^\infty n(h)dh = n(h)\, H\, Ch(X, \chi_h) \qquad 2.3$$

where $n(h)$ is the concentration of the atmospheric constituent at height h,

χ_h is the solar zenith angle at height h,

H is the scale height,

$X = (r_E + h)/H$, for r_E the earth's radius,

$Ch(X, \chi_h)$ is the Chapman function,

and it is assumed that

$$n(h) = n_0 \exp(- h/H) \qquad 2.4$$

Distinction must be made between the density scale height H_n and the pressure scale height H_p. H_n follows directly from Equation 2.4 viz

$$H_n = - \left[1/n(h) \frac{dn(h)}{dh} \right]^{-1} \qquad 2.5$$

Since, for atmospheric species of mass m at temperature T, the density is related to the pressure by the hydrostatic equation

$$\frac{dP}{dh} = - n(h)\, g\, m$$

and by the Ideal Gas Equation

$$P(h) = n(h)\ k\ T$$

then the pressure scale height is calculated to be

$$H_p = kT/mg \qquad 2.6$$

Only if hydrostatic and thermal equilibrium are assumed can the two scale heights be equated. However, it can be seen that the scale height gradient is approximately a temperature gradient since

$$\frac{dH_p}{dh} = (k/mg)\ \frac{dT}{dh}$$

The assumption of constant scale height, implicit in Chapman's calculations, is not necessarily valid for the terrestrial atmosphere, especially between 100 and 250 km where the temperature is observed to change with altitude (Section 1.2a). Nicolet (1945, 1954) introduced the concept of constant scale height gradients equal to one-half and one in determining the optical depth at large zenith angles for a real atmosphere. He defined a dimensionless parameter F, called the optical depth factor, which reduces to the Chapman function of Equation 2.3 when the scale height gradient is zero.

Approximate analytic functions for use in aeronomic computations have been given by Swider (1964), Fitzmaurice (1964), Weeks and Smith (1968a)and Smith and Smith (1972). Banks and Kockarts (1973) have analyzed the accuracy of each of the approximations. In particular, the optical depth factor for large $\chi < \pi/2$ can be calculated with better than 2% agreement with the Chapman function from the formula given by Fitzmaurice (1964) viz:

$$F(X, \chi) = (\pi\ X/2)^{\frac{1}{2}} \exp\ [(X/2)\cos^2\chi\ ]\ \mathrm{erfc}\ [(X/2)^{\frac{1}{2}}\cos\chi\ ] \qquad 2.7$$

When $\chi \geqslant \pi/2$ the function must be given in terms of the density

and scale height at the minimum altitude, and hence the maximum density, of the grazing solar ray, which is generally not equivalent to the location of the detector. In this case

$$F(Y, \chi) = 2F(Y, \pi/2) - F(X, \pi-\chi) \exp [Y(1 - \operatorname{cosec}\chi)]$$

with Y being the parameter X evaluated at the minimum ray height.

c. *Monochromatic Absorption by a Single Constituent*

If the constituents of a particular region of the atmosphere have absorbing properties such that there is one species i for which

$$\sigma_i(\lambda)\, n_i(h) >> \sum_{j \neq i} \sigma_j(\lambda)\, n_j(h) \qquad 2.8$$

then at height h the monochromatic solar flux will generate a detector signal

$$I(h,\lambda) = I_0(\lambda) \exp \left[- \int_h^\infty \sigma(\lambda)\, n(s)\, ds \right]$$

which can also be expressed as

$$I(h, \lambda) = I_0(\lambda) \exp [- \sigma(\lambda)\, N(h)] \qquad 2.9$$

with $N(h) = \int_h^\infty n(s)ds$

where $N(h)$ is the columnar density of the absorbing species above height h along the path of the radiation. Since, using Equation 2.2,

$$\frac{dN(h)}{dh} = - \sec \chi\, n(h)$$

the differential form of Equation 2.9, for $\chi < 65°$, is

$$\frac{1}{\sec \chi\, I(h, \lambda)} \frac{dI}{dh}(h, \lambda) = \sigma(\lambda)\, n(h) \qquad 2.10$$

where $\sigma(\lambda)$ is the monochromatic absorption cross-section and the product $\sigma(\lambda)n(h)$ has been termed by Hinteregger (1962) the monochromatic extinction coefficient $\mu(h, \lambda)$. When $\chi > 65^{\circ}$ the term $\sec \chi$ must be replaced with the optical depth factor $F(h)$, evaluated according to Equation 2.7 at height h. Since accurate determination of extinction coefficients involves only the linearity of intensity response, there is no requirement for absolute detector calibration.

Of practical importance, for experimental applications, are regions of the absorption spectrum where $\sigma(\lambda)$ is approximately constant over an interval of a few tenths of nanometre. Then, 'sufficiently' monochromatic attenuation can be observed with a monochromator of only modest resolution, which is compatible with the fast scanning speeds needed for adequate height resolution. In the case of a narrow solar emission line, for example, observed by a moderate resolution instrument, the width of the line defines the bandwidth over which the absorption cross-section must remain constant. Such a solar emission line of width $\Delta\lambda_s$, when viewed with a finite resolution spectrometer, produces a triangular line shape (for perfectly matched and aligned entrance and exit slits) of width $\Delta\lambda_1$ called the experimental line width, FWHM. A measure of the total signal due to the line can be found by integrating the detector signal across the line, relative to the background continuum. This total signal is then assumed to be truly monochromatically absorbed.

Once the optical depth factor has been calculated, and the extinction coefficient determined from a plot of flux with altitude, knowledge of the absorption cross-section enables direct determination of the density profile of the absorbing species.

d. Multiconstituent Monochromatic Absorption

When monochromatic, solar radiation, absorbed by more than one

species, is measured with an instrument for which the absorption cross-section of each species is approximately constant over the detector bandwidth, and hence constant with altitude, the attenuation of the detector signal is described by

$$I(h, \lambda) = I_0(\lambda) \exp \left[- \int_h^\infty \sum_i \sigma_i(\lambda)\, n_i(s) ds \right] \qquad 2.11$$

Differentiating and dividing by $I(h, \lambda)$ yields

$$\frac{1}{\sec \chi\, I(h, \lambda)} \frac{dI(h, \lambda)}{dh} = \sum_i \sigma_i(\lambda)\, n_i(h) \qquad 2.12$$

Since the total number density at height h is

$$n_T(h) = \sum_i h_i(h)$$

then

$$\frac{1}{\sec \chi\, I(h, \lambda)} \frac{dI(h, \lambda)}{dh} = \frac{\sum_i \sigma_i(\lambda)\, n_i(h)}{\sum_i n_i(h)} \cdot n_T(h)$$

$$= \bar{\sigma}(h, \lambda)\, n_T(h) \qquad 2.13$$

and $\bar{\sigma}(h, \lambda)$ is called the weighted mean absorption cross-section.

For complete compositional analysis, the minimum number of independent experimental absorption curves required is equal to the number of types of absorbing species. Individual densities can then be extracted by the solution of simultaneous equations.

e. *Broad Band Absorption by a Single Constituent*

If the detector is such that the absorption cross-section of a primary absorber varies across its width, then the measured detector signal is the integral of the attenuated solar flux $\phi(h, \lambda)$ within the detector

bandwidth;

$$I(h) = \int_{\lambda_1}^{\lambda_2} E(\lambda)\ \phi(h, \lambda)\ d\lambda$$

where $E(\lambda)$ is the normalized detector response. So, for a single absorber,

$$I(h) = \int_{\lambda_1}^{\lambda_2} E(\lambda)\ \phi_0(\lambda)\ \exp\left[- \int_{h}^{\infty} \sigma(\lambda) n(s) ds \right] d\lambda \qquad 2.14$$

On differentiating and dividing by $I(h)$

$$\frac{1}{\sec \chi\ I(h)} \frac{dI(h)}{dh} = n(h) \frac{\int_{\lambda_1}^{\lambda_2} \sigma(\lambda) E(\lambda) \phi_0(\lambda)\ \exp\left[- \sigma(\lambda) N(h) \right] d\lambda}{\int_{\lambda_1}^{\lambda_2} E(\lambda) \phi_0(\lambda) \exp\left[- \sigma(\lambda) N(h) \right] d\lambda}$$

$$= \sigma_{EFF}(h)\ n(h) \qquad 2.15$$

where $\sigma_{EFF}(h)$ is called the effective absorption cross-section.

To calculate $\sigma_{EFF}(h)$ it is necessary to know the relative solar flux distribution and the variation of the absorption cross-section with wavelength and with temperature across the detector bandwidth. Any absorption by minor species, which may have significant absorption cross-section values within the wavelength range defined by the detector bandwidth, must be accounted for in this analysis.

Use of this particular absorption spectroscopy technique requires that the spectral response of the detector be determined by laboratory calibration.

6. *Multiconstituent Broad Band Absorption*

The most complicated application of absorption spectroscopy for density determination occurs when the solar flux over a finite wavelength range is absorbed by a number of different gases, each of which is characterized by an absorption cross-section spectrum which varies across the detector bandwidth. In this case, the numerical theory of Section 2.1d and that of 2.1e are combined as follows. At height h the measured detector signal is

$$I(h) = \int_{\lambda_1}^{\lambda_2} E(\lambda)\ \phi(h, \lambda)\ d\lambda \qquad 2.16$$

where $\phi(h, \lambda) = \phi_0(\lambda)\ \exp\left[- \int_h^\infty \sum_i \sigma_i(\lambda)\ n_i(s)\ ds \right]$

so that

$$\frac{1}{\sec \chi\ I(h)} \frac{dI(h)}{dh} = \frac{\int_{\lambda_1}^{\lambda_2} E(\lambda)\ \phi(h, \lambda) \sum_i \sigma_i(\lambda) n_i(h)\ d\lambda}{\int_{\lambda_1}^{\lambda_2} E(\lambda)\ \phi(h, \lambda)\ d\lambda}$$

$$= \frac{\int_{\lambda_1}^{\lambda_2} E(\lambda)\ \phi(h, \lambda)\ \ \overline{\sigma}(h, \lambda)\ n_T(h)\ d\lambda}{\int_{\lambda_1}^{\lambda_2} E(\lambda)\ \phi(h, \lambda)\ d\lambda}$$

$$= \overline{\sigma}_{EFF}\ (h) n_T(h) \qquad 2.17$$

where $\overline{\sigma}_{EFF}(h)$ is the effective weighted mean absorption cross-section. Evaluation of $\overline{\sigma}_{EFF}$ may require time consuming computation so regions of the solar spectrum for which this type of analysis is required are usually least desirable for the application of absorption spectroscopy techniques.

However, because it is important to know how and where all of the solar ultraviolet radiant energy is deposited in the atmosphere, avoidance of this experimental situation is not always possible.

2.2 CALCULATIONS OF ATMOSPHERIC ULTRAVIOLET ABSORPTION

Prior to employing absorption spectroscopy for an experimental investigation of the neutral atmosphere composition, it is necessary to qualitatively estimate the attenuation of solar radiation at altitudes for which the densities are to be measured. Suitable solar wavelength regions can then be chosen such that the attenuation is a maximum in the height region of interest, and experimental parameters such as the zenith angle of the sun, detector spectral response and sensitivity can be co-ordinated to maximize data retrieval.

Generation of monochromatic attenuation profiles requires a model of the distribution of neutral gases in the atmosphere (Section 1.2) and knowledge of their absorption cross-sections (Section 1.3). For simulating the attenuation measured by a broad band detector, the relative solar flux (Section 1.1) and the detector spectral response for the observed wavelength range must also be incorporated in the calculations.

Using the equations developed in Section 2.1, calculations of attenuation by the atmosphere are described for three different wavelength regions of the solar spectrum, the EUV, FUV and MUV, to illustrate the typically expected results of various experimental applications of atmospheric absorption spectroscopy.

a. Thermospheric Absorption of EUV Radiation

When solar EUV wavelengths are observed by an instrument with sufficient resolution for the attenuation to be monochromatic, the ratio of

the signal $I(h,\lambda)$ at height h to the signal at the top of the absorbing atmosphere $I_0(\lambda)$ can be calculated from Equation 2.11;

$$\frac{I(h, \lambda)}{I_0(\lambda)} = \exp \left[- \sum_i \sigma_i(\lambda) \, N_i(h) \right]$$

Attenuation of four wavelengths, as illustrated in Figure 2.1, for a radiant source at two different zenith angles, was calculated using absorption cross-sections from Stolarski and Johnson (1972) and the U.S. Standard Atmosphere, 1976 thermospheric densities, as given in Figure 1.2. From this composition model, vertical column densities were calculated at height h by numerical integration using Simpson's rule over 5 km intervals, up to 600 km. Then, for zenith angle χ, the quantity $N_i(h)$ was determined by the product of $\sec \chi$ and the vertical column density at height h.

In some regions of the EUV, when using an instrument of only moderate resolution, it may be necessary to employ Equation 2.16 for attenuation calculations. As an example, for radiation at 87 nm, observed with a monochromator with FWHM = 0.4 nm, the attenuation was determined by integration from $\lambda_1 = 86.5$ nm to $\lambda_2 = 87.5$ nm, performed numerically using Simpson's rule over 0.005 nm intervals. Appropriate values of the Lyman continuum solar flux (Donnelly and Pope, 1973), absorption cross-sections for O_2 and N_2 (Cook and Metzger, 1964) and for O (Stolarski and Johnson, 1972) and detector response, assumed to be Gaussian, are plotted together in Figure 2.2 for this wavelength interval. In Figure 2.3 the calculated values of the broad band attenuation and the effective weighted mean absorption cross-section are compared with the monochromatic attenuation at 87 nm, from Figure 2.1, and also the weighted mean

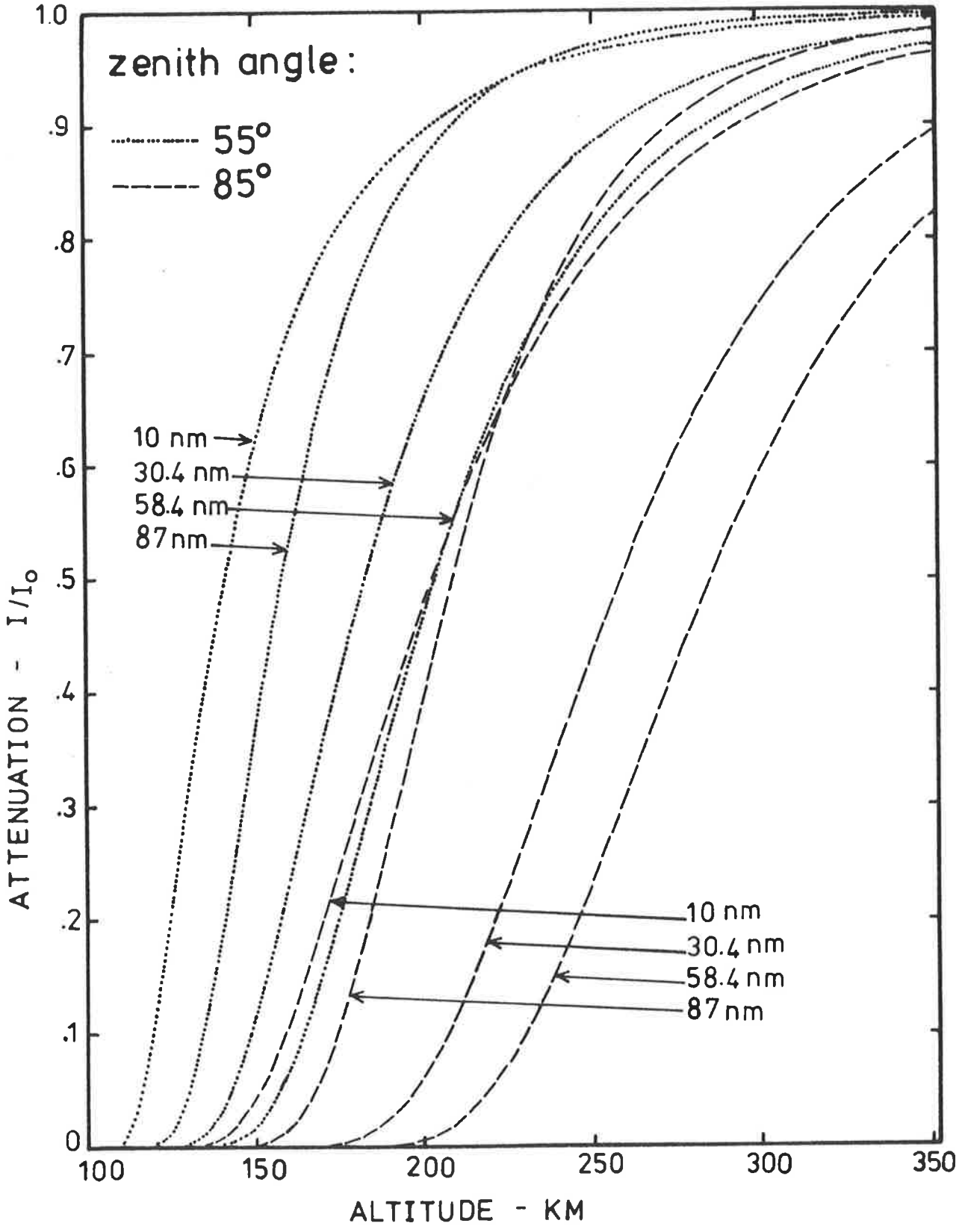

Figure 2.1 Calculated monochromatic attenuation in the EUV.

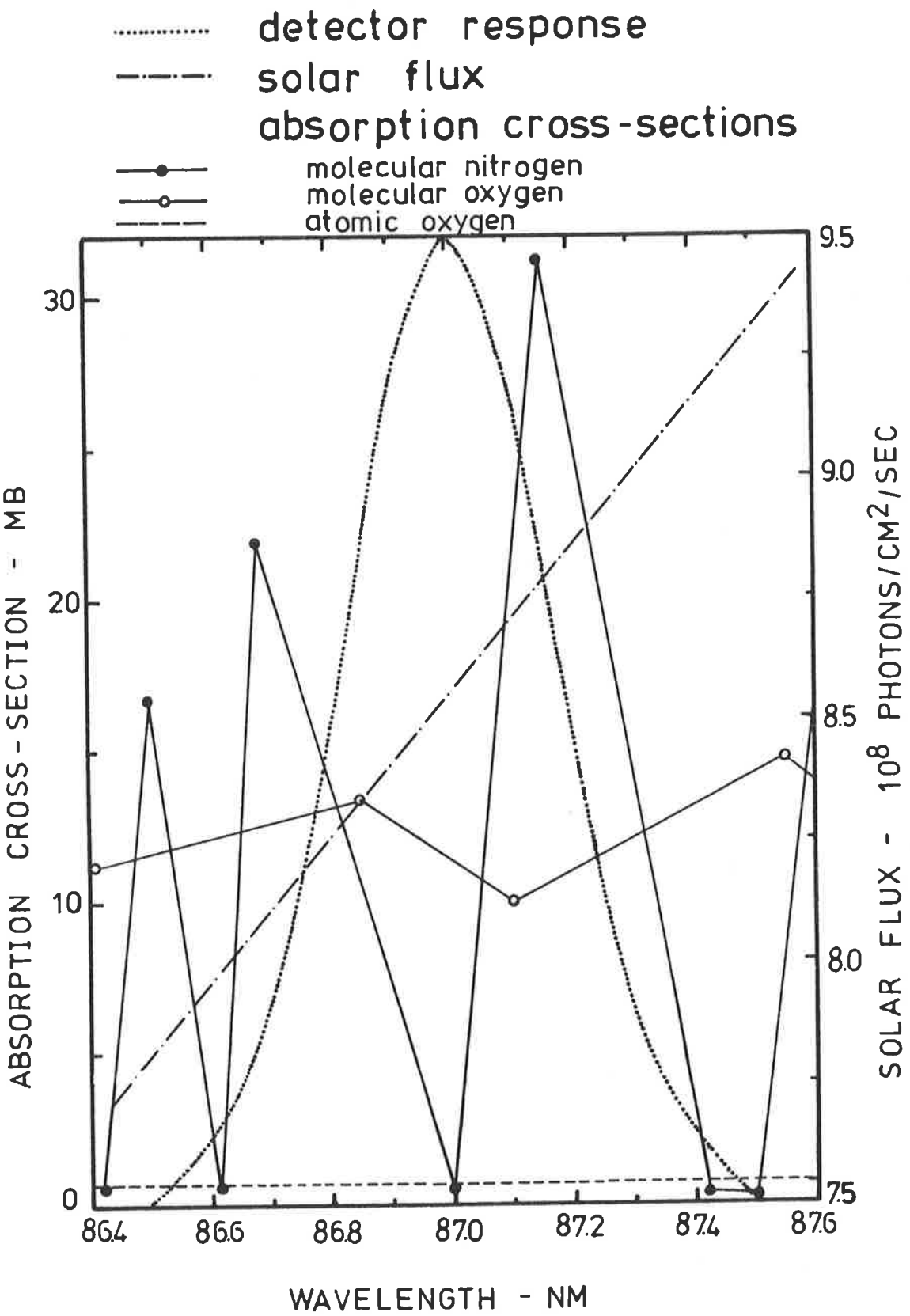

Figure 2.2 Parameters for broad band calculations at 87 nm.

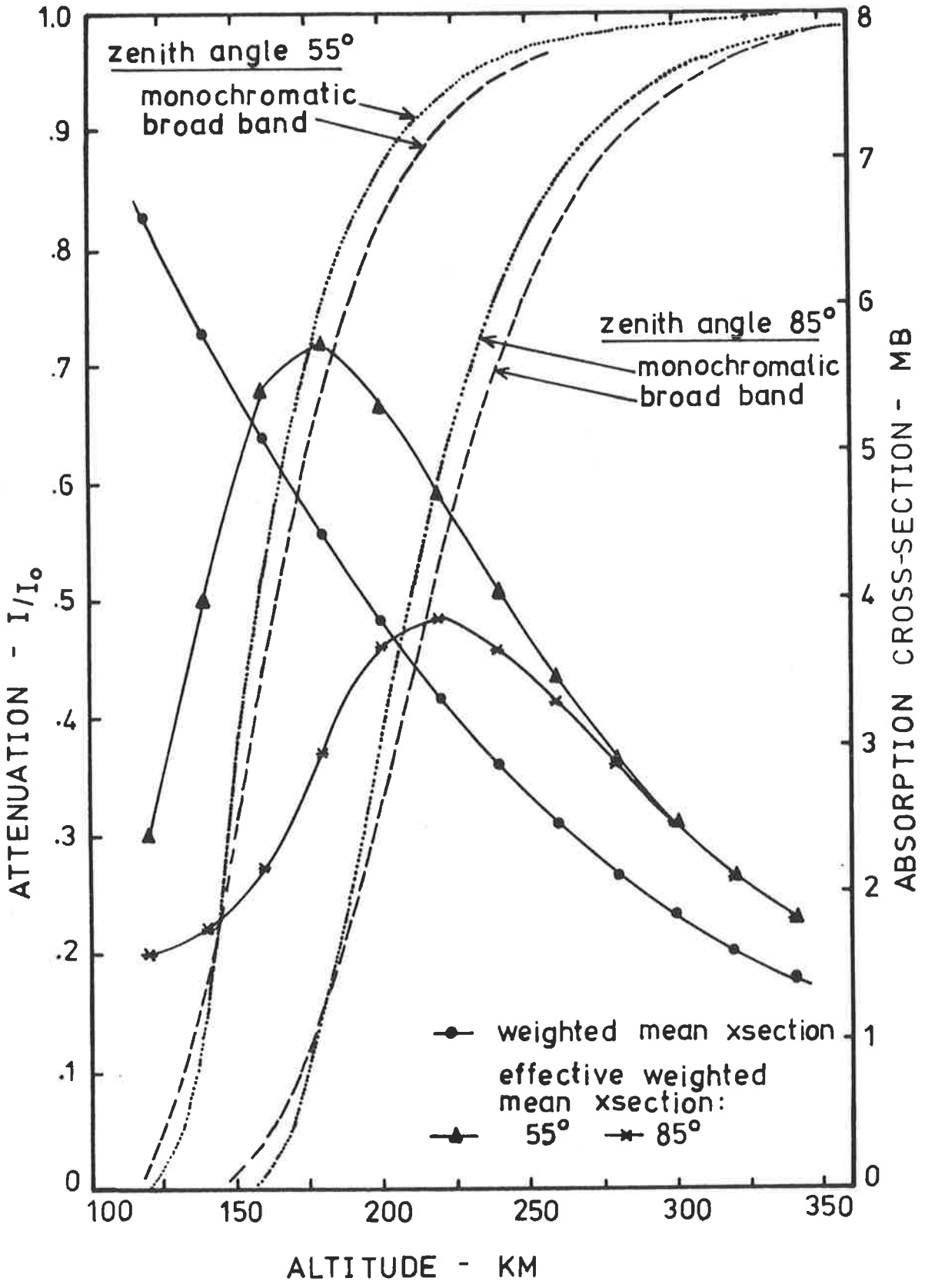

Figure 2.3 Calculated attenuation at 87 nm.

absorption cross-section.

b. *Absorption of FUV Radiation in the Schumann-Runge Continuum of O_2*

Since O_2 is the primary absorber of FUV radiation between 140 and 175 nm, monochromatic attenuation curves can be easily calculated from Equation 2.9 ;

$$\frac{I(h,\lambda)}{I_0(\lambda)} = \exp\ [\ -\ \sigma(\lambda)\ N(h)\ ]$$

Using column densities N(h) derived from the U.S. Standard Atmosphere, 1976, with two different zenith angles, and O_2 absorption cross-sections from Blake *et al* (1966) produced the profiles of Figure 2.4.

c. *Ozone Absorption of MUV Radiation in the Stratosphere and Mesosphere*

MUV radiation above 240 nm, where absorption by O_2 in the Herzberg continuum becomes negligible, is absorbed primarily in the strong Hartley band of ozone. Altitude profiles due to this absorption, measured by a broad band detector, were generated according to Equation 2.14 and are illustrated in Figure 2.5. Incorporated in these calculations were the solar flux model of Donnelly and Pope (1973), ozone densities from the empirical model of Krueger and Minzner (1976) and absorption cross-section values from Inn and Tanaka (1959). Effective absorption cross-sections were computed at two different wavelengths by numerical integration over the bandwidth of a detector whose response was assumed to be Gaussian with 10 nm FWHM. Figure 2.5 compares broad band and monochromatic calculations of attenuation of MUV radiation.

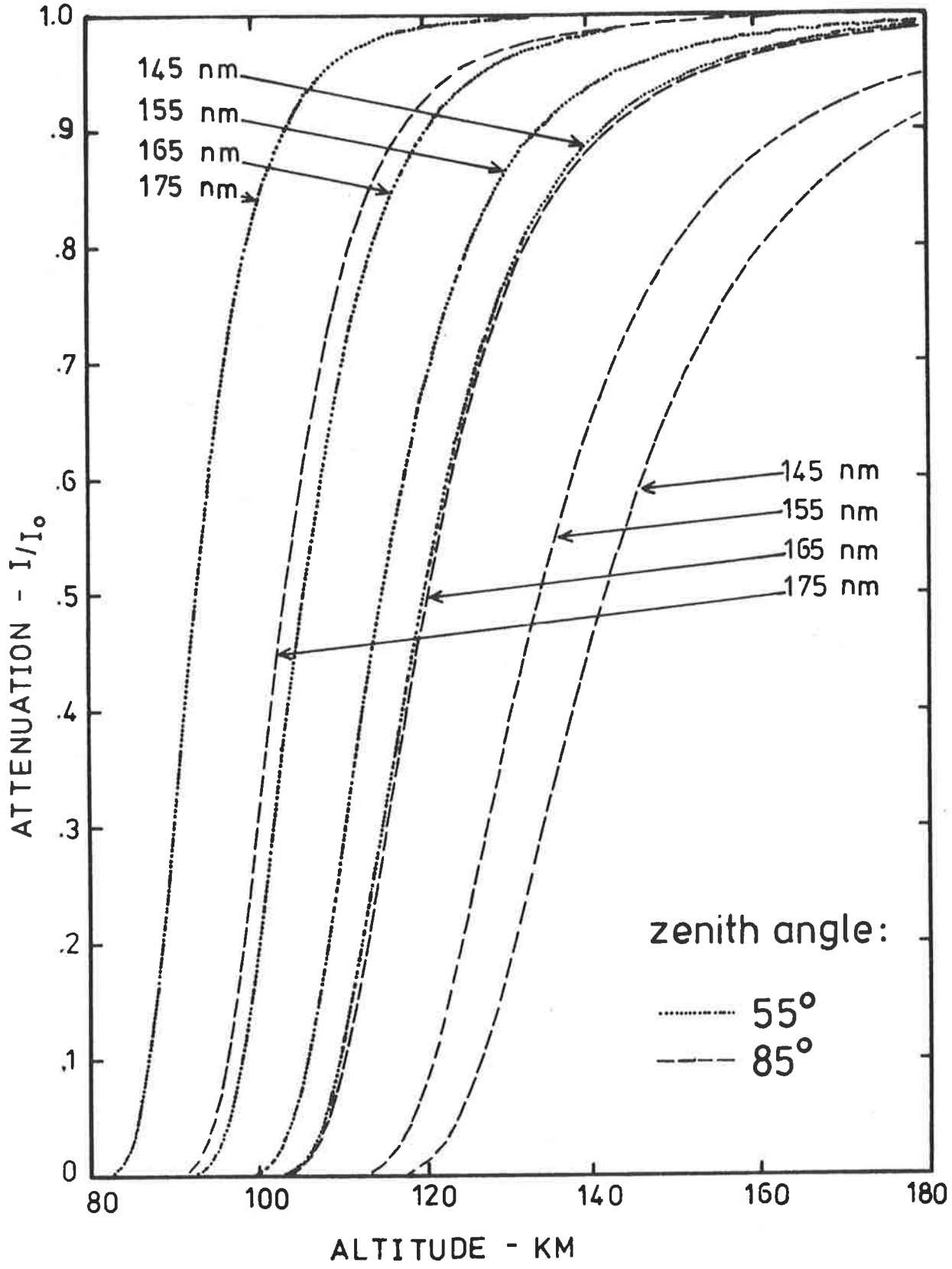

Figure 2.4 Calculated monochromatic attenuation in the FUV.

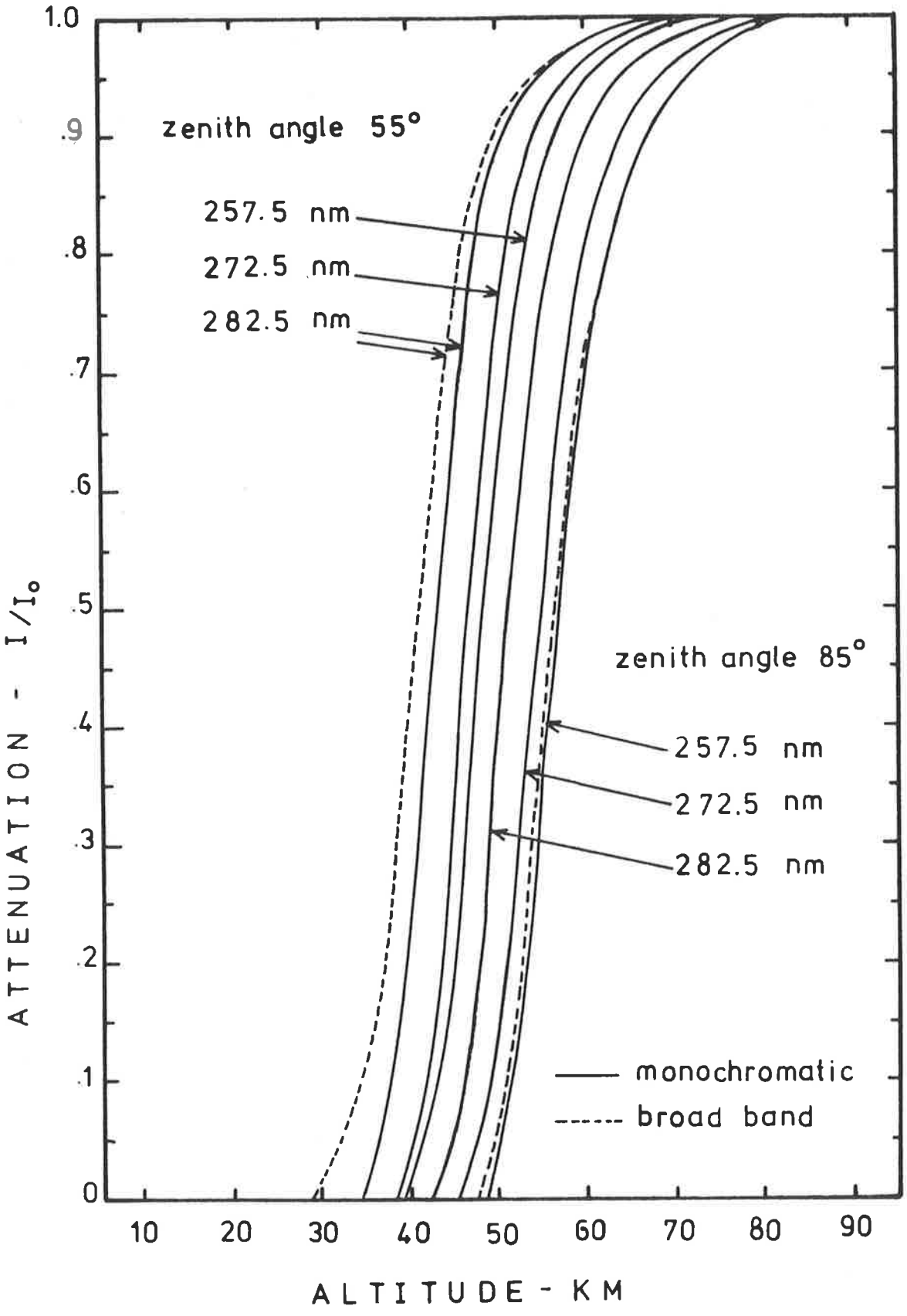

Figure 2.5 Calculated attenuation in the MUV.

2.3 REVIEW OF EXPERIMENTAL APPLICATIONS OF ULTRAVIOLET ABSORPTION SPECTROSCOPY

a. Extreme Ultraviolet Radiation

Radiation below 91.1 nm is absorbed in the lower thermosphere by O_2, O and N_2. In principle, determination of the concentrations of each of these species, by atmospheric absorption spectroscopy, requires attenuation measurements at three separate wavelengths and solution of the resultant set of simultaneous equations.

Casual acquaintance with the procedures developed in Sections 2.1d and 2.1f implies that such an exercise, while certainly not trivial, is reasonably straightforward. However, a myriad of experimental difficulties have meant that the technique has not yet been developed to provide reliable atmospheric compositional analysis, despite the integral nature of extreme ultraviolet absorption data for a multitude of atmospheric calculations. This is fundamentally because the character of the absorption cross-sections at these wavelengths necessitates the use of high spectral resolution optics, both in the laboratory where the cross-sections are measured and for monitoring atmospheric extinction from rockets and satellites.

The most suitable instrument for EUV absorption spectroscopy is one that disperses incident solar radiation into a number of monochromatic wavelength intervals which can each be detected at different altitudes. This involves the use of a grating, usually with grazing incidence optics, and thus a vehicle with attitude control. The technology associated with such an instrument, and its physical applications, have been discussed in detail by Hinteregger (1961).

Monochromators for EUV absorption experiments have had, typically, only moderate resolution (.1 - 1 nm) and while this appears sufficient for analysis at wavelengths such as 30.4 and 58.4 nm, where the absorption cross-sections are relatively well determined and constant over spectral

passbands of that order, their application at wavelengths such as 79 and 833 - 835 nm is more complicated. Here, as evident in Figure 1.6, the cross-sections are highly structured and, when observed with instruments of only moderate resolution, exhibit altitude dependence because of radiation hardening within the finite passband. Even at the most appropriate extreme ultraviolet wavelengths, compositional analysis is precluded unless the absorption cross-sections are sufficiently different to enable the contribution to the extinction by each species to be determined.

EUV atmospheric absorption spectroscopy was pioneered by Hinteregger and co-workers at the U.S.A. Air Force Cambridge Research Laboratories, using rocket borne monochromators that scanned almost the entire EUV spectrum - from 25 to 130 nm. (Hinteregger *et al*, 1960; Hall, Damon and Hinteregger, 1963; Hall, Schweizer and Hinteregger, 1963; Hinteregger *et al*, 1965). Data from these experiments implied that atomic oxygen, rather than molecular nitrogen, was the dominant atmospheric absorber at 200 km. From observations of extinction at nine appropriate EUV wavelengths, Hall *et al* (1965) derived thermospheric densities between 150 and 220 km. Absorption cross-sections were chosen from the available laboratory measurements to provide densities at 200 km that were consistent with the assumption of diffusive equilibrium. Diurnal variation investigated with this technique appeared to be of the same order as the uncertainties; 25% (Hall *et al*, 1967).

Detailed analysis of EUV absorption at 30.4, 58.4 and 102.6 nm was included in an experimental study of the daytime ionosphere by Timothy *et al* (1972). Neutral densities between 100 and 270 km were determined with an accuracy of 30%. In addition, the extinction profiles from a scanning spectrometer provided the basis for an estimate of primary ion and photoelectron production rates.

Currently, the usefulness of EUV absorption data emphasizes the measurement of atomic oxygen absorption cross-sections via solar occultation (Hinteregger and Hall, 1969; Knight *et al*, 1972). Above about 250 km the atmosphere is 95% atomic oxygen so that this experimental technique is one of the most reliable, to date, for acquiring these values. Absorption cross-sections for both atomic oxygen and molecular nitrogen have been reported from sunrise and sunset occultation experiments (Modali *et al*, 1976). A simultaneous investigation of the N_2 and O densities from 250 to 500 km revealed that measurements at sunset exhibited far less scatter than those at sunrise, and this was attributed to the complex nature of the earth's atmosphere while heating. EUV absorption measurements at sufficiently high altitudes, above about 280 km where the O_2 absorption is not important, have also been reported by Hinteregger and Chaikin (1977) and Schmidtke *et al* (1975).

Reliable interpretation of atmospheric extreme ultraviolet absorption depends on the availability of high resolution absorption cross-section data, ideally measured at temperatures and pressures characteristic of the upper atmosphere and using radiation simulating that from the sun. Any EUV laboratory measurement is difficult (Section 1.3b), even without the additional stringent requirements of the aeronomer, but EUV absorption cannot be ignored.

b. *Hydrogen Lyman-alpha Radiation*

Because the hydrogen Lyman-alpha emission is absorbed in the mesosphere, primarily by molecular oxygen, many experimenters have considered it to be eminently suitable for absorption spectroscopic determination of O_2 densities between altitudes 70 and 100 km. In most experiments, the attenuation of the line is monitored, from a rocket or satellite, with a

lithium fluoride-nitric oxide ion chamber (Carver and Mitchell, 1964) which is sensitive over the wavelength range 105 to 135 nm.

Inherent, however, in this apparently simple technique, is a network of complications. For the solar spectrum, only 90% of radiation within the passband of the ion chamber is due to Lyman-alpha and measurements are usually restricted to below 100 km to allow the natural filtering of the O_2 absorption cross-section window (Figure 1.7) to remove contaminating radiation from the wings. The effect of other mesospheric absorbers of Lyman-alpha, in particular N_2, H_2O, CO_2 and NO, is not negligible and may be as much as 5% (Smith and Miller, 1974) to 7% (Prinz and Brueckner, 1977). In addition, the O_2 absorption cross-section has been measured to vary across the width of the line (Ogawa, 1968; Carver *et al*, 1977a) and is also temperature dependent (Carver *et al*, 1977a), while the spectral shape of the line itself may vary with solar conditions (Vidal-Madjar, 1975).

Initial applications of Lyman-alpha absorption spectroscopy (Carver *et al*, 1964; Weeks and Smith, 1968a; Lockey *et al*, 1969; Subbaraya *et al*, 1972; Brannon and Hoffman, 1971) employed a constant absorption cross-section and ignored any contribution of absorbers other than O_2 to the attenuation. Mesospheric oxygen densities so obtained exhibited great variability which was considered to be of diurnal, seasonal and latitudinal origin (Carver, 1969). While the number of measurements was inadequate for establishing definite correlations, it did appear that seasonal differences below 90 km were paralleled by variations of the total neutral atmosphere (Weeks and Smith, 1968a; Carver *et al*, 1969).

To improve the accuracy of Lyman-alpha absorption measurements required a detailed calculation of the height dependence of the effective

absorption cross-section of the detector (Quessette, 1970; Hall, 1972) using, for example, the absorption cross-section profile of Ogawa (1968) and the spectral profile of Purcell and Tousey (1960). Additionally, a small qualitative correction for other absorbers was suggested (Hall, 1972).

Subsequent measurements adopted these recommendations and the general character of mesospheric oxygen that emerged is as follows. The densities are highly variable, they may exhibit structure between 70 and 90 km (Subbaraya *et al*, 1974; Weeks, 1975a)and are mostly always less than the models at lower altitudes, for example, by as much as 30% at 70 km (Hall, 1972). At the equator the height of the mesopause is lower than at higher latitudes (Subbaraya *et al*, 1974), while in the southern hemisphere densities may be lower by 10% to 30% (Ilyas, 1974). During spring the densities are lower than other seasons, both in the southern hemisphere (Ilyas, 1974) and the northern hemisphere (Weeks, 1975a) which is opposite to the trend predicted by CIRA 1972.

Measurements of O_2 densities by Lyman-alpha absorption between 70 and 90 km have been made simultaneously with independent measurements of the total neutral density (Smith and Miller, 1974). Comparison of the ratio of both results with that predicted by CIRA 1965 indicated that the absorption technique predicted densities which were too low by about 20%. This was attributed to the inappropriateness of laboratory cross-section measurements for temperatures and pressure encountered in the atmosphere. The need for temperature dependent Lyman-alpha absorption cross-sections was echoed by Weeks (1975a) in a detailed discussion and error evaluation of the technique.

The temperature dependence of Lyman-alpha absorption by molecular oxygen, as measured by Carver *et al* (1977a), provided confirmation that at 194 K there is a 20% reduction in the magnitude of the cross-section.

Data from 34 rocket flights have since been re-analyzed to include this dependence (Carver *et al*, 1977b) and the resultant observational mean density was reported to be 20% higher than that of CIRA 1972 at 70 km and 9% higher at 90 km. Measurements over a twelve year period from Woomera were generally consistent and indicated only a small seasonal variation. In contrast, measurements of mesospheric molecular oxygen in the mid-latitude northern hemisphere, also derived from Lyman-alpha absorption incorporating the temperature dependent cross-sections of Carver *et al* (1977a), have indicated a marked seasonal variation in which the density at 70 km in summer is about twice that during winter (Williams, 1980).

For Lyman-alpha absorption spectroscopy the remaining question is that of other absorbers, with its legacy of additional 6% errors. This will remain unanswered until reliable values for the absorption cross-section and atmospheric concentration are available for each minor constituent in the mesosphere.

c. *Far Ultraviolet Radiation*

From absorption of wavelengths 140 to 175 nm, molecular oxygen densities can be reliably determined between 100 and 170 km. Atmospheric absorption spectroscopy is intrinsically less complicated here than in the mesosphere because oxygen is the primary absorber of this far ultraviolet radiation and the strong Schumann-Runge continuum varies only slowly with wavelength (Figure 1.7).

In particular, across the bandwidth of sapphire xylene ion chambers (SX : 142 to 147 nm) the cross-section is virtually constant at its maximum value. Quartz-triethylamine ion chambers (QT : 157 to 168 nm) also exhibit suitable spectral characteristics for far ultraviolet absorption spectroscopy (Carver *et al*, 1969).

Unfortunately, the sensitivity of ion chambers has been observed to change during the first few minutes of flight (Wildman *et al*, 1969) so that measurements during flight downleg are generally more reliable than during ascent. This effect has been attributed to dissociation of the gas and temperature changes of the window when the ion chambers are first exposed to ultraviolet radiation (Carver and Mitchell, 1967).

Ion chambers on satellites (Parker and Stewart, 1972; May, 1973) have been used for sunrise and sunset occultation to establish the general nature of O_2 variability at 180 km. Both experimenters confirmed the dependence of thermospheric molecular oxygen on geomagnetic activity, the effect being stronger at high latitudes. However, a quantitative correlation was difficult because the observed variations were not clearly represented by the K_p index, even with a 3-hour delay. Sunrise densities were reported to be higher than those at sunset by 16% to 20%, although for the air density, and also oxygen between 107 and 118 km (Carver *et al*, 1978a) this trend is reversed.

Subsequent measurements from satellites (Norton and Roble, 1974) and rockets (Weeks, 1975b; Higgins and Heroux, 1977; Carver *et al*, 1978a) have verified the connection between O_2 densities and geomagnetic activity but are inconclusive about its magnitude and definition. Weeks (1975b) has observed the densities between 135 and 180 km increase twofold following an increase in K_p from 2.2 to 5.8. Other observations, during more moderate excursions of K_p (1 to 4) have reported less drastic density changes. At 150 km Carver *et al* (1978a) noted an enhancement of 1.5 but Higgins and Heroux (1977) reported no change, although over limited altitude regions between 110 and 170 km they conceded possible increases of 10%, consistent with satellite observations (Parker and Stewart, 1972; May, 1973). The effect of geomagnetic activity on oxygen densities in the lower

thermosphere appears to be altitude-dependent, and may exhibit wave structure (Weeks, 1975b). Rocket observations, rather than satellite measurements which have limited height resolution, are needed for further investigations.

While broad band detectors have been extensively used for far ultraviolet absorption spectroscopy, only a few monochromatic measurements of the attenuated solar flux have been reported (Jursa *et al*, 1963; Jursa *et al* 1965; Ackerman *et al*, 1974; Brueckner *et al*, 1974; Garriott *et al*, 1977; Longmire *et al*, 1979). The dearth of such measurements at Schumann-Runge continuum wavelengths is reflective of the relative cost and complexity of dispersive instruments, rather than their unsuitability.

Use of the technique with radiation sources other than the sun is difficult and has occurred infrequently. Nighttime oxygen densities, which appear to be the same as daytime densities, have been derived from stellar absorption (Opal and Moos, 1969; Hays and Roble, 1973b) while observation of an aurora (Opal *et al*, 1970) has indicated that at high latitudes the winter oxygen density near 115 km might be a factor of 2 greater than at temperate latitudes.

Absolute molecular oxygen densities are, it is generally concluded, overestimated by Jacchia's 1971 model, especially at higher altitudes. At 180 km the model is high by 35% to 50% (Weeks, 1975b: Parker and Stewart, 1972; Ackerman *et al*, 1974; Higgins and Heroux, 1977) and this is attributed to the inability of the model to account for dissociation at these altitudes, and possibly to high thermospheric temperatures used by the model.

d. Middle Ultraviolet Radiation

Measurements of the atmospheric attenuation of MUV radiation from sources such as the sun, the moon, a star or airglow, have been

extensively employed to determine ozone densities.

For this purpose, broad band detectors have been carried on rockets and satellites in a variety of experimental configurations.

Daytime ozone densities can be derived from solar absorption spectroscopy over a typical altitude range of 20 to 60 km with an accuracy of 10%-20%. Since 1965, Krueger (1969a,1973) has conducted regular ozone soundings with a four channel filter wheel photometer which descends through the stratosphere, suspended below a high altitude parachute. The optical entrance of this detector is a planar diffuser plate which ensures that the MUV radiation is incident normally on the filters, and provides a 120° field of view. These measurements, made primarily at local noon, over a wide range of latitudinal and seasonal conditions, have established the general character of the vertical distribution of stratospheric ozone. The maximum density occurs at a mean altitude of 24 km and shifts to lower altitudes with increasing latitude. The range of observed values is ± 40% of the mean value at 30 km, decreasing to ± 30% at 50 km. In particular, the results of measurements made between 41°N and 47°N have been incorporated in a mid latitude model for the 1976 U.S. Standard Atmosphere (Krueger and Minzner, 1976).

The seasonal variation of daytime ozone has been investigated statistically using results from broad band MUV photometers on spinning rockets (Nagata *et al*, 1971; Tohmatsu *et al*, 1974) launched between 1965 and 1975. Corrections for the aspect of the sun with respect to the rocket axis were provided by the signal from a reference visible channel. Above 35 km the ratio of winter to summer densities was observed to increase, reaching a maximum value of 2.8 at 65 km (Watanabe and Tohmatsu, 1976).

This seasonal variation is greater than the variability reflected in the Krueger results, which included measurements over different seasons.

Equatorial daytime ozone has also been measured with broad band detectors on spinning rockets (Acharya *et al*, 1979). The results confirm that at low latitudes the peak concentration occurs at a slightly higher altitude (31 km) than at mid-latitude, with a maximum concentration lower by a factor of 2 to 2.5.

A detector with peak response at two MUV wavelengths has been used for density determination in the altitude range 0 to 70 km (Brezgin *et al*, 1977). Solar radiation was diffused by an Ulbricht sphere and then incident normally on the detectors. Concentrations differing by a factor of 3 to 4 from the U.S. Standard Atmosphere, 1976, with a possible secondary maximum at 50 km, have been reported.

At twilight, when the solar zenith angle is large, absorption spectroscopy can be used to measure ozone densities at altitudes from 50 to 90 km. Such measurements have been made with broad band solar MUV detectors carried on rockets (Weeks and Smith, 1968b; Weeks *et al*, 1972; Miller and Ryder, 1973) and satellites (Rawcliffe *et al*, 1963; Miller and Stewart, 1965).

For solar zenith angles greater than 90°, the analysis of the raw absorption data to yield O_3 densities is complicated by the finite width of the solar disc. Rays from the upper and lower limbs are absorbed at different altitudes and this limits the height resolution of the experimental absorption profile.

During the twilight zone photochemically induced changes in the ozone density, especially at altitudes between 55 and 70 km, may cause the height of maximum density to differ from the minimum ray height.

Calculations of the number of absorbing ozone molecules along the path from the detector to the sun is then more difficult and the assumption of a spherically symmetric atmosphere is generally incorporated in analysis of the experimental data.

Below 80 km, the results of twilight ozone measurements are in broad agreement with each other and with the US Standard Atmosphere, 1976 model but the variability is larger than that existing in the daytime data, and is greater than 50% for altitudes from 68 to 74 km. Between 80 and 90 km Miller and Ryder (1973) have observed a secondary maximum.

Solar occultation measurements of atmospheric ozone at morning twilight have been made with a moderate resolution (1 nm) detector on the satellite AE-5 (Guenther *et al*, 1977). While the results agree with those of the US Standard Atmosphere, 1976 between 55 and 80 km, they are as much as a factor of two less than the model at altitudes below 50 km. Investigation of the measured column densities above 80 km inferred that any secondary maximum would be small.

Atmospheric extinction of solar emission lines at MUV wavelengths has been monitored with a high resolution spectrometer (0.002 nm) on the satelitte OSO-8 (Millier *et al*, 1979). Because only a small area of the solar disc was observed in this experiment, the height resolution of the attenuation profile was greater than that characteristic of broad band occultation measurements. Sunset ozone densities at altitudes from 50 to 70 km were obtained at an average latitude of 22°N during solar minimum conditions. Reasonable agreement with the mid latitude US Standard Atmosphere densities, reflective of conditions near solar maximum, and with the summer mean densities of Watanabe and Tohmatsu (1976) was reported.

While the vertical density profile of ozone in a sunlit atmosphere has been experimentally determined within known limits at noon below 60 km, and less accurately at higher altitudes and in the twilight

zone, the distribution of atmospheric ozone when there is no sunlight is far less certain.

Absorption spectroscopy has been employed for density measurements less frequently at night than during the day and the results differ in the shape of the nocturnal ozone profile as well as its magnitude, especially above 80 km.

When the altitude variation of reflected radiation from the full moon is observed with sensitive detectors, it is possible to determine ozone densities between 30 and 75 km. Such measurements have been made by Carver *et al* (1966, 1967, 1972b)a few hours after local sunset, with broad band photometers carried on spinning rockets. Below 55 km they reported agreement with the daytime measurements of Miller and Stewart (1965) but at higher altitudes the ozone concentration was observed to be substantially increased above that of a sunlit atmosphere. In a similar experiment, Mikirov (1965) also observed a nighttime ozone increase.

Another nighttime radiation source suitable for absorption spectroscopy measurements is the night airglow emission, originating above 87 km. Observations of its attenuation by ozone have been made by Reed (1968), also using broad band detectors on a spinning rocket. Ozone densities from 48 to 56 km were similar to those of Carver *et al* but above 56 km the increase in ozone density was represented by a more pronounced maximum with a peak density, at 63 km, 10 times that of typical daytime values. The results of DeJonckheere and Miller (1974) for 65 to 75 km were consistent with previous measurements in indicating an increase in nighttime ozone at higher altitudes.

By observing the occultation of stellar MUV radiation with detectors on satellites, nighttime ozone densities can be measured over the altitude range 50 to 100 km. However, the results from broad band

stellar occultation with detectors on the satellite OAO-2 (Hays *et al*, 1972; Roble and Hays, 1973; Hays and Roble, 1973a; Roble and Hays, 1974) were markedly lower (by as much as a factor of 4) than those derived from rocket broad band spectroscopy, in the altitude region 50 to 70 km where both techniques are applicable. They also reported a minimum density at 75 km, with a maximum at 83 km, but were unable to establish any seasonal or diurnal pattern from their measurements, except that mesospheric ozone exhibits great variability.

Occultation profiles of monochromatic stellar radiation, obtained with an ultraviolet telescope-spectroscope on OAO-3 during equatorial midnights (Riegler *et al*, 1976; Riegler *et al*, 1977), provided results in conflict with those from broad band occultation, since they indicated that the ozone profile peaked at 97 km, with a minimum at 87 km. Additionally, the magnitude of the densities was larger, by a factor of 4 to 20, than the twilight measurements of Guenther *et al* (1977) and the US Standard Atmosphere, and larger still than the values of Hays *et al*.

When considering the definition of the nighttime ozone density in the atmosphere, there remains the serious problem of reconciling the experimental results, described above, even though the measurements have been made with essentially the same technique of absorption spectroscopy.

2.4 OTHER TECHNIQUES FOR MEASURING NEUTRAL DENSITIES IN THE UPPER ATMOSPHERE

a. Atomic Oxygen

Mass spectrometers carried on rockets (Offermann and Tatarczyk, 1973; von Zahn and Gross, 1969; Nier *et al*, 1972) and more recently on satellites (Nier *et al*, 1973; Pelz *et al*, 1973; Krankowsky *et al*, 1974;

Trinks and von Zahn,1975) have provided extensive atomic oxygen data, especially at altitudes above 120 km. Although this technique represents the primary source of *in situ* measurements, it is generally acknowledged that the absolute accuracy of the results is limited by quantitative uncertainties related to atomic oxygen recombination within the instrument - the 'atomic oxygen loss' (Sjolander, 1976). Some results may be low by a factor of 2.5 (Offermann, 1974) or even 3 to 4 (von Zahn, 1970). This uncertainty, coupled with the apparently highly variable nature of thermospheric atomic oxygen, is reflected in the wide range of atomic oxygen densities reported in the literature.

Early rocket experiments with mass spectrometers, conducted by the University of Minnesota (Nier *et al*, 1964; Krankowsky *et al*, 1968; Kasprzak *et al*, 1968), indicated that the day-to-day variation was at least as important as the diurnal variation and that, in contrast to the results of Schaefer and Nichols (1964), the nighttime atomic oxygen densities were 1.8 times greater than those in the daytime. They employed two types of mass spectrometers in order to estimate the degree of atomic oxygen recombination. In one instrument, the ion source was completely enclosed by a chamber, connected to the ambient atmosphere by a cylinder. It was assumed that there was complete recombination of all the atomic oxygen entering the chamber. The other instrument had an 'open' source, orientated so that, to the greatest possible extent, the ambient gas molecules were able to enter the ionization region with the minimum number of collisions. By comparing simultaneous results, the recombination factor was estimated to be 1.25.

However, in a review of all mass spectrometer measurements at 150 km, von Zahn (1970) reported an average density of $2.3 \times 10^{10}\ cm^{-3}$,

which was a factor of 3 to 4 higher than the average of the Minnesota experiments. That recombination uncertainties were an important consideration in atomic oxygen determination was further substantiated by the results from a 'nearly closed' mass spectrometer in which the ion source and walls were cryogenically cooled to freeze any colliding particles (Offermann and Grossmann, 1972, 1973). At 150 km their measured atomic oxygen density was $2.21 \times 10^{10}\ cm^{-3}$. Additionally, EUV experiments (Hall *et al*, 1965, 1967) and incoherent scatter experiments yielded high, rather than low, atomic oxygen densities.

Nier (1972) defended the 'low' densities because a comparison of mass spectrometer data from eight flights with satellite drag density measurements indicated that the Minnesota relative densities were in agreement. This implied that von Zahn's correction factor was far too high and a recombination of 20% was more appropriate. Laboratory investigations simulating the interaction of an atomic oxygen beam with a mass spectrometer (Lake and Nier, 1973) revealed that the recombination could indeed be as high as a factor of 2.5. They suggested that a 'conditioning' of the surfaces, effected by high levels of atomic oxygen, would reduce this factor to a value more applicable to the Minnesota experiments, since they were generally exposed to the ambient atmosphere below 100 km, well before measurements commenced. So effectively the dilemma remained unsolved.

Radio frequency mass spectrometers have been flown on Russian rockets primarily to investigate latitudinal, diurnal and seasonal composition changes (Pokhunkov, 1971; Pokhunkov, 1972; Mikhnevich *et al*, 1975; Chasovitin *et al*, 1976) and also in conjunction with an eclipse (Pokhunkov and Gorbunov, 1976). These experiments affirmed the highly variable day-to-day nature of atomic oxygen, especially at polar latitudes,

and suggested a daytime maximum. The effect of recombination was consistently reported to be less than 20%, and no corrections were applied to the results, which were reported primarily in ratio rather than absolute format.

Other experimenters have made rocket mass spectrometer measurements of atomic oxygen at high latitudes (von Zahn and Gross, 1969; Gross and von Zahn, 1971; Hickman and Nier, 1972) and at the equator (Danilov *et al*, 1979).

In a review of rocket composition measurements in the lower thermosphere, in which the 2.5 factor suggested by Lake and Nier (1973) was applied to the Minnesota data, Offermann (1974) reported the average atomic oxygen density at 150 km to be $1.22 \pm 0.19 \times 10^{10} cm^{-3}$, and identified a pronounced summer minimum but only a small diurnal variation.

More extensive investigation of the relation between thermospheric atomic oxygen densities and assorted geophysical parameters is afforded by mass spectrometer measurements from satellites. Patterns established by the rocket data have generally been confirmed. Atomic oxygen variations appear to be larger than is represented by static diffusion models (Philbrick, 1974, 1976) and mid latitudes exhibit a winter enhancement factor of about 3 near 120 km, which shifts to a summer bulge above 275 km (Keating *et al*, 1976).

Mass spectrometers on satellites are exposed to atomic oxygen environments for extended periods. The consequent surface 'conditioning' was expected to facilitate a more accurate determination of atomic oxygen densities by reducing problems with chemical reactions involving regularly observed impurities such as carbon compounds (Newton *et al*, 1974). Assuming, therefore, that all atomic oxygen either recombined or was not lost inside their closed source, magnetic mass spectrometer, Newton *et al* (1974) deduced total oxygen densities between altitudes 137 and 225 km

which were 30% below the von Zahn (1970) total oxygen average at 150 km.

Additional total oxygen data was acquired from the quasi-open ion source mass spectrometer of Nier *et al* (1976), since in the normal mode of satellite operation this behaves essentially as a closed source (Nier *et al*, 1974). Alternately, the 'fly-through' mode, utilizing the velocity of the satellite to distinguish between incoming ambient particles and those which have struck instrument surfaces, enables measurement of absolute atomic oxygen densities. Their reported value at 150 km of $9 \times 10^9 \text{ cm}^{-3} \pm 30\%$ is consistent, within quoted uncertainties, with the rocket average of Offermann (1974) at this altitude.

In their measurement of total oxygen, Nier *et al* (1976) applied a 5% correction to allow for the presence of uncombined atomic oxygen in the source. So the need to understand the complex mechanisms of atomic oxygen surface interactions remains a crucial aspect of mass spectrometric analysis. Lake and Krankowsky (1975) proposed a two layer surface model in which the more tightly bound layer desorbs from the surface as atomic oxygen with a relatively long time constant and the less tightly bound, more mobile layer recombines and desorbs as molecular oxygen at a much faster rate. Sjolander (1976), from laboratory atomic oxygen - metal surface studies, has qualified the general processes involved but reiterated the difficulty in obtaining quantitative data for the loss correction; it appears that to accurately measure atomic oxygen requires simultaneous measurements of H_2O, CO, CO_2 and O_2 with a mass spectrometer that excludes contribution to the ion current from gas molecules that have interacted with any surface of the instrument. Such experiments, it was suggested, were those of Nier *et al* (1974) and Offermann and Grossmann (1973).

Paradoxically, Nier and co-workers at the University of Minnesota are the acknowledged advocates of the lowest atomic oxygen densities for the lower thermosphere, while the results from the cryo-cooled mass spectrometer of Offermann and co-workers are among the highest reported in the literature. Recent measurements with the cooled instrument, in the altitude range 80 to 270 km (Trinks *et al*, 1978), have yielded an atomic oxygen density of 1.45 to 1.65 x 10^{10} cm^{-3} at 150 km. While this is consistent with Offermann's (1974) average value, it is 70% higher than that of Nier *et al* (1976).

Measurements of atomic oxygen densities in the mesosphere are no more definitive than in the thermosphere. With their cryo-cooled ion source mass spectrometer, Trinks *et al* (1978) determined the maximum density to be 6.5 x 10^{11} cm^{-3} ± 25% at 97.5 km, generally higher than previously reported values.

Other measurements have been made with a rocket borne resonance and fluorescence technique (Dickinson *et al*, 1974; Dickinson *et al*, 1976; Thomas *et al*, 1979). Radiation emitted at the atomic oxygen resonance triplet from 130.2 to 130.6 nm is reflected by a mirror deployed on a beam, and detected by an ion chamber. In-flight background radiation is monitored by a photomultiplier and the experiment is calibrated in the laboratory by determining the signal for known atomic oxygen concentrations. A number of measurements have been made at night, as well as in the daytime, and also in conjunction with experiments to examine the electron concentration. Densities have been reported over the altitude range 80 to 140 km, with the maximum concentration varying from 3 to 5 x 10^{11} cm^{-3}. However, from nighttime measurements employing a similar experimental technique, Sharp (1980) has determined a lower peak concentration of 1.1 x 10^{11} cm^{-3} at 93 km.

It is possible to derive the atomic oxygen density in the mesosphere by monitoring the emission of the OI green line at 557.7 nm (Donahue *et al*, 1974; Wasser and Donahue, 1979). Reported densities at the peak of the profile are low, typically less than $2.7 \times 10^{11} cm^{-3}$. Inherent in this technique is the major uncertainty of which of the theories of Chapman or Barth is most appropriate for describing the excitation mechanism of the airglow (Section 1.4b).

Rocket borne silver film sensors have been developed to measure atomic oxygen from 80 to 120 km (Henderson and Schiff, 1970). Contact with atomic oxygen causes the resistance of the sensor to change. Despite the simplicity of this technique there are difficulties with contamination, with producing uniform sensors and with reducing the raw data acquired during conditions of rocket flight. Only preliminary results have been reported (Henderson, 1974).

b. Molecular Oxygen

Molecular oxygen densities have been determined by virtually all the mass spectrometer experiments described in the previous section specifically for their application to atomic oxygen. Problems of recombination of atomic oxygen are similarly important, and may cause the measured molecular oxygen density to be higher than that of the ambient atmosphere. This has prompted a preference for presenting and comparing total oxygen densities.

In his review of 28 rocket measurements, primarily using mass spectrometers, Offermann (1974) calculated the average concentration at 150 km to be $2.56 \pm .19 \times 10^{9} cm^{-3}$, and observed that the scatter of the data was 'astonishingly large' - but better than that for atomic oxygen.

Since then, Nier *et al* (1976) have averaged 20 mass spectrometer rocket measurements and found an almost identical value at 150 km. For comparison, the average of their satellite data is $3.1 \times 10^9 cm^{-3}$. Total oxygen data reported by various laboratories has been compared by Newton *et al* (1974) and the average of $2.2 \times 10^{10} cm^{-3} \pm 22\%$ is only in reasonable agreement with Offermann's value, $1.73 \times 10^{10} cm^{-3}$.

An indication of the variability of O_2 density data, manifested probably by both real changes and lack of experimental reproducibility, is afforded from two measurements with the same technique, at different times. Specifically, using the cryo-cooled ion source mass spectrometer, Offermann and Grossmann (1973) deduced the molecular oxygen concentration at 150 km to be $1.6 \times 10^9 cm^{-3}$, and the same technique employed by Trinks *et al* (1978) yielded densities of $2.5 \times 10^9 cm^{-3}$. The range of these values, a factor of 1.5, is echoed in FUV determinations of the molecular oxygen density. Weeks's (1975b) result for the density at 150 km, using 145 nm ion chambers, was $2.8 \times 10^9 cm^{-3}$, while Higgins and Heroux (1977), employing the same experimental technique, reported it to be $1.95 \times 10^9 cm^{-3}$.

When molecular oxygen densities are derived from total oxygen data, assumptions must be made about the percentage of atomic oxygen that does not recombine in the mass spectrometer. Then the O_2 contribution to the measured signal is obtained as the difference between this signal and a fitted atomic oxygen profile (Kirby-Docken and Oppenheimer, 1977) or in conjunction with an open source mass spectrometer such as in the 'fly-through' mode (Nier *et al*, 1976). Below 200 km it appears that the contribution from uncombined atomic oxygen is 5% (Nier *et al*, 1976) to 7% (Lake and Krankowsky, 1975) but at 350 km this may increase to 15% (Lake and Krankowsky, 1975). The problem remains incompletely understood.

A comparison of FUV and mass spectrometry techniques for O_2 density determination has been reported by Ackerman *et al* (1974). Their results are an appropriate representation of the general uncertainties pertaining to current techniques for measuring molecular oxygen in the lower thermosphere. At 150 km data from the FUV experiment yielded a concentration of $1.9 \times 10^9 cm^{-3}$ but according to the mass spectrometer it was in the range 2.8 to $3.3 \times 10^9 cm^{-3}$. Ackerman *et al* deferred to the absorption spectroscopy results, citing the mass spectrometer results as an upper limit in view of the recognized recombination problem. Nier *et al* (1976) were not convinced and suggested they look elsewhere for the source of the discrepancy.

Molecular oxygen composition can be calculated from ion composition measurements using atmospheric ion chemistry (Oppenheimer *et al*, 1976; Mayr *et al*, 1976). Here, the major uncertainties are with the rate coefficients for the numerous chemical equations and, additionally, the accuracy of the calculations may be limited by restriction of the chemical reaction scheme. Potter *et al* (1977) have compared the simplified reaction scheme calculations of Oppenheimer *et al* with satellite measurements using both open and closed source mass spectrometers and have concluded that the technique is more appropriate for mid latitudes at about 200 km, during periods of low geomagnetic activity.

c. *Molecular Nitrogen*

The density of molecular nitrogen is usually measured by mass spectrometers simultaneously with that of O_2 and O. This experimental data base has been described in Section 2.4a. Mass spectrometers are considered to provide reliable data for N_2 because there is no incumbent analagous to the problem of atomic oxygen recombination. Atomic nitrogen

constitutes less than a few percent of the total thermospheric number density (Nier *et al*, 1964; Hickman and Nier, 1972) although it has been observed in greater concentration at higher altitudes (Pokhunkov, 1972). Molecular nitrogen densities should therefore be predicted with greater confidence than either O_2 or O densities. Despite this the data is widely scattered.

This implies that N_2 densities are quite variable, especially on a day-to-day basis. Offermann (1974) has identified a small summer maximum at 150 km, which becomes more pronounced at 200 km. He also noted a diurnal minimum occurring at 0400 hours local time. This was confirmed by Köhnlein *et al* (1975) who attributed it to the sensitivity of N_2 to thermospheric heat input.

At 150 km von Zahn (1970) reported the average of 37 density measurements, of which only two were from EUV experiments, to be $2.6 \times 10^{10}\,cm^{-3}$. This was updated by Offermann (1974) to $2.79 \pm 0.14 \times 10^{10}\,cm^{-3}$. Nier *et al* (1976) have recognized good agreement between the average of rocket mass spectrometry data ($2.73 \times 10^{10}\,cm^{-3}$) and satellite mass spectrometry data ($2.9 \times 10^{10}\,cm^{-3}$).

Recently, Trinks *et al* (1978) have reported new results from their cryo-cooled mass spectrometer. On the upleg of their rocket flight, the density was found to be $2.1 \times 10^{10}\,cm^{-3}$ and on the downleg it was $3.8 \times 10^{10}\,cm^{-3}$, the difference being attributed to a real variation. Earlier measurements with this same type of mass spectrometer were much lower, at $1.58 \times 10^{10}\,cm^{-3}$. Other mass spectrometry investigations by Ackerman *et al* (1974) have yielded higher values, in the range 3.4 to $3.7 \times 10^{10}\,cm^{-3}$.

It appears true for thermospheric N_2, as it is for O_2 and O,

that there have been insufficient measurements to identify the scatter of the available data with real thermospheric variations as opposed to experimental uncertainties.

d. *Ozone*

Accurate measurements of upper atmosphere ozone are essential for detecting changes that may be a consequence of the sensitivity of ozone densities to tropospheric pollutants. For this reason, the accuracy and precision of current techniques for determining ozone concentration have recently been considered in detail by two stratospheric workshops, as reported by Hudson (1977) and Hudson and Reed (1979).

The total ozone in a column above the earth's surface has been regularly monitored for over 50 years by a variety of ground based instruments, primarily the Dobson spectrophotometer and the Russian M-83 ozonemeter. Measurements with the Dobson instrument, which is a double prism monochromator, derive from observations of direct or of zenith sky scattered solar radiation at pairs of wavelengths in the range 300 to 340 nm, where ozone absorption changes greatly with wavelength. Systematic uncertainties in total ozone estimates arise from assumptions about the effects of light scattered by particles and the constancy of the extra-terrestrial solar spectrum, and also reflect uncertainties in the ozone absorption coefficients. However, 90% of Dobson total ozone measurements are considered to be uncertain by no more than 3% (Hudson, 1977). Bojkov (1969) has discussed the optimization of the ground based network for measuring total ozone, and Angell and Korshover (1976) have analyzed the available data for long term trends. Inherent in such a global study of total ozone are systematic errors between different stations.

From a statistical analysis of total ozone data from 9 Dobson

stations, to assess their trend detection capability, Hill *et al* (1977) claim that a global change of 0.26% persisting over 6 years is detectable. They also noted the absence of any abnormal global trend at the present time, and implied that predictions of ozone depletion may be exaggerated.

Total ozone is also monitored from satellites with instruments that detect ultraviolet radiation that has passed through the stratospheric ozone layer and is reflected back from the lower atmosphere or the earth's surface. Typically, for example on the Nimbus-4 satellite, the backscatter ultraviolet (BUV) instrument is a double Ebert-Fastie spectrometer with about 1 nm spectral resolution and a spatial resolution of better than 200 x 200 km^2. Ozone densities are determined by measuring the ratio of the backscattered UV to the incident total flux in the long wavelength end of the Hartley-Higgins bands. An additional measurement of radiance in an absorption free spectral region adjacent to the bands is necessary to model the lower boundary reflectivity. Uncertainties are associated with the absorption cross-sections (Klenk, 1980), instrument calibration (Guenther, 1978), the effect of aerosol scattering (Dave, 1978), the wavelength dependence of the surface reflectivity and the need to assume an ozone profile for the inversion formulae.

Extensive coverage of global total ozone has been provided from Nimbus-4 since 1970 (Krueger *et al*, 1980). Some of this data has been reported by Ghazi *et al* (1976), Finger *et al* (1976) and recently by Hilsenrath *et al* (1979_b) who interpreted the early data in terms of seasonal and interannual variations, in general agreement with the trends established by the Dobson measurements.

Dobson and BUV results have been compared by a number of experimenters (Mateer *et al*, 1971; Fleig *et al*, 1978), and Hudson and Reed

(1979) reported that the average BUV measurement is 3.4% lower than a simultaneous Dobson measurement. Improved versions of the BUV experiment, incorporating a scanning facility and increased spatial resolution (SBUV and TOMS), are currently collecting data on board the Nimbus-7 satellite.

Another technique for monitoring total ozone from satellites utilizes the earth emitted radiation in the 9.6 μm band. On Nimbus-4 this infrared interferometer spectrometer (IRIS) instrument has been described by Prabhakara *et al* (1976), and from an analysis of the experimental data Blackshear and Tolson (1978) have identified correlations between total ozone and geophysical variations such as the solar radio flux ($F_{10.7}$), the Zurich sunspot number and the total solar Lyman-alpha flux.

Measurements of total ozone, acquired over a nine month period and averaged over the globe in latitude bands of 10°, by both the BUV and IRIS experiments on Nimbus -4,have been compared with simultaneous ground based data from the Dobson and Russian ozonemeter instruments (Prior and Oza, 1978). Going from mid to high latitudes, in both the northern and southern hemispheres, the IRIS results became increasingly higher than both the BUV and ground based results which, however, displayed generally better mutual agreement. During summer at 75° N the discrepancy between the two satellite techniques was as much as 23%, while at equatorial latitudes, although the average difference was much smaller (2%), the IRIS data was systematically lower than that from the BUV experiment. Prior and Oza (1978) have stressed that before any changes in the total ozone, in response to anthropogenic factors, can be reliably identified, such systematic uncertainties, inherent in either the instruments, the sampling techniques or the data reduction methodologies, must be located.

Determination of the gross features, with about 15 km resolution, of the vertical ozone profile is possible from ground based absorption experiments. With the optical Umkehr technique, observations are made of the ratio of the intensities of downward scattered zenith radiation at two wavelengths in the Huggins bands, as the solar zenith varies from 60° to 90° (DeLuisi and Furukawa, 1970; DeLuisi, 1979). Profiles up to 45 km, with data averaged over 5 km intervals, have been acquired over the past 20 years and are the only long term data base for ozone variations above the level of its maximum (Dütsch, 1974).

Radio techniques which monitor the emission at 110.8 Ghz, in ozone's rotational spectrum, are also able to provide ground based measurements of the ozone vertical distribution (Shimabukuro *et al*, 1975). Unlike the Umkehr method, this experiment can be utilized during the nighttime. Penfield *et al* (1976) have thus observed the mesospheric ozone decay at sunrise and have reported that daytime densities at these altitudes are reduced by a factor of two over the nighttime densities.

Remote sensing of the vertical ozone profile, as well as the total ozone, is afforded by BUV instrumentation on the Nimbus-4 (Krueger *et al*, 1973) and OGO-4 (Anderson *et al*, 1969) satellites. Data for altitudes 30 to 55 km, consistent with other rocket and satellite data, indicated that here the ozone profile has significant vertical, geographical and temporal variations (London *et al*, 1977). For example, in winter the level of the maximum mixing ratio tilts upward with latitude and is also higher than in summer. Nimbus-4 BUV profiles have been compared with Umkehr data (DeLuisi *et al*, 1979), allowing biases to be assessed and revealing that between 28 and 38 km the two techniques agree only

roughly, although for 38 to 50 km measurements of the phase and magnitude of seasonal variations are more satisfactory.

When the atmosphere's infrared emissions are measured by radiometers as they scan across the earth's limb, the CO_2 emission at 15 μm provides information about the atmospheric temperature which can be used in conjunction with ozone's emission at 9.6 μm to derive a profile of the vertical ozone density. Preliminary results from the limb radiance inversion radiometer (LRIR) on Nimbus-6 indicate that this is a powerful technique for obtaining high resolution (~ 3 km) vertical ozone profiles from 11 to 70 km, both in the daytime and at nighttime (Gille *et al*, 1980a,b).In particular, measurements made simultaneously in space and time with the stellar occultation experiment of Riegler *et al* (1976) were reported to average a factor of 3 lower, but agreed well with other data sources, such as the Krueger and Minzner (1976) mid latitude daytime model. In Section 2.3d, comparisons with other UV optical measurements of ozone densities also implied that the data of Riegler *et al* (1976, 1977) were anonomously high.

Height resolution superior to that typically characteristic of remote sensings must be provided by *in situ* measurements. In the lower stratosphere, below 30 km, chemical and optical experiments have been carried regularly on balloons (Paetzold, 1969; Mani and Sreedharan, 1969; Hudson and Reed, 1979) and less frequently on aeroplanes (Gauntner *et al*, 1979). Comparisons with the Umkehr method have been reported by Dütsch and Ling (1969) and Angell and Korshover (1979) to verify trends established independently by the two techniques.

Above about 30 km the primary source of non-optical, high altitude resolution, *in situ* ozone data is the chemiluminescent experiment

employed by Randhawa (1971) and more often by Hilsenrath *et al* (1969, 1979a, 1980). The ratio of ozone molecules to the total air density, termed the mixing ratio, is measured during descent of the detector, from about 70 km, on a high altitude parachute. Air is sampled by means of the self-pumping action of a ballast chamber and ozone is detected via its chemiluminescent reaction with a rhodamine-B disc which is detected with a photomultiplier.

Hilsenrath *et al* (1979a) have reported a measurement precision of 8% and an accuracy of 14% for the altitude region 25 to 60 km and this has been generally confirmed by comparisons with the Kruger optical sonde (Section 2.3d) which yielded differences of about 10% above the mixing ratio peak, with the chemiluminescent sonde showing lower values.

With this technique ozone concentrations can be measured during the nighttime, although the accuracy decreases to about 35% above 60 km, in the altitude region where important diurnal changes are expected. Ozone densities also lower, by a factor of two, than the UV stellar occultation results of Reigler *et al* (1977) (Section 2.3d) have been reported. Experiments during the polar night evidence great ozone variability at all levels, which can only partly be explained by temperature and wind fields.

Both the chemiluminescent and optical rocket sondes provide most accurate data at altitudes less than 60 km. In the mesosphere, from 60 to 100 km, ozone concentrations can be inferred by monitoring the $O_2(^1\Delta_g)$ emission at 1.27 μm with infrared detectors carried on rockets (Evans and Llewellyn, 1970, 1972). Deduction of the ozone density requires knowledge of mesospheric photochemistry and the ozone dissociation coefficient at the time of the measurement, and hence reflects uncertainties in both the absolute solar MUV flux and the ozone absorption cross-sections.

The technique has been validated by simultaneous solar occultation measurements during an Arctic winter twilight, from which Llewellyn and Witt (1977) have observed a minimum density notch at 80 km with peak concentration of $5.1 \times 10^7 cm^{-3}$ between 85 and 90 km.

A comparison of ozone measurements with absorption, chemiluminescent, airglow and mass spectrometer experiments was conducted by Weeks *et al* (1978), in the altitude region 19 to 108 km, over a two-day interval. Where the techniques overlapped, the airglow and optical results were consistent within experimental error, and both indicated a density minimum at 81 km. However, the chemiluminescent results were higher than the absorption results, especially at higher altitudes, and above 90 km the mass spectrometer measured ozone densities considerably higher than was deduced from the airglow. Additionally, the experimental data and model predictions could be quite different.

Such inconsistencies in the present understanding of the stratosphere and mesosphere, and in measurements of the ozone densities, imply that truly reliable monitoring of the ozone concentration over a long period of time may be quite difficult.

CHAPTER THREE

ATMOSPHERIC ABSORPTION OF SOLAR EXTREME ULTRAVIOLET RADIATION

3.1 INTRODUCTION

Solar EUV radiation is absorbed by each of the three major thermospheric neutral constituents, causing excitation, dissociation and ionization at altitudes between 100 and 300 km. If the absorption cross-sections of the constituent gases are accurately known, measurements of the absorption profiles of EUV radiation can, in principle, enable direct determination of the composition of the neutral thermosphere. Absorption spectroscopy techniques pertaining to such an analysis have been described in Section 2.1.

When the energy of the radiation is more than the ionization potential of the gas, this absorption produces ions (O^+, O_2^+, N_2^+) and photoelectrons which carry away excess kinetic energy for distribution amongst the ambient particle population, thus initiating atmospheric energetics, as described in Section 1.4. Knowledge of the absolute intensity of the solar flux and of the photoionization cross-sections of the thermospheric gases enables the rates of formation of ions and photoelectrons to be derived from the absorption curves.

Monitoring the transmitted solar EUV spectrum is essential in any investigation of the neutral and charged constituents of the thermosphere because each of the three primary neutral species exhibit strong absorption at these wavelengths (Section 1.3). On an Aerobee rocket, details of which are available in Appendix A, measurements of the neutral atmosphere composition by EUV absorption spectroscopy were made

in conjunction with density determination afforded by a neutral mass spectrometer. For data on the distribution of photoelectrons, an electron retarding potential analyzer and a cylindrical electron energy analyzer were flown, and a positive ion retarding potential analyzer and a positive ion quadrupole mass spectrometer were incorporated for steady state ion density evaluation.

Although wavelengths longer than 50 nm are best observed at normal incidence, to cover the entire EUV with one instrument it is necessary to employ grazing incidence optics essential for shorter wavelengths. A number of investigators have flown grazing incidence monochromators on rockets for the purpose of solar EUV flux measurements (Hall *et al*, 1963b; Heroux *et al*, 1972; Higgins, 1976) and as a tool for absorption spectroscopy (Hinteregger, 1961; Hinteregger *et al*, 1965; Timothy *et al*, 1972). Review of the application of absorption spectroscopy techniques to these wavelengths (Section 2.3a) emphasizes that such experiments do not reflect the preferred criteria for compositional analysis. In practice, acquisition of useful data is most difficult. Absorption cross-sections for N_2 and O_2 (Section 1.3) are not known as accurately as required, while data on atomic oxygen remains largely theoretical; at best, semi-empirical. Nor has the temperature dependence of the cross-sections been usefully formulated for aeronomic applications.

While such uncertainties can often be tolerated in the case of uniquely characteristic absorption, the extension to multiconstituent absorption involves a tripling of the attendant errors, so that derived results are often ambiguous. For example, Timothy *et al* (1972) have reported that for their particular application; 'attempts to determine

the number densities of the three major neutral constituents (O_2, N_2, O) directly by the simultaneous solution of the measured extinction coefficients did not give realistic solutions'.

Extraction of density information from experimental absorption curves becomes extremely complicated in regions of the spectrum, such as 70 to 105 nm, where the absorption cross-sections exhibit sharp and detailed structure (Section 1.3). Absorption at these wavelengths becomes hardened with atmospheric penetration, causing the observed cross-section to change with altitude. Application of absorption spectroscopy techniques to such wavelengths requires broad band analysis (Section 2.1f) wherein it is necessary to know the shape of the solar line being monitored and the detector response function defined by the exit slit of the monochromator, since the measured profile is the integrated effect of these variables. Measurements of spectrally integrated atmospheric transmittance in the Schumann-Runge bands of O_2, used to derive O_2 column densities, have been reported by Longmire *et al* (1979) but this form of analysis has not yet been used for absorption of radiation at EUV wavelengths.

There remain a number of questions which must be answered to provide a more complete understanding of how the atmosphere absorbs solar EUV radiation. On the basis of emission lines observed in laboratory spectra it is possible that the absorption spectra of atomic oxygen and atomic nitrogen contain sharp lines which may overlap solar emission lines (Huffman and Larrabee, 1968). Secondly, measurements of the cross-sections of N_2 and O_2 are made using laboratory produced lines, of width < 0.01 nm, at solar wavelengths and it is uncertain just how representative these results are for *in situ* atmospheric absorption of solar lines whose widths are unknown (Samson and Cairns, 1964). Thirdly,

it is necessary to investigate possible absorption by excited molecular species (Huffman and Larrabee, 1968) and minor constituents such as N, since if the N_2 bands are predissociated the resultant production of N may mean it exists in sufficient quantity that its absorption cannot be ignored.

In view of the many uncertainties associated with multi-constituent absorption of EUV radiation, the inclusion of a grazing incidence monochromator for compositional data on the Aerobee rocket was conditioned by the availability of other experiments to provide simultaneous measurements which could be incorporated in the data analysis. In particular, molecular oxygen densities were determined independently, and N_2 and O densities, and their ratios,were provided by a neutral mass spectrometer.

It is important, for most accurate absorption measurements, that the rocket carries the detecting instrument to altitudes above the region of main absorption. Prediction of the absorption profiles from calculations of atmospheric attenuation of solar EUV radiation (Section 2.2) indicate that absorption of some EUV wavelengths begins above 250 km. For large zenith angles the region of main absorption shifts to higher altitudes. So the scientific objectives of the Aerobee experiment, requiring a large solar zenith angle, resulted in less than optimum flight conditions for the grazing incidence monochromator, since the maximum apogee that could be expected was 245 km.

3.2 SOLAR EUV FLUX MEASUREMENTS

Early investigations of the solar EUV spectrum were made with photographic techniques on rockets by experimenters at the United States Naval Research Laboratories (NRL) (Purcell *et al*, 1960; Austin *et al*, 1962; Tousey *et al*, 1963; Tousey *et al*, 1964; Austin *et al*, 1966) and photo-

electrically with rocket borne grazing incidence telemetering monochromators by a group at the Air Force Cambridge Research Centre (now the Air Force Geophysics Laboratory, AFGL) (Hinteregger *et al*, 1960; Hinteregger, 1961; Hall *et al*, 1963b; Zirin *et al*, 1963; Manson, 1967). Characteristics and results of these experiments have been reviewed by Tousey (1963, 1971).

Observations of the absolute EUV flux and its variation, from satellites OSO - I and OSO - III, reported by Neupert and Behring (1962), Neupert *et al* (1964) and Lindsay (1964), formed the data base for the aeronomical reference spectrums IAGA-69 (Hinteregger, 1970) and Donnelly and Pope (1973), suggested for medium activity, non-flaring solar conditions.

High resolution (0.004 nm) spectra from 6 to 77 nm, photographed with wavelength precision of 0.0008 nm, from the experiments of Behring *et al* (1972) and Behring *et al* (1976) provided relative line intensities with accuracy better than 30%, and absolute full disc fluxes from 5 to 122 nm, measured with 0.06 nm resolution and 25% accuracy, were obtained from six AFGL photoelectric grazing incidence spectrometers, flown on rockets launched between 1969 and 1976 (Heroux *et al*, 1972; Malinovsky and Heroux, 1973; Heroux *et al*, 1974; Higgins, 1976). Additional measurements below 20.5 nm, for both active and quiet solar conditions (Manson, 1967, 1972, 1976), indicated excellent agreement with the data of Heroux *et al* (1974), justifying a general error estimate for these fluxes of ± 20%.

Both Manson (1976) and Heroux and Higgins (1977), who reviewed the AFGL experiments, cautioned against scaling solar EUV fluxes with respect to the solar radio flux at 10.7 cm, despite the study of OSO - I and OSO - III data by Chapman and Neupert (1974) indicating that the $F_{10.7}$ cm flux could be used to predict some EUV fluxes.

For aeronomy, there still remains the question of what is an appropriate reference solar spectrum, capable of predicting temporal flux variabilities in various parts of the EUV spectrum. This problem is being addressed by two groups who have been monitoring the EUV fluxes from satellites. Experimenters at AFGL (Hinteregger *et al*, 1973) have flown, on each of the satellites AE-C, D and E, an EUV spectrophotometer for measurements in the region 14 to 185 nm. In Germany, the Institut fur Physikalische Weltraumforschung, Freiburg, has been monitoring full disc fluxes in the wavelength range 16 to 106 nm with a plane grating spectrometer aboard the German - USA satellites AEROS-A and B (Schmidtke *et al*, 1974a).

Observations from AE-C, AEROS-A and AEROS-B indicated that the earlier models, IAGA-69 and Donnelly and Pope (1973), urgently required upward revision and the validity of the satellite data was confirmed from an intercomparison of solar EUV flux measurements, including the results of AE-E, by Working Group IV of Cospar, which reported general agreement of absolute flux measurements from these two independent sets of satellite measurements. Solar cycle 20 was hence considered to have been approximately modelled for periods of low solar activity and the data is contained in empirical solar flux models R74113 (Hinteregger, 1976) and F74113 (Heroux and Hinteregger, 1978).

Both satellite experiments monitored the flux variation of selected wavelength intervals and were concordant that different wavelength groups showed different relationships to $F_{10.7}$ over different solar cycles. This emphasized the unsuitability of correlating EUV fluxes with the $F_{10.7}$ flux, which was expected from considerations of solar physics since the $F_{10.7}$ flux is coronal but each EUV emission finds its optimum condition at different levels of the solar atmosphere (Schmidtke, 1979).

In conclusion, the paucity of definitive EUV flux data is incompatible with their importance for atmospheric investigations. Current knowledge has been summarized by Timothy (1977) thus; during the solar rotation, the EUV fluxes vary because of the appearance and disappearance of active regions on the solar disc and over the 11-year solar cycle it is possible that there may be a variation of up to a factor of 2, but no systematic changes in the magnitude of EUV variability have been observed. Chromospheric and transition-region lines are expected to vary by ± 15% while variations of up to a factor of 3 have been identified in coronal emission lines. Such variations are, however, insufficient to account for a change of a factor of two in the EUV irradiance over the solar cycle.

Improved data on the EUV fluxes and their variability will not become available until the problem of detector calibration in space has been addressed. In particular, in-flight calibration is urgently needed (Schmidtke, 1976a) to monitor changes in spectrophotometrically critical components so that real flux variation can be reliably detected. This necessity is illustrated by new data for solar cycle 21, which commenced in July 1976 and indicates a much greater variation of the fluxes, together with a base level for the quiet disc that is well above the F74113 model. Hinteregger (1979) does not discount the possibility of future need to re-interpret this data on the basis of an instrumental artefact.

It would seem, for aeronomical calculations, the only relevant EUV flux data is that from truly time correlated observations (Schmidtke, 1976b).

3.3 DESIGN OF A GRAZING INCIDENCE MONOCHROMATOR FOR A ROCKET PAYLOAD

a. Concave Diffraction Grating Theory

Dispersion and focusing of solar EUV radiation is most efficiently achieved by use of a concave diffraction grating. Theoretical

formulation of the analytic expressions required to describe the dispersive properties and aberrations associated with this type of grating have been derived from physical optics by Mack *et al* (1932) and from geometric optics by Namioka (1959).

Illustration of the principles pertaining to concave diffraction grating optics is provided by Figure 3.1. Light of wavelength λ, incident at angle α on a grating with $1/d$ lines per mm, is diffracted at an angle β, both angles being measured with respect to the grating normal N. If the entrance slit S_1 and tangent to the grating T lie on a circle of diameter R equal to the radius of curvature of the grating, then the diffracted ray is focused on to this circle, called the Rowland circle, at the exit slit S_2.

Two rays reflected from grooves separated by distance w reinforce at S_2 if the path difference between them is equal to an integral number of wavelengths. Reinforcement of all rays at S_2, for an arbitrary light path S_1GS_2, is determined by application of Fermat's principle of least time to the light path F which is given by

$$F = S_1G + S_2G + m \lambda w/d.$$

S_2 is located so that F is an extreme for any point G and is determined by differentiating F with respect to y and z parameters across the grating.

Since the derivatives of F with respect to each variable cannot be zero simultaneously, it is impossible to achieve, with the concave diffraction grating, a point of perfect focus. While the point of horizontal focus is predicted as lying on the Rowland circle, vertical focus occurs along a straight line tangent to the Rowland circle at the normal to the grating. Physically this means that a point source from S_1 is imaged first into a vertical line at S_2 and then into a horizontal

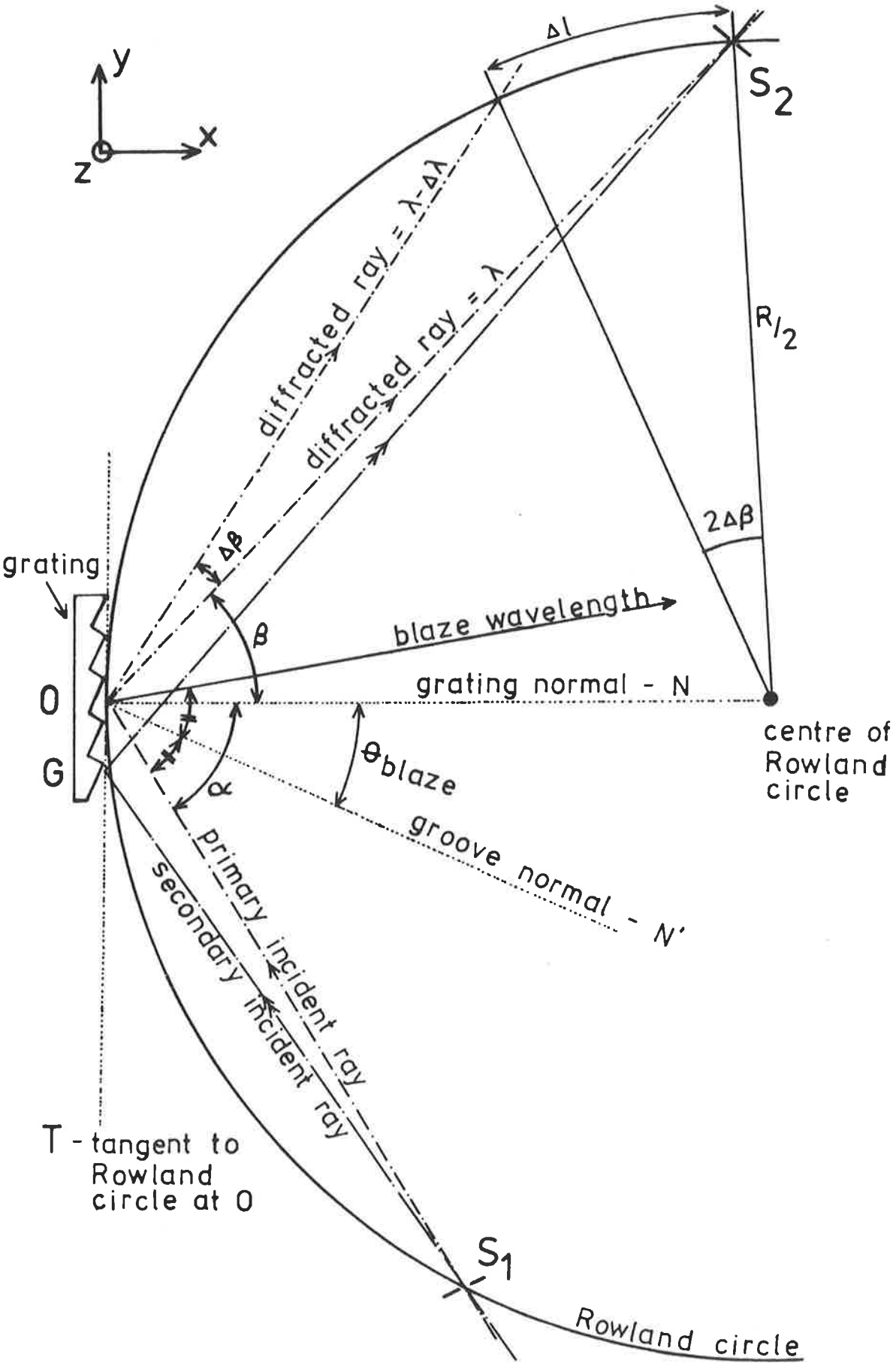

Figure 3.1 Concave diffraction grating optics.

line at some distance beyond. The lack of coincidence of the focusing planes, called astigmatism, is not a problem at small angles of incidence but becomes increasingly important at larger incident angles since it reduces the intensity per unit area of the image and imposes strict focusing conditions to achieve maximum resolution.

Practically, it is most useful in a monochromator to employ vertical slits, parallel to the grating, in which case astigmatism can usually be tolerated because only horizontal focusing is required to separate the various wavelengths.

Application of Fermat's principle to the principle ray S_1OS_2 enables the grating equation to be derived;

$$\pm m \lambda/d = \sin \alpha - \sin \beta \qquad 3.1$$

For observations of inside orders the sign is positive and for outside orders it is negative. The spectral order m represents the principal maximum of the diffraction pattern arising from each monochromatic beam of wavelength λ. Secondary maxima intensity decreases as the number of rules lines exposed to the radiation increases. Angular half width of the principal maximum provides a theoretical limit to the resolving power of the grating.

A measure of the percentage of incident flux returned by the grating into a particular wavelength range of a given spectral order is an indication of the grating efficiency. Concentration of radiation into a given order is controlled by the groove shape, characterized by the blaze angle θ_b. Specular reflection from the surface of the facets (normal N') determines the blaze wavelength which, from Figure 3.1 and Equation 3.1, is derived as

$$\lambda_b = 2 d \sin \theta_b \cos(\alpha - \theta_b) \qquad 3.2$$

To maintain a constant blaze angle it is usual to rule the grating lines in three sections - the resultant grating is termed tripartite.

Distribution of wavelengths along the Rowland circle is determined by the linear dispersion

$$\frac{d\ell}{d\lambda} = (d/mR) \cos \lambda \qquad 3.3$$

and the resolving power R determines whether the separation $\Delta\lambda$ of wavelengths along an arc length $\Delta\ell$ can be distinguished. Refinement of the theory of the resolving power of a concave grating, beyond the first approximation afforded by plane grating calculations, involves the use of a modified Rayleigh criteria (Namioka, 1959) and results in the resolution being dependent on the grating width. When the grating is illuminated beyond an optimum width W_{opt} the resolving power tends to oscillate about a mean value, and has been best expressed by Samson (1967) as

$$R = 0.75\, W_{opt}(m/d) \qquad 3.4$$

$$W_{opt} = 2.51 \left(R^3 \lambda \frac{\cos \alpha \cos \beta}{\sin^2 \alpha \cos \beta + \sin^2 \beta \cos \alpha} \right)^{1/4}$$

Since the measured resolution of a concave diffraction grating instrument is the convoluted result of elements such as the entrance and exit slits and alignment accuracy, superimposed on qualities of the grating such as uniformity of groove spacing, often the theoretical resolution is not the limiting factor of instrument resolution. In particular, the resolving power of a concave grating monochromator is never better than

$$R_{slit} = \frac{\lambda}{\Delta\lambda_{slit}}$$

where $\Delta\lambda_{slit}$ is determined from Equation 3.3 for a slit width $\Delta\ell$.

b. *Grazing Incidence Optics*

Reflection by grating surfaces of short wavelengths is very inefficient unless the light is incident at an angle greater than the critical angle, where total reflection occurs. Grazing incidence monochromators make use of this principle to access the EUV spectrum below 50 nm.

At large angles, although the dispersion increases, the optimum grating width, and hence the resolution, decreases and also astigmatism increases rapidly. Scattered light becomes a problem too, as the distance between the grating and the slits decreases.

Depending on the grating surface material, a particular glancing angle θ ($= 90 - \alpha$) defines a minimum wavelength λ_{min} that can be reflected, according to the formula from Landon (1963);

$$\sin \theta = \lambda_{min} \, e/c \, (n/\pi m)^{\frac{1}{2}} \qquad 3.5$$

where e and m are the electron charge and mass, c is the velocity of light and n is the number of electrons per unit volume of the reflecting material.

Astigmatism can be reduced by the use of a toroidal mirror to provide horizontal focus at the entrance slit and vertical focus at the vertical focus of the grating (Rense and Violett, 1959; Namioka, 1962; Kozlenkov and Belov, 1977; Tondello, 1979).

In general, when employing grazing incidence monochromators, it is preferable to avoid the aberrations attendant with large angles of incidence since '....it is clear that there are benefits to be reaped by maintaining the glancing angle as large as possible commensurate with the shortest wavelength to be studied' (Landon, 1964).

c. *Optical Design Parameters*

The grazing incidence monochromator incorporated in the Aerobee experiment was required to continually scan, with moderate resolution, the solar wavelengths from below 10 nm to above 100 nm. For a monochromator with a concave diffraction grating the useful wavelength range is determined by application of the grating equation (3.1) which, for first inside order, when the incident and diffracted rays are on opposite sides of the grating normal N, is

$$\lambda = d(\sin \alpha - \sin \beta) \qquad 3.6$$

The incident angle α is chosen to ensure that the shortest required wavelength can be detected, using Equation 3.6.

Typically, the linear dispersion (Equation 3.3) is required to be as large as practical, for improved resolution, so preferential design criteria is for both 1/d and R to be large. But rocket dimensions limit the Rowland circle arc available for a given wavelength range, thus imposing restrictions on both of these parameters.

For the rocket payload, it was required that the monochromator be contained within a cylindrical volume of base diameter 13" and height 9". The instrument must be pointed at the sun, constraining the line from the entrance slit to the grating to be aligned perpendicular to the rocket axis. The most useful configuration was chosen to be one in which the plane of the Rowland circle lay parallel to the rocket longitudinal axis.

A Bausch and Lomb tripartite grating (Model 32-52-00-41-(t)) of concave radius 400.7 nm and 600 lines/mm, in a ruled area of 30 x 38 mm, was considered physically and optically most suitable. It was

overcoated with platinum and the grating grooves were blazed at an angle $\theta_b = 2^\circ 35'$. Having chosen the grating for the monochromator, a number of specific optical parameters were calculated, as follows.

That portion of the Rowland circle where the wavelengths of interest are focused was located using Equation 3.6. With reference to the quantities identified in Figure 3.1, it was calculated that, for radiation incident at an angle $\alpha = 77^\circ$, photons of wavelength 10 nm are diffracted at an angle $\beta_{10} = 75.5^\circ$ while for photons at 110 nm, $\beta_{110} = 65.3^\circ$. Since these diffracted rays represented the extremities of the wavelength interval to be monitored, their intersection with the Rowland circle defined the particular portion of it to be scanned. Further, from the geometry in Figure 3.1, it can be seen that

$$\Delta l = R \Delta \beta$$

so, with $R = 400.7$ mm and $\Delta\beta = \beta_{10} - \beta_{110} = 10.2^\circ$, the length of the Rowland circle arc that required scanning was 71.3 mm. Since four detectors were available for use in the monochromator, this arc was subdivided into four equal intervals. Coverage of each wavelength region thus corresponded to an arc length of 17.8 mm or, alternately, an increment in the diffraction angle of 2.55°. To illustrate these concepts, Figure 3.2 provides schematics of the layout of the monochromator's components within the physical confines of the rocket. Here, the Rowland circle is half-scale but the components have been drawn only approximately half-scale. The four diffracted rays represent the paths of photons at approximately the average wavelength of each of the four wavelength intervals.

The wavelength for which the grating was most efficient, the blaze wavelength, was calculated from Equation 3.2 as $\lambda_b = 40.4$ nm

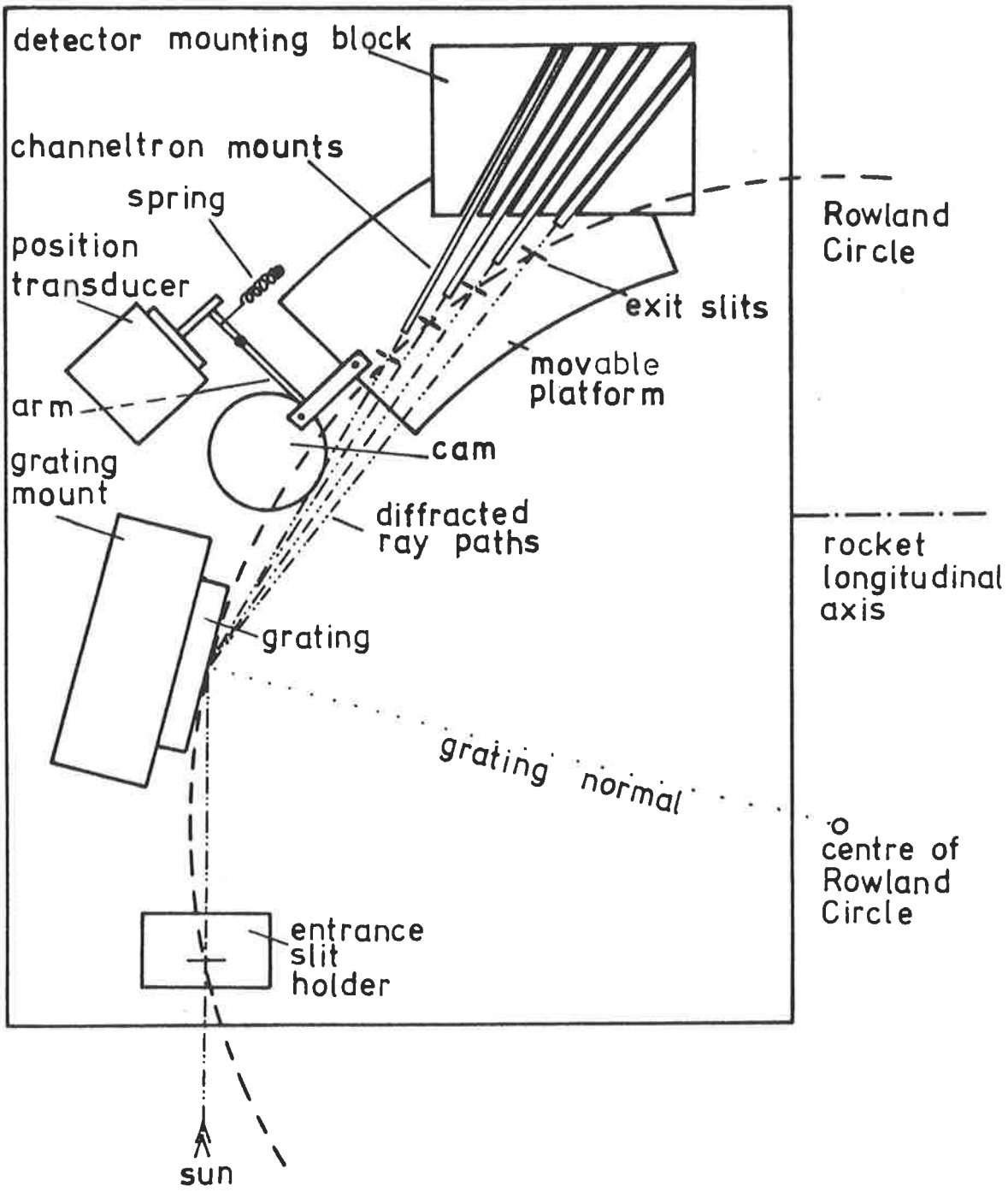

Figure 3.2 Grazing incidence monochromator.

which was appropriately central in the total wavelength range observed. An estimate of the minimum wavelength reflected from the grating was found from Equation 3.5. For light incident at a glancing angle $\theta = 13^{\circ}$ on platinum, which has an electron number density n of $6.6 \times 10^{22} cm^{-3}$, λ_{min} equalled 3.3 nm.

Particulars of the grating, wavelength and angular configuration employed by the monochromator enabled the optimum width of grating illumination to be determined from Equation 3.4. At 10 nm W_{opt} was 7.5 mm and increased to 14.7 mm at 110 nm. For the grating, of ruled width W = 38 nm, fully illuminated $W >> W_{opt}$ and the theoretical resolving power, given by Equation 3.4, was equal to 3375 at 10 nm and 6615 at 110 nm, corresponding to $\Delta\lambda = 0.003$ nm at 10 nm and $\Delta\lambda = 0.017$ nm at 110 nm.

Experimental details, in particular the slit widths, which were 125μ, limited the resolution. The exit slit of 125μ corresponded, according to Equation 3.3, to $\Delta\lambda = 0.15$ nm at 10 nm and $\Delta\lambda = 0.2$ nm at 110 nm. These values represented best expected resolution of the monochromator. In addition, there was further degradation of the resolution, due to scanning.

d. Photoelectric Detectors

To detect the extreme ultraviolet radiation diffracted at each wavelength, channel electron multipliers (Mullard channeltrons) were mechanically mounted behind each of four coupled exit slits which scanned the Rowland circle. Because of minimum dimension, weight and power requirements, channeltrons are most suitable for space experiments, as confirmed in the literature by many workers (Timothy, 1973; Timothy and Lapson, 1974; Mack *et al*, 1976).

Laboratory calibrations representative of a broad range of models (Mack *et al*, 1976) have indicated that channeltrons respond most sensitively to the spectral region 1 to 150 nm with a maximum efficiency of around 0.16 counts/photon at 75 nm. The background is characteristically low - of the order of 4 counts/minute - resulting in an overall sensitivity which exceeds that of any other presently available detector.

Physically, this detector is a hollow glass cylinder with a resistive secondary emission coating on the inside surface. Its ability to detect radiation is based on the concept of a resistive strip dynode. A photon striking the wall releases an electron which is accelerated by an applied axial electric field until it strikes the wall again to produce secondary electrons, so that of the order of 10^8 electrons are collected at the anode. Positive ion feedback is inhibited by curving the channeltron tube.

The gain of a channeltron is defined as the ratio of the charge in the output pulse to the electron charge. This output charge is used to raise the potential across the input capacitor of a pulse amplifier and the resultant voltage is referred to as the pulse height. Because of the statistical nature of electron multiplication processes in a channeltron, the output pulses are not all the same size so that the nominal gain is not always achieved every time an output pulse is produced. However, as the gain, which depends on the operational voltage applied to the channeltron funnel, is increased, the output pulses become more constant in amplitude. In this pulse saturated mode, each detected photon produces an output pulse which remains constant in amplitude even with relatively large fluctuations in the channeltron bias voltage.

In absorption spectroscopy experiments, the response of the photodetector must be linear over a wide dynamic range, as defined by

the incident solar flux, and channeltrons are quite satisfactory providing their output count rate is less than, typically, 10^5 counts/sec. The count rate is limited by current depletion when the signal current approaches the quiescent channel current and this may be caused by excessive radiation. However, since the limit is strictly a function of the tube resistance, it is apparent that the linearity of response can be extended to higher count rates by decreasing the tube resistance.

At rocket apogee, if this is above the main absorbing region of solar EUV flux, the intensity of, for example, 58.4 nm radiation will be 1.3×10^9 photons $cm^{-2} sec^{-1}$ (Heroux and Hinteregger, 1978). Since the area of the entrance slit is $0.0125\ cm^2$, there will be 1.6×10^7 photons/sec incident on the grating. Assuming that 50% of these are diffracted into the exit slit and that the channeltron efficiency is 16% the output count rate will be 1.3×10^6 counts/sec, which could be in the non-linear region of channeltron operation.

Dr G. Bibbo, as a postgraduate student involved with preliminary organization of the rocket payload, consulted Mullard on the availability of small channeltrons capable of handling count rates of at least 10^6/sec. Mullard agreed to manufacture a special batch of low resistance channeltrons Consequently, two models were incorporated in the monochromator. Photographed in Figure 3.3, the larger channeltron is a Mullard B413BL with entrance funnel 15 mm x 4 mm and the smaller is the 'experimental' model B312BL with entrance funnel 10 mm x 2.5 mm.

Operation of these detectors in the pulse saturated mode required that a potential of - 3KV be applied to the channeltron funnel and on the Aerobee rocket this was obtained from a +28 Volt battery, isolated by a DC-DC convertor. Output pulses were fed to a pre-amplifier, thence digitally to the PCM telemetry. Figure 3.4 is the electronic

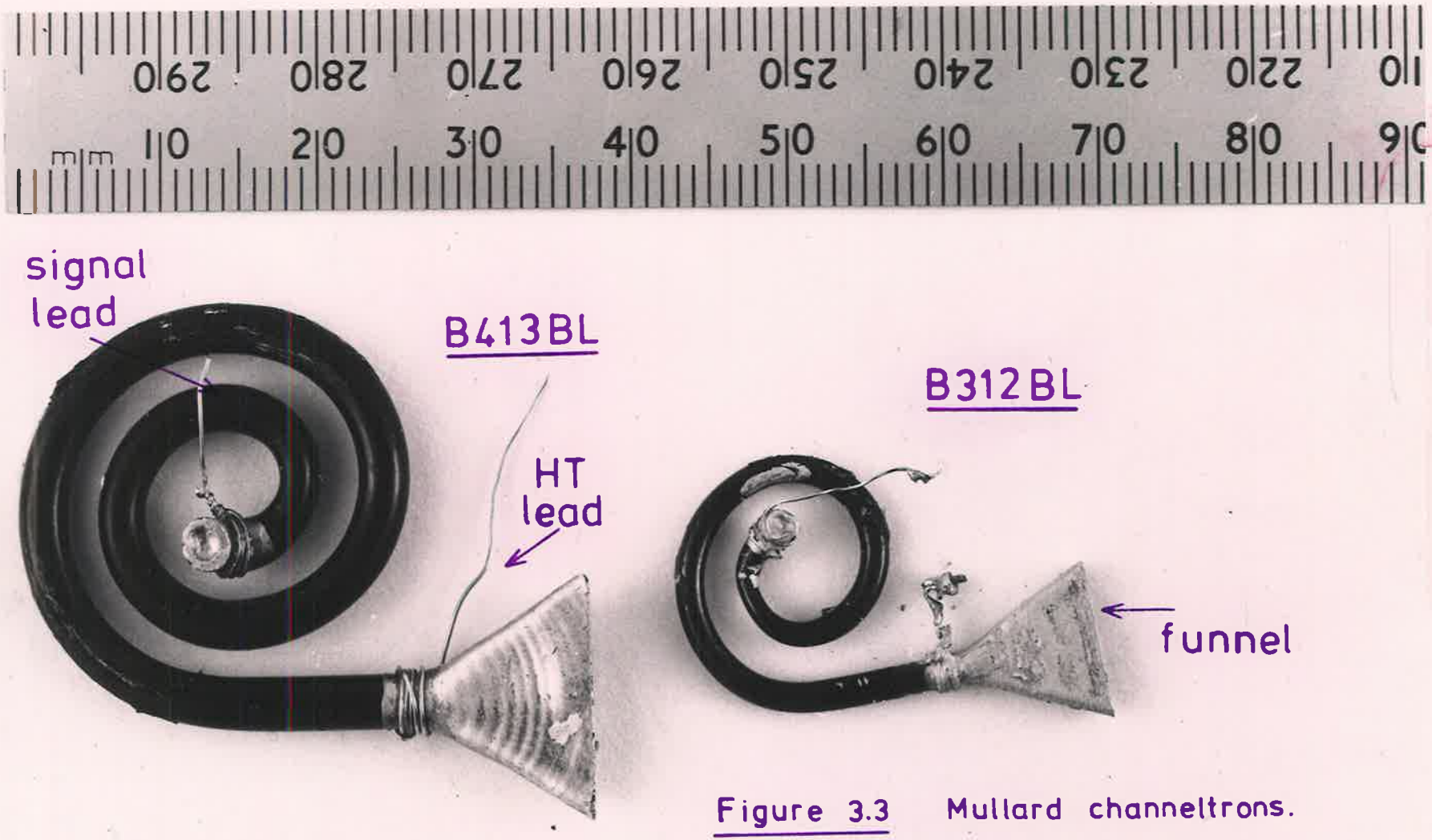

Figure 3.3 Mullard channeltrons.

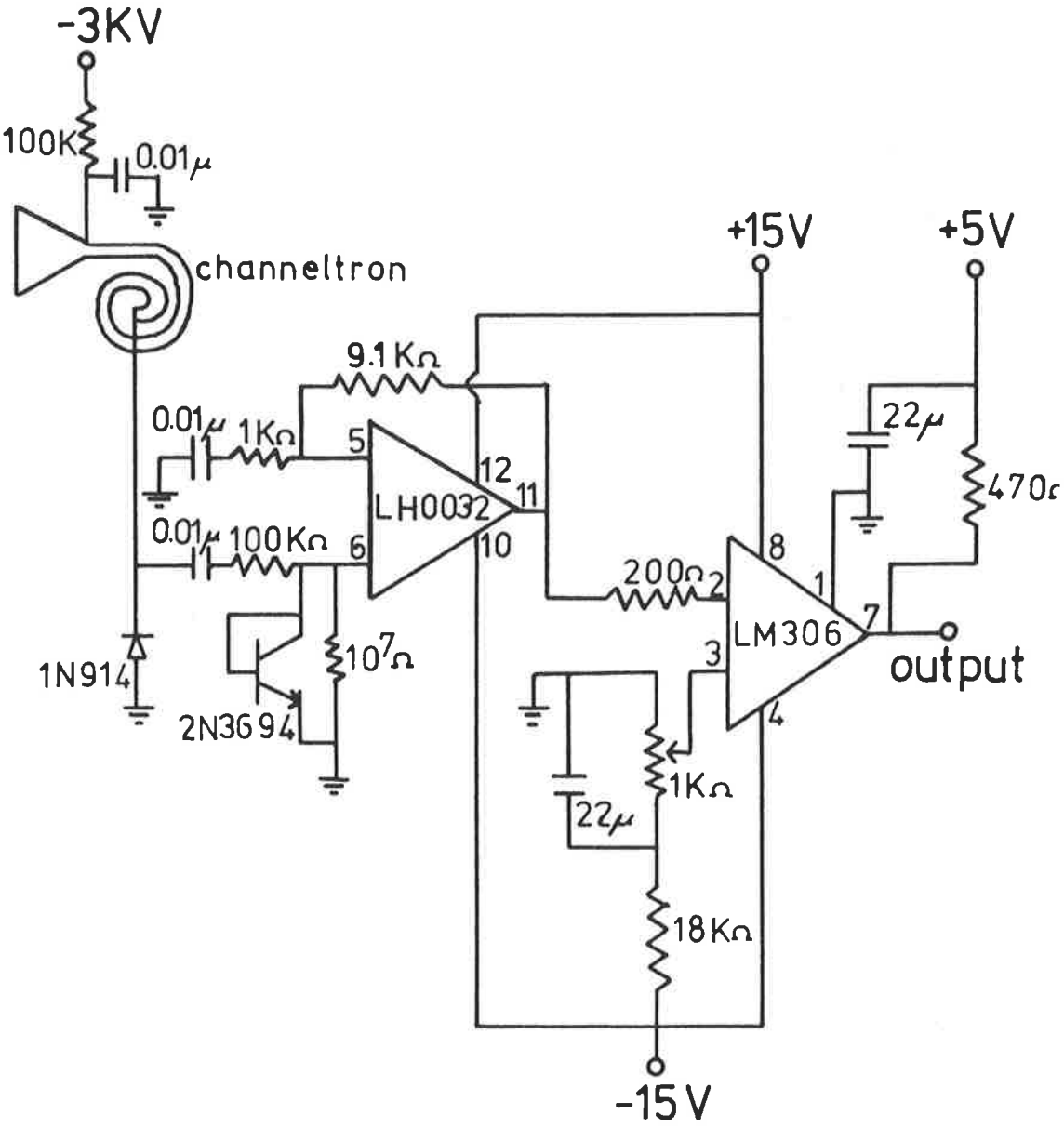

Figure 3.4 Electronic schematics for channeltron photon detector.

schematics for the detectors employed in the monochromator.

e. *Detector Scanning Mechanism*

To scan the wide wavelength range of interest, the photoelectric detectors must be translated along the Rowland circle. In Section 3.3c it was calculated that each of the four detectors must traverse a distance of 17.8 mm. Scanning was achieved, with reference to Figure 3.5, using the following mechanical configuration. Two grooves with curvature equal to that of the Rowland circle were machined in a curved way which was then mounted in a raised position above a base plate. A platform for carrying the exit slits, channeltrons and preamplifier electronics moved on ball bearings in these grooves. Additional ball bearings, constrained beneath the curved way, ensured that the motion of the carriage remained in the plane of the Rowland circle. The complete scanning mechanism, assembled for flight, can be seen in the photograph, Figure 3.6.

Transit along the curved way was produced by the action of a motor driven cam which is identified in Figure 3.6 and also, more clearly, in Figure 3.2. A brass disc was mounted eccentrically on the motor shaft and connected to the movable carriage by a rod which was free to pivot about its attachments to both the carriage and the disc. Hence the rod was constrained to accompany the disc as it spun, thereby converting this rotation to translational motion of the carriage along the Rowland circle arc.

In Figure 3.2 it can be seen that an arm on a pivot pressed tangentially against the disc. Because the disc was mounted off-axis, its rotation caused a linear displacement of this tangent point, which was transferred, via the pivoting arm, to the transducer. As a result,

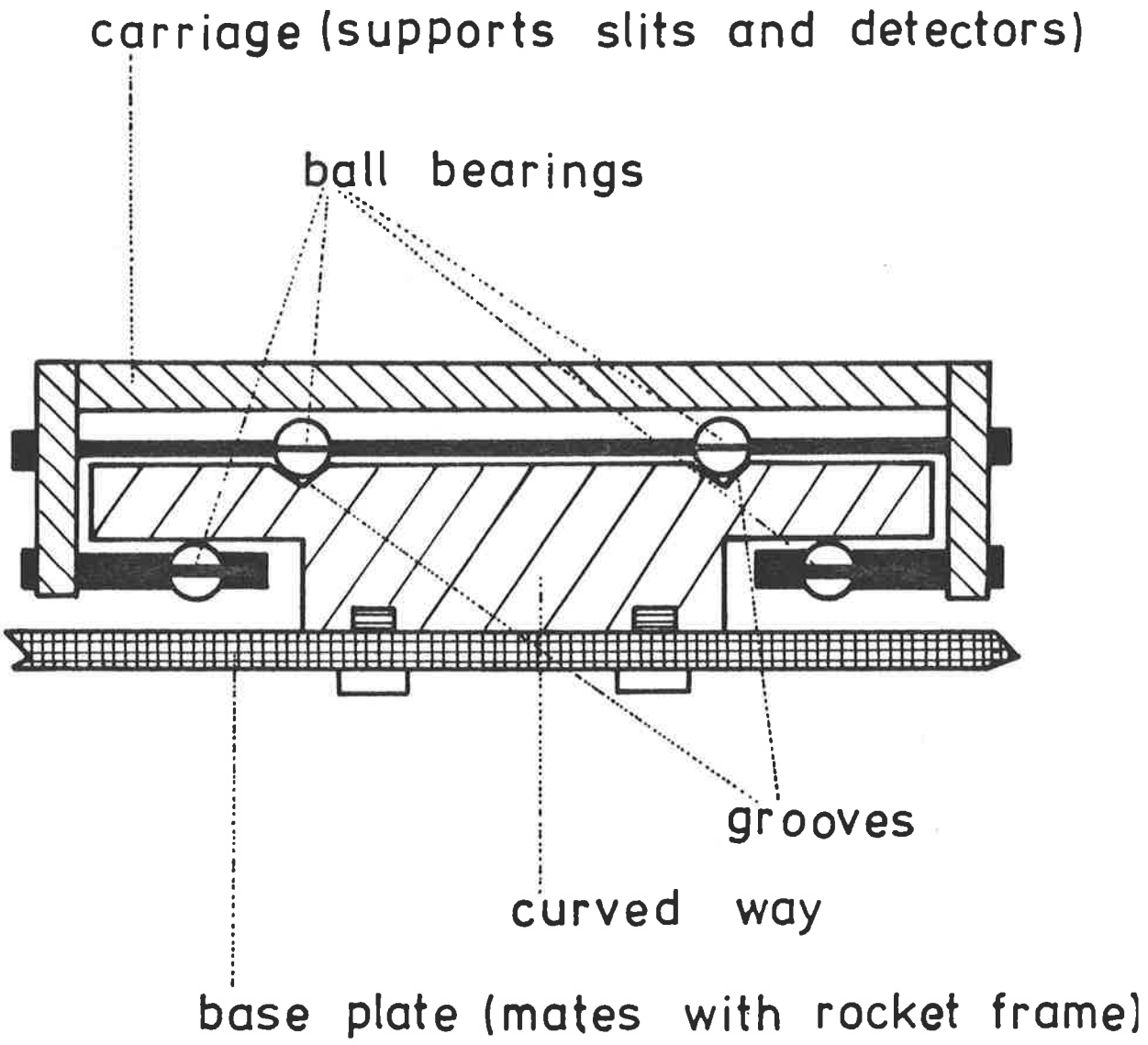

Figure 3.5 Cross sectional view of detector scanning mechanism.

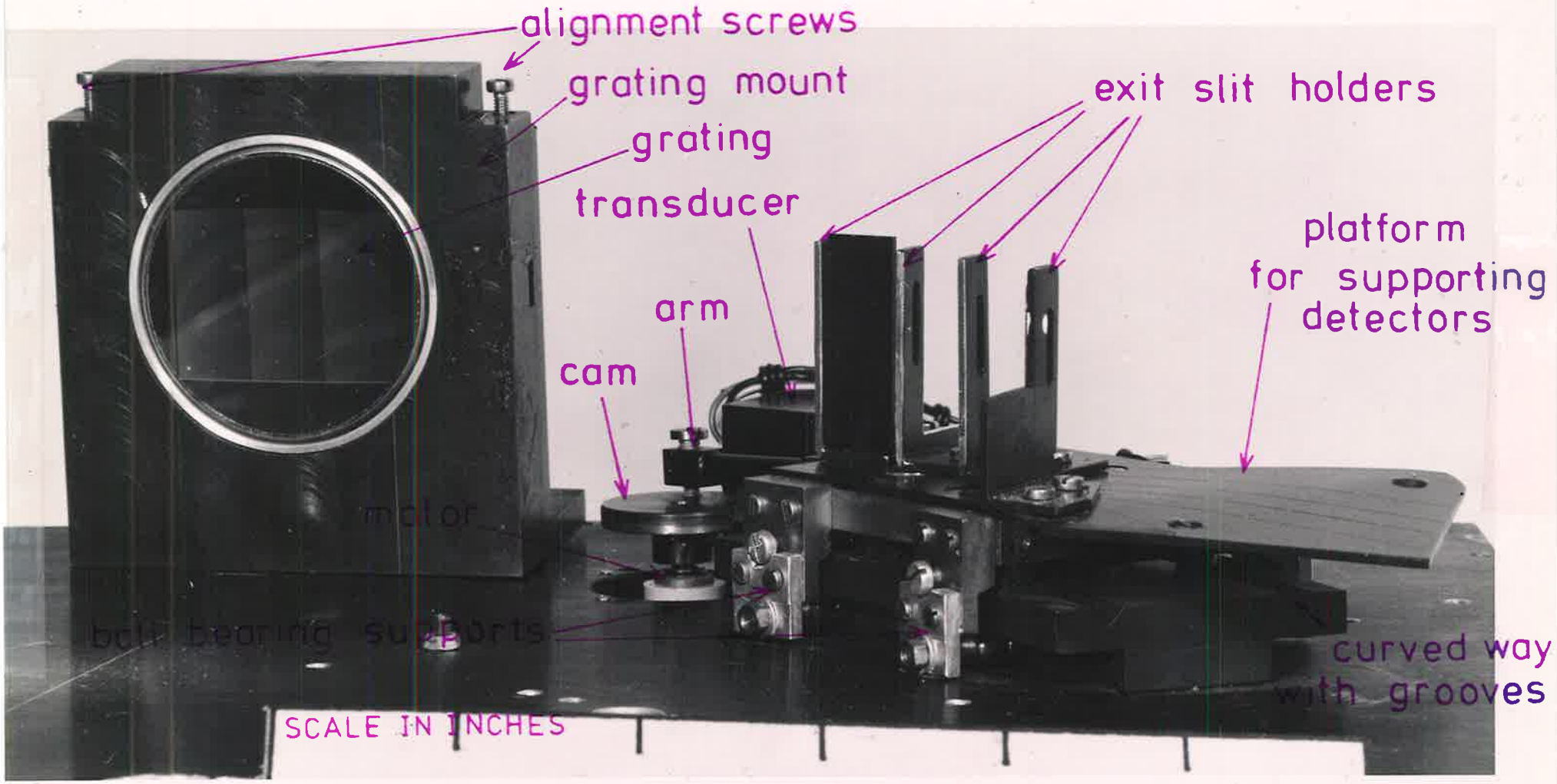

Figure 3.6 Grating and detector scanning mechanism of the grazing incidence monochromator.

the location of the carriage in its scan was uniquely identified by the transducer.

The scanning motor was driven from a regulated +28 volt supply and the transducer required 5 volts.

3.4 PRE-FLIGHT ALIGNMENT AND OPERATION

a. Assembly

Construction of the grazing incidence monochromator was undertaken by the workshop at the Department of Physics, University of Adelaide. Materials used were brass and aluminium and the components were blackened then positioned on a 6 mm thick aluminium sheet which mated with the rocket frame.

It is necessary when mounting a grating to provide, for ease of alignment, a small degree of freedom of rotation about the X, Y and Z axes of Figure 3.1. This was achieved by bonding the grating onto a flat surface which was then located, using strategically placed screws, in a rigid holder that bolted firmly to the base plate. The grating in its mount can be seen in Figure 3.6.

Each channeltron funnel was painted with highly conducting paint 'Acheson Silver Dag 915', to ensure a uniform potential, then potted with Dow Corning silastic in insulating teflon holders. These were slotted, at the appropriate angle to the grating normal, as illustrated in Figure 3.2, into a large teflon block which also supported the four detector pre-amplifiers. The complete block was screwed onto the movable carriage.

The exit slits were formed by bonding razor edges to aluminium supports which were then screwed perpendicularly onto the carriage, at the correct position on the Rowland circle. Throughout the assembly, strict attention was given to the requirements of concave grating, Rowland

circle mount geometry. Centres of the slits and grating were physically checked to be at uniform height above the rigid mounting board.

Finally, to inhibit stray and scattered light, a black cover was made to enclose the instrument, with allowance for pumping through a 5 cm square mesh port.

b. *Visible Alignment*

The necessity of careful assembly and pre-alignment to produce required wavelength accuracy and resolution has been emphasized by Madden *et al* (1967). In a correctly aligned monochromator, the centre of the slits and the grating lie on the Rowland circle, which defines the Rowland plane. Grating lines must be perpendicular to the Rowland plane and in the plane defined by the tangent to the Rowland circle at the centre of the grating.

To align the monochromator, the following procedure was used. A laser beam, confined to pass through the entrance slit and then a pinhole in the Rowland plane, hit the grating centre. Simultaneously, another laser beam was incident on the grating centre through pinholes along the normal to the grating tangent. By adjusting the grating location in its holder, the zero, first and second order diffracted rays were made to lie in the Rowland plane, and the normal ray collimated. Once aligned, the grating position was rendered invariant against possible rocket vibration with silastic on the locating screws.

The actual wavelengths that would be scanned by the fully aligned monochromator were estimated from Equation 3.6 and measurements, with a protractor, of the angle between each exit slit and the grating normal, for various locations of the movable carriage as monitored by the transducer. The four detectors, labelled A, B, C and D, were thus

determined to scan, respectively, the wavelength intervals 104 to 75.4 nm, 75.4 to 48 nm, 50.5 to 25.9 nm and 26 to 6 nm.

c. *Vacuum Operation*

The mechanical measurements described above afforded only a crude estimation of the wavelength scale of the monochromator; an uncertainty of 0.5° in the measured angle between the grating normal and either of the incident or diffracted ray paths effected a wavelength uncertainty of 3 nm. A more accurate calibration could have been made with emission lines at a variety of wavelengths from 10 to 110 nm but this was not possible because no suitable laboratory light source was available. Rather, it was assumed that identification of a few of the many emission lines which characterize the EUV solar spectrum would provide a wavelength scale.

However, the optical and electrical operation of the monochromator was checked under vacuum with the system described in Figure 3.7. A McPherson half-metre normal incidence monochromator was used to disperse light from an AC powered Hinteregger capillary discharge lamp. The exiting beam was incident at an angle of 45° on a mesh covered with sodium salicylate which converted the ultraviolet radiation from the laboratory monochromator to visible radiation that was monitored by a photomultiplier.

The rocket instrument was positioned in the adjacent vacuum chamber so that the light fell on the centre of its entrance slit and illuminated the grating. This correct placement could only be physically ascertained in zero order and was done with both a laser beam and a dispersed white light source.

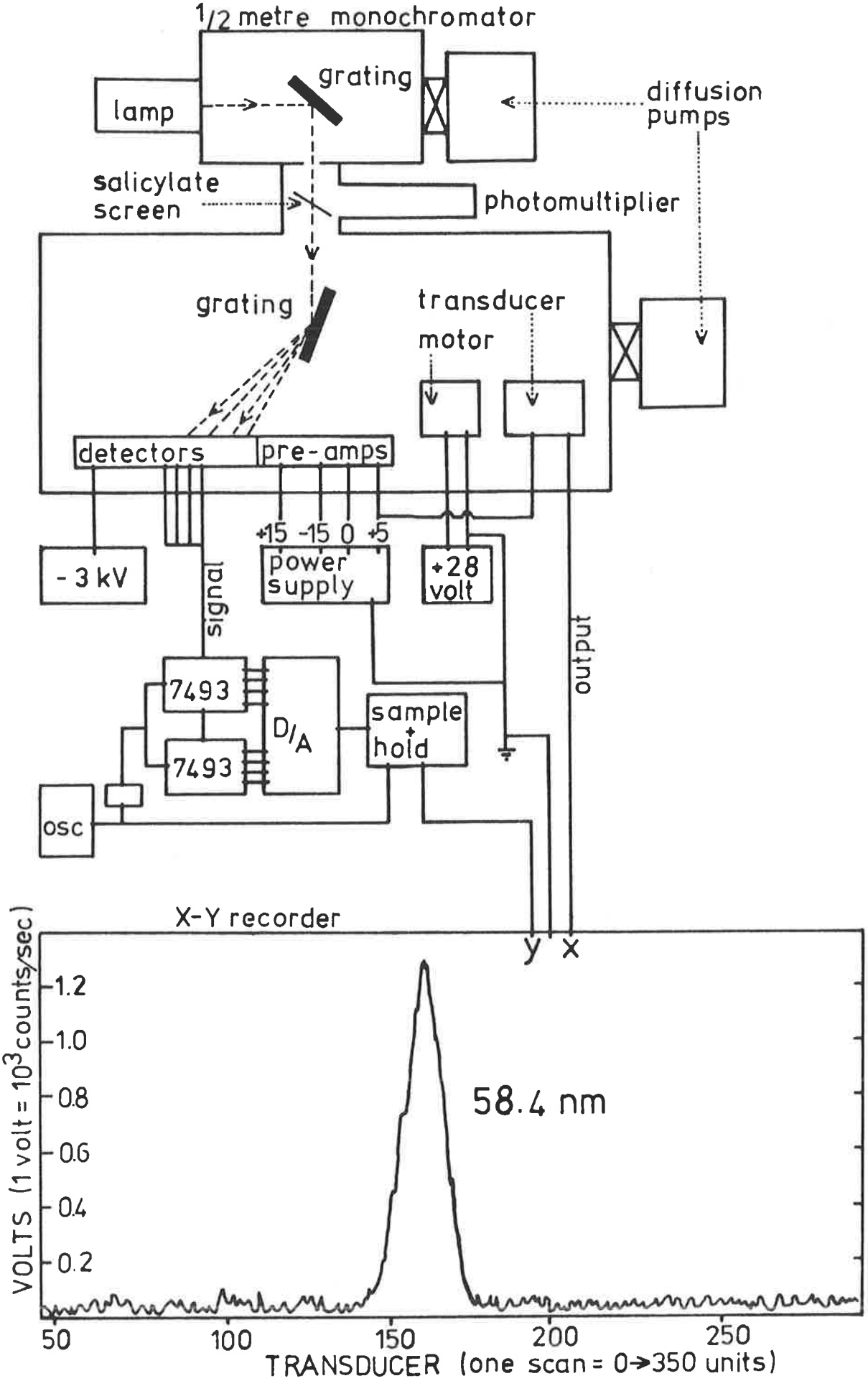

Figure 3.7 Diagram of monochromator laboratory operation.

To observe the amplified channeltron pulses, a digital-to-analog convertor was used to produce an output voltage directly proportional to the number of counts per second received. This was displayed as the Y signal of an X-Y recorder, the X input of which was the transducer output.

It was confirmed that each channeltron detected light by removing the entrance slit of the rocket monochromator and allowing zero order radiation to fall directly on the grating. Included in Figure 3.7 is a scan of 58.4 nm, recorded by the monochromator with the motor spinning once every 75 seconds.

3.5 FLIGHT DATA

The grazing incidence monochromator was flown on an Aerobee 170 rocket, launched from Woomera, S.A., at 0636 hours C.S.T., when the sun was at a zenith angle of 85°.

Recalling the calculations presented in Figure 2.1, solar EUV radiation, incident on the atmosphere at this zenith angle, is attenuated primarily over the altitude region 150 to 350 km. An Aerobee 170 rocket, with apogee anticipated to be 209 km, is certainly not the preferred rocket vehicle for EUV absorption spectroscopy experiments at large zenith angles. Explanation of this anomaly is afforded by the following brief recount.

At inception, proposals for a composite experimental package to measure a variety of thermospheric parameters required that a more powerful Aerobee 200 rocket be launched when the zenith angle was near 45°; a similar investigation in which a Skylark rocket, launched also from Woomera, attained an apogee of 273 km when the zenith angle was 43.5°, had been reported by Timothy *et al* (1972). A grazing incidence monochromator

for monitoring the attenuation of solar EUV radiation was therefore an important and viable component of the payload, as originally conceived. The utility of the experiment was considerably lessened when the priorities of the principal investigators re-focused on the early morning ionosphere, with its attendant large zenith angles. It was anticipated, however, that useful data would be collected from a few wavelength intervals in the EUV spectrum where the absorption cross-sections of the thermospheric constituents were sufficiently small to allow solar flux to penetrate to the lower thermosphere (Horton, 1979). And, since the monochromator was accounted for, both financially and in the payload design, it remained. That an Aerobee 170, rather than the more suitable Aerobee 200, was used resulted from poor communication between the University of Adelaide and NASA's Goddard Space Flight Centre.

In Figure 3.8 the location of the monochromator in the Aerobee rocket payload is indicated. Figure 3.9 is a photograph of the Aerobee vehicle on the launcher just prior to lift-off. The rocket under-performed and attained an apogee of only 177 km; thus the quality of the data was further reduced.

Throughout the flight, the solar eye, situated above the entrance slit, ensured that the monochromator was pointed at the sun. The amplified output from each channeltron and the transducer's analog signal were sampled by the PCM telemetry 320 times per second. At 107 km on the upleg the HT was activated and data was acquired for 270 seconds until the HT was turned OFF at 85 km on the downleg. With the motor period equal to 1.3 seconds, a total of 216 scans in each direction of transit was obtained over the entire rocket flight.

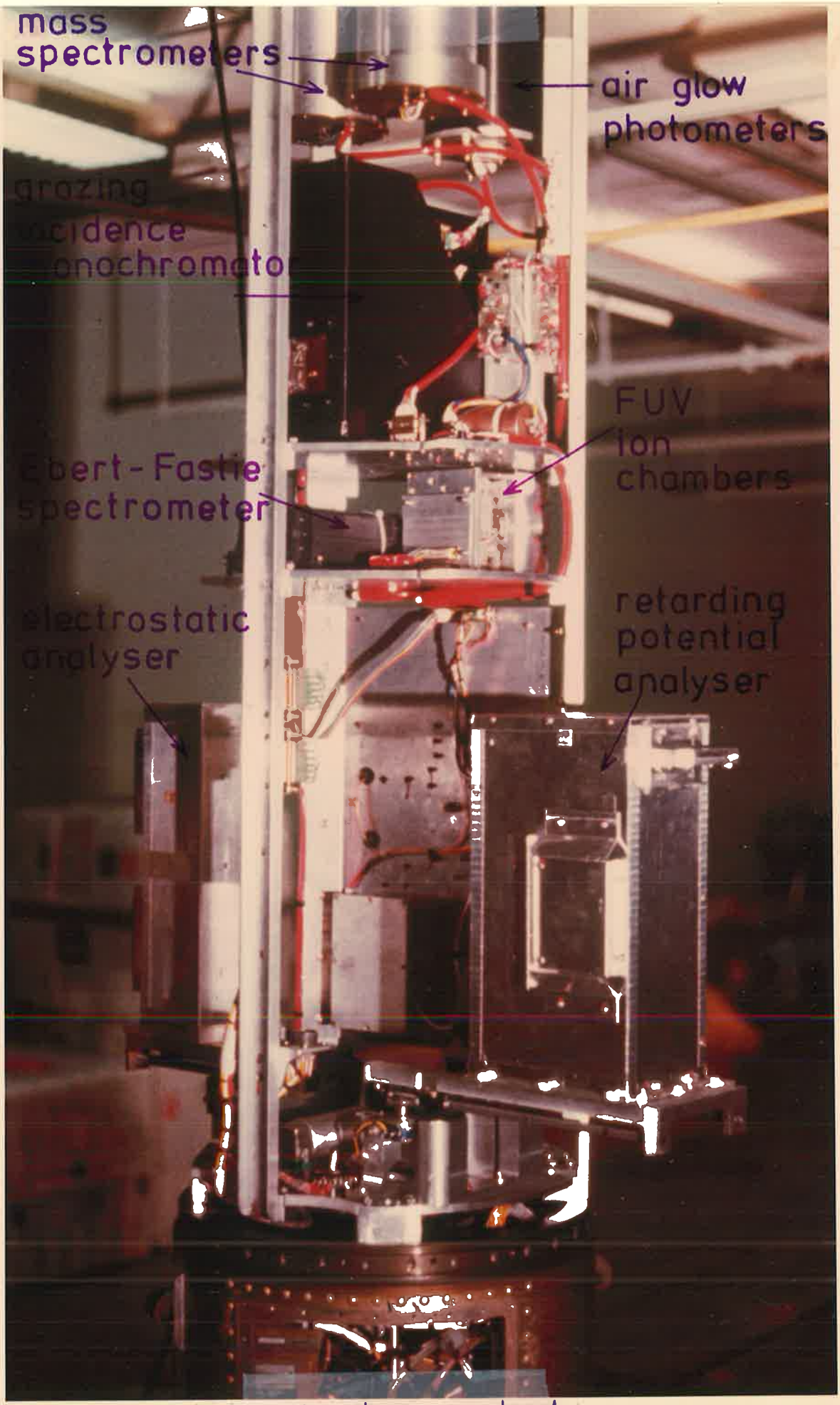

Figure 3.8 Aerobee payload.

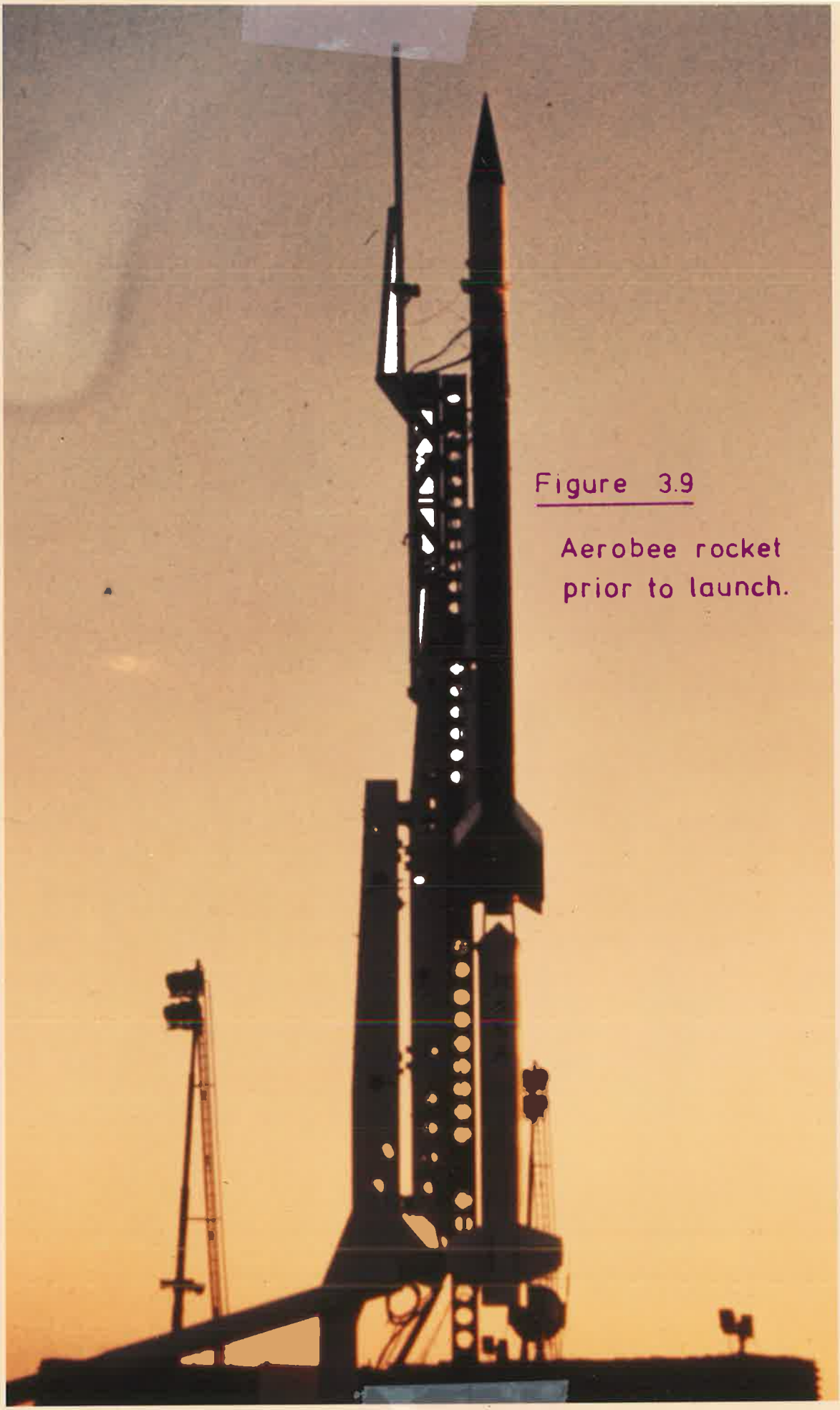

Figure 3.9

Aerobee rocket prior to launch.

Figure 3.10 is a sample of the quicklook records, in which the digital detector signals are displayed in analog format. This was achieved by repeatedly accumulating telemetry pulses from zero to a pre-set maximum voltage so that the data display is, effectively, compressed. The salient feature of Figure 3.10 is the approximately constant and very low count rate of detector B, implying that it was not responding to the transmitted solar flux. For the other three detectors, high count rates near apogee caused a randomization of the quicklook records while below 90 km the count rates were reduced and almost constant.

a. Solar Spectral Scans

Signals telemetered from each detector were apportioned to successive solar spectral scans according to the corresponding transducer output which has been illustrated qualitatively in Figure 3.10 and which ranged in magnitude from 0 to 350 units. To increase their reproducibility by increasing the statistical accuracy at selected wavelength intervals, the scans were divided into 70 steps and the channeltron signals were averaged over consecutive steps defined by 5 transducer units.

Nine such scans were then averaged at apogee to provide the lease attenuated spectral scan for each detector. From detector B, an experimental channeltron (type B312BL), no useful signal was obtained. As noted previously, the telemetry output remained constant, at approximately 1.5×10^3 counts/sec and this slow count rate has been evidenced in the quicklook record of Figure 3.10. It is possible that either the HT lead to the funnel, or the channeltron itself, had been broken and the measured count rate was probably caused by pre-amplifier pickup. These channeltrons are fragile and, despite being cushioned in silastic, this

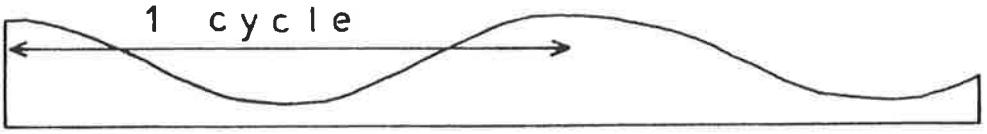

transducer

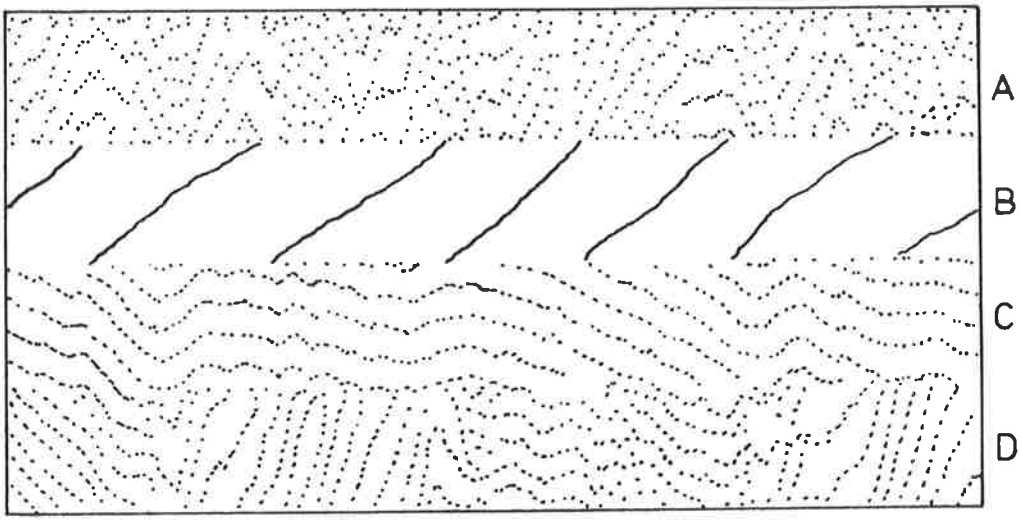

detector signals near apogee

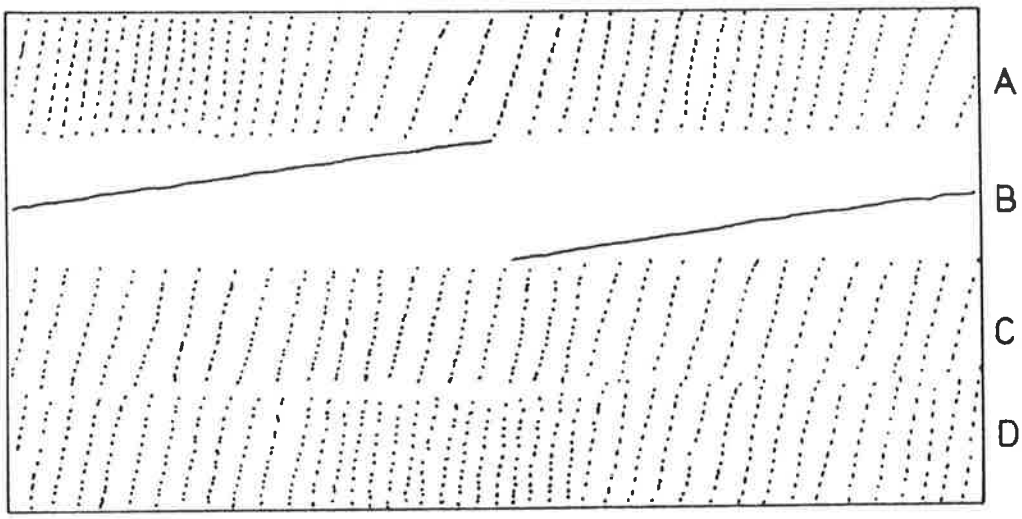

detector signals below 90 km

A : channeltron type B413BL, longest wavelengths

B, C } experimental channeltrons, type B312BL

D : channeltron type B413BL, shortest wavelengths

Figure 3.10 Quick-look records of telemetered outputs from the grazing incidence monochromator.

detector may not have survived the severe vibrations accompanying a rocket launch.

Neither did detector C, also an experimental channeltron (type B312BL) provide useful spectral data. Analysis of the scans indicated that, while the detector responded to solar radiation, the count rate was about half that of the larger channeltrons (type B413BL) and no reproducible or identifiable spectrum could be extracted. It was concluded that, although the B312BL model channeltron can detect light, its response was too slow to resolve the rapidly scanned solar spectrum. This observed unsatisfactory flight performance has been confirmed in post flight calibration, as requested by Mullard and reported in Appendix B. An alternative explanation is that at an altitude of 177 km there is complete attenuation of the flux at 30.4 nm, which was expected to have provided the signature wavelength for the spectral region scanned by this detector.

An average scan of the highest wavelength interval monitored by the monochromator (detector A) is shown in Figure 3.11 and the laboratory-determined wavelength scale is provided in Figure 3.12. Wavelength identification, as indicated in Figure 3.11, was acquired from consultation of the unattenuated solar spectrum over the wavelength interval 75 to 95 nm (Dupree and Reeves, 1971), Figure 3.13, in conjunction with Figure 3.12. Structure observed in the Lyman continuum is probably related to the many strong lines in the nitrogen absorption spectrum throughout this wavelength range, as evident in Figure 1.6. It is apparent that the range of the solar spectrum scanned by the monochromator was not as complete as anticipated, indicating that the cam configuration provided less than the intended coverage of the Rowland circle arc.

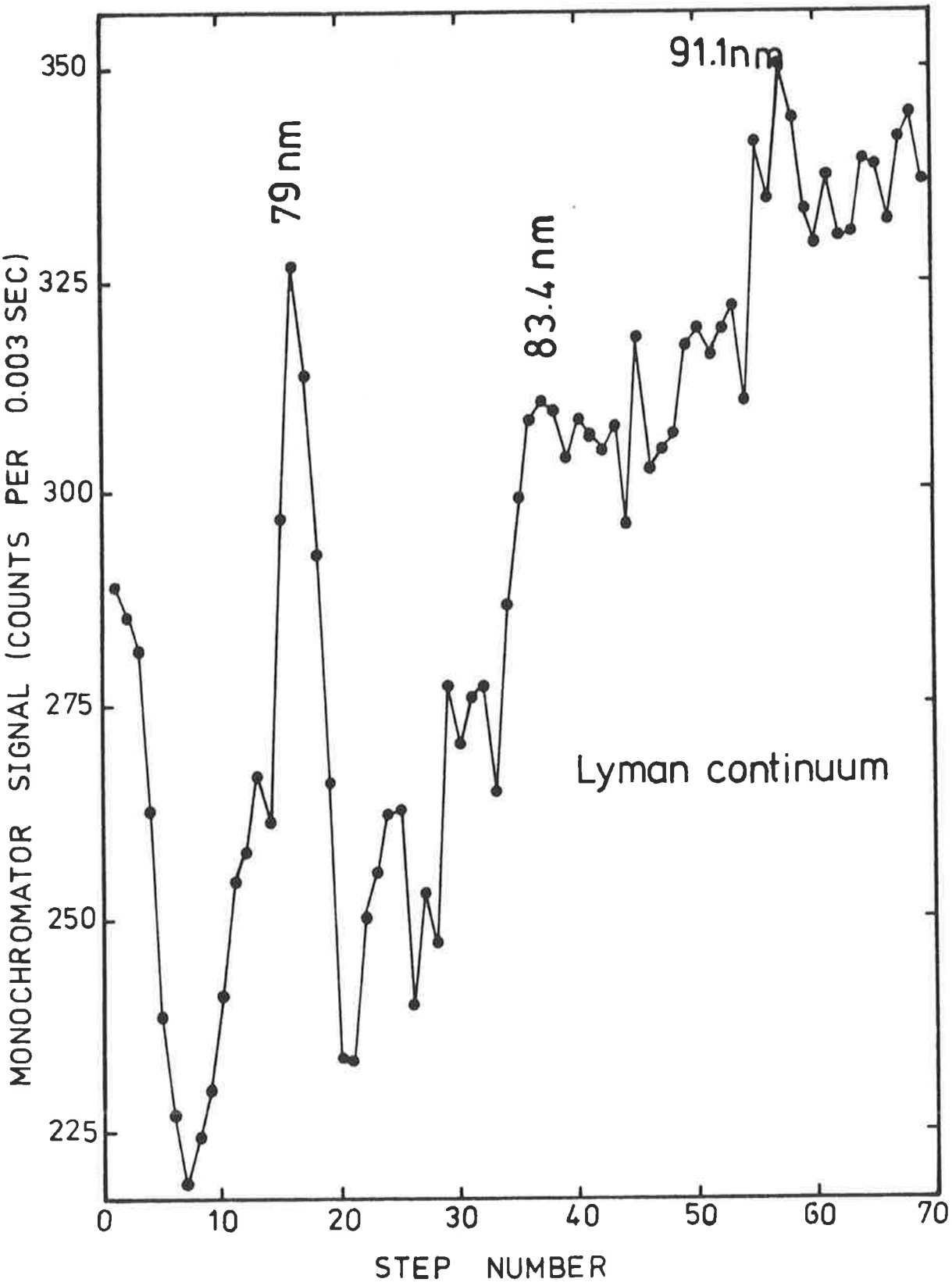

Figure 3.11 Long wavelength scan of solar spectrum, near apogee (detector A).

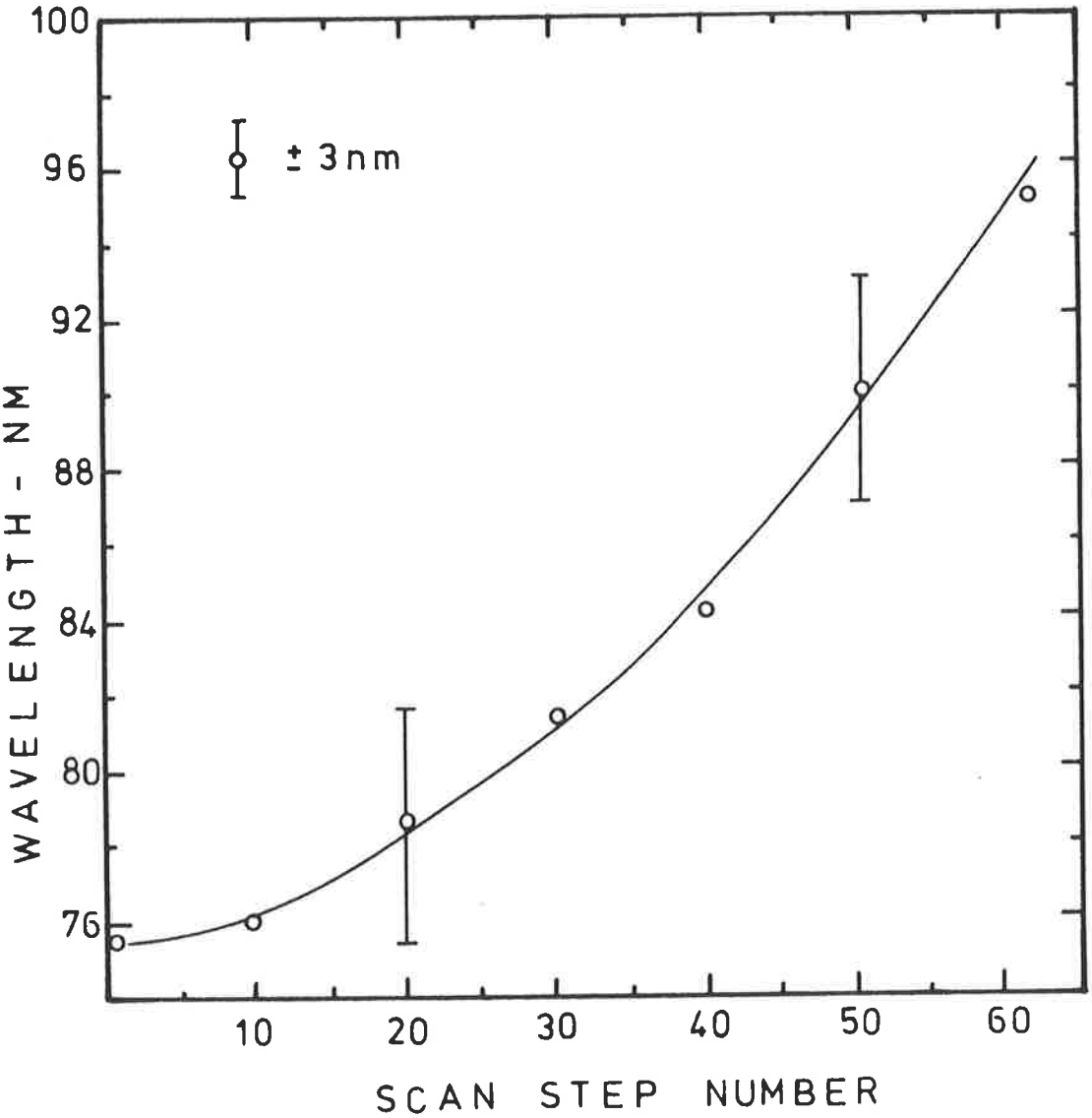

Figure 3.12 Approximate wavelength scale for Figure 3.11, determined in the laboratory using Equation 3.6.

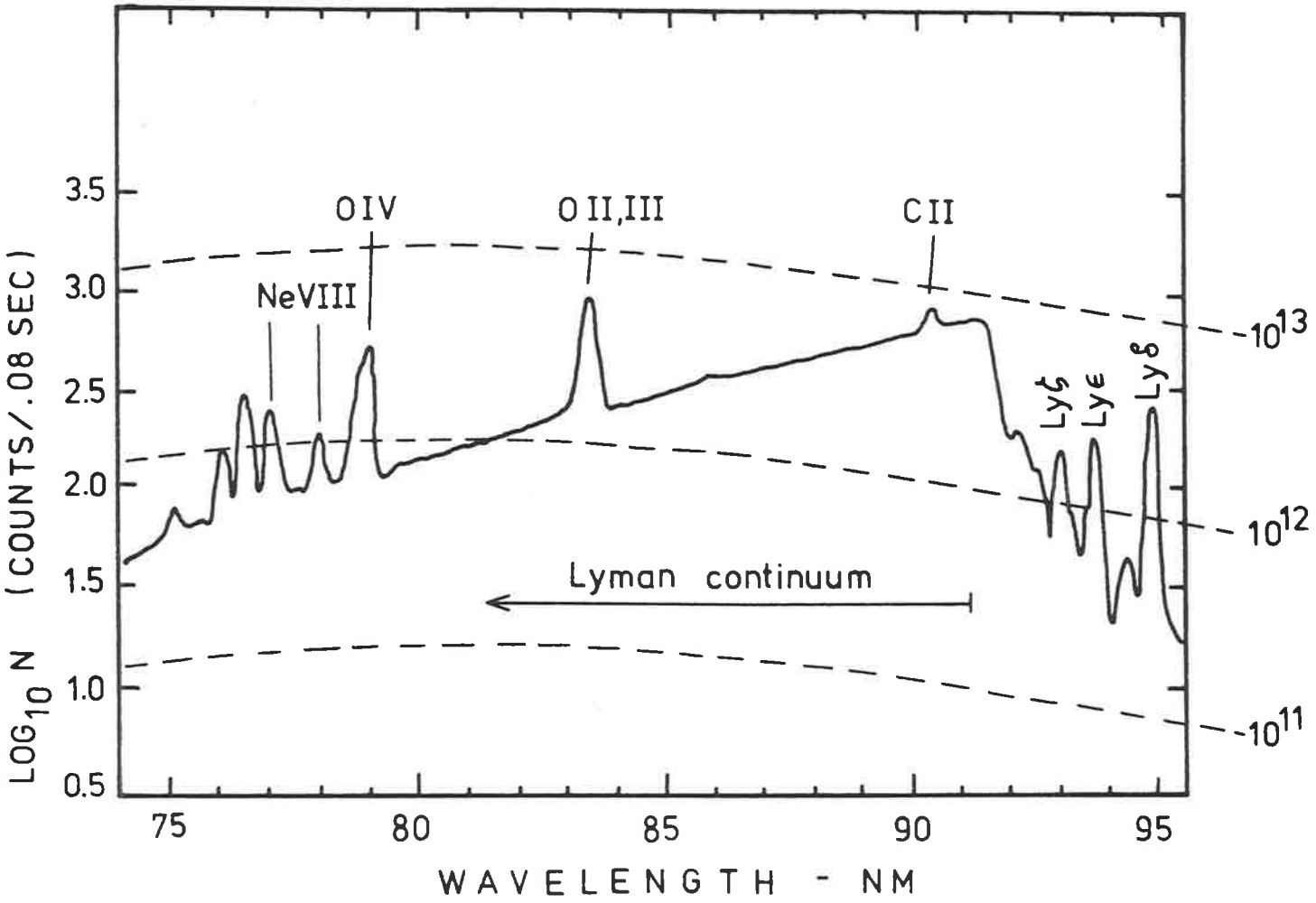

Figure 3.13 Spectrum of the quiet sun, 75 to 95nm. (Dupree and Reeves, 1971)

Figure 3.14 is the spectral scan recorded at apogee by detector D (channeltron type B413BL) which monitored the shortest wavelengths. Calculations in Figure 2.1, with $\chi = 85^{\circ}$, indicate that, at 180 km, the transmitted flux at 10 nm is 0.4 of the incident flux. Although Figure 3.14 is not a scan of the unattenuated solar spectrum, it is possible to compare the two because, at the shortest EUV wavelengths, the absorption cross-sections of the thermospheric species vary only slowly and smoothly with wavelength (see Figure 1.6) so the relative spectral distribution of the unattenuated solar flux will be generally preserved during its transmission through the atmosphere. It must be noted, however, that the solar spectrum at these short EUV wavelengths may vary markedly with solar activity (Section 1.1a) and this may affect such a comparison.

When the Aerobee rocket was launched, the solar radio flux was $82 \times 10^{-22} Wm^{-2} Hz^{-1}$, and superimposed on the experimental spectrum in Figure 3.14 is the flux data of Manson (1972), obtained when the solar radio flux was $81 \times 10^{-22} Wm^{-2} Hz^{-1}$, summed over 0.4 nm intervals. Accompanying any comparison between the two spectra in Figure 3.14 is the following caveat; there are no singularly prominant solar lines shortward of the He II emission at 30.4 nm and the only feature of the experimental scan, useful for wavelength identification purposes, is the sharp signal decrease about step # 40. While this enabled adequate wavelength identification within its vicinity, since the monochromator wavelength was not a strictly linear function of the step number, the wavelength scale in Figure 3.14 is of qualitative rather than quantitative relevance to the experimental scan.

b. *Experimental Absorption Profile*

An experimental absorption curve is the height profile of the

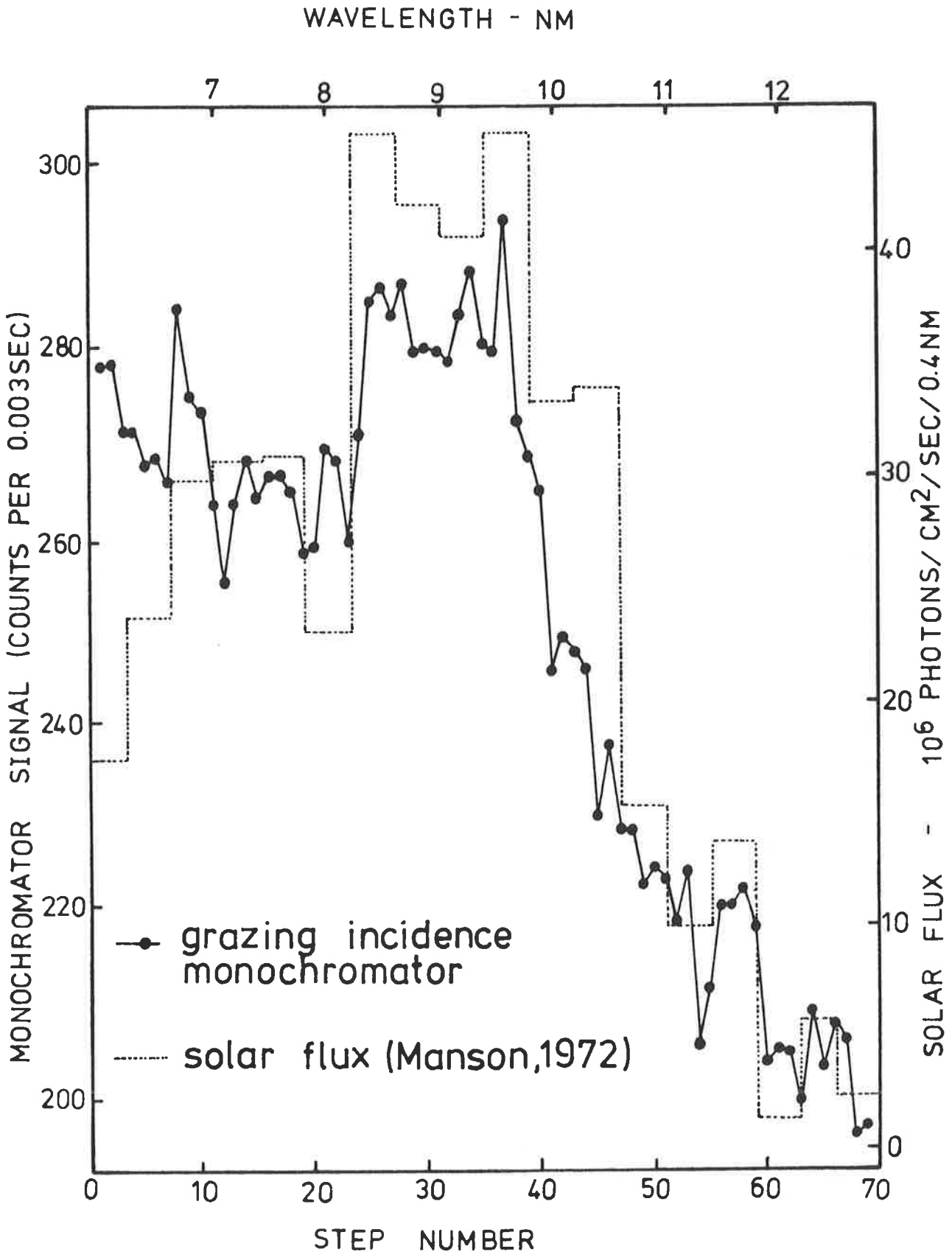

Figure 3.14 Short wavelength scan of solar spectrum, near apogee (detector D) - see text.

signal from a finite wavelength interval of the spectrum scanned by the monochromator (Figures 3.11 and 3.14). Illustrated in Figure 3.15 is the altitude variation of the average signal at steps 36 + 37 + 38 of Figure 3.14. Above about 120 km the signal increased monotonically due to solar flux at approximately 9.6 nm. A large non-zero background, which decreased at altitudes less than 120 km, was attributed to scattered Lyman-alpha radiation. As previously noted (Section 1.1b), this line is singularly the most intense of all solar ultraviolet emissions. Its flux of 3×10^{11} photons/cm^2/sec is about 300 times the total flux - 9×10^8 photons/cm^2/sec - from all other wavelengths less than 15 nm (Donnelly and Pope, 1973). The observed attenuation of the background signal corresponds to absorption of Lyman-alpha in the mesosphere.

A more appropriate perspective of the absorption curve is afforded by recalling the calculated attenuation profiles of Figure 2.1. It has been noted previously that, at 180 km, with $\chi = 85^\circ$, the monochromatic flux at 10 nm, where the attenuation will be similar to that at 9.6 nm, is 0.4 of its incident value. Therefore, the experimental curve in Figure 3.15, truncated by the apogee limit of the Aerobee rocket, represents only the low altitude portion of the complete profile for absorption of solar flux at 9.6 nm.

Scans of the solar spectrum monitored by detector A (Figure 3.11), at four different altitudes, are shown in Figure 3.16.

3.6 EXTREME ULTRAVIOLET ABSORPTION CROSS-SECTIONS

The ease with which composition information can be extracted from the experimental data provided by the grazing incidence monochromator

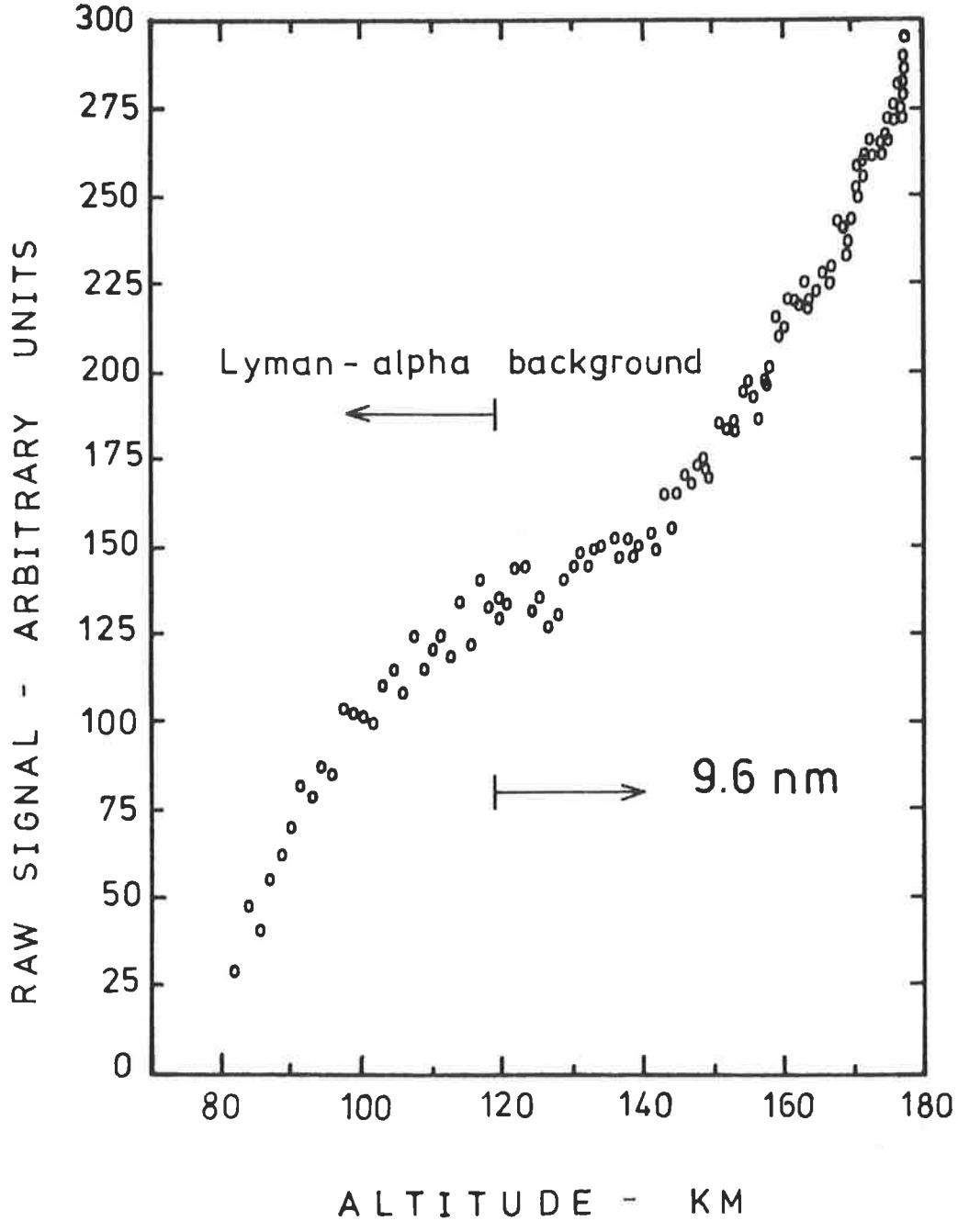

Figure 3.15 Altitude profile of the average signal at steps 36, 37 & 38 of Figure 3.14.

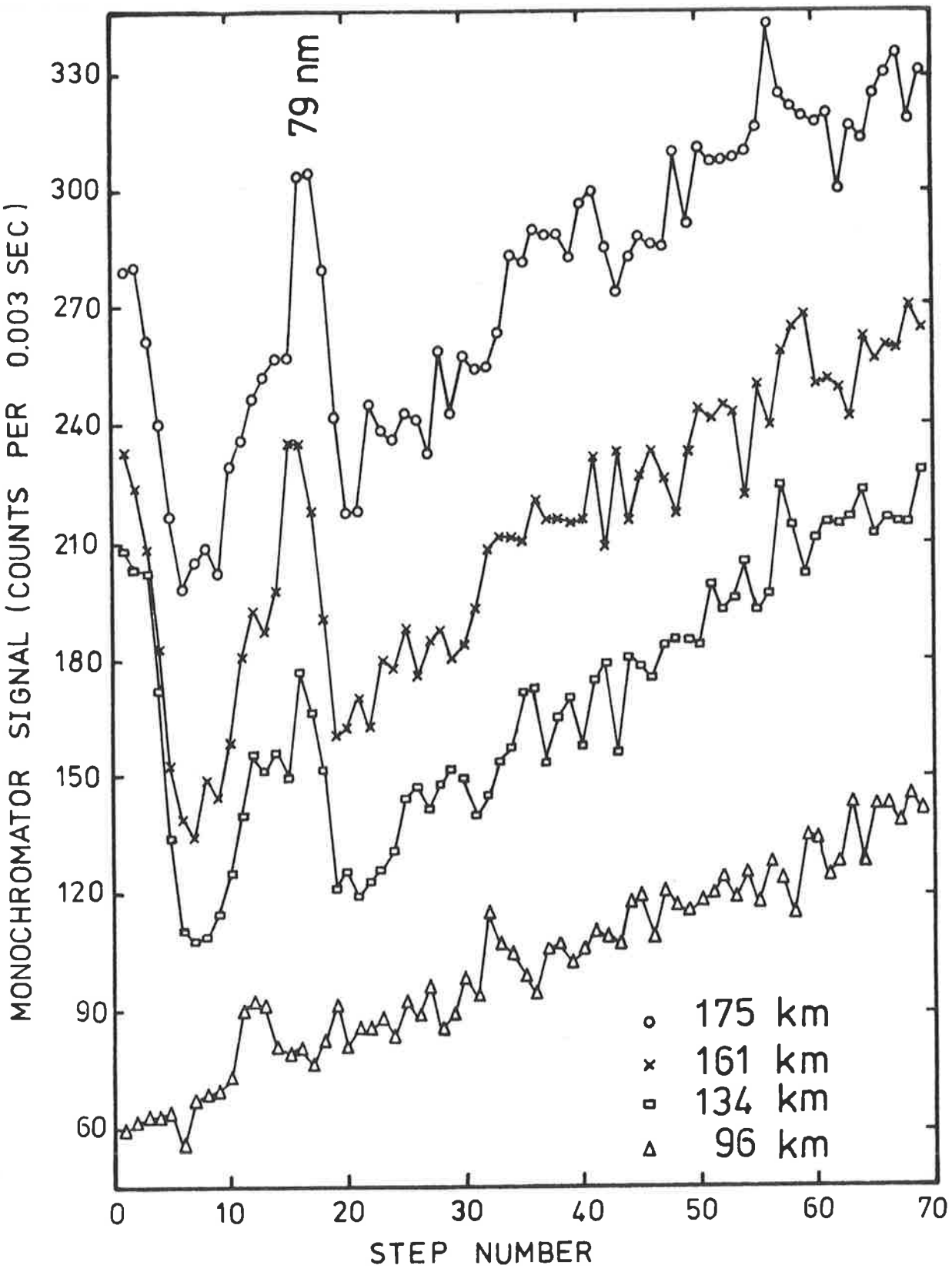

Figure 3.16 Altitude profile of solar spectral scan.

depends on the variation of the absorption cross-sections of each absorbing species across the wavelength 'window' defined by the steps of the scan used to generate an absorption curve. If this is small the absorption curve can be considered monochromatic, and the formulae of Section 2.1d are applicable. Otherwise, the far more complicated approach of Section 2.1f must be utilized. The importance of adequately accommodating the variation of the cross-sections across the detector bandwidth, in absorption spectroscopy calculations, has been emphasized in Section 2.2 and illustrated in Figure 2.3 for a detector of bandwidth 0.4 nm at 87 nm. In the thermosphere the three absorbers of EUV radiation are N_2, O_2 and O, so the structure of their absorption cross-sections must be known as accurately as possible, and this is considered below. Then, calculations of weighted mean absorption cross-sections and effective weighted mean absorption cross-sections, incorporating appropriate experimental absorption cross-section data, are described in Sections 3.6d and 3.6e, respectively.

a. Atomic Oxygen

In addition to the normal difficulties associated with EUV laboratory spectroscopy, as described in Section 1.3b, any experimental investigation of atomic oxygen is confronted with the problem of producing it in sufficient quantity, free from excited atomic and molecular states. Three measurements of atomic oxygen absorption cross-sections at photon energies above the ionization threshold have been reported (Cairns and Samson, 1965; Comes *et al*, 1968; Kohl *et al*, 1978). Each observation employed a line source and was hence restricted to certain selected wavelengths.

Between 91 and 50.4 nm Cairns and Samson obtained results at 45 wavelengths, with a passband of 0.18 nm. Atomic oxygen was produced in a microwave discharge and allowed to flow through an absorption cell, where its cross-section was measured with an estimated accuracy of ± 30%. The results of Comes *et al*, with 0.1 nm passband, were a factor of two lower. Between 89.9 and 76.2 nm, corresponding to a transition from the ground state atom to the ground state ion, Kohl *et al* have made measurements at five wavelengths, utilizing atomic oxygen produced in a shock tube. Within the quoted ± 7% uncertainty, their results support the higher values of Cairns and Samson. High resolution laboratory measurements with a continuum source are needed to establish the precise structure in atomic oxygen's absorption spectrum, since, according to the calculations of Henry (1968), the autoionization linewidths may vary from 0.0001 nm to 0.01 nm.

In the absence of abundant laboratory data, theoretical approaches have been relied on to provide numerical cross-section values. The general procedure is to consider absorption due to all, or just the lowest three, of the five transitions arising from ejection of either a p or s electron (see Section 1.3b) (Dalgarno *et al*, 1964; Starace *et al*, 1974). Refinements of this basic technique have incorporated a close-coupling of the final-state open-channels (Henry, 1967). Inclusion of autoionizing states in the wavefunctions for the e^-O^+ system (closed-channels) has provided formulation of resonances in the absorption cross-section (Henry, 1968).

More rigorous analyses have replaced the Hartree-Fock wave-function for the initial ground state, as used by Henry, with a close-coupling wavefunction similar to that used for the continuum (ion + electron)

This means that correlation effects are incorporated in both the initial and final wavefunctions (Taylor and Burke, 1976; Pradhan and Saraph, 1977; Pradhan, 1978). While these calculated cross-sections are some 45% higher than the original results of Henry, they are still lower than the available experimental data (Cairns and Samson, 1965; Kohl *et al*, 1978). Current discrepancies between experimental and theoretical estimates of the atomic oxygen absorption cross-sections in the important region 91 to 74 nm, where autoionization is abundant, are shown in Figure 3.17. To indicate the location of possibly significant lines, the relative absorption cross-section spectrum of Dehmer *et al* (1973) is included.

Below about 66 nm the cross-section spectrum is expected to be less structured, but there has been no experimental confirmation of this. For wavelengths shorter than 34 nm it has been suggested that an appropriate value is half of the molecular oxygen absorption cross-section (Cole and Dexter, 1978a). At high energies the atomic parts of the molecule tend to dominate absorption processes, but the suitability of this approximation, on a theoretical basis, is admitted by Cole and Dexter to be questionable.

It is possible that reliable measurements of the atomic oxygen absorption cross-section in the EUV spectral range, especially at short wavelengths, can be provided by high altitude (350 to 450 km) solar occultation experiments on satellites. Some preliminary results have been reported by Hinteregger and Hall (1969), Knight *et al* (1972) and Modali *et al* (1976).

On the basis of current knowledge it is not apparent which are the most appropriate values for the absorption cross-section of atomic oxygen in the EUV. The problem has been addressed by Kirby *et al* (1979) and their recommendations derive from the following considerations. Above

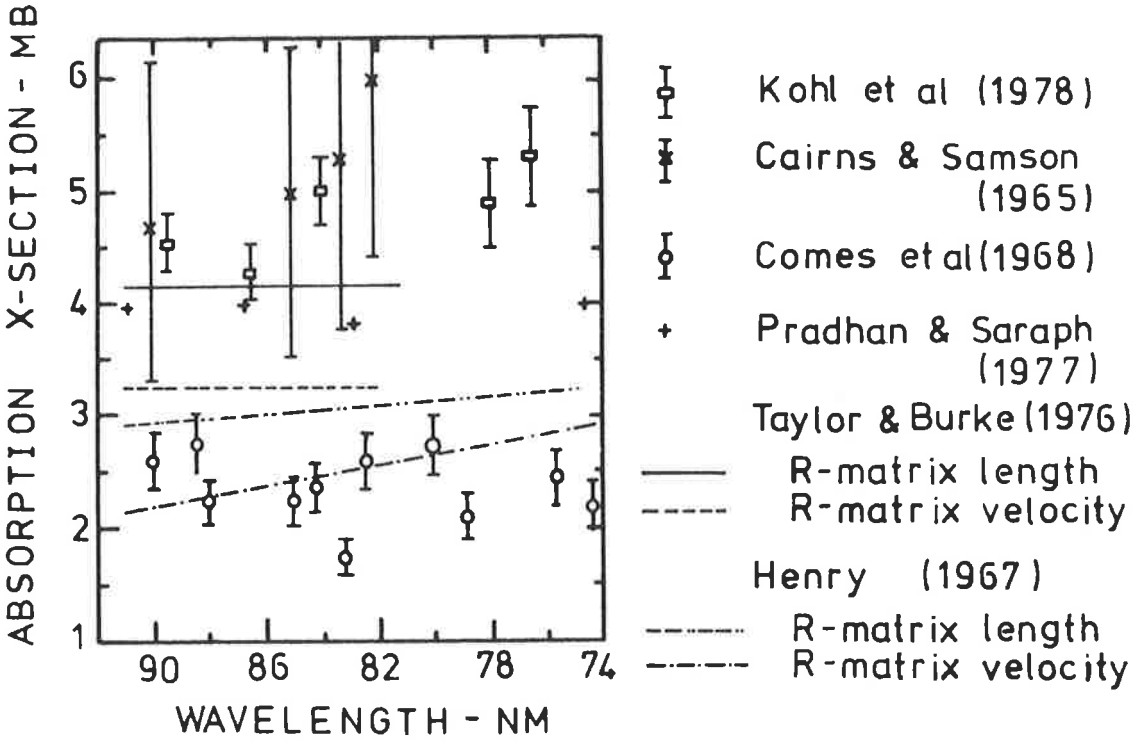

Figure 3.17a Atomic oxygen absorption cross-sections: 74 to 91nm.

(Kohl et al, 1978)

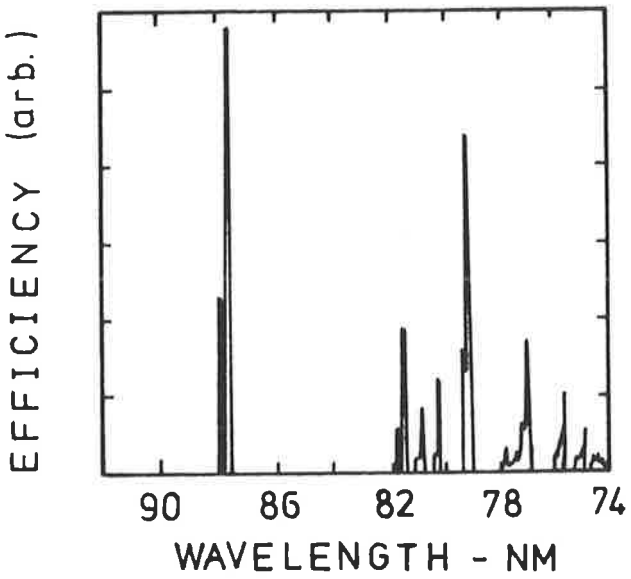

Figure 3.17b Relative photoionization efficiency of atomic oxygen.

(Adapted from Dehmer et al, 1973)

43.5 nm the calculated total cross-section for photoionization of the 2p valence electron of Taylor and Burke (1976) tend to be confirmed by Pradhan and Saraph (1977) and, near threshold, by Kohl *et al* (1978). From 70.6 to 60.8 nm there are several resonances which have also been calculated by Taylor and Burke (1976). Below 43.5 nm total photoionization cross-sections can be obtained by adding to the calculations pertaining to a 2p electron (Taylor and Burke, 1976), the partial cross-sections for removing the 2s electron. These have been calculated by Dalgarno *et al* (1964) and modified by Henry (1967).

b. *Molecular Oxygen*

At wavelengths less than 50 nm, where the molecular oxygen absorption spectrum is continuous and structureless, experimental investigations usually concur about the magnitude and shape of the cross-section, especially below 35 nm. Using synchrotron radiation and a grazing incidence monochromator with a passband of 0.0065 nm, Mehlman *et al* (1978) have measured the absorption cross-section between 55 and 35 nm, at four different pressures, and have reported absolute accuracies better than 5%. Their results are in agreement with those of Lee *et al* (1973) who also employed synchrotron radiation, with the measurements of Samson and Cairns (1964, 1965) at specific wavelengths dictated by their high-voltage, condensed spark discharge line source and with De Reilhac and Damany (1977) who used a BRV source and photographic detection. Recent measurements (Cole and Dexter, 1978b) observing synchrotron radiation with 0.02 nm passband have confirmed the magnitude of the molecular oxygen absorption cross-section at these shortest extreme ultraviolet wavelengths.

The majority of cross-section measurements between 30 and 55 nm have used line sources (Weisler and Po Lee, 1952; Wainfan *et al*, 1955;

Samson and Cairns, 1964, 1965). While the results appear to indicate reasonable agreement, comparison is difficult, limited as it is to specific wavelengths.

Detailed investigation of the complex structure above 55 nm requires a continuum radiation source and extensive use has been made of the Hopfield continuum of helium, generated by a repetitive high-voltage condensed spark discharge through helium at high pressure. With this source, both Cook and Metzger (1964) and Huffman *et al* (1964a) have made cross-section measurements from 60 to 110 nm with 0.005 nm passband, over a wide range of pressures. Other experiments in this spectral region have used line sources (Watanabe and Marmo, 1956; Samson and Cairns, 1964; Matsunaga and Watanabe, 1967). In particular, using the H_2 'many-line' spectrum, Matsunaga and Watanabe have reported measurements at 0.02 nm passband. The relative shape of the absorption spectrum has been consistently reported by all of these experiments between 60 and 110 nm. Discrepancies exist, however, in the magnitude of the cross-section at the extremities of the individual bands, especially the maxima. Here, the measured cross-section may depend on the pressure and bandwidth pertaining to a particular experimental investigation. For example, from 85 to 100 nm, the minima reported by Cook and Metzger (1964) are higher than those of Watanabe and Marmo (1956), but for wavelengths less than 85 nm, they are lower than those of Wainfan *et al* (1955). Watanabe and Marmo (1956) indicate substantial agreement with both Matsunaga and Watanabe (1967) and Samson and Cairns (1964). Huffman's values are lower than these by about 20%, above 90 nm, while for 60 to 80 nm they are considerably higher. Hudson (1971) has attributed this to a systematic error in Huffman's experiment.

c. *Molecular Nitrogen*

Experimental investigations of molecular nitrogen absorption have been generally concurrent with similar investigations of molecular oxygen, as described in the previous section.

At wavelengths less than 50 nm, where the absorption cross-section is smooth, the reported values are consistent (Lee *et al*, 1973; De Reilhac and Damany, 1977; Cole and Dexter, 1978b).

Above 50 nm cross-section data has been provided by Wainfan *et al* (1955), Watanabe and Marmo (1956), Huffman *et al* (1963), Samson and Cairns (1964), Cook and Metzger (1964), Cook *et al* (1964) and most recently by Gürtler *et al* (1977). Measurements below 66 nm are complicated by the fluorescence of N_2^+ (Huffman *et al*, 1963). From 66 nm to the first threshold of ionization at 79.6 nm the absorption cross-sections across the bands appear to be independent of pressure. Despite this, there is general disagreement about the magnitude of the maxima and minima although, as for the molecular oxygen cross-section, the relative intensity distribution is more certain. From 80 to 100 nm the bands exhibit exaggerated pressure dependence to the extent that it is meaningless to compare the results of different experiments, especially those for which the resolution was only modest. In fact, no data was reported by Samson and Cairns (1964) in the wavelength intervals 832 to 835 nm and 921 to 924 nm, because Beer's law was not obeyed by the absorption cross-sections. Neither did Hudson (1971), in his critical review of absorption cross-section measurements, attempt to compare the available data for this spectral region, although he did recommend that the results of Samson and Cairns be used.

Gürtler *et al* (1977) have determined absorption cross-sections for molecular nitrogen in the wavelength range 40 to 100 nm, utilizing the continuum of synchrotron radiation and a 3-metre grazing incidence monochromator with 0.003 nm resolution. Because of the higher resolution and the continuous wavelength coverage, these results are probably the most relevant of all the measurements, and have been incorporated in the extensive compilation of absorption cross-section data reported by Kirby *et al* (1979).

d. Weighted Mean Absorption Cross-Sections

For the spectral scan of Figure 3.14, recorded by detector D, the corresponding numerical values for the absorption cross-sections of O, O_2 and N_2, in the wavelength interval 5 to 15 nm, are illustrated in Figure 3.18. Across wavelength intervals of 0.4 nm, the estimated FWHM of the monochromator response, the absorption spectra are smooth and only slowly varying.

In Figure 3.14 the most prominant spectral feature occurs at 9.6 nm and this wavelength was considered the most suitable for generating an absorption curve. At 9.6 nm the average change in the magnitude of the absorption cross-sections across the wavelength increment ± 0.2 nm is ± 4%. The absorption profile shown in Figure 3.15 was therefore considered, in the following analysis, to be 'sufficiently' monochromatic and, following Section 2.1d, weighted mean absorption cross-sections $\bar{\sigma}(h)$ at 9.6 nm were calculated at altitudes h in the range 120 to 180 km, where

$$\bar{\sigma}(h) = \frac{\sum_i \sigma_i \, n_i(h)}{\sum_i n_i(h)}$$

This required, as input parameters, numerical absorption cross-section data

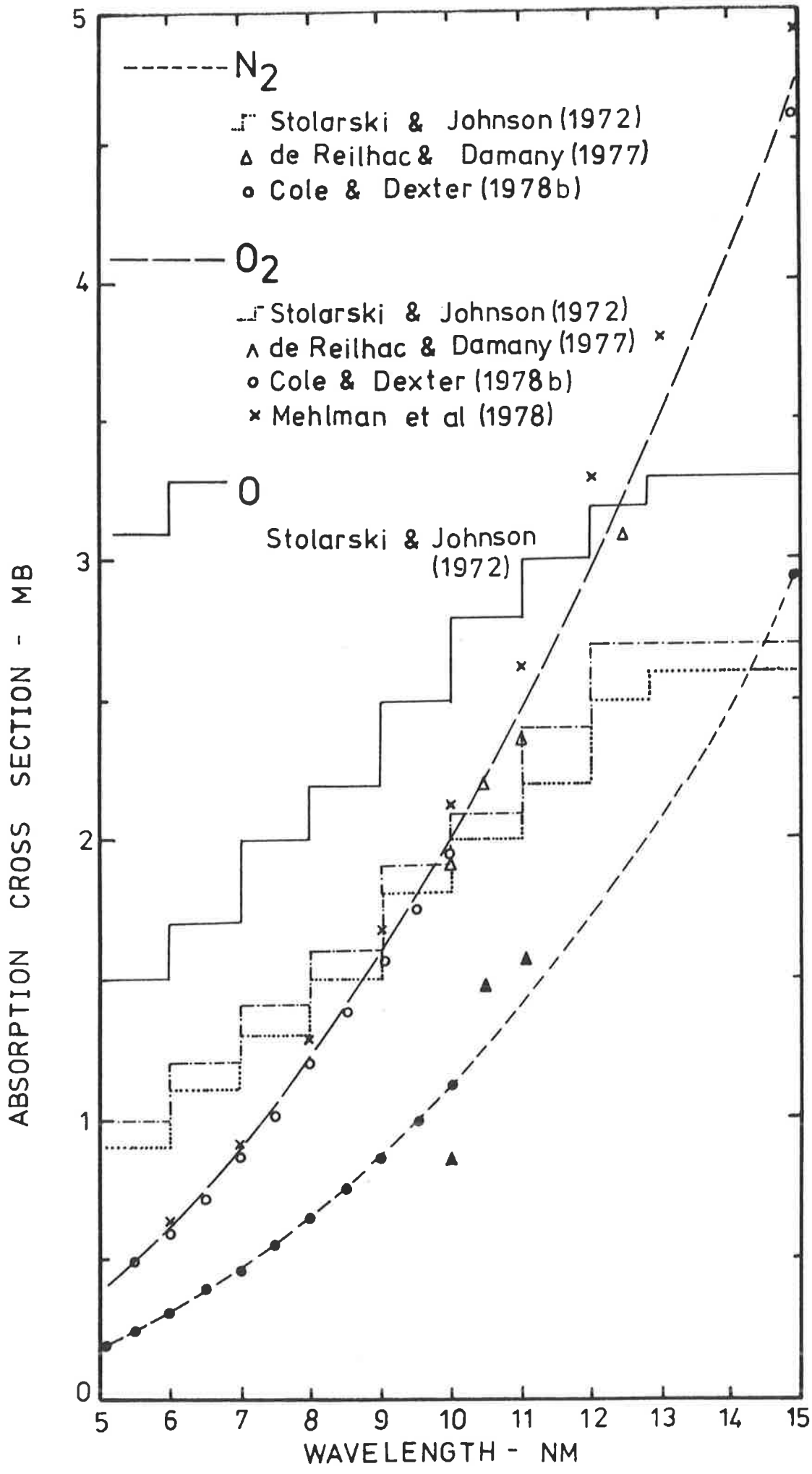

Figure 3.18 EUV absorption cross-sections: 5 to 15 nm.

for each of N_2, O_2 and O ($i = 1, 3$), plus a model of their density distributions in the lower thermosphere.

Huffman (1969) and Stolarski and Johnson (1972) have both presented photoabsorption cross-sections in a form useful for aeronomic calculations. Subsequent to their recommendations, additional experimental results have been reported, as illustrated in Figure 3.18 and described in the previous sections. These new measurements have been included in the recent compilation of Kirby *et al* (1979).

Weighted mean absorption cross-sections at 9.6 nm were determined from the cross-sections of Kirby *et al* (1979), using three different composition models. With reference to Figure 3.19, both CIRA 1972 and the U.S. Standard Atmosphere,1976 are mean atmospheres, representative of typical conditions, but the Jacchia (1977) model was evaluated at the time of the Aerobee launch, according to the procedures in Appendix C. In all the calculations of the weighted mean absorption cross-sections only the model densities for N_2 and O were required since the O_2 densities were determined experimentally by other instrumentation carried on the Aerobee (Appendix A and Chapter 4).

In Figure 3.20 the weighted mean absorption cross-sections at 9.6 nm are illustrated for four different combinations of the input parameters. Curves X, Y and Z were generated using the cross-sections of Kirby *et al* (1979) with three models, respectively CIRA 1972, Jacchia (1977) and the U.S. Standard Atmosphere, 1976, for the N_2 and O density profiles. There is little difference between the results incorporating the two most recent models but CIRA 1972 effected an increase in the weighted mean absorption cross-section of about 9%. For comparison, the calculations were repeated (curve A, Figure 3.20) with the Jacchia (1977) density model and another set of absorption cross-sections recommended by Stolarski and Johnson (1972), with the result that at 121 km the weighted mean absorption cross-section was increased by 87% and at 171 km

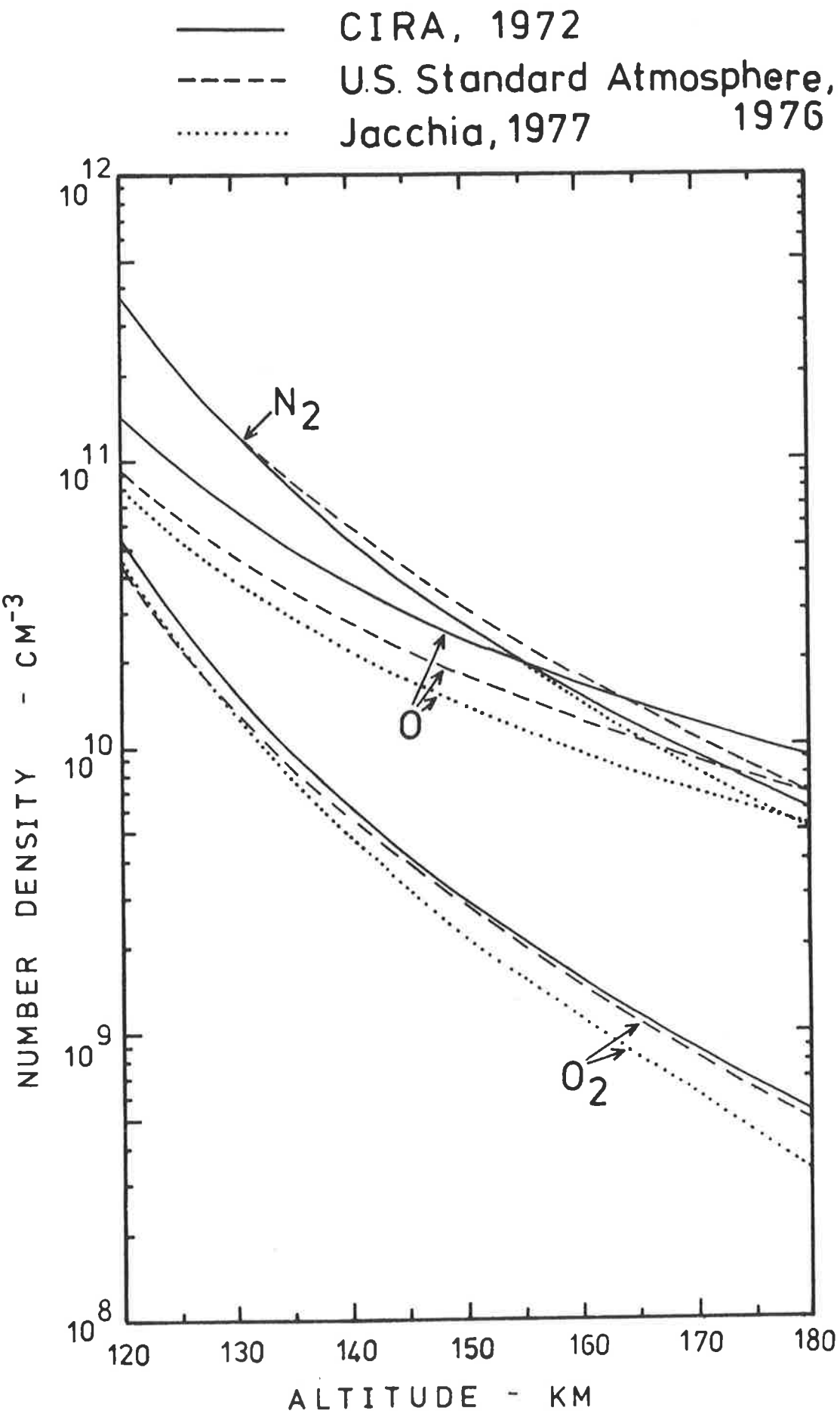

Figure 3.19 Comparison of composition models for the lower thermosphere.

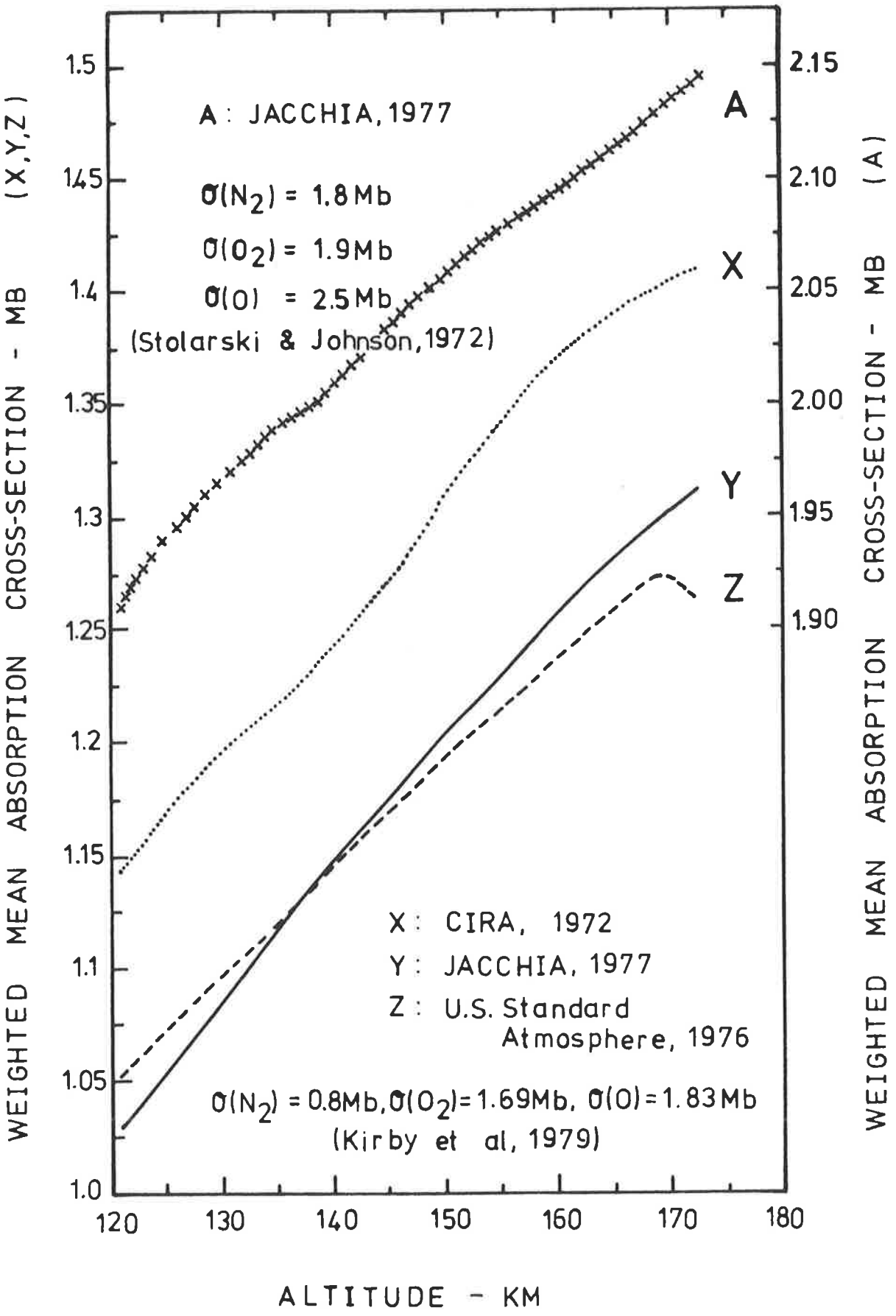

Figure 3.20 Weighted mean absorption cross-sections at 9.6 nm.

by 63%.

So, while the calculated values of the weighted mean absorption cross-sections did not vary greatly when different model densities were used as input parameters, they were relatively more sensitive to numerical values for the absorption cross-sections. Since there was no conclusive evidence to suggest a preference for a particular set of absorption cross-sections, both of the sets of cross-section data in Figure 3.20 were incorporated in evaluation of the densities described in Section 3.7.

e. *Effective Weighted Mean Absorption Cross-Sections*

The solar scan in Figure 3.11, recorded by detector A, lies within the wavelength interval 75 to 90 nm and the absorption cross-sections of O, O_2 and N_2 over this spectral range, from Kirby *et al* (1979), are illustrated in Figure 3.21. Nowhere in this spectral region is it possible for a detector with a passband of 0.4 nm to generate a monochromatic absorption curve. Any attempted analysis of the experimental data thus required an approach similar to that described in Section 2.1f where an effective weighted mean absorption cross-section was defined by Equation 2.17. Such calculations were performed for the spectral line identified in Figures 3.11 and 3.16 at 79 nm which was considered to arise from solar emission lines at 78.65, 78.77 and 79.02 nm.

Parameters for evaluating effective weighted mean absorption cross-sections at 78.9 nm are illustrated in Figure 3.22. The solar flux is from Donnelly and Pope (1973) and the shape of each of the emission lines at 78.65, 78.77 and 79.02 nm was represented by a Gaussian function with FWHM = 0.01 nm. Such approximations of the shape and width of the solar lines can provide only a crude estimate of their effect on the integrated absorption measured by a detector. These characteristics of solar emission lines remain generally unknown, requiring high resolution

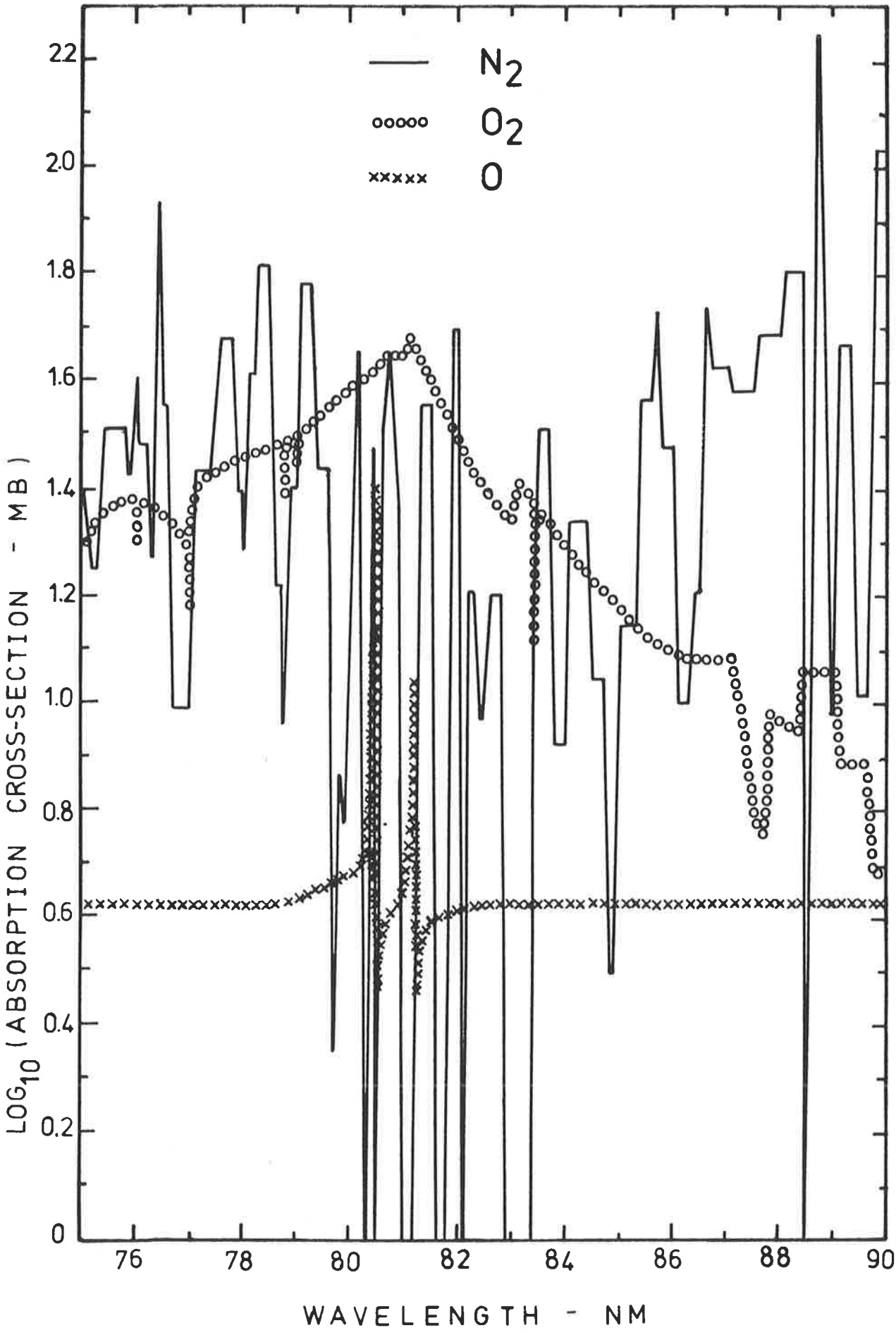

Figure 3.21 EUV absorption cross-sections: 75 to 90 nm. (Kirby et al, 1979)

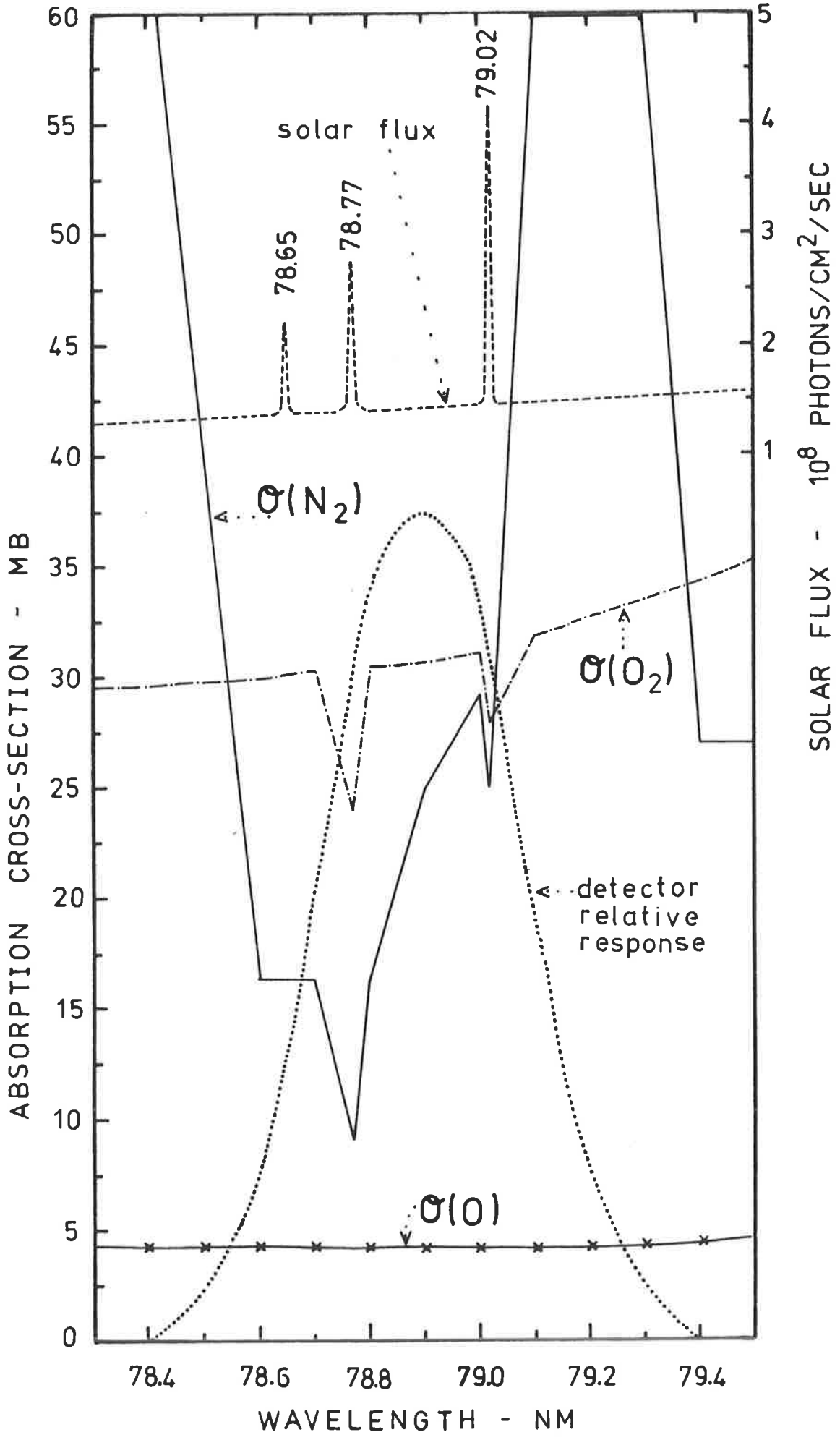

Figure 3.22 Parameters for broad band calculations at 78.9 nm.

instrumentation for their investigation. Huffman and Larrabee (1968) have suggested that, since H Lyman-alpha (121.6 nm) and H Lyman-beta (102.5 nm) are broad lines (FWHM = .12 and .06 nm respectively), it is likely that other lines will be found to be broad. Measurements of the profile of the He I solar emission at 58.4 nm have indicated that it can be represented by a Gaussian profile with FWHM = 0.0122 nm (Maloy *et al*, 1978). It is possible that none of the above examples of solar linewidths are directly relevant to the solar lines in Figure 3.22 since they may be emitted from different levels of the solar atmosphere, under different environments. In view of the meagre data for solar line widths, the use of linewidths narrower than 0.01 nm, necessitating computer calculations with finer spectral resolution, seemed unwarranted.

The detector response was also represented by a Gaussian function, with FWHM = 0.4 nm. The cross-sections in Figure 3.22 are from Kirby *et al* (1979). At each altitude, $\overline{\sigma}_{EFF}(h)$ was determined by integrating from 78.4 to 79.4 nm, using Simpson's rule with 0.005 nm increments. At each step, the monochromatically attenuated flux $\phi(h, \lambda)$ was evaluated using column densities generated from the U.S. Standard Atmosphere, 1976 .

It is also possible to calculate a profile for the attenuation of 78.9 nm radiation, as monitored by a detector with 0.4 nm bandwidth, using Equation 2.11. The effective weighted mean absorption cross-sections and the calculated attenuation at 78.9 nm when the zenith angle is 85° are shown together in Figure 3.23. At 180 km the transmitted flux is less than 1% of the incident flux, according to these calculations. Also shown in Figure 3.23 are similar calculations using the N_2 and O_2 absorption cross-sections tabulated by Cook and Metzger (1964). For comparison, within the wavelength interval 78.4 to 79.4 nm the shape

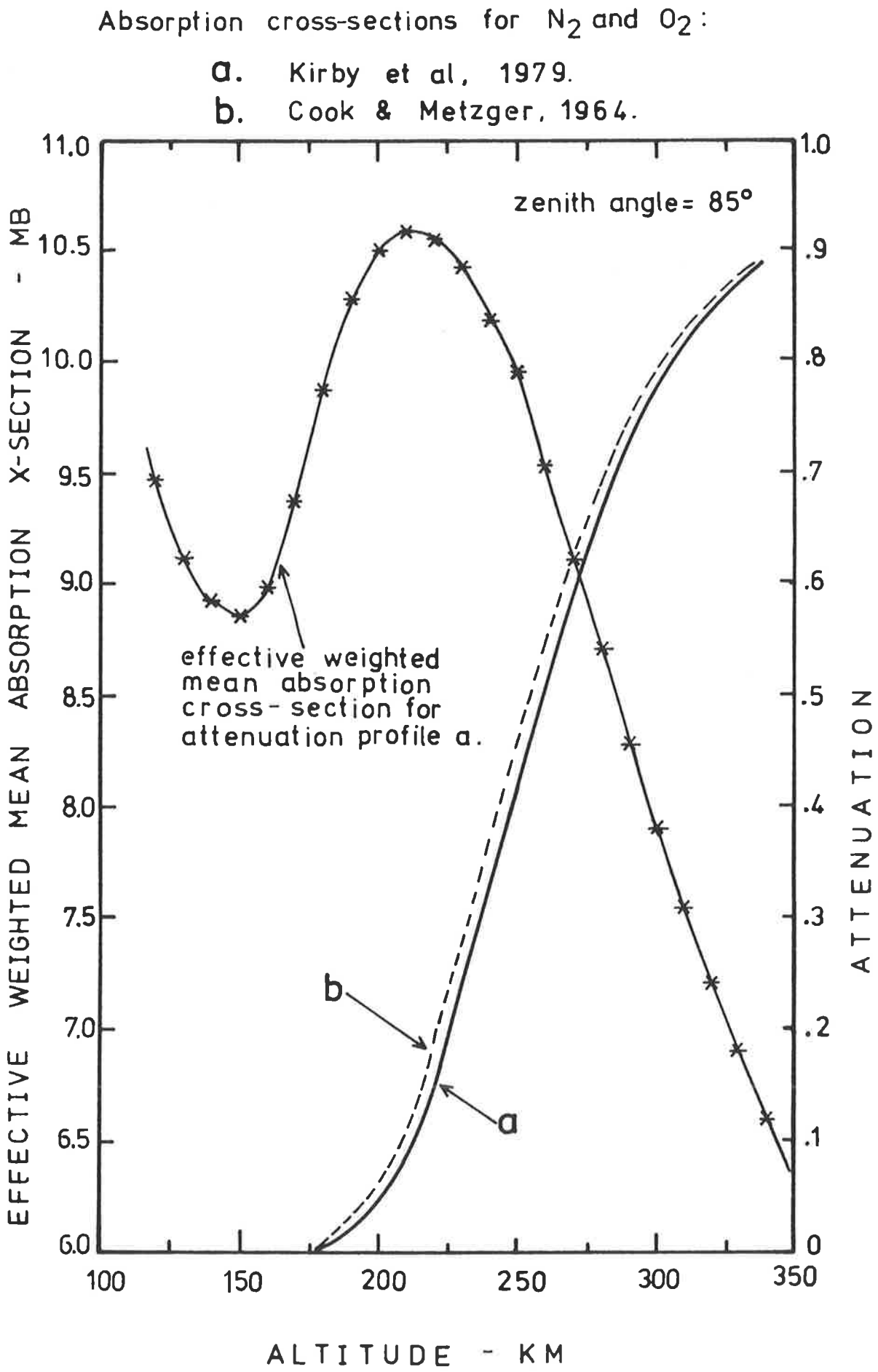

Figure 3.23 Calculated attenuation at 78.9 nm.

of their N_2 absorption spectrum is similar to that of Kirby *et al*, but the average value is lower; 30.4 Mb compared to 37.9 Mb. The O_2 absorption spectra from both sets of data are similar in shape and magnitude, with an average value across the 1 nm interval of 30.5 Mb. Consequently, the calculations involving the cross-section data of Cook and Metzger yielded effective weighted mean absorption cross-sections lower than those derived, at a particular altitude, from the data of Kirby *et al*, and the attenuation was shifted to slightly lower altitudes. This is evident in Figure 3.23.

3.7 DEDUCED ATMOSPHERIC COMPOSITION

a. Total Densities

The total number of particles $n_T(h)$ at height h which absorb monochromatic radiation at a particular wavelength can be derived from the experimental curve describing the atmosphere's absorption at that wavelength since, from Equation 2.13,

$$n_T(h) = \frac{1}{\bar{\sigma}(h)\ F(h)\ I(h)} \frac{dI(h)}{dh}$$

Monochromatic absorption data at 9.6 nm was analyzed to provide estimates of total thermospheric densities at altitudes between 145 and 165 km.

Evaluation of the weighted mean absorption cross-section $\bar{\sigma}(h)$ at 9.6 nm has been detailed in Section 3.6d, where it was apparent from the numerical results illustrated in Figure 3.20 that $\bar{\sigma}(h)$ was less sensitive to uncertainty in the model density input parameter than to that of the monochromatic absorption cross-sections for each species.

The optical depth factor F(h) has been discussed in Section 2.1b and must be used here instead of $\sec \chi$ because of the large zenith angle χ at the time of the Aerobee launch. Procedures employed for

its evaluation, using the formula of Fitzmaurice (1964), Equation 2.7, are available in Appendix D.

In the numerical calculations of $n_T(h)$, rather than determining $\bar{\sigma}(h)$ and $F(h)$ independently, a weighted mean value of the product $\sigma_i F_i(h)$ was used because $F_i(h)$ is slightly different for each of the absorbing species $i = 1, 3$. This difference was sufficiently small that the approximation $\bar{\sigma}(h)\, F_{AV}(h)$ was only 2% greater than $[\sum_i \sigma_i F_i(h) n_i(h)]/\Sigma n_i(h)$.

At successive altitudes h the experimental quantity $[1/I(h)]dI(h)/dh$ was obtained by subtracting the background then least-squares fitting a polynomial to the raw data points in Figure 3.15, lying within $\pm$ 7 km of h.

In Figure 3.24 are the total densities evaluated using the absorption cross-sections recommended by Stolarski and Johnson (1972) and by Kirby *et al* (1979) which correspond respectively to the weighted mean absorption cross-section curves A and Y of Figure 3.20. As noted in Section 3.6d, in these calculations Jacchia's 1977 model provided the density inputs for N_2 and O while the average Aerobee result (Appendix A) was used for O_2. In addition, total densities were derived using a third set of absorption cross-sections selected from the numerical values plotted in Figure 3.18, and these results are also indicated in Figure 3.24. This latter cross-section data represents the average magnitude of the recent experimental results discussed in Section 3.6 for each of N_2 (De Reilhac and Damany, 1977; Cole and Dexter, 1978b) and O_2 (De Reilhac and Damany, 1977; Cole and Dexter, 1978b; Mehlmann *et al*, 1978), with the atomic oxygen cross-section according to Stolarski and Johnson (1972).

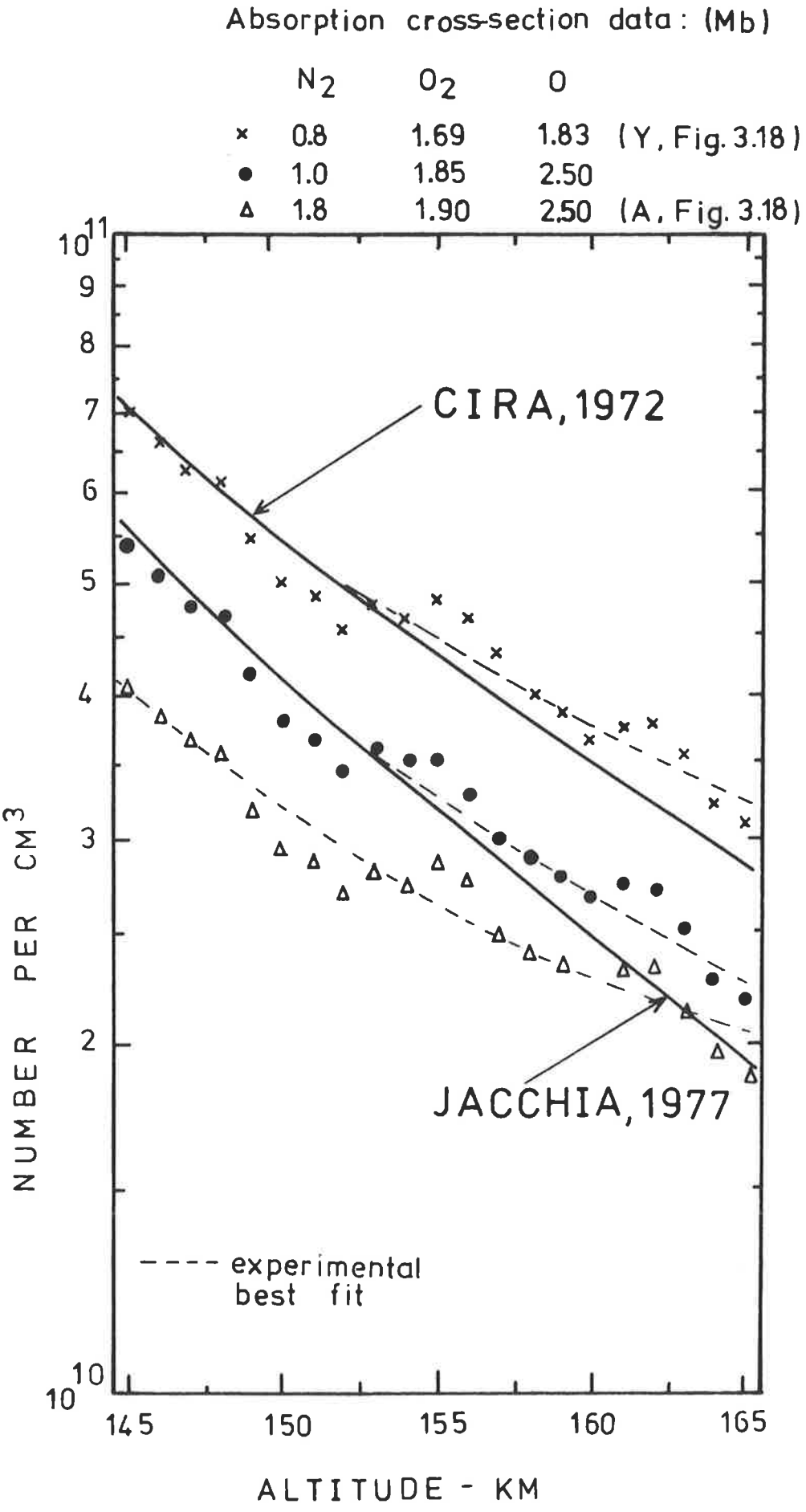

Figure 3.24 Total densities derived from absorption at 9.6 nm.

Total densities can also be derived from absorption at 78.9 nm, using Equation 2.17;

$$n_T(h) = \frac{1}{\bar{\sigma}_{EFF}(h)\ F(h)\ I(h)} \frac{dI(h)}{dh}$$

where the effective weighted mean absorption cross-section $\bar{\sigma}_{EFF}(h)$ has been illustrated in Figure 3.23. The experimental quantity $[\ 1/I(h)\ ]dI(h)/dh$ was available from the absorption profile of the spectral line observed at 79 nm, as displayed qualitatively in Figure 3.16. Such calculations yielded densities low by a factor of 10 at 145 km, the disagreement decreasing monotonically with altitude to a factor of 2 at 170 km.

It was expected that insensible results would be obtained from analysis of this experimental data because at the base of an absorption curve the analysis techniques rapidly become invalid. This has been discussed by Hinteregger (1961). The data from this channel of the monochromator was only analyzed qualitatively to illustrate the procedures that are required, and that would have been employed had the vehicle attained greater altitudes.

More specifically, at 180 km the experimental signal was calculated to be only 1% of the expected maximum. Generally, a signal that is less than 0.1 times the maximum signal caused by the unattenuated solar flux will not be useful because the signal to noise ratio is extremely small, as is the signal rate of change, both of which are required to determine the density. Additionally, a non-zero background signal, as is characteristic of this data, will significantly perturb the true magnitude of the signal and the slope.

There is no reason to assume that, had data at higher altitudes been available, the techniques described in this section would not have

been applicable. However, the difficulties in deriving accurate results from absorption at this particular wavelength must be acknowledged. Figure 3.22 is evidence of extreme and abrupt changes in the absorption spectra, especially for N_2, within the moderate passband of the monochromator.

b. N_2 and O Density Profiles

Deduction of the absolute concentrations of N_2 and O from the absorption curve at 9.6 nm was facilitated by measurements made with other Aerobee instrumentation. Specifically, the molecular oxygen density was considered to be well defined by far ultraviolet absorption spectroscopy experiments (Appendix A and Chapter 4), while the mass spectrometer provided a height profile of the ratio K of the density of atomic oxygen to that of molecular nitrogen (Appendix A). Then the N_2 and O densities were reckoned using Equation 2.13 as follows:

$$\sum_i n_i(h)\ \sigma_i\ F_i(h) = \frac{1}{I(h)}\ \frac{dI(h)}{dh}$$

with $i = 1, 2, 3$ pertaining respectively to N_2, O_2 and O.

Each $F_i(h)$ is documented in Appendix D and $n_2(h)$, the average Aerobee molecular oxygen density, is tabulated in Appendix A. Also from Appendix A, $n_3(h) = Kn_1(h)$ so the above equation was solved for $n_1(h)$, via

$$n_1(h)\sigma_1F_1(h) + n_3(h)\sigma_3F_3(h) = \frac{1}{I(h)}\ \frac{dI(h)}{dh} - n_2(h)\sigma_2F_2(h)$$

$$\therefore \quad n_1(h) = \left[\ \frac{1}{I(h)}\ \frac{dI(h)}{dh} - n_2(h)\sigma_2F_2(h)\ \right] / \left[\ \sigma_1F_1(h) + K\sigma_3F_3(h)\ \right]$$

by using numerical values for the absorption cross-sections σ_i, $i = 1, 3$, and molecular nitrogen and atomic oxygen densities thus obtained were independent of any model densities.

Uncertainty in each of the absorption cross-sections was seen in Figure 3.24 to generate a wide latitude for the magnitude of the total densities; thus it was essential to establish the most appropriate numerical values but the criteria for this decision was not obvious. Since the recommendations of Stolarski and Johnson (1972), new experimental results, as illustrated in Figure 3.18, have been reported and from this data σ_1 = 1.0 Mb and σ_2 = 1.85 Mb, in reasonable agreement with the recommendation of Kirby *et al* (1979) that σ_1 = 0.8 Mb and σ_2 = 1.69 Mb. The primary dilemma was caused by the large uncertainty in the absorption cross-section of atomic oxygen at 9.6 nm. No experimental measurements have been reported, making it difficult to assess the accuracy of the theoretical calculations. At longer wavelengths (see Section 3.6a and Figure 3.17a) theoretical calculations of the atomic oxygen absorption cross-sections have been reported which are a factor of two lower than experimental measurements.

In Figure 3.25 are N_2 and O densities derived from two sets of absorption cross-section data: XSA; σ_1 = 1.0 Mb, σ_2 = 1.85 Mb, σ_3 = 2.50 Mb and XSB; σ_1 = 0.8 Mb, σ_2 = 1.69 Mb, σ_3 = 1.83 Mb. Also included in Figure 3.25 are the N_2 densities measured by the mass spectrometer flown on the Aerobee rocket. At these altitudes the mass spectrometer data is uncertain by about 22% (G. Bibbo, 1980). Densities obtained from the absorption cross-sections (XSA) are compared, in Figure 3.26, with the model densities of Jacchia (1977) and CIRA 1972, and in the following discussions are considered 'preferred' data because of the superior agreement between the N_2 data derived with these absorption cross-sections and the N_2 data from the mass spectrometer.

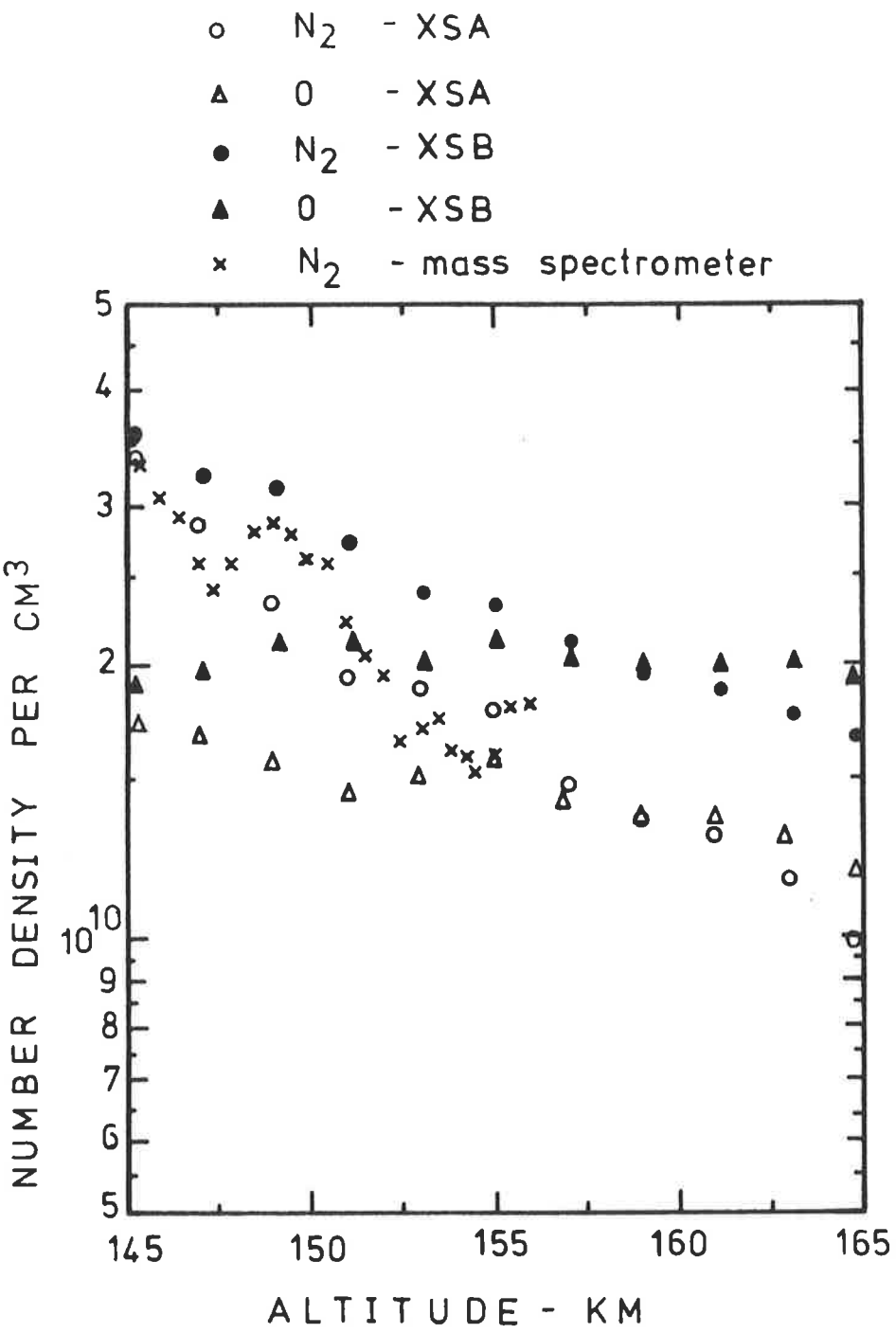

Figure 3.25 Comparison of N_2 and O number densities derived from absorption at 9.6 nm with N_2 number densities measured by the mass spectrometer:

	$\sigma(N_2)$	$\sigma(O_2)$	$\sigma(O)$ - Mb
XSA	1.0	1.85	2.5
XSB	0.8	1.69	1.83

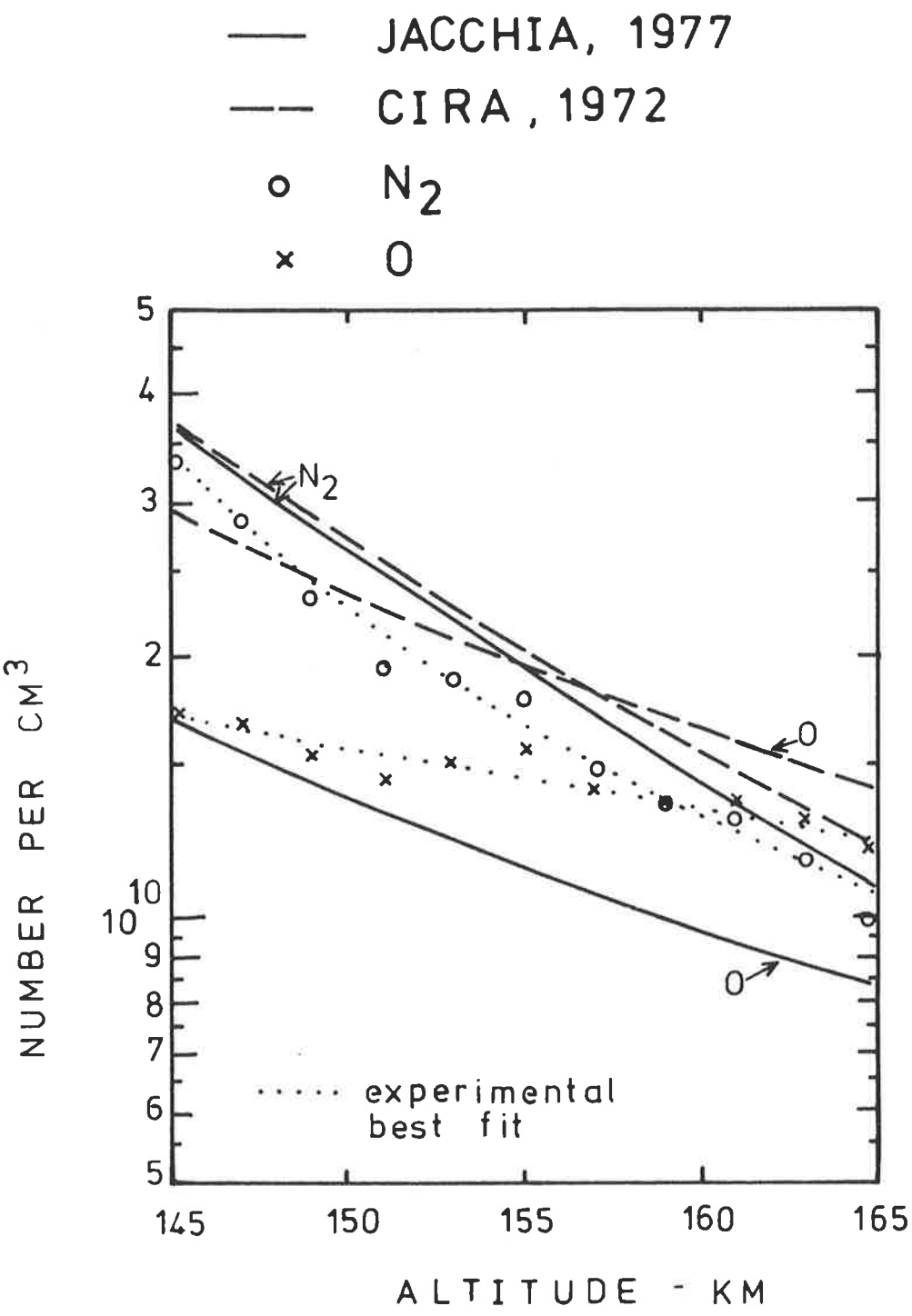

Figure 3.26 N_2 and O densities derived from absorption at 9.6 nm (XSA - see text) compared with model densities.

3.8 DISCUSSION

a. The Experimental Technique

The predominant source of uncertainty in any extreme ultraviolet absorption analysis is in the magnitude of the absorption cross-sections of the atmospheric gases, especially atomic oxygen. From the example at 9.6 nm the disagreement between two sets of absorption cross-section data which have been recommended in the literature (Stolarski and Johnson, 1972; Kirby *et al*, 1979) caused the total densities derived with them to differ by as much as 60%. For the N_2 and O density profiles in Figure 3.25, evaluated with two sets of absorption cross-section data, it was found that decreasing the absorption cross-sections of N_2, O_2 and O by, respectively, 20%, 8.6% and 26.8% effected an increase in the N_2 density of 45% at 150 km and 71% at 65 km. Here, the larger discrepancy at higher altitudes was identified with the least certain atomic oxygen absorption cross-section being emphasized as the atomic oxygen densities increase with respect to the N_2 densities, and especially with respect to the O_2 densities.

For the N_2 and O densities derived in Section 3.7, in addition to the uncertainties corresponding to the absorption cross-sections, as described above, are uncertainties due to the procedure for fitting the experimental data, and its 'low' position in the perspective of the complete absorption profile for 9.6 nm. There is also a contribution from the uncertainty in the ratio of the atomic oxygen and molecular nitrogen densities measured by the mass spectrometer. Overall, an average uncertainty for the data is probably 30%, excluding systematic errors arising from the magnitudes of the absorption cross-sections.

Since there are no reports in the literature of lower thermospheric densities derived from rocket absorption spectroscopy utilizing wavelengths

shorter than 10 nm, it is not possible to specifically compare the experimental data in Figure 3.26. Other extreme ultraviolet composition investigations have been reviewed in Section 2.3a. Such experiments have not been frequent, as testified by Offermann's (1974) review of absolute density data at 150 km, in which, of 19 reported measurements, only 2 (Hall *et al*, 1965; Hall *et al*, 1967) employed absorption spectroscopy techniques. In both examples, molecular oxygen was determined independently from its unique absorption at 120.65 nm and N_2 and O were obtained from simultaneous absorption at 30.38 and 62.97 nm. In another rocket flight reported by Timothy *et al* (1972), absorption at 102.6 nm provided O_2 densities and two other absorption curves at 30.38 and 58.43 nm were analyzed for the N_2 and O concentrations. The composition data from each of these three extreme ultraviolet absorption experiments are plotted together with the present data in Figure 3.27.

In each of these three EUV experiments, useful data for deriving N_2 and O composition was obtained from absorption at wavelengths less than 66 nm. Figure 1.6 indicates that here the absorption spectra are much less structured than at higher wavelengths. Hall *et al* (1965) monitored absorption at 79 nm and 83.3-83.5 nm with 0.3 nm resolution but the altitude dependence of the absorption cross-sections precluded a sensible analysis. Timothy *et al's* (1972) observations in the wavelength intervals 83.3-83.5 nm and 86.5-88.5 nm with 1 nm resolution were similarly unsuccessful. Between 66 and 90 nm the N_2 absorption cross-section may change by more than 100 Mb in less than 0.1 nm, so that spectral resolution many times higher than 0.3 to 1 nm is required. While such high resolution instruments have been used for solar EUV flux

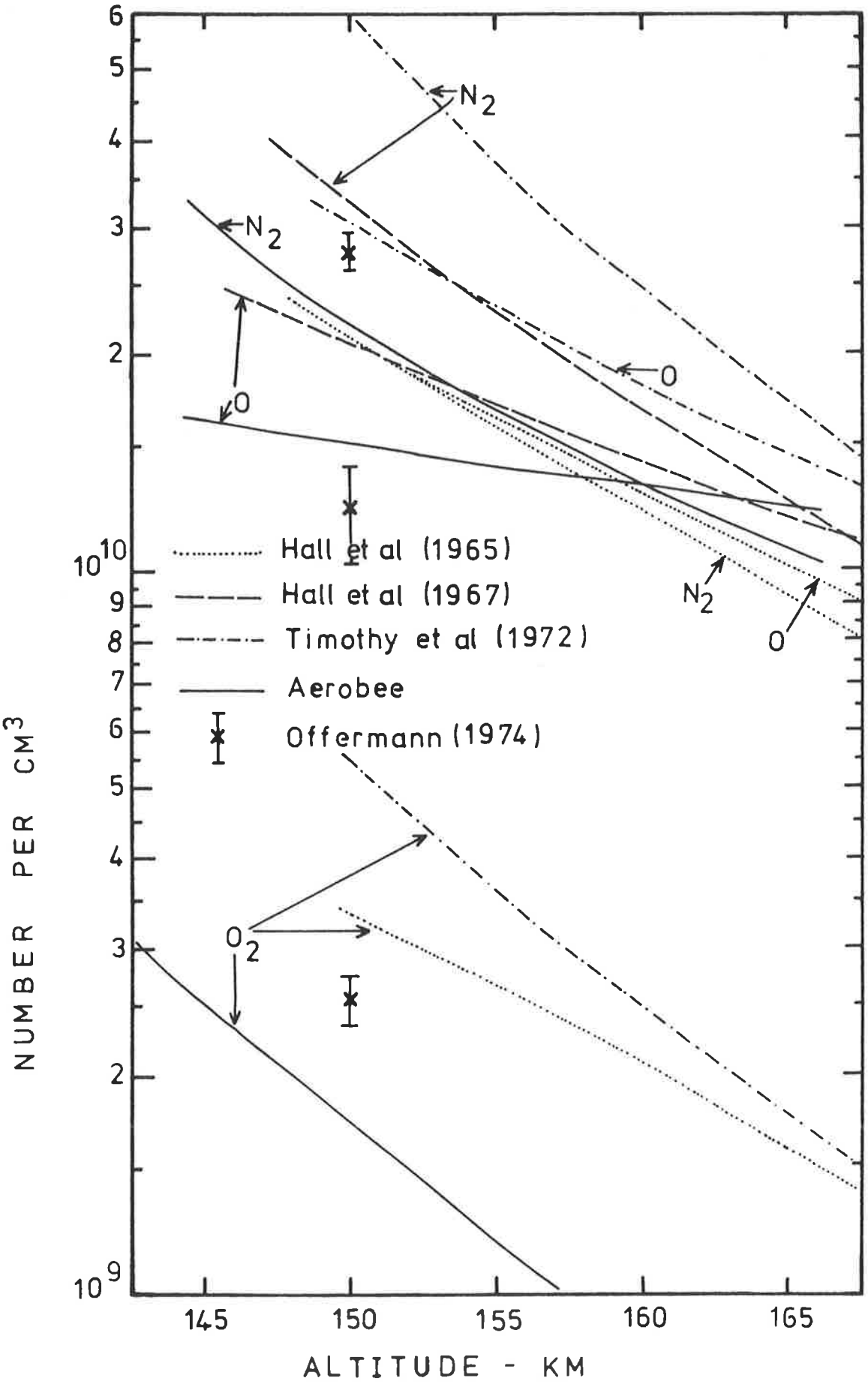

Figure 3.27 Composition of the lower thermosphere determined by EUV absorption spectroscopy.

measurements, usually with photographic rather than photoelectric detection (Behring *et al*, 1972, 1976), they have not been well utilized in absorption spectroscopy experiments. Nor has the alternative broad band approach of Section 3.6e been developed at these wavelengths.

Independent evaluation of molecular oxygen densities from analysis at a wavelength for which it is the primary absorber appears to be mandatory in any application of EUV absorption spectroscopy, since the successful simultaneous solution of three absorption profiles has not yet been reported. However, the most appropriate choice of this wavelength is not obvious. The Si III solar emission line at 120.65 nm, used by Hall *et al* (1965, 1967), is seen in Figure 1.7 to coincide with a strong line in the O_2 absorption spectrum. In the wavelength interval 119 to 121.5 nm, the absorption cross-section varies from near 0.01 Mb to a peak value of 18.6 Mb. At the H Lyman-beta line, 102.6 nm, used by Timothy *et al* (1972), the absorption cross-section is far less variable but also much smaller in magnitude (1.1 Mb), causing this wavelength radiation to be deposited at lower altitudes than that of other EUV emissions such as 30.4 and 58.4 nm. There may also be a discrete atomic oxygen transition at this wavelength (Huffman, 1969). Incorporated in the derivation of the N_2 and O densities discussed in this chapter were O_2 densities measured by Schumann-Runge continuum absorption, but only in an altitude region coincident with absorption of the very shortest EUV wavelengths.

Calculations of the attenuation of radiation at different wavelengths, Figures 2.1 and 2.4, illustrate an important limitation for EUV absorption spectroscopy, namely that the requirement for the individual absorption cross-sections to be sufficiently different to provide sensible density measurements may be incompatible with the prerequisite that

simultaneous absorption in different wavelength intervals occur in a common altitude region. This effectively restricts the range of altitude for which EUV absorption spectroscopy can provide an accurate composition analysis.

The only obvious feature of Figure 3.27 is that none of the density profiles obtained from EUV absorption spectroscopy experiments agree with each other. However, the validity of each measurement, and the extent of the contribution of experimental uncertainties to the range of the data, is not easily discerned. Thermospheric composition is known to depend on a variety of geophysical parameters (Section 1.2b) and such real changes obscure and perturb differences which may otherwise reflect the typical boundary of experimental uncertainty for this technique. Referring to the list of geophysical parameters in Table 3.1, all the measurements in Figure 3.27 occurred at mid latitudes during periods of quiet to moderate geomagnetic activity, but in different seasons. Of special significance are the two following aspects; the Aerobee rocket was launched near dawn while the other three measurements were made mid to late morning and for the data of Timothy *et al* (1972) the sun was very active and near the maximum of its 11-year cycle while the other data was acquired during times of quiet solar activity and near minima of the 11-year cycle. Offermann (1974) has identified an early morning minimum and little seasonal variation for N_2 densities at 150 km, and comparison of the present N_2 results with Offermann's average density in Figure 3.27 supports this. While the influence of solar activity on thermospheric constituents has not yet been unequivocally established, Roble and Schmidtke (1979) have reported that in general all atmospheric properties increase with increasing solar activity so this

TABLE 3.1 Measurements of thermospheric composition by EUV absorption spectroscopy.

Reference	Lat	Local Time	$F_{10.7}$	K_p	Wave-length (nm)
Hall *et al*, 1965 10/7/63	32N	1004	77	2^-	30.4 63.0 120.7
Hall *et al*, 1967 2/3/65	38N	1255	81	1^-	30.4 63.0 120.7
Timothy *et al*, 1972 3/4/69	31S	1035	189.8	2	30.4 58.4 102.6
Aerobee 21/2/77	31S	0636	82	3^-	9.6 SR ctm.

could explain why the data of Timothy *et al* is noticeably higher than the other data.

EUV experiments on satellites have been employed for thermospheric composition investigations with varying degrees of success. From the analysis of occultation profiles at four wavelengths between 62.5 and 77 nm, Reid (1971) concluded that when there is more than one absorbing species the individual number densities cannot be determined uniquely. Since then, Delaboudinière and Millier (1977) have presented a preliminary description of occultation at eight wavelengths in the range 17 to 127 nm.

Above about 200 km, where the molecular oxygen density is small, EUV radiation is absorbed by two rather than three species. At these altitudes occultation experiments at 30.4 and 58.4 nm have provided numerical values for N_2 and O densities (Schmidtke *et al*, 1974b; Schmidtke *et al*, 1975; Schmidtke, 1975; Rawer *et al*, 1976). An alternate application of satellite absorption spectroscopy at high altitudes is the aeronomic determination of the absorption cross-sections of atomic oxygen and molecular nitrogen (Hinteregger and Hall, 1969; Knight *et al*, 1972; Modali *et al*, 1976).

In the present experiment it was possible to use the absorption of short wavelength radiation in the EUV to derive N_2 and O densities by incorporating simultaneous measurements of the O_2 concentration and the ratio of the densities O/N_2, from other experiments.

It is apparent that these shortest EUV wavelengths are quite suitable for absorption spectroscopy. The absorption spectra of N_2 and O_2 are smooth and the magnitude of the cross-sections have been well established by laboratory measurements using synchrotron radiation. Cross-

section data for O are potentially available from high altitude satellite measurements.

Theoretical evaluation of EUV absorption spectroscopy belies the impractibility of its use for a complete composition analysis of the lower thermosphere, and this is why there have been so few measurements. However, the mutual benefits available from a combination of absorption spectroscopy and mass spectrometry techniques are apparent.

Accurate analytic representation of atmospheric EUV absorption remains a challenge, and also provides a stringent test of the validity of cross-section data for the atmospheric absorbers.

b. *The Results*

Comparison, in Figure 3.27, of the N_2 and O densities derived in this chapter with similar results from other EUV absorption experiments implied that measurements of thermospheric composition were not entirely reproducible. Hence it was difficult to conclude whether the present results are within the experimental uncertainty characteristic of absorption spectroscopy measurements.

In Figure 3.28 the Aerobee data is compared with similar data acquired with a different technique. Of all the data compiled by Offermann (1974), the mass spectrometer results of Hedin *et al* (1964) were characterized by geophysical parameters most nearly approaching those for the Aerobee launch. Between the two sets of measurements there is substantial agreement, especially since there is an uncertainty of at least $\pm$ 30% associated with the N_2 and O profiles derived from absorption. It must be noted that the atomic oxygen densities of Hedin *et al* (1964) were multiplied by a factor of 2.5, as recommended by Offermann (1974), and discussed in Section 2.4a, and that since the mass

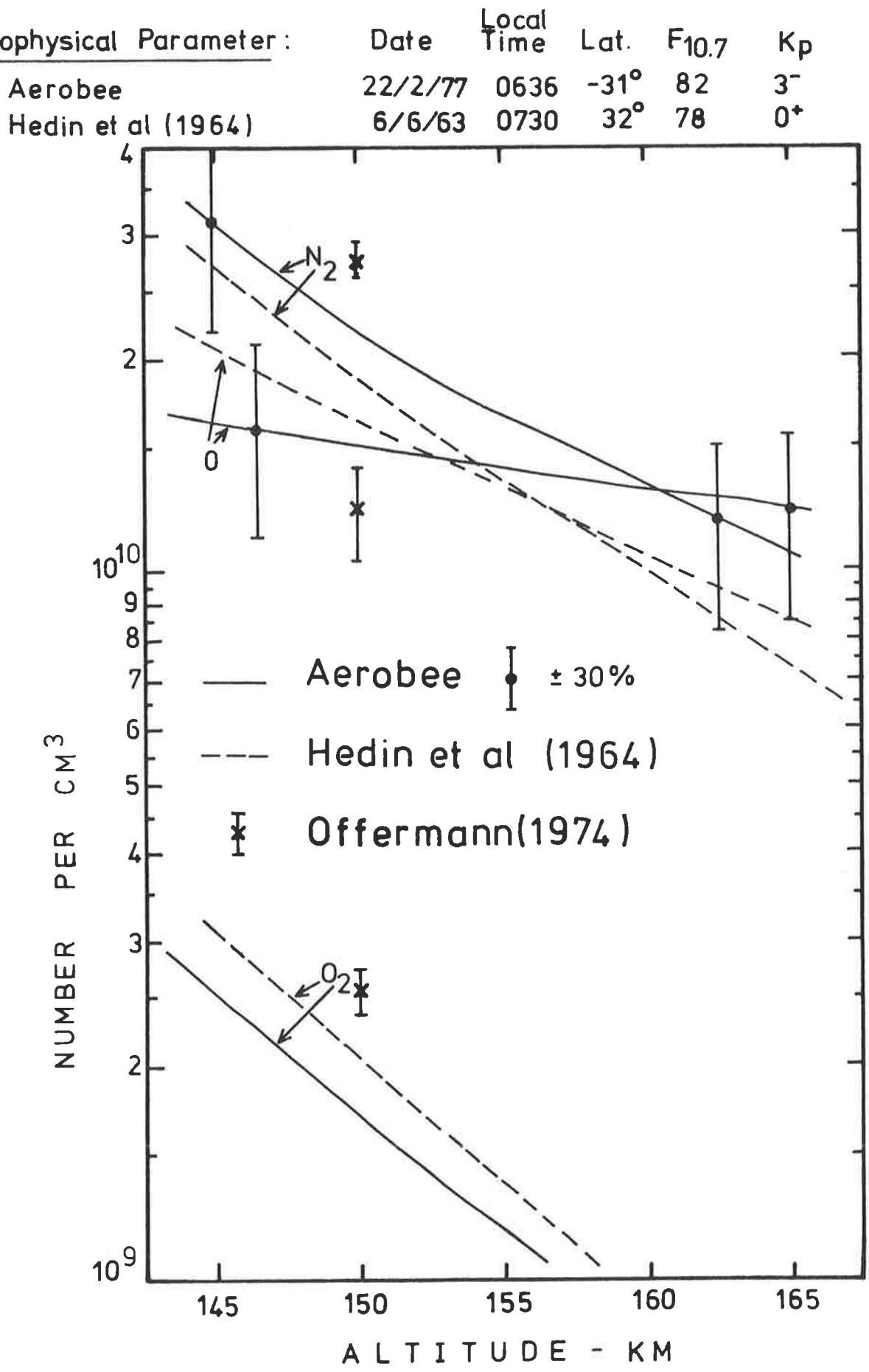

Figure 3.28 Comparison of thermospheric composition measurements during similar geophysical conditions.

spectrometer was uncooled, the O_2 densities may well be slightly high.

Included in Figure 3.28 are the average densities at 150 km of all the data considered by Offermann. That both the mass spectrometer results and the absorption results lie on the same side of the average value for each individual species suggests the existence of real variability, arising from, for example, seasonal or diurnal or solar activity effects.

Offermann (1974) has tried to establish the extent of the seasonal and diurnal variability of both N_2 and O. In Figure 3.29, are plots of his results for the density of N_2 at 150 km, with the present data included. It appears that N_2 varies little throughout the seasons and the N_2 density determined from this experiment lies well within the scatter of the total data base. In contrast, there is a distinct diurnal variation which is positively confirmed by the present data.

An examination of the atomic oxygen variability in the context established by Offermann is provided in Figure 3.30. The experimental ratio of densities O/O_2 at 150 km is in excellent agreement with the seasonal changes of this ratio, as inferred from Offermann's figure, and from OGO 6 mass spectrometer data, as explained in the text of Offermann's (1974) review. It is difficult to establish from Offermann's plot whether or not there is a diurnal variation of atomic oxygen. Since all the uncooled mass spectrometer data have been multiplied by a factor of 2.5, it is reasonable to assume that some of this data may have been over-corrected. In general, the present result lies midway between the corrected and uncorrected mass spectrometer data.

Recently in the literature, Trinks *et al* (1978) reported thermospheric densities measured by their cryo-cooled mass spectrometer,

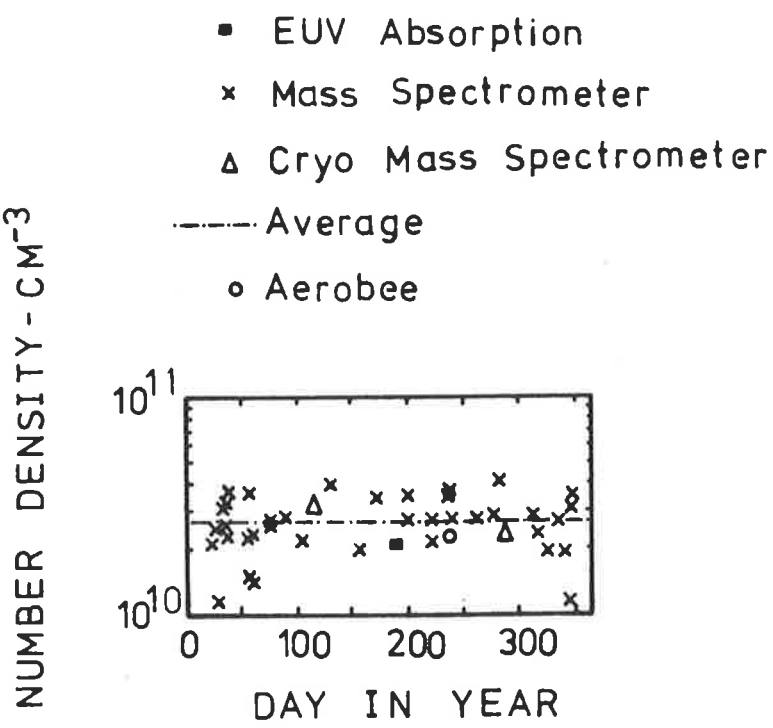

Figure 3.29a Seasonal variation of N_2 number density at 150 km. (Offermann, 1974)

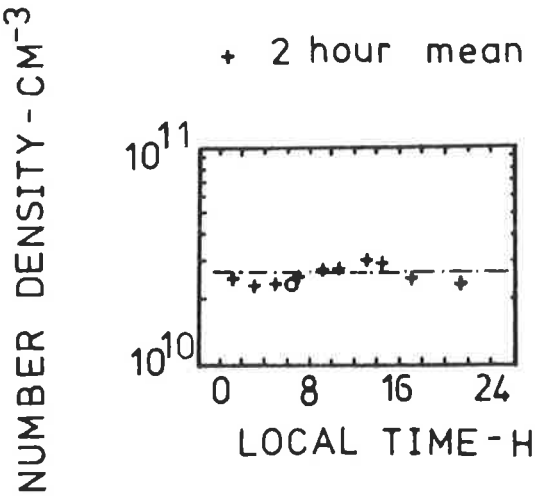

Figure 3.29b Diurnal variation of N_2 number density at 150 km. (Offermann, 1974)

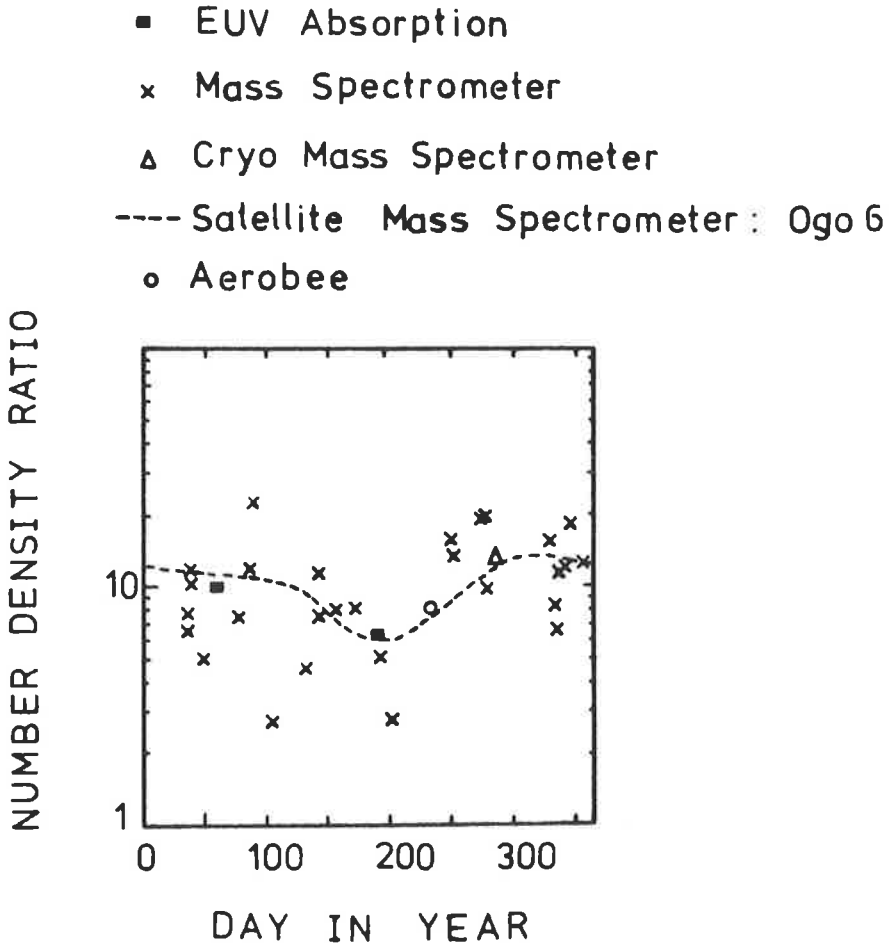

Figure 3.30a Seasonal variation of the number density ratio of atomic and molecular oxygen at 150 km. (Offermann, 1974)

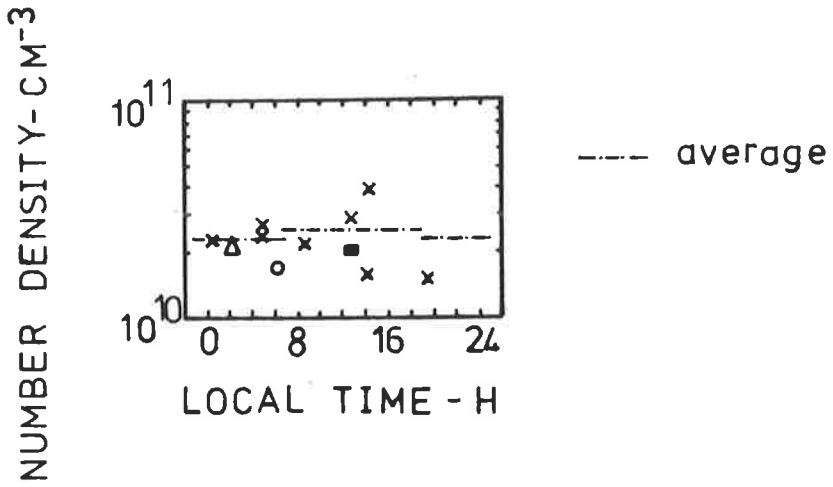

Figure 3.30b Atomic oxygen number density v local time at 150 km. (Offermann, 1974)

in which recombination of atomic oxygen is thought not to be a problem (Section 2.4a). Apart from the local time of launch, at 1514 hours, this flight occurred when most other geophysical conditions were similar to those for the Aerobee launch. Their mass spectrometer data is compared with the present results in Figure 3.31. It is instructive to observe the range of the measurements made by the mass spectrometer on the upleg and downleg of its flight. If, as was concluded by Trinks *et al* (1978), the changes are real, the data is an excellent illustration of extreme composition variability in the lower thermosphere.

Agreement between the N_2 density profiles in Figure 3.31 is particularly good, especially since the diurnal variation predicted by Figure 3.29b suggests that at 1514 hours the density is just slightly increased above its value at 0630 hours.

Jacchia's (1977) model, evaluated for the time of the Aerobee flight (Appendix C), is seen in Figure 3.31 to be more representative of the mid-afternoon data of Trinks *et al* (1978), implying that the model has not adequately incorporated the true extent of composition variability. Other experimenters have similarly reported this apparent failing of the thermospheric composition models (Krankowsky *et al*, 1968; Philbrick, 1974).

The singularly most pronounced feature of Figure 3.31 is the quite different slopes of the atomic oxygen profiles. This observed atomic oxygen distribution may well result from a combination of season and diurnal effects. Atomic oxygen has been reported to have a distinct summer minimum at 120 km, converting to a summer maximum at 275 km (Keating *et al*, 1976), implying that the slope of the profile will be less in summer than in winter. Further, many workers have observed extreme

Geophysical Parameter :	Date	Local Time	Lat.	$F_{10.7}$	K_p	$T_{exo.}$
Aerobee	22/2/77	0636	-31°	82	3⁻	768K
Trinks et al (1978)	29/6/74	1514	38°	83	4.1	910K

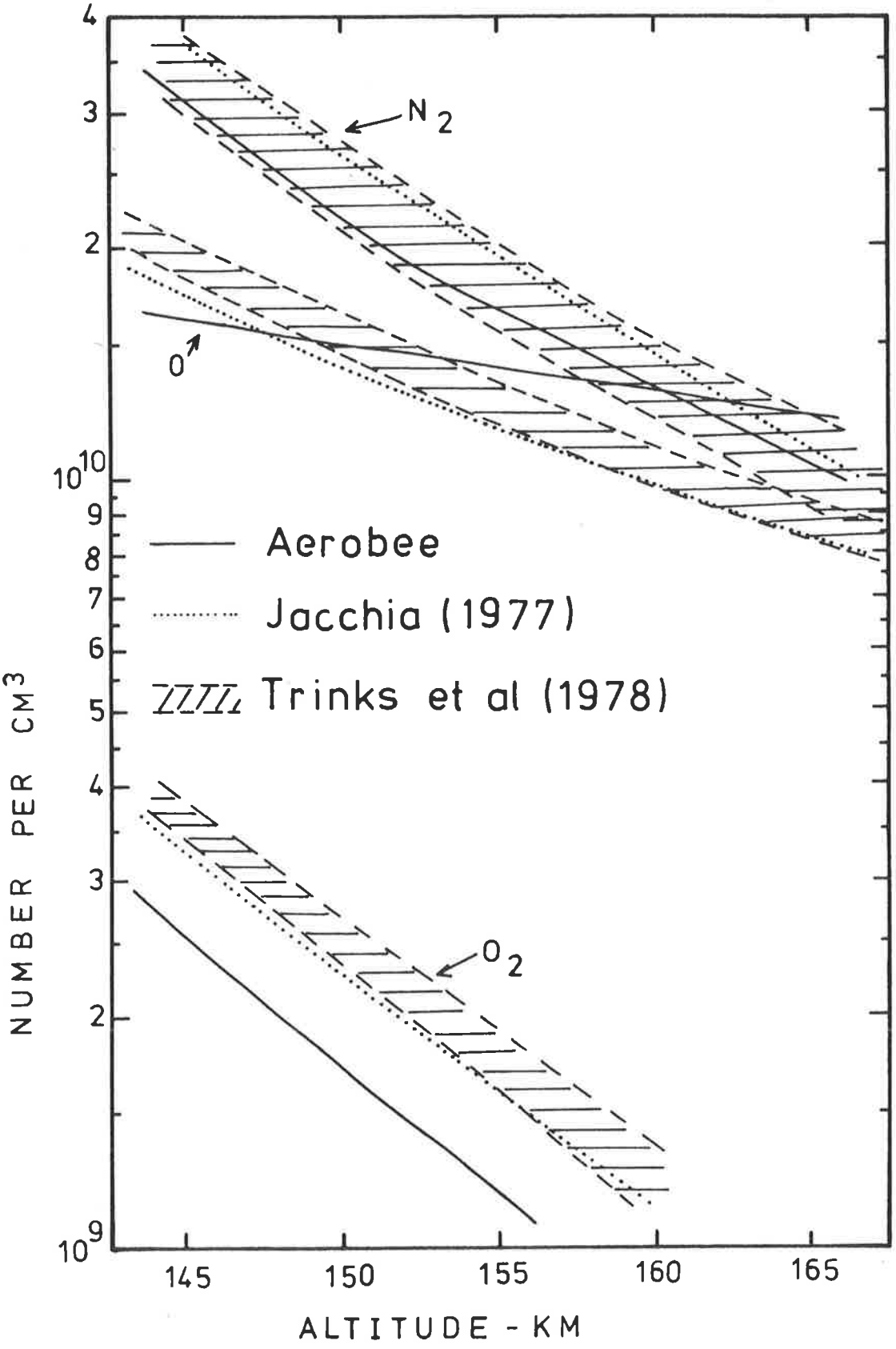

Figure 3.31 Comparison of Aerobee data with cryo-cooled mass spectrometer measurements.

variability in early morning composition (Modali *et al*, 1976; Danilov *et al*, 1979), attributed to dynamical phenomenon during heating of the thermosphere, and Alcayde *et al* (1979) have observed that in summer the lower thermosphere is more turbulent than in winter. The Aerobee rocket was launched in late summer, at sunrise, while the flight of Trinks *et al* (1978) occurred in early summer and mid-afternoon, when the thermosphere is expected to have become more stable.

Measurements of atomic oxygen have, in general, been characterized by a wide variety of results in both magnitude and shape, and this is illustrated by some profiles in Figure 3.32. More so for atomic oxygen, than for N_2 and O_2, is the contribution of real variability to the scatter of the data uncertain, and this reflects the special problems manifested by its extreme reactivity, causing recombination both in mass spectrometers and in laboratory experiments that measure its absorption cross-section.

The present results conclusively support higher numerical values for the atomic oxygen densities as opposed to the 'low' values from the uncooled mass spectrometer experiments discussed in Section 2.4a. When recombination is a problem, the absolute atomic oxygen and molecular oxygen concentrations will be more uncertain than that of total oxygen ($2O_2 + O$). Increasingly, experimenters are reporting total oxygen values and, by considering the results from a variety of experimental groups, Newton *et al* (1974) have reported the average amount of total oxygen at 150 km to be $2.2 \times 10^{10}\,cm^{-3} \pm 22\%$. Since then, other measurements have yielded 2.19×10^{10}, 1.92×10^{10} (Trinks *et al*, 1978) and $1.9 \times 10^{10}\,cm^{-3}$ (Nier *et al*, 1976) which decreases the average to about $2.0 \pm 0.5 \times 10^{10}\,cm^{-3}$. The total oxygen concentration measured by Aerobee is $1.87 \times 10^{10}\,cm^{-3}$, in good agreement with this average value and well within its uncertainty.

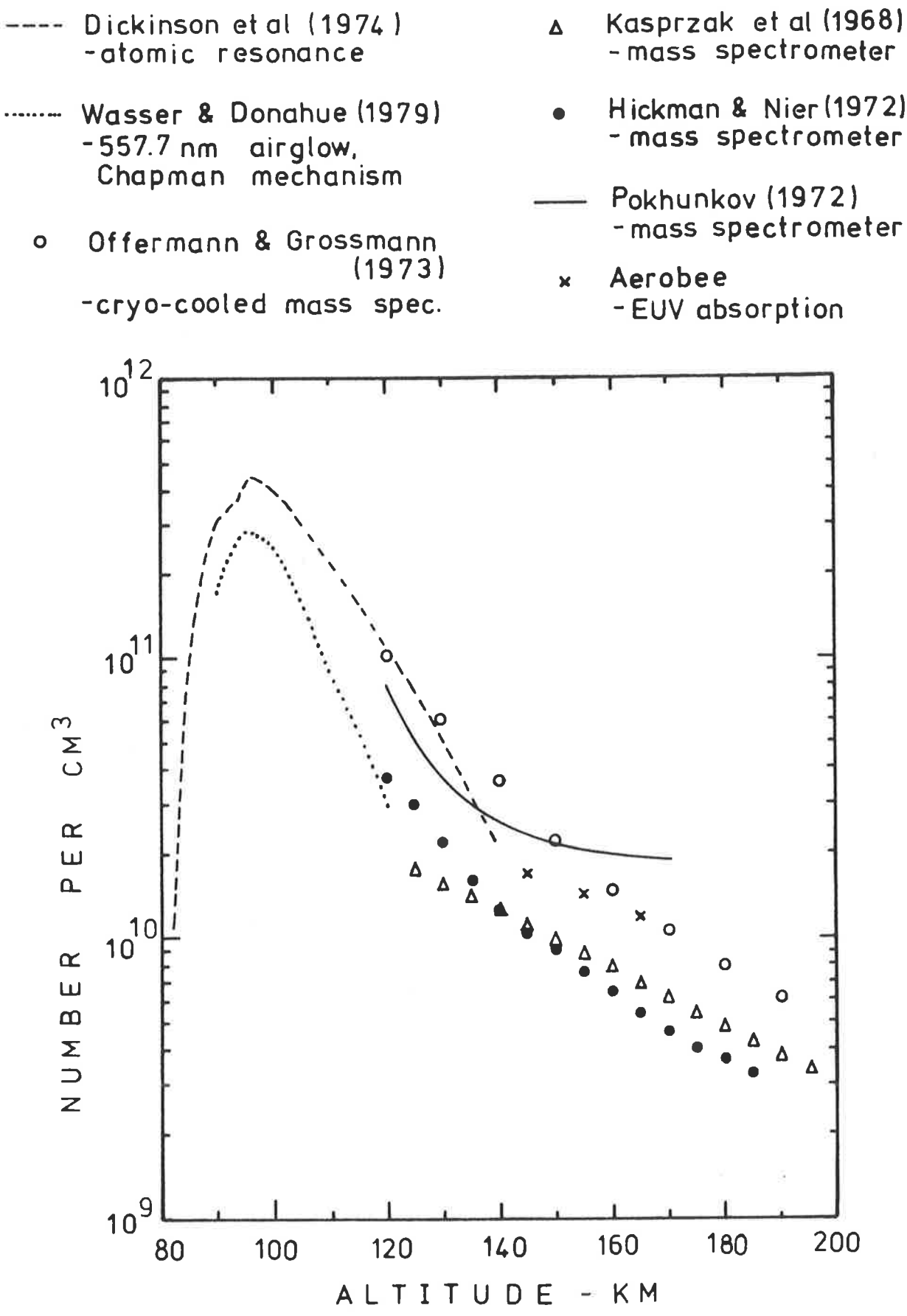

Figure 3.32 Measurements of atomic oxygen number densities.

There are no definitive conclusions available from the results of this experiment. The difficulties inherent in accurate composition measurements of the lower thermosphere have been emphasized, so too has its apparent variability. While composition changes are implied to be in response to a wide range of geophysical parameters, analytic formulae to describe these changes, if they exist, remain obscure. There are probably more factors influencing thermospheric composition than there have been measurements, and this makes a comprehensive treatment of correlations difficult, if not impossible, as yet.

Some broad trends established from the data base of all previous measurements have generally been confirmed by the present results. Many experimenters have suggested that day-to-day fluctuations may obscure more subtle, but regular, diurnal and seasonal changes (Hall *et al*, 1967; Kasprzak *et al*, 1968; Pokhunkov, 1972). It is therefore essential to establish whether observed day-to-day changes are real, or a consequence of the lack of experimental reproducibility. If they are real, an ultimate challenge for atmospheric physics will be to model them.

CHAPTER FOUR

MOLECULAR OXYGEN ABSORPTION OF SOLAR FAR ULTRAVIOLET RADIATION IN THE SCHUMANN-RUNGE CONTINUUM

4.1 INTRODUCTION

An integral requirement for any experimental study of the lower thermosphere is the determination of molecular oxygen number densities as accurately as possible. For this purpose the Aerobee rocket, discussed in the previous chapter, was equipped with a far ultraviolet spectrometer as well as broad band ion chambers and a neutral mass spectrometer.

Absorption spectroscopy techniques applied to solar FUV radiation are particularly appropriate for measuring O_2 concentrations because at these wavelengths the absorption cross-section of O_2 reaches its maximum value, in the Schumann-Runge continuum, and the radiation is absorbed primarily by O_2 in the lower thermosphere. This corresponds to the convenient case of uniquely characteristic absorption, described in Section 2.1c. Laboratory measurements have indicated that the absorption cross-sections in the Schumann-Runge continuum are temperature dependent (Blake *et al*, 1980), so for derivation of the most accurate O_2 densities this effect must be incorporated in the analysis of the raw absorption data.

For monitoring solar FUV radiation on board a rocket vehicle, the Ebert-Fastie spectrometer is extremely suitable (Fastie, 1967) because it is compact, rugged and efficient. A number of experimenters have used this instrument to determine O_2 densities (Ackerman *et al*, 1974) and for solar FUV flux measurements (Parkinson and Reeves, 1969; Rottman, 1974; Heroux and Swirbalus, 1976; Heroux and Higgins, 1977).

On the Aerobee rocket, the use of the FUV spectrometer in conjunction with other instrumentation for measuring the molecular oxygen concentrations provided particular advantages. By using a number of monochromatic wavelengths for density determination, the precision of this technique for composition analysis could be estimated. Comparison with the results of other techniques enabled the accuracy of the method to be evaluated, leading to oxygen densities for which uncertainties could be sensibly predicted, and which were used as input parameters for the reduction of data from other experiments on the rocket (Chapter 3).

4.2 SOLAR FUV FLUX MEASUREMENTS

Initial investigations of the solar far ultraviolet flux were with NRL rocket spectrographs (Johnson *et al*, 1958; Detwiler *et al*, 1961) and have been reviewed by Tousey (1963). Parkinson and Reeves (1969) reported fluxes, acquired with an Ebert-Fastie spectrometer and telescope, which were a factor of three lower than Detwiler *et al*. Other measurements by Widing *et al* (1970) and Bonnet (1968) agreed with each other at 195 nm but were lower than the data of Parkinson and Reeves, by a factor of two at 187 nm and a factor of three at 160 nm.

Photographic investigations by Brueckner and Moe (1972) supported Widing *et al's* values but photoelectric measurements by Nishi (1973) determined fluxes slightly lower than those of Parkinson and Reeves. Nor was the factor of three dilemma resolved by absolute full disc irradiances, measured with broad band ion chambers (Carver *et al*, 1972a) and with a moderate resolution Ebert-Fastie spectrometer (Ackerman and Simon, 1973) since both these results were midway between the extremes of the previous experimental values.

High resolution (0.01 nm) full disc fluxes from 123 to 194 nm, obtained with an accuracy of ± 20% with rocket borne Ebert-Fastie

spectrometers (Heroux and Swirbulus, 1976), agreed with the similarly determined fluxes of Rottman (1974) and indicated that the data of Parkinson and Reeves was more appropriate. Further confirmation came from the integrated spatially resolved spectra of Samain and Simon (1976) for wavelengths less than 180 nm, but above this wavelength they recommended that the values of both Heroux and Swirbulus and Rottman be recognized only as a lower limit, due to the low efficiency of their photoelectric detectors at these high wavelengths. Further investigation of the average disc intensities in the range 175 to 210 nm (Brueckner *et al*, 1976) were 13% higher than those of Rottman, in agreement with the results for the same wavelength region of Jordan and Ridgeley (1974) and Widing *et al* (1970). They concluded that in this region of the solar spectrum, when the proper quantities were compared, different measurements, using entirely different methods, agreed within an error of 25% or better. Recent spatially resolved high resolution spectra of the solar flux from 150 to 210 nm (Samain, 1979) have yielded mean full disc intensities of better than 10% accuracy, which are in agreement with Nishi's 1973 values.

A review of the FUV solar fluxes by Simon (1978) concluded that the discrepancies at 190 nm are 50%, improving to better than 30% between 160 and 175 nm and reaching 40% for 150 to 160 nm and lower. Hinteregger's F74113 reference spectrum incorporated the tabulation of full disc fluxes, in 1 nm intervals, as given by Heroux and Swirbalus (1976).

The question of irradiance variability has been investigated by Hinteregger *et al* (1977) by means of the AE-C satellite. Maximum variability is indicated to be 25% at 155 nm, decreasing to 9% at 170 nm and beyond. Brueckner *et al* (1976) estimated the solar FUV flux variability as 3%, in agreement with the observations of Heath (1973) who reported 5% variation with solar rotation. Obviously, while experimental

uncertainties remain in the range 10% to 20%, evidence for variability of the FUV solar flux remains inconclusive. However, recent preliminary observations of the spectrometer experiment on AE-E have indicated that any variations are indeed quite small since the solar flux for cycle 21 appears at most 10% higher than that for cycle 20, where at least part of this may be due to increased Lyman-alpha for which corrections have not yet been made (Hinteregger, 1979).

4.3 THE EBERT-FASTIE SPECTROMETER

a. Description

The Ebert-Fastie spectrometer is a spherical mirror, auto-collimating, plane grating monochromator developed by Fastie (1952a, 1952b) from the original optical system described by Ebert in 1889.

Optical and electrical features of the spectrometer are illustrated in Figure 4.1. The entrance slit S_1 and the exit slit S_2 lie on the focal plane of the spherical concave mirror M and are equidistant from the mirror axis line A. Light from S_1 is thus rendered parallel by M before reaching the grating G. The diffracted light is then focused by M onto S_2. The slits are curved to lie on the Ebert circle which has a radius of curvature equal to the distance of the slits from the optical axis A and is centred on it. Because of this curvature the effect of astigmatism due to the spherical mirror is removed and, simultaneously, wavelength errors at the exit slit, arising from curvature of the spectrum when a plane grating is employed, are avoided. Near theoretical resolution can thus be achieved.

In addition, this type of spectrometer has the advantage of fixed slits, compact design and a simple scanning mechanism which can be driven to provide a linear wavelength scale, and which allows accurate determination of the wavelength (Fastie *et al*, 1958).

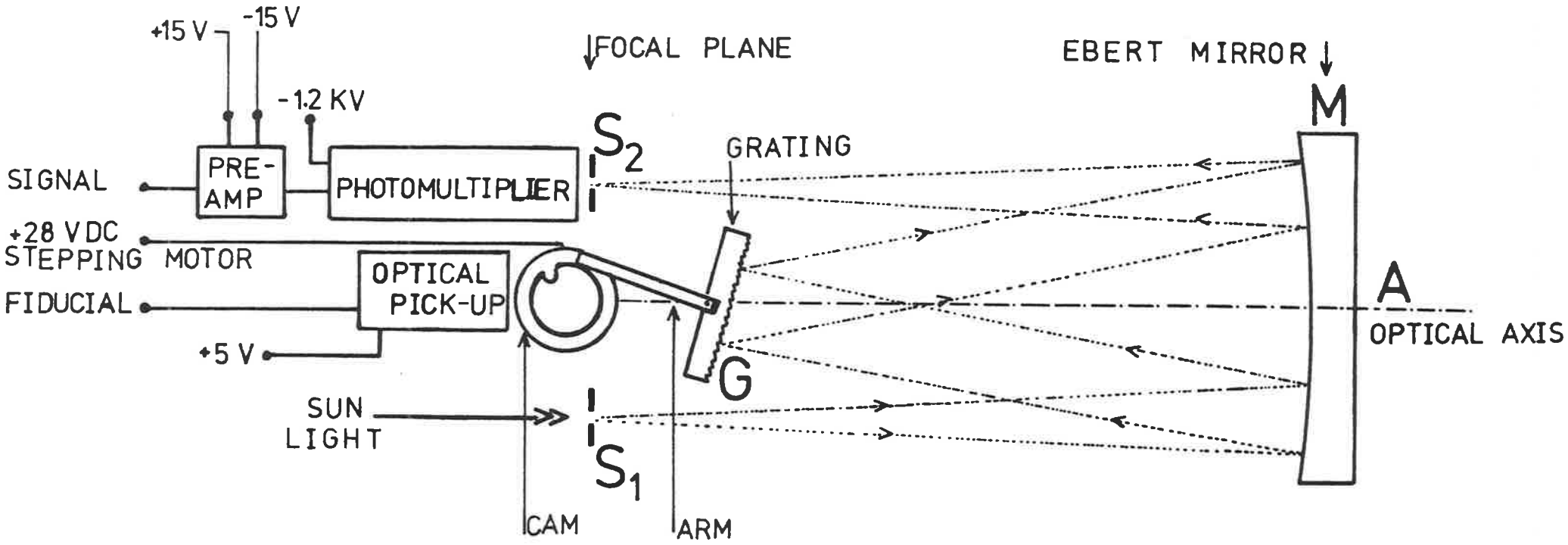

Figure 4.1 Spectrometer optical and electrical schematics.

The spectrometer for the Aerobee rocket was provided by Ray Lee Instruments (Model 15-125) and consisted of an Ebert mirror (62mm x 38mm) of focal length 125mm, a grating (ruled area 26mm x 26mm) with 3600 lines/mm (from the Apollo master) blazed for 140 nm and matched slits 100 micron wide and 2mm long. With dispersion of 2 nm/mm the resolution was expected to be 0.2 nm. The spectrometer housing was aluminium with a low outgassing optical black finish. The mirror, also of aluminium, and the grating were both coated with magnesium fluoride to give maximum reflectance near 140 nm. Wavelength scanning was accomplished by driving a cam with a stepping motor. The grating was thus rotated always in the same direction, in successive angular steps, each step equivalent spectrally to 0.133 nm. At the completion of each scan the grating was reset to its original position by cam flyback. Cam position was determined by use of an optical pickup utilizing an infrared LED and phototransistor, and the commencement of each scan registered a large negative pulse, called the fiducial. Spectrometer exit slit signals were monitored by an integrated detector system, also supplied by Ray Lee instruments (Model SE-315). This contained an EMR 510F-09-13-1000 miniature ceramic photomultiplier with cesium telluride cathode (long wavelength cut-off at 350 nm) and magnesium fluoride window (short wavelength cut-off at 115 nm) which operated in the pulse counting mode with grounded grid and gain between 10^6 and 5×10^6.

Figure 4.2 is a view of the fully assembled flight spectrometer in which the entrance slit, stepping motor and potted detector are apparent.

b. *Calibration*

The wavelength at each step of the spectrometer grating was determined in the laboratory for the spectral range 137 to 175 nm.*

* This was carried out by Dr R. Schaeffer, at the time a Post-Doctoral Fellow in the Department of Physics, University of Adelaide.

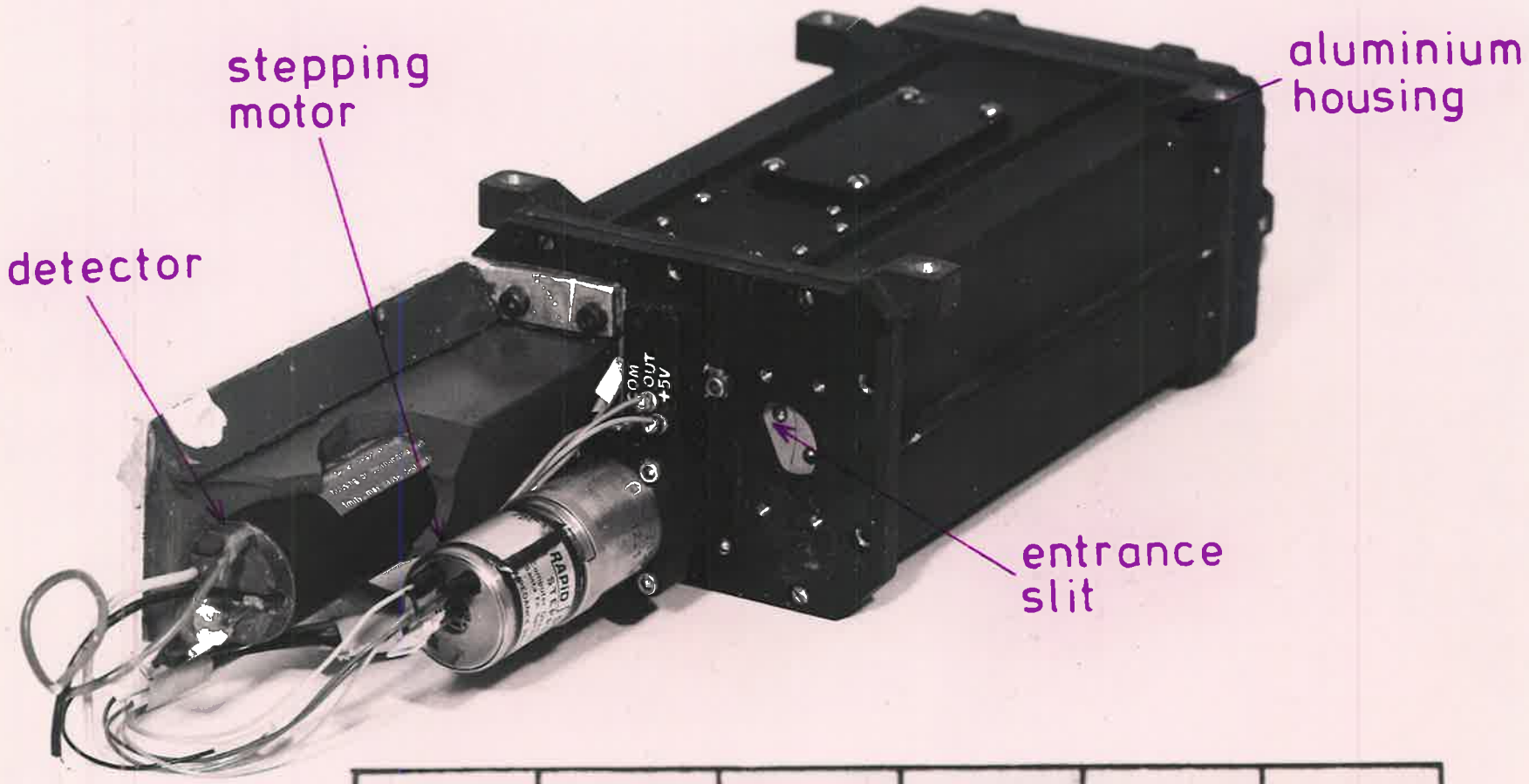

Figure 4.2 Ebert - Fastie spectrometer

Light was provided by a water cooled capillary discharge lamp powered by a thyratron capacitance discharge circuit used to excite a discharge in hydrogen. Spectral lines produced by the lamp were identified with a six metre vacuum ultraviolet monochromator (Carver *et al*, 1978b). Figure 4.3 is the lamp spectrum as resolved by the Ebert-Fastie spectrometer, by counting for three seconds per step and advancing manually every fourth second. Figure 4.4 is a graph of the wavelength as a function of step number, as determined from the scan in Figure 4.3.

4.4 SPECTROMETER FLIGHT PERFORMANCE

a. Data Acquisition

The 1/8th meter FUV scanning spectrometer was flown on the same Aerobee rocket that carried the grazing incidence monochromator discussed in Chapter 3. This sun-pointed vehicle was launched from Woomera, S.A., at 0636 hours C.S.T. and reached an apogee of 177 km at a time when the solar zenith angle was 84.5°. Description of the rocket payload and additional flight details are provided in Appendix A. The location of the spectrometer in the payload can be seen in Figure 3.8.

When the solar zenith angle is 85°, attenuation of FUV radiation occurs primarily between the altitudes 100 and 180 km and useful experimental data was recorded after the acquisition system took control at 107 km on the upleg until 85 km on the downleg, at which height the instrument power supplies were turned OFF. A total of 79 complete scans of the solar spectrum between 137 and 175 nm, at the rate of one cycle (290 steps) every 3.5 seconds, was obtained.

The signal from the spectrometer photomultiplier, and this signal attenuated by a factor of 16, were fed directly to the digital input PCM telemetry system carried by the Aerobee, at a rate of 625/sec. The analog fiducial signal was sampled at a rate of 160/sec. Flight data was

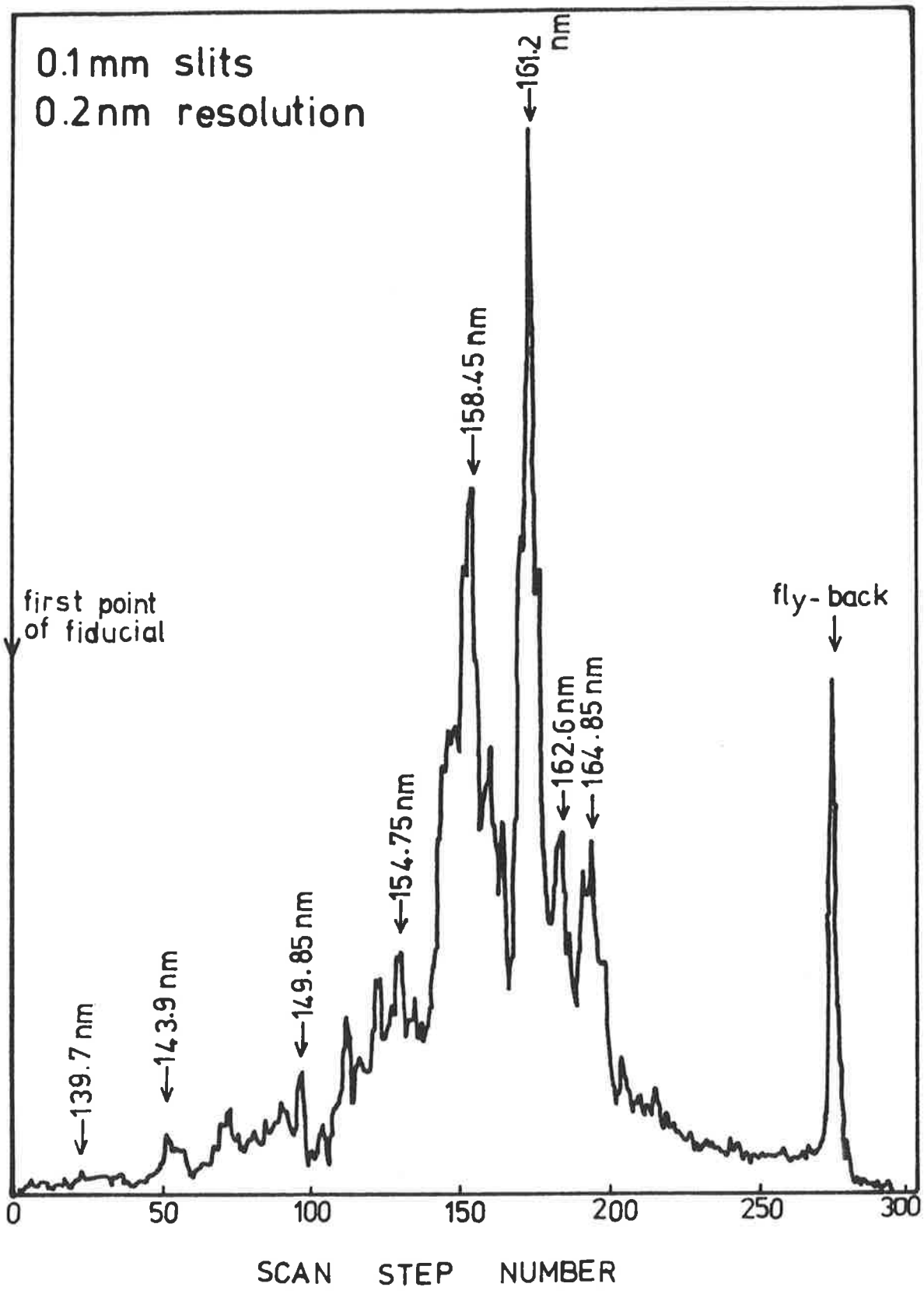

Figure 4.3 Hydrogen lamp spectrum resolved by spectrometer.

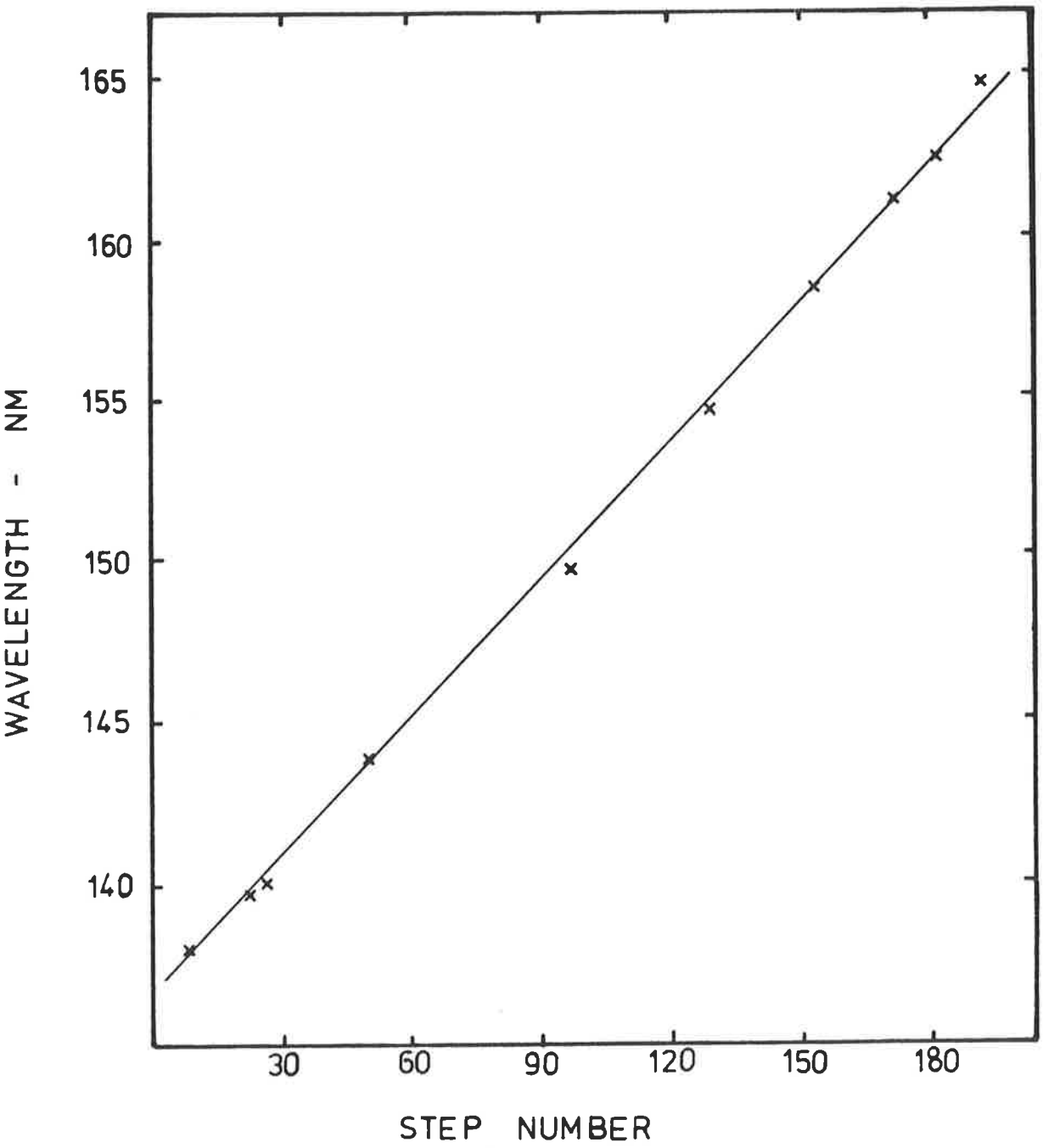

Figure 4.4 Spectrometer wavelength calibration curve.

stored on seven track magnetic tape and analyzed using the University of Adelaide's CDC Cyber 173 computer.

Vehicle trajectory and velocity were acquired with a Weapons Research Establishment FPS16 radar and provided in printout form as a function of time. A fourth order polynomial was least-squares fitted to the rocket altitude so it could be calculated at any time during the flight.

b. *Solar Spectral Scans*

Telemetry data records were surveyed over the whole flight for the times when the fiducials occurred. Each scan required 290 steps of the grating and the scan period was determined from the time between successive fiducials. Dividing by 290 then gave the absolute time interval that data were collected at each particular step of a scan. By averaging all telemetered signals at a single step, spectral scans were generated for different altitudes. Because the fiducial was not exactly reproducible an error was associated with the scanning frequencies deduced in this way and with choosing the exact position for the start of each scan. Average scan period was found to be 3.53 seconds with an uncertainty of ± 0.01 second, indicating that the error was of the order of the time per step (0.012 sec) which was equivalent (Section 4.2a) to 0.13 nm. Rottman (1976) has noted that the Ray Lee cam drive for the wavelength scan is not as precise as desirable because of the difficulty in polishing the cam track sufficiently. His scans showed wavelength shifts as large as ± 0.1 nm and this may have affected the 0.2 nm resolution.

The solar spectrum observed with the scanning far ultraviolet spectrometer, and shown in Figure 4.5, is an average of eleven scans near apogee. The background, an average of seven scans below 100 km, was attributed to light of wavelength longer than 200 nm which is not absorbed by atmospheric constituents above about 90 km, and to Lyman-alpha radiation.

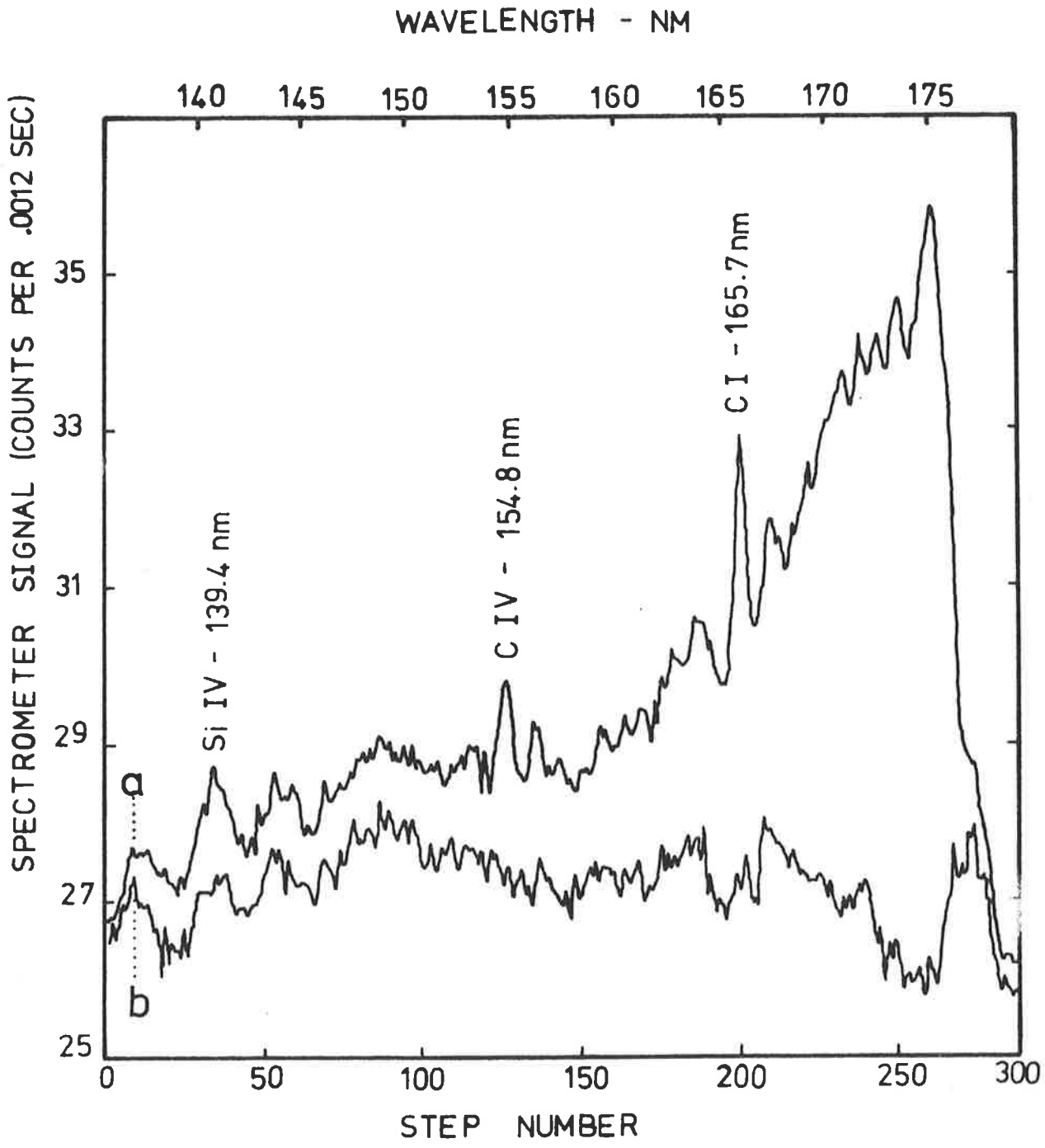

Figure 4.5 a) Solar spectrum observed with spectrometer near apogee.

b) Background.

Solar emission wavelengths were identified with the help of Figure 4.4 and Widing *et al* (1970).

4.5 EXPERIMENTAL ABSORPTION CURVES

a. Smoothing the Spectral Altitude Profile

The time allowed for the spectrometer to measure the solar flux at each step was small (0.3% of the total period of each scan). The number of observed counts was only 6 or 7 per step hence the statistical error was large (~ 40%). The spectrum recorded by the spectrometer thus represented a very small random sample of the parent distribution - the solar spectrum. To obtain spectral scans in which the relative spectral distribution was reproducible, a small degree of smoothing was applied to the data.

This involved obtaining a better estimate of the signal for each step at the expense of altitude information and was achieved by successive weighted averaging over five scans. A narrow weighting function was used, for which the half-width was only slightly wider than the altitude resolution afforded by the rate of acquisition of the raw scans.

For a particular step in the scan i ($i = 1, 5$) the signal s_i recorded at height h_i was weighted by a factor w_i calculated according to

$$w_i = \exp\left[- \tfrac{1}{2} \frac{(h_i - h_a)^2}{x} \right]$$

where h_a is the height of the same step averaged over the five scans -

$$h_a = \frac{\Sigma h_i}{5}$$

and x is given by

$$x = \sqrt{\frac{\Sigma(h_i - h_a)^2}{5}}$$

The weighted signal s_a for this step was then

$$s_a = \frac{\Sigma w_i s_i}{\Sigma w_i}$$

The weighting function as applied to five low altitude scans is shown in Figure 4.6a. From this, the height resolution of the raw data was obtained from the FWHM value and varied with altitude as indicated in Figure 4.6b.

b. Absorption Curves

In the far ultraviolet region the solar spectrum, as described in Section 1.1c, is a continuum, superimposed with emission lines below 168 nm and Fraunhofer absorption lines above 176 nm. The 0.2 nm spectrometer resolution was sufficient to define the radiation received at each step of the spectral scan as being monochromatic and absorption curves were available, for example, from the altitude variation of the signals at individual steps.

Since the statistical accuracy corresponding to a single step was poor, two or three steps from the continuum region of the spectrum were used to provide narrow wavelength 'windows' for which the average signal was plotted as a function of altitude.

For solar emission lines such as CI emission at 165.7 nm, monochromatic absorption curves were generated by monitoring the height variation of the average of the signal at each step across the line.

A total of ten absorption curves were extracted from 38 downleg scans. On the upleg, the measured signal was smaller than on the downleg and this was attributed to insufficient outgassing of the spectrometer.

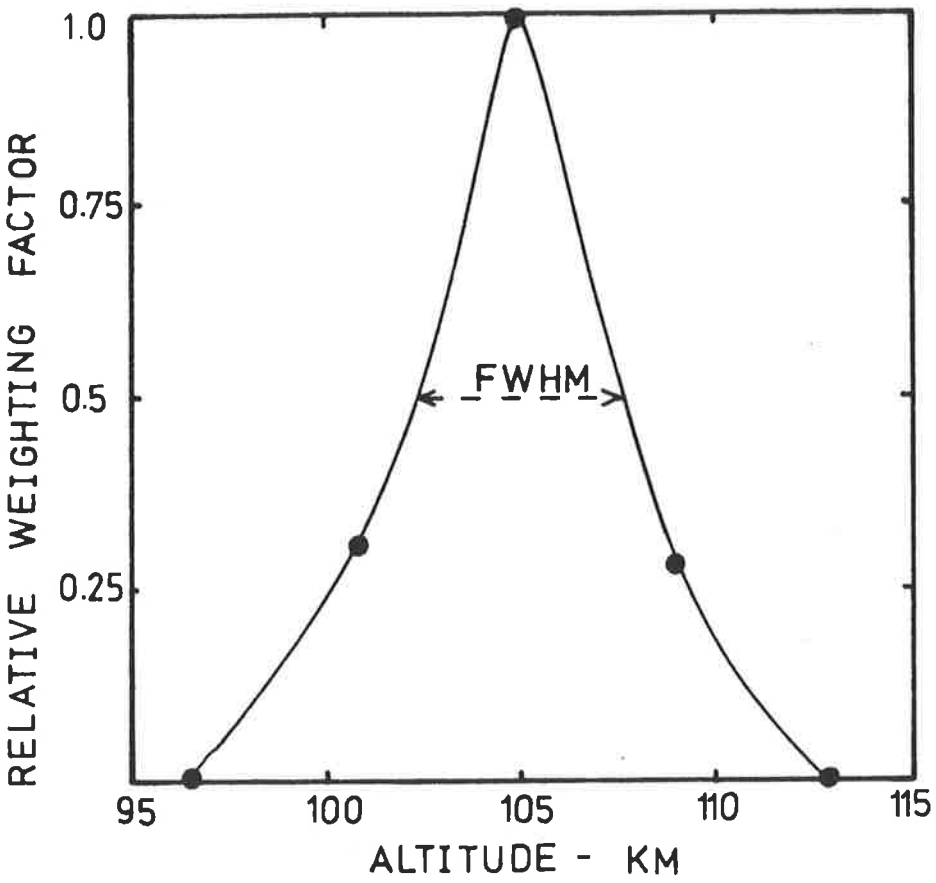

Figure 4.6a Smoothing window at 105 km.

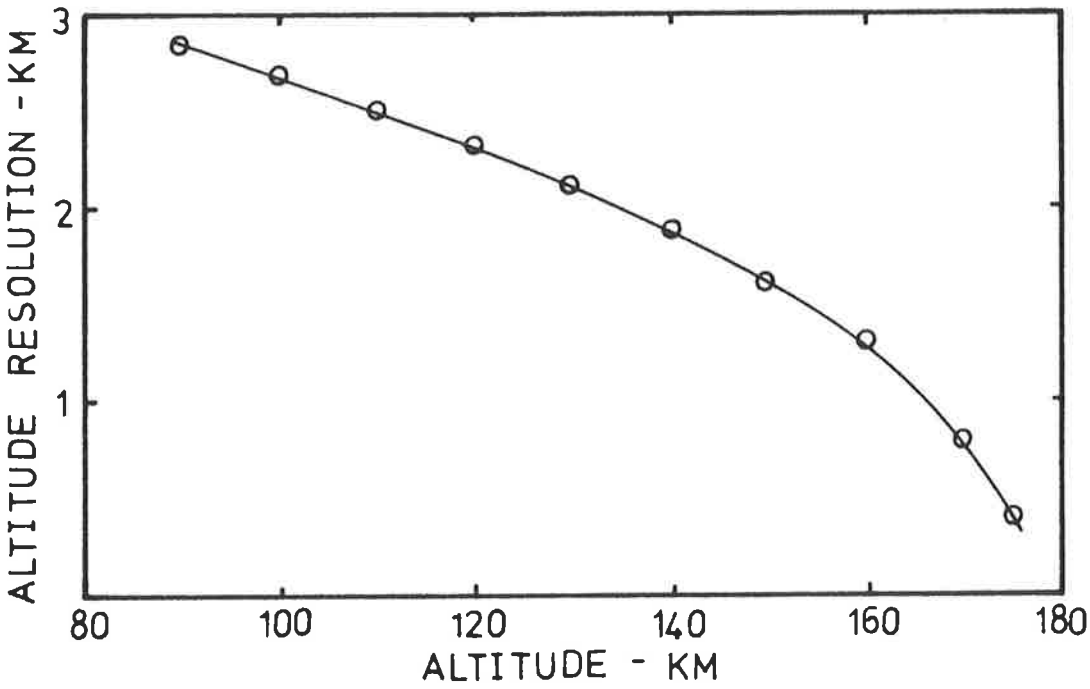

Figure 4.6b Altitude resolution determined by smoothing.

c. *Curvefitting*

Since the height resolution (Figure 4.6b) was about 2 km at altitudes where the far ultraviolet solar flux was attenuated, only the coarse structure of this attenuation was provided by the experimental absorption curves. To facilitate efficient data manipulation and to provide additional smoothing in the region of low attenuation, each absorption profile was fitted as a composite curve.

An analytical function used to fit experimental data must in no way presuppose the theoretical expressions which describe the data trends and must be sufficiently flexible to accommodate any real asymmetries and irregularities. Each absorption curve was fitted with a function of the form

$$I_e = I_b + \frac{I_o}{1 + \exp[- (h - h_o)k + (h - h_o)^2\ 1 - (h - h_o)^3 m]} \qquad 4.1$$

using the least-squares procedure for fitting data with a function non-linear in its parameters, as described by Bevington (1969). I_e is the signal measured at height h and I_b, I_o, h_o, k, 1, and m are six fitting parameters. I_b corresponds to the background signal and the unabsorbed signal is $I_b + I_o$. At the height h_o, dI_e/dh is a maximum, while 1 and m determine respectively the shape of the curve about h_o and its asymmetry.

Table 4.1 gives the best values of the parameters, as determined by the fitting routine, for each absorption curve. In Figure 4.7 the data points and fitted functions are presented for four of the ten curves and it can be seen by visual inspection that the chosen analytic function was an appropriate one. Additional confirmation was afforded by successfully fitting some typical attenuation curves, such as those calculated in Section 2.2 and illustrated in Figure 2.4.

Wavelength - nm	I_b	I_o	h_o	k	l x 10	m x 10^3
165.7	27.090	4.8831	117.75	.15309	.02608	.029
167.1	27.651	4.2324	115.15	.13255	.01372	.002
168.3	27.216	4.5247	113.46	.16961	.05401	.106
170.5	26.750	6.9975	110.85	.21885	.08360	.126
171.2	26.804	7.2196	110.44	.25384	.10926	.198
171.4	26.986	6.9247	110.22	.21766	.08990	.244
172.1	26.265	7.9401	109.00	.28485	.12493	.212
172.9	26.093	8.5151	108.27	.22129	.05822	.069
173.4	25.887	8.0226	107.73	.30727	.14784	.276
174.4	25.614	10.2439	106.49	.24009	.06199	.064

TABLE 4.1 Fitting parameters for ten absorption curves.

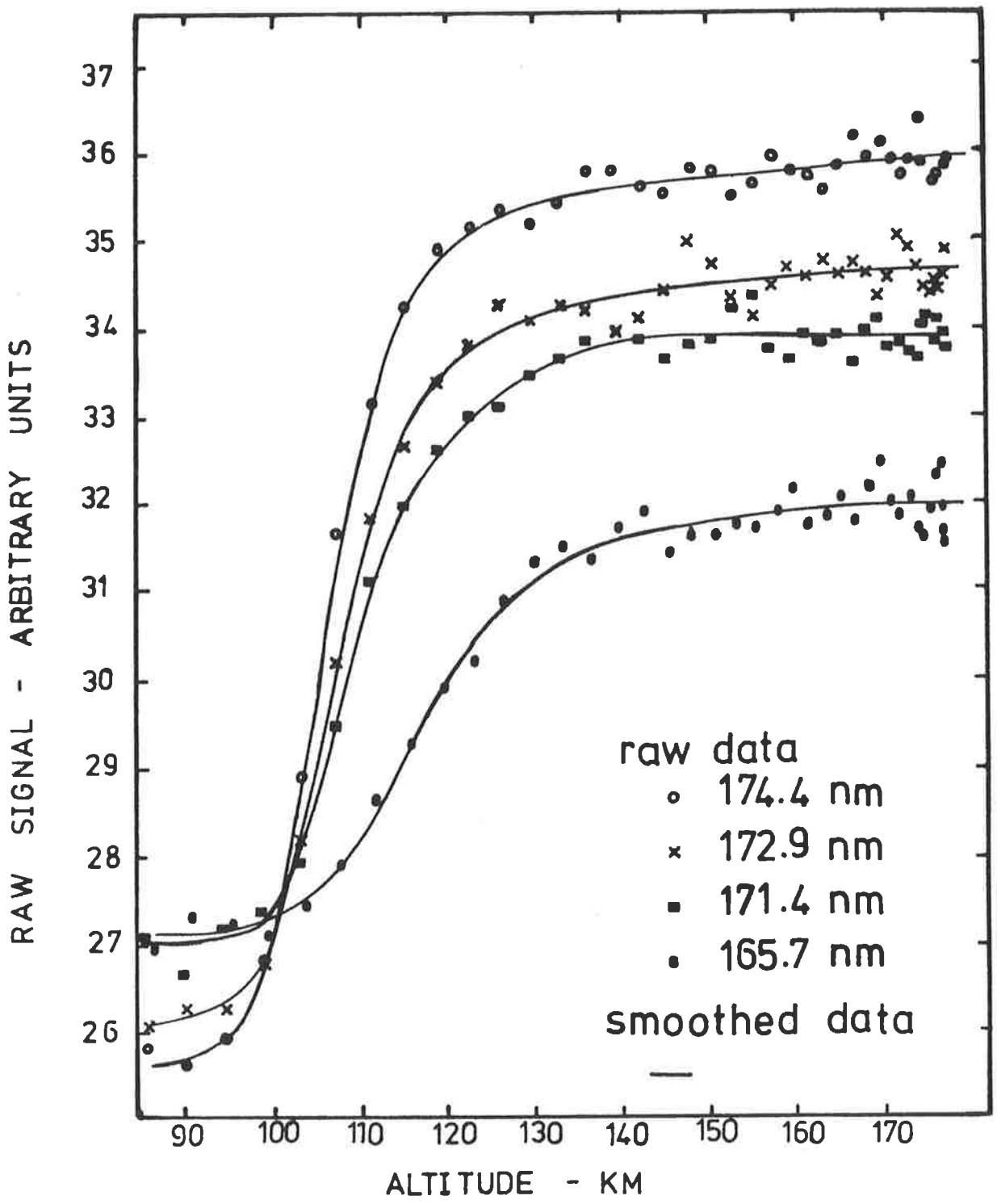

Figure 4.7 Experimental absorption curves.

4.6 OXYGEN ABSORPTION CROSS-SECTIONS IN THE SCHUMANN-RUNGE CONTINUUM

To derive atmospheric densities from the experimental absorption curves in Figure 4.7 it is necessary to know the values of the absorption cross-sections of molecular oxygen in the Schumann-Runge continuum and these must be measured in the laboratory. Absorption properties of gases have been reviewed in Section 1.3 and the particular case of the Schumann-Runge continuum is now considered in greater detail.

a. Theoretical Models

The Schumann-Runge continuum corresponds to transitions from discrete vibrational-rotational energy levels of the $X^3\Sigma_g^-$ state to the energy region above the dissociation limit of the $B^3\Sigma_u^-$ state. Continuum absorption processes have been formulated theoretically by Jarmain and Nicolls (1964). Following their notation, the absorption coefficient at wavenumber ν cm^{-1} for a particular vibrational level v'' of the ground electronic state is given by

$$K(\nu) = (8\pi^3 \nu N_{v''}/3hcg_{v''}) S_{\nu v''} \qquad 4.2$$

$$S_{\nu v''} = \left| \int \psi_\nu R_e(r) \psi_{v''} dr \right|^2 \qquad 4.3$$

In these equations

$g_{v''}$ is the statistical weight of the level v'',

$N_{v''}$ is the species concentration at standard temperature and pressure in the level v'',

ψ_ν is the upper state wave function,

$\psi_{v''}$ is the wave function associated with the lower state vibrational level and,

$R_e(r)$ is the electronic transition moment and is a function of the internuclear separation r.

To enable $S_{\nu v''}$ to be evaluated, it is assumed that R_e varies slowly with r, since the range of r involved in significant overlap of the two wavefunctions is small. Then $R_e(r)$ is removed from the integral (Equation 4.3) and evaluated at the r-centroid

$$\bar{r}_{\nu v''} = \frac{\int \psi_\nu \; r \, \psi_{v''} \, dr}{\int \psi_\nu \, \psi_{v''} \, dr}$$

Because of the single valued relationship between $\bar{r}$ and ν (Jarmain and Nicholls, 1964), the electronic transition moment R_e can be expressed as a function of ν and the transition strength $S_{\nu v''}$ is then given by

$$S_{\nu v''} = R_e(\nu)^2 \left| \int \psi_\nu \, \psi_{v''} \, dr \right|^2$$

where the Franck-Condon density is the term for

$$q_{\nu v''} = \left| \int \psi_\nu \, \psi_{v''} \, dr \right|^2$$

Hence the Equation 4.2 for the absorption cross-section reduces to

$$\sigma(\nu) = 4.083 \times 10^{-24} \; \nu \, R_e(\nu)^2 \; q_{\nu v''}$$

In practice, numerical values for $\sigma(\nu)$ with $v'' = 0$ are available from laboratory measurements at room temperature, and these are combined with knowledge of the potential energy curves and wavefunctions of the upper and lower states to provide an estimate for R_e which is then utilized for calculations with $v'' \neq 0$.

Such calculations were done by Jarmain and Nicolls using Klein-Funham potentials to develop suitable wavefunctions for determing Frank-

Condon densities. From the measured absorption coefficients they deduced the variation of the electronic transition moment R_e across the continuum for the ground state level $v'' = 0$. Extension of this technique was reported by Allison *et al* (1971) for higher ground state vibrational levels, $v'' = 1$ and $v'' = 2$. A trial and error procedure, in which R_e was allowed to vary slowly with r, was used to find a plausible combination of the upper state potential $V'(r)$ and $R_e(r)$ that reproduced the measured absorption and emission data. These results were then used to predict the continuous absorption cross-sections for the three lowest ground state vibrational levels. Their computed cross-sections are illustrated in Figure 4.8.

More recently, Julienne *et al* (1976) have used multi-configuration self consistent field wavefunctions to calculate the transition moment function necessary to interpret the Schumann-Runge absorption cross-sections. Their data is different from that of Allison *et al* and the reason was attributed to the procedure employed by the latter to fit the upper state potential $V'(r)$ beyond the dissociation limit. This state is not well known and may have an inflection point so that the resultant Frank-Condon densities will also be uncertain. Julienne *et al* hence cautioned against the extraction of the transition moment from experimental data.

Theoretical calculations of absorption from the $v'' = 0$ vibrational level can be directly compared with experimental measurements of the cross-sections at room temperature but at higher temperatures transitions from excited vibration states must be considered. This can be done, if rotational energy is ignored, as suggested by Allison *et al* (1971), by weighting the contribution to the cross-section from each vibration state according to its population, so that at temperature T and wavelength λ,

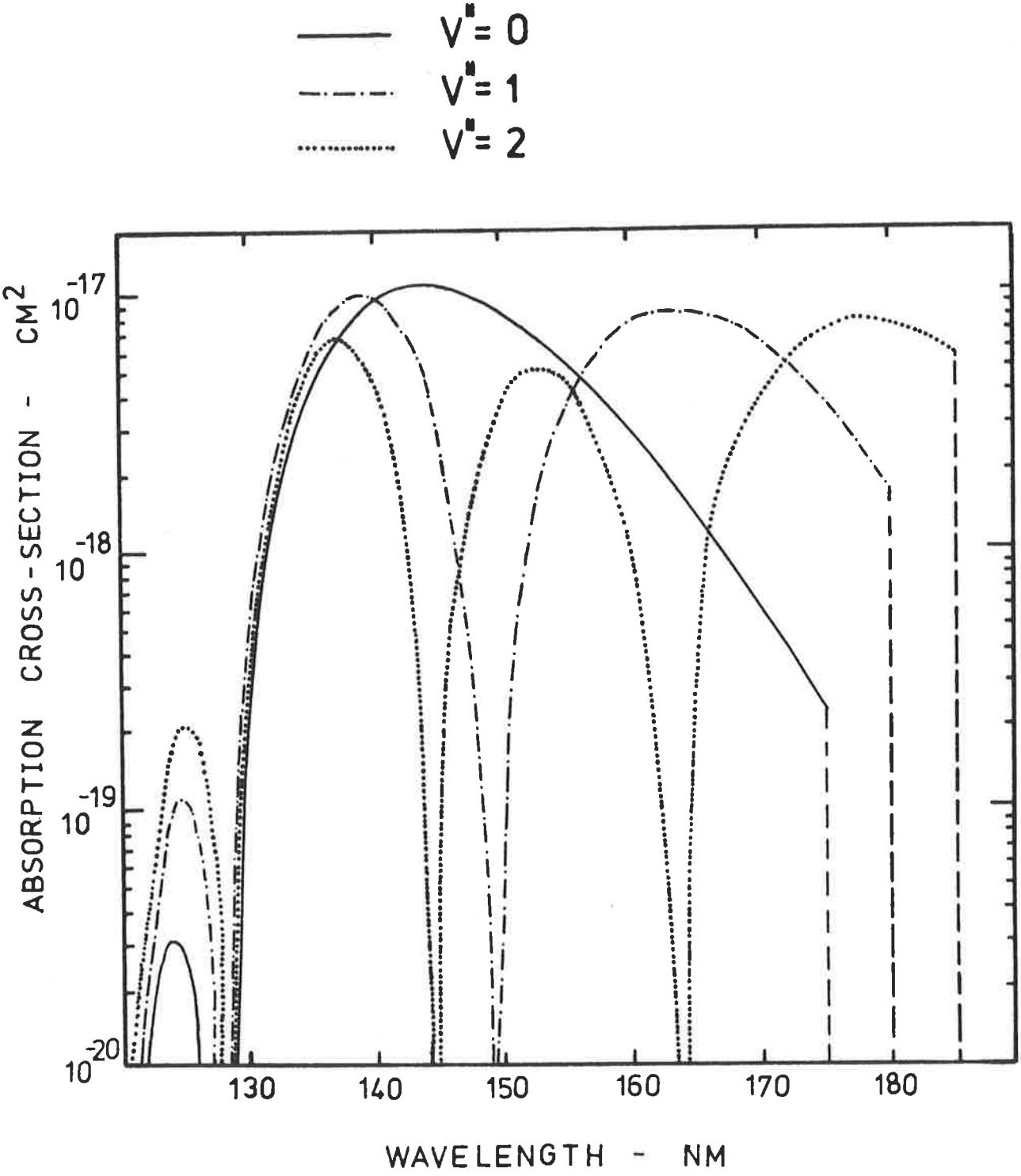

Figure 4.8 Theoretical absorption cross-sections for molecular oxygen.

(Allison et al. 1971)

$$\sigma(T, \lambda) = \frac{\sum_{v''} \sigma_{v''}(\lambda) \exp(- G_{v''}hc/kT)}{\sum_{v''} \exp(- G_{v''}hc/kT)} \qquad 4.4$$

where $G_{v''}$ is the conventional spectroscopic constant (Herzberg,1950). In particular, σ_0, σ_1 and σ_2 are the cross-sections, illustrated in Figure 4.8, of the ground state, first and second excited states respectively.

b. *Numerical Values at Room Temperature*

There is general agreement between different experimenters about the magnitude of the Schumann-Runge continuum cross-sections at room temperature. Laboratory measurements of the type described in Section 1.3b are relatively straightforward, and Beer's law is observed to be appropriate for data collected over a wide range of pressures.

The three diffuse bands between 125 and 135 nm were first resolved by Watanabe *et al* (1952, 1953) who also identified the asymmetry of the absorption spectrum over the entire photodissociation continuum. At the wavelength for which the absorption is a maximum, the cross-section was reported to be 25% lower than previous measurements which had used photographic absorption spectroscopy (Ditchburn and Heddle, 1953). Watanabe's results were subsequently confirmed by additional photoelectric measurements (Huffman *et al*, 1964b; Metzger and Cook, 1964; Blake *et al*, 1966; Hudson *et al*, 1966). In particular, Hudson *et al* used a 2.2 metre monochromator with a passband of 0.0075 nm to provide results with a quoted systematic error of only 1%. New measurements have been made from 150 to 175 nm, using a 6-metre monochromator with 0.01 nm resolution (Blake *et al*, 1980).

In the wavelength region corresponding to the absorption curves of Section 4.5, tabulated numerical values of the oxygen absorption cross-sections at room temperature have been provided by Watanabe *et al* (1953),

Hudson *et al* (1966), Blake *et al* (1966) and most recently by the six-metre group at the Department of Physics, University of Adelaide (Blake *et al*, 1980). Data from each experimental group is plotted together in Figure 4.9. At the wavelength corresponding to each absorption curve, the best estimate of the absorption cross-section $\bar{\sigma}(\lambda)$ was considered to be the average of all experimental data ;

$$\bar{\sigma}(\lambda) = [\sum_i \sigma_i(\lambda)] /N, \quad N = 4$$

Calculation of the sample standard deviation s according to

$$s^2(\lambda) = \{ \Sigma_i [\sigma_i(\lambda) - \bar{\sigma}(\lambda)]^2 \}/(N - 1)$$

enabled the uncertainty $\Delta \bar{\sigma}(\lambda)$ in this average value to be estimated since $\Delta \bar{\sigma}(\lambda) = s/\sqrt{N}$. Numerical cross-section data and the results of the averaging are listed in Table 4.2.

c. *Temperature Dependence*

It is possible to predict the nature of the temperature dependence of the absorption cross-section $\sigma(T, \lambda)$ by considering Figure 4.8. According to Blake *et al* (1980), as the temperature increases from 300 to 600K, the temperature coefficient will be positive or negative as $\sigma_1(\lambda)$ is respectively greater or less than $\sigma_0(\lambda)$. In particular, at about 140 nm and also at 157 nm, these two cross-sections are equal and there will be no temperature effect. Near 149 nm Figure 4.8 indicates that $\sigma_1(149)$ is some 10^3 times smaller than $\sigma_0(149)$ so a redistribution of the ground state population by 2%, corresponding to a temperature increase from 300 to 600K, will cause a negative temperature effect of similar magnitude. For wavelengths greater than 157 nm, since $\sigma_1(\lambda)$ now exceeds $\sigma_0(\lambda)$, an increasingly large positive temperature effect is

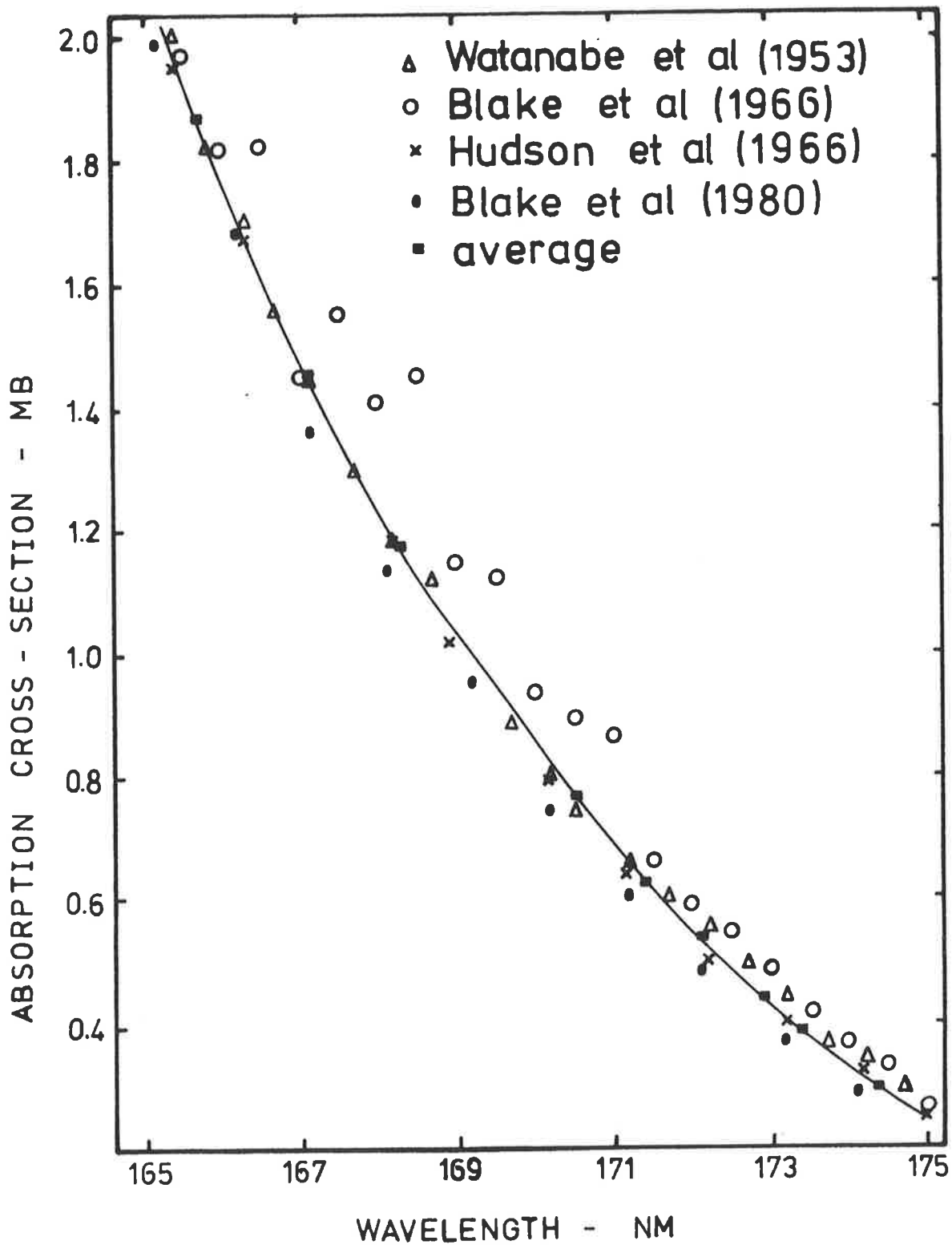

Figure 4.9 Molecular oxygen absorption cross - sections.

Wavelength - nm	Absorption cross-section - Mb					
	Blake *et al* (1966)	Hudson *et al* (1966)	Watanabe *et al* (1953)	Blake *et al* (1980)	Average	Percent Uncertainty
165.7	1.96	1.86	1.88	1.81	1.88	1.7
167.1	1.60	1.44	1.45	1.39	1.47	3.1
168.3	1.31	1.16	1.18	1.10	1.19	3.7
170.5	0.88	0.75	0.75	0.72	0.77	4.8
171.2	0.73	0.64	0.68	0.62	0.67	3.8
171.4	0.70	0.60	0.65	0.59	0.64	3.9
172.1	0.60	0.51	0.57	0.50	0.55	4.4
172.9	0.48	0.42	0.48	0.41	0.45	4.2
173.4	0.42	0.38	0.42	0.36	0.39	4.1
174.4	0.33	0.29	0.33	0.27	0.31	4.6

TABLE 4.2 Laboratory measurements of molecular oxygen absorption cross-sections at room-temperature in the Schumann-Runge continuum.

predicted.

Measurements of the absorption cross-sections $\sigma(T, \lambda)$, for $T < 900K$, have been made by Hudson *et al* (1966) and by the group at the University of Adelaide. Both sets of results are plotted in Figure 4.10 and for comparison the average room temperature cross-sections calculated in the previous section are included.

Using the first two terms of the summation in Equation 4.4, the absorption cross-section can be expressed analytically as

$$\sigma(T, \lambda) = \frac{\sigma_0(\lambda) \exp(- G_0hc/kT) + \sigma_1(\lambda) \exp(- G_1hc/kT)}{\exp(- G_0hc/kT) + \exp(- G_1hc/kT)}$$

The constant $G_{v''}$ is evaluated from the expression (Herzberg, 1950)

$$G_{v''} = w_e(v'' + \tfrac{1}{2}) - w_ex_e(v'' + \tfrac{1}{2})^2 + w_ey_e(v'' + \tfrac{1}{2})^3$$

where, for the $X^3\Sigma_g^-$ state, the constants have the following values;

$$w_e = 1580.361, \quad w_ex_e = 12.073, \quad w_ey_e = 0.0546.$$

Using the numerical values $G_0 = 787.17$, $G_1 = G_0 + \Delta G$ and $\Delta G = 1556.39$ cm^{-1}, the expression for the absorption cross-section reduces to

$$\sigma(T, \lambda) = \frac{\sigma_0(\lambda) + \sigma_1(\lambda) \exp(- 2239.29/T)}{1 + \exp(- 2239.29/T)} \qquad 4.5$$

From the data of Blake *et al* (1980), values of $\sigma(290, \lambda)$ and $\sigma(570, \lambda)$ were obtained by graphical interpolation of Figure 4.10 at the particular wavelengths of the absorption curves. At room temperature $\sigma(270, \lambda) = \sigma_0(\lambda)$ so that Equation 4.5 can be solved by substituting $\sigma(570, \lambda)$ to obtain the value of the constant $\sigma_1(\lambda)$. This meant that $\sigma(T, \lambda)$ could then be predicted, as a first approximation, at any temperature. For

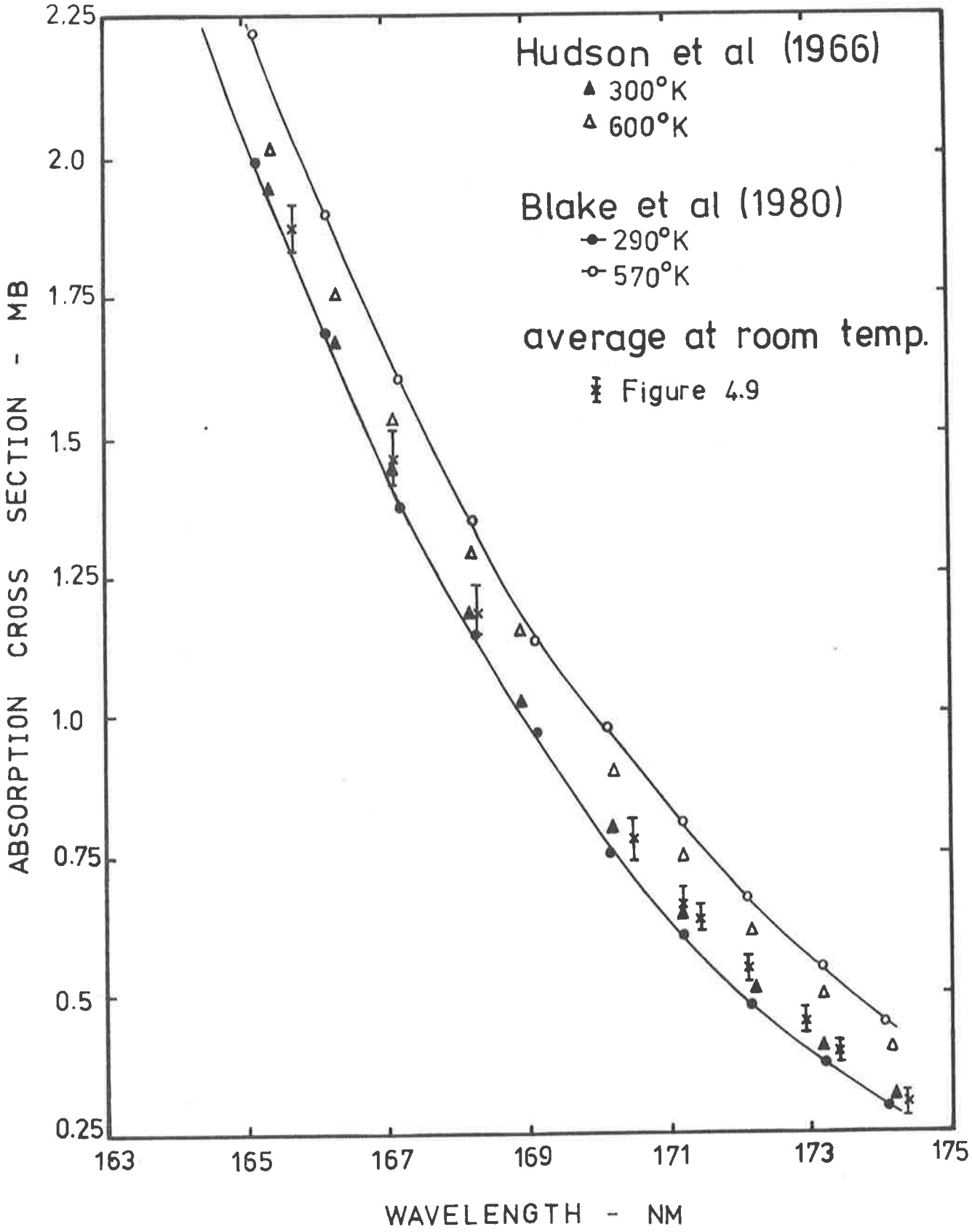

Figure 4.10 Temperature dependence of molecular oxygen absorption cross - sections: laboratory measurements.

evaluating this semi-empirical variation of the absorption cross-sections with temperature, the average room temperature cross-sections, as calculated in the previous section, were resubstituted into Equation 4.5, and these results are displayed in Figure 4.11.

4.7 MOLECULAR OXYGEN NUMBER DENSITIES

In deducing O_2 densities, the following analysis assumed that the Schumann-Runge continuum of molecular oxygen is the dominant absorber of FUV flux between 140 and 175 nm. Absorption cross-sections for O_2, as discussed in Section 1.3, are such that the requirement of Equation 2.8 was satisfied. Absorption spectroscopy techniques developed in Section 2.1c for monochromatic absorption by a single constituent were applied on assumption that the experimental absorption curves were 'sufficiently' monochromatic. Then molecular oxygen densities were determined directly from the absorption curves generated from the spectral scans, since rearranging Equation 2.10 expresses the density as

$$n(h) = \frac{1}{F(h)\ \sigma(\lambda)\ I(h,\ \lambda)} \quad \frac{dI(h,\ \lambda)}{dh} \qquad 4.6$$

F(h) is the optical depth factor and has been discussed in Section 2.1b. Because of the large solar zenith angle when the Aerobee was launched it was necessary to use Equation 2.7 to determine F(h) as a function of altitude. These calculations are provided in Appendix D, and incorporated the use of height dependent zenith angles and scale heights derived, using Equation 2.5, from the O_2 densities predicted by Jacchia (1977) at the time of launch.

Numerical values for (1/I)dI/dh were obtained by differentiating the analytical functions, Equation 4.1, determined in Section 4.4c. The most accurate densities derived from that part of the absorption curve where

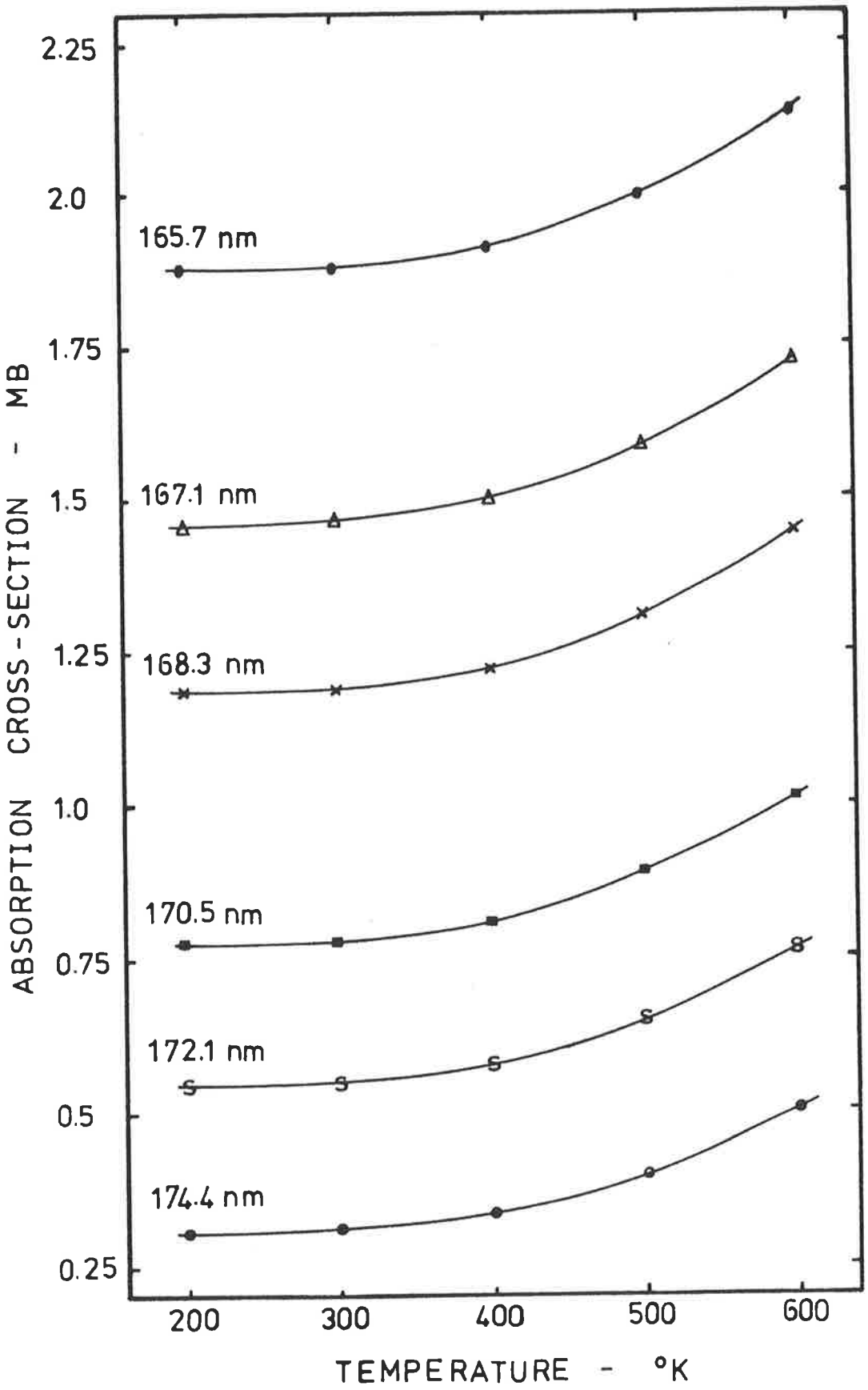

Figure 4.11 Temperature dependence of O_2 absorption cross-sections: semi-empirical model.

dI/dh was greatest. The altitude region for which this rate of attenuation was a maximum differed for each absorption curve. As illustrated in Figure 4.12, normalized absorption curves generated at wavelengths for which the absorption cross-section is large were displaced to higher altitudes with respect to those curves corresponding to weaker absorption.

For the absorption cross-sections, the values presented in Section 4.5 were used. Initially, room temperature cross-sections were incorporated in density determination (Section 4.6a, below) then perturbation of the results due to the temperature dependence of the cross-sections was investigated (Section 4.6b, below).

a. Results for Room Temperature Cross-Sections

O_2 density profiles were extracted from each absorption curve using Equation 4.6. At each altitude for which the density was determined, the uncertainty in the density was calculated from

$$\left[\frac{\Delta n(\lambda, h)}{n(\lambda, h)}\right]^2 = \left[\frac{\Delta F(h)}{F(h)}\right]^2 + \left[\frac{\Delta \sigma(\lambda)}{\sigma(\lambda)}\right]^2 + \left[\frac{\Delta I(\lambda, h)}{I(\lambda, h)}\right]^2 + \left[\frac{\Delta dI(\lambda, h)/dh}{dI(\lambda, h)/dh}\right]^2$$

Since the accuracy of the optical depth factor approximation was given in Section 2.1b as better than 2%, the relative error arising from the evaluation of the optical depth factor in Appendix D was taken as $\Delta F/F = 3\%$ and constant with altitude. Average absorption cross-sections and their mean standard deviations were determined in Section 4.5 so that $\Delta\sigma/\sigma$ was better than 5% and differed with wavelength (Table 4.2) but not altitude.

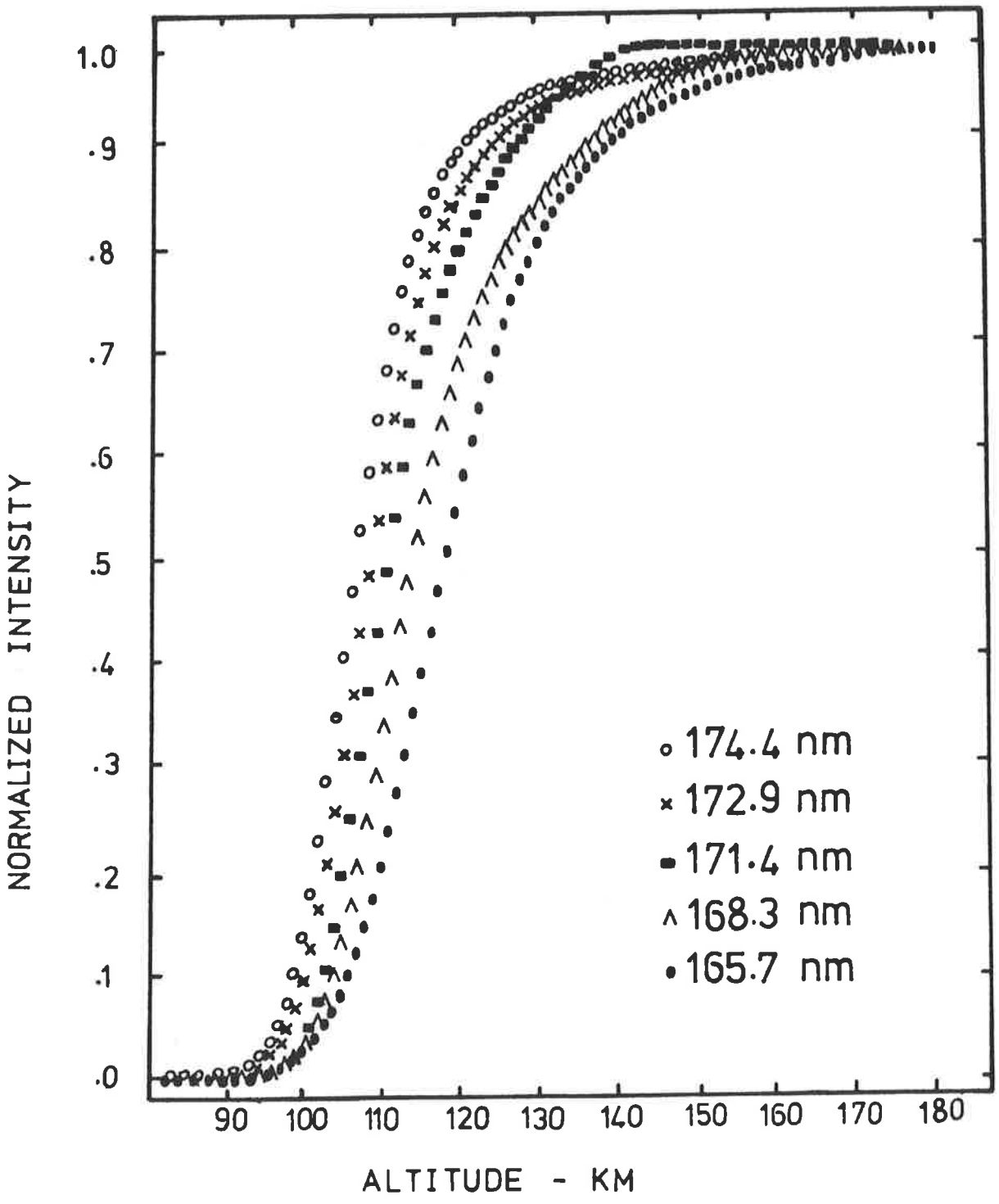

Figure 4.12 Normalized absorption curves.

$I(\lambda, h)$ corresponds to the raw signal and the associated error was assumed to be the telemetry error, equivalent to 25 mV for a telemetry output of 0 - 5V. This relative error was less than 1% and decreased slowly with altitude as the signal increased.

Having ascribed telemetry errors to the raw signal, it was supposed that the error in the slope dI/dh derived only from the numerical techniques used for its evaluation. As an estimate of the magnitude of this error, the slope at the point of inflection was calculated graphically and compared with the numerical value resulting from differentiating the fitted curve. At this point when dI/dh was a maximum, the relative error was found to be about 2.5% so that the derivative at the inflection point of each curve was normalized to this value. Consequently, on either side of the inflection point, the relative error increased as the slope decreased in magnitude.

Once the standard deviation $\Delta n(\lambda_i, h)$ was evaluated for the densities $n(\lambda_i, h)$, determined at selected altitudes from individual absorption curves $(i = 1, 10)$, it was possible to obtain a weighted average density profile. This was done according to

$$\bar{n}(h) = \frac{\sum_i w(\lambda_i, h)\, n(\lambda_i, h)}{\sum_i w(\lambda_i, h)}$$

$$w(\lambda_i, h) = 1/\Delta n(\lambda_i, h)^2$$

For this calculated average, the sample standard deviation at altitude h was determined from

$$s^2(h) = \frac{N \sum_i w(\lambda_i, h)\, [n(\lambda_i, h) - \bar{n}(h)]^2}{(N-1) \sum_i w(\lambda_i, h)}, \quad N = 10$$

and the uncertainty in the mean density from

$$\Delta \bar{n}_1(h) = s(h)/\sqrt{10}$$

An additional uncertainty $\Delta \bar{n}_2(h)$ was incorporated in the density results to reflect the finite height resolution associated with each density estimate at a given altitude. This was obtained from the uncertainty in the altitude given in Figure 4.6b. For the final uncertainty in the O_2 densities ;

$$\Delta \bar{n}(h) = \sqrt{\Delta n_1(h)^2 + \Delta n_2(h)^2}$$

b. *The Effect of Temperature Dependence of the Absorption Cross-Sections on Density Calculations*

To incorporate temperature dependent absorption cross-sections in aeronomic calculations, it is necessary to assume a temperature profile of the atmosphere in the height region of interest. Jacchia's (1977) thermospheric model was evaluated (Appendix E) for the temperature profile at the time of the Aerobee launch. It is plotted in Figure E.1,together with the temperature profile of the U.S. Standard Atmosphere, 1976 which is representative of more typical thermospheric conditions.

The procedure for determining the O_2 densities, described in Section 4.7a, was repeated but the temperature dependence of the absorption cross-sections, effectively a height dependence, was included. At each altitude the temperature of Jacchia (1977) was used to calculate the absorption cross-section from Equation 4.5, for each of the ten absorption curves.

Oxygen densities deduced from the FUV spectrometer data, using both room temperature absorption cross-sections and temperature dependent cross-sections, are given in Table 4.3. In Figure 4.13 the results which incorporated the temperature dependence of the cross-sections are plotted, together with the O_2 densities predicted by Jacchia (1977) and CIRA 1972.

TABLE 4.3 Molecular oxygen number densities deduced from FUV spectrometer data.

Altitude - km	Room temperature absorption cross-sections			Temperature dependent absorption cross-sections		
	$n(O_2)$ cm^{-3}	Uncertainty $\Delta n(O_2)$	%	$n(O_2)$ cm^{-3}	Uncertainty $\Delta n(O_2)$	%
103	1.70×10^{11}	0.53×10^{11}	31.3	1.70×10^{11}	$.53 \times 10^{11}$	31.1
105	1.58	0.43	27.5	1.58	.43	27.5
107	1.41	0.32	23.0	1.41	.32	23.0
109	1.22	0.22	18.2	1.22	.22	18.2
111	1.00	0.13	13.5	1.00	.13	13.4
113	7.88×10^{10}	0.70×10^{10}	9.2	7.87×10^{10}	$.72 \times 10^{10}$	9.2
115	6.01	0.35	5.9	5.99	.35	5.8
117	4.55	0.18	3.9	4.52	.18	3.9
119	3.48	0.13	3.8	3.45	.13	3.8
121	2.71	0.12	4.5	2.68	.12	4.5
123	2.14	0.11	5.1	2.11	.11	5.2
125	1.72	0.09	5.4	1.68	$.94 \times 10^{9}$	5.6
127	1.40	0.08	5.4	1.36	.76	5.6
129	1.15	0.06	5.2	1.11	.59	5.4
131	9.50×10^{9}	0.48×10^{9}	5.0	9.10×10^{9}	.46	5.1
133	7.95	0.41	5.1	7.55	.38	5.0
135	6.71	0.40	5.9	6.32	.35	5.5
137	5.72	0.43	7.5	5.34	.37	6.9
139	4.91	0.47	9.6	4.54	.40	8.9
141	4.23	0.50	11.8	3.88	.43	11.0
143	3.65	0.50	13.8	3.31	.43	12.9
145	3.13	0.48	15.4	2.82	.41	14.4
147	2.67	0.45	16.7	2.39	.38	15.8
149	2.26	0.40	17.9	2.00	.34	17.0
151	1.88	0.36	18.9	1.65	.30	18.0
153	1.56	0.30	19.4	1.35	.25	18.6
155	1.27	0.25	19.3	1.09	.20	18.7
157	1.03	0.19	18.8	8.76×10^{8}	.16	18.4
159	8.33×10^{8}	1.53×10^{8}	18.3	6.99	.13	18.2
161	6.71	1.26	18.8	5.57	.11	19.0
163	5.59	1.09	20.3	4.42	$.92 \times 10^{8}$	20.9
165	4.30	0.98	22.8	3.49	.83	23.8

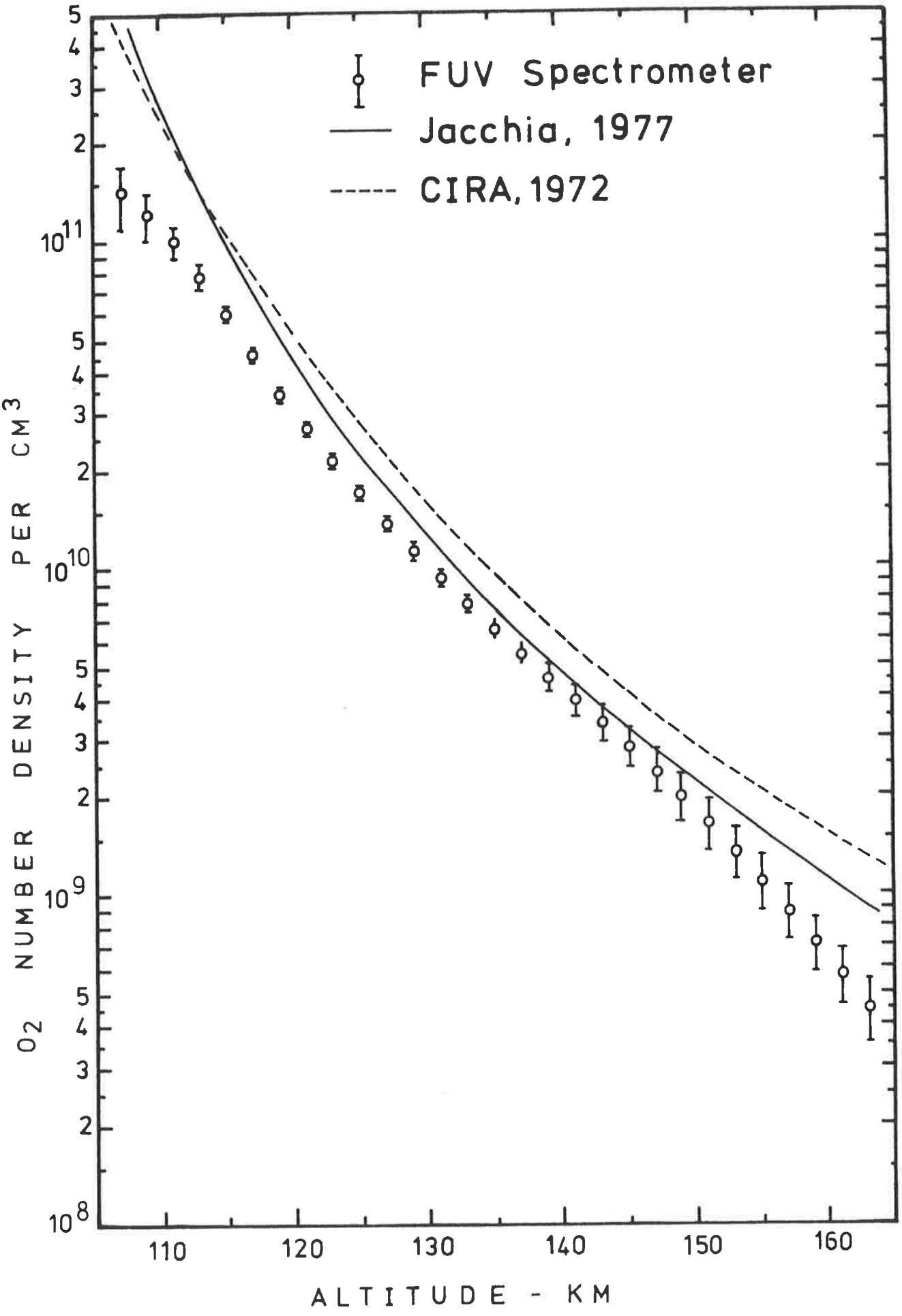

Figure 4.13 Molecular oxygen number densities.

c. *Discussion of the Temperature Effect*

In general, inclusion of the temperature dependence of the cross-sections leads to smaller numerical values for the oxygen densities. At 120 km the thermosphere is approximately at room temperature and it is above this altitude that the temperature dependence was observed to become important. By 145 km the temperature, according to profile (b) of Figure E.1, is 536K and the room temperature cross-sections yielded densities which were 11% higher than those derived from temperature dependent cross-sections. At 165 km the densities were overestimated by 23% when the temperature effect was not included.

The importance of using the temperature dependent absorption cross-sections in these calculations was substantiated by an observed decrease in the weighted mean standard deviation of the densities obtained using absorption at different wavelengths when the temperature effect was included. This implies that the densities predicted individually by each of the ten absorption curves were in better agreement with each other because the temperature dependence of the cross-section varies with wavelength.

It can be seen from Figure 4.14 that the oxygen densities obtained from the absorption data are sensitive to the difference between the temperature profiles shown in Figure E.1. At an altitude of 145 km the temperature from profile (a) gave densities which were 5% less than those obtained using profile (b) while at 165 km the difference increased to 11%. The Aerobee was launched during a period of low solar activity ($F_{10.7} = 82 \times 10^{-22} Wm^{-2} Hz$, $K_p = 1^-$) at a time (0636 hours local time) when the diurnal variation of the thermospheric temperature was near its minimum. These conditions are reflected in the lower temperature profile of (b) compared to profile (a) which represents more typical conditions.

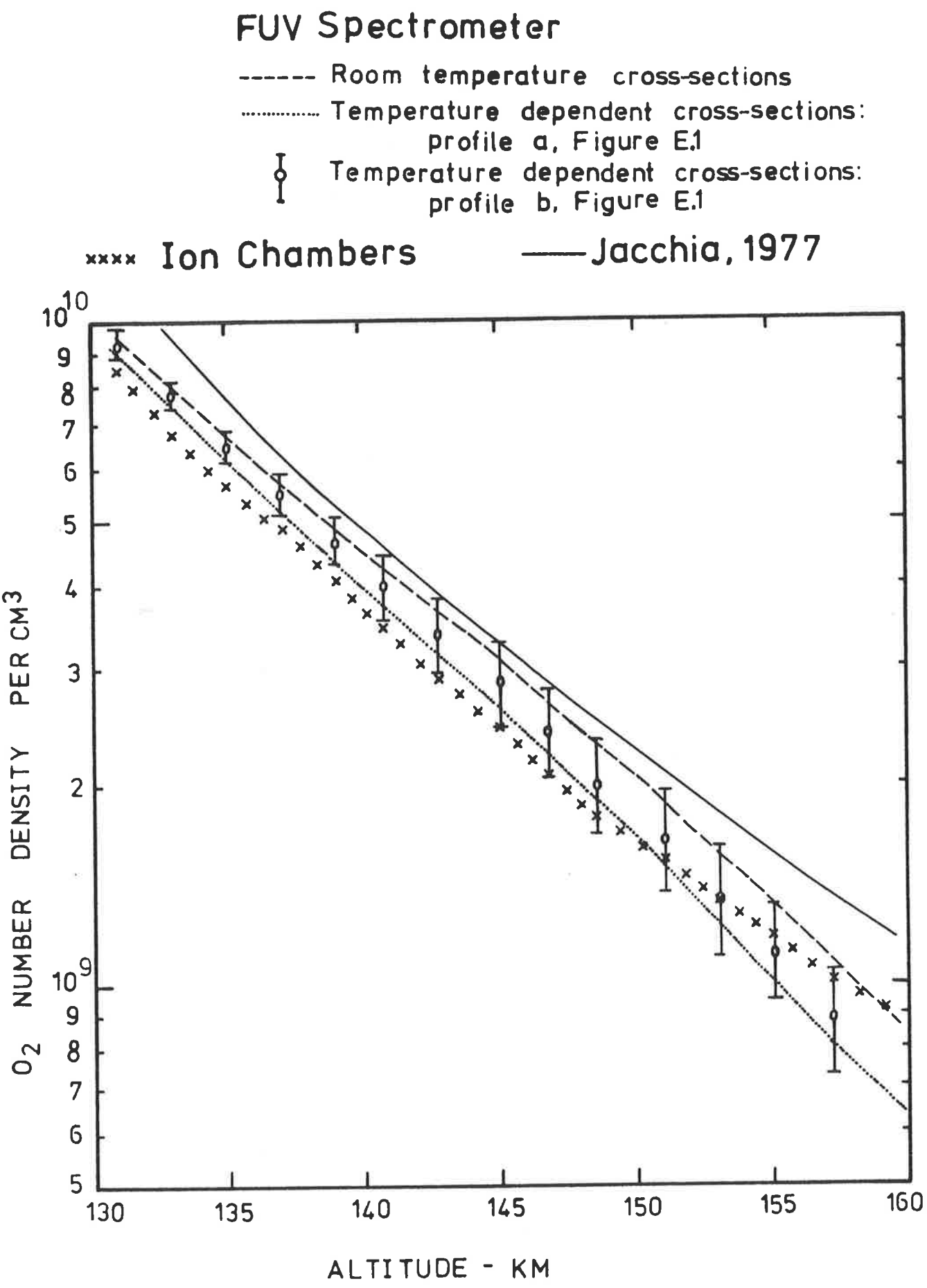

Figure 4.14 The effect of absorption cross-section temperature dependence on O_2 number densities derived from FUV absorption spectroscopy.

In Figure 4.14, the O_2 densities derived from the temperature dependent analysis are compared with the average measurements of two types of broad band ion chambers (QT : 156-165 nm, SX : 142.5-149 nm) flown on the Aerobee rocket. Investigation of the temperature effect on the QT results indicated 3% decrease in the density at 145 km (Davis, 1980). Since the temperature coefficient for the cross-section at the SX chamber wavelengths is small and negative (Blake *et al*, 1980), the average density calculations shown in Figure 4.14 were relatively insensitive to temperature. At 145 km the FUV spectrometer results are 13% higher than the ion chamber densities. Since the associated uncertainty for the spectrometer results at this altitude is ± 15%, when the error of the ion chamber results is applied, the results from these two independent techniques indicate substantial agreement. However, this cannot be said of the densities derived using room temperature cross-sections, since at 145 km they are 29% higher than the ion chamber results.

It must be concluded that the temperature dependence of the molecular oxygen absorption cross-section in the Schumann-Runge continuum should not be neglected in evaluation of atmospheric absorption and that it is important to choose the most appropriate temperature profile.

4.8 INTERPRETATION OF THE RESULTS

An attempt to interpret the available molecular oxygen data between 100 and 200 km in terms of geophysical parameters (local time, latitude, season, solar radio flux, geomagnetic activity) has been reported by Offermann (1974). In addition, some experimenters have provided a comparison of their measurements of O_2 with a selection of other results (Ackerman *et al*, 1974; Carver *et al*, 1974; Carver *et al*, 1978a) and

almost every published profile has been referenced to one or other of the thermospheric models, usually Jacchia (1971) or CIRA 1972 which incorporated Jacchia (1971).

The prominent feature that emerges from the literature is the wide scatter of the data, and some examples of this have been provided by Figures 3.27, 3.28 and 3.31. While part of this variation undoubtedly reflects real geophysical changes, the contribution of instrumental biases must be acknowledged. Offermann's analysis concluded that O_2 seasonal variations at 150 km are very small, and slightly more pronounced at 120 km. An asymmetric diurnal variation is apparent at 150 km, but less so at 120 km. Geomagnetic effects are small, and there is no obvious regular response to different solar radio fluxes. It must be concluded that, while oxygen densities do indeed vary, the trends are as yet obscure and have defied analytic formulation on the basis of infrequent measurements, using techniques with unknown biases.

The O_2 profile from the FUV spectrometer experiment is compared, in Figure 4.15, with three other profiles, chosen because the appropriate experimental parameters more nearly approached those of the spectrometer measurement than other profiles reported in the literature. They also, incidently, are in best agreement. Table 4.4 provides the relevant information for the different measurements. Each of the O_2 profiles in Figure 4.16 is the result of an absorption measurement at wavelengths for which only O_2 contributed to the observed extinction. At 6.7 hours prior to launch, the geomagnetic activity varied by no more than a K_p increment of 1.6, and the range of the calculated exospheric temperature was only 145 K. All are mid-latitude measurements, but at different seasons. For all except profile B, the zenith angle was greater than 84°.

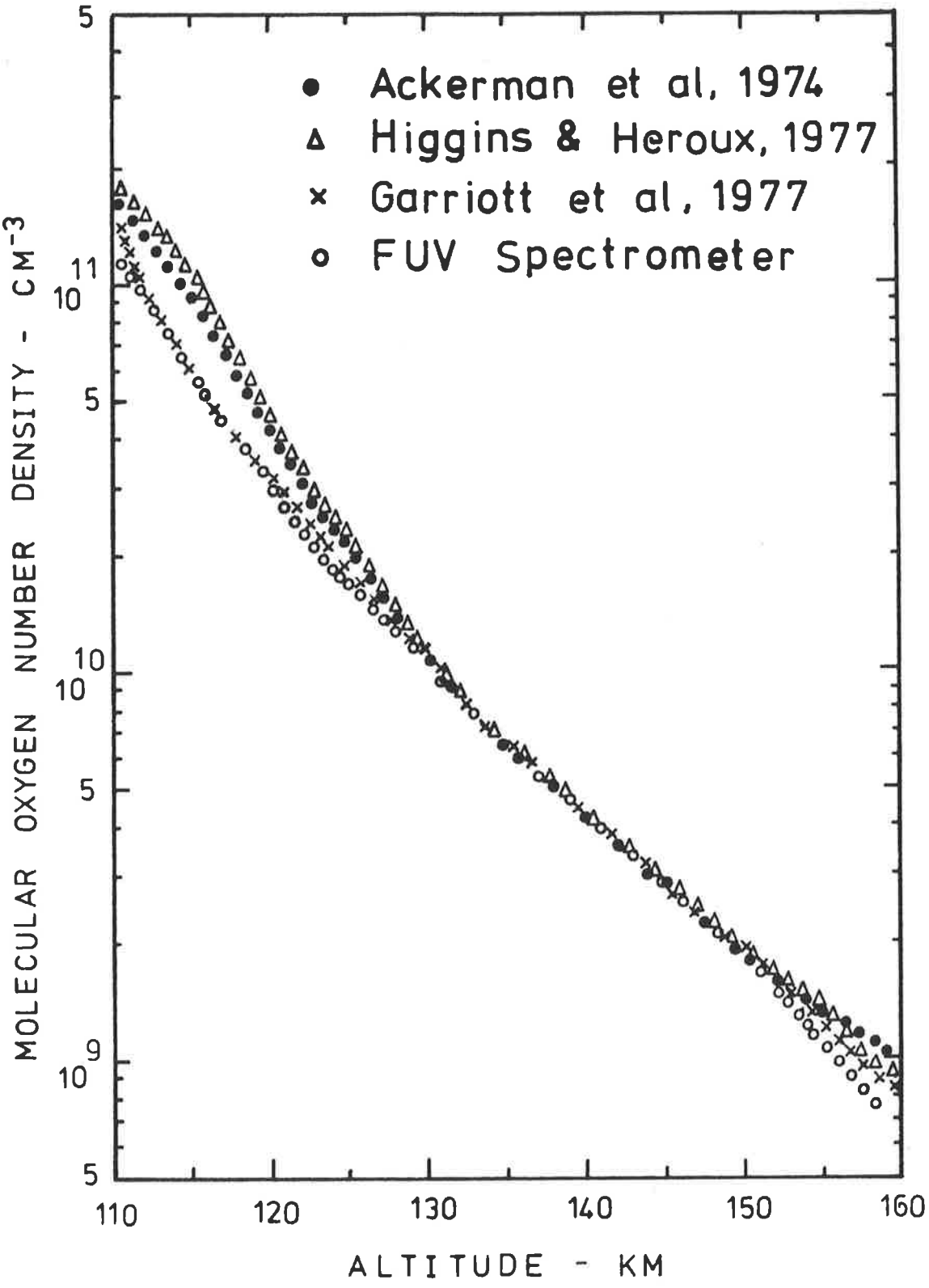

Figure 4.15 Comparison of measured O_2 density profiles.

TABLE 4.4 Comparison of geophysical parameters for oxygen profile measurements - Figure 4.15.

	A	B	C	D
Reference	Ackerman *et al* (1974)	Higgins & Heroux (1977)	Garriott *et al* (1977)	Aerobee
Identification	S84	Spring	-	FUV Spect.
Date	28.2.72	23.4.74	30.7.73	21.2.77
Location	Sardinia	White Sands	Satellite	Woomera
Latitude	39° 36'N	32° 24'N	36° S (?)	30° 56'S
Season	Winter	Spring	Winter	Summer
Universal Time		1802	0454	2106
Local Time	0654	1102	sunrise	0636
Zenith Angle	89.8°	24°	90°	84.5°
$F_{10.7}$	124.5 (Average)	74	86.1	77 (Average)
K_p (-6 hrs)	3^-	4^+	3 to 4	3^-
T_{exo}	913K	853K	800K	768K
Experiment Description	145 & 171 nm monochrom. absorptn.	145 nm broad band absorptn.	103.2 & 133.5 nm monochrom. absorptn.	165.7 - 174.4 nm monochrom. absorptn.

Between 130 and 150 km the excellent agreement of the four results confirms Offermann's conclusion that there is little seasonal variation at 150 km, but contradicts the supposition of a significant diurnal variation since although profiles A, C and D were measured at sunrise, B was at mid-morning. Below 130 km, especially between 100 and 110 km, wide variability and anomalous structure have been reported by a number of workers (Lockey *et al*, 1969; Timothy *et al*, 1972; Atreya *et al*, 1976; Garriott *et al*, 1977; Trinks *et al*, 1978), so the observed differences here are probably real. It may not be coincidental that below 130 km measurements made in the same hemispheres agree with each other. Mayr *et al* (1976) have observed such a hemispheric asymmetry. At 120 km the O_2 density at mid to high northern winter latitudes was reported to be a factor of two higher than at low southern summer latitudes. Since their measurements occurred when the average $F_{10.7}$ was 80 and the average K_p was 3, they should be relevant for the data base in Table 4.4. Comparison of the data of Ackermann *et al* (1974) (profile A, Figure 4.15) with the data from the FUV spectrometer (profile D , Figure 4.15) confirms their results.

Above 150 km the divergence of the data is probably an artifact of the absorption technique, the most reliable measurements being provided by absorption at 145 nm, with the largest zenith angle. This corresponds to profile A, Figure 4.15 (Ackerman *et al*, 1974). Depending on the relative contributions to the reported average result by respective absorption at 145 nm and 171 nm, inclusion of the temperature effect may reduce the densities and improve the agreement with the other profiles. At 171 nm the absorption cross-section increases by 30%, from 0.618 Mb to 0.808 Mb, as the temperature increases from 290 K to 570 K.

Offermann's investigation of the seasonal and diurnal variations of molecular oxygen at 120 km and 150 km are reproduced in Figure 4.16,

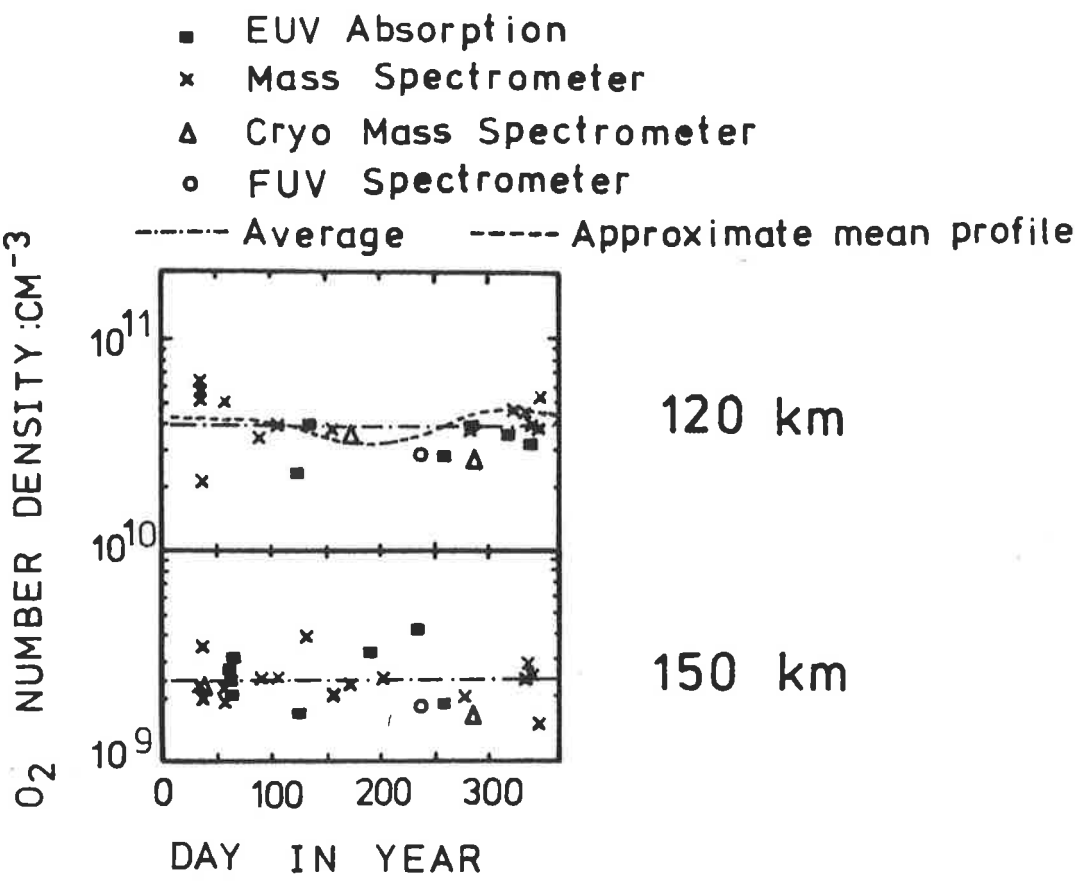

Figure 4.16a Seasonal variation of O_2 number density at 120 km and 150 km. (Offermann, 1974)

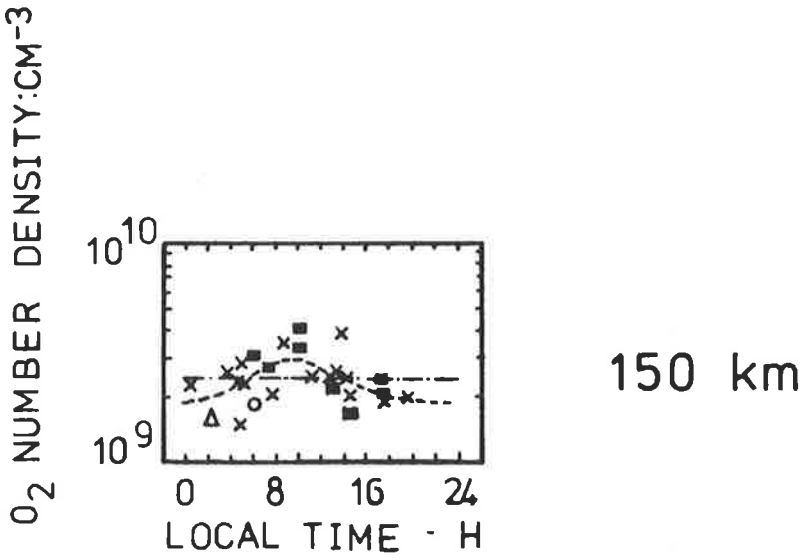

Figure 4.16b Diurnal variation of O_2 number density at 150 km. (Offermann, 1974)

and the present results have been included. Since then, new data at 150 km has increased the number of measurements from 28 to 42, of which 18 are from absorption spectroscopy techniques. A survey of the more recent experiments, not considered by Offermann (1974), is provided in Table 4.5.

The Aerobee spectrometer result at 150 km is well below the new average of $2.4 \pm 0.1 \times 10^9 \text{ cm}^{-3}$ and the densities at 120 km are also lower than the average. While the most plausible explanation is the diurnal effect, evident in Figure 4.16b, it is possible that the average value might be too high, reflective of data from mass spectrometers in which recombined atomic oxygen has contributed to the measurement. An indication that this might be so is provided by the following comparison. At 150 km, Offermann (1974) reported the concentration of molecular oxygen to be $2.56 \times 10^9 \text{ cm}^{-3}$ which is higher than the FUV spectrometer value of $1.84 \times 10^9 \text{ cm}^{-3}$. For atomic oxygen the average density of $1.22 \times 10^{10} \text{ cm}^{-3}$ is lower than the Aerobee result of $1.5 \times 10^{10} \text{ cm}^{-3}$. According to Offermann's values the average total oxygen concentration at 150 km is $1.73 \times 10^{10} \text{ cm}^{-3}$, which is slightly lower than the Aerobee value of $1.87 \times 10^{10} \text{ cm}^{-3}$ but certainly in better agreement than either of the individual data for O_2 or O.

The apparently irreconcilable disagreement between mass spectrometry and absorption spectroscopy investigations of thermospheric molecular oxygen was typified by the comparison of the two techniques reported by Ackerman *et al* (1974). As discussed in Section 2.3b, the mass spectrometer measured O_2 densities 75% higher than those provided by the absorption analysis. The latter are seen in Figure 4.15 to be in excellent agreement with the present spectrometer results.

Kayser (1980) has very recently reported that the molecular oxygen densities at both 150 km and 120 km are inversely dependent on the

TABLE 4.5 Recent measurements of molecular oxygen number density at 150 km.

Reference	Type	Lat	Local Time	$F_{10.7}$	K_p	$n(O_2)$ x 10^9 cm^{-3}
Ackerman *et al*, 1974						
28.2.72						
S84	UV	40N	0654	143	3^-	1.9
S84	MS	40N	0654	143	3^-	3.33
S90	MS	40N	1047	143	3^-	2.78
Norton & Roble, 1974 Aug-Sept. 1971	UV Sat.	mid	PM twilight	110	average quiet	3.0
Weeks, 1975 5.10.71 A07.913	UV	38N	sunset	106	2.2	2.78
Nier *et al*, 1976						
Feb-June, 1974	MS Sat	mid	sunset	70 to 90	moderate	3.1
Garriott *et al*, 1977						
30.7.73	UV Sat	36S(?)	0454	86.1	3	1.5
Higgins & Heroux, 1977						
23.4.74 Spring	UV	32N	1102	74	4.2	2.0
2.11.73 Fall	UV	32N	1132	83	1.5	2.0
Trinks *et al*, 1978						
29.6.74 Ascent	MS	38N	1514	83	4.1	2.7
Descent	MS	38N	1514	83	4.1	2.35
Carver *et al*, 1978a						
11.12.72 (SL1005)	UV	30S	0930	105	1^-	1.9
23.4.74 (SL1207)	UV	30S	1033	73	4^+	3.4
Aerobee						
21.2.77	UV	30S	0636	82	3^-	1.84

$F_{10.7}$ index. At 120 km, as $F_{10.7}$ varies from 70 to 150 x 10^{22} Wm^{-2} Hz^{-1} the O_2 concentration decreases by about 30%. These conclusions derived from satellite measurements for the ratio O_2/N_2 and also from a re-analysis of virtually the same data base used by Offermann (1974), with the addition of some of the new data listed in Table 4.5.

In his investigation of seasonal and diurnal changes, Offermann (1974) considered densities measured over a wide range of $F_{10.7}$ values. Likewise, the results used by Kayser (1980) to confirm a functional relationship between O_2 concentrations and $F_{10.7}$ indices, were made at many different times of day. Although the data base is small, it was attempted to separate the diurnal and solar activity effects to see if changes induced by solar activity are more pronounced at different times of day. For this purpose the 42 available O_2 density measurements were separated into two groups according to whether the $F_{10.7}$ index was greater than or less than 120. Each group was analyzed for diurnal variations by following Offermann's procedure of averaging over 4 hours. All the data is plotted in Figure 4.17a as a function of $F_{10.7}$ and labelled by a diurnal tag. The predictions of Kayser (1980) are included, and the data points omitted in his analysis, because of greater than moderate geomagnetic activity or a high latitude parameter, are identified. The results of the diurnal averaging for both active and quiet solar conditions are listed in Table 4.6 and plotted in Figure 4.17b. While the diurnal variation identified by Offermann (Figure 4.16b) is evident in both sets of data, the conclusions of Kayser (1980) appear to be contradicted at 150 km for the sunlit atmosphere. It must be noted that the average density measurement when the $F_{10.7}$ value is less than 120 is higher than when $F_{10.7}$ is greater than 120, and from this it could be deduced that molecular oxygen densities are inversely dependent on solar activity. However, Figure 4.17b suggests that at local times between 0600 and 1400

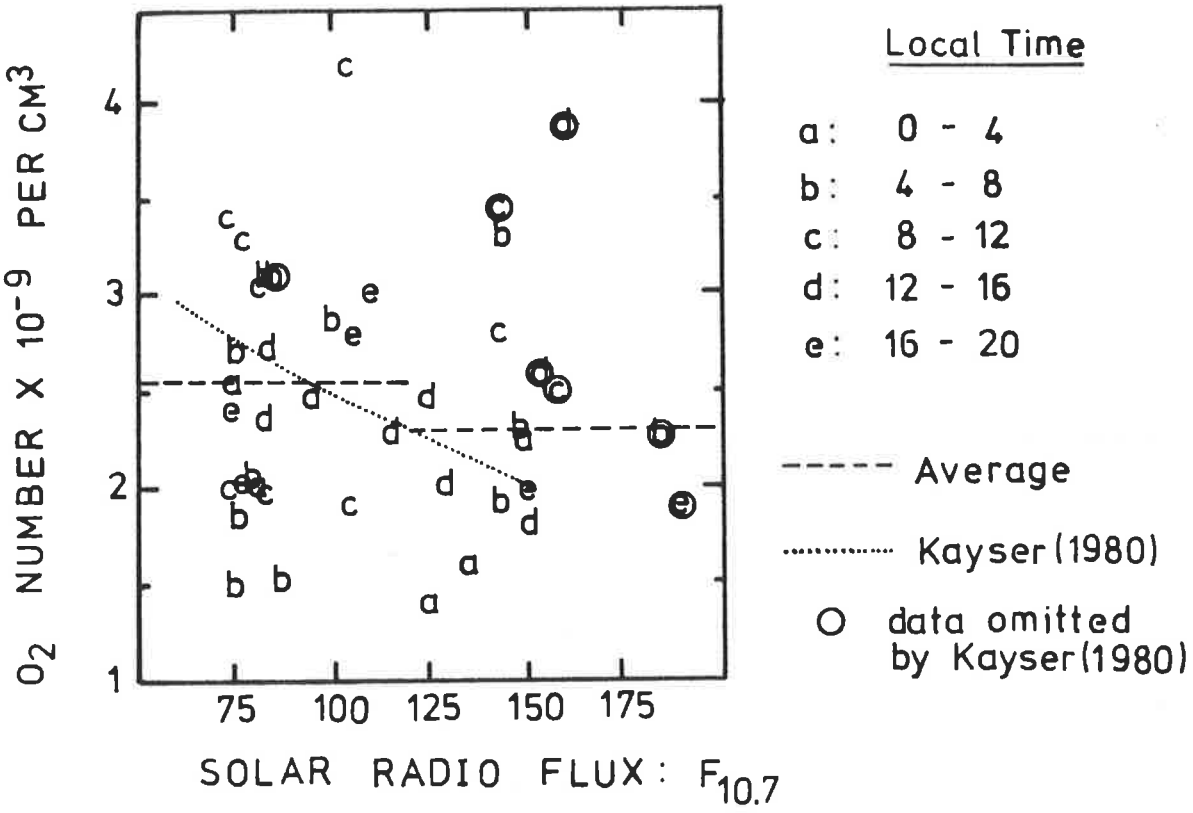

Figure 4.17a O_2 densities at 150 km.

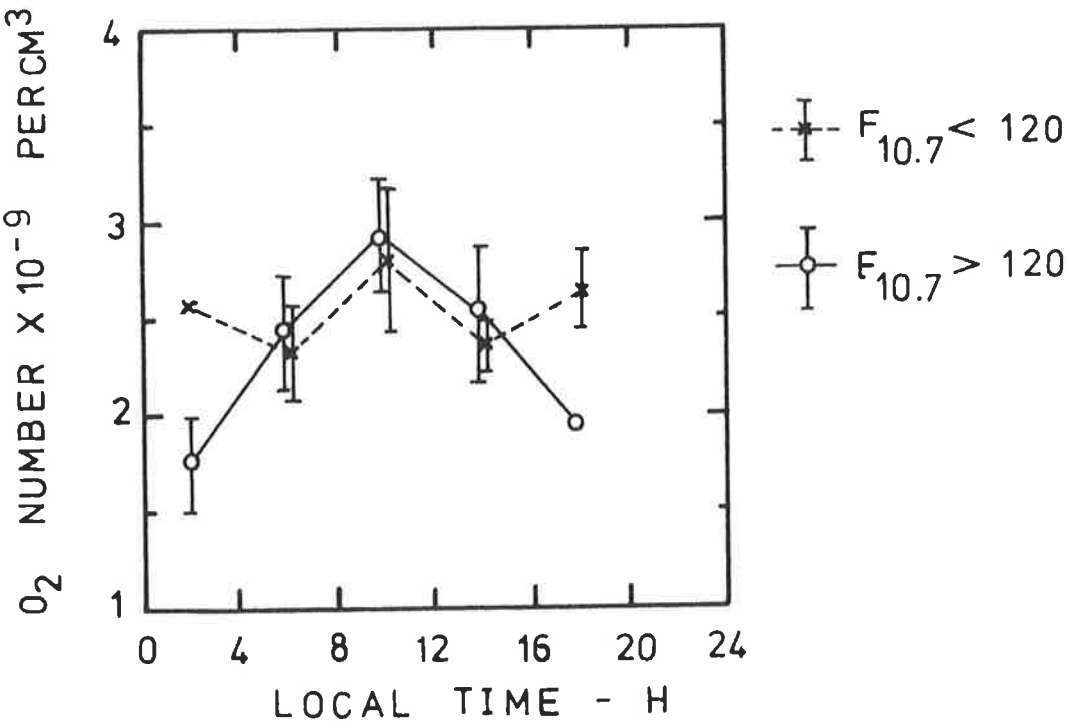

Figure 4.17b Diurnal variation of O_2 at 150 km for two conditions of the solar radio flux.

TABLE 4.6 Investigation of the diurnal variation of molecular oxygen number densities at 150 km under two conditions of solar activity.

Local Time - hours	$F_{10.7} < 120$		$F_{10.7} > 120$	
	No.	Average Density x 10^9 cm^{-3}	No.	Average Density x 10^9 cm^{-3}
0 - 4	1	2.56	3	1.75 ± 0.26
4 - 8	8	2.33 ± 0.24	4	2.43 ± 0.30
8 - 12	6	2.80 ± 0.39	3	2.92 ± 0.29
12 - 16	5	2.38 ± 0.10	5	2.52 ± 0.38
16 - 20	5	2.65 ± 0.19	2	1.94 ± 0.04
Total Number	25		17	
Average of Total		2.53 ± 0.13		2.37 ± 0.17

hours, the dependence is small and in the reverse direction.

It is difficult to confirm or refute the FUV spectrometer measurement on the basis of trends which have not yet been properly qualified, but the agreement with simultaneous measurements by ion chambers (Appendix A) and with other experiments during similar geophysical conditions (Figure 4.15) afford general confirmation that it was reliable, and hence that it provides one more sample of thermospheric molecular oxygen densities, adding to a very sparse data base.

CHAPTER FIVE

ABSORPTION OF MIDDLE ULTRAVIOLET RADIATION BY OZONE

5.1 INTRODUCTION

Middle ultraviolet radiation is harmful to life, and the importance of atmospheric ozone as a strong absorber of this radiation, preventing it from reaching the earth's surface, has long been recognized. Whether or not pollutants, originating in the troposphere and diffusing up to the stratosphere, are effecting irreversible ozone depletion is at present uncertain, and aspects of this potential environmental threat have been discussed frequently and enthusiastically in the literature, for example, by Crutzen *et al* (1978), Ellsaesser (1978), Gribbin (1979), Thrush (1979), Panofsky (1980), Pyle and Derwent (1980) and Allaby and Lovelock (1980).

Since the first theoretical postulation of atmospheric ozone by Chapman (1930), the photochemistry of the stratosphere and mesosphere has been refined and advanced by many workers to include numerous complex reactions between ozone and free radicals, some of which have been described in Section 1.4. In summary, ozone is formed by atomic oxygen recombining with molecular oxygen in the presence of a third body. This occurs in the stratosphere and mesosphere where atomic oxygen is produced by photo-dissociation of molecular oxygen in the Schumann-Runge bands and Herzberg continuum, respectively. Destruction of ozone arises partly from its photodissociation by radiation at wavelengths less than 1.08 μm, especially MUV radiation which is the origin of stratospheric heating, and partly via chemical activity involving oxygen, hydrogen, nitrogen, chlorine and possibly bromine radicals.

Over the past decade, investigations of the distributions of ozone and other minor upper atmosphere constituents have expanded beyond the initial photochemical schemes which incorporated only oxygen and hydrogen families (Hunt, 1966; Crutzen, 1969; Leovy, 1969; Nicolet, 1971; Hesstvedt, 1971; Thomas and Bowman, 1972) to include nitrogen species (Crutzen, 1971; Whitten and Turco, 1974; Shimazaki and Ogawa, 1974) and, more recently, chlorine compounds (Wofsy and McElroy, 1974; Nicolet, 1975; Johnson and Podolske, 1978; Wofsy, 1978). So too has the importance of the transport term in the continuity equation for some species become apparent, and atmospheric models have attempted to account for this in one dimension (Shimazaki and Laird, 1970; Hunt, 1971; Moreels *et al*, 1977), two dimensions (Visconti *et al*, 1980; Harwood, 1980) and three dimensions (London and Park, 1974; Cunnold *et al*, 1980; Mahlman *et al*, 1980) with varying degrees of complexity, generally inversely proportional to the extent of the photochemical scheme. Additionally, for the minor species to be adequately modelled requires inclusion of Rayleigh scattering and ground albedo effects on the photodissociation rates, particularly when determining the distributions of NO and OH (Visconti *et al*, 1980) and, since the OH produced by the reaction of H with O_3 is preferentially excited, it is necessary for the photochemistry to accommodate these different excited vibrational levels (Moreels *et al*, 1977).

With the identification of anthropogenic sources of the naturally occurring species which participate in catalytic cycles that destroy ozone in an unpolluted atmosphere have come predictions by the models of possible future permanent ozone depletion. Calculations have indicated that ozone will be reduced by emissions of NO_x from high flying aircraft (Hesstvedt, 1974), the use of fertilizers which effect an increase in N_2O

via denitrification (Johnston, 1977a) and the presence of Cl and ClO, arising from the photodissociation, by radiation of wavelengths from 195 to 225 nm, of CF_2Cl_2 and $CFCl_3$, transported up from the troposphere (Molina and Rowland, 1974; Stolarski and Cicerone, 1974; Crutzen, 1974).

The magnitude of the ozone reductions predicted by these initial calculations have since been revised, following reinvestigation of the photochemical reaction schemes. In the case of the NO_x cycle, the impetus for this was the absence of observational evidence for long term ozone depletion following the injection of NO_x into the atmosphere during the nuclear tests of the 1950's and 1960's (Johston, 1977b; Chang *et al*, 1979). In particular, an increase by a factor of 40 in the rate of the reaction

$$HO_2 + NO \rightarrow NO_2 + OH \qquad 5.1$$

represented a much stronger interference between the NO_x and HO_x catalytic ozone destruction cycles that considerably reduced their individual effects. As a consequence, NO_x additions to the stratosphere are now thought to lead to decreasing ozone concentrations above 25 km but increasing concentrations below, so that total ozone may well increase (Crutzen, 1979).

However, the rate of the reaction 5.1 appears to have magnified the importance of ClX in the photochemical scheme, since additional OH implies that the reaction

$$OH + HCL \rightarrow H_2O + Cl$$

will be more frequent, causing a larger fraction of ClX to be present, rather than HCl which does not attack odd oxygen (Crutzen, 1979; Borucki *et al*, 1980). An increase in the rate of the reaction

$$HO_2 + O_3 \rightarrow 2O_2 + OH \qquad 5.2$$

has a similar effect. But, just as the reaction 5.1 inhibits the

catalytic agility of NO_x and HO_x to destroy ozone, so too is the effect of odd nitrogen and ozone-active chlorine compounds reduced by the formation of the inert reservoir chlorine nitrate $ClONO_2$ (Borucki *et al*, 1980). As Crutzen (1979) has emphasized, the realization that chemical interactions between ClX, HX and NX reactant groups are critical aspects of middle atmosphere photochemistry has increased the difficulty in predicting the effect of these substances on ozone and on one another. For example, because of reactions 5.1 and 5.2, the role of H_2O may be found to be more important so that water vapour injection from high flying aircraft may yet be considered another pollutant.

The following scenario for possible ozone depletion by chlorofluoromethanes is from the recent two-dimensional model of Borucki *et al* (1980) : by 1990, global and seasonal average ozone depletion is calculated to be 3.5%, with the reduction greater by 50% in polar regions than in the equatorial region. This is because the smaller optical depth at the equator enables increased photodissociation of molecular oxygen which nearly compensates for the loss of odd oxygen due to reactions of ClO and Cl. However, this self healing is not so effective at higher latitudes since here the optical depth is much greater. A similar latitudinal profile of the ozone depletion was reported by Pyle (1980) who also noted that, on a vertical scale, maximum depletion would occur at about 40 km.

The extensive network of uncertainties inherent in large scale atmospheric models has prompted inquiries into their general credibility (Ellsaesser, 1978; Ehhalt *et al*, 1979; Prather *et al*, 1979) and sensitivity to parameters such as reaction rates and products, boundary conditions, solar intensities and photolysis cross-sections (Butler, 1978). Ultimately, their validity will be determined by the availability of

reliable data on the distributions and natural variability of the atmospheric species which are being modelled, and this is true for active species such as NO, HO, ClO and O, as well as for O_3.

The dependence of ozone densities on solar input to the atmosphere initiates seasonal, latitudinal and diurnal variations which have been observed experimentally (Watanabe and Tohmatsu, 1976; London *et al*, 1977; De Luisi *et al*, 1979; Hilsenrath *et al*, 1979b) and broadly predicted by atmospheric models (Shimazaki and Laird, 1970, 1972; Thomas and Bowman, 1972; Shimazaki and Ogawa, 1974; Park and London, 1974; Wuebbles and Chang, 1975; Herman, 1979). Characteristics of this variability have been described by Dütsch (1974). In particular, total ozone exhibits a subpolar spring maximum with a minimum near the equator, all through the year. For the vertical distribution, the seasonal variations in a first approximation are produced by changes on the lower stratosphere, reflective of the total ozone. Going to higher latitudes, the height of the maximum density decreases and the concentration of this maximum increases. Diurnally, there is a nighttime maximum in the mesosphere.

Additionally, natural ozone variations may arise from changes in solar activity (Frederick, 1977; Penner and Chang, 1978; Blackshear and Tolson, 1978; London and Reber, 1979; Fishman *et al*, 1979) and general fluctuations in the stratospheric components which react with ozone and each other (Finger *et al*, 1976). As yet, the available data base is unable to provide conclusive correlations but this natural variability may be a useful precursor for meteorology (Dickinson, 1975b; Herman and Goldberg, 1978; Pollack *et al*, 1979).

Identification of possible anthropic effects on atmospheric ozone requires regular monitoring of the ozone densities with precision greater than the expected changes, coupled with a quantitatively well

defined appreciation of ozone's natural variability. With currently available measurement techniques this may be difficult, if not impossible, in the near future. For example, chlorofluoromethanes have been predicted to reduce the total ozone by 0.35% per year (Borucki *et al*, 1980) and, although Hill *et al* (1977) have claimed that it is possible to detect a change of 0.26% persisting over six years, the masking effect of nitrogen pollutants may mean that permanent trends are not identified for much longer than this. With regard to changes in the vertical ozone profile, the monitoring network is significantly less developed. Satellite BUV measurements near 50 km, acquired over a two year period, were recently reported to be consistently lower, by 4% to 16%, than data from 'ground truth' rockets (McPeters, 1980). The maximum ozone reduction is expected to occur near 40 km, at high latitudes, during winter-spring, implying a need to focus data acquisition here. However, BUV data, limited by large solar zenith angles, does not make such measurements and the results of scanty rocket investigations are highly variable (Hilsenrath, 1980) and not easily interpreted in terms of the dynamics, radiation and photochemistry of the atmosphere which, at high latitudes, appear to be more complicated.

The experiments described in this chapter formed a very small part of a campaign of intensive observation of mid latitude atmospheric ozone, using almost all of the currently available measurement techniques (Sundararaman *et al*, 1980). Rocket absorption spectroscopy experiments, primarily with broad band MUV photometers carried on spinning rockets, have provided information about ozone's vertical distribution for over 15 years. However, the resultant data base, like that pertaining to other atmospheric species (Chapters 3 and 4), is sparse and, similarly, potential information about real variability is concealed by instrument imprecision.

This is especially true of the vertical ozone distribution during the nighttime, for which recent measurements appear to conflict.

5.2 SOLAR MUV FLUX MEASUREMENTS

Early investigations of MUV solar flux were conducted at NRL, in particular by Purcell *et al* (1963) with an echelle rocket spectrograph of Littrow type mounting. From photoelectric spectra with 0.003 nm resolution, they estimated the existence of a total of 4000 Fraunhofer lines between 220 and 300 nm, and established wavelength identification accurate to approximately 0.001 nm.

No further rocket measurements of the MUV solar flux were reported until the experimental results of Broadfoot (1972) who used a ¼-metre Ebert-Fastie spectrometer with a pre-disperser to scan the wavelength region 170 to 350 nm. Since wavelength errors were ± 0.3 nm, the more accurate NRL spectrum was used to establish a wavelength scale. Intensities were presented with 10% accuracy in 0.1 nm intervals and also averaged over 1 nm. Excellent relative agreement between the two spectra was reported, with Broadfoot's intensities being less than those of NRL in the region 250 to 260 nm.

Other estimates of the solar MUV flux include balloon measurements by Simon (1974) which were 40% lower than previous balloon measurements by Ackerman (1971) and also lower than Broadfoot's results, except for 226 to 230 nm where the agreement was within 15%. Satellite measurements have been made of solar irradiances at ten discrete wavelengths between 250 and 350 nm by Heath (1973). Thekaekara *et al* (1969) obtained measurements from an aircraft and presented tables of irradiances integrated over 5 nm, based on an average of data from four instruments.

In a review of irradiation solar flux measurements, Simon (1978) has recommended the rocket measurements of Broadfoot as the most reliable contribution covering continuously the most important wavelength region for the photodissociation of ozone.

5.3 OPTICAL OZONE DETECTORS

Since ozone, in the Hartley band, is the principal absorber of MUV radiation, knowledge of the ozone absorption cross-section in this region together with the measured intensity change with altitude of a source of MUV radiation enables direct determination of the ozone number densities. For monitoring MUV radiation from both the sun and the moon, ozone detectors consisting of broad band MUV photometers were flown on a number of spin-stabilized rockets. Broad band absorption spectroscopy techniques have been described in Section 2.1e and examples of similar experiments were included in Section 2.3d.

a. Daytime Ozone Experiment

The daytime ozone experiment shown in Figure 5.1 consisted of two photometer channels with peak responses at the MUV wavelengths 257.5 and 282.5 nm, and a third visible photometer channel at 375 nm to monitor the background. Design details indicating the arrangement of the photometers in the detector block are shown in Figure 5.2a. The cross-section of each photometer channel, Figure 5.2b, consisted of an appropriate filter for transmitting the required solar flux, an ultraviolet enhanced PIN diode (UDT PIN 10/UV) for detecting this radiation and a logarithmic amplifier (Analog Devices 755P) which was capable of five decades of pre-telemetry signal amplification and provided output signals corresponding to currents in the range 10^{-10} to 10^{-5} amp.

To provide sufficient definition of the flux received by the two MUV photometers, the bandwidth of each of these channels was narrow (approximately 10 nm), as defined by a multilayer dielectric interference

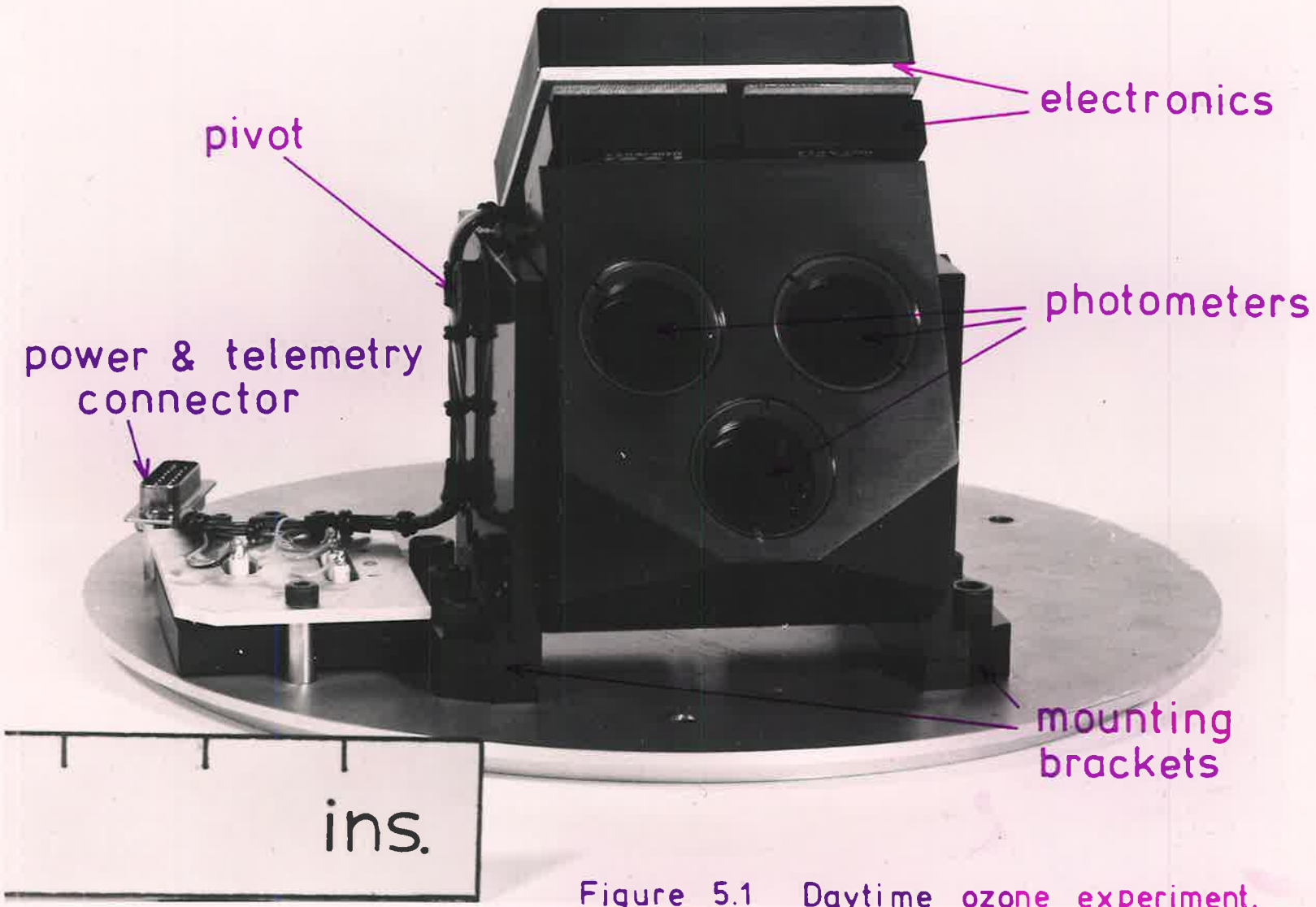

Figure 5.1 Daytime ozone experiment.

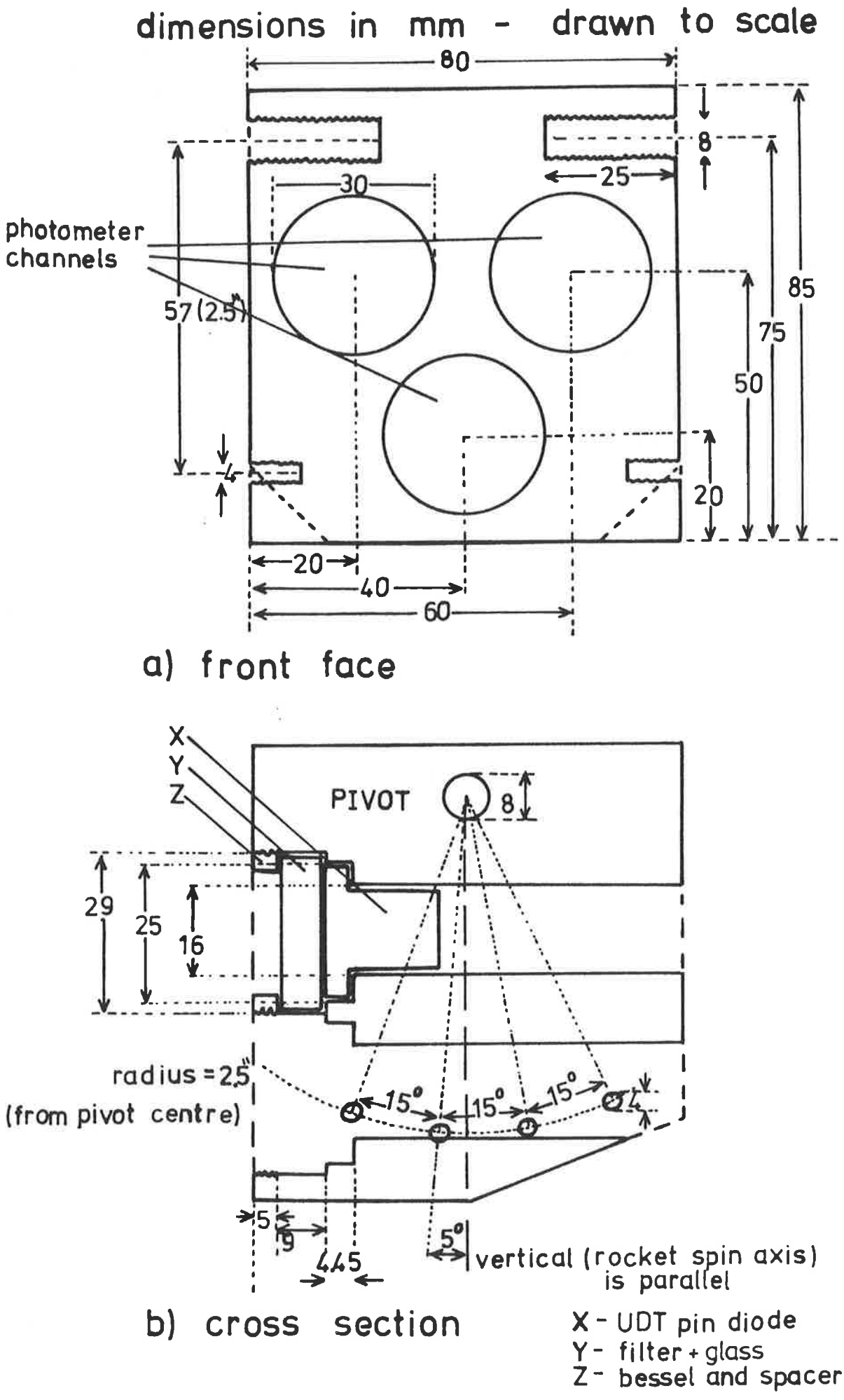

Figure 5.2 Daytime ozone detector schematics.

filter (Pomfret Research Optics Inc.). Use of these filters was complicated by the presence of leakage bands, the residues of the transmittance side bands which have only been partly suppressed in manufacture (Basher, 1977). Such bands were observed on either side of the nominal peak, at 230 and 400 nm approximately, and were suppressed by the addition of Corning 7-54 glass. The remaining visible and infrared leakage was measured to be less than 0.1% of the peak transmittance. However, because the pin diode spectral sensitivity was some 6 times higher at 900 nm than at 250 nm, and since the solar irradiance increases rapidly with wavelength, it was suspected that the integrated signal upward of 300 nm would not be exactly zero, resulting in a measurable background. This was confirmed by observing the detector signal due to direct sunlight. Solar radiation of wavelengths less than 300 nm is filtered out by the atmosphere and the radiation upward of 300 nm which is transmitted to the ground caused a measurable signal of the order of 10^{-8} amp which effectively reduced the dynamic range of the logarithmic amplifiers from five to three decades. The photometer channel at 375 nm, comprised of Corning 7-54 and Corning 7-39 glass, was included in the detector to monitor any variation with altitude of the solar flux beyond the Hartley band wavelengths. Figure 5.3 illustrates the relative transmittances of the filters and glass, as measured by a Perkin-Elmer 137UV spectrophotometer in the laboratory.

To accommodate the variety of zenith angles encountered by launches at different times of the day, provision was made for varying the 'look' angle of the detector block from 45° to 90°, in 5° increments, relative to the rocket spin axis. Figure 5.4 shows how the experiment was mounted in the rocket. Construction material was aluminium and the weight was approximately 2 kg.

Power requirements for the experiment were + 28V at 250 mA,

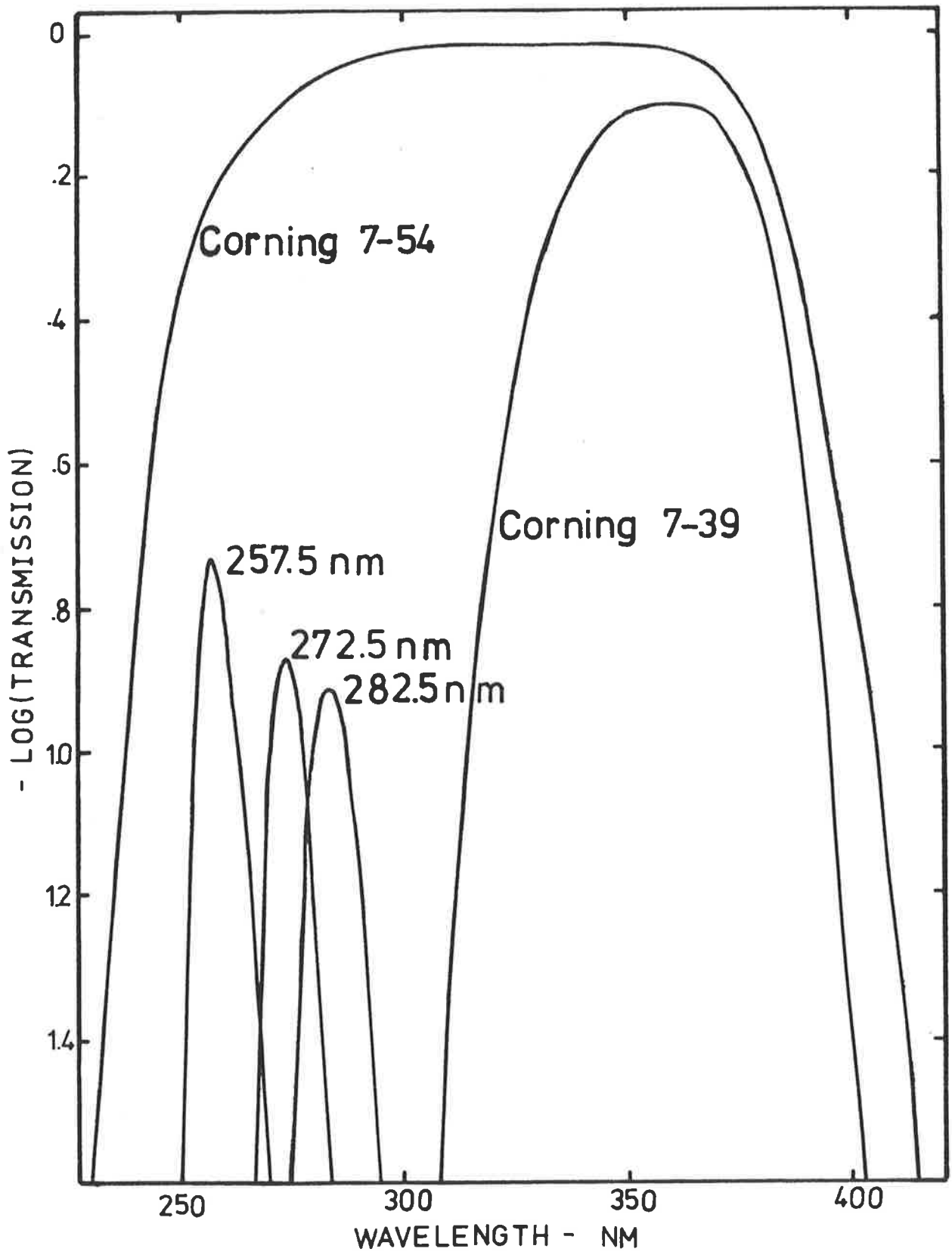

Figure 5.3 Transmission of filters for optical ozone detectors.

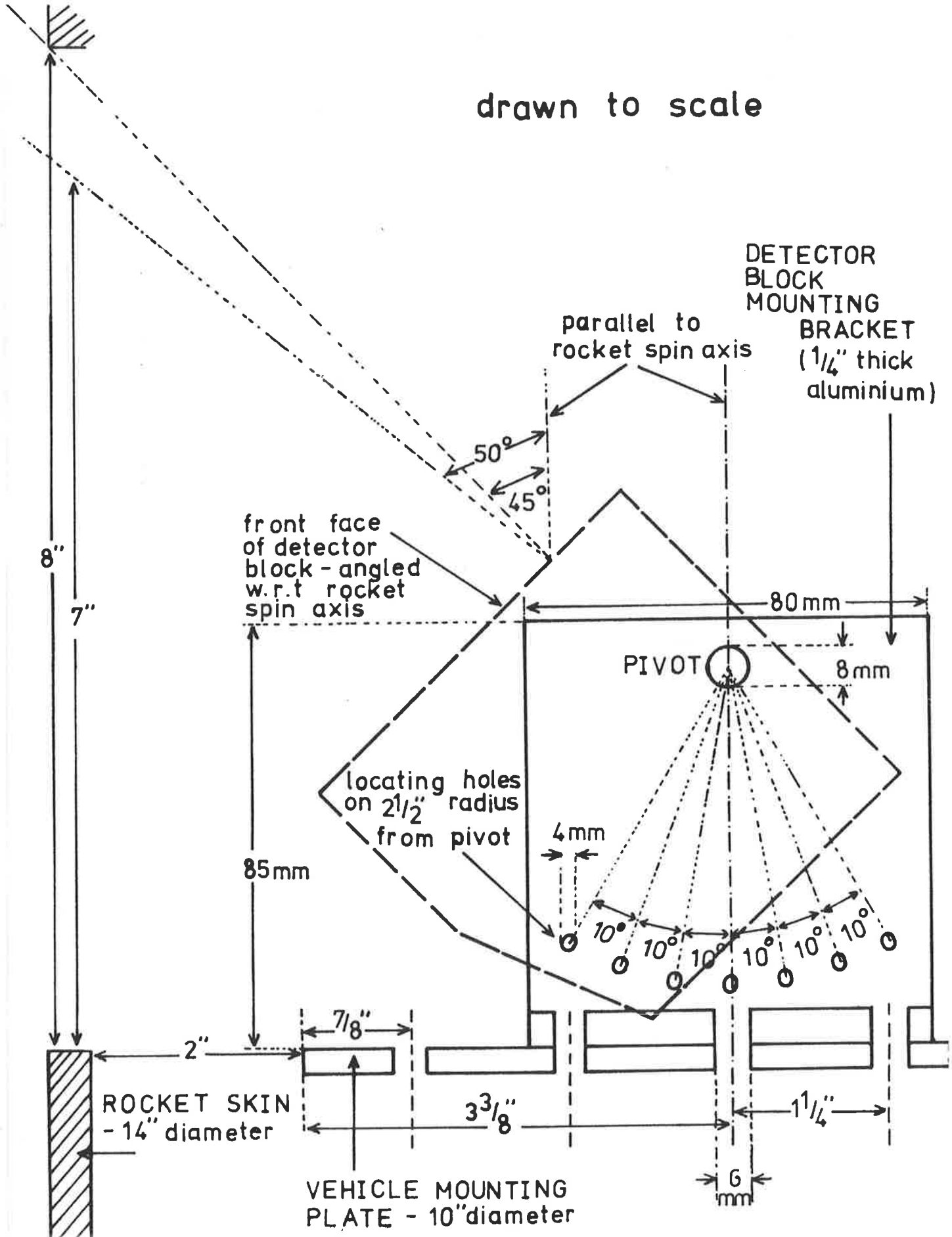

Figure 5.4 Mounting block configuration for daytime ozone detector.

switched ON with vehicle power. With reference to the electrical diagram, Figure 5.5, a DC-DC convertor (A/D 945) was used to isolate the experimental rails from the telemetry system and to eliminate possible ground loops. Detector block temperature was monitored with a National LX 5600 temperature transducer, operated with an external Zener diode, since extreme temperature changes may effect the filter and the detector characteristics.

Because the photometer response varied with the angle of the incident radiation it was necessary to know the angle between the sun and the rocket spin axis. This information was provided, in digital form, by a Solar Aspect Sensor (Bayshore System Model SS-11) mounted on the rocket spin axis.

b. Nighttime Ozone Experiment

For nighttime ozone measurements the moon was used as a source of MUV radiation. The lunar flux is some 10^4 times less than the solar flux (Carver and Horton, 1967) so it was necessary to replace the pin diodes used for the daytime experiment with more sensitive ultraviolet detectors. Ruggedized EMI QB9734 photomultipliers were located behind each filter and dynode amplification ensured that the signal reaching the log amp was in the same magnitude range as that provided by the pin diodes which are single stage devices. The front face of the nighttime detector block and a cross sectional view of a photometer channel are indicated in Figure 5.6. The photomultiplier and its dynode resistance chain, which operated at high voltage, were vacuum potted in Dow Corning Silicon Encapsulate RTV 3120 then activated under vacuum to check that there was no corona discharge.

power requirements: +28 Volts
250 mA

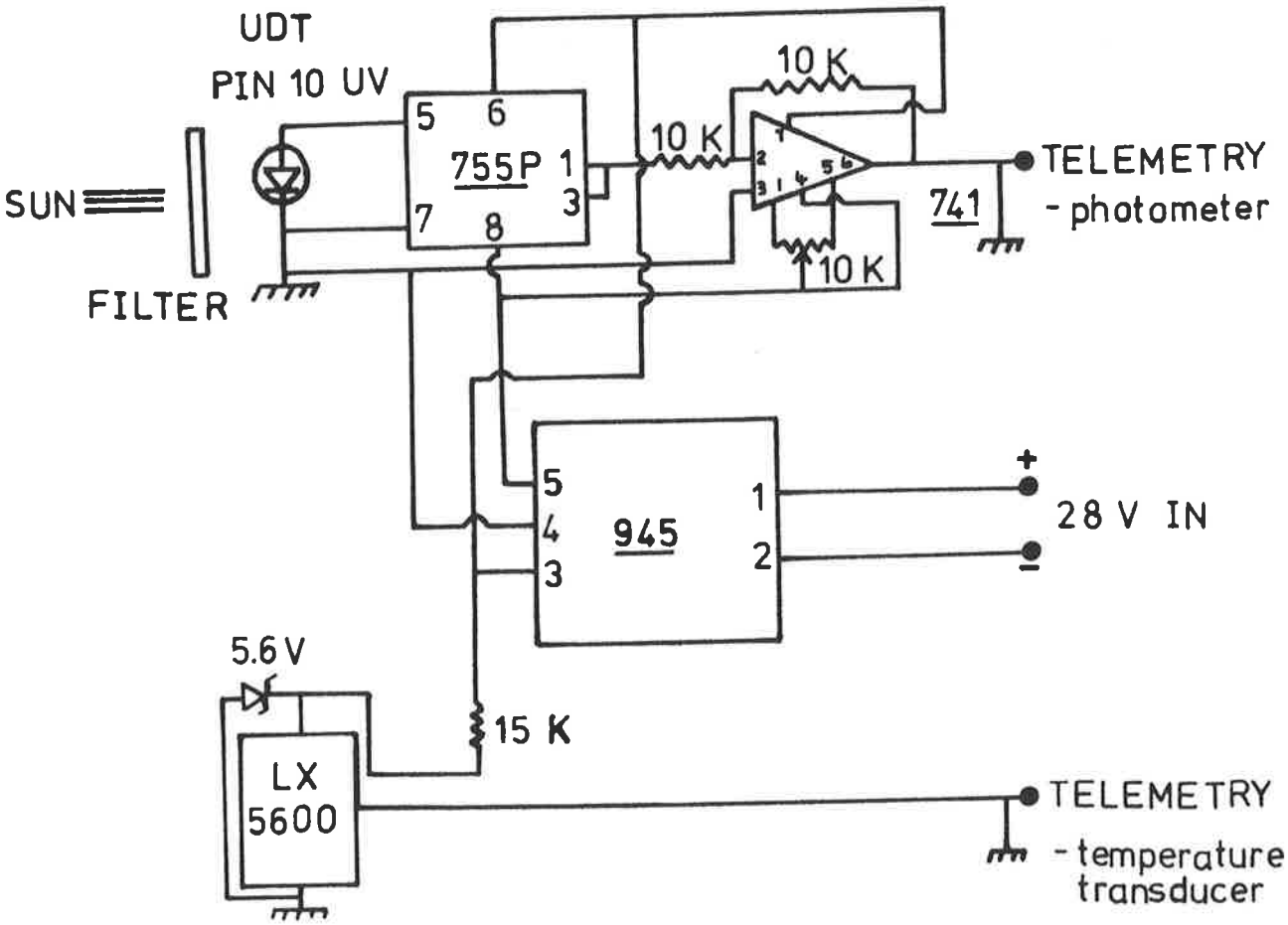

Figure 5.5 Electrical diagram for daytime ozone detector.

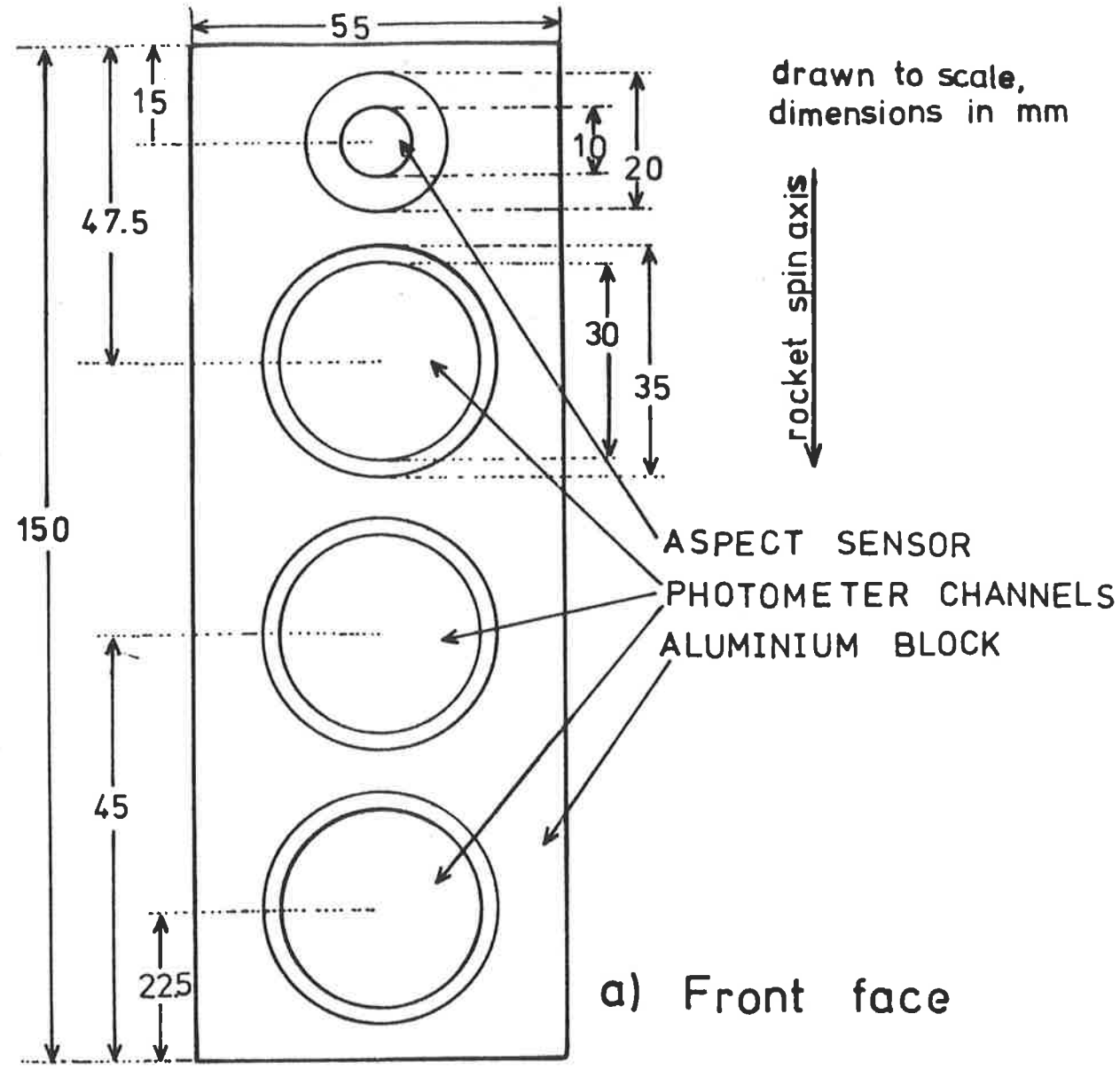

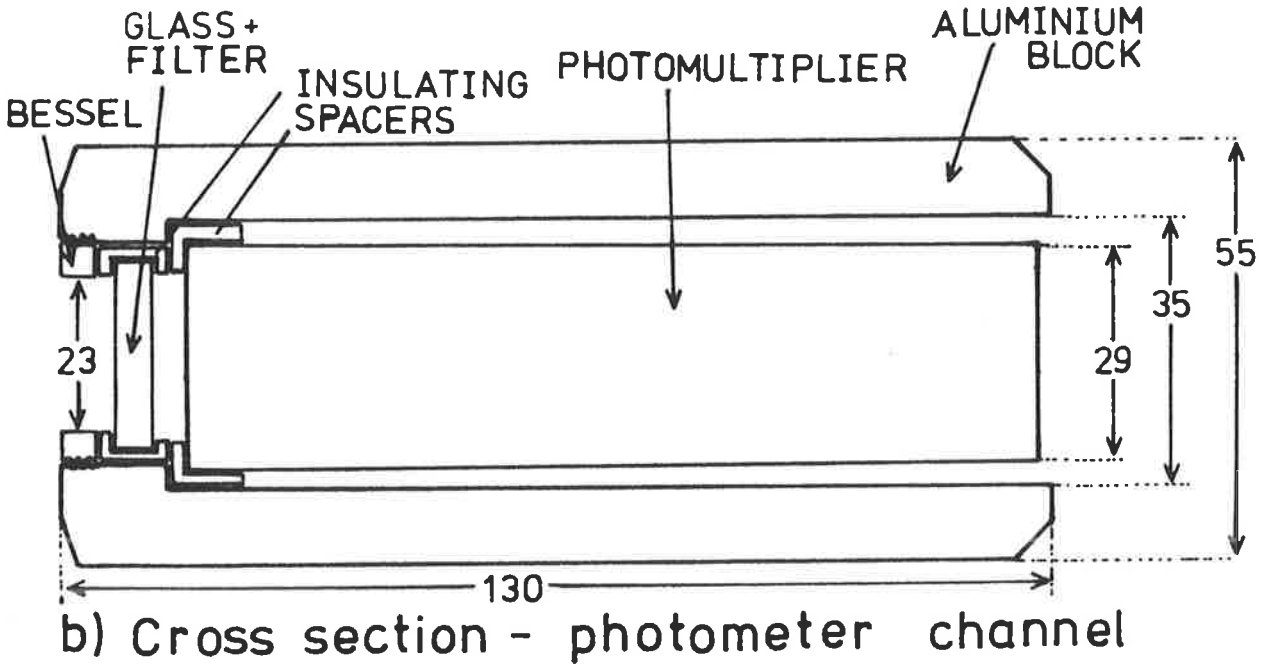

Figure 5.6 Nighttime ozone detector schematics.

Since the photomultiplier sensitivity peaked at 205 nm and was negligible in the infrared, it was unnecessary to monitor in flight the background signal. So the visible channel of the daytime experiment was replaced, for the night flight, with an additional MUV sensitive channel, centred at 272.5 nm. The fully assembled nighttime experiment, consisting of three complete detector blocks, each with three MUV photometers, is seen in Figure 5.7. Located on each detector block, as indicated in Figure 5.7, was a quadrant aspect sensor comprised of a PIN diode (UDT PINSPOT 4D) behind a square mask. From the ratios of the various quadrant signals, the angle between the moon and the rocket spin axis could be determined.

Figure 5.8 is the electrical diagram for the nighttime experiment. To prevent noisy photomultiplier dark currents, due to vehicle induced vibration of the dynodes, the high voltage was turned ON after motor burnout and after the doors had been ejected. This switching was achieved with a twin coil magnetic latching relay, located in the high voltage line, activated by a + 28V pulse of a few millisecond duration. The high voltage was monitored throughout flight and thermistors were located on each detector block for monitoring in-flight temperatures.

5.4 CALIBRATION

Broad band absorption spectroscopy requires knowledge of the relative spectral response of the detector (Section 2.1e). Additional absolute calibration, though not essential, is useful for predicting the maximum detector signal during flight. Conversely, from experimental data when the detector is above the absorbing layer, an estimate of the absolute integrated solar flux within the wavelength interval defined by

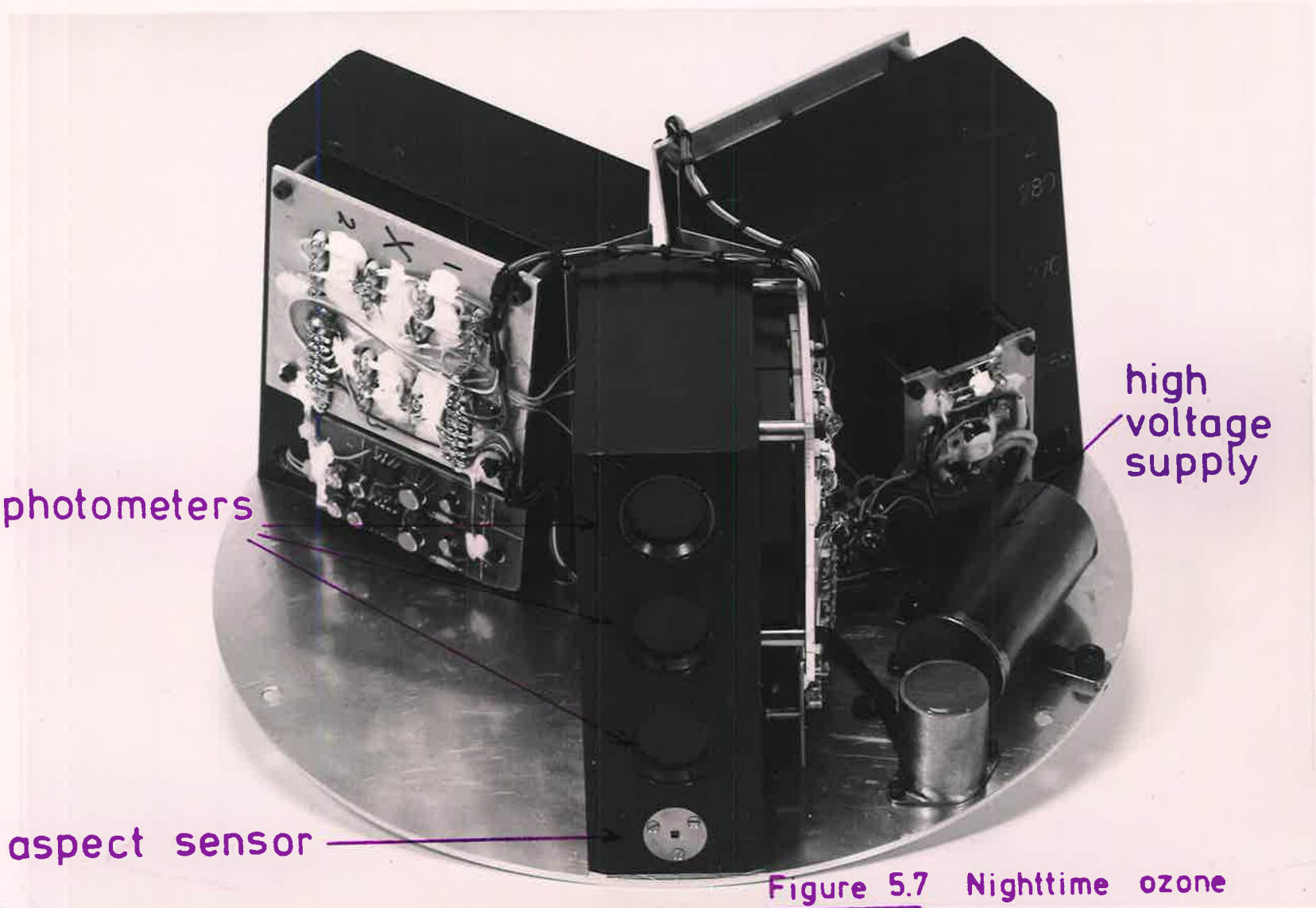

Figure 5.7 Nighttime ozone experiment.

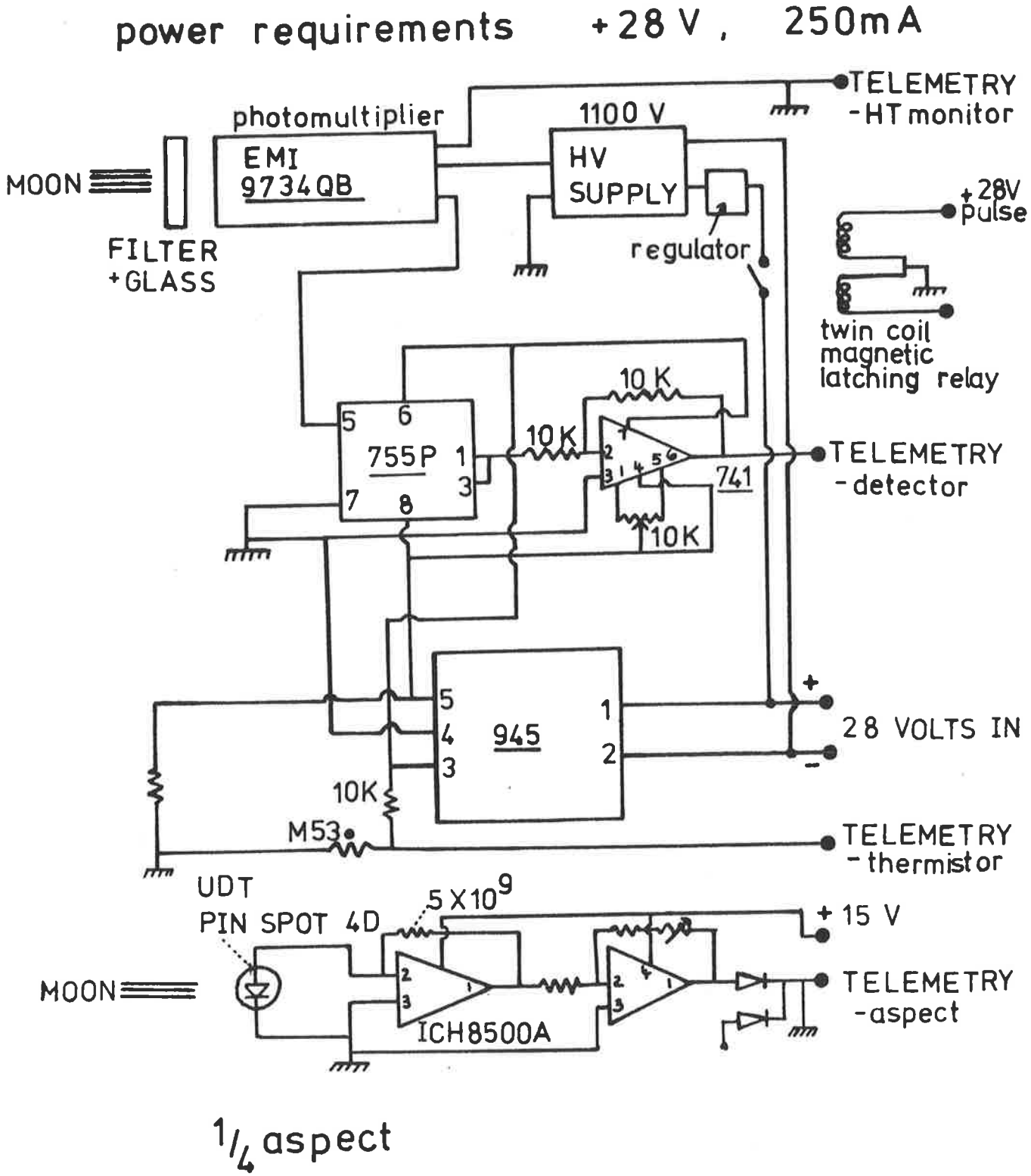

Figure 5.8 Electrical diagram for nighttime ozone detector.

the detector's response is possible.

a. Detector Spectral Response

The spectral responses of the MUV photometers for the nine detectors were determined using a 1/3rd metre Hilger Watt monochromator of 0.3 nm resolution to disperse light from an incandescent bulb. The relative spectral distribution of the lamp, which radiated approximately as a black body at 2400°K, was measured with an EMI 543P-09-00 photodiode, absolutely calibrated at the National Bureau of Standards, Washington D.C. A correction for the lamp spectrum was applied to the laboratory signal from the photometer, to obtain the best estimate of the relative spectral response.

Then, by placing the detectors on a rotatable table, additional spectral response curves were generated for different angles of incident radiation. This calibration was necessary because when detectors are carried on non-pointed rocket vehicles the angle between the radiation source and the normal of the detector surface may never be zero, or even constant. Radiation incident non-normally on interference filters causes the transmitted wavelength interval to shift to shorter wavelengths, accompanied by a decrease in transmission relative to that for normally incident radiation.

Typical response curves for each of the different wavelength photometers are illustrated in Figure 5.9. While the shift in peak response with the angle of incident radiation could be ascertained to within the resolution of the monochromator, the decrease in sensitivity was less accurately determined. Ideally, angular response experiments require a parallel monochromatic beam of sufficient width to illuminate the entire photometer surface. However, radiation emerging from the monochromator exit slit depends on the angle subtended at the slit by the grating, and was

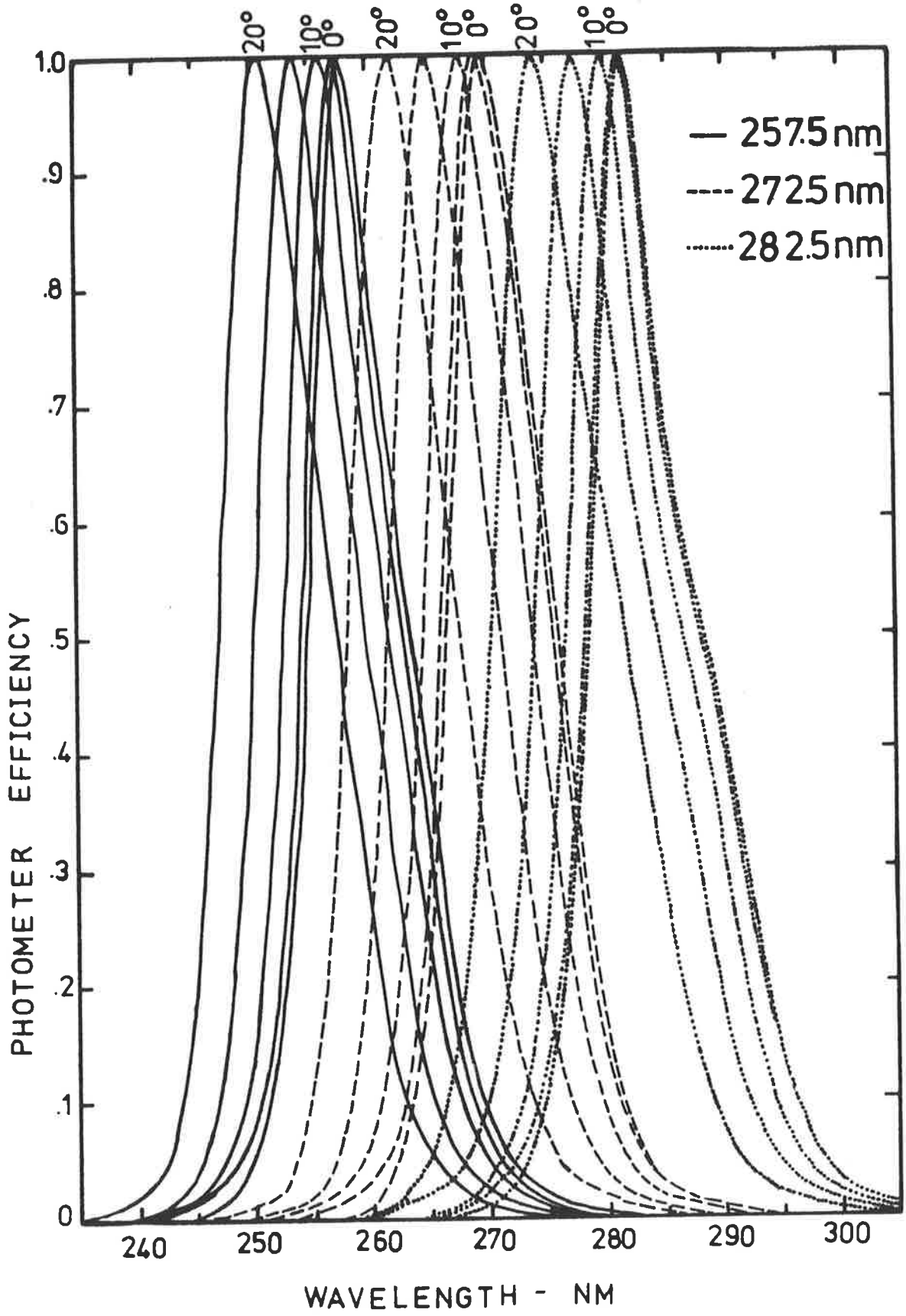

Figure 5.9 Spectral response of MUV photometers, illuminated at different angles.

found to diverge 2.5°. Neither was the beam wide enough, even with the detector placed at a finite distance from the exit slit to take advantage of the beam divergence, for complete and constant illumination. Consequently, measurements of the decreasing photometer sensitivity with increasing angle of incidence involved an uncertainty of about 40%.

In Figure 5.9 the photometer response curves have been normalized to the maximum signal because this aspect of their calibration was not crucial for the success of the experiment for two reasons. Firstly, an in-flight estimate of the photometer's angular response was provided by the variation in the signal when the rocket was above the altitudes of primary absorption. This corresponded to a measurement of the enveloping curve of the calibration profiles in Figure 5.9, prior to their normalization. Secondly, for broad band absorption spectroscopy experiments only the relative spectral responses of the photometers need be known for a given angle of the incident radiation. With regard to the absolute calibration of the photometers, which is described in the next section, the peak filter transmission occurred for normally incident radiation and absolute calibration was only performed for this condition.

b. Absolute Efficiency

A xenon lamp was used in conjunction with a low resolution (20 nm) Bausch and Lomb monochromator to provide an exit beam centred near the wavelength of the peak photometer response and wider than its bandpass. Using the Hilger Watt monochromator and photodiode, the relative spectral distribution of this beam was determined. Then, directing all the beam onto the photodiode provided a measure of the total number of photons per second exiting from the Bausch and Lomb monochromator. Integrating over the relative spectral distribution of the beam and dividing by the total intensity enabled the absolute intensity to be determined as a function of wavelength across the beam. These calculations

assumed that the spectral distribution, as sampled by the entrance slit of the Hilger Watt monochromator, was uniform across the beam from the Bausch and Lomb instrument.

When the photometer was illuminated with the calibration beam, such that all the incident flux was collected, the amplified signal from the photometer produced a current I_1. Referring to Figure 5.10, with $E(\lambda)$ the relative efficiency of the photometer, as typified by the curves in Figure 5.9, $B(\lambda)$ the absolute spectral intensity of the calibration beam and $\phi(\lambda)$ the solar flux, then the photometer signal on top of the absorbing atmosphere was estimated to be

$$I_s = I_1 \frac{\int \phi(\lambda)\ E(\lambda)\ d\lambda}{\int B(\lambda)\ E(\lambda)\ d\lambda}$$

A more accurate and less tedious absolute calibration technique was afforded by use of a solar simulator. This is a source of parallel light which reproduces the relative spectral distribution of the sun and is calibrated for equivalent total solar irradiance in photons/cm^2/sec. Use was made of the solar simulator facility at Goddard Space Flight Center, Maryland, U.S.A., for additional absolute calibration of the photometers for the daytime experiments, and also to provide estimates of their angular responses.

Both of the absolute calibration techniques described above indicated that the maximum signal measured by each of the photometers near apogee would be less than 10^{-5} amp, which was the limit of linearity of the PIN diode response. For photometers centred at 257.5 nm this maximum signal was calculated, on average, to be 0.47×10^{-6} amp, while the average measured response to the solar simulator light source was

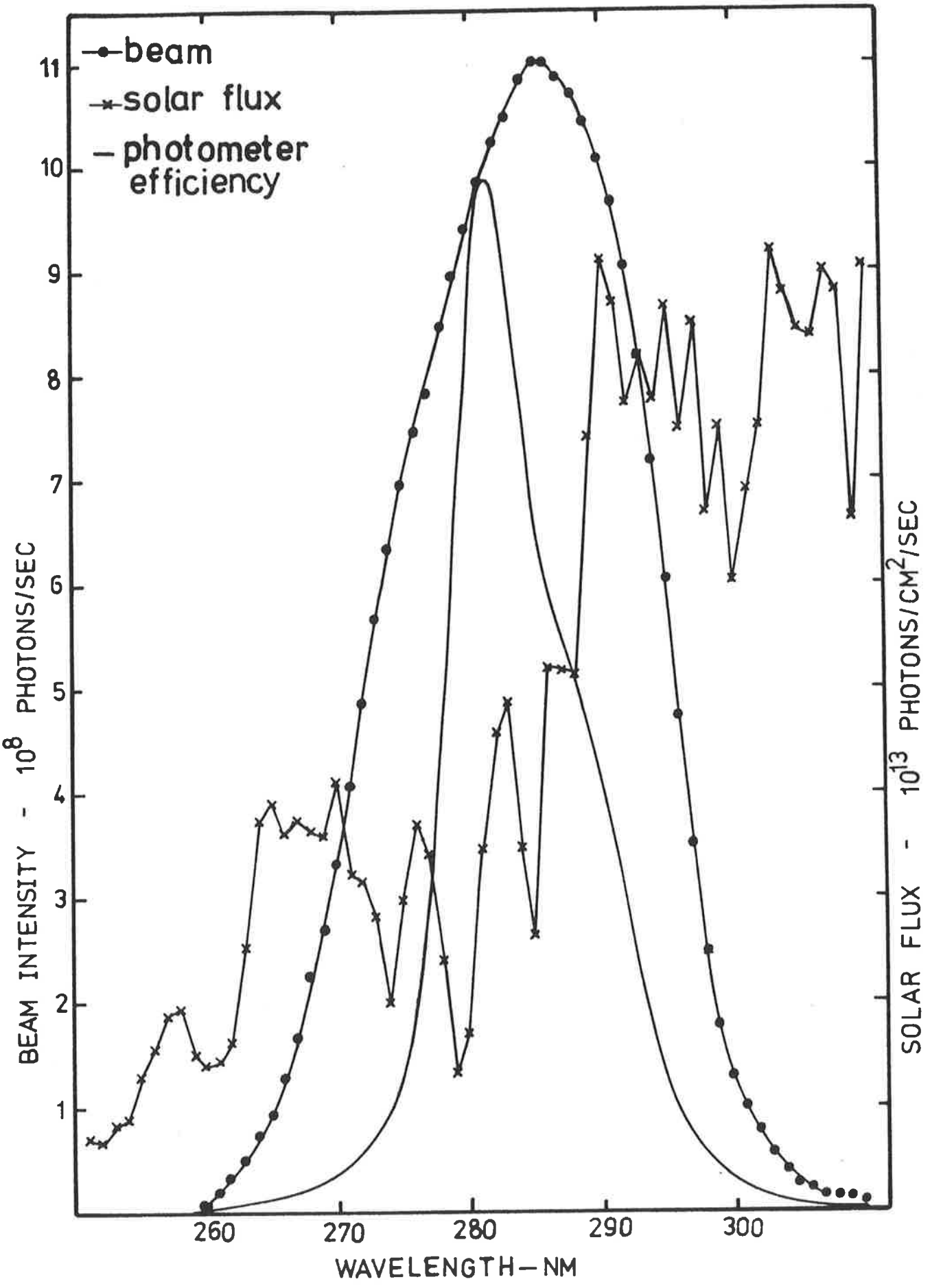

Figure 5.10 Parameters for absolute calibration of ozone detectors.

0.77×10^{-6} amp. The average of the calculated maximum signals for photometers at 282.5 nm was 1.14×10^{-6} amp and the average measured signal was 1.76×10^{-6} amp.

c. *Aspect Sensor Calibration*

The principle by which the aspect sensors provided information about the position of the radiation source, in both the zenith and azimuth planes, is that of shadowing, produced by a square mask over a photosensitive surface subdivided into four square regions of equal area.

For a perfectly aligned aspect sensor, the signal from each quadrant is equal when radiation is incident normally to the surface. If the radiation is not normally incident, the ratios of the signals from each quadrant indicate the complex angle of the source with respect to the detector normal.

Typically, the construction of the mask and the location of the sensor in the detector block contribute to overall imperfect alignment, necessitating calibration. This was achieved with a 3mm diameter source at a distance of 320 mm, simulating the moon as seen by the aspect sensor on the rocket. In Figure 5.11 are the recorded outputs from each quadrant of one of the three aspect sensors of the nighttime experiment, as a function of angle, which was varied in a plane parallel to the direction of the rocket spin axis.

5.5 *DATA RETRIEVAL*

The optical ozone detectors described in the previous sections were carried on spinning rockets, launched from Wallops Island, U.S.A., over the period 21 October to 4 November, 1979. To summarize the flight parameters: three rockets were launched during 2½ hours, near local noon, on 21 October, 1979, when the solar zenith angle was approximately 50°;

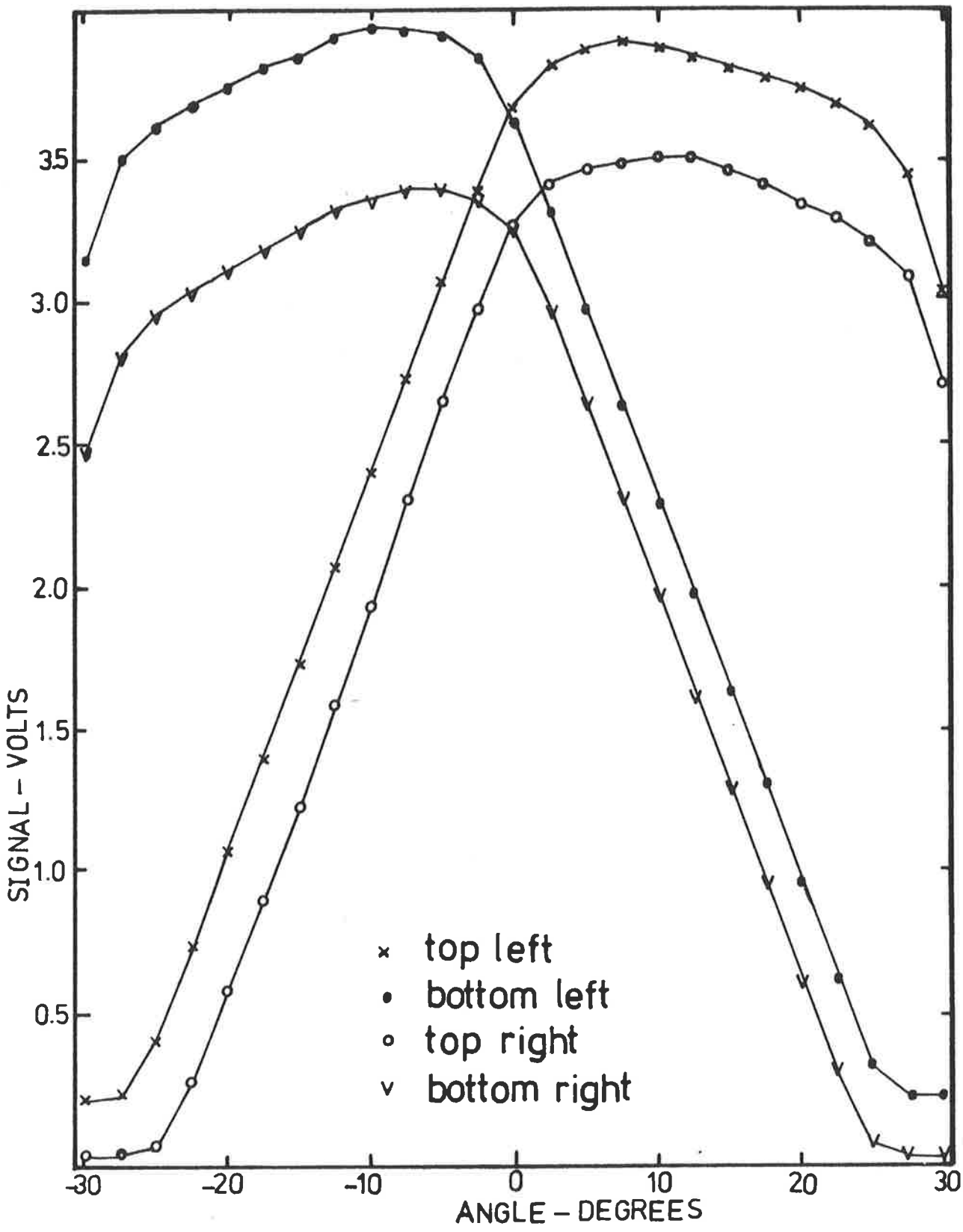

Figure 5.11 Calibration of the aspect sensor for the nighttime experiment.

two rockets were launched within an hour of each other on the morning of 1 November, 1979, for which the average solar zenith angle was 70°; the sixth daytime launch occurred at sunset on the same day, when the solar zenith angle was about 87°; and the nighttime ozone measurements were made on 4 November, 1979 at 0427 hours local time, when the lunar zenith angle was about 65°. Each of the rockets attained apogee near 80 km. Additional details pertaining to the flights are provided below.

a. Daytime Rocket Flights

To investigate daytime ozone densities, the optical detectors comprised of broad band photometers, described in Section 5.3a, were incorporated into composite payloads, as photographed in Figure 5.12, and characterized more fully in Appendix A. For each payload, the detector 'look' angle was adjusted, according to the calculated solar zenith angle, so that throughout the flight solar radiation would be incident on the photometers as near normally as possible. Figure 5.13 is a photograph of a fully assembled Nike Orion rocket vehicle, used for the daytime experimental payloads, prior to its ignition. Table 5.1 summarizes selected parameters for each of the six launches and Figure 5.14 illustrates the variation of the solar zenith angle for the duration of each flight.

Data was obtained on the upleg of all flights when the detectors were pointed at the sun by the rocket, spinning about 6 times per second. Five of the six payloads performed successfully in the descending mode and data was acquired as the experimental package rotated 3 times per second, suspended below a high altitude parachute. Data acquisition from one of the payloads was terminated near 60 km on the upleg when the parachute was deployed prematurely. The Nike Orions used proportional bandwidth (IRIG) telemetry to transmit the signals from the experiments to ground. Since this is an analog system, it was necessary to digitilize the signals for recording the data on magnetic tape.

Altitude information was provided by an FPS16 C-band radar which

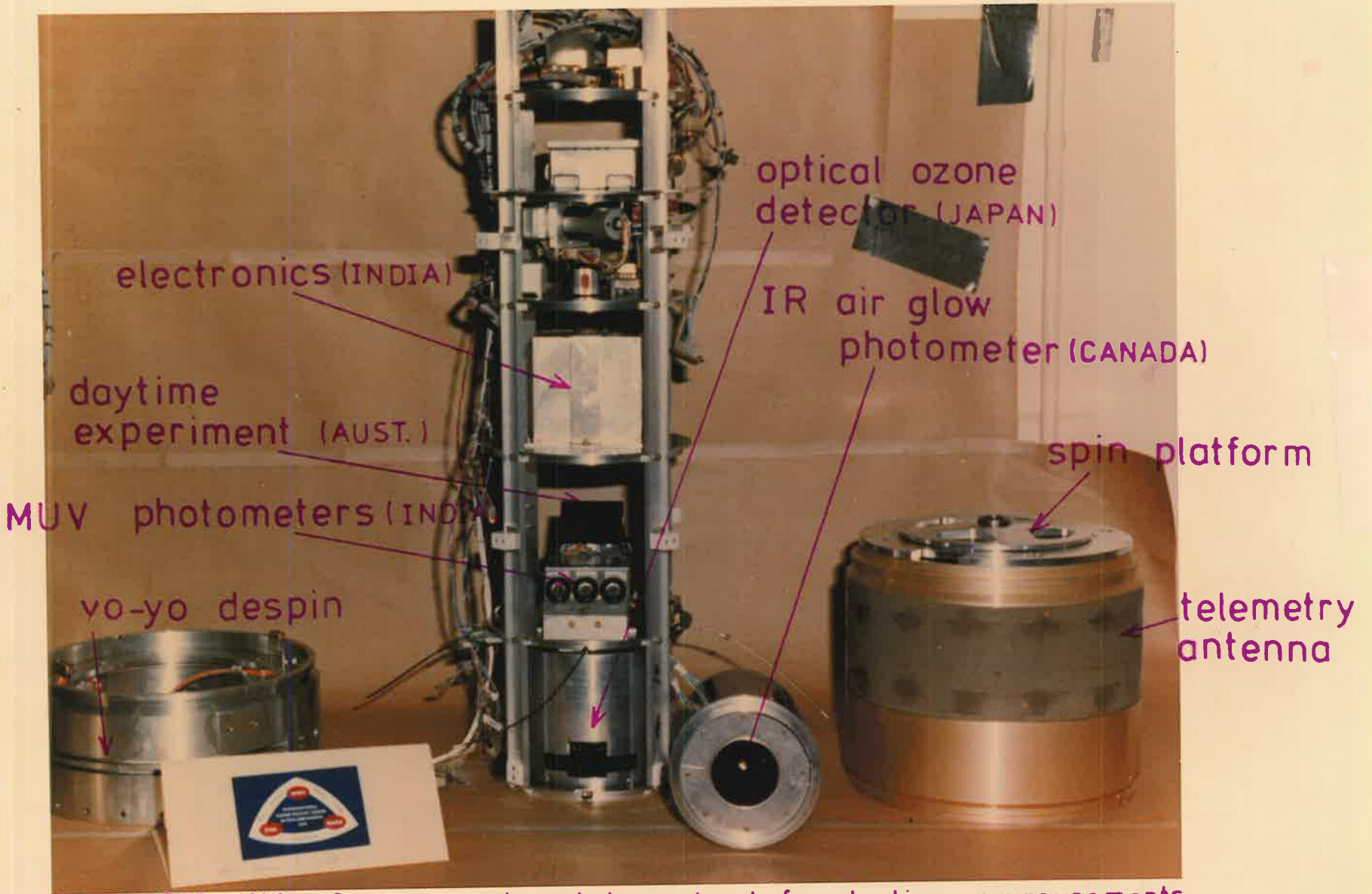

Figure 5.12 Nike Orion experimental payload, for daytime measurements.

Figure 5.13 Nike Orion rocket vehicle on launcher.

VEHICLE	31.010	31.009	31.008	31.011	31.012	31.013
Launch Time: Universal (Local)	21/10/79 1530 hrs (1127)	21/10/79 1625 hrs (1222)	21/10/79 1748 hrs (1345)	1/11/79 1300 hrs (0857)	1/11/79 1345 hrs (0942)	1/11/79 2140 hrs (1737)
GHA of Equinox	$1^h53^m59^s$	$1^h54^m06^s$	$1^h54^m19^s$	$2^h40^m53^s$	$2^h40^m57^s$	$s^h42^m15^s$
Apparent Right Ascension	$13^h38^m52^s$	$13^h38^m59^s$	$13^h39^m11^s$	$14^h24^m31^s$	$14^h24^m35^s$	$14^h25^m53^s$
Apparent Declination	$-10° 16^m28^s$	$-10° 17^m08^s$	$-10° 18^m14^s$	$-14° 20^m20^s$	$-14° 20^m41^s$	$-14° 27^m05^s$
Solar Zenith Angle at Apogee	51.0°	48.3°	50.4°	73.6°	66.6°	86.9°
Solar Radio Flux: $F_{10.7}$ cm	230.1	230.1	230.1	211.6	211.6	211.6
Geomagnetic Index: K_p	3^-	3^-	3^-	3	3	3
Apogee	83.16 km	80.63 km	83.20 km	83.72 km	84.94 km	82.00 km

TABLE 5.1 Parameters for Nike Orion launches from Wallops Island (37.84° N, 75.48° W).

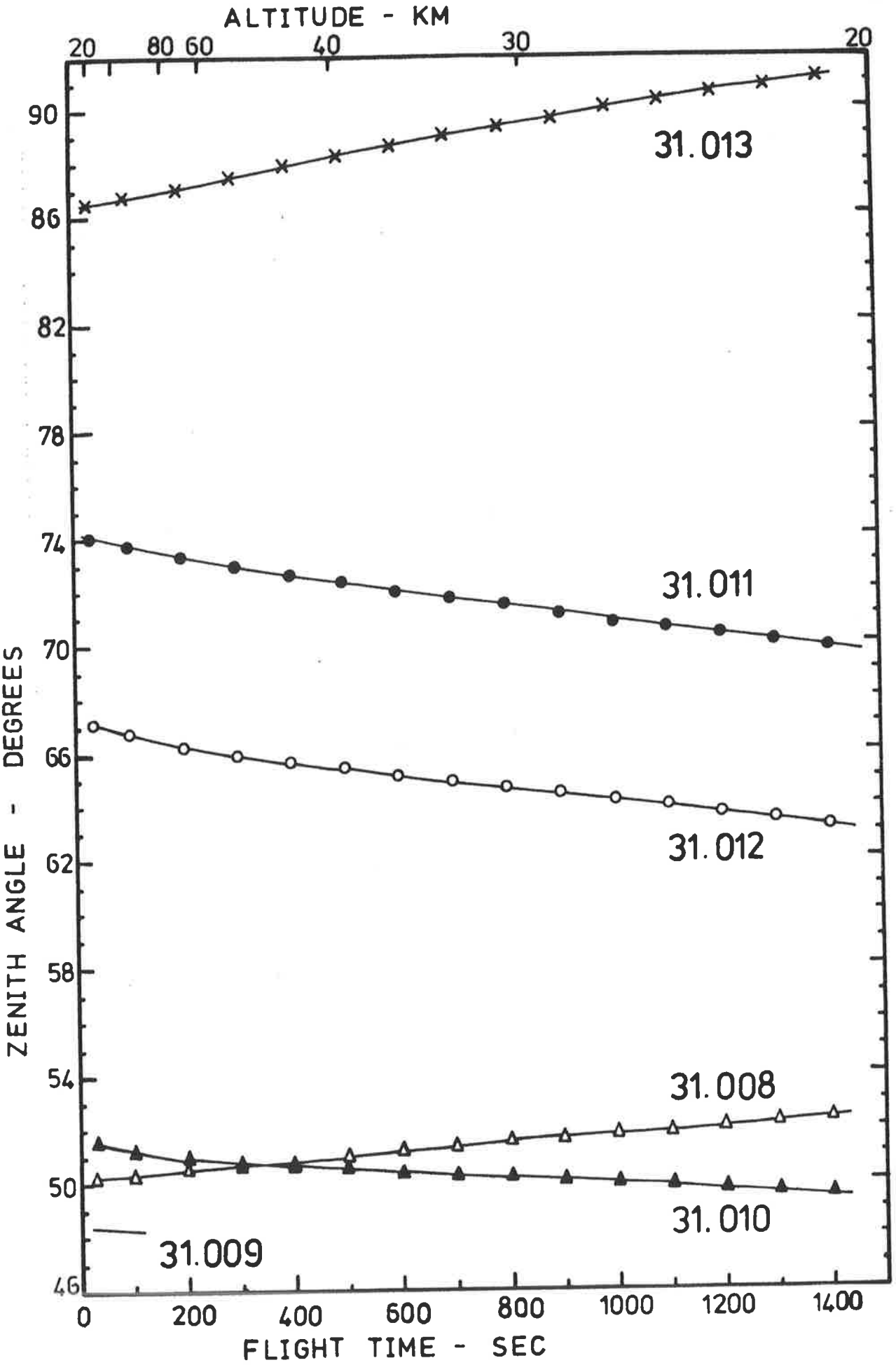

Figure 5.14 Solar zenith angles for Nike Orion flights

tracked the vehicles with an accuracy of ± 0.023 km. This data, together with the position and velocity of the vehicle throughout flight, was available in printout form. A typical altitude profile for the ascent and descent of the Nike Orion payload is shown in Figure 5.15a. Combining the rate at which the experimental package was spinning with its rate of change of altitude enabled an estimate to be made of the measurement height resolution associated with the raw data and this is illustrated in Figure 5.15b.

Solar aspect information for the experimental package was determined by a sensor which produced a digital pulse on traversing the source of the radiation. Specific combinations of seven binary digits were coded to represent an integral value for the angle with which the radiation was incident on the sensor. Had a digital (PCM) system been used to telemeter these pulses, decoding them would have been a routine computing procedure, yielding solar aspect angles accurate to ± 1°. However, converting the pulses to analog form for telemetry purposes then re-digitilizing them for analysis caused the original, precise code information to be degraded, requiring that the data be reduced manually. This tedious procedure was undertaken by Wallops Flight Centre and provided aspect angles uncertain by at least ± 2°.

b. Nighttime Rocket Flight

The experiment for measuring nighttime ozone densities, consisting of three identical detectors each with three MUV photometer channels, as described in Section 5.3b, was carried on a single stage Orion rocket, launched at 0930 hours UT (0427 hours LT) on 4 November, 1979, from Wallops Island. This vehicle can be seen in Figure 5.16 and is described in Appendix A. At the time of launch, the moon was at a zenith angle of 65.4° and at a phase angle of 0.3° from full moon. The sun was 27°

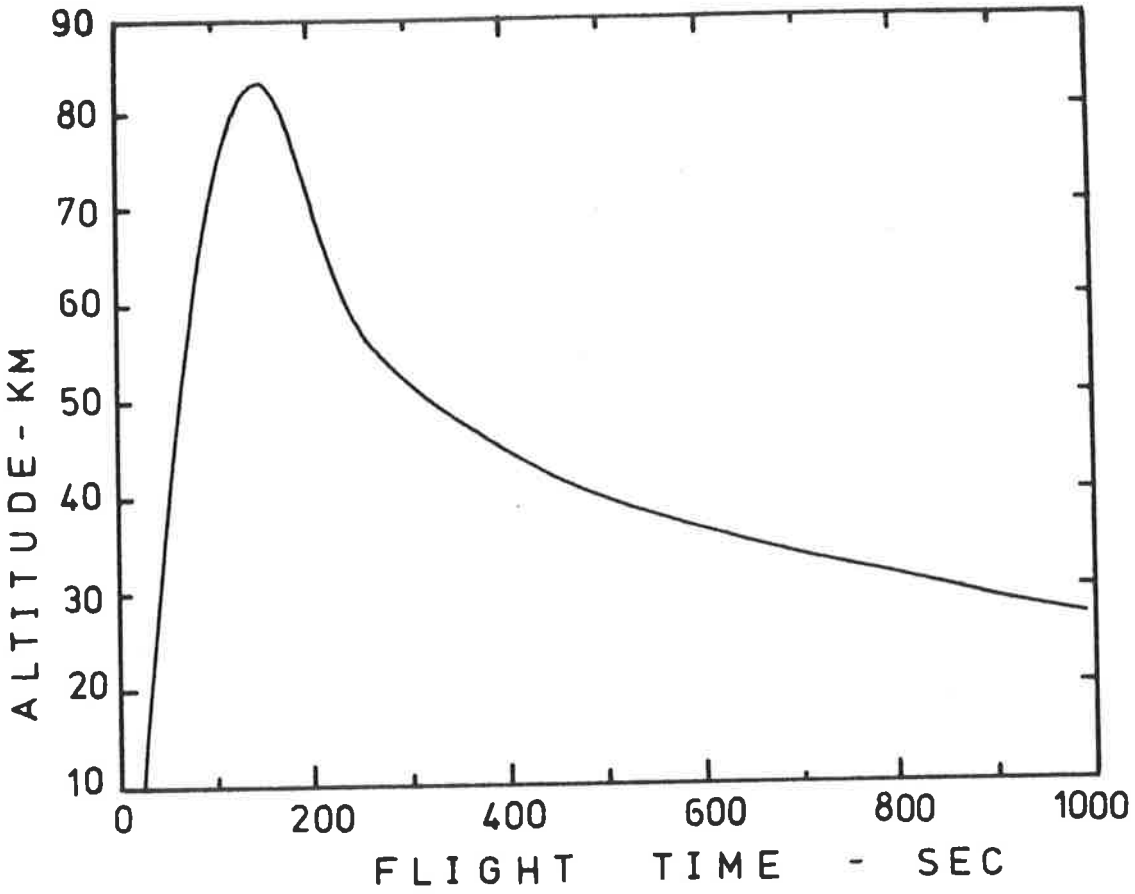

Figure 5.15a Altitude profile for Nike Orion flight.

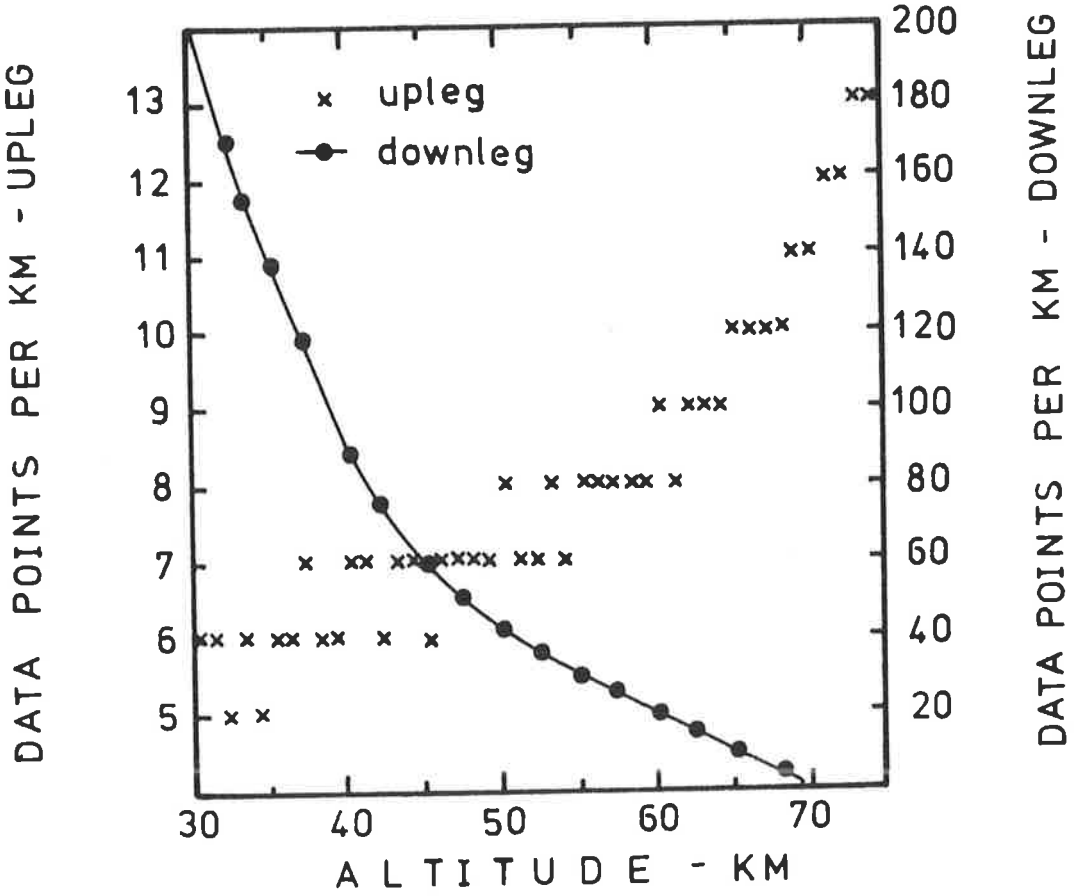

Figure 5.15b Data acquisition rate.

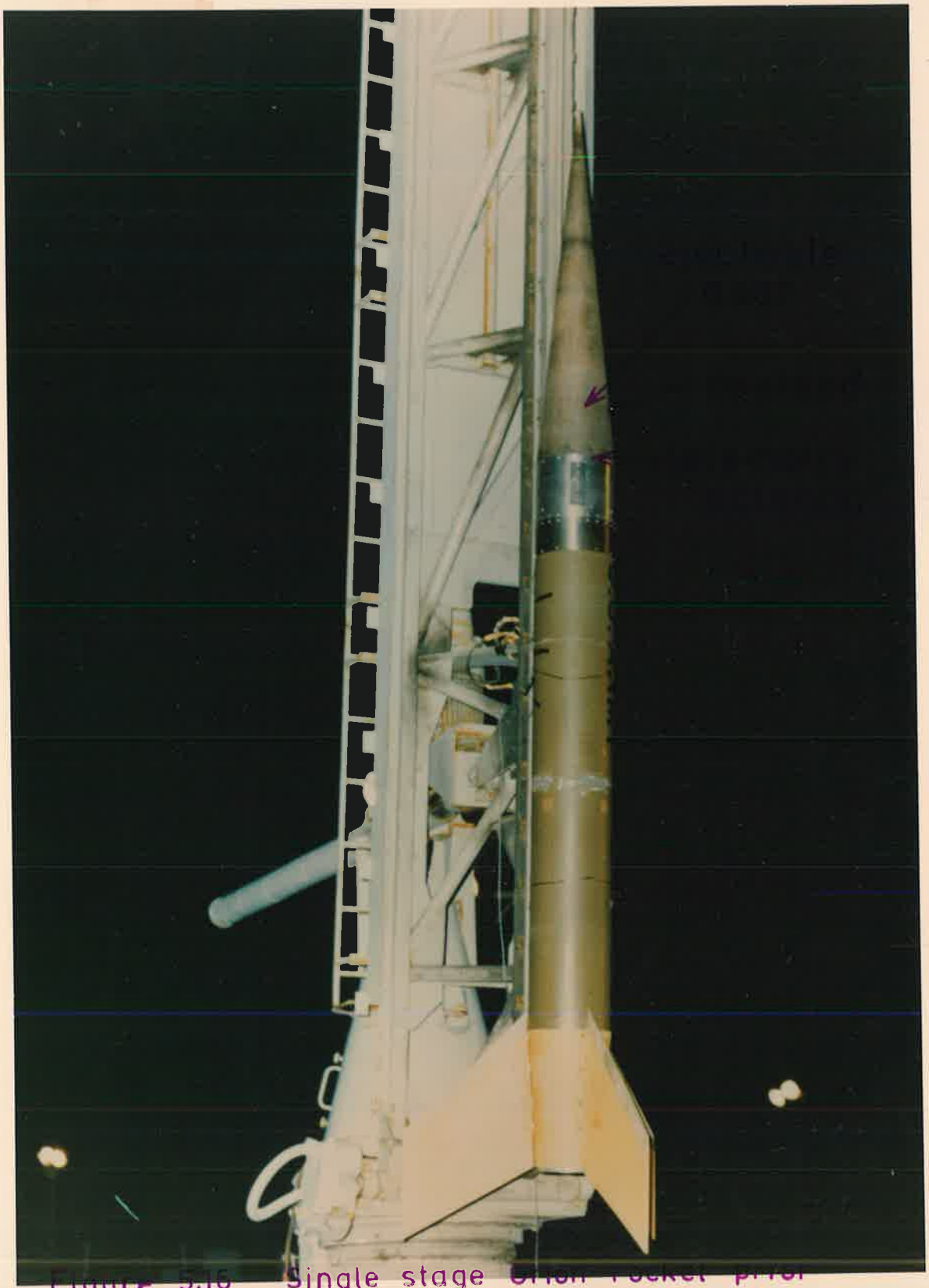

Figure 5.16 Single stage Orion rocket prior to nighttime launch.

below the horizon for which the earth's shadow extended to an altitude of 800 km, more than sufficient to ensure that no scattered sunlight would be seen by the photometers on reaching apogee at 82 km. Altitude during flight was obtained with an FPS16 C-band radar and is shown, together with the zenith angle, for upleg flight time, in Figure 5.17.

Primary data retrieval was afforded after the doors were pyrotechnically ejected and the high voltage activated, when the moon consecutively illuminated the three detectors as they spun past about 3½ times every second, looking outward at an angle of 83° to the rocket spin vector. Each detector block carried its own aspect sensor for information about the relative position of the moon at the time of its observation.

Data from three photometer channels, four aspect channels and one temperature sensor were thus telemetered to ground every 120° of rotation. Because of a limited number of high frequency IRIG channels, necessary to define the photometers' responses on sweeping past the moon, a number of photometer channels and aspect channels were multiplexed and transmitted to ground via common IRIG channels. Quicklook records of some analog signals from this experiment are shown in Figure 5.18. As for the daytime experiment, the data were stored on magnetic tape and transferred to the University of Adelaide for analysis.

5.6 EXPERIMENTAL ABSORPTION CURVES

a. Reduction of the Raw Data

At Wallops Flight Centre, the real time data from the seven rocket flights were written in 16-bit words onto 9-track magnetic tape. Initial processing of these tapes involved converting the 16-bit data words into 60-bits which could be read by the University of Adelaide's CDC

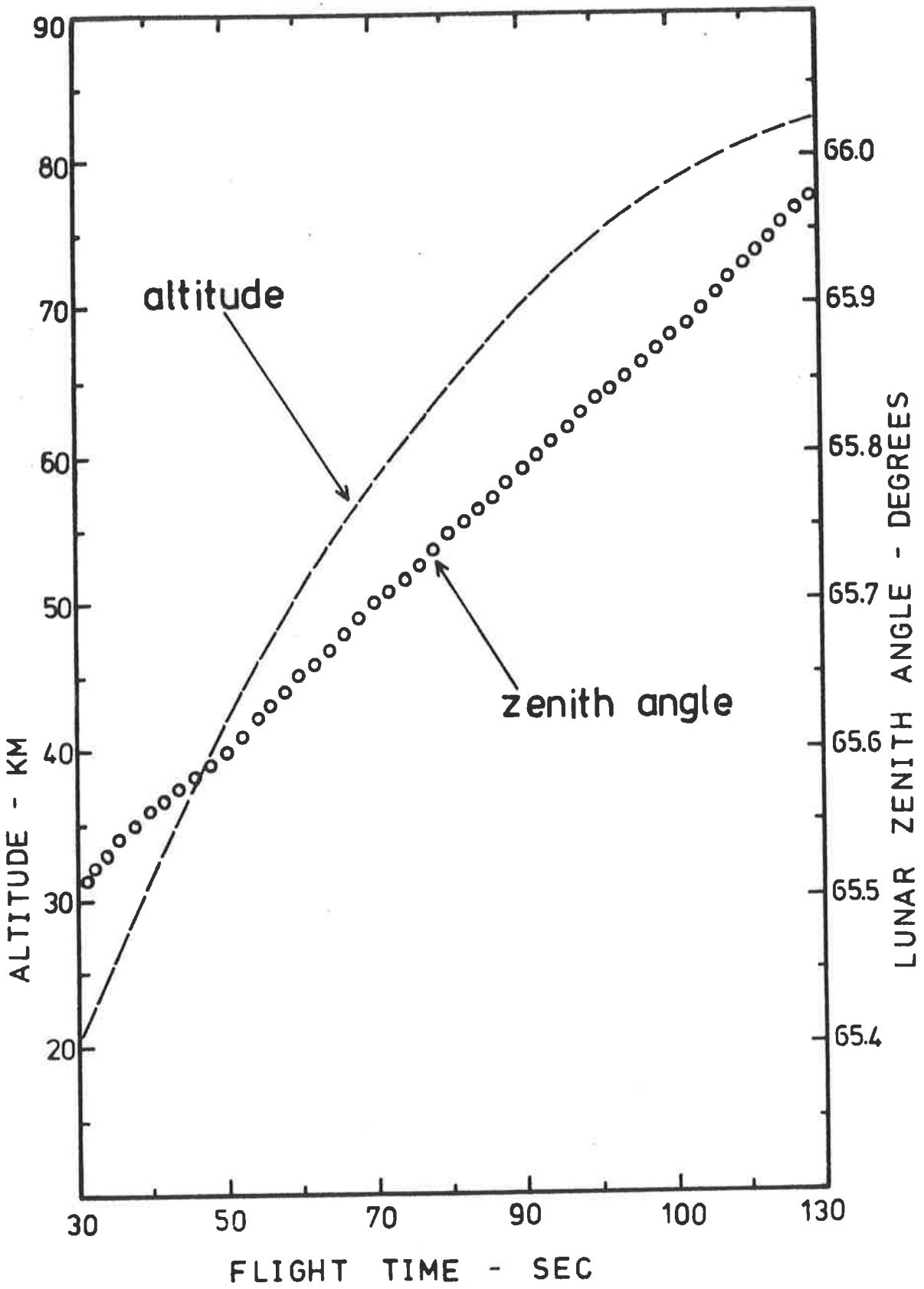

Figure 5.17 Flight parameters for single-stage Orion.

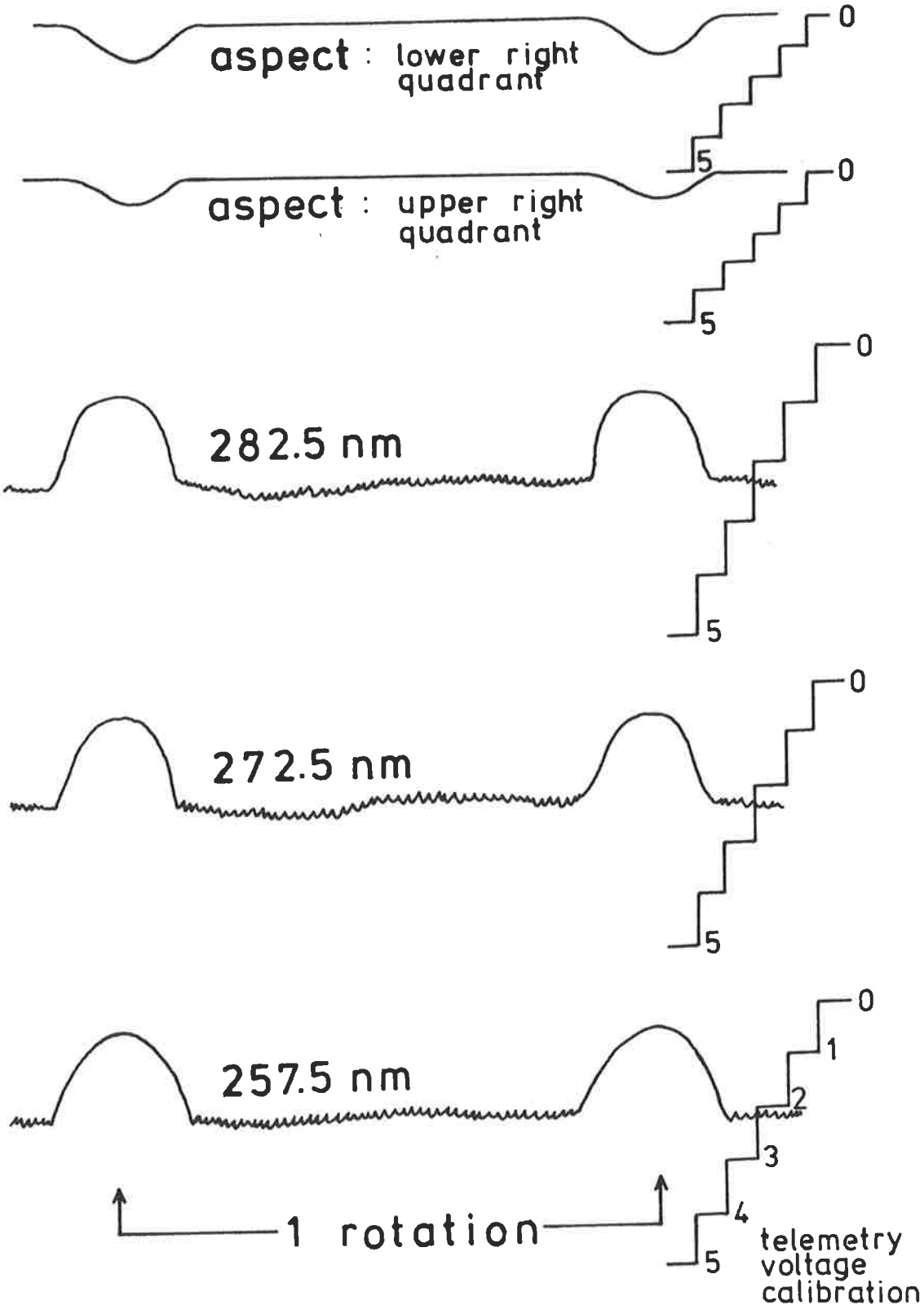

Figure 5.18 Quicklook records of telemetered signals from photometers and aspect sensor of the nighttime experiment, on the single-stage Orion rocket, near apogee.

Cyber 173 computer.

Data from appropriate telemetry channels, represented in base 10 by integral numbers with 4 significant figures, were arranged sequentially on the tapes, grouped in record blocks, each of which was identified by its own universal time. One block of data from a daytime rocket flight comprised 333 integer words from each of six telemetry channels, and occurred once every 0.3996 seconds, so that effectively the telemetry outputs from the daytime experiments were sampled every 0.0249 seconds.

From the night flight, it was required to record the output of 16 telemetry channels, each of which was sampled 125 times per record block. Since one such block was recorded every 0.1333 seconds, the telemetry channels of the nighttime experiment were hence sampled once per 0.00833 seconds.

Because only one time value was acquired for all the data within one record block, it was necessary to generate individual time tags for each integer of raw data and this was done by linearly interpolating between the time values corresponding to successive record blocks.

In the process of transferring the telemetry data onto magnetic tape, the 0-5 volt range of the telemetered experiment signals was modified by the voltage range defined by the data recording unit. For the recorded digital data to be referenced absolutely to the experimental signals required that it be scaled according to the magnitude of the upper, middle and lower band edge characteristic of the recording mechanism.

Following the initial processing procedures of time tagging and calibrating, the data extracted from the tapes were thus in the form of 4 digit integers, numerically equivalent to the experiment output voltage in millivolts, and represented a reconstruction of the original analog telemetry signals. However, the truly continuous nature of the original

signals had been impaired by random error associated with the 12th bit of the A/D convertor, requiring that the data be smoothed to more accurately reproduce the telemetered signal. This was done by successive averaging over groups of 7 data points, weighted according to 1:4:7:10:7:4:1.

Data from each photometer channel were recorded continuously with time as the rocket rotated, and were thus characterized by numerical maxima when the detector pointed most nearly in the direction of the MUV source, and minima when the detector looked away. The nature of the telemetered voltage has been illustrated previously in Figure 5.18. Only the signal maxima were of experimental relevance, since they contained information about the intensity profile of the source during the rocket trajectory. After smoothing, the digital data were sufficiently continuous for the peak signals, acquired during each rotation of the detector past the source, to be extracted as local maxima in the data.

From application of the above data processing techniques were obtained the signal maxima from each of the photometers, and from the aspect channels of the night flight, as functions of the flight time. Rocket trajectory information (for example, Figures 5.15a and 5.17) then enabled these peak signals to be obtained as functions of height. The height profile of a photometer signal, extracted in this way, represented the intensity variation of the MUV radiation within the wavelength band of the photometer, modulated by the response of the photometer to the changing angle at which this radiation was incident, following the changing aspect of the source with respect to the detector normal, as the rocket precessed. To obtain the best estimate of the absorption profile of the MUV radiation, it was necessary that corrections for the aspect variation be applied to the initial intensity profiles.

b. Correction for Aspect

The dependence of the photometer response on the angle of the incident radiation was established during the laboratory calibration of each detector (Section 5.4a) and involved a wavelength shift in the relative spectral response of the detector, accompanied by a reduction in the integrated spectral response. As the angle between the radiation source and the detector normal increased, the transmission of the filter, which defined the detector bandpass, decreased, causing the detector signal to decrease, while the shift in the filter bandpass to shorter wavelengths meant that the detector now observed a slightly different wavelength region of the source spectrum, for which the integrated spectral intensity was enhanced or reduced, depending on the relative spectral distribution of the source radiation.

The required absorption curve for ozone density determination is a profile for which the angle of the incident radiation, and hence the photometer spectral response, is known and constant. This can be obtained from the measured height profile of the photometer signal, using knowledge of the aspect angle of the source with respect to the photometer normal, in a number of ways, as follows.

Theoretically, the preferable approach is to choose the detector signal at some time in its spin such that its angle of rotation in the plane perpendicular to its spin vector and the angle of the position vector of the source together define a constant angle of incidence. The geometry of a detector rotating on a rocket is shown in Figure 5.19. Ideally for absorption measurements, the angle α between the source and the detector normal should remain constant. If γ is the angle between the source and the plane in which the detector rotates, and β the angle of rotation, there will always be some combination of γ and

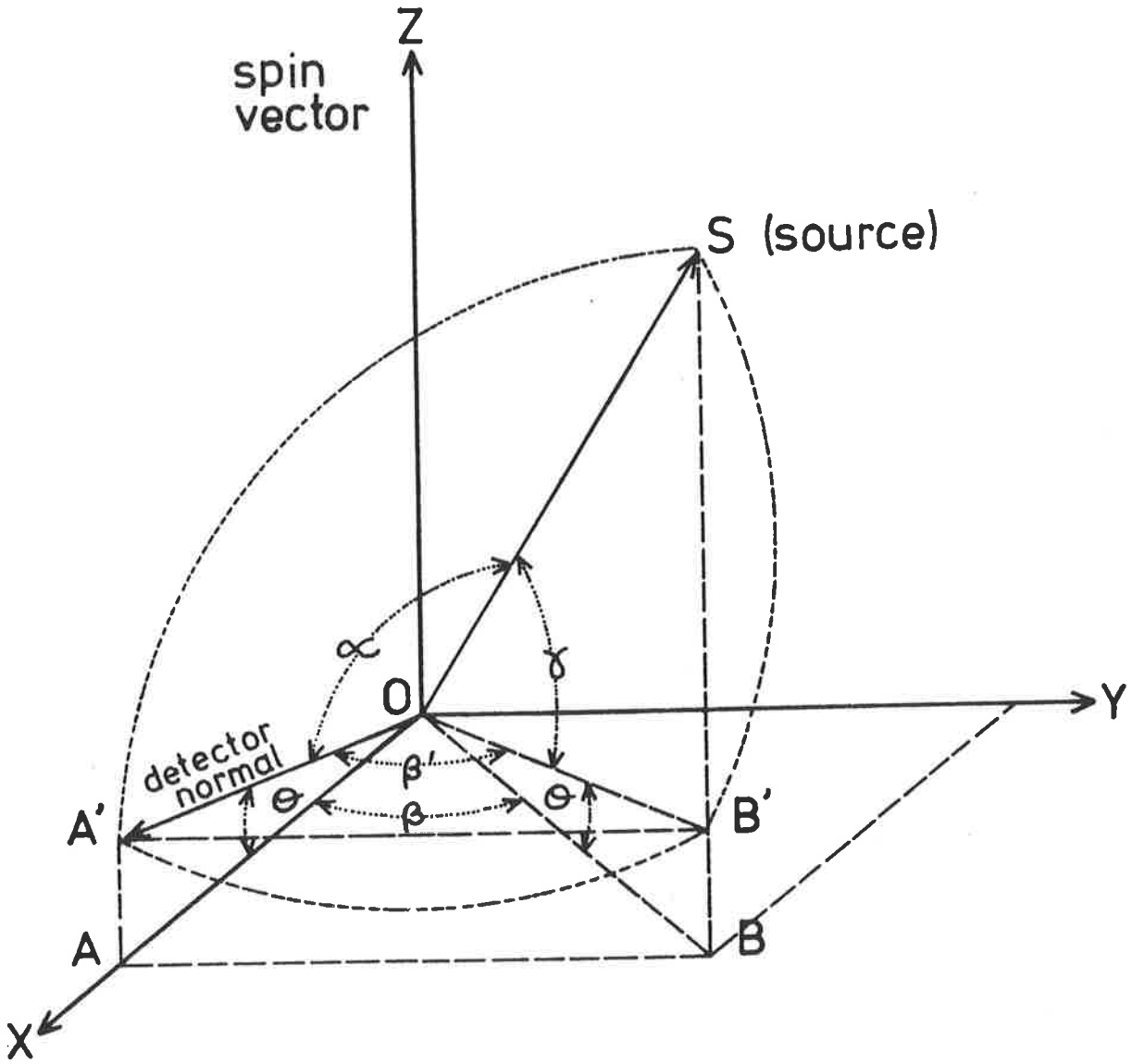

Figure 5.19 Geometry of a detector on a spinning rocket.

β for which α can be kept constant. Following the notation in Figure 5.19, analysis of the spherical triangle A'B'S yields the relationship

$$\cos \alpha = \cos \beta' \cos \gamma + \sin \beta' \sin \gamma \cos \hat{A'B'S}$$

and since $\hat{A'B'S} = 90^\circ$, then

$$\cos \alpha = \cos \beta' \cos \gamma \qquad 5.3$$

From the isosceles triangles A'OB' and AOB,

$$\sin \beta/2 = \cos \theta \sin \beta/2. \qquad 5.4$$

Combining Equations 5.3 and 5.4 gives

$$\cos \alpha = \cos \gamma (\sin^2 \theta + \cos^2 \theta \cos \beta) \qquad 5.5$$

If θ is known and γ is measured, it is possible to choose β such that α remains constant. For all flight data to be incorporated in this form of analysis, α must be chosen to be larger than the maximum measured value of γ.

Alternately, when the detector is above the altitude region in which there is significant absorption, any variation in its signal will be caused primarily by changes in the angle at which the radiation is incident. Above such altitudes it is possible to correlate the variation in signal with the variation in aspect. Having established this relationship, the detector signal throughout flight can then be adjusted for a constant aspect angle. This technique is more suitable when the coning about apogee extends over the entire range of aspect encountered in the data collection period. Possible errors may be generated at low altitudes where the solar spectral distribution is a modified version of the extraterrestrial distribution, due to the different rates of ozone absorption at different wavelengths within the detector bandpass.

A variation of the above approach for aspect correction of the detector signal involves laboratory determination of the angular dependence of the integrated detector response. This is then used to correct the measured intensity profile to a constant angle of illumination. An obvious limitation of this technique is the effectiveness of any laboratory source to accurately simulate the extraterrestrial source (sun or moon) or to provide the same geometry of irradiation.

If the data retrieval rate is sufficiently high, it may be possible to use only those signals recorded at the same aspect angle to generate a family of absorption curves. Or, if there are many experimental points within a small enough height range, the absorption of the MUV radiation can be analyzed in a step wise fashion through concentric spheres, avoiding the necessity of considering a composite absorption curve, or for correcting all the data for common aspect.

In any application of absorption spectroscopy involving detectors on spinning rockets the most useful approach for incorporating aspect variation into the analysis to deduce atmospheric density depends on a combination of many experimental parameters, including the number of data points acquired per km, the extent of coning of the rocket vehicle and the sensitivity of the detectors to variation in the angle of illumination.

c. *Daytime Measurements*

Examples of the raw data from a typical daytime experiment are provided in Figure 5.20 where the signals from each of the two MUV photometer are plotted as functions of flight time, for both the upleg, on a spinning Nike Orion rocket, and the downleg, on a rotating platform suspended beneath a high altitude parachute as described in Appendix A. Aspect data for the same flight is provided, also as a function of time, in Figure 5.21.

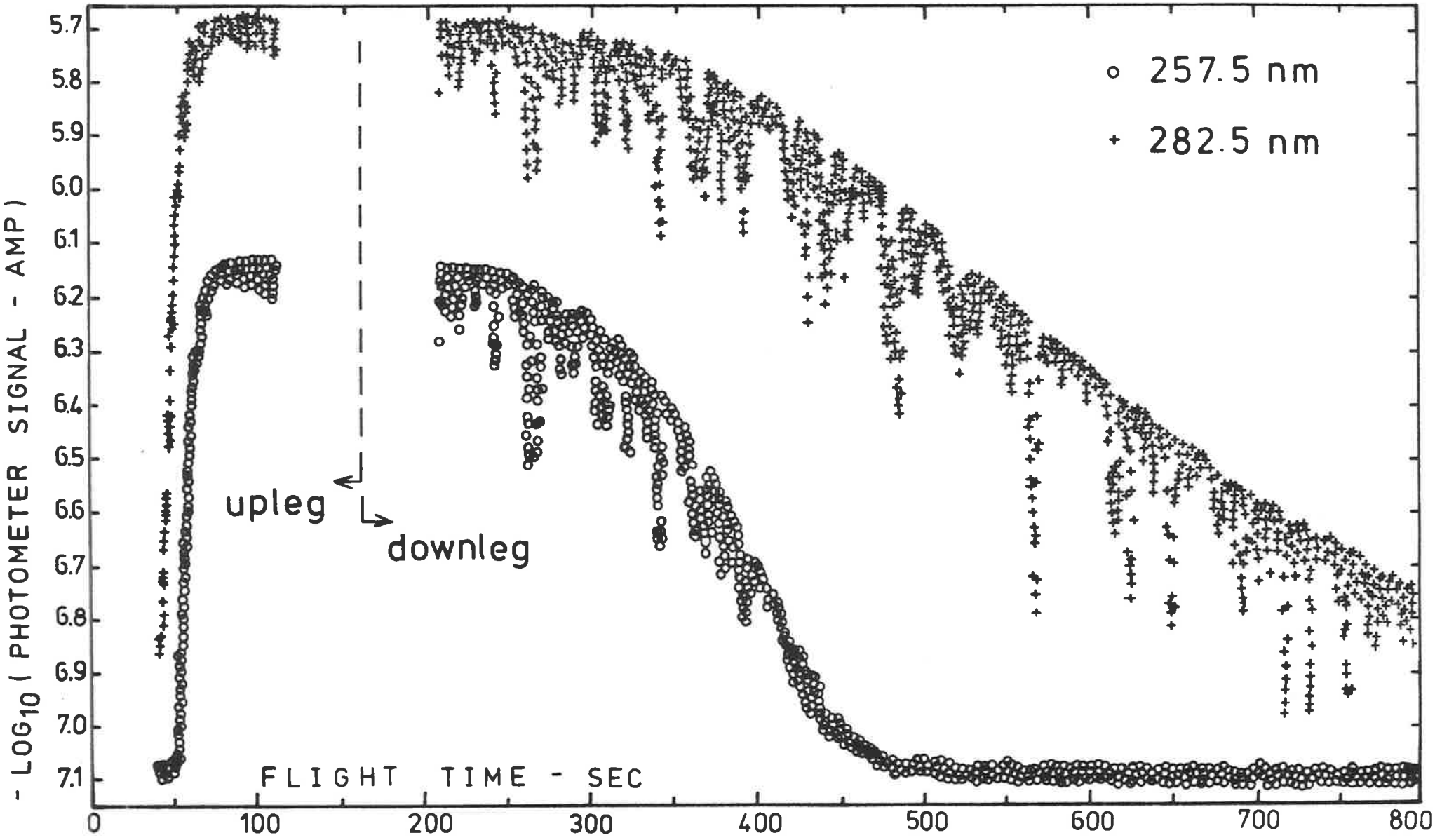

Figure 5.20 Time variation of the signals from the photometers of a daytime experiment.

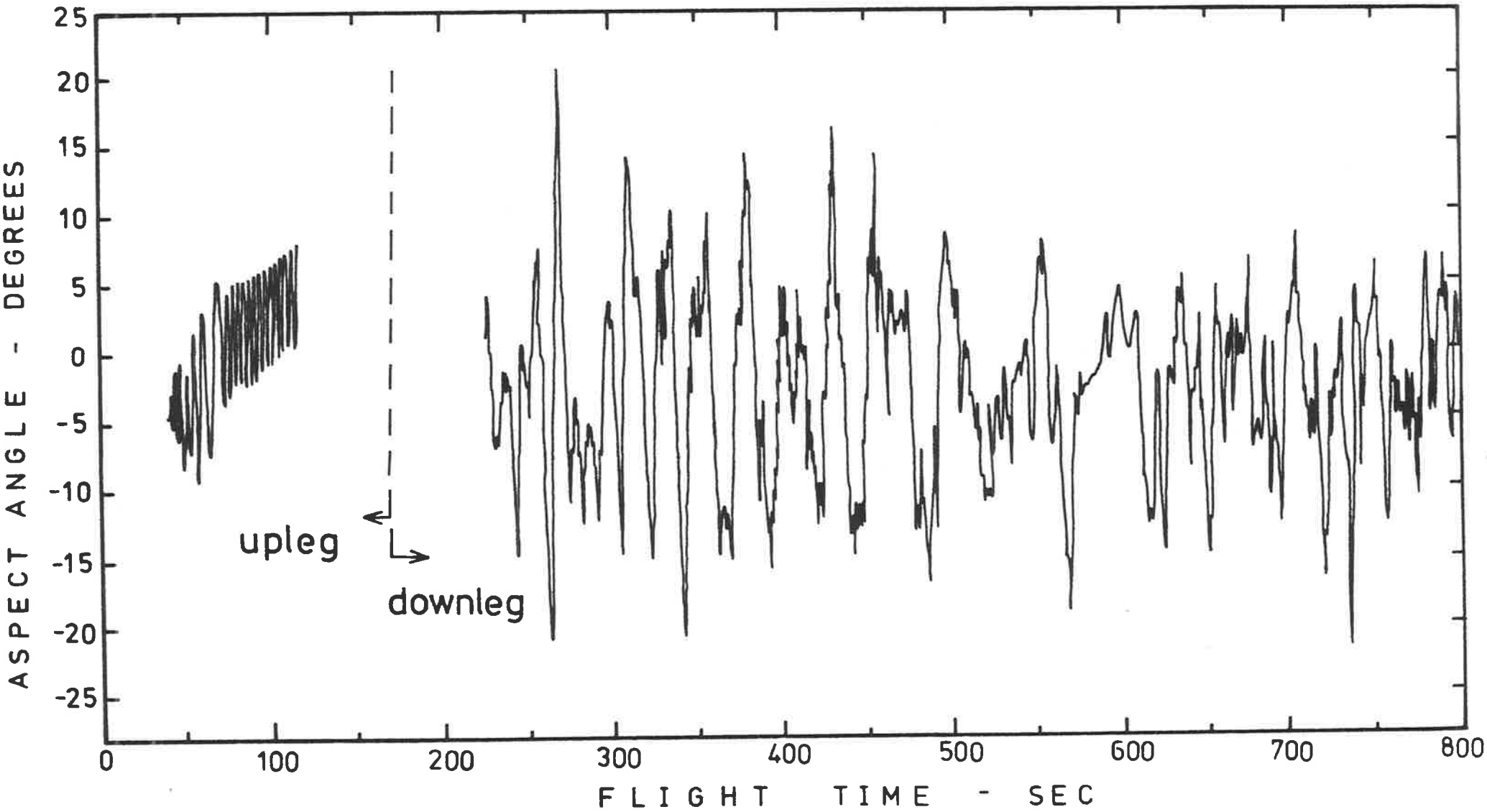

Figure 5.21 Aspect angle variation for the photometers of Figure 5.20.

That the parachute was not a very stable descent mechanism is apparent from the wide and only semi-regular excursions of the downleg aspect angle in Figure 5.21.

The need to apply aspect correction to the raw signals, and techniques for doing this, have been discussed in the previous section. For the daytime data, the variation of the raw signal with aspect, at altitudes corresponding to the plateau maximum of the absorption curve, was least squares fitted with a parabola. This was used to modify the raw data for constant illumination, at approximately the average aspect angle. With reference to the examples of Figures 5.20 and 5.21, the upleg data wereadjusted to zero illumination angle and the downleg data for constant illumination at 5°. More generally, the 'look' angles, θ in Figure 5.19, for the detectors were such that all the flight uplegs were adjusted for illumination at $\gamma=0$ while for three of the downlegs (31.010, 31.008, 31.013) $\gamma=5^\circ$ and for the remaining two (31.011, 31.012), $\gamma=10^\circ$. Height profiles of typical upleg and downleg aspect-corrected photometer signals are plotted, on a linear scale, in Figure 5.22. Drawn through the data points are curves representing the smoothed absorption profiles.

Smoothing of absorption curves is a contentious issue: although some such techniques are applied to most experimental data, there are no standard procedures and the intrinsic difficulty is with distinguishing real structure from scatter. The signal of a photometer must increase monotonically with altitude but, because the MUV flux transmitted to a particular altitude depends on the column density above that altitude, structure existent in the local density is not manifested directly as structure in the absorption curve.

If measurements of the flux transmitted through successive finite height intervals are sufficiently accurate that the incremental change in

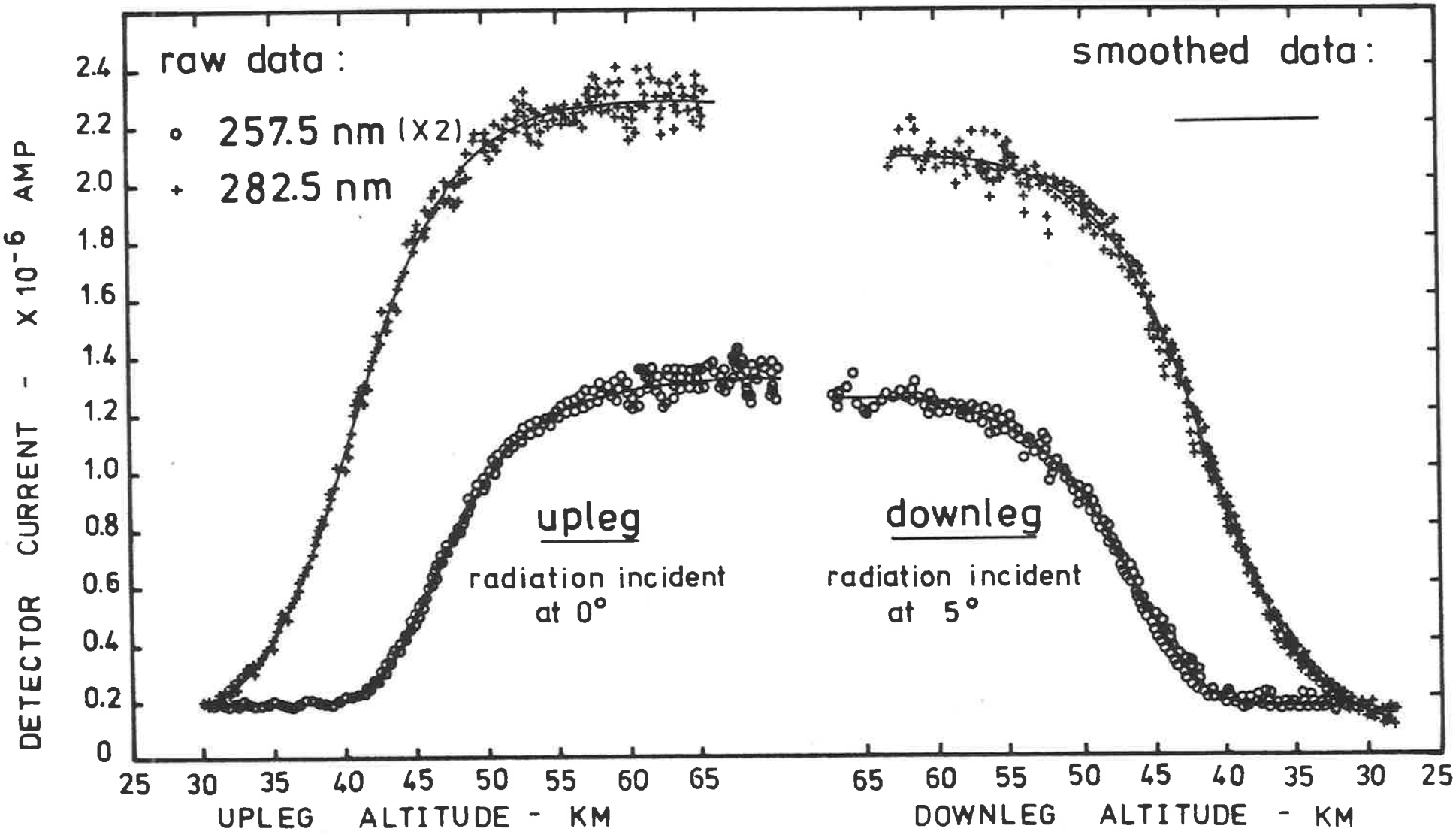

Figure 5.22 Aspect corrected absorption curves, measured near noon, with $\chi \div 50°$.

flux is unambiguously defined, direct application of the Lambert-Beer law provides an estimate of the density within each height interval. In rocket absorption spectroscopy this condition is most nearly achieved with a fixed detector on a pointed vehicle. Then the data acquisition rate is limited only by the telemetry sampling rate S and the rocket velocity V. For example, with S = 625 samples/sec and V = 1 km/sec there are 625 data points recorded every km. Primary uncertainties derive only from the telemetry noise and pointing inaccuracies, and smoothing over successive 1 km intervals would probably be sufficient.

When detectors are carried on spinning rockets the data acquisition rate is severely reduced, limited by the number of spins per km, to typical values as given in Figure 5.15b. The data is further degraded by the need for aspect correction, incorporating cumulative uncertainties from the detector's angular response and measurements of the aspect angle in flight. This is especially true when the coning is large, as in the downleg data in Figure 5.21. Rarely, in such experiments, does each consecutive detector signal increase monotonically with height, precluding direct application of the Lambert-Beer law independently to data within small height intervals. Rather, the data are scattered about a mean profile, representing the gross effects of the absorption, and the signature of local density structure may well be submerged in the scatter of this data. Smoothing the raw data to provide the best estimate of the mean absorption profile can be done with, for example, a weighted running mean, a moving polynomial, cubic spline interpolation, a fast fourier transform or by hand.

The smooth curves in Figure 5.22 are analytical representations of the absorption data, obtained by least squares fitting the raw data with functions of the form

$$I_{exp} = A + \frac{B}{1 + \exp[- (h-h_0)k + (h-h_0)^2\ 1 - (h-h_0)^3 m + (h-h_0)^4 n + (h-h_0)^5 p]}$$

where A, B, h_0, k, l, m, n and p are eight fitting parameters and I_{exp} is the smoothed value for the photometer signal at height h.

The appropriateness of this function as a suitable mathematical representation of this type of data is examined in Appendix F where a variety of ozone density profiles were used to generate attenuation curves which were then reproduced with fitted functions of the above form. It was considered that any real structure smoothed by this function would be within the experimental uncertainty of the measurement, as defined by the scatter of the raw data.

Figure 5.23 illustrates the typical altitude regions of the absorption curves measured by the two types of photometers, at four different zenith angles during the daytime. These curves were obtained from the least-squares fitted analytic functions by subtracting the background then dividing by the maximum signal. For each of the detectors the background signal monitored by the photometer at 375 nm was observed to remain constant, within telemetry and aspect induced uncertainties, for all altitudes throughout flight. The attenuation curves in Figure 5.23 provided a data base for evaluation of ozone densities and this is described in Section 4.7.

d. Nighttime Measurements

In Figure 5.24 are plotted the height variations of the signals from three MUV photometers, recorded when the spinning Orion rocket pointed them most nearly in the direction of the moon. Also shown is the variation in aspect for the flight upleg. This was determined using the ratio of the peak signals from the bottom right and top right quadrants

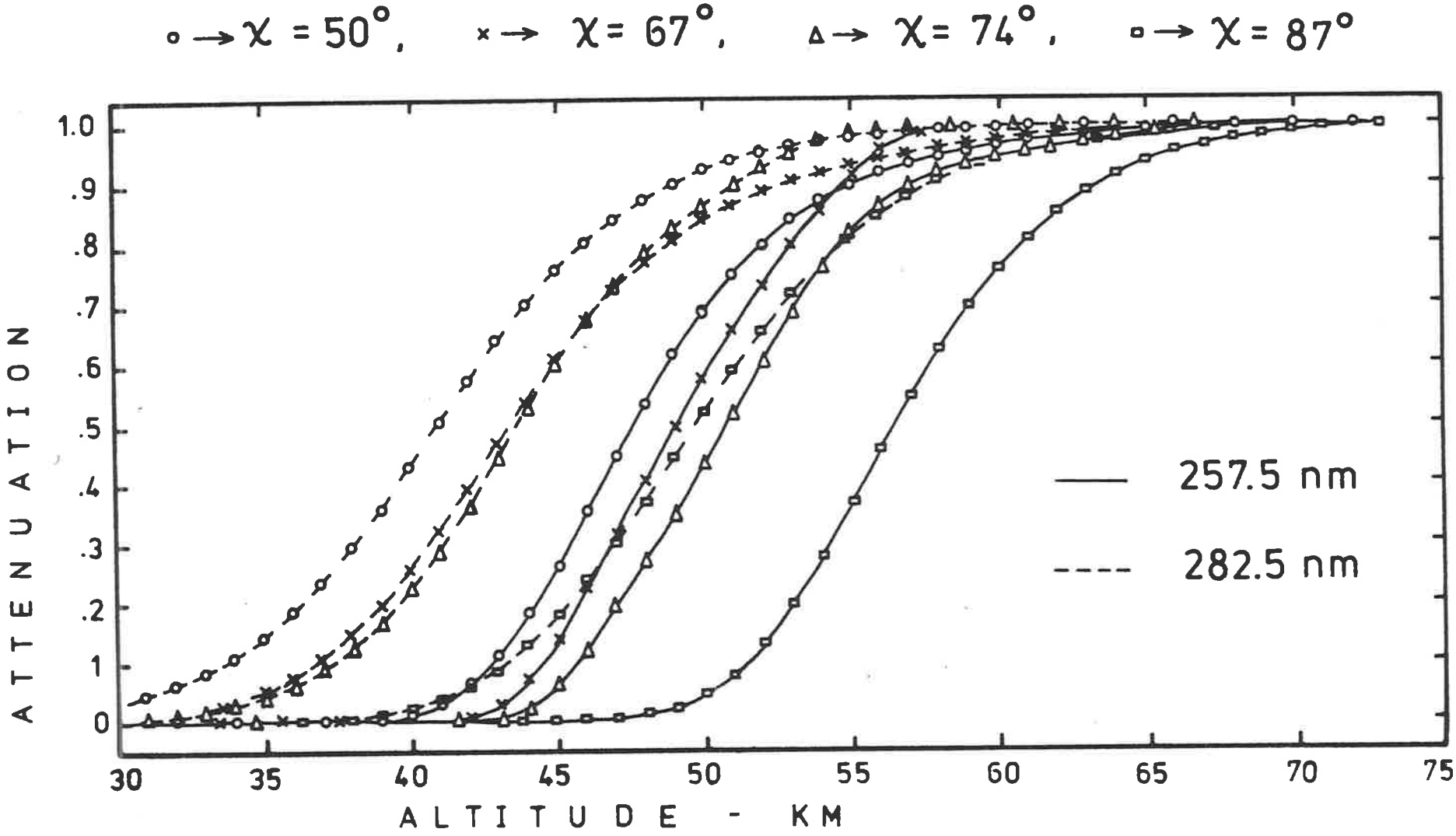

Figure 5.23 Experimental attenuation curves, measured at different solar zeniths.

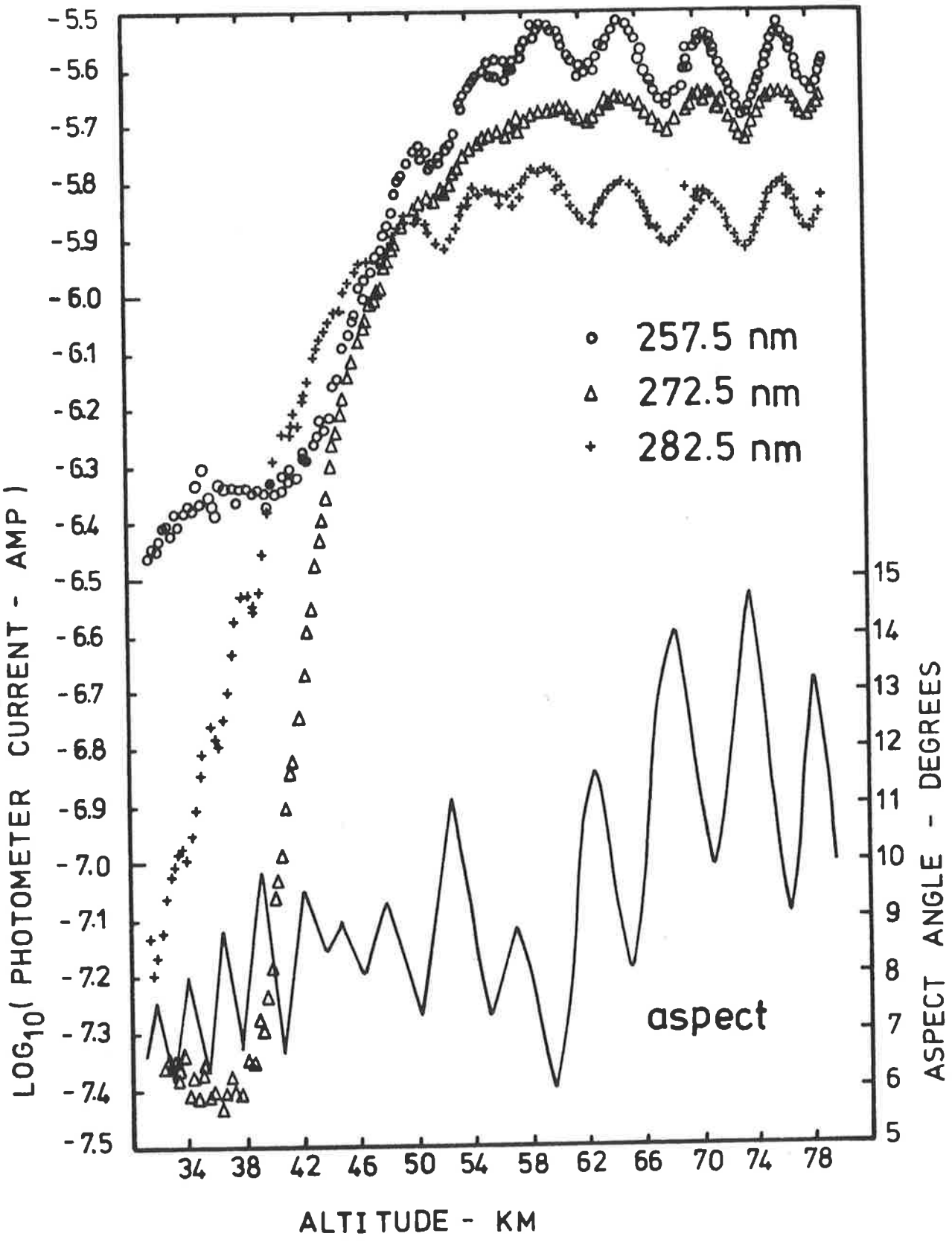

Figure 5.24 Height profiles of photometer signals and aspect angle, from the nighttime experiment.

of the aspect sensor in conjunction with the calibration curves provided in Figure 5.11. Referring to Figure 5.19, the detectors were inclined at an angle $\theta = 7^{\circ}$ to the plane of rotation and the angle measured by the aspect sensor was the value of γ when $\beta = 0$.

Initially, aspect corrected absorption curves were generated by using the measured value of γ to determine a value of β, via Equation 5.5, such that α remained constant at 15°. By fitting a parabola, in the region of signal maximum, to the signal data as a function of time and using the local period of rotation to convert β into an equivalent time, the signal from the photometer rotated through β was then obtained. An intensity profile generated in this way represented the output of the photometer due to MUV radiation incident at 15° to the normal. In practice, because the resultant absorption curves exhibited a large degree of scatter, use was made of an alternative approach for which the aspect corrected raw data was less scattered.

The correlation between photometer signal and aspect angle, visibly evident in Figure 5.24, was established analytically by fitting a parabola to the variation of signal with aspect, at altitudes above 72 km. This enabled modification of the curves of Figure 5.24 to provide intensity profiles of the photometer signals due to MUV radiation incident at 10° to the detector normal, and such aspect corrected profiles are illustrated in Figure 5.25.

The smooth curves in Figure 5.25 were drawn by hand using computer generated plots of the raw data for which the altitude scale was 1 km per cm and the signal scale was 0.05×10^{-6} amp per cm. Data from the nighttime experiment was analyzed prior to that of the daytime experiments and it was the tedium and inefficiency of manually smoothing the raw data that promoted the alternate analytic representation discussed

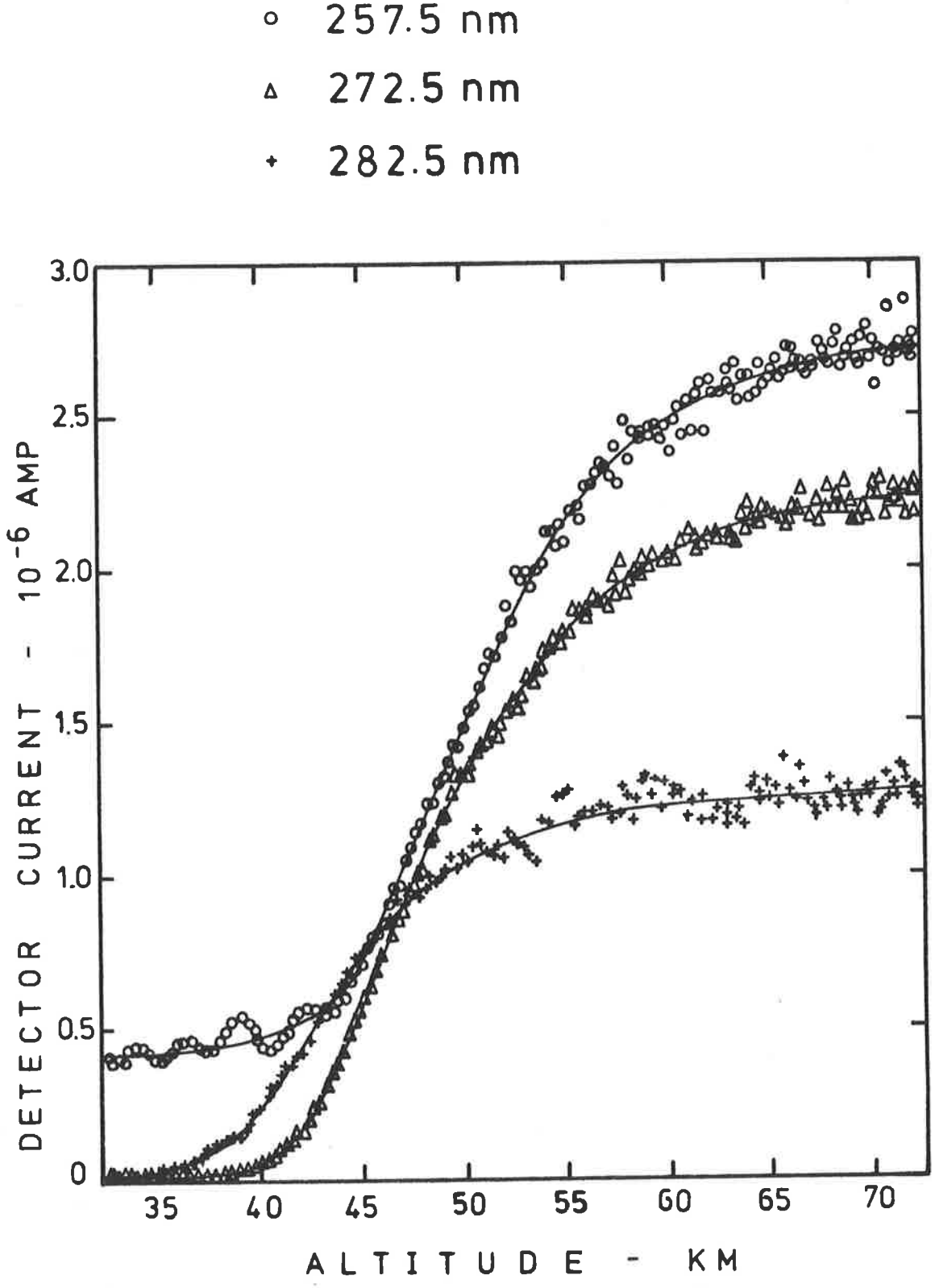

Figure 5.25 Experimental absorption curves from the nighttime experiment; the photometer signals have been corrected for lunar flux incident at 10°.

in the previous section. Typical attenuation profiles measured by the three types of photometers of the nighttime experiment are provided in Figure 5.26.

5.7 OZONE ABSORPTION CROSS-SECTIONS IN THE HARTLEY BAND

Having measured the attenuation of MUV radiation in the stratosphere and mesosphere, the number of absorbing ozone molecules, over the height range of the attenuation profile, can be obtained once the effective absorption cross-section of the detector (Equation 2.15) has been calculated.

This requires knowledge of the ozone absorption cross-sections in the wavelength region of the Hartley band, at temperatures which characterize the atmospheric environment of the absorbing ozone. For the photometer channels of the rocket-borne ozone detectors, effective absorption cross-sections were calculated following consideration of experimental investigations of how ozone molecules absorb MUV radiation in the Hartley band, both at room temperature and at lower temperatures typical of the altitude region 25 to 80 km.

a. Numerical Values

It is generally agreed in the literature that the early measurements by Inn and Tanaka (1953, 1959) have provided the most appropriate numerical values for the room temperature absorption cross-sections of ozone's Hartley band.

In their experiment, light from a continuum source was detected photoelectrically after passing through pure ozone in an absorption cell situated at the exit slit of a moderate resolution monochromator. Measurements of the absorption cross-sections, made over a wide range of

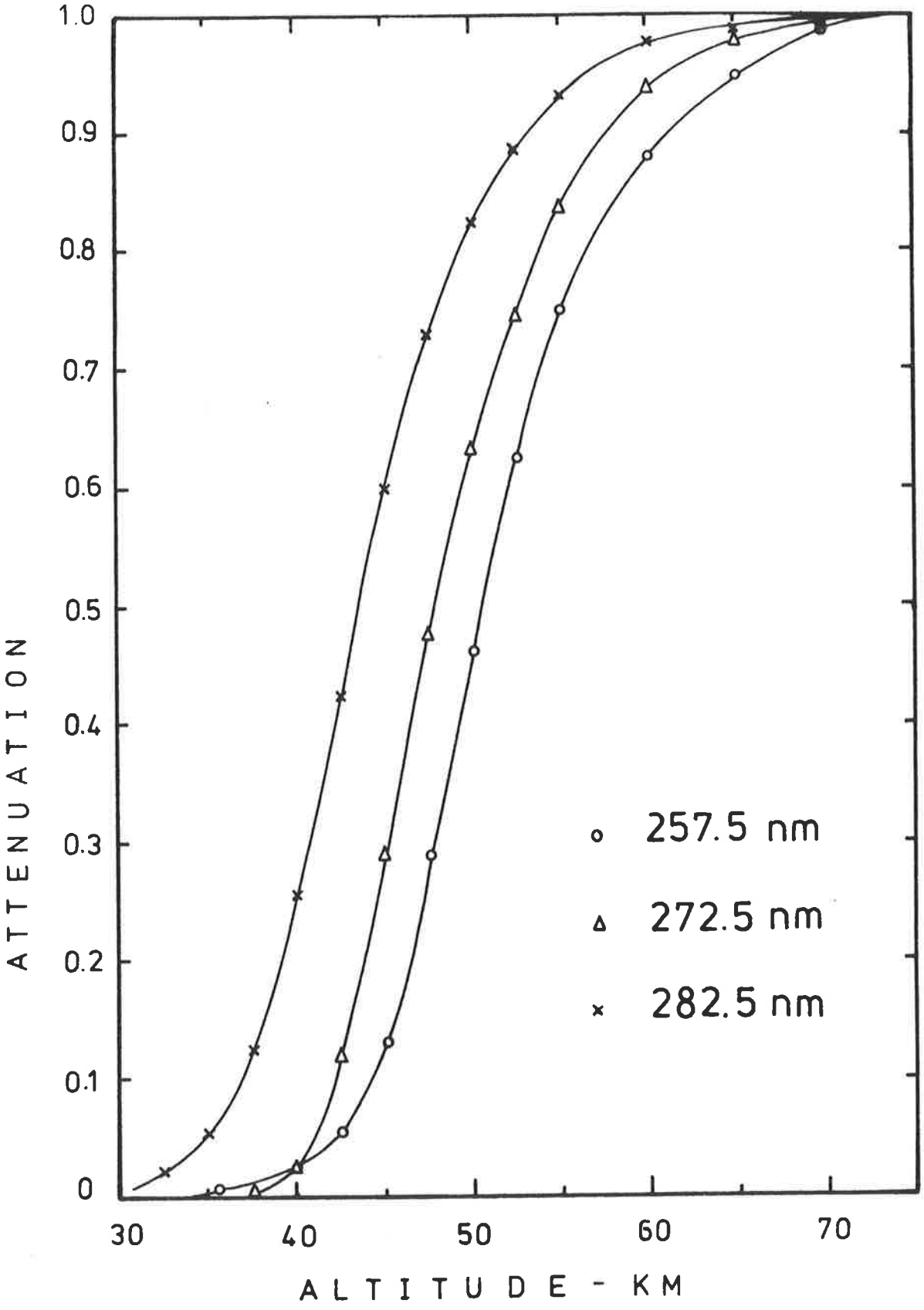

Figure 5.26 Experimental attenuation of lunar MUV radiation.

pressures, agreed within 5%, indicating the lack of any pressure effects.

From photographic measurements, Vigroux (1953) reported cross-sections 10% lower in the region of the maximum (235 to 270 nm) while similar measurements by Ny and Choong (1933) were as much as 20% higher than those of Inn and Tanaka (1953).

Additional photoelectric measurements using a continuum source (Griggs, 1968) and line emission sources (Hearn, 1961; DeMore and Raper, 1964) have verified the Inn and Tanaka values, and numerical results from these experiments agree within ± 2% (Hudson, 1971).

Despite the revision by Vigroux of his original results (Vigroux, 1969), the absorption cross-section at 287.6 nm remained 7% lower than the Inn and Tanaka values although the discrepancy at 255.5 nm was resolved.

Room temperature measurements made by Simons *et al* (1973) were reported to be 3% larger than those of Inn and Tanaka at 255.5 nm with the difference increasing monotonically to 12% at 301.9 nm.

In response to the requirement of accurate numerical cross-section values, essential for reliable investigation of atmospheric ozone densities, the National Bureau of Standards is currently undertaking new measurements, using a 2-metre Ebert monochromator. Until these results are available, the Inn and Tanaka results have been recommended (Hudson, 1971; Hudson, 1974; Griggs, 1968; Ackerman, 1972; Klenk, 1980) for use in aeronomic calculations.

b. Temperature Dependence

Inn and Tanaka (1953) measured the absorption cross-sections of ozone at 18° C. However, as illustrated in Figure 1.2, the equilibrium

temperature of ozone in the stratosphere and mesosphere ranges between 0°C and 80°C. Vigroux's experiments (Vigroux, 1953) included measurements at - 30°C, - 44°C, - 59°C and - 92°C as well as at 27°C. The ratio of the value of the cross-section at 27°C to its value at - 44°C, was observed to decrease from 0.98 at 255 nm to 0.90 at 310 nm.

From measurements at 27°C and - 78°C, Simons *et al* (1973) reported a temperature dependence different by 3 to 4% in the region 255 to 290 nm from that found by Vigroux.

While the effect of temperature on ozone's Hartley band absorption is not large, being only slightly greater than the experimental uncertainty for the wavelengths from 255 nm to 290 nm, it is preferable that it be included in atmospheric absorption spectroscopy analyses to reduce the uncertainties of the resultant ozone densities. From a survey of ozone absorption cross-section measurements, in an attempt to define a set of numerical values for use in processing satellite UV data, Klenk (1980) has recommended the absorption cross-sections of Inn and Tanaka (1953), adjusted to - 44°C with Vigroux's (1953) temperature coefficients. Experimental evidence from satellite measurements has confirmed that these values lead to the most consistent results among various determinations of total ozone.

With reference to Figure 1.2, it is evident that below 80 km the temperature of the atmosphere is not constant at - 44°C. The temperature dependence of atmospheric ozone absorption can be more appropriately defined by correcting Inn and Tanaka's values with Vigroux's coefficients, scaled according to a typical temperature profile of the stratosphere and mesosphere.

Hudson (1973) has tabulated Vigroux's temperature corrections for absorption at seven wavelengths in the Hartley band. This data was used, in conjunction with the U.S. Standard Atmosphere, 1976 temperature data (Figure 1.2), to generate the altitude dependence of the absorption cross-section at each of the seven wavelengths, and the results are plotted in Figure 5.27.

c. Effective Absorption Cross-Sections

Effective absorption cross-sections were calculated for each photometer from Equation 2.15 ;

$$\sigma_{EFF}(h) = \frac{\int_{\lambda_1}^{\lambda_2} \sigma(\lambda, h)\, E(\lambda)\, \phi_0(\lambda)\, \exp[-\sigma(\lambda, h) N(h)]\, d\lambda}{\int_{\lambda_1}^{\lambda_2} E(\lambda)\, \phi_0(\lambda)\, \exp[-\sigma(\lambda, h)\, N(h)]\, d\lambda} \qquad 5.6$$

where $\sigma(\lambda, h)$ is the ozone absorption cross-section at wavelength λ, corrected for the temperature at height h,

$E(\lambda)$ is the photometer efficiency at λ,

$\phi_0(\lambda)$ is the extraterrestrial solar flux at λ, and

$N(h)$ is the ozone column density above height h.

At each height, the attenuation of the photometer signal due to the column density $N(h)$ was also calculated ;

$$\frac{I(h)}{I_0} = \frac{\int_{\lambda_1}^{\lambda_2} E(\lambda)\, \phi_0(\lambda)\, \exp[-\sigma(\lambda, h)\, N(h)]\, d\lambda}{\int_{\lambda_1}^{\lambda_2} E(\lambda)\, \phi_0(\lambda) d\lambda} \qquad 5.7$$

Initially, Equations 5.6 and 5.7 were evaluated at successive km intervals by using Simpson's rule to numerically integrate from λ_1 to

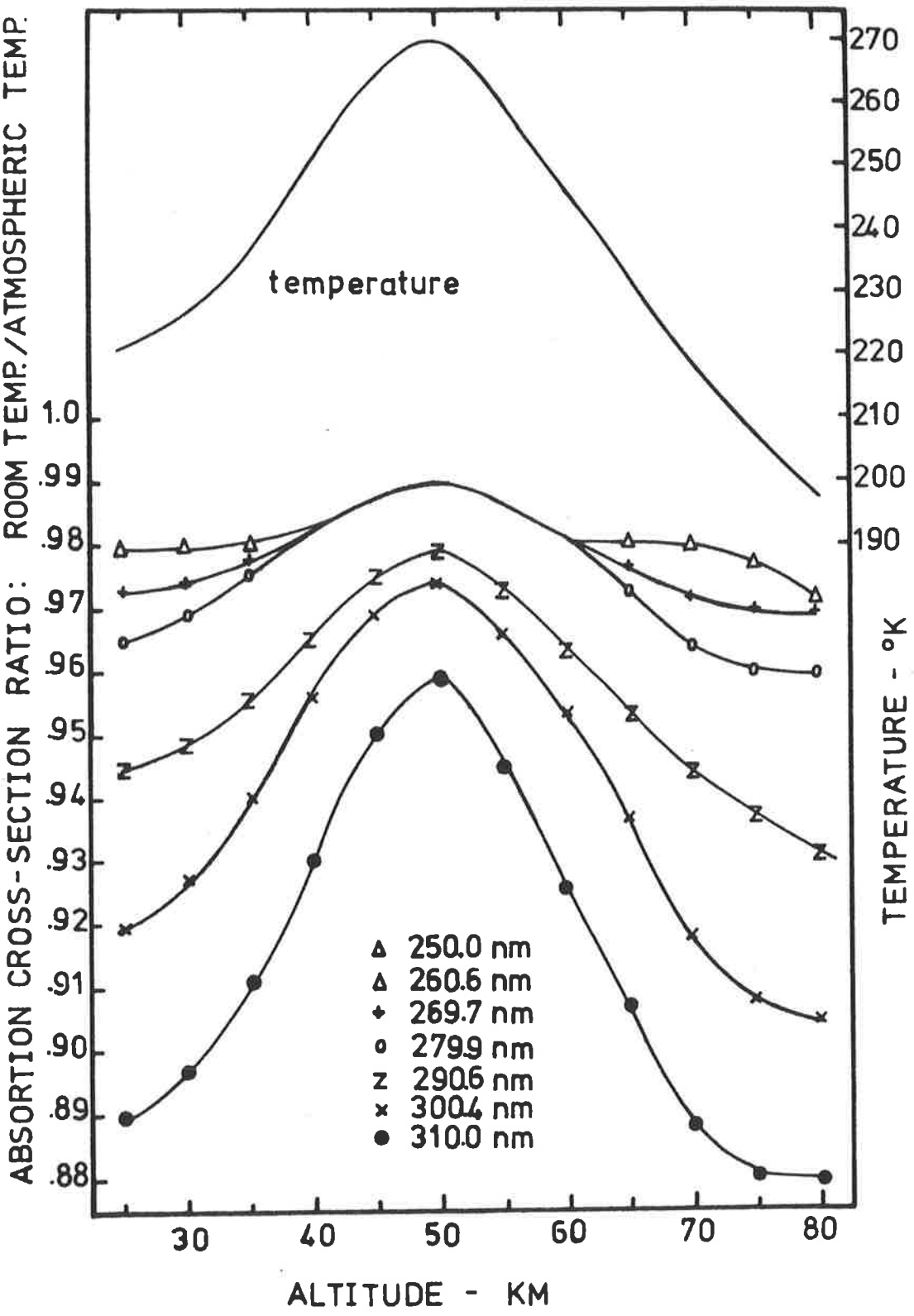

Figure 5.27 Dependence of ozone absorption cross-sections on atmospheric temperature.

λ_2, where $\lambda_1 - \lambda_2 = 50$ nm, in steps of 1 nm. $E(\lambda)$ was available for each photometer, over a range of angles of the incident radiation, from the laboratory calibrations described in Section 5.4a (Figure 5.9). For the extraterrestrial solar flux $\phi(\lambda)$, the tabulation, in 1 nm intervals, by Donnelly and Pope (1973), of Broadfoot's (1972) measurements was used. This solar spectral data is illustrated in Figure 5.28, together with the ozone absorption cross-sections $\sigma(\lambda)$ measured at room temperature by Inn and Tanaka (1953). A temperature correction for the absorption cross-section at each wavelength and height specified by Equations 5.6 and 5.7 was obtained from 2-way interpolation of a matrix representation of the data in Figure 5.27. Ozone column densities N(h) were generated from the U.S. Standard Atmosphere, 1976. In Figure 5.29, calculated effective absorption cross-sections for three MUV photometers which responded over different wavelength intervals are plotted as functions of the attenuated photometer signals, for illumination at 5°, 10° and 15°. The σ_{EFF} utilized in this way depended only on the total number of absorbing molecules between the source and the photometer, and were independent of the height profile of the model density used for input. Figure 5.29 emphasizes that it is essential to know the angle of the incident radiation with respect to the photometer normal, as well as the photometer spectral response at this angle, to enable the most appropriate estimates of σ_{EFF} to be included in subsequent analysis of the absorption profiles.

The most accurate ozone densities derive from the use of σ_{EFF} for which uncertainties have been minimized. For this reason, Equations 5.6 and 5.7 were also calculated with integration steps of 0.1 nm, using Broadfoot's (1972) solar flux data at 0.1 nm intervals and incorporating a more extensive representation of the temperature effect, as defined by Vigroux's (1953) measurements at five temperatures for 83 wavelengths between 244.8 and 311.2 nm.

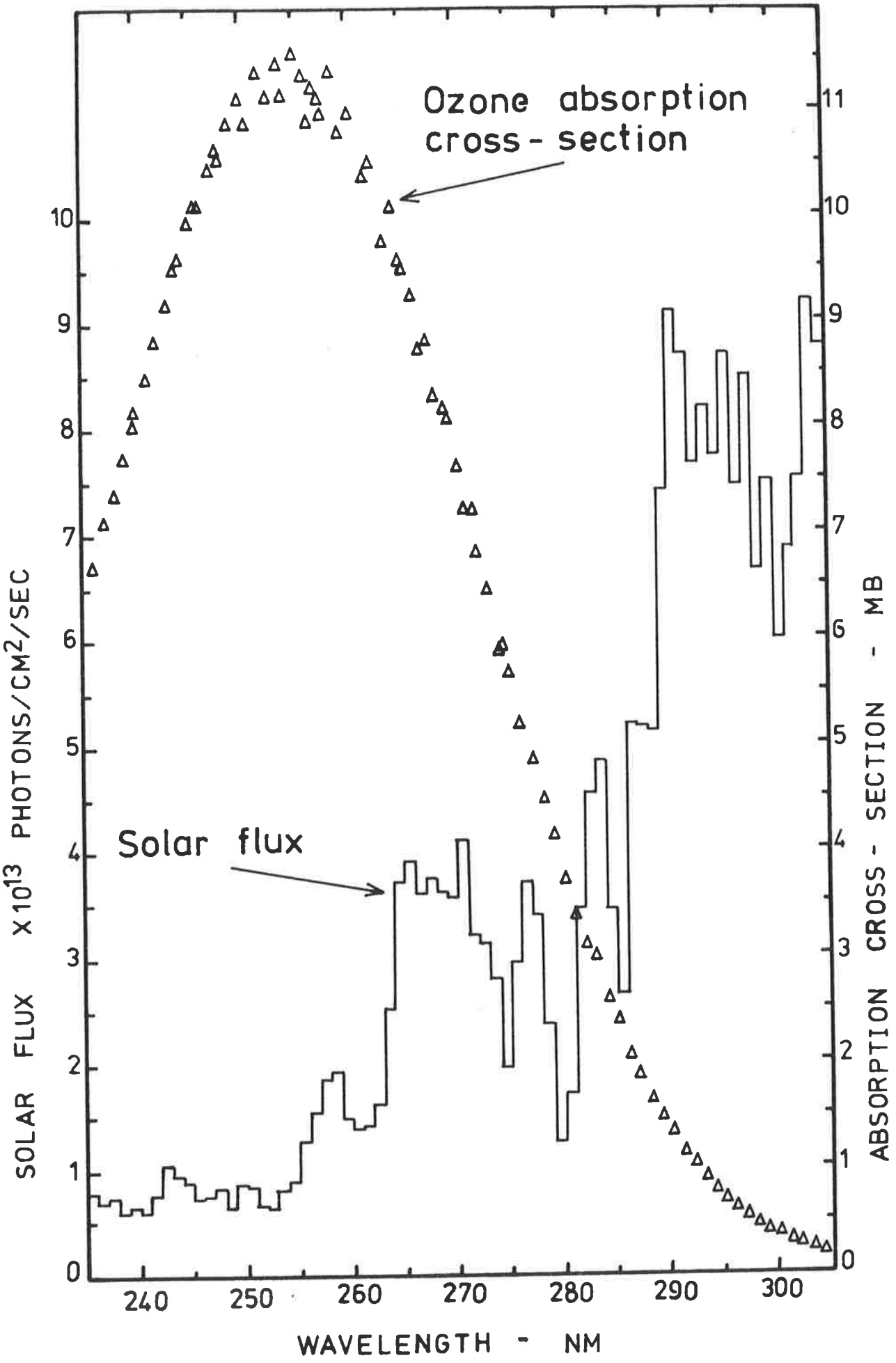

Figure 5.28 MUV solar flux (Donnelly & Pope, 1973) and ozone absorption cross-sections (Inn & Tanaka, 1953).

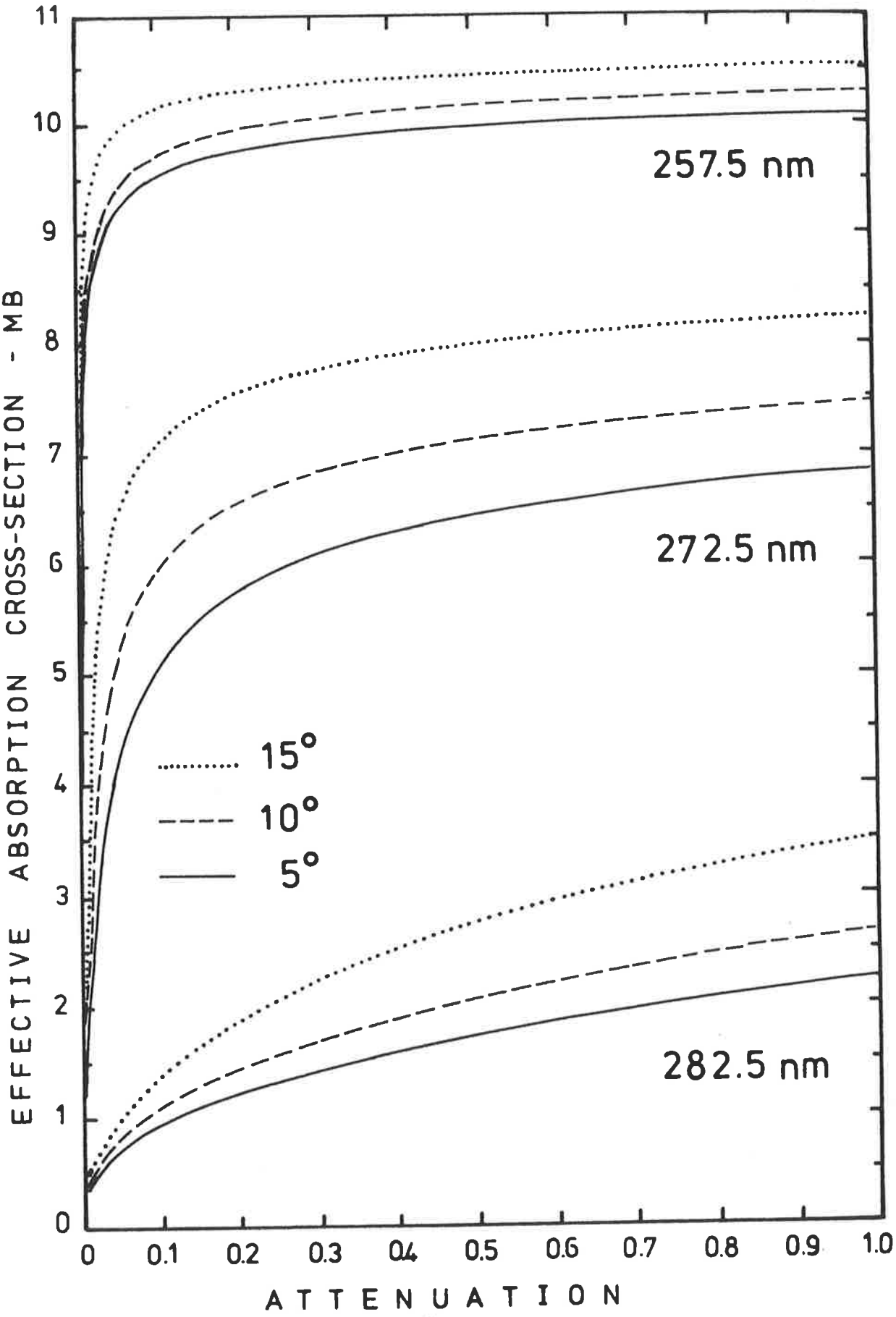

Figure 5.29 Angular dependence of the effective absorption cross-sections for MUV photometers.

Table 5.2 provides some examples of the results of such calculations, with the temperature

(a) constant at room temperature (17° C),

(b) provided from *in situ* experimental measurements at the time of the rocket flights (see Appendix E),

(c) constant at - 44° C, as recommended by Klenk (1980), and

(d) the U.S. Standard Atmosphere profile.

Also included in Table 5.2 are the σ_{EFF} determined with integration resolution 1 nm.

The effect of temperature on σ_{EFF}, for a photometer centred at 282.5 nm, is illustrated in Figure 5.30. Differences caused by the various temperature profiles were of the order of a few percent and smaller for the photometers at 257.5 nm than for those at 282.5 nm. Calculations with 0.1 nm integration steps, utilizing experimental temperature profiles, were assumed superior, and perturbations of this data due to less satisfactory input parameters are summarized, for respectively 257.5 nm and 282.5 nm, when the attenuation is 0.5, as follows: using room temperature cross-sections, σ_{EFF} was overestimated by 1.5% and 3.8%; with the temperature constant at - 44° C, σ_{EFF} was under-estimated by 1.6% and 2%; and using the U.S. Standard Atmosphere temperature profile, σ_{EFF} was over-estimated by 0.6% and 1.9%. In addition, integration with 1 nm steps effected differences of about 1% and 2.5% but the computing time was reduced by a factor of 50!

5.8 VERTICAL DISTRIBUTIONS OF OZONE

a. Density Calculations

From each measured attenuation curve (for example, Figures 5.23 and 5.26), the ozone density at height h was determined by

$$n(h) = \frac{1}{F(h)\ \sigma_{EFF}(h)\ I(h)} \frac{dI(h)}{dh}$$

TABLE 5.2 Calculations of the effective absorption cross-sections (Mb) for two MUV photometers.

	Experimental temp. - Figure E.2	Temp. = - 44°C	Room temp. = 17°C	U.S. Standard Atmosphere temp. - Figure E.2	
	Integration resolution = 0.1 nm				1.0 nm
	257.5 nm, 10° incidence (see Figure 5.9)				
.0	1.415	1.420	1.524	1.415	1.506
.1	9.684	9.598	9.910	9.712	9.699
.2	9.950	9.835	10.146	9.970	9.993
.3	10.072	9.935	10.250	10.089	10.034
.4	10.152	9.997	10.314	10.169	10.096
.5	10.207	10.041	10.359	10.231	10.140
.6	10.246	10.074	10.393	10.283	10.173
.7	10.272	10.099	10.419	10.314	10.199
.8	10.285	10.120	10.441	10.336	10.220
.9	10.274	10.138	10.459	10.314	10.237
1.0	10.171	10.153	10.475	10.171	10.253
	282.5 nm, 10° incidence (see Figure 5.9)				
.0	.356	.358	.363	.357	.349
.1	1.074	1.080	1.162	1.080	1.079
.2	1.409	1.411	1.515	1.431	1.413
.3	1.668	1.659	1.773	1.696	1.662
.4	1.888	1.863	1.980	1.910	1.866
.5	2.075	2.032	2.155	2.088	2.035
.6	2.236	2.181	2.305	2.244	2.184
.7	2.376	2.310	2.436	2.382	2.313
.8	2.502	2.426	2.553	2.508	2.429
.9	2.612	2.530	2.659	2.625	2.533
1.0	2.615	2.625	2.754	2.615	2.628

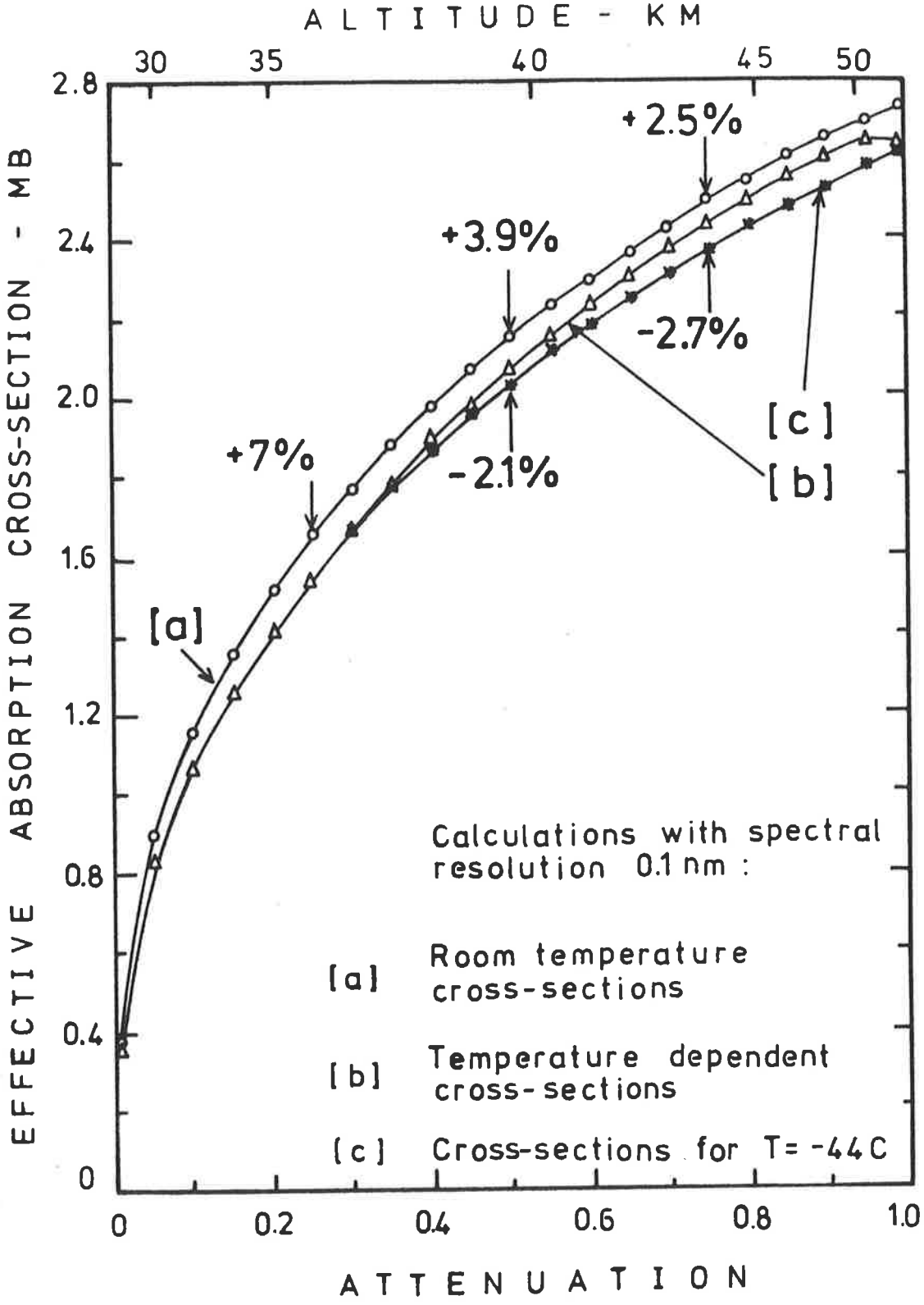

Figure 5.30 The effect of the upper atmosphere temperature on the effective absorption cross-section of the 282.5 nm channel illuminated at 10°.

The optical depth factor F(h) was calculated from Equation 2.7 for those measurements when the source zenith angle χ was $\geqslant 65^{\circ}$. These calculations, for flights 31.011, 31.012, 31.013, and 30.009, are provided in Appendix D. For data acquired on 21 October, the factor secχ was substituted for F(h).

Figure 5.31 illustrates the importance of using the optical depth factor instead of secχ for applications of absorption spectroscopy when the zenith angle is large. Here, the two qnaitities are compared throughout the upleg and downleg of the sunset flight 31.013. Near apogee the solar zenith angle was 87° for which secχ was 18.3% greater than the calculated optical depth factor. At smaller zenith angles this discrepancy diminishes rapidly; for flight 31.011, for which the zenith angle near apogee was 73.6°, secχ was 0.77% greater than F(h) and for flight 31.012, with $\chi = 66.6^{\circ}$ near apogee, the difference between secχ and F(h) was only 0.2%.

Effective absorption cross-sections σ_{EFF} were calculated over a range of altitudes, following the procedures described in Section 5.7c and incorporating the photometer's spectral response at the angle of the incident radiation for which the raw signals had been corrected. At a particular height, the appropriate value of σ_{EFF} was identified by the measured attenuation; examples of the dependence of σ_{EFF} on the attenuated signal have been provided in Figure 5.29.

I(h) was obtained directly from the smooth attenuation profile and the derivative of the analytic function provided the magnitude of dI/dh.

An estimate of the uncertainty $\Delta n(h)$ in n(h), derived from a particular attenuation profile, was calculated as

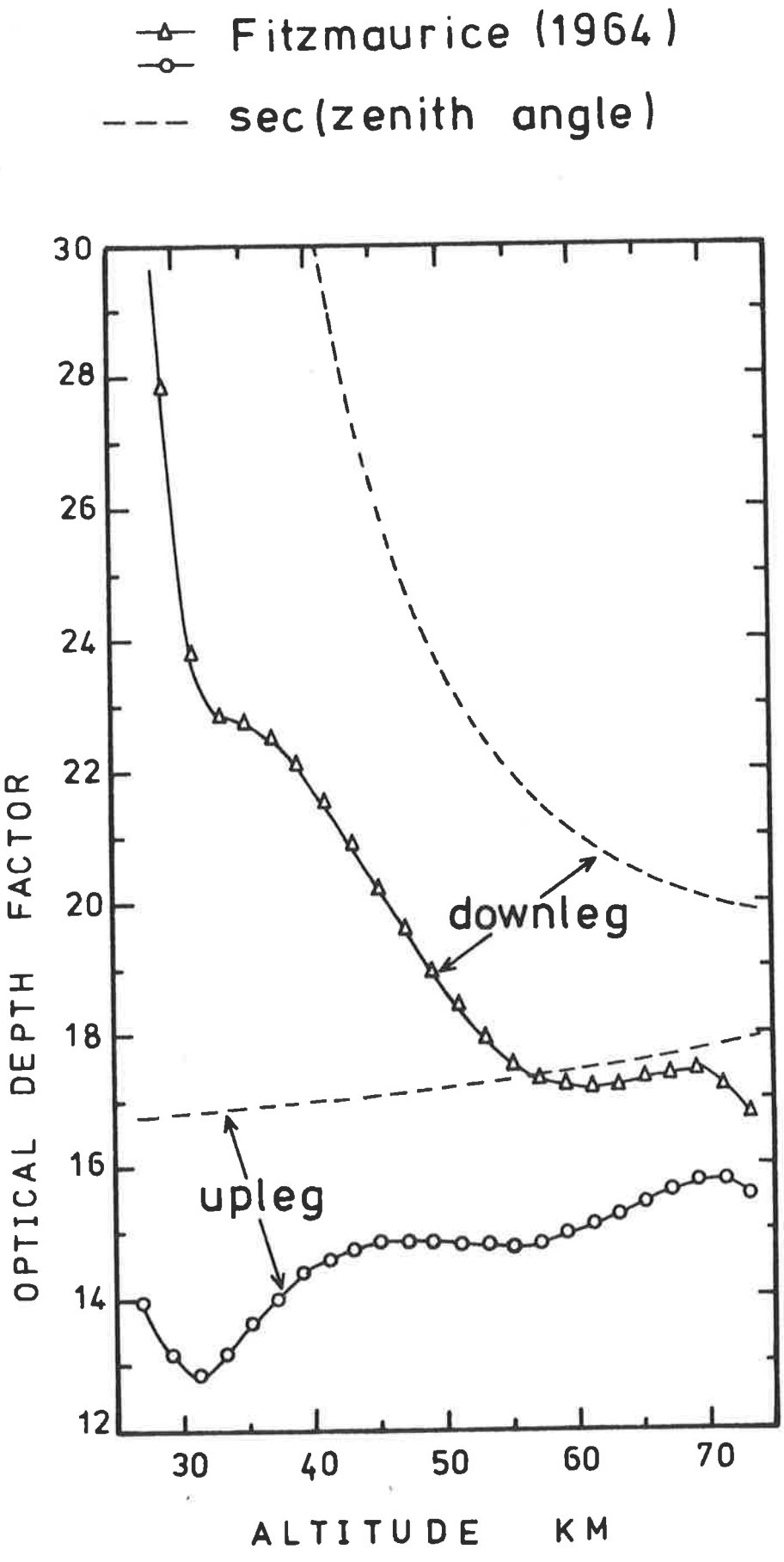

Figure 5.31 Optical depth factor calculations for flight 31.013, at sunset.

$$\left[\frac{\Delta n}{n}\right]^2 = \left[\frac{\Delta F}{F}\right]^2 + \left[\frac{\Delta\sigma_{EFF}}{\sigma_{EFF}}\right]^2 + \left[\frac{\Delta I}{I}\right]^2 + \left[\frac{\Delta dI/dh}{dI/dh}\right]^2$$

The relative uncertainty in the optical depth factor was taken as 3% for $\chi \geq 80^\circ$, 1% for $65^\circ \leq \chi < 80^\circ$ and negligible for $\chi < 65^\circ$.

The primary source of uncertainty in σ_{EFF} was considered to arise from the collective dependence on the angle of illumination of the detector of the photometer's spectral response and hence the relative solar flux and the ozone absorption cross-sections appropriate for height h. Assuming the angle of illumination was certain to within $\pm 2^\circ$, the corresponding range of σ_{EFF} was used to estimate $\Delta\sigma_{EFF}$. Therefore, $\Delta\sigma_{EFF}/\sigma_{EFF}$ was different for photometers which responded over different wavelength intervals and depended on the angle for which the raw absorption curve data had been corrected. This is summarized in Table 5.3.

Uncertainty in the attenuated signal was attributed to scatter of the raw data and also to uncertainties in estimating the maximum and minimum value of the detector signal. From the smoothed profile of the photometer signal were obtained estimates of the maximum and minimum signals, respectively I_{max} and I_{min}, and the attenuated signal at a particular height was determined from the smoothed photometer signal I_{exp} at that height, according to

$$I = \frac{I_{exp} - I_{min}}{I_{max} - I_{min}}$$

Then

$$\left[\frac{\Delta I}{I}\right]^2 = \left[\frac{\Delta I_{exp} + \Delta I_{min}}{I_{exp} - I_{min}}\right]^2 + \left[\frac{\Delta I_{max} + \Delta I_{min}}{I_{max} - I_{min}}\right]^2$$

so that $\Delta I/I$ exhibited a different height dependence for each photometer. Examples of typical numerical values for the quantities used to determine $\Delta I/I$ are provided, from the absorption curves in Figure 5.25, in Table

TABLE 5.3 Estimates of the uncertainties in the effective absorption cross-sections due to the angular dependence of the response of photometers at different MUV wavelengths.

Incident Angle	Wavelength of photometer's peak response - nm	$\Delta\sigma_{EFF}/\sigma_{EFF}$
0°	257.5	0.01
	282.5	0.04
10°	257.5	0.01
	272.5	0.03
	282.5	0.06
15°	257.5	0.01
	282.5	0.10

5.4. In particular, the magnitude of ΔI_{exp} was obtained by comparing the raw data I_{raw} with the smoothed data I_{fit} over a height interval of 1 km, centred on the height at which $\Delta I/I$ was evaluated;

$$\Delta I_{exp} = 1/2 \sqrt{\frac{\Sigma(I_{fit} - I_{raw})^2}{N(N-1)}}$$

where N varied from 3 to 5 for the nighttime flight, and has been given for the duration of a daytime flight in Figure 5.15b.

Evaluation of the uncertainty in the derivative $\Delta dI/dh$ has been described in Chapter 4. Values of the derivative dI/dh were normalized to the maximum which was attributed the least uncertainty, of magnitude 2.5%. Table 5.5 illustrates how the uncertainty in the density was partitioned amongst the various contributing sources. In those altitude regions where the attenuation was either very small or very large, the diminishingly small numerical value of the derivative caused its relative uncertainty to be large. For this reason, ozone densities were generally obtained from altitude regions where the attenuated signal was between 0.02 and 0.98.

It can be seen from Table 5.5 that, at a particular altitude, the uncertainties in the measurements by photometers covering different wavelength intervals may be quite different. The best estimate of the ozone density determined by each detector was considered to be a weighted average of the results from its individual photometers. Therefore,

$$\bar{n}(h) = \frac{\sum_{i=1}^{M} w_i(h)\, n_i(h)}{\sum_{i=1}^{M} w_i(h)}$$

where M is the number of photometer channels and

Wavelength of photometer's peak response - nm	$I_{max} \pm \Delta I_{max}$ x 10^{-6} amp	$I_{min} \pm \Delta I_{min}$ x 10^{-6} amp	$I_{exp} \pm \Delta I_{exp}$ x 10^{-6} amp	$\frac{\Delta I_{max} + \Delta I_{min}}{I_{max} - I_{min}}$	$\frac{\Delta I_{exp} \pm \Delta I_{min}}{I_{exp} - I_{min}}$	$\frac{\Delta I}{I}$
257.5						
40 km	2.74 ± 0.01	0.414 ± 0.01	0.473 ± 0.016	0.009	0.441	0.441
60 km	2.74 ± 0.01	0.414 ± 0.01	2.484 ± 0.019	0.009	0.014	0.017
282.5						
40 km	1.27 ± 0.01	0.013 ± 0.005	0.246 ± 0.005	0.012	0.042	0.044
60 km	1.27 ± 0.01	0.013 ± 0.005	1.226 ± 0.011	0.012	0.013	0.018

TABLE 5.4 Examples of the relative uncertainty of the attenuated signal.

Wavelength of photometer's peak response - nm	$\frac{\Delta F}{F}$	$\frac{\Delta \sigma_{EFF}}{\sigma_{EFF}}$	$\frac{\Delta I}{I}$	$\frac{\Delta dI/dh}{dI/dh}$	$\frac{\Delta n}{n}$
257.5					
40 km	0.01	0.01	0.44	0.23	0.50
60 km	0.01	0.01	0.017	0.105	0.11
282.5					
40 km	0.01	0.06	0.044	0.029	0.08
60 km	0.01	0.06	0.018	0.36	0.37

TABLE 5.5 Numerical examples of sources of uncertainty contributing to the total uncertainty in the measured ozone density.

$$w_i(h) = \frac{1}{\Delta n_i(h)^2}$$

The uncertainty in the average density was estimated as

$$\overline{\Delta n}(h) = \frac{\sum_{i=1}^{M} w_i(h) \quad \Delta n_i(h)}{\sum_{i=1}^{M} w_i(h)}$$

where each $\Delta n_i(h)$ was determined similarly to the example in Table 5.5.

b. Daytime Ozone Profiles

Daytime ozone densities were obtained from six detectors during their ascent on Nike Orion rocket vehicles and from five of these detectors as they descended on parachutes. Upleg and downleg data were considered independent and ozone profiles were grouped according to the local time of the measurement. On 21 October 1979, within 2½ hours of local noon, a total of 5 density profiles was obtained. These results are provided in Table 5.6, together with an average profile. In Table 5.7 are data pertaining to four measurements during the morning of 1 November, 1979 and in Table 5.8 are two ozone density profiles obtained at sunset on the same day.

Included in the Tables 5.6, 5.7 and 5.8 are two different estimates of the uncertainty in the average density for each of these sets of K near simultaneous measurements. Evaluation of the sample standard deviation of a set of measurements of a particular parameter indicates the reproducibility of the measuring technique. So for the precision of the ozone density at height h,

Height - km	Ozone number density per cm^3							
	31.010 upleg	31.010 downleg	31.009 upleg	31.008 upleg	31.008 downleg	Average	Precision	Accuracy
32	2.12×10^{12}	2.48×10^{12}	2.57×10^{12}	2.53×10^{12}	1.99×10^{12}	2.34×10^{12}	5.0%	15.1%
34	1.73	1.86	1.95	1.91	1.58	1.81	3.8	9.5
36	1.31	1.35	1.33	1.36	1.16	1.30	2.8	7.0
38	9.37×10^{11}	9.58×10^{11}	9.57×10^{11}	9.29×10^{11}	8.18×10^{11}	9.20×10^{11}	2.8	5.9
40	6.34	6.61	6.67	6.06	5.57	6.25	3.2	5.6
42	4.12	4.39	4.23	3.83	3.66	4.05	3.3	6.2
44	2.60	2.69	2.55	2.43	2.39	2.53	2.2	6.7
46	1.61	1.58	1.53	1.50	1.52	1.55	1.3	6.6
48	9.87×10^{10}	9.82×10^{10}	8.98×10^{10}	8.86×10^{10}	9.05×10^{10}	9.32×10^{10}	2.3	6.6
50	5.96	6.05	6.45	5.57	5.40	5.89	3.2	6.7
52	3.52	3.52		3.87	3.51	3.60	2.5	8.1
54	2.03	2.03		2.74	2.46	2.31	7.5	10.1
56	1.18	1.37		1.77	1.65	1.49	9.1	12.9
58	7.11×10^{9}			9.94×10^{9}	9.21×10^{9}	8.75×10^{9}	9.7	19.0
60	4.84			4.86	2.26	3.98	21.6	40.2

TABLE 5.6 Daytime ozone densities measured near noon on 21 October, 1979.

Height - km	Ozone number density per cm^3						
	31.011 upleg	31.011 downleg	31.012 upleg	31.012 downleg	Average	Precision	Accuracy
34	1.81×10^{12}		1.88×10^{12}	1.96×10^{12}	1.88×10^{12}	2.3%	44.0%
36	1.21		1.31	1.49	1.33	6.2	23.4
38	8.18×10^{11}		9.00×10^{11}	1.05	9.22×10^{11}	7.3	13.5
40	5.76	5.00×10^{11}	6.10	7.01×10^{11}	5.97	7.0	9.4
42	3.85	3.43	4.03	4.56	3.97	5.9	7.3
44	2.35	2.28	2.57	2.90	2.53	5.6	6.7
46	1.35	1.46	1.57	1.73	1.53	5.4	7.4
48	7.82×10^{10}	8.75×10^{10}	9.19×10^{10}	1.00	8.94×10^{10}	5.1	8.1
50	5.26	5.32	5.61	5.53×10^{10}	5.43	1.5	8.3
52	3.78	3.22	3.67	3.08	3.44	4.9	8.9
54	2.26	1.96	2.55	1.65	2.11	9.2	9.3
56	1.15	1.25	1.49		1.30	7.9	9.2
58	5.31×10^{9}	7.51×10^{9}			6.41×10^{9}	17.2	12.6
60	2.51	4.57			3.54	29.1	19.5

Table 5.7 Daytime ozone densities measured on the morning of 1 November, 1979.

Height - km	Ozone number density per cm^3			Precision	Accuracy
	31.013 upleg	31.013 downleg	Average		
40	5.79×10^{11}		5.79×10^{11}		25.8%
42	3.48	3.41×10^{11}	3.44	1.4%	31.2
44	2.18	2.22	2.20	1.5	15.4
46	1.39	1.47	1.43	4.1	9.4
48	8.84×10^{10}	9.60×10^{10}	9.22×10^{10}	5.9	7.2
50	5.59	6.12	5.86	6.4	6.4
52	3.48	3.87	3.67	7.5	6.8
54	2.17	2.45	2.31	8.4	6.7
56	1.35	1.54	1.44	9.3	7.6
58	8.18×10^{9}	9.87×10^{9}	9.03×10^{9}	13.2	7.9
60	4.95	5.96	5.45	13.0	8.4
62	2.99	3.07	3.03	1.8	9.6
64	1.76		1.76		11.9
66	9.73×10^{8}		9.73×10^{8}		19.3
68	5.03		5.03		35.6
70	2.34		2.34		63.6

Table 5.8 Ozone densities measured at sunset on 1 November, 1979.

$$\Delta n_{pre}(h) = \frac{\sum_{k=1}^{K} [\,\bar{n}_k(h) - n_{av}(h)\,]^2}{K(K-1)}$$

and this represented the repeatability of the measurement technique.

However, the precision is not necessarily equivalent to the absolute accuracy of the result which is more difficult to estimate. Rather, the accuracy of the average density at a particular height from a set of K near simultaneous measurements was obtained as the average of the uncertainties of the individual densities determined from each detector and these uncertainties have been previously expressed as $\Delta\bar{n}(h)$. So

$$\Delta n_{acc}(h) = \frac{\sum_{k=1}^{K} \Delta\,\bar{n}_k(h)}{K}$$

where each $\Delta\bar{n}_k(h)$ reflected an assessment of possible sources of uncertainty that could have influenced the ozone density derived from each detector to be different from the 'true' ozone density at height h.

Shown in Figure 5.32 are ozone density profiles obtained at noon, in the morning and at sunset. Included, for comparison, is the U.S. Standard Atmosphere, 1976 model of the mid latitude ozone distribution.

c. Nighttime Ozone Profile

Measurements of the nighttime ozone densities were made using three detectors during the upleg of a single rocket flight. Results for each of these independent measurements were acquired from the weighted average densities determined by three photometer channels.

Average nighttime densities, together with the data from each individual measurement, are given in Table 5.9. Methods of calculating uncertainties in the nighttime densities were similar to those described

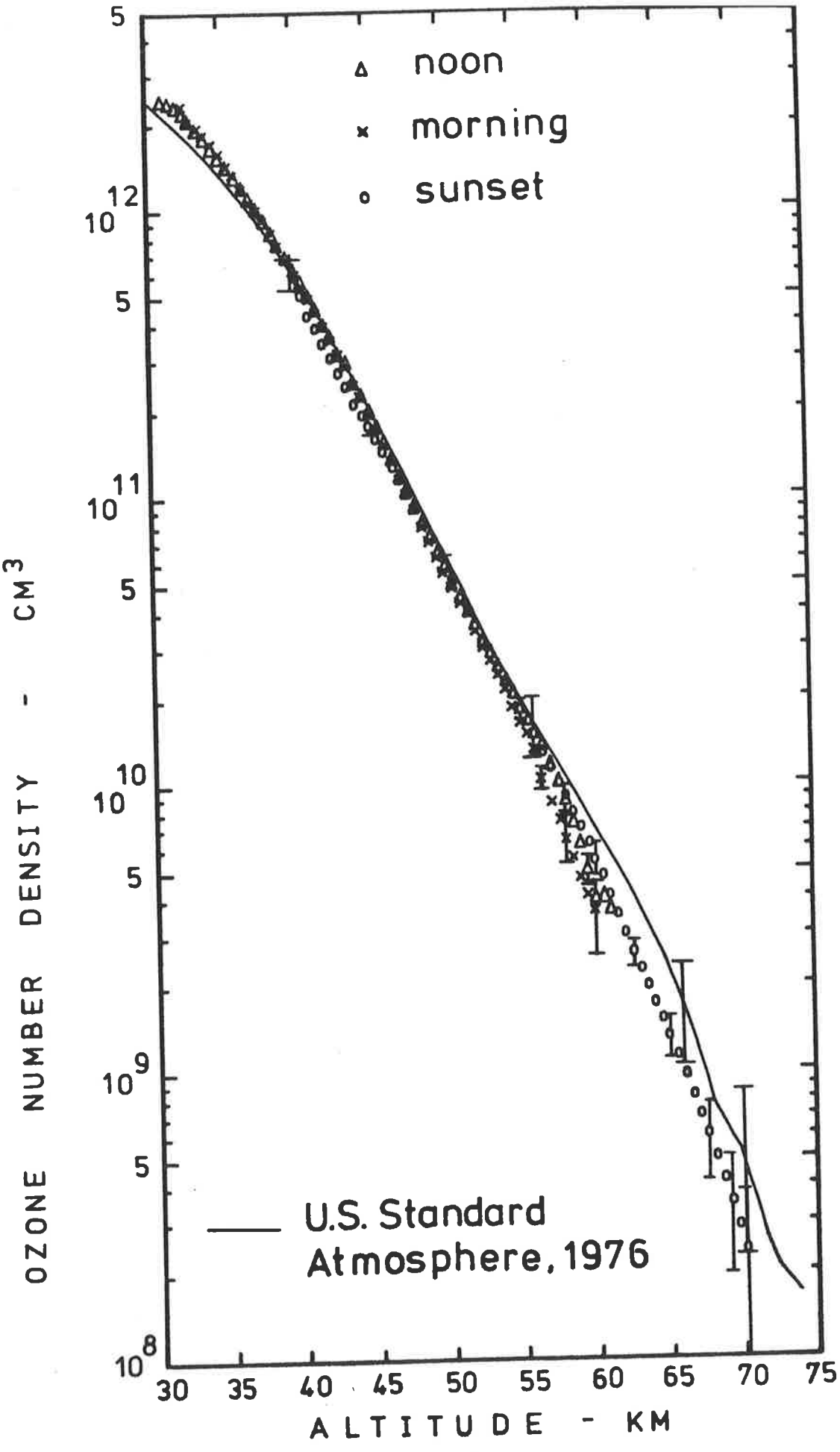

Figure 5.32 Ozone number densities measured at different times during the day.

Height - km	Ozone number density per cm^3				Precision	Accuracy
	1	2	3	Average		
34	2.20×10^{12}	1.95×10^{12}	-	2.07×10^{12}	6.0%	18.4%
36	1.27	1.55	1.30	1.37	6.5	14.2
38	9.80×10^{11}	9.78×10^{11}	8.19×10^{11}	9.26×10^{11}	5.8	9.7
40	5.02	5.36	6.52	5.64	8.0	11.0
42	3.17	3.47	3.17	3.27	3.1	8.7
44	2.29	2.18	2.02	2.16	3.6	6.3
46	1.33	1.32	1.26	1.30	1.8	5.5
48	8.56×10^{10}	8.27×10^{10}	7.72×10^{10}	8.19×10^{10}	3.0	4.8
50	5.83	5.58	5.25	5.55	3.0	4.7
52	3.65	4.03	3.48	3.72	4.4	5.3
54	2.92	2.70	2.49	2.70	4.6	5.7
56	2.13	1.83	1.70	1.88	6.7	7.0
58	1.30	1.19	1.24	1.24	2.4	9.4
60	8.74×10^{9}	7.80×10^{9}	7.63×10^{9}	8.06×10^{9}	4.3	13.5
62	5.87	5.54	5.41	5.61	2.5	18.5
64	3.81	4.00	3.55	3.79	3.5	26.7
66	2.50	3.04	2.65	2.73	5.9	36.4
68	3.38	2.15	1.81	2.45	19.4	43.8
70	1.52	1.40	1.59	1.50	3.7	63.2
72	-	8.68×10^{8}	1.64	1.25	30.7	84.9

TABLE 5.9 Nighttime ozone densities, measured on 4 November, 1979 at 0427 hours LT.

in the previous section, for the daytime data. The experimental nighttime ozone profile is shown in Figure 5.33.

d. Statistical Analysis for Measurement Precision

When three instruments are used to measure the same quantity it is possible to extract from the measurements estimates of the precision of each of the instruments. Techniques for doing this have been developed by Grubbs (1948) and modified for application to measurements of ozone densities by Grubbs (1980). Estimates of the precision of some instruments used to measure the ozone densities reported in this chapter proceeded via his instruction, as summarized below and described in mathematical detail in Appendix G.

By taking differences between each pair of simultaneous measurements of the ozone density at height h the true value of the density is cancelled leaving only the random errors and, if the errors between the instruments are uncorrelated, the three differences are independent random variables for which, if there is no measurement bias, the mean value is zero. The variance of a set of such differences, acquired, for example, from measurements at other heights, is related to the variance of each measurement instrument. Calculations of the variances for each of the three sets of differences therefore generate three simultaneous equations which can be solved to yield information about the variance of the measurements by each individual instrument, and hence the measurement precision which is the square root of the measurement variance. From the numerical examples provided in Appendix G, the typical precision of the ozone measurements described in this chapter, averaged over the entire altitude range where data was collected, was of the order of 7%. More generally, this varied from 5% to 10% for different combinations of the individual instruments used as input for the statistical analysis.

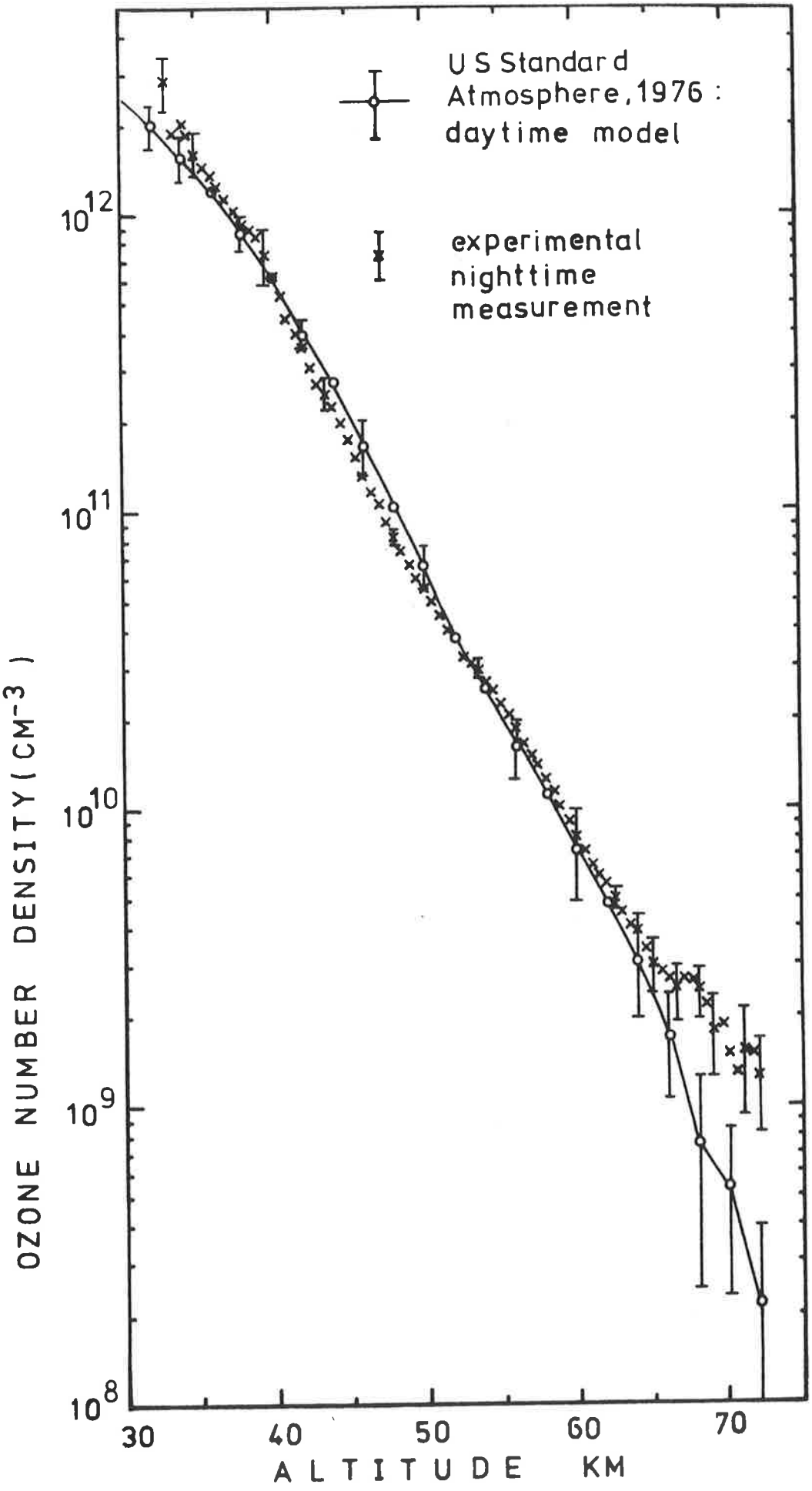

Figure 5.33 Ozone number densities measured at night.

5.9 DISCUSSION

a. Daytime Densities

In Figure 5.34 the average daytime ozone density profile measured by the experiments described in this chapter is compared with some other ozone profiles also measured, with the exception of the chemiluminescent data of Hilsenrath *et al* (1969), using absorption spectroscopy techniques. As noted previously in Section 2.3d, the U.S. Standard Atmosphere, 1976 is a mid latitude ozone model for which the data at altitudes less than about 55 km was obtained primarily at noon, with data at higher altitudes provided by twilight measurements. The model is more appropriate for times near the maximum of the 11-year solar cycle but includes data from a variety of seasons. Thus it is particularly appropriate to compare this model with the results of the present experiments which were also made at mid latitude (38°N) near a period of solar maximum. Figure 5.34 indicates that, within the variability of the model, there is excellent agreement between the two profiles at all altitudes where ozone densities were derived.

Comparison, in Figure 5.34, with the data of Watanabe and Tohmatsu (1976), also obtained at mid latitude (31°N), suggests that the average daytime profile may be the consequence of seasonal influences since its uncertainties, reflective of diurnal variability, are significantly less than the differences between their summer and winter profiles. In particular, between the altitudes 30 and 40 km the present results are consistent with the winter ozone densities of Watanabe and Tohmatsu (1976); from 40 to 55 km the present data is approximately midway between their winter and summer profiles; and at altitudes greater than 60 km there is excellent agreement between the present results and

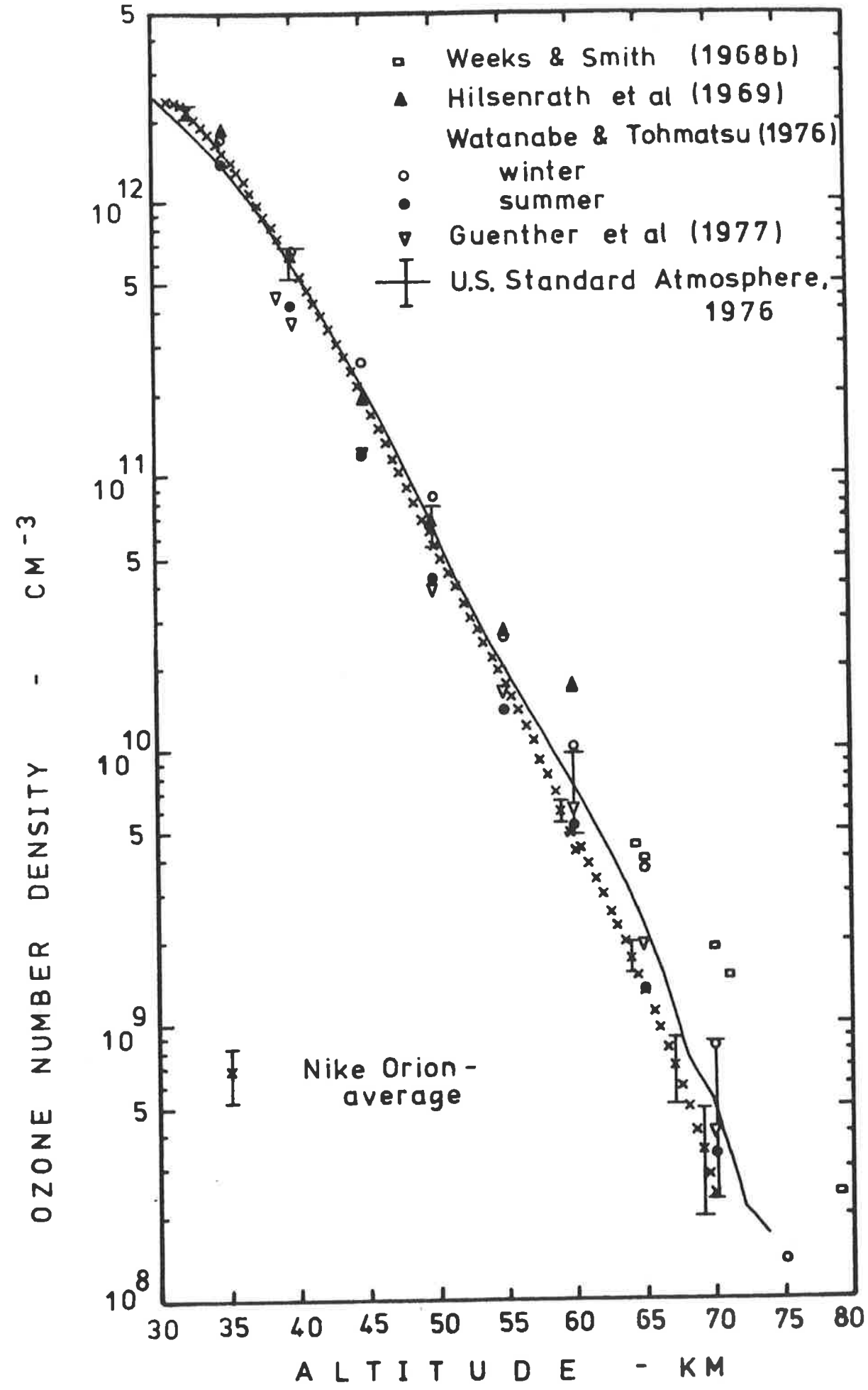

Figure 5.34 Comparison of measured daytime ozone densities.

summertime ozone densities. Since the experimental data described in this chapter were acquired during October it is not unreasonable to expect that in fall the ozone profile is being modified from its characteristic summer (June to September) distribution and assuming features of its winter (November to February) distribution.

Although the seasonal variability of atmospheric ozone, especially that of total ozone, appears qualitatively well established (see, for example, Hilsenrath *et al*, 1979b), quantitative details pertaining to seasonal variations of the vertical profile remain uncertain, and experimental data, such as that of Watanabe and Tohmatsu (1976) in Figure 5.34, conflict with some model predictions. For example, the model calculations of Park and London (1974) and also Shimazaki and Laird (1972), in which photochemical equilibrium conditions were assumed for altitudes above about 35 km, predicted ozone concentrations higher in summer than in winter, with the differences increasing at altitudes above 60 km. In the recent model of Cunnold *et al* (1980), ozone was reported to exhibit a summer maximum between 25 and 40 km with a winter maximum between 40 and 50 km, which was the upper altitude extent of the calculations.

While the production of atmospheric ozone depends directly on solar radiation, and thus is expected to display seasonal effects in response to changes in the solar zenith angle and the total hours of sunlight, it may not be sufficient to interpret seasonal differences solely in terms of these parameters. Difficulties in modelling ozone's seasonal patterns appear to originate in uncertainties about the abundances and chemical activity of the species which participate in mechanisms that destroy it. Of particular importance is the HO_x family, since above 40 km OH is the primary catalyst for ozone destruction (Wofsy, 1978). In fact, Wofsy (1978) has examined the temporal variations of HO_x, Clx and NO_x and found it difficult to reconcile upper stratosphere observations

of not only OH and ClO but also O_3; his calculations predicted a seasonal trend, between 40 and 60 km, contrary to that reported by Watanabe and Tohmatsu (1976).

Watanabe and Tohmatsu (1976) also interpreted their experimental data in terms of the reduction of odd oxygen by hydrogenic compounds in the mesosphere. Specifically, they suggested that an increase in water vapour concentration in summer, by a factor of 10 above the winter value, was consistent with their observations. And recently the apparent reality of this seasonal variation has been reiterated by Ogawa and Watanabe (1980).

With regard to the other experimental daytime ozone profiles in Figure 5.34; the data of Weeks and Smith (1968b) was obtained in June, 1966, at 38°N and at morning twilight ($\chi = 92.4°$) so the enhanced ozone densities at altitudes above 70 km may reflect the decay of the nighttime ozone buildup at these altitudes; Guenther *et al* (1977) measured ozone also at sunrise, in December 1976, but at low latitudes (5°N) where the concentrations are expected to be reduced with respect to mid latitudes, throughout the year; and for the chemiluminescent data of Hilsenrath *et al* (1969), acquired in September, 1968, at 38°N, there is general agreement with the present average daytime ozone profile and with the other mid latitude measurements at altitudes below 50 km.

It has been noted in the literature (Hilsenrath *et al*, 1979a, for example), that if the differences between ozone profiles such as those in Figure 5.34, especially near 50 km, are the consequence of geophysical influences, rather than experimental uncertainties, there are serious implications for one dimensional photochemical models which should be most accurate at these altitudes since here the chemistry is relatively simple and dynamical perturbations minimal. Butler (1978) has also emphasized the existence of discrepancies between experimental data and model

calculations, and although recent revision of the rates of the reactions 5.1 and 5.2 reduced such inconsistencies at 30 km and for the column densities it appears that there is still some disagreement at 50 km.

Until model calculations can accurately reproduce, in detail, all facets of the natural variability of atmospheric ozone densities they will have little credibility for predicting future trends. The obvious, and well recognized, (for example by Butler, 1978) paradox is that the models are imprecise because of uncertainties in atmospheric measurements which they use as input parameters.

b. Nighttime Densities

That nighttime ozone densities in the upper atmosphere are as yet poorly defined was evidenced by the reviews, in Sections 2.3d and 2.4d, of the results of various techniques employed to measure them. Some experimental profiles, together with the results from Section 5.8c, are plotted in Figure 5.35. Here, the conversion of the mixing ratio data of Gille *et al* (1980b) to number densities incorporated the U.S. Standard Atmosphere, 1976 total densities. If the wide scatter of the data in Figure 5.35 is real then the ozone densities are inconsistent with current mesospheric photochemistry, specifically the reactions between odd hydrogen and odd oxygen, and this possibility has been suggested by Riegler *et al* (1977). Alternately, the techniques themselves require re-evaluation but, as discussed by Gille *et al* (1980b), on the basis of data acquired during times characterized by different geophysical parameters, it is difficult to ascertain the extent to which this is necessary.

The two profiles in Figure 5.35 which are most different from each other, those of Roble and Hays (1973) and Riegler *et al* (1977), were both obtained with the technique of stellar occultation, although Roble

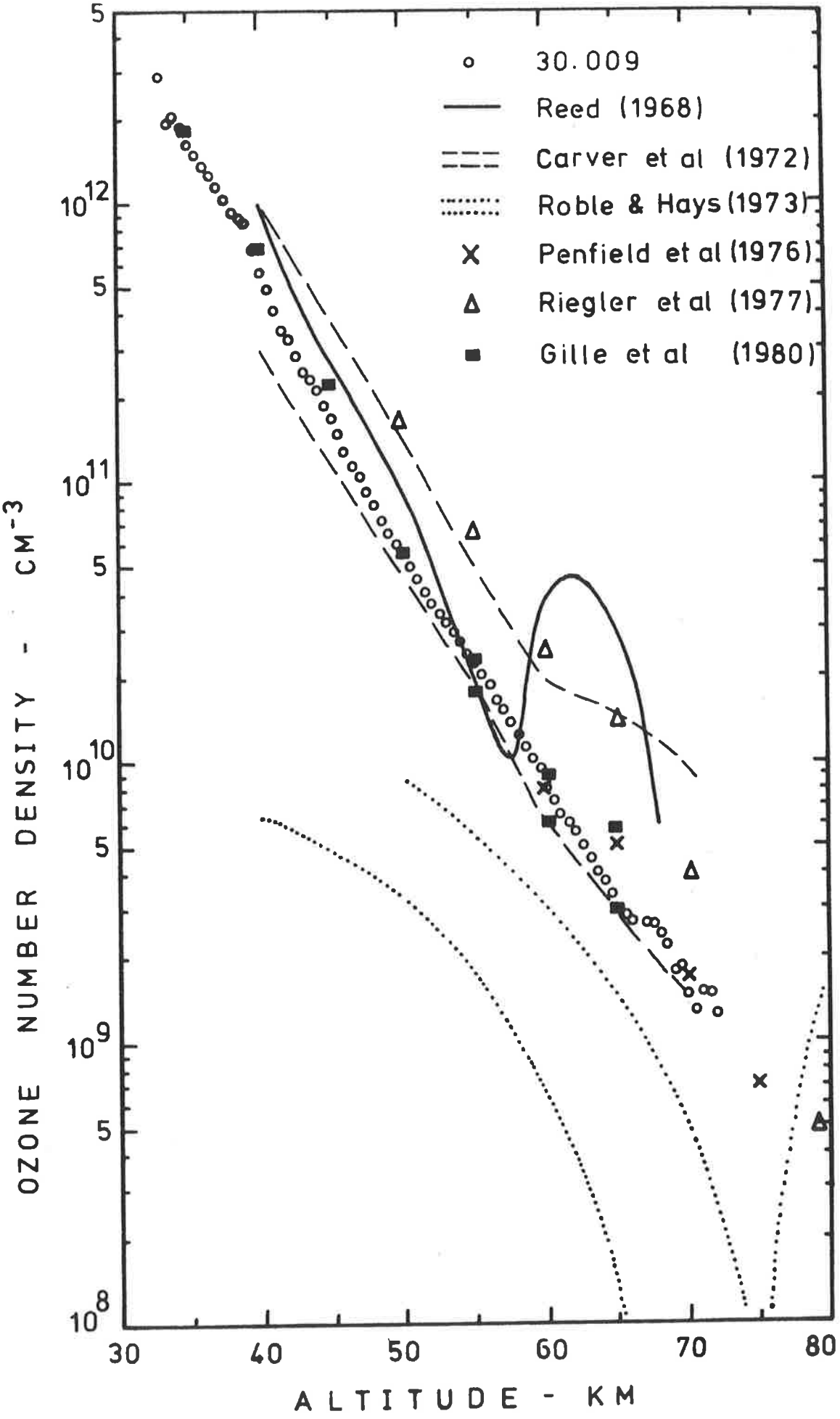

Figure 5.35 Comparison of measured nighttime ozone densities.

and Hays employed broad band detectors with FWHM $\doteq$ 40 nm while Riegler *et al* used a telescope and spectrometer to obtain monochromatic occultation profiles. It has been recognized that there may be a number of difficulties associated with the stellar occultation measurement technique. Rosenberg *et al* (1974a) suggested that the maximum above 75 km, prominant in the ozone profile of Roble and Hays (1973), was the result of additional 10% attenuation of stellar radiation by the atmospheric aerosol layer at 80 km. Assuming that the aerosol scattering cross-section is far less dependent on wavelength than ozone's absorption in its Hartley band, Roble and Hays (1974) refuted this suggestion because ozone densities determined by two detector channels at different wavelengths, 246 and 298 nm, were comparable. However, broad band stellar occultation measurements at 298 nm are contaminated by prominant atmospheric emissions from atomic oxygen at 297.2 nm and the Herzberg I bands of the O_2 molecule at 298 nm (Rosenberg *et al*, 1974b), so that the effect of atmospheric aerosols on stellar occultation measurements remained inconclusive. And with respect to the data of Riegler *et al* (1977), possible sources of a systematic error, exposed by the direct comparison in space and time with LRIR data (Gille *et al*, 1980b) (see Section 2.4b) also remain obscure.

There is excellent agreement in Figure 5.35 between the nighttime ozone profiles of Penfield *et al* (1976), Gille *et al* (1980b) and the present results. Each measurement was acquired using a different technique (Section 2.4d), employing respectively ozone's millimetre emission feature at 110.8 GHz, its infrared emission at 9.6 μm and its ultraviolet absorption in the Hartley band. In particular, the latter two sets of data agree well over the entire altitude range 30 to 70 km where measurements were made. Each of these three measurements occurred at different locations and at different times; Penfield *et al* measured nighttime ozone during February, 1975, at 31° N, the equatorial data of

Gille *et al* was collected in July, 1975 and the present measurements occurred at 38° N in November, 1979. While agreement between these data sets may be fortuitous, the alternative explanation is that nighttime ozone concentrations aren't greatly variable, especially below 50 km. Even if, at 65 km, the density data from the measurements of Gille *et al* reflect real variability, the extent of this is considerably less than is implied by Figure 5.35 if all the ozone profiles are equally valid. Further, it can be optimistically construed, from the agreement of each of these profiles, that none of the techniques is hampered by large systematic errors.

c. Diurnal Variation of Ozone

Theoretical investigations of the diurnal behaviour of an oxygen - hydrogen atmosphere unanimously predict a nighttime increase in ozone concentrations at altitudes between 60 and 80 km (Hunt, 1966; Leovy, 1969; Hesstvedt, 1971). Important species which participate in the numerous possible chemical reactions include O_3, $O(^1D)$, $O(^3P)$, H, HO_2, OH, H_2, H_2O, and H_2O_2, and some of the primary processes between the odd oxygen and odd hydrogen families, for both the daytime and the nighttime, are listed in Table 5.10.

With the cessation of solar radiation at sunset, all dissociation rates vanish and, below 80 km, virtually all atomic oxygen and atomic hydrogen disappear rapidly via very fast recombination with molecular oxygen. Since OH depends on $O(^1D)$ for its formation (Section 1.4c), and since it also combines rapidly with $O(^3P)$, it too is diminished during the night, as is HO_2. The depletion of these primary odd hydrogen species effectively means that the nighttime lower mesosphere, below 80 km, is characterized by the reactions of a pure oxygen atmosphere and with the

TABLE 5.10 Some primary photochemical processes in the atmosphere between 50 and 75 km, from the model of Park and London (1974).

	Odd Oxygen: O, O_3	Odd hydrogen: H, OH, HO_2
Daytime Processes		
Source	$O_2 + h\nu \rightarrow O + O$	$H_2O + O(^1D) \rightarrow OH + OH$
		$H_2O + h\nu \rightarrow H + OH$
Sink	$O + OH \rightarrow H + O_2$	$OH + HO_2 \rightarrow H_2O + O_2$
	$O + HO_2 \rightarrow OH + O_2$	$HO_2 + HO_2 \rightarrow H_2O_2 + O_2$
	$O_3 + H \rightarrow OH + O_2$	$H + HO_2 \rightarrow H_2 + O_2$
Conversion among odd particles		
	$O + O_2 + M \rightarrow O_3 + M$	$O + OH \rightarrow H + O_2$
	$O_3 + h\nu \rightarrow O + O_2$	$O + HO_2 \rightarrow OH + O_2$
		$O_3 + H \rightarrow OH + O_2$
		$H + O_2 + M \rightarrow HO_2 + M$
Nighttime Processes		
Source	None	None
Sink	$O_3 + OH \rightarrow HO_2 + O_2$	$OH + HO_2 \rightarrow H_2O + O_2$
	$O_3 + HO_2 \rightarrow OH + 2O_2$	$HO_2 + HO_2 \rightarrow H_2O_2 + O_2$
Conversion among odd particles		
	$*O + O_2 + M \rightarrow O_3 + M$	$O_3 + OH \rightarrow HO_2 + O_2$
		$O_3 + HO_2 \rightarrow OH + 2O_2$
		$*H + O_2 + M \rightarrow HO_2 + M$

* Very fast reaction

absence of photodissociation and atomic oxygen there are no efficient sinks for the increased ozone concentrations caused by the rapid atomic oxygen recombination at sunset. It is the significant concentration of H remaining above 80 km that prevents appreciable diurnal variation of ozone at higher altitudes.

During the nighttime there are further subtle and complex variations of the atmospheric species. Below about 60 km H, OH, and HO_2 are ultimately converted to H_2O_2, which thus increases throughout the night, while above about 75 km, the presence of H produces a net increase in OH and HO_2, as well as H_2O_2. In addition, while O_3, $O(^1D)$, OH and HO_2 are usually assumed to be in photochemical equilibrium, the species $O(^3P)$, H, H_2, H_2O, H_2O_2 and O_2 are diffusing gases for which atmospheric transport is an important factor in their distributions. This is especially true for $O(^3P)$ and H, and since they both strongly influence ozone's diurnal variations any realistic model of atmospheric diurnal variations must incorporate the effect of turbulence and eddy diffusion (Hunt, 1971; Shimazaki and Laird, 1970).

Typically, model calculations have predicted that nighttime ozone concentrations at 70 km are increased by an order of magnitude over the daytime concentrations (Hunt, 1971; Hesstevdt, 1971; Park and London, 1974). Possible verification of these predictions by *in situ* measurements has been largely precluded, over the past decade, by the sparseness of the experimental data set, acquired over a variety of geophysical parameters, with unknown measurement uncertainties, and this has been discussed in Section 5.9b. From the comparison in Figure 5.36, of ozone densities measured at sunset and at night by the present experiments, the magnitude of the nighttime increase over the sunset concentrations was determined to be a factor of

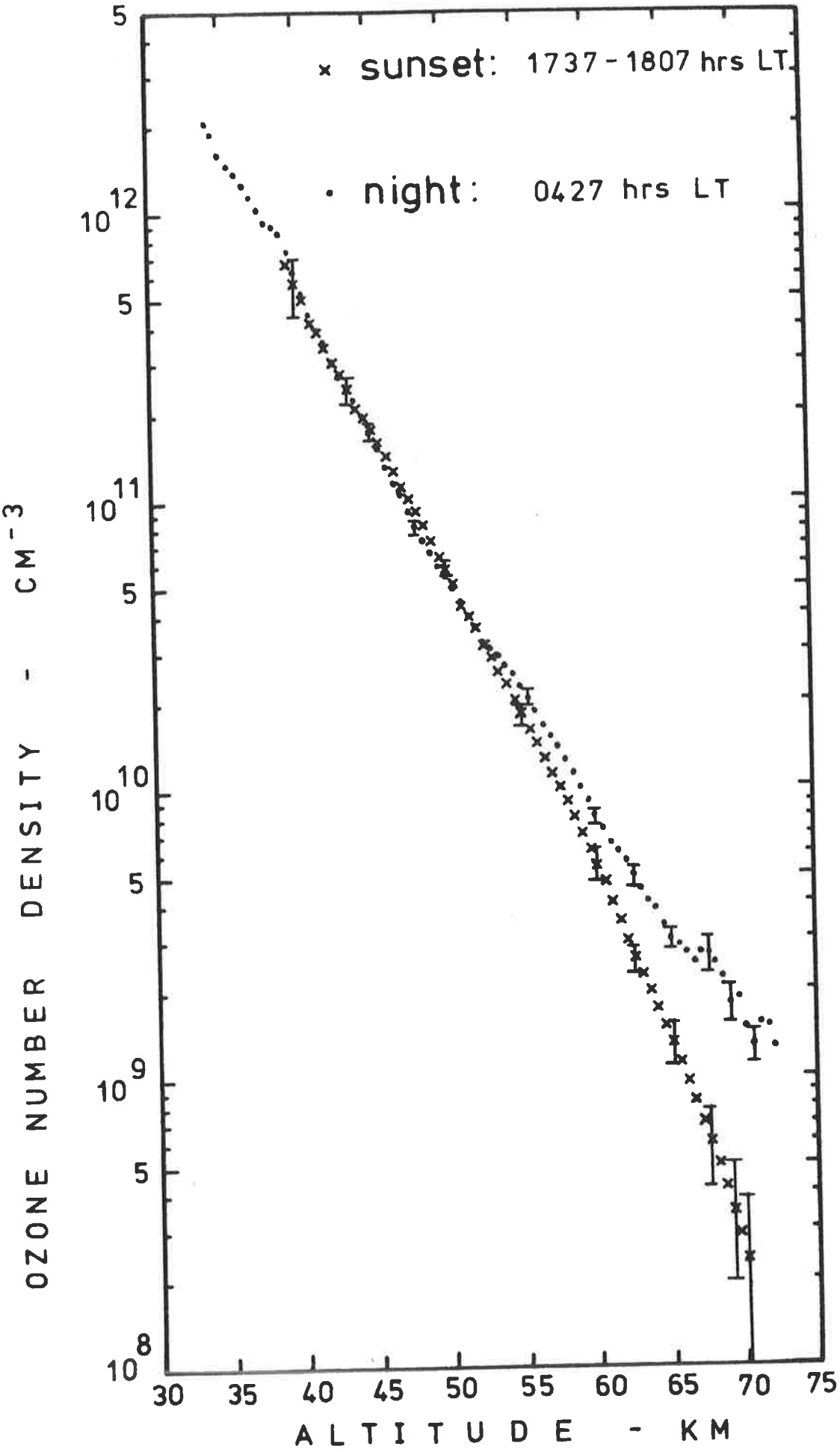

Figure 5.36 Comparison of ozone densities measured at sunset and at night.

.25 at 55 km,

.50 at 60 km,

1.3 at 65 km,

and 5.4 at 70 km.

Consideration of the maximum uncertainties, taken as the accuracy in each measurement (about ± 60%), in the data at 70 km indicated that the nighttime increase might be as little as a factor of 1.25 or as great as a factor of 10.1. This experimental data is compared with the theoretical calculations of Hunt (1971) in Figure 5.37a where it is evident that although the general trends of the experimental results are qualitatively predicted by the model, there are significant differences in both the shape and magnitude of the ozone profiles.

Keneshea *et al* (1979) have computed the diurnal variation of ozone using a one dimensional chemical transport model in which particular consideration was given to the dynamics of turbulence and which incorporated *in situ* measurements of transport parameters. Their results, for the altitudes 50 to 75 km, are illustrated in Figure 5.37b. At 70 km the increase from the sunset concentration of $5 \times 10^9 cm^{-3}$ to the nighttime concentration of $3 \times 10^{10} cm^{-3}$ was a factor of 5 which agrees well with the present experimental determination. However, the magnitudes of the ozone densities in the model are at least 20 times higher than the measured ozone densities.

A distinctive feature of Figure 5.37b is the asymmetry of ozone's diurnal variation at altitudes above 60 km, and this has been predicted by a number of other models (for example, Hesstvedt, 1971; Park and London, 1974). At sunrise the solar photon flux increases by many orders of magnitude in a time that is short compared to the chemical time constants of many upper atmosphere species. After sunrise the stratosphere

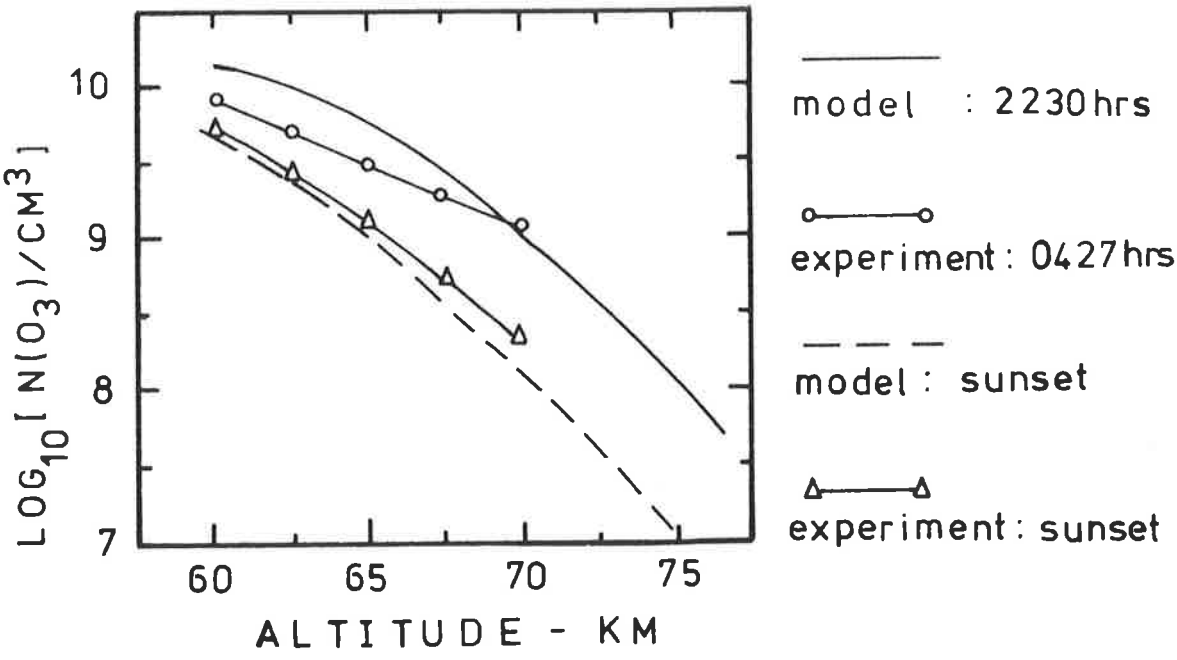

Figure 5.37a Comparison of ozone profiles measured at sunset and at night with the diffusive-photochemical model calculations of Hunt (1971).

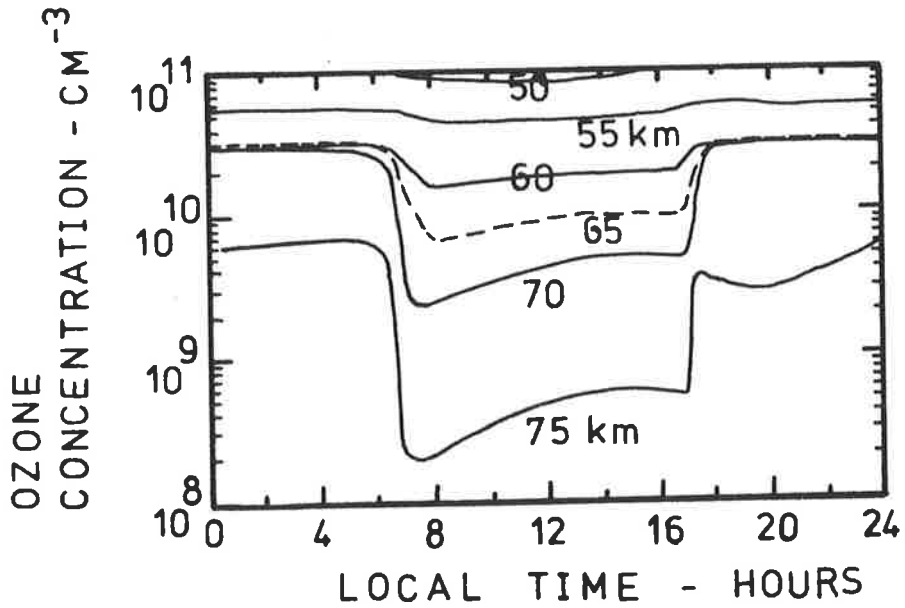

Figure 5.37b Diurnal variation of ozone calculated by the one-dimensional chemical transport model of Keneshea et al (1979).

and lower mesosphere are far from chemical equilibrium for times that depend on the species under consideration and also the altitude. For ozone, rapid dissociation at sunrise destroys the nighttime enhancement and results in the minimum concentration for the day. Following this, there is a steady increase in the ozone densities at all altitudes. Below 60 km, equilibrium concentrations are reached by noon after which there is a reduction, following the decrease in O_2 dissociation with increasing solar zenith angle. But above about 70 km this buildup may increase until sunset when the nighttime enhancement again commences. Now, the individual chemical decay time constants of the atmospheric species govern the post sunset chemistry.

It is generally considered that, below about 50 km, ozone is diurnally invariant. Comparison, in Figure 5.38, of the nighttime and noon ozone profiles measured by the experiments in this chapter suggest that this is not so at altitudes between 40 and 50 km; at 45 km the noon ozone concentration is 17% higher than the nighttime concentration and this difference is well beyond the uncertainty of the measurements as represented by the mean sample standard deviation of each of the average densities. Recent investigations by Herman (1979) have also indicated that at altitudes above 30 km the percent changes in ozone are substantial. Results of his calculations are provided in Figure 5.39a and are explained by him thus; the various maxima and minima at each altitude are simple displacements in time from similar features at other altitudes, arising from altitude dependence of the chemistry rates. While atoms and some radical molecules quickly come to equilibrium with each other and with the long-lived species, the latter may remain significantly out of equilibrium for the better part of the day and may appear to 'ring' after sunrise in response to changes occurring in the densities of other minor constituents.

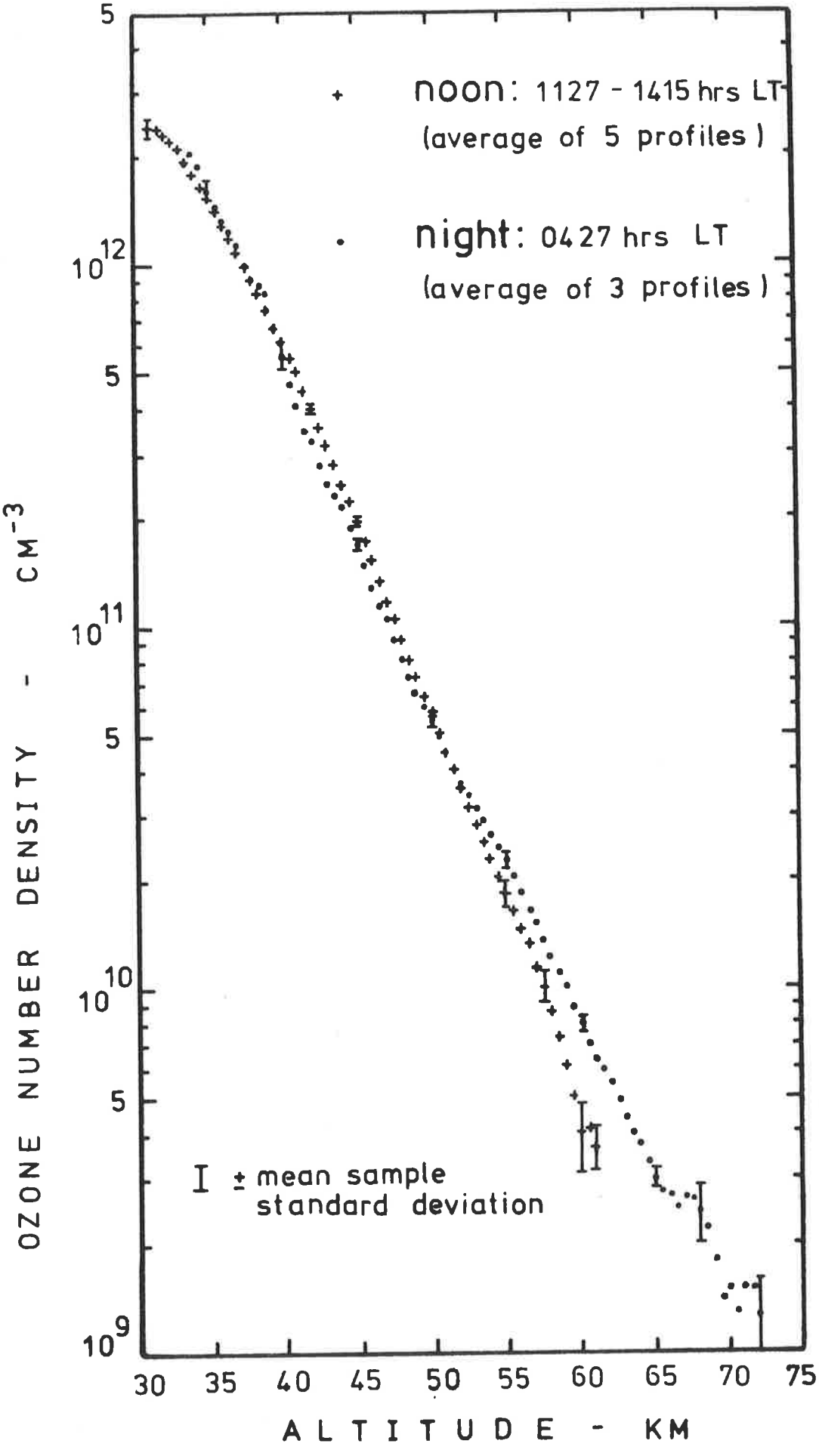

Figure 5.38 Comparison of ozone densities measured near noon and at night.

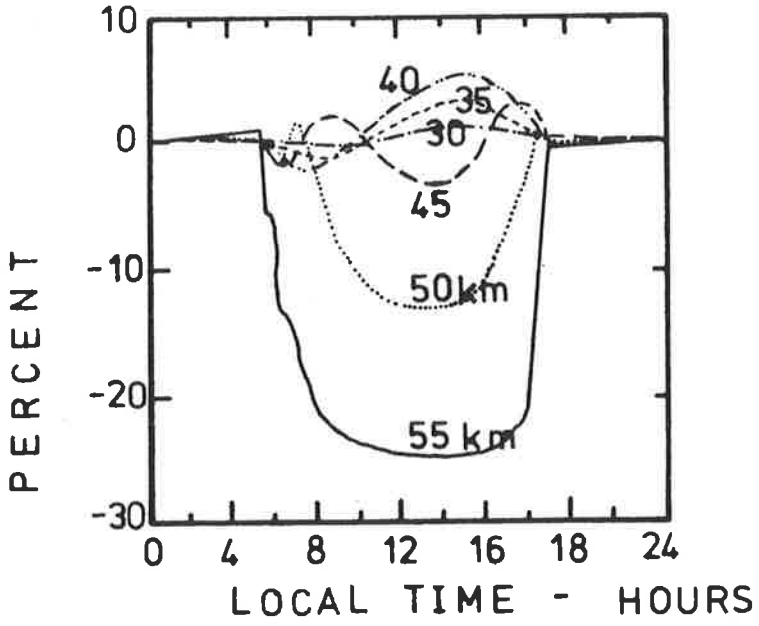

Figure 5.39a Model calculations of the percentage change time variation of ozone in relation to its midnight value. (Herman, 1979)

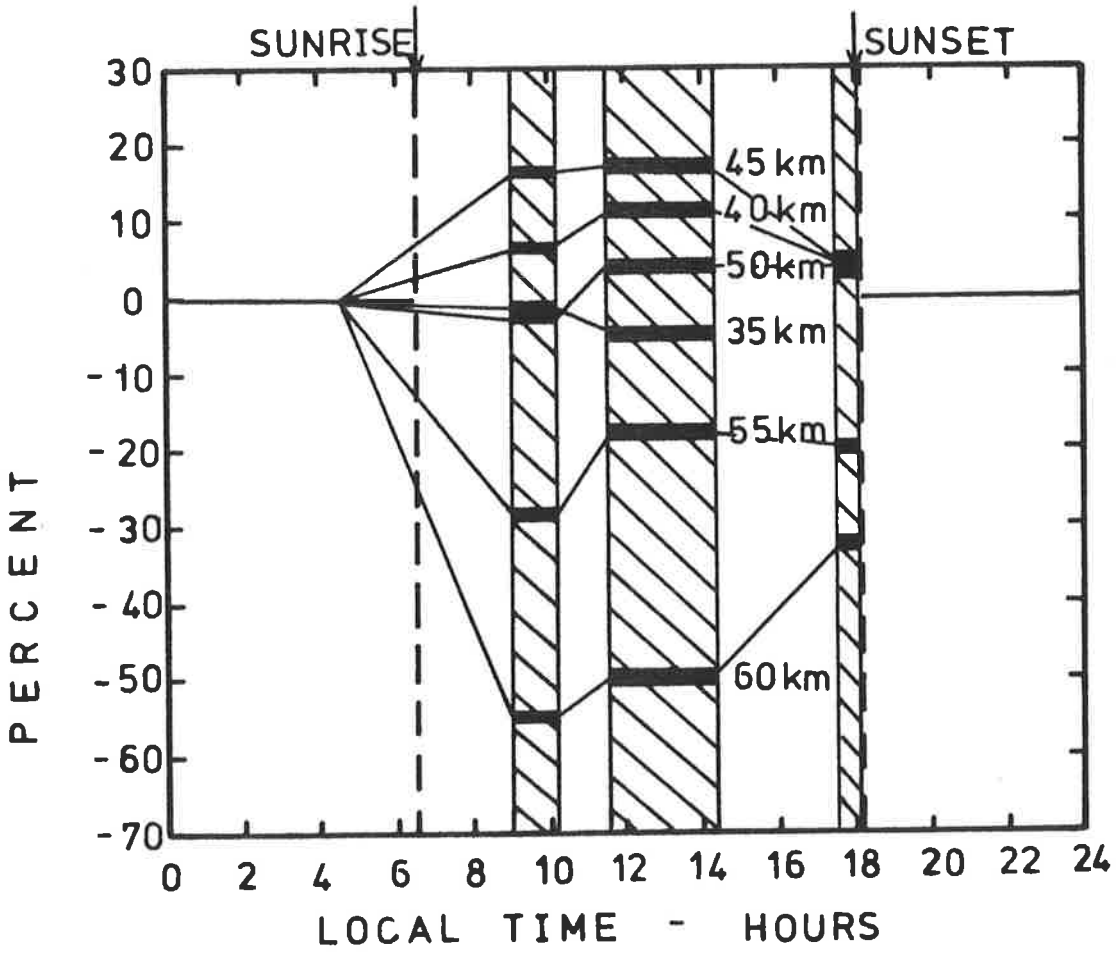

Figure 5.39b Experimental measurements of the percentage change time variation of ozone in relation to its value at 0427hrs.

Following the procedure employed by Herman (1979) for representing ozone's diurnal variations (Figure 5.39a), the percentage change in the daytime densities measured by the present experiments, with respect to the measured nighttime densities, are provided, for six altitudes, in Table 5.11 and this data is illustrated in Figure 5.39b. Overall, the trends inherent in the model and in the experimental data are similar; specifically that at altitudes less than about 45 km the noontime ozone concentrations are higher than the nighttime concentrations while at altitudes above 55 km the differences are in the reverse direction. However, this changeover is predicted by the model to occur at 45 km but from the experimental data appears to be at 50 km. And, while the maximum calculated noontime increase is about 5% at 40 km, it was measured to be 17% at 45 km. Thus the observed differences between the model and the experimental results appear, at lower altitudes, to be systematic and may arise from uncertainties about the altitude dependence of the chemical reaction rates. At 55 km both the model and the experiments indicate a noontime ozone concentration about 20% less than at nighttime.

More generally, the experimental investigation of the diurnal changes in ozone densities which have been described in this section suffer from important limitations in that for both the morning and noontime measurements the uncertainties are large at 60 km and there is no data above this altitude, while sunset ozone densities were not determined below 40 km. Such are the fundamental constraints on the technique of atmospheric absorption spectroscopy. The altitude region where data are most reliably retrieved depends on the column density of the absorbing species, hence on the solar zenith angle and hence on the diurnal time of the measurement. Additional aspects of this measurement technique are discussed in the final section of this chapter.

Height - km	Night: 0427 hrs	Morning: 0857 - 1012 hrs		Noon: 1127 - 1415 hrs		Sunset: 1737 - 1807 hrs	
	$n(O_3)/cm^3$	$n(O_3)/cm^3$	Change	$n(O_3)/cm^3$	Change	$n(O_3)/cm^3$	Change
35	$1.62 \pm .10 \times 10^{12}$	$1.60 \pm .07 \times 10^{12}$	- 1.2%	$1.54 \pm .05 \times 10^{12}$	- 5%		
40	$5.63 \pm .45 \times 10^{11}$	$5.97 \pm .42 \times 10^{11}$	+ 6%	$6.25 \pm .20 \times 10^{11}$	+ 11%	$5.79 \pm 1.5 \times 10^{11}$	+ 2.8%
45	$1.70 \pm .04 \times 10^{11}$	$1.97 \pm .10 \times 10^{11}$	+ 15.8%	$1.99 \pm .03 \times 10^{11}$	+ 17%	$1.76 \pm .05 \times 10^{11}$	+ 4.7%
50	$5.55 \pm .17 \times 10^{10}$	$5.43 \pm .08 \times 10^{10}$	- 2.2%	$5.89 \pm .19 \times 10^{10}$	+ 6%	$5.86 \pm .37 \times 10^{10}$	+ 5.6%
55	$2.28 \pm .10 \times 10^{10}$	$1.62 \pm .18 \times 10^{10}$	- 29%	$1.86 \pm .17 \times 10^{10}$	- 18%	$1.82 \pm .14 \times 10^{10}$	- 20%
60	$8.06 \pm .35 \times 10^{9}$	$3.54 \pm 1.03 \times 10^{9}$	- 56%	$3.98 \pm .86 \times 10^{9}$	- 50%	$5.45 \pm .71 \times 10^{9}$	- 32%

Table 5.11 Experimental measurements of the diurnal variation of ozone in the stratosphere and mesosphere, expressed as the percentage change in relation to the nighttime measurement.

d. The Measurement Technique

Broad band MUV photometers carried on spinning rockets are regularly employed by a number of investigators to measure ozone densities but, from the results of the experiments described in this chapter, it appears doubtful whether this particular application of atmospheric ultraviolet absorption spectroscopy is sufficiently precise to furnish reliable data on subtle changes in ozone concentrations, such as those predicted to be the consequence of atmospheric pollution. Recalling that the reduction in ozone concentration by chlorofluormethanes was predicted by recent models (Borucki *et al*, 1980) to be 0.35% per year, and that statistical analysis of the broad band absorption spectroscopy measurement technique implied that the average precision over the altitude range where data was collected was of the order of 7%, suggests that, if real changes in ozone concentrations are occurring, it may be 20 years before they are conclusively recognized. By this time, the accumulation of chlorofluoromethanes in the stratospheric reservoir will make it impossible to control their effect on the environment.

There are, primarily, two features of this technique which limit the quality of the data; that the detector responds over a wide wavelength interval, typically defined by an interference filter, and that it is spinning. Because of the former, the detector's spectral response, the relative distribution of the solar flux and the ozone absorption cross-sections must be accurately known over a wavelength interval of about 20 nm. Additionally, detectors incorporating interference filters often have non-zero background signals due to leakage bands. That the transmission of these filters changes with the angle of the incident radiation compounds these inherent uncertainties when they are carried on spinning rockets which are prone to coning motions.

The need to correct the data for the changing aspect of the source is eliminated when the detector is slaved to a sun tracker. Such experiments have been successfully flown on spinning rockets (Ogawa and Watanabe, 1980), providing raw data of apparently significantly improved quality. However, uncertainties associated with broad band detectors still remain and the data acquisition rate is never better than the number of spins per km.

Although spinning rockets are the most widely used *in situ* detector platforms, high altitude parachutes may also be quite suitable, in the future, for carrying experiments which view the sun directly. Data acquired during the descent of such parachutes, in these experiments, indicated that this detector platform was not as stable as anticipated but certainly implied the potential of the configuration. NASA's Wallops Flight Center have recently extended the deployment altitude to 98 km (Gurkin, 1980) and have repeatedly demonstrated that parachute payloads can be recovered in the air and reflown.

Using a sun seaker to control the attitude and elevation of an experimental package suspended beneath a high altitude parachute would facilitate, through the use of dispersive instrumentation, the application of monochromatic, rather than broad band, absorption spectroscopy techniques for ozone concentration measurements. Grating monochromators and pointed experiments have collected data from balloons for many years (Ackerman *et al*, 1971; Farmer *et al*, 1980) and so, for example, an Ebert-Fastie scanning monochromator could be repeatedly used to acquire absorption profiles having both high spectral and height resolution.

Regarding the absolute accuracy of upper atmosphere ozone densities derived from absorption spectroscopy utilizing Hartley band wavelengths, the question of other absorbers of radiation at these wave-

lengths remains unanswered. It has been speculated that some excited states of both O_2 and O_3 may exhibit absorption features at MUV wavelengths but laboratory verification of this is scanty; nor are the atmospheric distributions of such species, with the exception of $O_2(^1\Delta_g)$, well known.

Krueger (1969b) attributed observed anomalies in broad band measurements of the absorption of solar flux near 300 nm to previously unidentified absorption bands in either of the $O_2(^1\Delta_g)$ or $O_2(^1\Sigma_g^+)$ metastable excited states. However, according to Noxon (1970), both of these species are precluded from absorbing MUV flux near 300 nm because the consequences of their having absorption cross-sections of sufficient magnitude would be inconsistent with observations of their respective airglows.

Ozone is considered to have a number of low lying stable excited states which have been predicted theoretically (Section 1.3f) and correlated in the laboratory with infrared emissions at wavelengths not corresponding to vibrational transitions in ground state ozone (Wraight, 1977). Additionally, when ozone is formed by recombination of O and O_2, significant changes in the spectral region of the Hartley band have been observed (Kleindienst *et al*, 1980). A separate maximum appears and decays on the long wavelength side of the Hartley band and this has been attributed to the presence of excited ozone. However, there is little agreement in the literature as to whether this energetic 'precursor' is an electronically excited state (Wraight, 1977) or a vibrationally excited state corresponding to a secondary minimum in the ground state energy surface (Prasad and Burton, 1979) and, while Kleindienst *et al* (1980) attributed the observed changes to vibrational excitation of ozone, they did not discount the possibility of an unobserved metastable state as an intermediate.

If excited ozone precursors exist in sufficient quantities in the atmosphere there are wide implications for atmospheric photochemistry and energetics and these have been discussed by Wraight (1977) and Prasad and Burton (1979). Since excited ozone is more reactive than ground state ozone these species may participate in important reactions which govern the distributions of the minor atmospheric constituents and, more significantly for the experiments described in this chapter, they represent a potential contamination of MUV absorption data. Verification of the role of excited ozone species in the atmosphere requires extensive additional laboratory data on their lifetimes against both radiative transitions and collisional quenching and on the complex kinetics of the reactions which produce them.

While the agreement between the results in this chapter with ozone profiles acquired using other experimental techniques (Figures 5.34 and 5.35) implies that there are no obvious systematic errors inherent in MUV absorption spectroscopy techniques, it may be that the combination of a number of minor uncertainties pertaining to, for instance, the absolute magnitudes and temperature dependence of the absorption cross-sections, the role of other MUV absorbers and the temporal variations of ozone at twilight will prevent the technique from being sufficiently precise without more knowledge about reaction rates and absorption processes in atmospheric constituents, especially polyatomics, and their involvement in the composite mechanisms of the atmosphere itself.

APPENDIX A

ROCKET VEHICLES

A.1 THE AEROBEE ROCKET

a. Scientific Objectives

As an integrated experiment, the Aerobee payload was designed to study atmospheric processes important in the E and F region when the layers of ionization are developing quickly. For this purpose it was capable of simultaneously investigating absorption of EUV and FUV solar radiation, the energy spectra of thermospheric photoelectrons and ions, the abundance of both neutral and ionized atmospheric constituents, and certain day airglow emissions from lines and bands of oxygen and nitrogen.

To achieve these objectives, initial planning requirements were that the rocket be launched when the solar zenith angle was greater than 45° and that the rocket attain an apogee of 245 km.

b. Vehicle Description

The Aerobee 170 is a 15" diameter, free-flight, expendable liquid-propellant vehicle, stabilized in flight by four equally spaced, fixed fins. An initial spin rate of 2.5 sec^{-1} is reduced to zero by a yo-yo despin mechanism. It has a cylindrical nose cone with tip eject mechanism and carries an attitude control system, a parachute for land recovery and a 15 channel PCM telemetry transmitter.

With a net payload weight of 145 kg, burnout altitude was calculated to occur at 42.2 km and the vehicle was expected to reach an apogee of 209 km.

c. Instrumentation

Schematics of the Aerobee payload are shown in Figure A.1 and details of the instrumentation are summarized in Table A.1. Total power requirements were + 28V at 5 amp.

An ACS sunseeker unit was used to control the attitude of the payload after vehicle burnout. This provided pointing accuracy of ± 1 arc minute for two axes and ± 3 degrees for the third axis.

d. Flight Parameters

Launched from Woomera, S.A., at 0636 hours C.S.T. on 22nd February, 1977, the rocket reached an apogee of 177 km at a time when the zenith angle was 84.7°.

Prior to despin at 60 km, three fly-away doors were released and at 86 km the nose cone tip was ejected, the analyzers (Figure A.1) deployed and a portion of the experimental high voltage turned ON. At 100 km, when pressure was sufficiently low, the remaining experiments were activated. The rocket was programmed to point the ultraviolet experiments at the sun after the acquisition system took control at an upleg altitude of 107 km. Data was transmitted until the high voltages were turned OFF at 85 km on the downleg, at which point the analyzers were retracted, ready for recovery separation at 79 km.

The vehicle was successfully tracked through flight by Weapons Research Establishment FPS16 radar.

Parameters pertaining to the launch of the Aerobee rocket, necessary for data reduction, are given in Table A.2.

e. Results

Data was acquired by all instrumentation except the airglow photometers which saturated.

Preliminary results from the mass spectrometers, the ion chambers

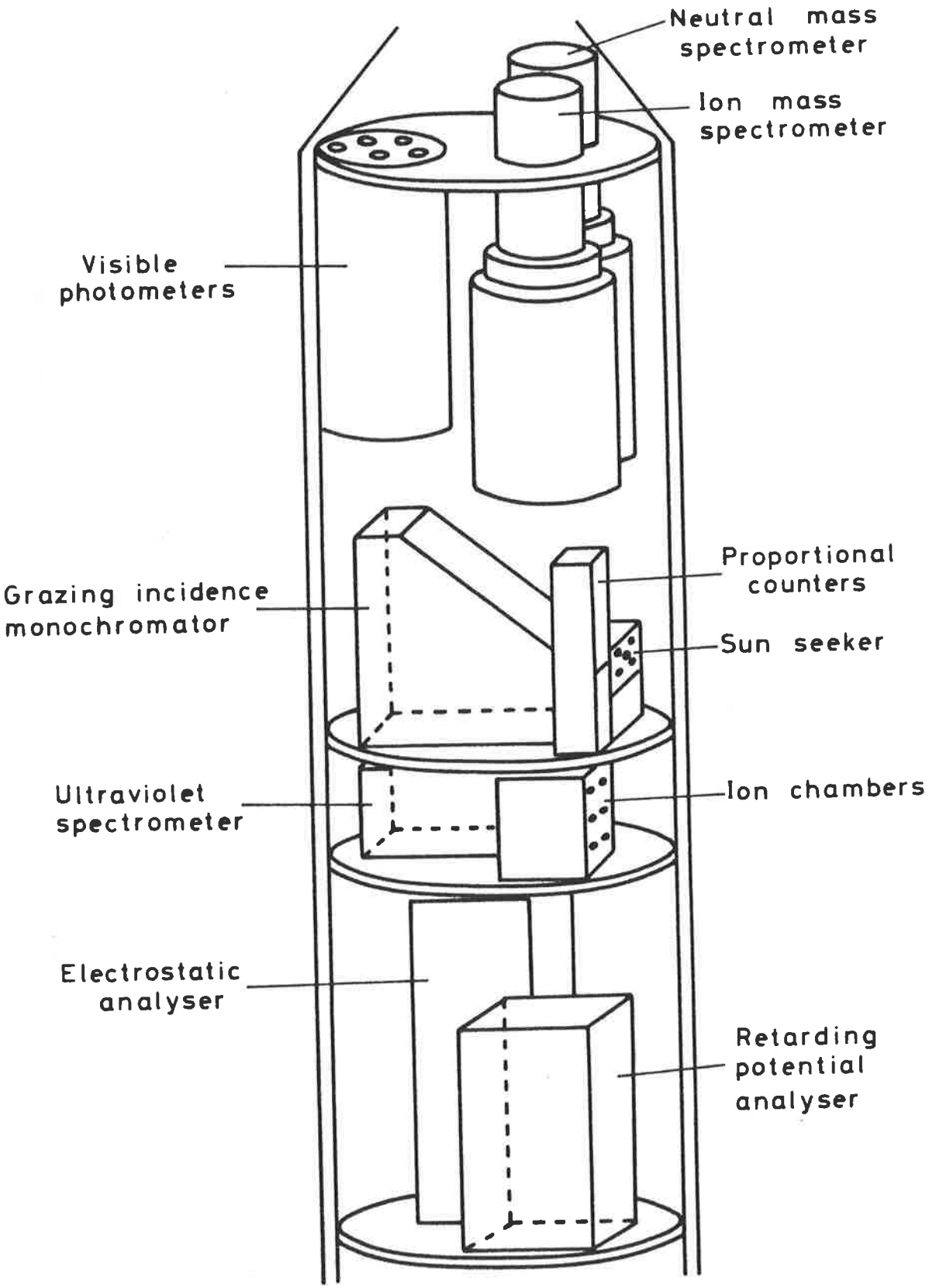

Figure A.1 Diagram of Aerobee Payload.

Scale 1:6

TABLE A.1 Aerobee instrumentation.

Solar aligned	2 X-ray proportional counters 550 mm Hg P-10 gas filling - polypropylene window 1 four channel scanning EUV grazing incidence monochromator 9 to 110 nm scan 1 $\frac{1}{8}$ metre Ebert-Fastie spectrometer (Ray Lee) scanning the wavelength range 135 to 175 nm 1 Lithium Fluoride-Nitric Oxide ion chamber 1 Magnesium Fluoride-Nitric Oxide ion chamber 2 Quartz-Triethylamine ion chambers 2 Sapphire-Xylene ion chambers 1 NASA Solar position seeker
Aligned at right angles to Sun in horizon plane	1 cylindrical electrode electron energy analyzer (southerly looking) 1 electron retarding potential analyzer 1 positive ion retarding potential analyzer (northerly looking)
Aligned parallel to rocket axis (rear- zenith aligned)	1 full channel (762, 630, 557, 391 and 337 nm) airglow photometer 1 neutral particle quadrupole mass spectrometer 1 positive ion quadrupole mass spectrometer

TABLE A.2 Aerobee flight parameters.

Latitude	ϕ	$-30^{\circ}\,56'\,40.393''$
Longitude	θ	$136^{\circ}\,27'\,41.117''$ East
Launch Time (Universal)	T_0	$21^h06^m00^s$, 21/2/77
Greenwich Hour Angle of the Equinox	GHA	10.11110556^h
Apparent Right Ascension	RA	22.33802322^h
Apparent Declination	δ_0	-10.35641748°
Solar Radio Flux at launch	$F_{10.7}$	$82 \times 10^{-22}\,Wm^{-2}Hz^{-1}$
Geomagnetic Index	K_p	1^- (at launch) 3^- (6 hours prior to launch)

and the FUV spectrometer have been published (Bibbo *et al*, 1979) and more detailed analyses have since been completed. Aerobee results of immediate relevance are those pertaining to the densities of the three major neutral constituents of the lower thermosphere - N_2, O_2 and O. Molecular oxygen densities were derived from the ion chamber data by L.A. Davis, and G. Bibbo analyzed the mass spectrometer data. In Table A.3 are listed the average O_2 densities measured by optical techniques on the Aerobee rocket vehicle while Figure A.2 provides the ratios of atomic oxygen and molecular nitrogen densities estimated by the mass spectrometer. Since an evaluation of the degree of atomic oxygen recombination in the mass spectrometer incorporated the optically determined O_2 densities, the absolute densities provided by the mass spectrometer were not considered to be independent measurements, nor compared as such.

A.2 NIKE ORION AND SINGLE-STAGE ORION ROCKETS

Both the Nike Orion and single-stage Orion rocket vehicles, and the payloads for the International Ozone Rocketsonde Intercomparison (IORI), have been documented in detail by Wallops Flight Centre (1979a, 1979b) and this appendix provides only a brief description.

a. Nike Orions for Daytime Launches

The Nike Orion is a two stage, solid propellant fin stabilized sounding rocket. The first stage is a Nike booster (diameter 41.9 cm, length 365 cm) with three fins and the second stage is an Orion (diameter 35.6 cm, length 281.4 cm) with four fins, canted to provide a spin rate of 4 to 6 revs/sec at motor burnout. Stage separation occurs after first stage burnout, at about 3.5 seconds, following which the second stage is activated by an on-board ignition system.

TABLE A.3 Average molecular oxygen densities determined optically on the Aerobee vehicle.

Altitude - km	$n(O_2)$ per cm^3	Sample standard deviation	Number of measurements	Mean sample standard deviation
109	1.88×10^{11}	0.61×10^{11}	3	18.7%
111	1.02	0.02	3	1.1
113	6.60×10^{10}	1.11×10^{10}	3	9.7
115	4.88	0.97	3	11.5
117	3.83	0.63	3	9.5
119	2.77	0.51	4	9.2
121	2.58	0.69	5	12.0
123	1.99	0.47	5	10.6
125	1.57	0.20	5	5.7
127	1.31	0.13	5	4.4
129	1.05	0.10	5	4.3
131	8.70×10^{9}	0.86×10^{9}	5	4.4
133	7.00	0.64	5	4.1
135	5.85	0.49	5	3.7
137	4.99	0.42	5	3.8
139	4.20	0.38	5	4.0
141	3.57	0.33	5	4.1
143	3.00	0.26	5	3.9
145	2.53	0.21	5	3.7
147	2.15	0.19	5	4.0
149	1.84	0.17	5	4.1
151	1.58	0.11	5	3.1
153	1.36	0.09	5	3.0
155	1.17	0.07	5	2.7
157	9.85×10^{8}	0.71×10^{8}	4	3.7
159	8.46	0.93	4	5.5
161	7.41	1.16	4	7.8
163	6.28	1.53	3	14.1
165	5.34	1.55	3	16.8

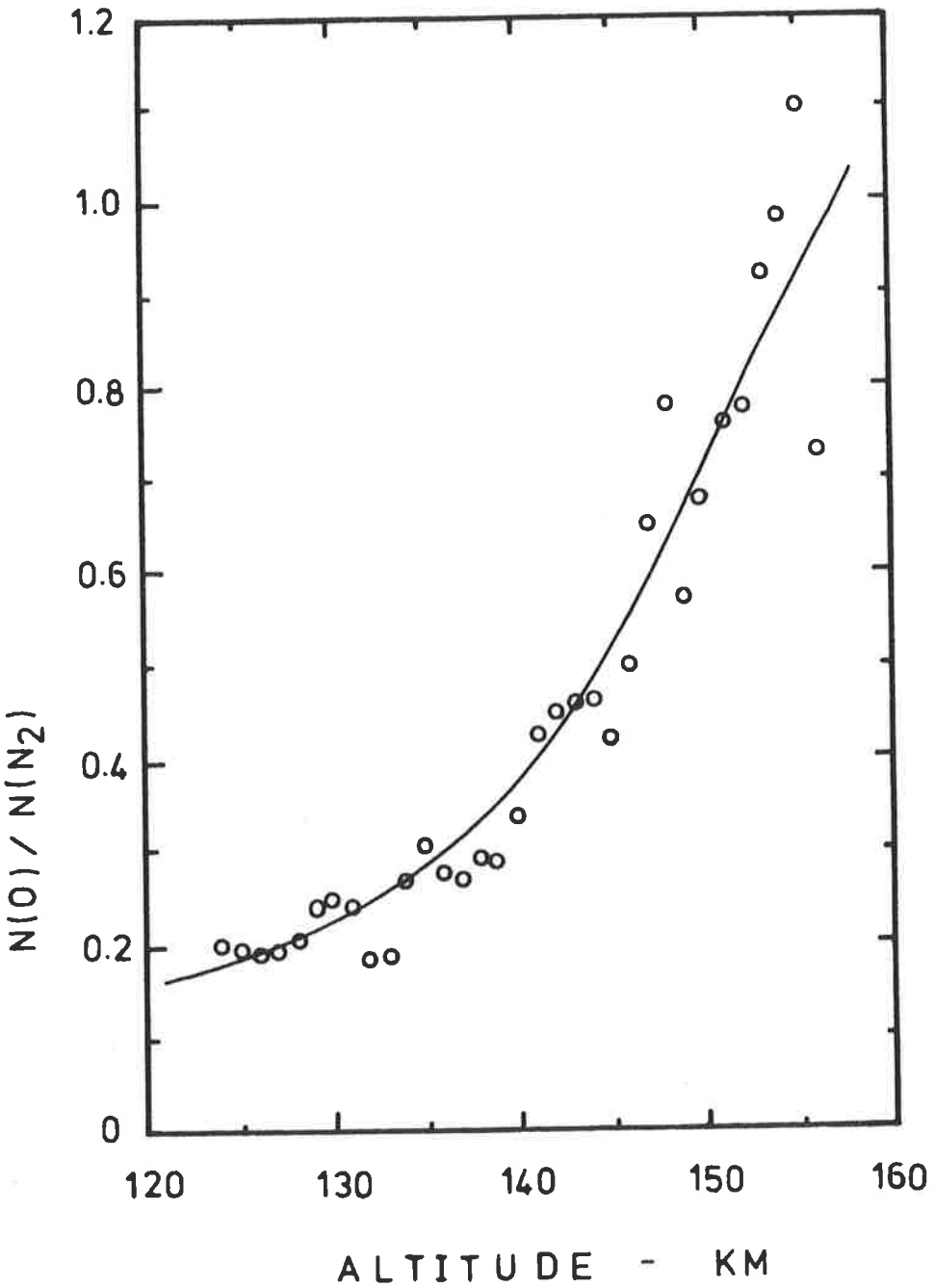

Figure A.2 Ratios of atomic oxygen and molecular nitrogen densities measured by the neutral mass spectrometer on the Aerobee rocket.

For the IORI, four experiments for measuring ozone densities were assembled in a composite payload for the Nike Orion. Three of these experiments, those of Australia, Japan and India, used optical broad band detectors to monitor the attenuation of solar MUV by ozone absorption, and thus required to view the sun directly, looking at an angle to the rocket spin axis. The fourth experiment, from Canada, was sensitive to the 1.27 μm radiation of the $O_2(a^1\Delta_g)$ photodissociation product of ozone and was constrained to look parallel to the rocket spin axis, shielded from direct sunlight.

At an altitude of 30 km four equally spaced doors were released through pyrotechnic severence of attachment cables, so that the three outward-looking optical detectors were exposed to solar radiation once every cycle as the rocket spun. Nose tip ejection occurred at 40 km, enabling the Canadian experiment to look through the nose cone and commence data acquisition. At 58 km on the upleg, the spinning payload separated from the Orion motor and continued spinning to apogee. Shortly after apogee was reached, the payload was despun, followed by ejection of the experimental package which initiated the deployment of two parachutes. To the larger, a 48 foot disk-gap band high altitude parachute, was attached the experimental payload. At 75 km during descent a motor commenced to spin the experimental package relative to the 'stable' parachute platform and this continued until 3 km when the payload was retrieved by an airborne recovery system.

b. A Single Stage Orion for Nighttime Launch

The single-stage Orion uses a solid propellant rocket motor which causes relatively low acceleration and a low vibration environment. It utilizes a tail fin assembly consisting of three adjustable fins that

provide a spin rate of 2 to 3 revs/sec at motor burnout.

At 30 km three doors were pyrotechnically ejected, exposing the three sets of broad band MUV detectors to moonlight as the vehicle spun. Data collection continued from this point to apogee at 82 km and no attempt was made to recover the payload.

c. *Pre-Flight Testing*

It was required that each rocket payload be subjected to rigorous pre-flight testing, as follows;

(a) random sweep, low power vibration tests,

(b) low power sinusoidal sweeps (50 Hz - 2 KHz), in each of three perpendicular directions, to look for resonances,

(c) full power sinusoidal sweeps,

(d) shock testing (8g) parallel to the rocket's longitudinal axis,

(e) spinning, door deployment and V band release tests, and

(f) complete operation of the integrated experiment and telemetry systems, on INTERNAL power.

Throughout each test the daytime experiments performed reliably but the nighttime experiment, with its more sensitive detectors, suffered from the shock of door deployment, causing one of the nine photometer channels to become noisy. However, by launch the dark current had returned to a sufficiently low value and was not a problem during flight, the high tension being activated immediately after, rather than prior to, door ejection.

APPENDIX B

CALIBRATION OF MULLARD SPECIAL CHANNELTRONS

Since two of the channeltrons (model B312BL) used in the grazing incidence monochromator which was flown on the Aerobee rocket were especially developed to have a fast response and high counting rate, a report on their performance was requested by the manufacturers (Mullard). This appendix describes the laboratory calibration, as contained in that report, and the ensuing reply from Mullard.

B.1 EXPERIMENTAL DETAILS

Figure B.1a is the experimental schematics. A McPherson half-metre, normal incidence monochromator dispersed light from a Hinteregger capillary discharge lamp (McPherson type # 630). Attached to the exit slit was the channeltron holder, behind which was an EMR photodiode, Model 543, whose spectral cutoff was 115 nm.

The B312BL channeltron, mounted on an externally controlled rotatable arm, could be positioned in or out of the light from the exit slit of the monochromator. On another arm, on the same axis but perpendicular to the arm holding the channeltron, was a mask with a slot equal in area to that of the channeltron input aperture (10 mm x 2 mm). This mask, when turned into the light path, sat at the same distance from the exit slit as the channeltron and ensured that, for a constant number of photons/sec from the light source, the flux reaching the photodiode was the same as that seen by the channeltron.

The channeltron was operated with - 3 KV on the funnel and with counting electronics as indicated in Figure B.1b. Output pulses from the channeltron were amplified and fed to a digital-to-analog convertor. The output voltage thus produced was directly proportional to

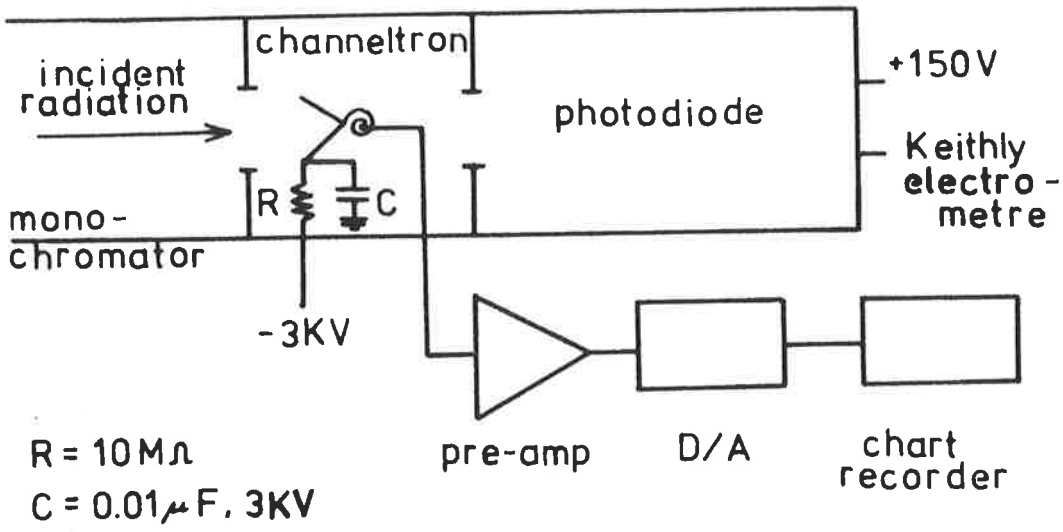

Figure B.1a Experimental schematics for channeltron calibration.

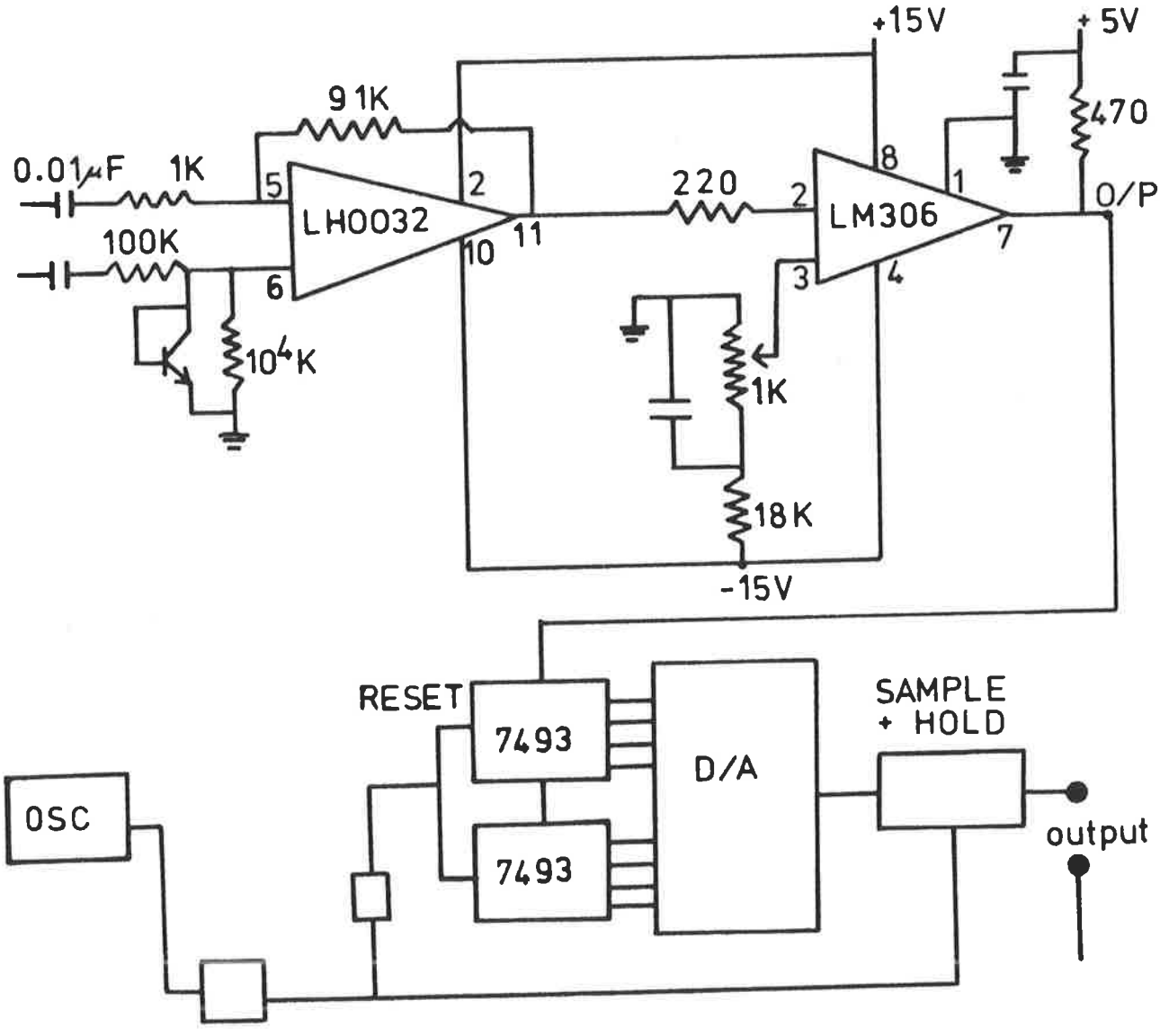

Figure B.1b Channeltron counting electronics.

the number of counts/sec received. Current from the photodiode was measured by a Keithly Electrometer and was directly proportional to the light intensity.

B.2 CALIBRATION RESULTS

Results of the calibration are shown in Figure B.2. Data for the graphs were obtained using the NI line at 116.8 nm which is an unresolved doublet of lines at 116.85 nm and 116.74 nm. The entrance slit width was 350 micron and the exit slit width was 375 micron. In the region of the channeltron the pressure was 3×10^{-4} torr.

Figure B.2a illustrates the voltage plateau for the channeltron and confirms that 3 KV was an appropriate starting voltage. Figure B.2b shows the variation of output pulse with changing light intensity. It can be seen that a saturated pulse height distribution was not produced until the input count rate was greater than 10^7 photons/sec and that until saturation was reached, the output count rate changed linearly with the change in the number of incident photons/sec.

From Figure B.2 it is evident that the output count rate was very low, at 10^3 counts/sec, and the channeltron quantum efficiency (counts/photon) was of the order of 10^{-4} which, in comparison to other commercially available channeltrons, is extremely low. Mack *et al* (1976) reported a quantum efficiency, at 120 nm, of 0.02 counts/photon as being representative of a large range of channeltron models. Timothy and Lapson (1974) quoted the detection efficiency of Mullard B419BL cone channeltrons as 0.05 counts/photon.

B.3 MANUFACTURER'S COMMENTS

Mullard concurred that the performance of the experimental channeltrons was disappointing and suggested that this was caused by the

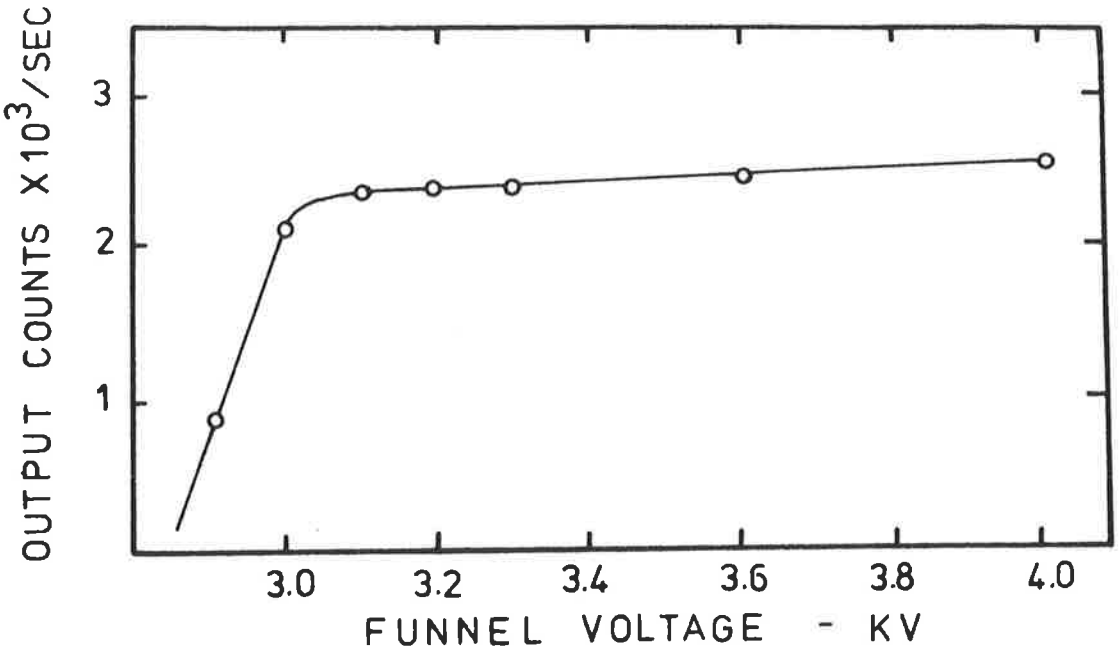

Figure B.2a Channeltron count rate v. funnel voltage.

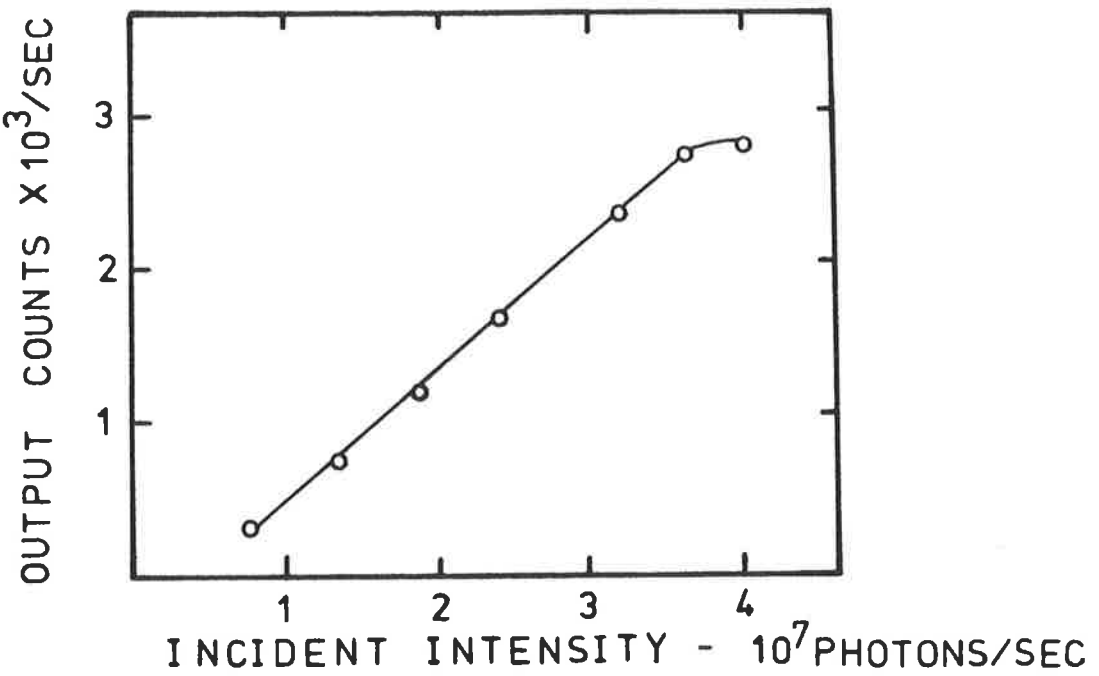

Figure B.2b Channeltron count rate v. incident radiant intensity.

low efficiency with which the input funnel converted incident photons to electrons, rather than the electron multiplying mechanism, which seemed to have performed satisfactorily.

A contributor to this low conversion efficiency may have been the high work function of the low resistance glass, causing the experimental channeltrons to be characterized by a plateau starting voltage of 3KV, compared to the normal 2KV. For this reason, Mullard noted that it would have been preferable to operate the channeltrons at 3.5 KV, rather than on the knee of the curve in Figure B.2a, at 3KV.

No further use of the particular low resistance glass used for the experimental channeltrons is proposed by Mullard, but developmental work on low resistance glasses is continuing.

APPENDIX C

EVALUATION OF JACCHIA (1977) THERMOSPHERIC COMPOSITION MODEL AT THE TIME OF THE AEROBEE LAUNCH

Jacchia's (1977) model consists of two parts;

I - basic static models which give temperature and density profiles for atmospheric constituents for any specified exospheric temperature, and

II - analytic formulae for computing the exospheric temperature and the expected deviations from the static models as a result of recognized types of thermospheric variations of the following origin;

(a) solar activity

(b) diurnal

(c) geomagnetic activity

(d) seasonal - latitudinal

(e) semi - annual

These variations are subject to some amount of regularity and can be predicted with varying degrees of accuracy on the basis of ground based observations.

Instructions for evaluating the model composition of the thermosphere at a particular location and time have been well documented by Jacchia (1977) and the following calculations were performed with the guidance of this manual. Values of the constants used in the model, and of the numerical calculations at the time of launch, are given simultaneously with the relevant equations.

C.I *SOLAR ACTIVITY*

Thermospheric and exospheric temperature depend on solar activity. The disc component of solar radiation can be linearly related to the 10.7 cm radio flux $F_{10.7}$ averaged or smoothed over a few solar rotations. Thus the temperature can also be related to this index of

solar activity, and this is expressed by

$$T_{\frac{1}{2}} = 5.48\,\overline{F}^{0.8} + 101.8\,F^{0.4}$$

where $T_{\frac{1}{2}}$ is the arithmetic mean of the global extrema of the diurnal variation in the exospheric temperature under quiet magnetic conditions, $K_p = 0$.

F is the 10.7 cm solar radio flux at the time t_o of evaluation,

$\overline{F}$ is a weighted average of the 10.7 cm flux over six solar rotations, centred on t_o, thus

$$\overline{F} = \frac{\Sigma\, w.F}{\Sigma w}, \quad w = \exp\left[- \left(\frac{t - t_o}{\tau} \right)^2 \right], \quad \tau = 70 \text{ days}$$

For the Aerobee launch :

t_o = 21st February, 1977

$F = 82 \times 10^{-22} \text{Wm}^{-2}\text{Hz}^{-1}$

$\overline{F} = 77.1 \times 10^{-22} \text{Wm}^{-2}\text{Hz}^{-1}$
(average of F values from 3rd December 1976 to 13th May 1977)

$T_{\frac{1}{2}}$ = 768 K

C.2 *DIURNAL VARIATIONS*

Once the exospheric temperature is known, the diurnal temperature T for given latitude and season is calculated from

$$T/T_{\frac{1}{2}} = 1 + c_1 \frac{\delta_0}{e} \sin\phi + c_2 \frac{\delta_0}{e} \cos\phi \left[f(H) - \tfrac{1}{2} \right]$$

where δ_0 is the solar declination,

c_1 and c_2 are constants,

e is the obliquity of the ecliptic,

ϕ is latitude, and

$f(H) = \cos^n \tfrac{1}{2}(H + \beta) + c_3 \cos [3(H + \beta) + \chi_c]$

is a function which varies from 0 to 1.

H is the Hour angle of the sun, and

$n = 2 + \cos^2 (\phi^2/90^2)$

where β is variable for each atmospheric constituent since, while the total density always peaks at the same time, the density of each atmospheric constituent peaks at different times of the day;

$\beta_i = \beta_0 + \beta_1 (\bar{M}/M_i - 1)$

where β_0 and β_1 are constants,

M_i is the mass of atmospheric species i,

$\bar{M}$ is the mean molecular mass, given at different altitudes by the static models for the calculated exospheric temperature T_{∞}.

For the Aerobee launch :

$c_1 = 0.15, \quad c_2 = 0.24, \quad c_3 = 0.08$

$\delta_0 = -10.36$

$e = 23^\circ.44$

$\phi = -30.56^\circ$

$H = -81^\circ$

$\chi_c = -75^\circ$

$\beta_0 = -35^\circ, \quad \beta_1 = 27^\circ$

$M(N_2) = 28, \quad M(O_2) = 32, \quad M(O) = 16.$

The diurnal temperature T, calculated at different heights for each species, is called the pseudo temperature and this is used to determine, from the static models, densities for each species corresponding to 'quiet' solar conditions, $K_p = 0$.

C.3 GEOMAGNETIC ACTIVITY

When $K_p \neq 0$, geomagnetic activity produces a temperature increase $\Delta_G T$, which depends on magnetic latitude and induces a density change $\Delta_T \log(n_i)$. Simultaneously, atmospheric composition changes arise not only because of the change in scale height induced by $\Delta_G T$, but also because of a change in the interface between the regions of mixing and diffusion. Effectively, the height of the homopause changes by an amount Δz_H and this contributes an amount $\Delta_H \log(n_i)$ to the change in the densities of the atmospheric constituents in the diffusion region. Also, a density wave propagates from high to low magnetic latitudes causing a further density change $\Delta_e \log(n_i)$. Thus, the resultant change in density due to geomagnetic activity is the sum of these three effects, vis

$$\Delta_G \log(n_i) = \Delta_T \log(n_i) + \Delta_H \log(n_i) + \Delta_e \log(n_i)$$

and in the model each of these effects is individually evaluated to determine the corresponding density increment, as follows.

The change in temperature due to geomagnetic activity is calculated at each height z according to

$$\Delta_G T(z) = \Delta_G T_\infty \tanh [\, c\,(z - z_0)\,],$$

$$\Delta_G T_\infty = A \sin^4 \phi',$$

$$\sin \phi' = 0.9792 \sin \phi + 0.2028 \cos \phi \cos(\theta - 291)$$

$$A = 57.5\ ^\circ K'_p\ [\, 1 + 0.027 \exp(0.4\ K'_p)\,]$$

where c and z_0 are constants

ϕ' is the centred-dipole geomagnetic latitude

ϕ is latitude, θ is longitude

K'_p is the K_p value at a time $t_0 - t'$ where $t' = 0.1^d + 0.2^d \cos^2 \phi$.

For the Aerobee launch :

$$c = 0.006, \quad z_0 = 90 \text{ km}$$

$$\phi = -30.56^\circ, \quad \theta = 136.46^\circ E$$

$$K_p = 1^-, \quad K'_p = 3^-$$

Once calculated, $\Delta_G T$ is added to the pseudo temperature for each species and the static models consulted again to obtain 'disturbed' density profiles.

The change in the height of the homopause due to the temperature change generated by geomagnetic activity is

$$\Delta z_H = 5000 \sinh^{-1} (0.01\ \Delta_G T_\infty)$$

from which the density variation of each species is

$$\Delta_H \log(n_i) = \alpha_i\ \Delta\ z_H$$

Each species is affected equally by the equatorial wave, by an amount

$$\Delta_e \log(n_i) = 5.2 \times 10^{-4} A \cos^4 \phi'$$

For the Aerobee launch :

$$\Delta z_H = 1.492 \text{ km}$$

$$\alpha(N_2) = 0, \quad \Delta_H \log(n_{N_2}) = 0$$

$$\alpha(O_2) = 1.03 \times 10^{-5} \text{ (mks)}, \quad \Delta_H \log(n_{O_2}) = 0.01537$$

$$\alpha(O) = -4.85 \times 10^{-5} \text{ (mks)}, \quad \Delta_H \log(n_O) = -0.07238$$

$$\Delta_e \log(n_i) = 0.02813$$

C.4 *SEASONAL-LATITUDINAL VARIATION*

Seasonal - latitudinal variations influence thermosphere composition directly, causing a density change $\Delta_{TSL} \log(n_i)$. Also, the seasonal variation of temperature and density in the stratosphere and mesosphere spills into the lower thermosphere (up to about 150 km) causing a further density change $\Delta_{MSL} \log(n_i)$. These variations are given analytically by

$$\Delta_{TSL} \log(n_i) = c_i \frac{\delta_0}{e} \sin \phi$$

$$\Delta_{MSL} \log(n_i) = \left|\frac{\phi}{\phi}\right| S P \sin^2 \phi$$

$$S = 0.014 (z - 91) \exp [- 0.0013 (z - 91)^2]$$

$$P = \sin (2\pi\Phi + 1.72)$$

$$\Phi = (t_o - \text{Jan. } 1)/365$$

For the Aerobee launch :

$c(N_2) = c(O_2) = 0$

$c(0) = -0.16, \quad \Delta_{TSL}\log(n_0) = -0.03594$

t_o - Jan. 1 = 51, P = 0.0453

C.5 SEMI-ANNUAL VARIATION

The semi-annual density variation is a product of two functions, one of height and the other of time. This is expressed as

$$\Delta_{sa}\log(n) = f(z)\ g(t)$$

$$f(z) = [\ 0.04(z/100)^2 + 0.05\ ] \exp(-0.25z/100)$$

$$g(t) = 0.0284 + 0.382\ [\ 1 + 0.467 \sin(2\pi T + 4.14)\ ] \sin(4\pi T + 4.26)$$

$$T = \Phi + 0.0954\ \{\ [\ \tfrac{1}{2} + \tfrac{1}{2} \sin(2\pi\Phi + 6.04)\ ]^{1.65} - \tfrac{1}{2}\ \}$$

Final densities, after correcting the static models for all the variations described above, are listed in Table C.1 and illustrated in Figure C.1.

TABLE C.1 Neutral thermospheric densities predicted by Jacchia's 1977 composition model, for the time of the Aerobee launch.

Altitude - km	$n(N_2)$ - cm^{-3}	$n(O_2)$ - cm^{-3}	$n(O)$ - cm^{-3}
100	9.70×10^{12}	2.26×10^{12}	3.73×10^{11}
102	6.81	1.51	3.20
104	4.79	1.00	2.80
106	3.37	6.58×10^{11}	2.46
108	2.38	4.29	2.15
110	1.69	2.78	1.85
115	7.59×10^{11}	1.01	1.21
120	3.82	4.46×10^{10}	7.91×10^{10}
125	2.11	2.28	5.36
130	1.26	1.28	3.81
135	8.00×10^{10}	7.74×10^{9}	2.83
140	5.35	4.93	2.18
145	3.72	3.29	1.73
150	2.66	2.26	1.40
155	1.95	1.59	1.15
160	1.45	1.14	9.65×10^{9}
170	8.40×10^{9}	6.12×10^{8}	6.95
180	5.03	3.41	5.13
190	3.08	1.96	3.86
200	1.92	1.14	2.94

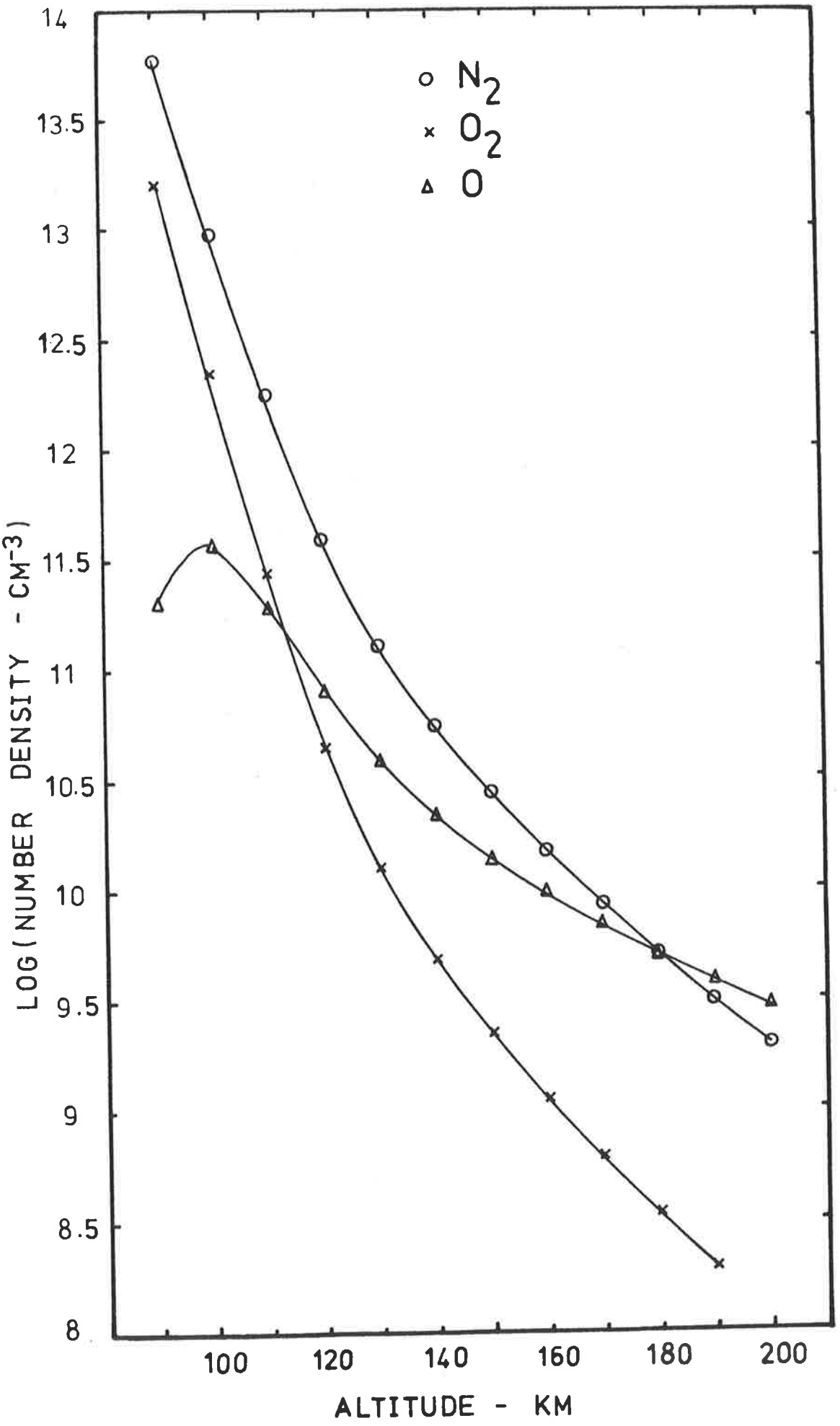

Figure C.1 Jacchia(1977) thermospheric composition model.

APPENDIX D

CALCULATION OF OPTICAL DEPTH FACTORS

Analytical expressions for the optical depth factor have been discussed in Section 2.1b. The following calculations used Equation 2.7 which gives the optical depth factor as

$$F(X, \chi) = (\pi X/2)^{\frac{1}{2}} \exp[\ (X/2)\cos^2\chi\ ]\ \text{erfc}\ [(X/2)^{\frac{1}{2}}\cos\ \chi\ ]$$

with $X = (r_e + h)/H_n$

where r_e is the radius of the earth,

h is the altitude,

H_n is the density scale height, and

χ is the zenith angle.

D.1 ZENITH ANGLES

Explanation of the terminology used in this section can be found in "The Astronomical Ephemeris for the Year 1977" (1975) and is applicable for the calculations of both solar and lunar zenith angles.

At a given latitude ϕ, on the earth's surface, the angle between the vertical and the position vector of the sun, called the zenith angle χ, can be determined from spherical geometry by

$$\cos\chi = \sin\phi \sin\delta_0 + \cos\phi \cos\delta_0 \cos \text{LHA}$$

where δ_0 is the solar declination and LHA is the Local Hour Angle of the sun. The LHA depends on the longitude θ and the universal time UT at which the zenith angle is being calculated;

$$\text{LHA} = \text{GHA} - \text{RA} + \text{UT} + \theta$$

where GHA is the Greenwich Hour Angle of the Equinox and RA is the Apparent Right Ascension. θ is positive eastward. Values of these

Parameters at the times T_0 of the Nike Orion launches have been given in Table 5.1, and in Table A.2 are those pertaining to the Aerobee lift off. In particular, ϕ and θ correspond to the origin of the range coordinate system.

Knowing the rocket location with respect to the range coordinates at some time $UT = T_0 + \Delta T$ after lift off enabled its latitude and longitude to be calculated for the duration of flight. At consecutive time intervals the instantaneous latitude and longitude were used in conjunction with interpolated values of GHA, δ_0 and RA to determine the zenith angle. Application of such procedures to the Nike Orion flight parameters produced the data in Figure 5.14. Alternatively, since the altitude was known as a function of time, it was also possible to obtain the height variation of the zenith angle, and this has been illustrated in Figure 5.17 for the single-stage Orion flight and is provided in Figure D.1 for the Aerobee downleg.

D.2 DENSITY SCALE HEIGHTS

At an altitude h, it is possible to estimate the density scale height $H_n(h)$ of a neutral atmospheric constituent from a model profile of its distribution $n(h)$ since, from Equation 2.5

$$H_n(h) = - \left[\frac{1}{n(h)} \frac{d\, n(h)}{dh} \right]^{-1}$$

Density scale heights were thus determined for N_2, O_2 and O from Jacchia's 1977 thermospheric composition model, evaluated in Appendix C, and ozone density scale heights were determined from the ozone density profile of the U.S. Standard Atmosphere, 1976 model.

D.3 NUMERICAL CALCULATIONS

Once the zenith angle and density scale height are known it is easy to calculate the optical depth factor when the rocket is at an

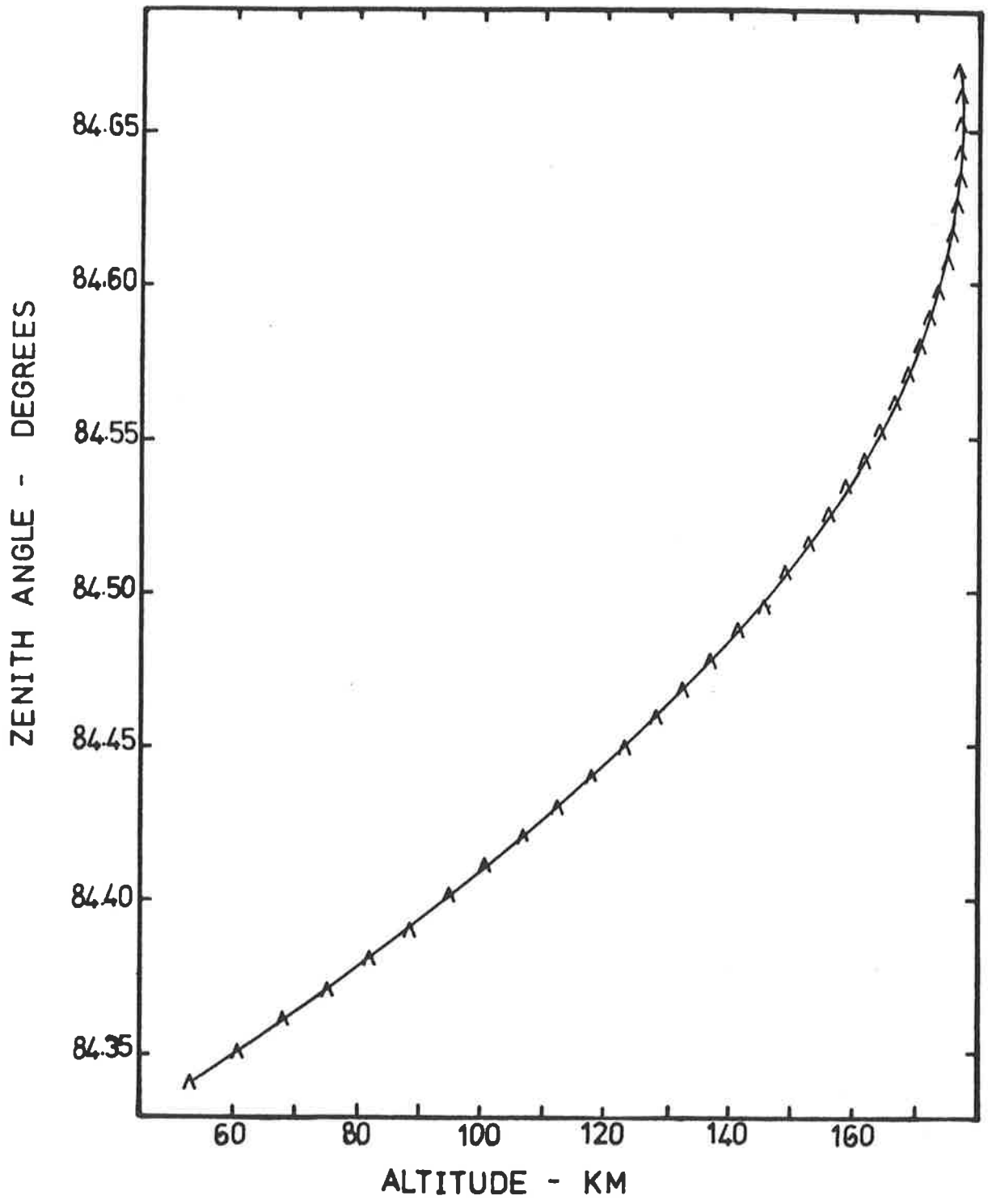

Figure D.1 Zenith angles for Aerobee downleg.

altitude h. To evaluate the complementary error function in Equation 2.7, the International Mathematical and Statistical Library (IMSL) function ERFC was used. Figure D.2 illustrates the variation of the optical depth factors pertaining to the neutral thermospheric constituents and data for this figure is provided in Table D.1, together with the scale heights. For the ozone measurements, optical depth factors and scale heights are available in Table D.2.

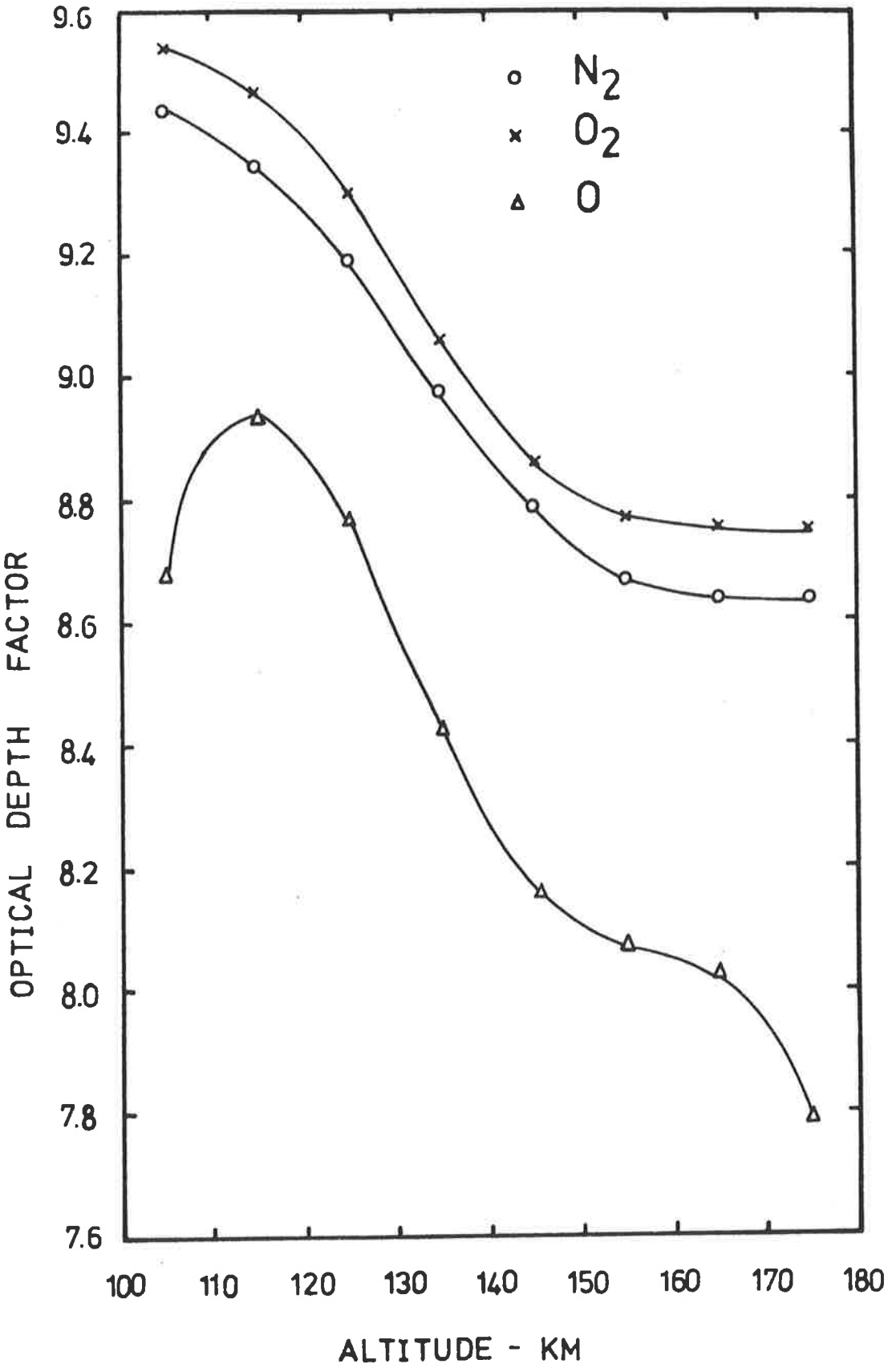

Figure D.2 Optical depth factors for neutral thermospheric constituents, determined at downleg Aerobee zenith angles.

TABLE D.1 Optical depth factor calculations for the Aerobee flight.

Altitude - km	Zenith Angle - degrees	N_2		O_2		O	
		Scale height - km	ODF	Scale height - km	ODF	Scale height - km	ODF
101	84.403	5.445	9.447	4.632	9.538	24.335	8.042
103	84.406	5.528	9.444	4.641	9.543	17.235	8.464
105	84.409	5.650	9.436	4.702	9.542	14.159	8.683
107	84.413	5.808	9.426	4.810	9.536	12.571	8.809
109	84.416	6.002	9.412	4.960	9.526	11.717	8.882
111	84.420	6.230	9.394	5.151	9.511	11.292	8.923
113	84.424	6.493	9.373	5.383	9.493	11.155	8.941
115	84.428	6.791	9.350	5.656	9.470	11.232	8.941
117	84.432	7.124	9.343	5.971	9.443	11.482	8.926
119	84.436	7.492	9.294	6.328	9.413	11.882	8.900
121	84.440	7.895	9.262	6.729	9.379	12.418	8.864
123	84.445	8.333	9.227	7.173	9.341	13.081	8.819
125	84.449	8.804	9.190	7.661	9.300	13.864	8.766
127	84.454	9.306	9.151	8.189	9.256	14.759	8.706
129	84.458	9.837	9.110	8.755	9.210	15.756	8.641
131	84.463	10.392	9.068	9.353	9.161	16.838	8.572
133	83.467	10.967	9.026	9.975	9.113	17.984	8.502
135	84.472	11.554	8.983	10.612	9.064	19.164	8.432
137	84.476	12.146	8.941	11.250	9.016	20.345	8.365
139	84.480	12.736	8.901	11.877	8.970	21.485	8.303
141	84.484	13.313	8.862	12.477	8.928	22.546	8.247
143	84.489	13.870	8.825	13.038	8.890	23.492	8.199
145	84.493	14.399	8.791	13.547	8.856	24.299	8.159
147	84.497	14.894	8.761	13.997	8.828	24.955	8.129
149	84.501	15.348	8.734	14.384	8.805	25.464	8.107
151	84.505	15.760	8.710	14.707	8.787	25.844	8.093
153	84.509	16.129	8.690	14.971	8.774	26.125	8.083
155	84.514	16.456	8.674	15.186	8.765	26.345	8.078
157	84.519	16.746	8.661	15.361	8.760	26.547	8.073
159	84.525	17.003	8.651	15.511	8.757	26.775	8.068
161	84.531	17.325	8.643	15.649	8.756	27.073	8.060
163	84.538	17.450	8.638	15.788	8.755	27.485	8.047
165	84.547	17.654	8.635	15.943	8.755	28.055	8.028
167	84.557	17.856	8.634	16.124	8.755	28.827	8.000
169	84.568	18.063	8.634	16.344	8.754	29.849	7.962
171	84.582	18.281	8.637	16.611	8.753	21.174	7.913
173	84.598	18.515	8.640	16.933	8.750	32.856	7.851
175	84.617	18.769	8.646	17.314	8.747	34.949	7.776
177	84.640	19.043	8.655	17.754	8.744	37.497	7.688

* sec(84.5) = 10.43.

TABLE D.2 Optical depth factor calculations for Nike Orion and single stage Orion flights.

Altitude - km	Scale height-km	31.011	31.012	31.013	30.009
		UPLEG			
27	6.106	3.604	2.549	13.992	2.4019
29	9.328	3.580	2.540	13.161	2.3959
31	10.735	3.568	2.536	12.868	2.3938
33	9.477	3.575	2.538	13.165	2.3973
35	7.588	3.586	2.542	13.656	2.4021
37	6.150	3.594	2.544	14.091	2.4060
39	5.224	3.598	2.546	14.414	2.4086
41	4.668	3.600	2.546	14.634	2.4106
43	4.367	3.600	2.546	14.771	2.4122
45	4.248	3.598	2.545	14.845	2.4134
47	4.261	3.596	2.544	14.870	2.4147
49	4.371	3.593	2.542	14.859	2.4157
51	4.537	3.589	2.541	14.828	2.4165
53	4.705	3.585	2.539	14.798	2.4172
55	4.808	3.582	2.538	14.793	2.4181
57	4.783	3.579	2.537	14.837	2.4194
59	4.602	3.578	2.536	14.946	2.4210
61	4.294	3.577	2.535	15.111	2.4230
63	3.928	3.576	2.535	15.293	2.4251
65	3.583	3.576	2.534	15.481	2.4273
67	3.324	3.574	2.533	15.645	2.4293
69	3.210	3.571	2.532	15.751	2.4311
71	3.335	3.567	2.530	15.751	2.4326
73	3.983	3.558	2.527	15.524	2.4330
		DOWNLEG			
27	6.106	3.034	2.291	39.368	
29	9.328	3.072	2.308	27.938	
31	10.735	3.110	2.326	23.785	
33	9.477	3.156	2.347	22.869	
35	7.588	3.201	2.367	22.762	
37	6.150	3.329	2.384	22.552	
39	5.224	3.271	2.398	22.153	
41	5.668	3.300	2.411	21.596	
43	4.367	3.323	2.421	20.936	
45	4.248	3.343	2.430	20.257	
47	4.261	3.360	2.437	19.596	
49	4.371	3.376	2.444	18.987	
51	4.537	3.388	2.449	18.428	
53	4.705	3.399	2.453	17.959	
55	4.808	3.409	2.458	17.595	
57	4.783	3.419	2.462	17.354	
59	4.602	3.428	2.466	17.237	
61	4.294	3.437	2.470	17.223	
63	3.928	3.445	2.473	17.277	
65	3.583	3.453	2.475	17.352	
67	3.324	3.459	2.478	17.402	
69	3.210	3.454	2.480	17.377	
71	3.335	3.467	2.481	17.217	
73	3.983	3.468	2.481	16.775	

APPENDIX E

TEMPERATURE PROFILES FOR THE UPPER ATMOSPHERE

As noted in Section 1.2a, temperature profiles such as the U.S. Standard Atmosphere, 1976 profile in Figure 1.2, are illustrative of an idealized steady-state representation of the earth's upper atmosphere. Realistically, the upper atmosphere temperature is attuned to a variety of geophysical perturbations.

Hence, when temperature is required as an input parameter for analysis of experimental data, the preferred profile is one derived from correlated *in situ* measurements. Usually such data is unavailable and semi-empirical models (Section 1.2c) must be consulted for an estimate of the temperature appropriate for the time and location of the experiment.

Alternately, the density profiles of the neutral constituents can infer the temperature. Under conditions of hydrostatic and thermal equilibrium, the density scale height H_n and the pressure scale height H_p are equivalent so the temperature at a given altitude h can be calculated, using Equations 2.5 and 2.6, from

$$T(h) = \frac{m\, g\, H_n(h)}{k}$$

$$= \frac{M\, g\, H_n(h)}{N_A\, k}$$

where m is the mass of a neutral constituent with molecular weight M, k is Boltzmann's constant and N_A is Avagadro's number.

In Figure E.1 are three temperature profiles for the lower thermosphere: the U.S. Standard Atmosphere, 1976 profile for typical thermospheric conditions; the particular prediction of Jacchia's (1977) model for the time of the Aerobee launch, incorporating corrections for exospheric temperature, latitude, season, geomagnetic activity and local time; and an estimate deduced from the molecular oxygen densities in Figure C.1 and the corresponding density scale heights in Table D.1.

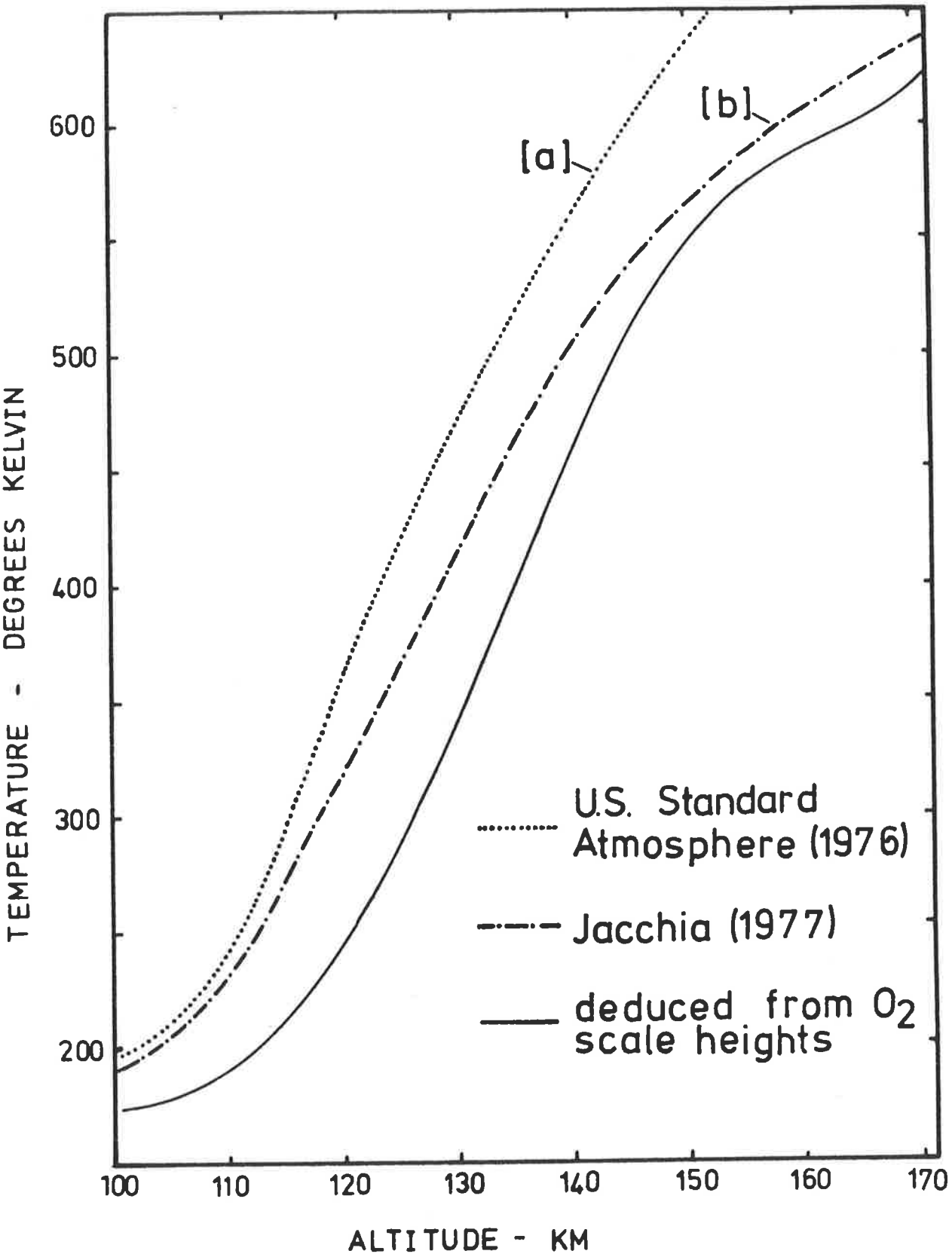

Figure E.1 Temperature profiles for the lower thermosphere.

In Figure E.2 the U.S. Standard Atmosphere, 1976 temperature profile for the stratosphere and mesosphere is compared with data from *in situ* measurements coincident with the rocket flights detailed in Chapter 5 (Table 5.1). Experimental data was acquired between altitudes 20 and 70 km from rocket-launched meteorological payloads, called 'super loki datasondes' (Wallops Flight Center, 1979a), which descended from apogee suspended below a Starute decelerator. The temperature sensor employed by these datasondes is a small spherical aluminized bead thermistor, about 0.25 mm in diameter, whose electrical resistance varies inversely with temperature.

experimental measurements (datasondes):

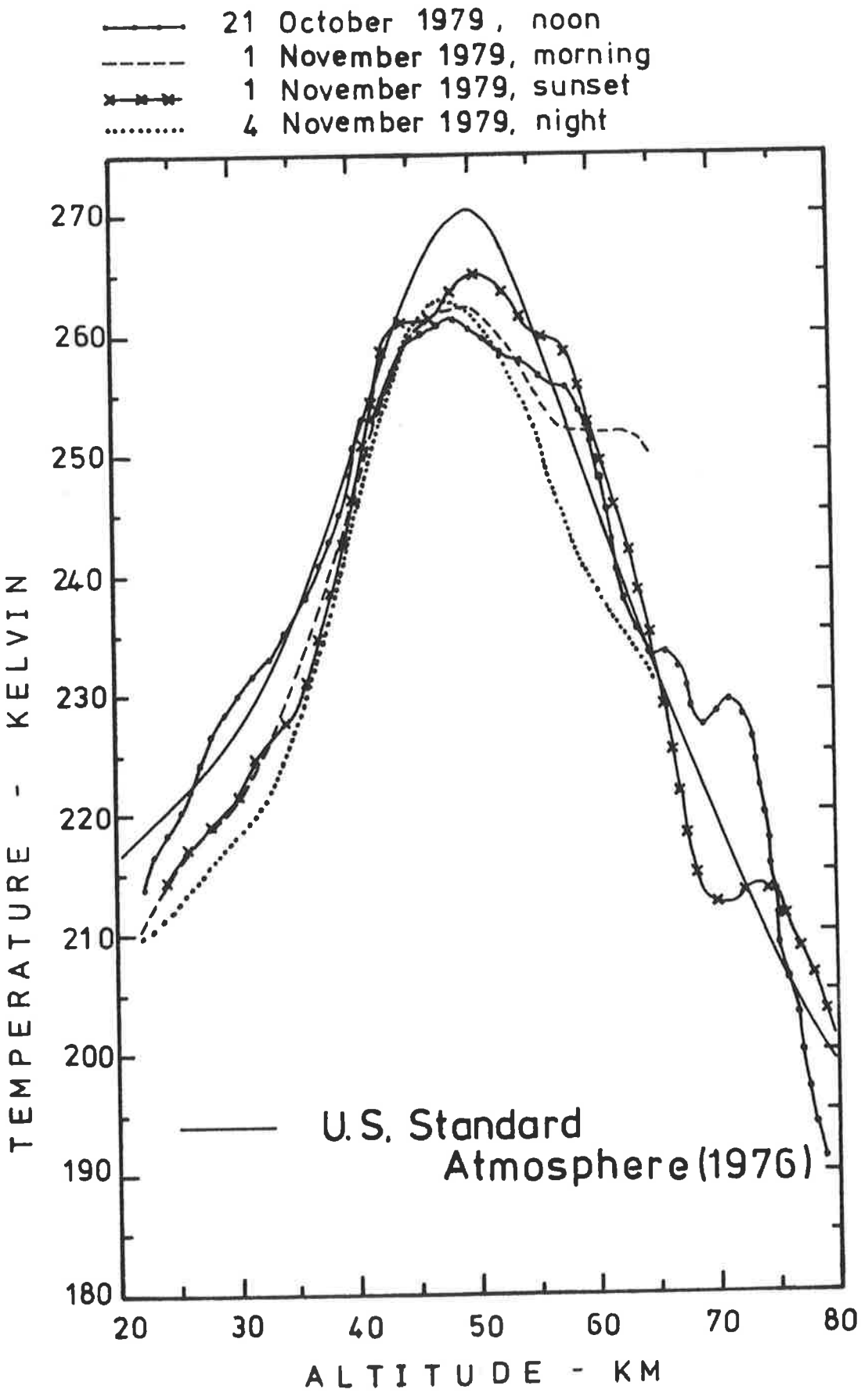

Figure E.2 Temperature profiles for the stratosphere and mesosphere.

APPENDIX F

DATA SMOOTHING PROCEDURES

In Chapter 5, experimental absorption curves were smoothed by least-squares fitting the data points with functions of the form

$$y(x) = a_1 + \frac{a_2}{1 + \exp[- (x-a_3)a_4 + (x-a_3)^2 a_5 - (x-a_3)^3 a_6 + (x-a_3)^4 a_7 + (x-a_3)^5 a_8]}$$

where a_j $(j = 1,8)$ are 8 fitting parameters. These functions afforded analytic representations of the data and did not attempt to approximate any theoretical models for describing atmospheric absorption.

To verify the ability of such functions to reproduce the typical characteristics of absorption profiles, they were least-squares fitted to calculated data points that represented the attenuation of MUV radiation within wavelength intervals monitored by the photometers employed in the ozone detectors. Calculations of the atmospheric absorption of MUV radiation have been described in Section 2.2c. In particular, to provide a wide variety of absorption profiles, use was made of the four different ozone density models identified in Figure F.1 as A, B, C and D. Ozone profile A corresponds to the U.S. Standard Atmosphere, 1976 and the variability of ozone concentrations, according to this model, is also indicated in Figure F.1. The other profiles B, C and D represent alternate ozone distributions that might possibly occur in the upper atmosphere. For example, the altitude of the maximum concentration has been observed experimentally to vary and this is reflected in the differences between the profiles B and C. Wave structure, evident in profile D, has also been observed experimentally and may be the consequence of vertically propagating gravity waves.

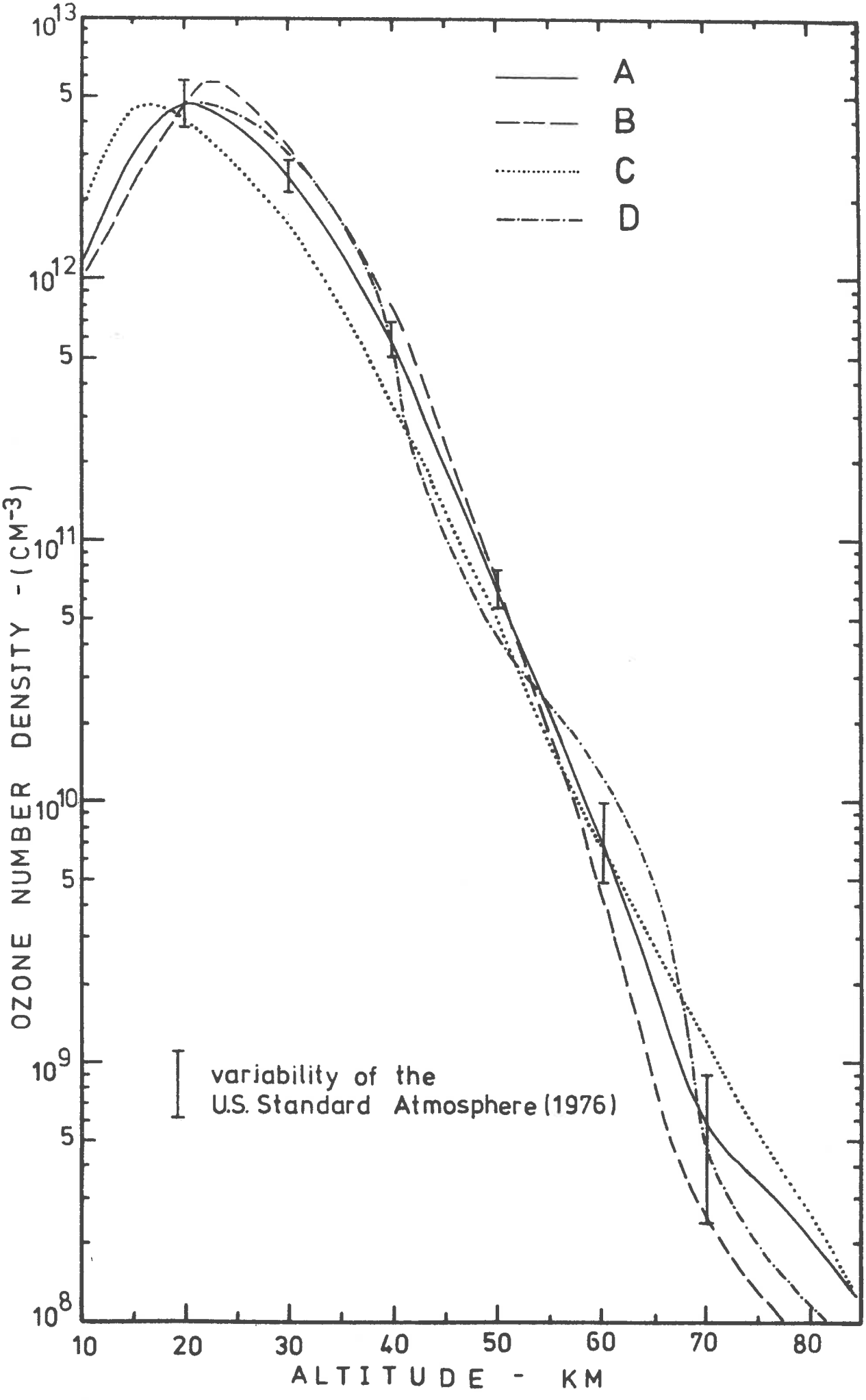

Figure F.1 Model ozone profiles for theoretical calculations.

In Figure F.2 are four attenuation profiles, calculated for a photometer centred at 257.5 nm, when the solar zenith angle is 70°, corresponding to each of the four ozone density profiles in Figure F.1. The smooth curves through the calculated data points were obtained from least-squares fitted analytic functions.

Techniques for non-linear least-squares fitting have been described by Bevington (1969), who incorporated them into a computer routine called CURFIT. The optimum values of the parameters a_i are obtained by minimizing the quantity

$$\chi^2 = \Sigma \{ \frac{1}{\sigma_i^2} [y_i - y(x_i)]^2 \}$$

with respect to each of the n parameters a_j simultaneously. Here, (x_i, y_i) are the experimental data points, $y(x_i)$ are the fitted points and σ_i are estimates of the relative uncertainties of the experimental data, effectively weighting parameters, which were set equal to unity. For the purpose of minimizing it, χ^2 is considered a continuous function of n parameters, describing a hypersurface in n dimensional space, and the space is searched for the minimum value.

In the program CURFIT, the minimum in parameter space is located by combining an initial gradient search with an analytic solution developed from linearizing the fitting function. In the gradient search method of least-squares, all the parameters a_j are incremented simultaneously with the relative magnitude adjusted so that the resultant direction of travel in parameter space is along the direction of the maximum variation of χ^2. Because the gradient search becomes insensitive as it approaches the minimum, where the variation of the gradient becomes increasingly small, another technique is then employed to locate the actual minimum. This involves expanding the

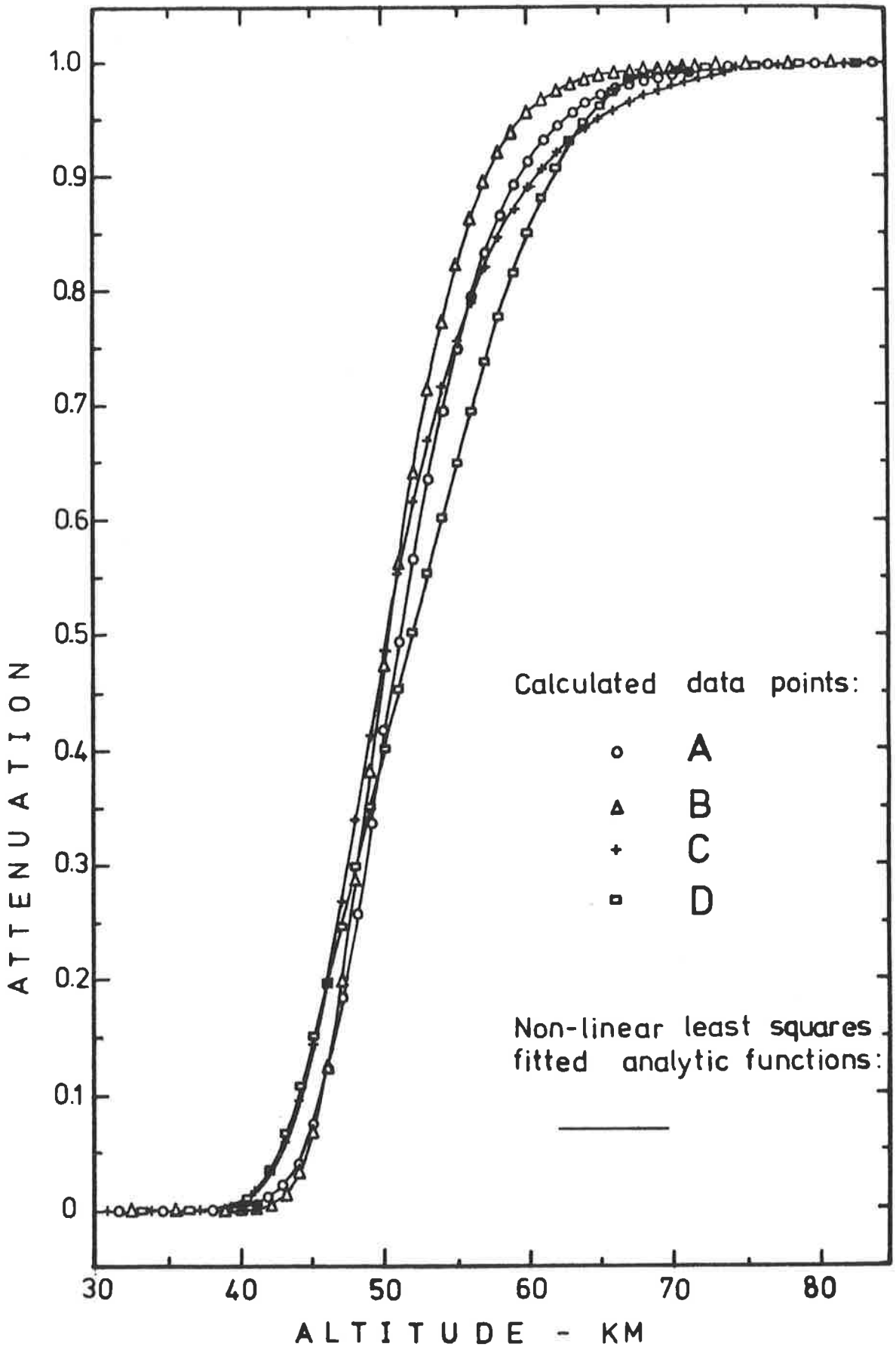

Figure F.2 Theoretical attenuation of MUV radiation, measured by a broad band detector centred at 257.5 nm, for the model ozone profiles in Figure F.1, when the zenith angle is 70°.

fitting function $y(x)$ as a function of the parameters a_j. For example, to first order, this can be done in a Taylor's expansion

$$y(x) = y_o(x) + \sum_{j=1,n}^{n} \left[\frac{\partial y_o(x)}{\partial a_j} \Delta a_j \right]$$

to provide a function which is linear in the parameter increments Δa_j so that the method of linear least squares can be applied to determine their optimum values.

It is important, for the most rapid convergence of the fitting routine, that appropriate initial values for a_j be chosen. These were estimated from the experimental data; a_1 was taken to be the minimum value of the absorption curve, $a_1 + a_2$ as the maximum value and a_3 was approximately equivalent to the altitude where the signal was $a_1 + a_2/2$. For the remaining 5 parameters, initial values were determined by using 5 pairs of data points to generate 5 linear equations which were solved simultaneously with the IMSL library routine LEQT1F.

Comparison of the calculated data points with the smooth function obtained from the fitting procedures was afforded by evaluating the sample variance which, for fitting 70 data points with a function having 8 parameters, is

$$s^2 = \frac{\Sigma \left[y_i - y(x_i) \right]^2}{62}$$

For the most reliable functional forms of the data, this is small. With reference to the 4 smooth curves in Figure F.2, as well as 4 additional curves generated for a photometer at 282.5 nm, the average variance was 3.02×10^{-6}, giving a standard deviation of 1.74×10^{-3}. So, for example, when the attenuation was 0.5 the fitted function differed from the calculated data point by 0.3%. It was concluded, therefore, that the analytic functions described in this appendix were most suitable for providing analytic representations of atmospheric absorption profiles.

APPENDIX G

STATISTICAL ANALYSIS TECHNIQUES

This appendix describes treatment of the ozone data sets reported in Chapter 5 to extract the precision of the measurement instruments, using the methodology of Grubbs (1980) which is as follows.

G.1 MATHEMATICAL THEORY

The result of an unbiased measurement x is the sum of the true value T and a random error E ;

$$x = T + E$$

A series of J measurements by three instruments yields the results

$$x_{11} = T_1 + E_{11} \qquad x_{12} = T_1 + E_{12} \qquad x_{13} = T_1 + E_{13}$$

$$x_{21} = T_2 + E_{21} \qquad x_{22} = T_2 + E_{22} \qquad x_{23} = T_2 + E_{23}$$

$$x_{j1} = T_j + E_{j1} \qquad x_{j2} = T_j + E_{j2} \qquad x_{j3} = T_j + E_{j3}$$

$$x_{J_1} = T_J + E_{J_1} \qquad x_{J_2} = T_J + E_{J_2} \qquad x_{J_3} = T_J + E_{J_3}$$

from which can be calculated sets of differences

$$D_{j12} = E_{j1} - E_{j2}$$

$$D_{j13} = E_{j1} - E_{j3}$$

$$D_{j23} = E_{j2} - E_{j3}$$

where $j = 1, J$.

The average of a set of differences generated, for example, by instruments 1 and 2 is

$$\bar{D}_{12} = \frac{\sum_{j=1}^{J} D_{j12}}{J}$$

and the variance is then

$$\sigma_{12}^2 = \frac{\sum_{j=1}^{J} [\, D_{j12} - \bar{D}_{12} \,]^2}{J - 1}$$

$$= \frac{\sum_{j=1}^{J} [\, D_{j12} \,]^2 - J \bar{D}_{12}^2}{J - 1}$$

where

$$\Sigma [\, D_{j12} \,]^2 = \Sigma [\, E_{j1} - E_{j2} \,]^2$$

$$= \Sigma [\, E_{j1} \,]^2 + \Sigma [\, E_{j2} \,]^2$$

since, for uncorrelated instruments, the cross product term is, on average, zero. Also

$$\bar{D}_{12}^2 = \bar{D}_1^2 - \bar{D}_2^2 \quad \text{so that}$$

$$\sigma_{12}^2 = \frac{\sum_{j=1}^{J} (E_{j1})^2 - J\bar{E}_1^2 + \sum_{j=1}^{J} (E_{j2})^2 - J\bar{E}_2^2}{J - 1}$$

$$= \sigma_1^2 + \sigma_2^2 .$$

More generally, there are three equations;

$$\sigma_{12}^2 = \sigma_1^2 + \sigma_2^2$$

$$\sigma_{13}^2 = \sigma_1^2 + \sigma_3^2$$

$$\sigma_{23}^2 = \sigma_2^2 + \sigma_3^2$$

which can be solved to provide numerical values for σ_1^2, σ_2^2 and σ_3^2, viz;

$$\sigma_1^2 = 0.5(\sigma_{12}^2 + \sigma_{13}^2 - \sigma_{23}^2)$$

$$\sigma_2^2 = 0.5(\sigma_{12}^2 + \sigma_{23}^2 - \sigma_{13}^2)$$

$$\sigma_3^2 = 0.5(\sigma_{13}^2 + \sigma_{23}^2 - \sigma_{12}^2)$$

G.2 APPLICATIONS

Because of the wide dynamic range of the ozone number densities over the altitude range where measurements were accumulated, the ratio of each measurement to the average measurement at a particular height was computed for input to the difference equations of the previous section.

As an example of the results of the application of this statistical technique to the ozone data, the treatment of the three instruments used to measure the nighttime ozone densities is summarized in Table G.1 while Table G.2 provides an example of the application of this statistical technique for determining the precision of three daytime measurements near noon.

TABLE G.1 Determining the precision of the measurement of nighttime ozone densities.

Altitude range	34.5 to 71 km, inclusive		
Altitude increment	one data point every 0.5 km		
No. of data points	74		
Differences set	D_{12}	D_{13}	D_{23}
Average of differences	0.02323	0.10050	0.07727
Variance of differences	0.02267	0.02260	0.01183
Instrument	1	2	3
Average of densities normalized to the U.S. Standard Atmosphere	1.3476	1.2744	1.1765
Instrument variance	0.01672	0.00595	0.00589
Precision	9.59%	6.05%	6.52%
Average Precision	7.39%		

TABLE G.2 Application of statistical analysis techniques for determining the precision of three daytime measurements, near noon.

Altitude range	31 to 57 km, inclusive		
Altitude increment	one data point every 0.5 km		
No. of data points	74		
Differences set	D_{12}	D_{13}	D_{23}
Average of differences	-0.00673	0.08109	0.08782
Variance of differences	0.01671	0.01534	0.00560
Instrument	1	2	3
Identification	31.010/UP	31.008/UP	31.008/DN
Average of densities normalized to the U.S. Standard Atmosphere	1.0032	1.0077	0.9180
Instrument variance	0.01322	0.00348	0.00212
Precision	11.46%	5.86%	5.01%
Average precision	7.44%		

BIBLIOGRAPHY

Acharya, Y.B., R.N. Misra, S.Lal and B.H. Subbaraya, A rocket borne solar MUV photometer for measurement of ozone concentrations in the stratosphere, J. Instn Electronics and Telecom. Engrs, 25, 256, (1979).

Ackerman, M., Molecular absorption cross-sections, Ann. Geophys., 28, 79, (1972).

Ackerman, M. and P. Simon, Rocket measurement of solar fluxes at 1216Å, 1450Å and 1710Å, Solar Phys., 30, 345, (1973).

Ackerman, M., D. Frimout and R. Pastiels, New ultraviolet solar flux measurements at 2000Å using a balloon borne instrument, in New Techniques in Space Astronomy, Labuhn and Lust (eds.), D. Reidel Publishing Company, Dordrecht-Holland, 251, (1971).

Ackerman, M., P. Simon, U. von Zahn and U. Laux, Simultaneous upper air composition measurements by means of UV monochromators and mass spectrometers, J. Geophys. Res., 79, 4757, (1974).

Alcayde, D., J. Fontanari, G. Kockarts, P. Bauer and R. Bernard, Temperature, molecular nitrogen concentration and turbulence in the lower thermosphere inferred from incoherent scatter data, Ann. Geophys., 35, 41, (1979).

Allaby, M. and J. Lovelock, Spray cans: the threat that never was, New Scientist, 87, 212, (1980).

Allison, A.C., A. Dalgarno and N.W. Pasachoff, Absorption by vibrationally excited molecular oxygen in the Schumann-Runge continuum, Planet. Space Sci., 19, 1463, (1971).

Amayenc, P., D. Alcayde and G. Kockarts, Solar extreme ultraviolet heating and dynamical processes in the mid latitude thermosphere, J. Geophys. Res., 80, 2887, (1975).

Anderson, G.P., C.A. Barth, F. Cayla and J. London, Satellite observations of the vertical ozone distribution in the upper stratosphere, Ann. Geophys., 25, 341, (1969).

Angell, J.K. and J. Korshover, Quasi-biennial and long term fluctuations in total ozone, Mon. Weather Rev., 101, 426, (1976).

Angell, J.K. and J. Korshover, Comparison of ozone variations derived from ozonesondes and Umkehr measurements for the period 1969-76, Mon. Weather Rev., 107, 599, (1979).

Astronomical Ephemeris for the Year 1977, Her Majesty's Stationery Office, London, (1975).

Atreya, S.K., T.M. Donahue, N.E. Sharp, B. Wasser, J.G. Drake and G.R. Riegler, Ultraviolet stellar occultation measurement of the H_2 and O_2 densities near 100 km in the earth's atmosphere, Geophys. Res. Lett., 3, 607, (1976).

Austin, W.E., J.D. Purcell and R. Tousey, A spectrum of the sun from 168 to 700Å, Astron. J., 67, 110, (1962).

Austin, W.E., J.D. Purcell, R. Tousey and K.G. Widing, Coronal emission line intensities in the extreme ultraviolet, Astrophys. J., 145, 373, (1966).

Avrett, E.H., Models of the solar atmosphere, in The Solar Output and its Variation, O. White (ed.), Colorado Associated University Press, Boulder, 327, (1977).

Banks, P.M. and G. Kockarts, Aeronomy, Academic Press, New York and London, (1973).

Banwell, C.N., Fundamentals of Molecular Spectroscopy, McGraw-Hill Book Company (UK) Ltd., (1972).

Basher, R.E. and W.A. Matthews, Problems in the use of interference filters for spectrophotometric determination of total ozone, J. Appl. Meteor., 16, 795, (1977).

Barlier, F., C. Berger, J.L. Falin, G. Kockarts and G. Thuillier, A new three-dimensional thermospheric model based on satellite drag data, Space Res., 17, 207, (1977).

Barlier, F., C. Berger, J.L. Falin, G. Kockarts and G. Thuillier, A thermospheric model based on satellite drag data, Ann. Geophys., 34, 9, (1978).

Barlier, F., C. Berger, J.L. Falin, G. Kockarts and G. Thuillier, Comparisons between various semi-empirical thermospheric models of the terrestrial atmosphere, J. Atmos. Terrest. Phys., 41, 527, (1979).

Behring, W.E., L. Cohen and U. Feldman, The solar spectrum: Wavelengths and identification from 60 to 385Å, Astrophys, J., 175, 493, (1972).

Behring, W.E., L. Cohen, U. Feldman and G.A. Doschek, The solar spectrum: Wavelengths and identification from 160 to 770Å, Astrophys. J., 203, 521, (1976).

Bevington, P.R., Data Reduction and Error Analysis for the Physical Sciences, McGraw-Hill Book Company, (1969).

Bibbo, G., Private communication, (1980).

Bibbo, G., J.H. Carver, L.A. Davis, B.H. Horton and J.L. Lean, UV extinction and mass spectrometer rocket measurements of atmospheric composition over Woomera, Space Res., 19, 255, (1979).

Blackshear, W.T. and R.H. Tolson, High Correlations between variations in monthly averages of solar activity and total atmospheric ozone, Geophys. Res. Lett., 5, 921, (1978).

Blake, A.J., An atmospheric absorption model for the Schumann-Runge bands of oxygen, J. Geophys. Res., 84, 3272, (1979).

Blake, A.J., J.H. Carver and G.N. Haddad, Photo-absorption cross-sections of molecular oxygen between 1250Å and 2350Å, J. Quant. Spectrosc. Radiat. Transfer, 6, 451, (1966).

Blake, A.J., D.G. McCoy, H.P.F. Gies and S.T. Gibson, Photoabsorption in molecular oxygen, Interim Sci. Rep., 15 Sept. 1978 - 30 Nov. 1979, Air Force Geophys. Lab., Hanscom AFB, MA, (1980).

Blum, P.W., K.G.H. Schuchardt and U. von Zahn, Semi-empirical models of the neutral atmosphere based on turbopause height and exospheric temperature variations, J. Atmos. Terrest. Phys., 40, 1131, (1978).

Bojkov, R.D., Some characteristics of the total ozone deduced from Dobson-spectrophotometer and filter-ozonemeter data and their application to a determination of the effectiveness of the ozone station network, Ann. Geophys., 25, 293, (1969).

Bonnet, R., Recherches sur l'emission continue du soleil entre 1950 et 3000Å, Ann. Astrophys., 31, 597, (1968).

Borucki, W.J., R.C. Witten, H.T. Woodward, L.A. Capone., C.A. Riegel and S. Gaines, Stratospheric ozone decrease due to chlorofluoro-methane photolysis : Predictions of latitude dependence, J. Atmos. Sci., 37, 686, (1980).

Brannon, P.J. and J.M. Hoffman, Molecular oxygen density measurements from 80 to 140 km, J. Geophys. Res., 76, 4630, (1971).

Brasseur, G., Long term effects on the ozone layer of nitrogen oxides produced by thermonuclear explosions in the atmosphere, Ann. Geophys., 4, 301, (1978).

Breig, E.L., Aeronomic consequences of solar flux variations between 2000 and 1325Å, J. Geophys. Res., 78, 5718, (1973).

Breig, E.L., M.E. Brennan and R.J. McNeal, Effect of atomic oxygen on the N_2 vibrational temperature in the lower thermosphere, J. Geophys. Res., 78, 1225, (1973).

Brezgin, N.I., G.I. Kuznetsov, A.F. Chizhov and O.V. Shtyrkov, Results of the measurement of the vertical profile of ozone up to a height of 70 km by means of the M-12 and M-100 sounding rockets, Meteorologichiskiye Issledovaniya, 23, 30, (1977).

Broadfoot, A.L., The solar spectrum 2100-3200Å, Astrophys. J., 173, 681, (1972).

Brueckner, G.E. and O.K. Moe, High angular resolution absolute intensity of the solar continuum from 1400Å to 1790Å, Space Res., 12, 1595, (1972).

Brueckner, G.E., D.F. Bartoe, C.M. Brown, D.K. Prinz., S.G. Tilford and M.E. van Hoosier, Oxygen densities at altitudes between 70 km and 120 km, Paper presented at 17th meeting of COSPAR, Sao Paulo, Brazil, (1974).

Brueckner, G.E., F. Bartoe, O.K. Moe and M.E. van Hoosier, Absolute solar ultraviolet intensities and their variations with solar activity. I. The wavelength region 1750 - 2100Å, Astrophys. J., 209, 935, (1976).

Butler, D.M., The uncertainty in ozone calculations by a stratospheric photochemistry model, Geophys. Res. Lett., 5, 769, (1978).

Cairns, R.B. and J.A.R. Samson, Total absorption cross-section of atomic oxygen below 910Å, Phys. Rev., 139, A1403, (1965).

Cantu, A.M. and G. Tondello, Continuum source and a focusing technique for the 80-500Å spectral range : Improvements, Appl. Opt., 14, 996, (1975).

Carignan, G.R., Thermospheric composition, Rev. Geophys. Space Phys ., 13, 885, (1975).

Carroll, P.K. and C.P. Collins, High resolution absorption studies of the $b'\pi_u \leftarrow X'\Sigma_g^+$ system of nitrogen, Can. J. Phys., 47, 563, (1969).

Carver, J.H., The atmospheric density of molecular oxygen, Ann. IQSY, 6, 259, (1969).

Carver, J.H. and B.H. Horton, Rocket determination of the ultraviolet reflectivity of the moon, Proc. Astron. Soc. Aust., 1, 11, (1967).

Carver, J.H. and P. Mitchell, Ionization chambers for the vacuum ultraviolet, J. Sci. Instrum., 41, 555, (1964).

Carver, J.H. and P. Mitchell, Effects of temperature and irradiation on the characteristics of ultraviolet ion chambers, J. Opt. Soc. Amer., 57, 738, (1967).

Carver, J.H., P. Mitchell, E.L. Murray and B.G. Hunt, Molecular oxygen density and Lyman-alpha absorption in the upper atmosphere, J. Geophys. Res., 69, 3755, (1964).

Carver, J.H., B.H. Horton and F.G. Burger, Nocturnal ozone distribution in the upper atmosphere, J. Geophys. Res., 71, 4189, (1966).

Carver, J.H., B.H. Horton and F.G. Burger, Rocket determination of the night ozone distribution and the lunar ultraviolet flux, Space Res., 7, 1020, (1967).

Carver, J.H., P.J. Edwards, P.L. Gough., A.G. Gregory , B. Rofe and S.G. Johnson, Solar absorption photometry and the determination of atmospheric composition, J. Atmos. Terrest. Phys., 31, 563, (1969).

Carver, J.H., B.H. Horton, G.W.A. Lockey and B. Rofe, Ultraviolet ion chamber measurements of the solar minimum brightness temperature, Solar Phys., 27, 347, (1972a).

Carver, J.H., B.H. Horton, R.S. O'Brien and B. Rofe, Ozone determinations by lunar rocket photometry, Planet. Space Sci., 20, 217, (1972b).

Carver, J.H., B.H. Horton, M. Ilyas and G.G. O'Connor, Rocket measurements of high altitude molecular oxygen, Paper presented at IAMAP/IAPSO First Special Assemblies, Melbourne, Aust., January (1974).

Carver, J.H., H.P.F. Gies, T.I. Hobbs., B.R. Lewis and D.G. McCoy, Temperature dependence of the molecular oxygen photoabsorption cross-section near the H-Lyman-alpha line, J. Geophys. Res., 82, 1955, (1977a).

Carver, J.H., B.H. Horton, M. Ilyas and B.R. Lewis, Molecular oxygen densities and the atmospheric absorption of solar Lyman-alpha radiation, J. Geophys. Res., 82, 2613, (1977b).

Carver, J.H., L.A. Davis, B.H. Horton and M. Ilyas, Ultraviolet extinction measurements of molecular oxygen density, J. Geophys. Res., 83, 4377, (1978a).

Carver, J.H., G.N. Haddad, T.I. Hobbs, B.R. Lewis and D.G. McCoy, Vacuum ultraviolet six metre monochromator, Appl. Opt., 17, 420, (1978b).

Chakrabarty, P., D.K. Chakrabarty and A.K. Saha, Solar flux estimated from electron density and ion composition measurements in the lower thermosphere, J. Geophys. Res., 82, 3299, (1977).

Chamberlain, J.W., Theory of Planetary Atmospheres : An Introduction to their Physics and Chemistry, International Geophysics Series, 22, Academic Press, (1978).

Chandra, S. and A.K. Sinha, The diurnal heat budget of the thermosphere, Planet. Space Sci., 21, 593, (1973).

Chang, J.S., W.H. Duewer and D.F. Wuebbles, The atmospheric nuclear tests of the 1950's and 1960's : A possible test of ozone depletion theories, J. Geophys. Res., 84, 1755, (1979).

Chapman, S., A theory of upper atmosphere ozone, Mem. Roy. Meteorol. Soc., 3, 103, (1930).

Chapman, S., The absorption and dissociative or ionizing effect of monochromatic radiation in an atmosphere on a rotating earth, Proc. Phys. Soc., 43, 26 and 483, (1931).

Chapman, R.D. and W.M. Neupert, Slowly varying component of extreme ultraviolet solar radiation and its relation to solar radio radiation, J. Geophys. Res., 79, 4138, (1974).

Chasovitin, Yu. K., A.A. Pokhunkov, N.M. Klyueva, G.F. Tulinov and V.G. Khryukin, Mass spectrometer and probe measurements of upper atmosphere parameters from Heiss Island, Space Res., 16, 445, (1976).

Chernyshev, V.I., A.G. Kolesnik and M.N. Vlasov, Rate of heating of the ionospheric plasma by solar radiation. II. Heating by emission in the Schumann-Runge continuum and as a result of chemical reactions, Geomagn. i aeronomiya, 18, 164, (1978).

CIRA 1972, The Mean COSPAR International Reference Atmosphere.

Codling, K., Structure of the photo-ionization continuum of N_2 near 500Å, Astrophys. J., 143, 552, (1966).

Cole, B.E. and R.N. Dexter, Empirical photoabsorption cross-sections for C, N, O, F and Cl obtained from molecular measurements between 50 and 340Å, J. Quant. Spectrosc. Radiat. Transfer, 19, 467, (1978a).

Cole, B.E. and R.N. Dexter, Photoabsorption and photoionization measurements on some atmospheric gases in the wavelength region 50 - 340Å, J. Phys. B : Atom. Molec. Phys., 11, 1011, (1978b).

Comes, F.J., F. Speier and A. Elzer, Photoionizationsuntersuchungen an atomstrahlen, Z. Naturforsch, 23, 125, (1968).

Cook, G.R. and P.H. Metzger, Photoionization and absorption cross-sections of O_2 and N_2 in the 600 to 1000Å region, J. Chem. Phys., 41, 321, (1964).

Cook, G.R., B.K. Ching and R.A. Becker, Absorption by, and photo-ionization of, N_2 and O_2 in the 830 - 1000Å range, Faraday Soc., Discussions, 31, 149, (1964).

Crutzen, P., Determination of parameters appearing in the oxygen-hydrogen atmosphere, Ann. Geophys., 25, 275, (1969).

Crutzen, P., Ozone production rates in an oxygen-hydrogen-nitrogen oxide atmosphere, J. Geophys. Res., 76, 7311, (1971).

Crutzen, P.J., Estimates of possible future ozone reductions from continued use of fluoro-chloro-methanes (CF_2Cl_2,$CFCl_3$), Geophys. Res. Lett., 1, 205, (1974).

Crutzen, P.J., Chlorofluoromethanes: Threats to the ozone layer, Rev. Geophys. Space Phys., 17, 1824, (1979).

Crutzen, P.J., I.S. Isaksen and J.R. NcAfee, The impact of the chloro-carbon industry on the ozone layer, J. Geophys. Res., 83, 345, (1978).

Cunnold, D.M., F.N. Alyea and R.G. Prinn, Preliminary calculations concerning the maintenance of the zonal mean ozone distribution in the northern hemisphere, Pure Appl. Geophys., 118, 329, (1980).

Cvetanović, R.J., Excited state chemistry in the stratosphere, Can. J. Chem., 52, 1452, (1974).

Dalgarno, A., Metastable species in the ionosphere, Ann. Geophys., 26, 601, (1970).

Dalgarno, A., R.J.W. Henry and A.L. Stewart, The photoionization of atomic oxygen, Planet. Space Sci., 12, 235, (1964).

Danilov, A.D., A.A. Pokhunkov, V.K. Semenov, V.A. Yarfolomeev, J.S. Shirke, R. Sridharan and S.P. Gupta, The variability of the upper atmosphere composition at the Dip equator, Paper presented at 22nd meeting of COSPAR, Bangalore,India, (1979).

Dave, J.V., Effects of aerosols on the estimation of total ozone in an atmospheric column from the measurements of its ultraviolet radiance, J. Atmos. Sci., 35, 899, (1978).

Davis, L.A., Private communication, (1980).

Deans, A.J., G.G. Shepherd and W.F.J. Evans, A rocket measurement of the O_2 ($b'\Sigma_g^+ - X^3\Sigma_g^-$) atmospheric band nightglow altitude distribution, Geophys. Res. Lett., 3, 441, (1976).

Dehmer, P.M., J. Berkowitz and W.A. Chupka, Photoionization of atomic oxygen from 920 to 650Å, J. Chem. Phys., 59, 5777, (1973).

De Jonckheere, C.G. and D.E. Miller, A measurement of the ozone concentration from 65 to 75 km at night, Planet. Space Sci., 22, 497, (1974).

Delaboudinière, J.P. and F. Millier, Preliminary results obtained from the solar EUV experiment on board the D2B Aura satellite, Space Res., 17, 519, (1977).

Delaboudinière, J.P., R.F. Donnelly, H.E. Hinteregger, G. Schmidtke and P.C. Simon, Intercomparison/compilation of relevant solar flux data related to aeronomy, Report to Working Group IV of Cospar, (1977).

DeLuisi, J.J., Shortened version of the Umkehr method for observing the vertical distribution of ozone, Appl. Opt., 18, 3190, (1979).

De Luisi, J.J. and P.M. Furukawa, An explanation for the worldwide anomaly in the concentrations of ozone above 40 km, J. Atmos. Sci., 27, 968, (1970).

DeLuisi, J.J., C.L. Mateer and D.F. Heath, Comparison of seasonal variations of upper stratospheric ozone concentrations revealed by Umkehr and Nimbus 4 BUV observations, J. Geophys. Res., 84, 3728, (1979).

De More, W.B. and O.F. Raper, Hartley band extinction coefficients of ozone in the gas phase and in liquid nitrogen, carbon monoxide and argon, J. Phys. Chem., 68, 412, (1964).

De Reilhac, L. and N. Damany, Photoabsorption cross-section measurements of some gases, from 10 to 50 nm, J. Quant. Spectrosc. Radiat. Transfer, 18, 121, (1977).

Detwiler, C.R., D.L. Garrett, J.D. Purcell and R. Tousey, The intensity distribution in the ultraviolet solar spectrum, Ann. Geophys., 17, 263, (1961).

Dickinson, R.E., Meteorology of the upper atmosphere, Rev. Geophys. Space Phys., 13, 771, (1975a).

Dickinson, R.E., Solar variability and the lower atmosphere, Bull. Amer. Meteorol. Soc., 56, 1240, (1975b).

Dickinson, P.H.G., R.C. Bolden and R.A. Young, Measurement of atomic oxygen in the lower ionosphere using a rocket borne resonance lamp, Nature, 252, 289, (1974).

Dickinson, P.G.H., N.D. Twiddy and R.A. Young, Atomic oxygen concentrations in the lower thermosphere, Space Res., 16, 301, (1976).

Ditchburn, R.W. and D.W.O. Heddle, Absorption cross-sections in the vacuum ultraviolet. I. Continuous absorption of oxygen (1800 to 1300Å), Proc. Roy. Soc. Lond., A220, 61, (1953).

Donahue, R.M., B. Guenther and R.J. Thomas, Spatial and temporal behaviour of atomic oxygen determined by Ogo 6 airglow observations, J. Geophys. Res., 79, 1959, (1974).

Donnelly, R.F. and J.H. Pope, The 1-3000Å solar flux for a moderate level of solar activity for use in modelling the ionosphere and upper atmosphere, NOAA Technical Report ERL 276-SEL 25, (1973).

Dressler, K., The lowest valence and Rydberg states in the dipole - allowed absorption spectrum of nitrogen. A survey of their interactions, Can. J. Phys., 47, 547, (1969).

Dupree, A.K. and E.M. Reeves, The extreme ultraviolet spectrum of the quiet sun, Astrophys. J., 165, 599, (1971).

Dütsch, H.U., The ozone distribution in the atmosphere, Can. J. Chem., 52, 1491, (1974).

Dütsch, H.U. and C. Ling, Critical comparison of the determination of vertical ozone distribution by the Umkehr method and by the electro-chemical sonde, Ann. Geophys., 25, 211, (1969).

Ehhalt, D.H., J.S. Chang and D.M. Butler, The probability distribution of the predicted CFM - induced ozone depletion, J. Geophys, Res., 84, 7889, (1979).

Ellsaesser, H.W., Ozone destruction by catalysis : Credibility of the threat, Atmos. Environ., 12, 1849, (1978).

Evans, W.F.J. and E.J. Llewellyn, Molecular oxygen emissions in the airglow, Ann. Geophys., 26, 167, (1970).

Evans, W.F.J. and E.J. Llewellyn, Measurements of mesospheric ozone from observations of the 1.27μm band, Radio Sci., 7, 45, (1972).

Evans, W.F.J. and E.J. Llewellyn, Atomic hydrogen concentrations in the mesosphere and the hydroxyl emissions, J. Geophys. Res., 78, 323, (1973).

Evans, W.F.J., D.M. Hunten, E.J. Llewellyn and A. Vallance Jones, Altitude profile of the infrared atmospheric system of oxygen in the dayglow, J. Geophys. Res., 73, 2885, (1968).

Farmer, C.B., O.F. Raper, B.D. Robbins, R.A. Toth and C. Muller, Simultaneous spectroscopic measurements of stratospheric species : O_3, CH_4, CO, CO_2, N_2O, H_2O, HCL and HF at northern and southern mid latitudes, J. Geophys. Res., 85, 1621, (1980).

Fastie, W.G., A small plane grating monochromator, J. Opt. Soc. Amer., 42, 641, (1952a).

Fastie, W.G., Image forming properties of the Ebert monochromator, J. Opt. Soc. Amer., 42, 647, (1952b).

Fastie, W.G., Ultraviolet measurements in planetary atmospheres, Appl. Opt., 6, 397, (1967).

Fastie, W.G., H.M. Crosswhite and P. Gloersen, Vacuum Ebert grating spectrometer, J. Opt. Soc. Amer., 48, 106, (1958).

Feldman, P.D. and P.Z. Takacs, Nitric oxide gamma and delta band emission at twilight, Geophys. Res. Lett., 1, 169, (1974).

Finger, F.G., A.J. Miller, D.F. Heath, A.J. Krueger and K. Labitzke, Examples of synoptic changes in ozone and circulation in the stratosphere, Space Res., 16, 121, (1976).

Fiocco, G., A. Mugnai and W. Forlizzi, Effects of radiation scattered by aerosols on the photodissociation of ozone, J. Atmos. Terrest. Phys., 40, 949, (1978).

Fishman, J., V. Ramanathan, P.J. Crutzen and S.C. Liu, Tropospheric ozone and climate, Nature, 282, 818, (1979).

Fitzmaurice, J.A., Simplification of the Chapman function for atmospheric attenuation, Appl. Opt., 3, 640, (1964).

Fleig, A.J., R.S. Fraser, B.W. Guenther, D.F. Heath, E. Hilsenrath, L.V. Novak, V.G. Kaveeschwar, R.D. McPeters, C.L. Mateer and A.J. Miller, Remote sensing of the atmosphere, in Developments in Atmospheric Science, A.L. Fymat and V.E. Zuer (eds.), Elsevier, New York, 97, (1978).

Forbes, J.M., Tidal variations in thermospheric O, O_2, N_2, Ar, He and H, J. Geophys. Res., 83, 3691, (1978).

Forbes, J.M. and H.B. Garrett, Theoretical studies of atmospheric tides, Rev. Geophys. Space Phys., 17, 1951, (1979).

Fox, J.N. and J.E.G. Wheaton, The BRV continuum source, J. Phys. E : Sci. Instrum., 6, 655, (1973).

Frederick, J.E., Chemical response of the middle atmosphere to changes in the ultraviolet solar flux, Planet. Space Sci., 25, 1, (1977).

Frederick, J.E., Influence of gravity wave activity on lower thermospheric photochemistry and composition, Planet. Space Sci., 27, 1469, (1979).

Frederick, J.E. and R.D. Hudson, Dissociation of molecular oxygen in the Schumann-Runge bands, J. Atmos. Sci., 37, 1099, (1980a).

Frederick, J.E. and R.D. Hudson, Atmospheric opacity in the Schumann-Runge bands and the aeronomic dissociation of water vapour, J. Atmos. Sci., 37, 1088, (1980b).

Garriott, O.K., R.B. Norton and J.G. Timothy, Molecular oxygen concentrations and absorption cross-sections in the thermosphere derived from extreme ultraviolet occultation profiles, J. Geophys. Res., 82, 4973, (1977).

Garton, W.R.S., J.P. Connerade, M.W.D. Mansfield and J.E.G. Wheaton, Atomic absorption spectroscopy in the 100 - 600Å wavelength interval, Appl. Opt., 8, 919, (1969).

Gauntner, D.J., T. Nyland, M. Tiefermann and T. Dudzinski, Measurements of carbon monoxide, condensation nuclei, and ozone on a B 747SP aircraft flight around the world, Geophys. Res. Lett., 6, 167, (1979)

Ghazi, A., A. Ebel and D.F. Heath, A study of satellite observations of ozone and stratospheric temperature during 1970-1971, J. Geophys. Res., 81, 5365, (1976).

Gille, J.C., P.L. Bailey and J.M. Russell III, Temperature and composition measurements from the LRIR and LIMS experiments on Nimbus 6 and 7, Phil. Trans. R. Soc. Lond. A, 296, 205, (1980a).

Gille, J.C., G.P. Anderson and P.L. Bailey, Comparison of near coincident LRIR and OAO-3 measurements of equatorial night ozone profiles, Geophys. Res. Lett., 7, 525, (1980b).

Gilmore, F.R., Potential energy curves for N_2, NO, O_2 and corresponding ions, J. Quant. Spectros. Radiat. Transfer, 5, 369, (1965).

Gribbin, J., Disappearing threat to ozone, New Scientist, 81, 474, (1979).

Griggs, M., Absorption coefficients of ozone in the ultraviolet and visible regions, J. Chem. Phys., 49, 857, (1968).

Gross, J. and U. von Zahn, Air density and composition in the lower thermosphere above Fort Churchill, Space Res., 11, 875, (1971).

Grubbs, F.E., On estimating precision of measuring instruments and product variability, J. Amer. Stat. Assoc., 43, 243, (1948).

Grubbs, F.E., Private communication, Japan, (1980).

Guenther, B., Maintaining calibration of long term satellite monitoring devices as performed on the ozone sensing BUV instruments, Amer. Chem. Soc., Proceedings, 4th Joint Conference on Sensing of Environmental Pollutants, 218, (1978).

Guenther, B., R. Dasgupta and D. Heath, Twilight ozone measurements by solar occultation from AE-5, Geophys. Res. Lett., 4, 434, (1977).

Gurkin, W., Private communication, (1980).

Gurtler, P., V. Saile and E.E. Koch, High resolution absorption spectrum of nitrogen in the vacuum ultraviolet, Chem. Phys. Lett., 48, 245, (1977).

Hall, J.E., Atmospheric pressure, density and scale height calculated from H Lyman-alpha absorption allowing for the variation in cross-section with wavelength, J. Atmos. Terrest. Phys., 34, 1337, (1972).

Hall, L.A., W. Schweizer and H.E. Hinteregger, Diurnal variation of the atmosphere around 190 km derived from solar extreme ultraviolet absorption measurements, J. Geophys. Res., 68, 6413, (1963a).

Hall, L.A., K.R. Damon and H.E. Hinteregger, Solar extreme ultraviolet photon flux measurements in the upper atmosphere of August 1961, Space Res., 3, 745, (1963b).

Hall, L.A., W. Schweizer and H.E. Hinteregger, Improved extreme ultraviolet absorption measurements in the upper atmosphere, J. Geophys. Res., 70, 105, (1965).

Hall, L.A., C.W. Chagnon and H.E. Hinteregger, Daytime variations in the composition of the upper atmosphere, J. Geophys. Res., 72, 3425, (1967).

Harwood, R.S., Dynamical models of the middle atmosphere for tracer studies, Phil. Trans. R. Soc. Lond. A, 296, 103, (1980).

Hasson, V. and R.W. Nicholls, Absolute spectral absorption measurements on molecular oxygen from 2640 - 1920Å : I. Herzberg I ($A^3\Sigma_u^+ - X^3\Sigma_g^-$) bands (2640 - 2430Å), J. Phys. B : Atom. Molec. Phys., 4, 1778, (1971a).

Hasson, V. and R.W. Nicholls, Absolute spectral absorption measurements on molecular oxygen from 2640 - 1920Å : II. Continuum measurements 2430 - 1920Å, J. Phys. B : Atom. Molec. Phys., 4, 1789, (1971b).

Hay, P.J. and W.A. Goddard III, Theoretical results for the excited states of ozone, Chem. Phys. Lett., 14, 46, (1972).

Hay, P.J., T.H. Dunning (Jr) and W.A. Goddard III, Theoretical evidence for bound electronic excited states of ozone, Chem. Phys. Lett., 23, 457, (1973).

Hay, P.J., T.H. Dunning (Jr) and W.A. Goddard III, Configuration interaction studies of O_3 and O_3^+. Ground and excited states, J. Chem. Phys., 62, 3912, (1975).

Hays, P.B. and R.G. Roble, Atmospheric properties from the inversion of planetary occultation data, Planet. Space Sci., 16, 1197, (1968).

Hays, P.B. and R.G. Roble, Observations of mesospheric ozone at low latitudes, Planet. Space Sci., 21, 273, (1973a).

Hays, P.B. and R.G. Roble, Stellar occultation measurements of molecular oxygen in the lower thermosphere, Planet. Space Sci., 21, 339, (1973b).

Hays, P.B., R.G. Roble and A.N. Shah, Terrestrial atmospheric composition from stellar occultations, Science, 176, 793, (1972).

Hays, P.B., D.W. Rusch, R.G. Roble and J.C.G. Walker, The OI (6300Å) airglow, Rev. Geophys. Space Phys., 16, 225, (1978).

Hearn, A.G., The absorption of ozone in the ultraviolet and visible regions of the spectrum, Proc. Phys. Soc., 78, 932, (1961).

Heath, D.F., Space observations of the variability of solar irradiance in the near and far ultraviolet, J. Geophys. Res., 78, 2779, (1973).

Hedin, A.E., C.P. Avery and C.D. Tschetter, An analysis of spin modulation effects on data obtained with a rocket borne mass spectrometer, J. Geophys. Res., 69, 4637, (1964).

Hedin, A.E., H.G. Mayr, C.A. Reber, N.W. Spencer and G.R. Carignan, Empirical model of global thermospheric temperature and composition based on data from the Ogo 6 quadrupole mass spectrometer, J. Geophys. Res., 79, 215, (1974).

Hedin, A.E., J.E. Salah, J.V. Evans, C.A. Reber, G.P. Newton, N.W. Spencer, D.C. Kayser, D. Alcayde, P. Bauer, L. Cogger and J.P. McClure, A global thermospheric model based on mass spectrometer and incoherent scatter data. MSIS1.N_2 density and temperature, J. Geophys. Res., 82, 2139, (1977a).

Hedin, A.E., C.A. Reber, G.P. Newton, N.W. Spencer, H.C. Brinton, H.G. Mayr and W.E. Potter, A global thermospheric model based on mass spectrometer and incoherent scatter data. MSIS2. Composition, J. Geophys. Res., 82, 2148, (1977b).

Henderson, W.R., Atomic oxygen profile measurement, J. Geophys. Res., 79, 3819, (1974).

Henderson, W.R. and H.I. Schiff, A simple sensor for the measurement of atomic oxygen height profiles in the upper atmosphere, Planet. Space Sci., 18, 1527, (1970).

Henry, R.J.W., Photoionization cross-sections for atomic oxygen, Planet. Space Sci., 15, 1747, (1967).

Henry, R.J.W., The influence of autoionizing states on absorption cross-sections for atomic oxygen, Planet. Space Sci., 16, 1503, (1968).

Herman, J.R., The response of stratospheric constituents to a solar eclipse, sunrise and sunset, J. Geophys. Res., 84, 3701, (1979).

Herman, J.R. and R.A. Goldberg, Sun, Weather and Climate, NASA SP-426, (1978).

Heroux, L. and J.E. Higgins, Summary of full-disc solar fluxes between 250 and 1940Å, J. Geophys. Res., 82, 3307, (1977).

Heroux, L. and H.E. Hinteregger, Aeronomical reference spectrum for solar UV below 2000Å, J. Geophys. Res., 83, 5305, (1978).

Heroux, L. and R.A. Swirbalus, Full-disc solar fluxes between 1230 and 1940Å, J. Geophys. Res., 81, 436, (1976).

Heroux, L., M. Cohen and M. Malinovsky, The interpretation of XUV rocket measurements of intensity ratios of solar spectral lines of the lithiumlike ions OVI, Ne VIII and MgX, Solar Phys.,23, 369, (1972).

Heroux, L., M. Cohen and J.E. Higgins, Electron densities between 110 and 300 km derived from solar EUV fluxes of August 23, 1972, J. Geophys. Res., 79, 5237, (1974).

Herzberg, G., Atomic spectra and atomic structure, Dover Publications, New York, (1944).

Herzberg, G., Spectra of Diatomic Molecules, van Nostrand Reinhold, (1950).

Herzberg, G., Molecular Spectra and Molecular Structure III Electronic Spectra and Electronic Structure of Polyatomic Molecules, van Nostrand Company, Inc, (1966).

Hesstvedt, E., A meridional model of the oxygen-hydrogen atmosphere, in Mesospheric Models and Related Experiments, G. Fiocco (ed.), D. Reidel Publishing Co, Dordrecht-Holland, 52, (1971).

Hesstvedt, E., Reduction of stratospheric ozone from high-flying aircraft, studied in a two-dimensional photochemical model with transport, Can. J. Chem., 52, 1592, (1974).

Hickman, D.R. and A.O. Nier, Measurement of the neutral composition of the lower thermosphere above Fort Churchill by rocket borne mass spectrometer, J. Geophys. Res., 77, 2880, (1972).

Higgins, J.E., The solar EUV flux between 230 and 1220Å on November 9, 1971, J. Geophys. Res., 81, 1301, (1976).

Higgins, J.E. and L. Heroux, Determination of molecular oxygen density between 110 and 170 km from a 1450Å photometer, J. Geophys. Res., 82, 3295, (1977).

Hill, R.M., Application of curve of growth to absorption spectral lines, J. Quant. Spectros. Radiat. Transfer, 21, 19, (1979).

Hill, W.J., P.N. Sheldon and J.J. Tiede, Analyzing world wide total ozone for trends, Geophys. Res. Lett., 4, 21, (1977).

Hilsenrath, E., Rocket observations of the vertical distribution of ozone in the Polar night and during a mid winter stratosphere warming, Geophys. Res. Lett., 7, 581, (1980).

Hilsenrath, E., L. Seiden and P. Goodman, An ozone measurement in the mesosphere and stratosphere by means of a rocket sonde, J. Geophys. Res., 74, 6873, (1969).

Hilsenrath, E., R.L. Coley, P.T. Kirschener and B. Gammill, A rocket ozonesonde for geophysical research and satellite intercomparison, NASA Tech. Mem. 79712, (1979a).

Hilsenrath, E., D.F. Heath and B.M. Schlesinger, Seasonal and interannual variations in total ozone revealed by the Nimbus-4 backscattered ultraviolet experiment, J. Geophys. Res., 84, 6969, (1979b).

Hinteregger, H.E., Telemetering monochromator measurements of extreme ultraviolet radiation. Part I : Introduction and technology. Part II : Physical Applications, in Space Astrophysics, W. Liller (ed.), McGraw-Hill Inc, New York, 34, (1961).

Hinteregger, H.E., Absorption spectrometric analysis of the upper atmosphere in the EUV region, J. Atmos. Sci., 19, 351, (1962).

Hinteregger, H.E., The extreme ultraviolet solar spectrum and its variation during a solar cycle, Ann. Geophys., 26, 547, (1970).

Hinteregger, H.E., EUV fluxes in the solar spectrum below 2000Å, J. Atmos. Terrest. Phys., 38, 791, (1976).

Hinteregger, H.E., Development of solar cycle 21 observed in EUV spectrum and atmospheric absorption, J. Geophys. Res., 84, 1933, (1979).

Hinteregger, H.E. and L.M. Chaikin, EUV absorption analysis of thermospheric structure from AE satellite observations of 1974-76, Space Res., 17, 525, (1977).

Hinteregger, H.E. and L.A. Hall, Thermospheric densities and temperature from EUV absorption measurements by OSO-III, Space Res., 9, 519, (1969).

Hinteregger, H.E., K.R. Damon, L. Heroux and L.A. Hall, Telemetering monochromator measurements of solar 304Å radiation and its attenuation in the upper atmosphere, Space Res., 1, 615, (1960).

Hinteregger, H.E., L.A. Hall and G. Schmidtke, Solar radiation and neutral particle distribution in July 1963 thermosphere, Space Res., 5, 1175, (1965).

Hinteregger, H.E., D.E. Bedo and J.E. Manson, The EUV spectrophotometer on Atmospheric Explorer, Radio Sci., 8, 349, (1973).

Hinteregger, H.E., D.E. Bedo, J.E. Manson and D.R. Skillman, EUV flux variations with solar rotation observed during 1974-1976 from the AE-C satellite, Space Res., 17, 533, (1977).

Horton, B.H., Private communication, (1979).

Hudson, R.D., Critical review of ultraviolet photoabsorption cross-sections for molecules of astrophysical and aeronomic interest, Rev. Geophys. Space Phys., 9, 305, (1971).

Hudson, R.D., Absorption cross-sections of stratospheric molecules, Can. J. Chem., 52, 1465, (1974).

Hudson, R.D. (ed.), Chlorofluoromethanes and the Stratosphere, NASA Reference Publication 1010, (1977).

Hudson, R.D. and E.I. Reed (eds.), The Stratosphere : Present and Future, NASA Reference Publication 1049, (1979).

Hudson, R.D., V.L. Carter and J.A. Stein, An investigation of the effect of temperature on the Schumann-Runge absorption continuum of oxygen, 1580 - 1950Å, J. Geophys. Res., 71, 2295, (1966).

Huffman, R.E., Absorption cross-sections of atmospheric gases for use in aeronomy, Can. J. Chem., 47, 1823, (1969).

Huffman, R.E. and J.C. Larrabee, Effect of absorption by atomic oxygen and atomic nitrogen lines on upper atmosphere composition measurements, J. Geophys. Res., 73, 7419, (1968).

Huffman, R.E., Y. Tanaka and J.C. Larrabee, Absorption coefficients of nitrogen in the 1000 - 580Å wavelength region, J. Chem. Phys., 39, 910, (1963).

Huffman, R.E., J.C. Larrabee and Y. Tanaka, Absorption coefficients of oxygen in the 1060 - 580Å wavelength region, J. Chem. Phys., 40, 356, (1964a).

Huffman, R.E., Y. Tanaka and J.C. Larrabee, Nitrogen and oxygen absorption cross-sections in the vacuum ultraviolet, Discussions Faraday Soc., 37, 159, (1964b).

Huffman, R.E., J.C. Larrabee and Y. Tanaka, Rare gas continuum light sources for photoelectric scanning in the vacuum ultraviolet, Appl. Opt., 4, 1581, (1965).

Huffman, R.E., J.C. Larrabee and Y. Tanaka, New absorption spectra of atomic and molecular oxygen in the vacuum ultraviolet. I. Rydberg series from OI ground state and new excited O_2 bands, J. Chem. Phys., 46, 2213, (1967a).

Huffman, R.E., J.C. Larrabee and Y. Tanaka, New absorption spectra of atomic and molecular oxygen in the vacuum ultraviolet. II. Rydberg series of OI ($^1D_2$) and OI ($^1S_0$) metastable states, J. Chem. Phys., 47, 4462, (1967b).

Huffman, R.E., F.J. Le Blanc, J.C. Larrabee and D.E. Paulsen, Satellite vacuum ultraviolet airglow and auroral observations, J. Geophys. Res., 85, 2201, (1980).

Hunt B.G., Photochemistry of ozone in a moist atmosphere, J. Geophys. Res., 71, 1385, (1966).

Hunt, D.C., Photon heating of the atmosphere at F-region heights, Planet. Space Sci., 18, 1745, (1970).

Hunt, B.G., A diffuse-photochemical study of the mesosphere and lower thermosphere and the associated conservation mechanisms, J. Atmos. Terrest. Phys., 33, 1869, (1971).

Hunt, B.G., Atmospheric vacillations in a general circulation model II. Tropospheric-stratospheric coupling and stratospheric variability, J. Atmos. Sci., 35, 2052, (1978).

Hunten, D.M. and M.B. McElroy, Quenching of metastable states of atomic and molecular oxygen and nitrogen, Rev. Geophys. Space Phys., 4, 303, (1966).

Hunter, W.R., A pulsed light source for the extreme ultraviolet, Proceedings of the 10th Colloquium of International Spectroscopy, 247, (1962).

Ilyas, M., Diurnal, seasonal and latitudinal variations of molecular oxygen and temperature in the mesosphere, Paper presented at the Aust. Instit. Phys. National Congress, Adelaide, Australia (1974).

Inn, E.C.Y. and Y. Tanaka, Absorption coefficient of ozone in the ultraviolet and visible regions, J. Opt. Soc. Amer., 43, 870, (1953).

Inn, E.C.Y. and Y. Tanaka, Ozone absorption coefficients in the visible and ultraviolet regions, in Ozone Chemistry and Technology, Advances in Technology, 21, 263, (1959).

Institute for Electronic Engineers, Conference Publication No. 65, (1970).

Jacchia, L.G., The Earth's upper atmosphere - I, Sky and Telescope, 49, 155: The Earth's upper atmosphere - II, Sky and Telescope, 49, 229: The Earth's upper atmosphere - III, Sky and Telescope, 49, 294, (1975).

Jacchia, L.G., Thermospheric temperature, density and composition : New models, Smithsonian Astrophysical Observatory, Special Report 375, (1977).

Jacchia, L.G., CIRA 72,recent atmospheric models and improvements in progress, Invited paper, 21st meeting of COSPAR, Innsbruck, Austria, (1978).

Jaeglé, P., P. Dhez and F. Wuilleumier, Versatile grazing incidence spectromonochromator for the XUV region, Rev. Sci. Instrum., 48, 978, (1977).

Jarmain, W.R. and R.W. Nicholls, A theoretical study of the O_2 $X^3\Sigma_g^-$ - $B^3\Sigma_u^-$ photodissociation continuum, Proc. Phys. Soc., 84, 417, (1964).

Johnson, F.S., H.H. Malitson, J.D. Purcell and R. Tousey, Emission lines in the extreme ultraviolet spectra of the sun, Astrophys. J., 127, 80, (1958).

Johnston, H.S., Analysis of the independent variables in the perturbation of stratospheric ozone by nitrogen fertilizers, J. Geophys. Res., 82, 1767, (1977a).

Johnston, H.S., Expected short term local effect of nuclear bombs on stratospheric ozone, J. Geophys. Res., 82, 3119, (1977b).

Johnston, H.S. and J. Podolske, Interpretations of stratospheric photochemistry, Rev. Geophys. Space Phys., 16, 491, (1978).

Jordan, C. and A. Ridgeley, M.N.R.A.S., 168, 553, (1974).

Julienne, P.S., D. Neumann and M. Krauss, Transition moments for the $B^3\Sigma_u^-$ - $X^3\Sigma_g^-$ and $^3\pi_u$ - $X^3\Sigma_g^-$ transitions in O_2, J. Chem. Phys., 64, 2990, (1976).

Jursa, A.S., M. Nakamura and Y. Tanaka, Molecular oxygen distribution in the upper atmosphere, J. Geophys. Res., 68, 6145, (1963).

Jursa, A.S., M. Nakamura and Y. Tanaka, Molecular oxygen distribution in the upper atmosphere, 2. J. Geophys. Res., 70, 2699, (1965).

Kasprzak, W.T., D. Krankowsky and A.O. Nier, A study of day-night variations in the neutral composition of the lower thermosphere, J. Geophys. Res., 73, 6765, (1968).

Kayser, D.C., Solar flux variation of the thermospheric molecular oxygen density, J. Geophys. Res., 85, 695, (1980).

Keating, G.M., E.J. Prior, R.B. Lee III, E.W. Hinson, K.H. Fricke and H. Trinks, The distribution of helium and molecular nitrogen in the lower thermosphere as measured by ESRO 4, Space Res., 16, 281, (1976).

Keneshea, T.J., S.P. Zimmerman and C.R. Philbrick, A dynamical model of the mesosphere and lower thermosphere, Planet. Space Sci., 27, 385, (1979).

King-Hele, D.G., The earth's neutral upper atmosphere, Rev. Geophys. Space Phys., 16, 733, (1978).

Kirby, K., E.R. Constantinides, S. Babeu, M. Oppenheimer and G.A. Victor, Photoionization and photoabsorption cross-sections of He, O, N_2, and O_2 for aeronomic calculations, Atomic Data and Nuclear Data Tables, 23, 63, (1979).

Kirby-Docken, K. and M. Oppenheimer, Indirect determination of molecular oxygen densities in the daytime thermosphere from Atmospheric Explorer C composition measurements, J. Geophys. Res., 82, 3503, (1977).

Kleindienst, T., J.B. Burkholder and E.J. Bair, The spectrum of ozone during formation by recombination, Chem. Phys. Lett., 70, 117, (1980).

Klenk, K.F., Absorption coefficients of ozone for the backscatter ultraviolet experiment, Appl. Opt., 19, 236, (1980).

Knight, D.E., R. Uribe and B.E. Woodgate, Extreme ultraviolet absorption cross-sections in the earth's upper atmosphere, Planet. Space Sci., 20, 161, (1972).

Kockarts, G., Penetration of solar radiation in the Schumann-Runge bands of molecular oxygen, in Mesospheric Models and Related Experiments, G. Fiocco (ed.), 160, (1971).

Kockarts, G., Absorption and photodissociation in the Schumann-Runge bands of molecular oxygen in the terrestrial atmosphere, Planet, Space Sci., 24, 589, (1976).

Kockarts, G., Nitric oxide cooling in the terrestrial thermosphere, Geophys. Res. Lett., 7, 137, (1980).

Kohl, J.L., G.P. Lafyatis, H.P. Palenius and W.H. Parkinson, Absolute cross-sections for photoionization of atomic oxygen, Phys. Rev. A, 18, 571, (1978).

Köhnlein, W., H. Trinks and H. Volland, The O to N_2 density ratio in the thermosphere derived from ESRO-4 data, Space Res., 15, 287, (1975).

Kolesnik, A.G. and V.I. Chernyshev, Rate of heating of the ionospheric plasma by solar radiation. I. Heating by photoelectrons, Geomagn. i aeronomiya, 18, 15, (1978).

Kozlenkov, A.I. and Y.I. Belov, Simple method for correcting astigmatism in grazing incidence spectrometers, Opt. Spectrosc., 42, 319, (1977).

Krankowsky, D., W.T. Kasprzak and A.O. Nier, Maws spectrometric studies of the composition of the lower thermosphere during summer 1967, J. Geophys. Res., 73, 7291, (1968).

Krankowsky, D., P. Lämmerzahl, F. Bonner and H. Wieder, The AEROS neutral and ion mass spectrometer, J. Geophys. Res., 40, 601, (1974).

Krueger, A.J., Rocket measurements of ozone over Hawaii, Ann. Geophys., 25, 307, (1969a).

Krueger, A., Atmospheric absorption anomalies in the ultraviolet near an altitude of 50 km, Science, 166, 998, (1969b).

Krueger, A.J., The mean ozone distribution from several series of rocket soundings to 52 km at latitudes from 58°S to 64°N, Pure Appl. Geophys., 106-108, 1272, (1973).

Krueger, A.J. and R.A. Minzner, A mid latitude ozone model for the 1976 U.S. Standard Atmosphere, J. Geophys. Res., 81, 4477, (1976).

Krueger, A.J., D.F. Heath and C.L. Mateer, Variations in the stratospheric ozone field inferred from Nimbus satellite observations, Pure Appl. Geophys., 106-108, 1254, (1973).

Krueger, A.J., B. Guenther, A.J. Fleig, D.F. Heath, E. Hilsenrath, R. McPeters and C. Prabhakara, Satellite ozone measurements, Phil. Trans. R. Soc. Lond. A, 296, 191, (1980).

Kuhn, H.G., Atomic Spectra, Longmans, Green and Co. Ltd., (1969).

Lake, L.R. and D. Krankowsky, Influence of surface recombination in satellite atomic oxygen measurements inferred from the AEROS-A mass spectrometer, Geophys. Res. Lett., 2, 545, (1975).

Lake, L.R. and A.O. Nier, Loss of atomic oxygen in mass spectrometer ion sources, J. Geophys. Res., 78, 1645, (1973).

Landon, D.O., Use of platinum or gold grating surfaces at grazing incidence, Appl. Opt., 2, 450, (1963).

Landon, D.O., A new grazing incidence spectrometric mounting, Appl. Opt., 3, 115, (1964).

Lee, L.C., R.W. Carlson, D.L. Judge and M. Ogawa, The absorption cross-sections of N_2, O_2, CO, NO, CO_2, N_2O, CH_4, C_2H_4, C_2H_6 and C_4H_{10} from 180 to 700Å, J. Quant. Spectros. Radiat. Transfer, 13, 1023, (1973).

Leovy, C.B., Atmospheric ozone : An analytic model for photochemistry in the presence of water vapour, J. Geophys. Res., 74, 417, (1969).

Lewis, B.R., J.H. Carver, T.I. Hobbs, D.G. McCoy and H.P.F. Gies, Experimentally determined oscillator strengths and linewidths for the Schumann-Runge band system of molecular oxygen - I. The (6-0) to (14-0) bands, J. Quant. Spectros. Radiat. Transfer, 20, 191, (1978).

Lewis, B.R., J.H. Carver, T.I. Hobbs, D.G. McCoy and H.P.F. Gies, Experimentally determined oscillator strengths and linewidths for the Schumann-Runge band system of molecular oxygen - II. The (2-0) to (5-0) bands, J. Quant. Spectros. Radiat. Transfer, 22, 213, (1979).

Lindsay, J.C., The solar extreme ultraviolet radiation (1-400Å), Planet. Space Sci., 12, 379, (1964).

Llewellyn, E.J. and B.H. Solheim, The excitation of the infrared atmospheric oxygen bands in the nightglow, Planet. Space Sci., 26, 533, (1978).

Llewellyn, E.J. and G. Witt, The measurement of ozone concentrations at high latitudes during the twilight, Planet. Space Sci., 25, 165, (1977).

Llewellyn, E.J., B.H. Solheim, J. Stegman and G. Witt, A measurement of the O_2 ultraviolet nightglow emission, Planet. Space Sci., 27, 1507, (1979).

Lockey, G.W.A., B.H. Horton and B. Rofe, Satellite measurements of upper atmospheric molecular oxygen densities, Nature, 223, 387, (1969).

London, J. and J.H. Park, The interaction of ozone photochemistry and dynamics in the stratosphere. A three dimensional atmospheric model, Can. J. Chem., 52, 1599, (1974).

London, J. and C.A. Reber, Solar activity and total atmospheric ozone, Geophys. Res. Lett., 6, 869, (1979).

London, J., J.E. Frederick and G.P. Anderson, Satellite observations of the global distribution of stratospheric ozone, J. Geophys. Res., 82, 2543, (1977).

Longmire, M.S., J.D.F. Bartoe, C.M. Brown, G.E. Brueckner and R. Tousey, Measurements of spectrally integrated atmospheric transmittance in the O_2 Schumann-Runge bands and the derived oxygen column densities : 72-102 km, J. Geophys. Res., 84, 1277, (1979).

Luther, F.M. and R.J. Gelinas, Effect of molecular multiple scattering and surface albedo on atmospheric photodissociation rates, J. Geophys. Res., 81, 1125, (1976).

Mack, J.E., J.R. Stehn and B. Edlen, On the concave grating spectrograph, especially at large angles of incidence, J. Opt. Soc. Amer., 22, 245, (1932).

Mack, J.E., F. Paresce and S. Bowyer, Channel electron multiplier : its quantum efficiency at soft X-ray and vacuum ultraviolet wavelengths, Appl. Opt., 15, 861, (1976).

Madden, R.P., D.L. Ederer and K. Codling, Instrumental aspects of synchrotron XUV spectroscopy, Appl. Opt., 6, 31, (1967).

Mahlman, J.D., H. Levy II and W.J. Moxim, Three-dimensional tracer structure and behaviour as simulated in two ozone precursor experiments, J. Atmos. Sci., 37, 655, (1980).

Malinovsky, M. and L. Heroux, An analysis of the solar extreme ultraviolet spectrum between 50 and 300Å, Astrophys. J., 181, 1009, (1973).

Maloy, J.O., R.W. Carlson, U.G. Hartmann and D.L. Judge, Measurement of the profile and intensity of the solar He I 584Å resonance line, J. Geophys. Res., 83, 5685, (1978).

Mani, A. and C.R. Sreedharan, Variations in the vertical distribution of ozone over India, Ann. Geophys., 25, 173, (1969).

Manson, J.E., The spectrum of the quiet sun between 30 and 128Å for November, 1965, Astrophys. J., 147, 703, (1967).

Manson, J.E., Measurement of the solar spectrum between 30 and 128Å, Solar Phys., 27, 107, (1972).

Manson, J.E., The solar extreme ultraviolet between 30 and 205Å on November 9, 1971, compared with previous measurements of this spectral region, J. Geophys. Res., 81, 1629, (1976).

Mateer, C.L., D.F. Heath and A.J. Krueger, Estimation of total ozone from satellite measurements of backscattered ultraviolet radiances, J. Atmos. Sci., 28, 1307, (1971).

Matsunaga, F.M. and K. Watanabe, Total and photoionization coefficients and dissociation of O_2 in the 580 - 1070Å region, Sci. Light, 16, 31, (1967).

May, B.R., Molecular oxygen density in the lower thermosphere from May to November 1967, Space Res., 13, 243, (1973).

Mayr, H.G. and I. Harris, F-region dynamics, Rev. Geophys. Space Phys., 17, 492, (1979).

Mayr, H.G., P. Bauer, H.C. Brinton, L.H. Brace and W.E. Potter, Diurnal and seasonal variations in atomic and molecular oxygen inferred from Atmospheric Explorer - C, Geophys. Res. Lett., 3, 77, (1976).

Mayr, H.G., I. Harris and N.W. Spencer, Some properties of upper atmosphere dynamics, Rev. Geophys. Space Phys., 16, 539, (1978).

McNeal, R.J., M.E. Whitson (Jr) and G.R. Cook, Temperature dependence of the quenching of vibrationally excited nitrogen by atomic oxygen, J. Geophys. Res., 79, 1527, (1974).

McPeters, R.D., The behaviour of ozone near the stratopause from two years of BUV observations, J. Geophys. Res., 85, 4545, (1980).

Mehlman, G., D.L. Ederer and E.B. Saloman, The photoabsorption cross-section of O_2 from 55 to 350Å, J. Chem. Phys., 68, 1862, (1978).

Messmer, R.P. and D.R. Salahub, Molecular orbital study of the ground and excited states of ozone, J. Chem. Phys., 65, 779, (1976).

Metzger, P.H. and G.R. Cook, A reinvestigation of the absorption cross-sections of molecular oxygen in the 1050 - 1800Å region, J. Quant. Spectrosc. Radiat. Transfer, 4, 107, (1964).

Mikhnevich, V.V., A.A. Pokhunkov, E.N. Golubev, Y.F. Ivanov and S.V. Gorbunov, Neutral atmosphere variations according to measurements made in tropical and mid latitudes, Space Res., 15, 227, (1975).

Mikirov, A.Y., Estimate of ozone concentration at heights of 44 - 102 km during night launchings of geophysical rockets, Geomagn. i. aeronomiya, 5, 882, (1965).

Miller, D.E. and P. Ryder, Measurement of the ozone concentration from 55 to 95 km at sunset, Planet. Space Sci., 21, 963, (1973).

Miller, D.E. and K.H. Stewart, Observations of atmospheric ozone from an artificial earth satellite, Proc. Roy. Soc. Lond., A288, 540, (1965).

Millier, F., A. Vidal-Madjar, J. Guidon and R.G. Roble, Ozone nummber density profiles in the lower mesosphere as determined by the French experiment on board OSO-8, Geophys. Res. Lett., 6, 863, (1979).

Minzner, R.A., The 1976 Standard Atmosphere and its relation to earlier standards, Rev. Geophys. Space Phys., 15, 375, (1977).

Misawa, K., I Takeuchi, Y. Kato and I. Aoyama, Emission mechanism of OI 557.7 nm radiation, J. Atmos. Terrest. Phys., 42, 299, (1980).

Modali, S.B., R.W.L. Thomas, R.D. Chapman and R.J. Thomas, OSO-7 measurements of atomic oxygen and molecular nitrogen densities in the earth's upper atmosphere, J. Geophys. Res., 81, 6203, (1976).

Molina, M.J. and F.S. Rowland, Stratospheric sink for chlorofluoromethanes - chlorine atom destruction of ozone, Nature, 249, 810, (1974).

Moreels, G., G. Megie, A. Vallence Jones and R.L. Gattinger, An oxygen-hydrogen atmosphere model and its application to the OH emission problem, J. Atmos. Terrest. Phys., 39, 551, (1977).

Mugnai, A., P. Petroncelli and G. Fiocco, Sensitivity of the photodissociation of NO_2, NO_3, HNO_3 and H_2O_2 to the solar radiation diffused by the ground and by atmospheric particles, J. Atmos. Terrest. Phys., 41, 351, (1979).

Murrell, J.N. and S. Farantos, An analytic function for the potential energy surface of ozone, Molec. Phys., 34, 1185, (1977).

Murrell, J.N., K.S. Sorbie and A.J.C. Varandas, Analytic potentials for triatomic molecules from spectroscopic data. II. Application to ozone, Molec. Phys., 32, 1359, (1976).

Nagata, T., T. Tohmatsu and T. Ogawa, Sounding rocket measurement of atmospheric ozone density, 1965-1970, Space Res., 11, 849, (1971).

Namioka, T., Theory of the concave grating. I, J. Opt. Soc. Amer., 49, 446, (1959).

Namioka, T., Grating theories and their applications to grating instruments for vacuum ultraviolet spectroscopy, J. Quant. Spectrosc. Radiat. Transfer, 2, 697, (1962).

Neupert, W.M. and W.E. Behring, Solar observations with a soft X-ray spectrometer, J. Quant. Spectrosc. Radiat. Transfer, 2, 527, (1962).

Neupert, W.M., W.E. Behring and J.C. Lindsay, The solar spectrum from 50 to 400Å, Space Res., 4, 719, (1964).

Newton, G.P., W.T. Kasprzak and D.T. Pelz, Equatorial composition in the 137 to 225 km region from the San Marco 3 mass spectrometer, J. Geophys. Res., 79, 1929, (1974).

Nicolet, M., Inst. Roy. Met. Belg. Mem., 19, 74, (1945).

Nicolet, M., in The Earth as a Planet, G.P. Kuiper (ed.), University of Chicago Press, Ch. 13, (1954).

Nicolet, M., Aeronomic reactions of hydrogen and ozone, in Mesospheric Models and Related Experiments, G. Fiocco (ed.), D. Reidal Publishing Co., Dordrecht - Holland, 1, (1971).

Nicolet, M., Stratospheric ozone : An introduction to its study, Rev. Geophys. Space Phys., 13, 593, (1975).

Nicolet, M., Solar UV radiation and its absorption in the mesosphere and stratosphere, Pure Appl. Geophys., 118, 3, (1980).

Nicolet, M. and P. Mange, The dissociation of oxygen in the high atmosphere, J. Geophys. Res., 59, 15, (1954).

Nicolet, M. and W. Peetermans, Atmospheric absorption in the O_2 Schumann-Runge band spectral range and photodissociation rates in the stratosphere and mesosphere, Planet. Space Sci., 28, 85, (1979).

Nier, A.O., Measurement of thermospheric composition, Space Res., 12, 881, (1972).

Nier, A.O., J.H. Hoffman, C.Y. Johnson and J.C. Holmes, Neutral composition of the atmosphere in the 100 to 200 km range, J. Geophys. Res., 69, 979, (1964).

Nier, A.O., J.L. Hayden, J.B. French and N.M. Reid, On the determination of thermospheric atomic oxygen densities with rocket borne mass spectrometers, J. Geophys. Res., 77, 1987, (1972).

Nier, A.O., W.E. Potter, D.R. Hickman and K. Mauersberger, The open-source neutral-mass spectrometer on Atmospheric Explorer - C, D and E, Radio Sci., 8, 271, (1973).

Nier, A.O., W.E. Potter, D.C. Kayser and R.G. Finstad, The measurement of chemically reactive atmospheric constituents by mass spectrometers carried on high-speed spacecraft, Geophys. Res. Lett., 1, 197, (1974).

Nier, A.O., W.E. Potter and D.C. Kayser, Atomic and molecular oxygen densities in the lower thermosphere, J. Geophys. Res., 81, 17, (1976).

Nishi, K., Observations of the absolute intensity and the centre-to- limb variation of the sun in the vacuum ultraviolet, Solar Phys., 33, 23, (1973).

Norton, R.B. and R.G. Roble, Molecular oxygen between 95 and 210 km determined from Solrad 10 occultation measurements, J. Geophys. Res., 79, 3876, (1974).

Noxon, J.F., Metastable oxygen : Origin of atmospheric absorption near 50 km, Science, 168, 1120, (1970).

Ny, T.Z. and S.P. Choong, Chinese J. Phys., 1, 38, (1933).

Offermann, D., Composition variations in the lower thermosphere, J. Geophys. Res., 79, 4281, (1974).

Offermann, D. and K.U. Grossman, Neutral composition measurements in the lower thermosphere by means of a mass spectrometer with helium cooled ion source, Space Res., 12, 665, (1972).

Offermann, D. and K.Y. Grossman, Thermospheric density and composition as determined by a mass spectrometer with cryo ion source, J. Geophys. Res., 78, 8296, (1973).

Offermann, D. and H. Tatarczyk, A cryo-cooled mass spectrometer ion source for atmospheric composition measurements at supersonic rocket velocities, Rev. Sci. Instrum., 44, 1569, (1973).

Ogawa, M., Absorption coefficients of O_2 at the Lyman-alpha line and its vicinity, J. Geophys, Res., 73, 6759, (1968).

Ogawa, M. and G.R. Cook, Absorption coefficients of O_3 in the vacuum ultraviolet region, J. Chem. Phys., 28, 173, (1958).

Ogawa, T. and Y. Kondo, Diurnal variability of thermospheric N and NO, Planet. Space Sci., 25, 735, (1977).

Ogawa, T. and T. Shimazaki, Diurnal variations of odd nitrogen and ionic densities in the mesosphere and lower thermosphere : Simultaneous solution of photochemical diffusive equations, J. Geophys. Res., 80, 3945, (1975).

Ogawa, M. and Y. Tanaka, Rydberg absorption series of N_2, Can. J. Phys., 40, 1593, (1962).

Ogawa, T. and T. Watanabe, Summary of the mesospheric ozone measurements during 1970-1979 in Japan, Quadrennial International Ozone Symposium, Boulder, Colorado, 4-9 August, Program and Abstracts, 107, (1980).

Opal, C.B. and H.W. Moos, Nighttime molecular oxygen densities in the 100 to 130 km region from Schumann-Runge absorption, J. Geophys. Res., 74, 2398, (1969).

Opal, C.B., H.W. Moos and W.G. Fastie, Far ultraviolet altitude profiles and molecular oxygen densities in an aurora, J. Geophys. Res., 75, 788, (1970).

Oppenheimer, M., A. Dalgarno and H.C. Brinton, Molecular oxygen abundances in the thermosphere from Atmospheric Explorer - C ion composition measurements, J. Geophys. Res., 81, 4678, (1976).

Oppenheimer, M., S. Babeu, J.H. Hoffman and E. Breig, The EUV flux inferred from AE-C He^+ abundances, Geophys. Res. Lett., 5, 773, (1978).

Oran, E.S. and D.F. Strobel, Photochemically induced departures of O and O_2 from diffusive equilibrium distributions, J. Geophys. Res., 81, 257, (1976).

Oran, E. and D.F. Strobel, Photochemical deviations of thermospheric O and O_2 densities from diffusive equilibrium, J. Geophys. Res., 82, 696, (1977).

Oran, E.S., P.S. Julienne and D.F. Strobel, The aeronomy of odd nitrogen in the thermosphere, J. Geophys. Res., 80, 3068, (1975).

Pack, R.T., Simple theory of diffusive vibrational structure in continuous UV spectra of polyatomic molecules. I. Collinear photodissociation of symmetric triatomics, J. Chem. Phys., 65, 4765, (1976).

Paetzold, H., Variation of the vertical ozone profile over middle Europe from 1951 to 1968, Ann. Geophys., 25, 347, (1969).

Panofsky, H.A., Threats to the ozone layer, Pure Appl. Geophys., 118, 636, (1980).

Paresce, F., S. Kumar and C.S. Bowyer, Continuous discharge line source for the extreme ultraviolet, Appl. Opt., 10, 1904, (1971).

Park, J.H. and J. London, Ozone photochemistry and radiative heating of the middle atmosphere, J. Atmos. Sci., 31, 1898, (1974).

Parker, A.E. and K.H. Stewart, Measurements of molecular oxygen in the thermosphere, J. Atmos. Terrest. Phys., 34, 1223, (1972).

Parkes, D.A., L.F. Kayser and F. Kaufman, Oscillator strength of the resonance triplet of atomic oxygen, Astrophys. J., 149, 217, (1967).

Parkinson, W.H. and E.M. Reeves, Measurements in the solar spectrum between 1400 and 1875Å with a rocket borne spectrometer, Solar Phys., 10, 342, (1969).

Peatman, W.B., B. Gotchev, P. Gurtler, E.E. Koch and V. Saile, Transition probabilities at threshold for the photoionization of molecular nitrogen, J. Chem. Phys., 69, 2089, (1978).

Pelz, D.T., G.P. Newton, W.T. Kasprzak and T.D. Clem, The San Marco - 3 neutral atmospheric composition experiment, NASA Doc. GSFC X-623-73-142, (1973).

Penfield, H., M.M. Litvak, C.A. Gottlieb and A.E. Lilley, Mesospheric ozone measured from ground-based millimetre wave observations, J. Geophys. Res., 81, 6115, (1976).

Penner, J.E. and J.S. Chang, Possible variations in atmospheric ozone related to the eleven-year solar cycle, Geophys. Res. Lett., 5, 817, (1978).

Petitdidier, M. and H. Teitelbaum, $O(^1S)$ excitation mechanism and atmospheric tides, Planet. Space Sci., 27, 1409, (1979).

Philbrick, C.R., Satellite measurements of neutral atmospheric composition in the altitude range 150 to 450 km, Space Res., 14, 151, (1974).

Philbrick, C.R., Recent satellite measurements of upper atmospheric composition, Space Res., 16, 289, (1976).

Pokhunkov, A.A., On atomic oxygen in the lower thermosphere, Space Res., 11, 839, (1971).

Pokhunkov, A.A., Mass spectrometric investigations of upper atmosphere neutral composition at equatorial, middle and polar latitudes, Space Res., 12, 657, (1972).

Pokhunkov, A.A. and S.V. Gorbunov, Upper atmosphere neutral composition measurements during the solar eclipse of 30 June, 1973, Space Res., 16, 351, (1976).

Pollack, J.B., W.J. Borucki and O.B. Toon, Are solar spectral variations a drive for climate change ?, Nature, 282, 600, (1979).

Potter, W.E., D.C. Kayser, H.C. Brinton, L.H. Brace and M. Oppenheimer, Comparison of measured and calculated thermospheric molecular oxygen densities, J. Geophys. Res., 82, 5243, (1977).

Prabhakara, C., E.B. Rodgers, B.J. Conrath, R.A. Hanel and V.G. Kande, The Nimbus 4 infrared spectroscopy experiment 3. Observations of the lower stratospheric thermal structure and total ozone, J. Geophys. Res., 81, 36, (1976).

Pradhan, A.K., Photoionization cross-section of atomic oxygen, J. Phys. B: Atom. Molec. Phys., 11, L729, (1978).

Pradhan, A.K. and H.E. Saraph, Oscillator strengths for dipole transitions in neutral oxygen, J. Phys. B: Atom. Molec. Phys., 10, 3365, (1977).

Prasad, S.S. and P.G. Burton, Possible existence and role of excited ozone precursors in the stratosphere, Planet. Space Sci., 27, 411, (1979).

Prasad, S.S. and D.R. Furman, Is there a real need for doubling the solar EUV fluxes ? J. Geophys. Res., 79, 2463, (1974).

Prather, M.J., M.B. McElroy, S.C. Wofsy and J.A. Logan, Stratospheric chemistry : Multiple solutions, Geophys. Res. Lett., 6, 163, (1979).

Prinz, D.K. and G.E. Brueckner, Observations of the O_2 column density between 120 and 70 km and the absorption cross-section in the vicinity of H Lyman-alpha, J. Geophys. Res., 82, 1481, (1977).

Prior, E. and B.J. Oza, First comparison of simultaneous IRIS, BUV and ground-based measurements of total ozone, Geophys. Res. Lett., 5, 547, (1978).

Purcell, J.D. and R. Tousey, The profile of solar hydrogen Lyman-alpha, J. Geophys. Res., 65, 370, (1960).

Purcell, J.D., D.M. Packer and R. Tousey, The ultraviolet spectrum of the sun, Space Res., 1, 581, (1960).

Purcell, J.D., D.L. Garrett and R. Tousey, Solar spectra from 3500 to 2200Å at 30 mÅ resolution, Space Res., 3, 781, (1963).

Pyle, J.A., A calculation of the possible depletion of ozone by chlorofluorocarbons using a two-dimensional model, Pure Appl. Geophys., 118, 355, (1980).

Pyle, J.A. and R.G. Derwent, Possible ozone reductions and UV changes at the earth's surface, Nature, 286, 373, (1980).

Quessette, J.A., On the measurement of molecular oxygen concentration by absorption spectroscopy, J. Geophys. Res., 75, 839, (1970).

Quiroz, R.S., Stratospheric temperature during solar cycle 20, J. Geophys. Res., 84, 2415, (1979).

Randhawa, J.S., The vertical distribution of ozone near the equator, J. Geophys. Res., 76, 8139, (1971).

Rawcliffe, R.D., G.E. Meloy, R.M. Friedman and E.H. Rogers, Measurement of the vertical distribution of ozone from a polar orbiting satellite, J. Geophys. Res., 68, 6425, (1963).

Rawer, B., K. Rawer, G. Schmidtke, R. Matzke and C. Munther, Aeros A atomic oxygen profiles compared with the OGO 6 model, Space Res., 16, 251, (1976).

Reed, E.I., A night measurement of mesospheric ozone by observations of ultraviolet airglow, J. Geophys. Rev., 73, 2951, (1968).

Reid, R.H.G., Number densities of atomic oxygen and molecular nitrogen in the thermosphere, Planet. Space Sci., 19, 801, (1971).

Rense, W.A. and T. Violett, Method of increasing the speed of a grazing incidence spectrograph, J. Opt. Soc. Amer., 49, 139, (1959).

Richmond, A.D., Thermospheric heating in a magnetic storm : Dynamic transport of energy from high to low latitudes, J. Geophys. Res., 84, 5259, (1979).

Riegler, G.R., J.F. Drake, S.C. Liu and R.J. Cicerone, Stellar occultation measurements of atmospheric ozone and chlorine from OAO-3, J. Geophys. Res., 81, 4997, (1976).

Riegler, G.R., S.K. Atreya, T.M. Donahue, S.C. Liu, B. Wasser and J.F. Drake, UV stellar occultation measurements of nighttime equatorial ozone, Geophys. Res. Lett., 4, 145, (1977).

Roble, R.G., Solar EUV flux variation during a solar cycle as derived from ionospheric modelling considerations, J. Geophys. Res., 81, 265, (1976).

Roble, R.G. and R.E. Dickinson, Is there enough solar extreme ultraviolet radiation to maintain the global mean thermospheric temperature ?, J. Geophys. Res., 78, 249, (1973).

Roble, R.G. and P.B. Hays, A technique for recovering the vertical number density profile of atmospheric gases from planetary occultation data, Planet. Space Sci., 20, 1727, (1972).

Roble, R.G. and P.B. Hays, The nighttime distribution of ozone in the low latitude mesosphere, Pure Appl. Geophys., 106-108, 1281, (1973).

Roble, R.G. and P.B. Hays, On determining the ozone number density distribution from OAO-2 satellite occultation, Planet. Space Sci., 22, 1337, (1974).

Roble, R.G. and G. Schmidtke, Calculated ionospheric variations due to changes in the solar EUV flux measured by the AEROS spacecraft, J. Atmos. Terrest. Phys., 41, 153, (1979).

Roble, R.G., R.E. Dickinson and E.C. Ridley, Seasonal and solar cycle variations of the zonal mean circulation in the thermosphere, J. Geophys. Res., 82, 5493, (1977).

Rosenberg, G.V., A.I. Semenov and N.N. Shefov, On the influence of the aerosols for satellite measurements of ozone at the thermospheric base, Planet. Space Sci., 22, 1035, (1974a).

Rosenberg, G.V., A.I. Semenov and N.N. Shefov, Commont on the Note by R.G. Noble and P.B. Hays on : Determining the ozone number density distribution from OAO-2 stellar occultation measurements, Planet. Space Sci., 22, 1455, (1974b).

Rottman, G.L., Disc values of the solar UV flux, 1150 - 1850Å, Trans. An. Geophys. Un., 56, 1175, (1974).

Rottman, G.J., Private communication with R.C. Schaeffer, (1976).

Rusch, D.W., A.I. Stewart, P.B. Hays and J.H. Hoffman, The NI(5200Å) dayglow, J. Geophys. Res., 80, 2300, (1975a).

Rusch, D.W., W.E. Sharp, and P.B. Hays, Twilight airglow 3. OI 6300Å radiation, J. Geophys. Res., 80, 1832, (1975b).

Saloman, E.B., Unfolding first and second order diffracted radiation when using synchrotron radiation sources : A technique, Appl. Opt., 14, 1391, (1975).

Samain, D., Solar continuum data on absolute intensities, centre to limb variations and Laplace inversion between 1400 and 2100Å, Aston. Astrophys., 74, 225, (1979).

Samain, D. and P.C. Simon, Solar flux determination in the spectral range 150-210 nm, Solar Phys., 49, 33, (1976).

Samson, J.A.R., Techniques of Vacuum Ultraviolet Spectroscopy, John Wiley and Sons, Inc., (1967).

Samson, J.A.R. and R.B. Cairns, Absorption and photoionization cross-sections of O_2 and N_2 at intense solar emission lines, J. Geophys. Res., 69, 4583, (1964).

Samson, J.A.R. and R.B. Cairns, Total absorption cross-sections of H_2, N_2 and O_2 in the region 550 - 200Å, J. Opt. Soc. Amer., 55, 1035, (1965).

Schaefer, E.J. and M.H. Nichols, Upper air neutral composition measurements by a mass spectrometer, J. Geophys. Res., 69, 4649, (1964).

Schmidtke, G., Phase lag of atomic oxygen density increase in the thermosphere, J. Geophys. Res., 80, 1367, (1975).

Schmidtke, G., Solar XUV measurements with in-flight calibration needed for aeronomy, Space Res., 16, 229, (1976a).

Schmidtke, G., EUV indices for solar-terrestrial relations, Geophys. Res. Lett., 3, 573, (1976b).

Schmidtke, G., Variability of solar ultraviolet flux and its significance to models of the neutral upper atmosphere, Space Res., 19, 193, (1979).

Schmidtke, G., W. Schweizer and M. Knothe, The Aeros EUV Spectrometer, Z. Geophys., 40, 577, (1974a).

Schmidtke, G., K. Rawer, T. Fischer and W. Lotze, Atomic oxygen density profiles determined by EUV absorption analysis, Space Res., 14, 169, (1974b).

Schmidtke, G., C. Munther and K. Rawer, Variations of atomic oxygen densities in the thermosphere, Space Res., 15, 221, (1975).

Schmidtke, G., K. Rawer, H. Botzek, D. Norbet and K. Holzer, Solar EUV photon fluxes measured aboard Aeros A, J. Geophys. Res., 82, 2423, (1977).

Schoeberl, M.R. and D.F. Strobel, The zonally averaged circulation of the middle atmosphere, J. Atmos. Sci., 35, 577, (1978a).

Schoeberl, M.R. and D.F. Strobel, The response of the zonally averaged circulation to stratospheric ozone reductions, J. Atmos. Sci., 35, 1751, (1978b).

Sharp, W.E., Absolute concentrations of $O(^3P)$ in the lower thermosphere at night, Geophys. Res. Lett., 7, 485, (1980).

Shemansky, D.E., Transition probabilities and collision broadening cross-sections of the N_2 Lyman-Birge-Hopfield system, J. Chem. Phys., 51, 5487, (1969).

Shimabukuro, F.I., P.L. Smith and W.J. Wilson, Estimation of the ozone distribution from millimetre wavelength absorption measurements, J. Geophys. Res., 80, 2957, (1975).

Shimazaki, T. and A.R. Laird, A model calculation of the diurnal variation in minor neutral constituents in the mesosphere and lower thermosphere including transport effects, J. Geophys. Res., 75, 3221, (1970).

Shimazaki, T. and A.R. Laird, Seasonal effects on distributions of minor neutral constituents in the mesosphere and lower thermosphere, Radio Sci., 7, 23, (1972).

Shimazaki, T. and T. Ogawa, A theoretical model of minor constituent distributions in the stratosphere including diurnal variation, J. Geophys. Res., 79, 3411, (1974).

Simon, P.C., Balloon measurements of solar fluxes between 1960 and 2300Å, Proceedings of the Third Conference on the climatic impact assessment program, DOT - TSC - OST - 74 - 15, Broderick and Hard (eds.), 137, (1974).

Simon, P.C., Irradiation solar flux measurements between 120 and 400 nm. Current position and future needs, Planet. Space Sci., 26, 355, (1978).

Simons, J.W., R.J. Paur, H.A. Webster III and E.J. Bair, Ozone ultraviolet photolysis. VI. The ultraviolet spectrum, J. Chem. Phys., 59, 1203, (1973).

Sjolander, G.W., Atomic oxygen-metal surface studies as applied to mass spectrometer measurements of upper planetary atmosphere, J. Geophys. Res., 81, 3767, (1976).

Smith, L.G. and K.L. Miller, The measurement of O_2 number density by absorption of Lyman-alpha, J. Geophys. Res., 79, 1965, (1974).

Smith III, F.L. and C. Smith, Numerical evaluation of Chapman's grazing incidence integral Ch (X,χ), J. Geophys, Res., 77, 3592, (1972).

Sorbie, K.S. and J.N. Murrell, Analytical potentials for triatomic molecules from spectroscopic data, Molec. Phys., 29, 1387, (1975).

Starace, A.F., S.T. Manson and D.J. Kennedy, Photoelectron angular distributions, cross-sections and branching ratios for atomic oxygen, Phys. Rev. A, 9, 2453, (1974).

Stolarski, R.S., Energetics of the mid latitude thermosphere, Planet. Space Sci., 38, 863, (1976).

Stolarski, R.S. and R.J. Cicerone, Stratospheric chlorine : A possible sink for ozone, Can. J. Chem., 52, 1610, (1974).

Stolarski, R.S. and N.P. Johnson, Photoionization and photoabsorption cross-sections for ionospheric calculations, J. Atmos. Terrest. Phys., 34, 1691, (1972).

Stolarski, R.S., P.B. Hays and R.G. Roble, Atmospheric heating by solar EUV radiation, J. Geophys. Res., 80, 2266, (1975).

Strobel, D.F., Minor neutral constituents in the mesosphere and lower thermosphere, Radio Sci., 7, 1, (1972).

Strobel, D.F., Parameterization of the atmospheric heating rate from 15 to 120 km due to O_2 and O_3 absorption of solar radiation, J. Geophys. Res., 83, 6225, (1978).

Strobel, D.F., E.S. Oran and P.D. Feldman, The aeronomy of odd nitrogen in the thermosphere, 2. Twilight emissions, J. Geophys. Res., 81, 3745, (1976).

Subbaraya, B.H., S. Prakash and P.N. Pareek, Molecular oxygen concentrations in the equatorial mesosphere, J. Atmos. Terrest. Phys., 34, 1141, (1972).

Subbaraya, B.H., S. Prakash, V. Kumar and P.N. Pareek, Molecular oxygen concentrations at the equator derived from solar ultraviolet absorption measurements, Space Res., 14, 173, (1974).

Sundararaman, N., T. Perry (Jr), W. Gurkin, E. Jackson, J. Lean, E.Llewellyn, B. Solheim, S. Lal, B.H. Subbaraya, T. Ogawa, T. Watanabe, E. Hilsenrath and A. Krueger, International ozone rocksonde intercomparison, Quadrennial International Ozone Symposium, Program and Abstracts, J. London (ed.), 68, Boulder, Colorado, 4-9 August, (1980).

Swartz, W.E. and J.S. Nisbet, Incompatibility of solar EUV fluxes and incoherent scatter measurements at Arecibo, J. Geophys. Res., 78, 5640, (1973).

Swider, W. (Jr), The determination of the optical depth at large zenith distances, Planet. Space Sci., 12, 761, (1964).

Tanaka, Y., E.C.Y. Inn and K. Watanabe, Absorption coefficients in the vacuum ultraviolet. Part IV. Ozone, J. Chem. Phys., 21, 1651, (1953).

Tanaka, Y., M. Ogawa and A.S. Jursa, Forbidden absorption band systems of N_2 in the vacuum ultraviolet region, J. Chem. Phys., 40, 3690, (1964).

Taylor, K.T. and P.G. Burke, Photoionization of ground-state carbon and oxygen atoms, J. Phys. B : Atom. Molec. Phys., 9, L353, (1976).

Thekaekara, M.P., A. Krueger and C.H. Duncan, Solar irradiance measurements from a research aircraft, Appl. Opt., 8, 1713, (1969).

Thomas, L., in Mesospheric Models and Related Experiments, D. Reidel Publishing Co., Holland, G. Fiocco (ed.), 65, (1971).

Thomas, L. and M.R. Bowman, The diurnal variations of hydrogen and oxygen constituents in the mesosphere and lower thermosphere, J. Atmos. Terrest. Phys., 34, 1843, (1972).

Thomas, L., R.G.H. Greer and P.H.G. Dickinson, The excitation of the 557.7 nm line and Herzberg bands in the nightglow, Planet. Space Sci., 27, 925, (1979).

Thomas, G.E., C.A. Barth, E.R. Hansen, C.W. Hord, G.M. Lawrence, G.H. Mount, G.J.Rottman, D.W. Rusch, A.I. Stewart, R.J. Thomas, J. London, P.L. Bailey, P.J. Crutzen, R.E. Dickenson, J.C. Gille, S.C. Liu, J.F. Noxon and C.B. Farmer, Scientific objectives of the solar mesosphere explorer mission, Pure Appl. Geophys., 118, 591, (1980).

Thrush, B.A., Aspects of the chemistry of ozone depletion, Phil. Trans. R. Soc. Lond. A, 290, 505, (1979).

Thuillier, G., J.L. Falin and C. Wachtel, Experimental temperature based on measurements from the Fabry-Perot interferometer on board the OGO-6 satellite - discussion of the data and properties of the model, J. Atmos. Terrest. Phys., 39, 399, (1977).

Timothy, J.G., Use of open-structure channel electron multipliers in sounding rocket experiments, Rev. Sci. Instrum., 44, 207, (1973).

Timothy, J.G., The solar spectrum between 300 and 1200Å, in The Solar Output and its Variation, O.R. White (ed.), Colorado Associated University Press, Boulder, 237, (1977).

Timothy, J.G. and L.B. Lapson, Use of channel electron multipliers as secondary standard detectors at EUV wavelengths, Appl. Opt., 13, 1417, (1974).

Timothy, A.F., J.G. Timothy, A.P. Willmore and J.H. Wager, The ion chemistry and thermal balance of the E and lower F-regions of the daytime ionosphere : An experimental study, J. Atmos. Terrest. Phys., 34, 969, (1972).

Tohmatsu, T., T. Ogawa and T. Watanabe, Absorption by the upper atmosphere in the middle ultraviolet region, Space Res., 14, 177, (1974).

Tondello, G., The use of a toroidal mirror as a focusing element for a stigmatic grazing incidence spectrometer, Optica Acta, 26, 357, (1979).

Torr, M.R. and D.G. Torr, Dissociative recombination of N_2^+ in the thermosphere, Geophys. Res. Lett., 6, 775, (1979).

Torr, M.R., D.G. Torr and P.G. Richards, The solar ultraviolet heating efficiency of the mid latitude thermosphere, Geophys. Res. Lett., 7, 373, (1980a).

Torr, D.G., P.G. Richards and M.R. Torr, Destruction of $N(^2D)$ by O_2 : A major source of 6300Å dayglow emission, Geophys. Res. Lett., 7, 410, (1980b).

Torr, M.R., D.G. Torr and R.A. Ong, Comparison of the N_2^+ photochemistry at different phases of the solar cycle, J. Geophys, Res., 85, 2171, (1980c).

Tousey, R., The extreme ultraviolet spectrum of the sun, Space Sci. Rev., 2, 3, (1963).

Tousey, R., Observations of the extreme ultraviolet solar spectrum. II. Chromosphere and corona, Phil. Trans. Roy. Soc. Lond. A, 270, 59, (1971).

Tousey, R., W.E. Austin, J.D. Purcell and K.G. Widing, Some emission lines in the region 168 to 1000Å, Space Res., 3, 772, (1963).

Tousey, R., J.D. Purcell, W.E. Austin, D.L. Garrett and K.G. Widing, New photographic spectra of the sun in the extreme ultraviolet, Space Res., 4, 703, (1964).

Trinks, H. and U. von Zahn, The Esro 4 gas analyzer, Rev. Sci. Instrum., 46, 213, (1975).

Trinks, H., D. Offermann, U. von Zahn and C. Steinhauer, Neutral composition measurements between 90 and 220 km altitude by rocket borne mass spectrometer, J. Geophys. Res., 83, 2169, (1978).

Tuck, A.F., A comparison of one-, two- and three-dimensional model representation of stratospheric gases, Phil. Trans. R. Soc. Lond. A, 290, 477, (1979).

Vidal-Madjar, A., Evolution of the solar Lyman-alpha flux during four consecutive years, Solar Phys., 40, 69, (1975).

Vidal-Madjar, A., The solar spectrum at Lyman-alpha 1216Å, in The Solar Output and its Variation, O.R. White (ed.), Colorado Associated University Press, Boulder, 213, (1977).

Vidal-Madjar, A., J.E. Blamont and B. Phissamay, Solar Lyman-alpha changes and related hydrogen density distribution at the earth's exobase (1969-1970), J. Geophys. Res., 78, 1115, (1973).

Vigroux, E., Ann. Phys., 8, 709, (1953).

Vigroux, E., Coefficients d'absorption de l'ozone dans la bande de Hartley, Ann. Geophys., 25, 169, (1969).

Visconti, G., G. Pitari and D. Cunnold, A two-dimensional photochemical model of the stratosphere with Rayleigh scattering, Pure Appl. Geophys., 118, 1033, (1980).

Vlasov, M.N., The photochemistry of excited species, J. Atmos. Terrest, Phys., 38, 807, (1976).

Volland, H. and H.G. Mayr, Theoretical aspects of tidal and planetary wave propagation at thermospheric heights, J. Geophys. Res., 15, 203, (1977).

von Zahn, U., Neutral air density and composition at 150 km, J. Geophys. Res., 75, 5517, (1970).

von Zahn, U. and J. Gross, Mass spectrometric investigation of the thermosphere at high latitudes, J. Geophys. Res., 74, 4055, (1969).

von Zahn, U., W. Kohnlein, K.H. Fricke, U. Laux, H. Trinks and H. Volland, ESRO 4 model of global thermospheric composition and temperatures during times of low solar activity, Geophys. Res. Lett., 4, 33, (1977).

Wainfan, N., W.C. Walker and G.L. Weissler, Photoionization efficiencies and cross-sections in O_2, N_2, CO_2, A, H_2O, H_2 and CH_4, Phys. Rev., 99, 542, (1955).

Wallops Flight Centre, Vehicles and sensors, March, (1979a).

Wallops Flight Centre, Project Planning Document - International Ozone Rocketsonde, Intercomparison, October, (1979b).

Wasser, B. and T.M. Donahue, Atomic oxygen between 80 and 120 km : Evidence for a latitudinal variation in vertical transport near the mesopause, J. Geophys. Res., 84, 1297, (1979).

Watanabe, K. and F.F. Marmo, Photoionization and total absorption cross-sections of gases. II. O_2 and N_2 in the region 850 - 1500Å, J. Chem. Phys., 25, 965, (1956).

Watanabe, T. and T. Tohmatsu, An observational evidence for the seasonal variation of ozone concentration in the upper stratosphere and the mesosphere, Rep. Ionos. Space Res. Jap., 30, 47, (1976).

Watanabe, K., E.C.Y. Inn and M. Zelikoff, Absorption coefficients of gases in the vacuum ultraviolet, J. Chem. Phys., 20, 1969, (1952).

Watanabe, K., E.C.Y. Inn and M. Zelikoff, Absorption coefficients of oxygen in the vacuum ultraviolet, J. Chem. Phys., 21, 1026, (1953).

Weeks, L.H., Determination of O_2 density from Lyman-alpha ion chambers, J. Geophys. Res., 80, 3655, (1975a).

Weeks, L.H., Observation of O_2 variability at mid latitudes from 1450Å measurements, J. Geophys. Res., 80, 3661, (1975b).

Weeks, L.H. and L.G. Smith, Molecular oxygen concentrations in the upper atmosphere by absorption spectroscopy, J. Geophys. Res., 73, 4835, (1968a).

Weeks, L.H. and L.G. Smith, A rocket measurement of ozone near sunrise, Planet. Space Sci., 16, 1189, (1968b).

Weeks, L.H., R.S. Cuikay and J.R. Corbin, Ozone measurements in the mesosphere during the solar proton event of 2 November, 1969, J. Atmos. Sci., 29, 1138, (1972).

Weeks, L.H., R.E. Good, J.S. Randhawa and H. Trinks, Ozone measurements in the stratosphere, mesosphere and lower thermosphere during Aladdin 74, J. Geophys. Res., 83, 978, (1978).

Weissler, G.L. and Po Lee, Absorption coefficients of oxygen in the vacuum ultraviolet, J. Opt. Soc. Amer., 42, 200, (1952).

White, O.R. (ed.), The Solar Output and its Variation, Colorado Associated University Press, Boulder, (1977).

Whitten, R.C. and R.P. Turco, Diurnal variations of HO_x and NO_x in the stratosphere, J. Geophys. Res., 79, 1302, (1974).

Widing, K.G., J.D. Purcell and G.D. Sandlin, The UV continuum 1450 - 2100Å and the problem of the solar temperature minimum, Solar Phys., 12, 52, (1970).

Wildman, P.J.L., M.J. Kerley and M.S. Shaw, Molecular oxygen measurements from 100 to 150 km at Woomera, Australia, J. Atmos. Terrest. Phys., 31, 951, (1969).

Wilkinson, P.G. and R.S. Mulliken, Forbidden band systems in nitrogen. II. The $a'\ ^1\Sigma_u^- - X\ ^1\Sigma_g^+$ system in absorption, J. Chem. Phys., 31, 674, (1959).

Williams, E.R., A series of daytime Lyman-alpha extinction measurements at mid latitudes, J. Atmos. Terrest. Phys., 42, 307, (1980).

Witt, G., J. Stegman, B.H. Solheim and E.J. Llewellyn, A measurement of the O_2 ($b'\ ^1\Sigma_g^+ - X^3\Sigma_g^-$) atmospheric band and the OI(^{1}S) green line in the nightglow, Planet. Space Sci., 27, 341, (1979).

Wofsy, S.C., Temporal and latitudinal variation of stratospheric trace gases : A critical comparison between theory and experiment, J. Geophys. Res., 83, 364, (1978).

Wofsy, S.C. and M.B. McElroy, HO_x, NO_x and ClO_x : Their role in atmospheric photochemistry, Can. J. Chem., 52, 1582, (1974).

Wraight, P.C., Electronically excited ozone in the atmosphere, Planet. Space Sci., 25, 1177, (1977).

Wuebbles, D.J. and J.S. Chang, Sensitivity of time varying parameters in stratospheric modeling, J. Geophys. Res., 80, 2637, (1975).

Zipf, E.C., The collisional deactivation of metastable atoms and molecules in the upper atmosphere, Can. J. Chem., 47, 1863, (1969).

Zirin, H., L.A. Hall and H.E. Hinteregger, Analysis of the solar emission spectrum from 1300 to 250Å as observed in August 1961, Space Res., 3, 760, (1963).